

STUDY ON THE SYNTHESIS AND PROPERTIES OF SMART CEMENT
C3AH6/RGO NANO-COMPOSITE AND DEVELOPMENT OF
THERMOELECTRIC GENERATOR USING CaMnO_3



A THESIS SUBMITTED IN PARTIAL FULFILLMENT OF THE REQUIREMENT FOR THE
DEGREE OF DOCTOR OF PHILOSOPHY IN APPLIED PHYSICS

DEPARTMENT OF PHYSICS

FACULTY OF SCIENCE

KING MONGKUT'S INSTITUTE OF TECHNOLOGY LADKRABANG

2020

KMITL-2020-SC-D-030-021

การศึกษาการสังเคราะห์และสมบัติของสมาร์ตซีเมนต์ไตรแคลเซียมอลูมิเนต
เฮกซะไฮเดรต/รีดิวซ์กราฟีนออกไซด์นาโนคอมโพสิตและการพัฒนาเครื่อง
กำเนิดไฟฟ้าเทอร์โมอิเล็กทริกโดยใช้แคลเซียมแมงกานีสออกไซด์

STUDY ON THE SYNTHESIS AND PROPERTIES OF SMART CEMENT
C3AH6/RGO NANO-COMPOSITE AND DEVELOPMENT OF
THERMOELECTRIC GENERATOR USING CaMnO_3

ชัยวัฒน์ พรหมเพชร
CHAIWAT PHROMPET

วิทยานิพนธ์นี้เป็นส่วนหนึ่งของการศึกษาตามหลักสูตร
ปริญญาดุษฎีบัณฑิต สาขาวิชาฟิสิกส์ประยุกต์
ภาควิชาฟิสิกส์ คณะวิทยาศาสตร์
สถาบันเทคโนโลยีพระจอมเกล้าเจ้าคุณทหารลาดกระบัง
พ.ศ. 2563

เอกสารนี้เป็นเอกสารที่สงวนไว้สำหรับการใช้งานเพื่อการศึกษาเท่านั้น เมื่ออนุญาตให้นำไปใช้ประโยชน์ด้านการค้า
ไม่ว่ากรณีใดๆ ทั้งสิ้น อีกทั้งห้ามมิให้ดัดแปลงเนื้อหา และต้องอ้างอิงถึงเจ้าของเอกสารทุกครั้งที่มีการนำไปใช้

KMITL-2020-SC-D-030-021

STUDY ON THE SYNTHESIS AND PROPERTIES OF SMART CEMENT
C₃AH₆/RGO NANO-COMPOSITE AND DEVELOPMENT OF
THERMOELECTRIC GENERATOR USING CaMnO₃



A THESIS SUBMITTED IN PARTIAL FULFILLMENT OF THE REQUIREMENT FOR THE
DEGREE OF DOCTOR OF PHILOSOPHY IN APPLIED PHYSICS
DEPARTMENT OF PHYSICS
FACULTY OF SCIENCE
KING MONGKUT'S INSTITUTE OF TECHNOLOGY LADKRABANG
2020

KMITL-2020-SC-D-030-021

เอกสารนี้เป็นเอกสารที่สงวนไว้สำหรับการใช้งานเพื่อการศึกษาเท่านั้น ไม่นิยมนำไปใช้ประโยชน์ด้านการค้า
ไม่ว่ากรณีใดๆ ทั้งสิ้น อีกทั้งห้ามมิให้ดัดแปลงเนื้อหา และต้องอ้างอิงถึงเจ้าของเอกสารทุกครั้งที่มีการนำไปใช้



COPYRIGHT 2020

FACULTY OF SCIENCE

KING MONGKUT'S INSTITUTE OF TECHNOLOGY LADKRABANG

เอกสารนี้เป็นเอกสารที่สงวนไว้สำหรับการใช้งานเพื่อการศึกษาเท่านั้น ไม่อนุญาตให้นำไปใช้ประโยชน์ด้านการค้า
ไม่ว่ากรณีใดๆ ทั้งสิ้น อีกทั้งห้ามมิให้ดัดแปลงเนื้อหา และต้องอ้างอิงถึงเจ้าของเอกสารทุกครั้งที่มีการนำไปใช้

หัวข้อวิทยานิพนธ์	การศึกษาการสังเคราะห์และสมบัติของสารซีเมนต์ไตรแคลเซียมอลูมิเนตเฮกซะไฮเดรต/รีดิวซ์กราฟีนออกไซด์นาโนคอมโพสิตและการพัฒนาเครื่องกำเนิดไฟฟ้าเทอร์โมอิเล็กทริกโดยใช้แคลเซียมแมงกานีสออกไซด์
ชื่อนักศึกษา	ชัยวัฒน์ พรหมเพชร
รหัสประจำตัว	58605014
ปริญญา	ปรัชญาดุษฎีบัณฑิต (ฟิสิกส์ประยุกต์)
ภาควิชา	ฟิสิกส์
พ.ศ.	2563
อาจารย์ที่ปรึกษาวิทยานิพนธ์	รองศาสตราจารย์ ดร. เสรษฐา รัตนพันธ์
อาจารย์ที่ปรึกษาวิทยานิพนธ์ร่วม	ผู้ช่วยศาสตราจารย์ ดร. ขวาลย์ ศรีวงษ์

บทคัดย่อ

วัตถุประสงค์ของวิทยานิพนธ์นี้ คือการศึกษาการสังเคราะห์การพิสูจน์เอกลักษณ์และการศึกษาคุณสมบัตินาโนซีเมนต์ไตรแคลเซียมอลูมิเนตเฮกซะไฮเดรต (C3AH6) และนาโนซีเมนต์ C3AH6 ร่วมกับรีดิวซ์กราฟีนออกไซด์ (C3AH6/rGO) รวมทั้งยังได้ทำการศึกษาพัฒนาคอนกรีตบล็อกผลิตไฟฟ้าจากความร้อนโดยใช้แคลเซียมแมงกานีสออกไซด์ (CaMnO₃) เป็นวัสดุเทอร์โมอิเล็กทริก หลังจากนั้นตัวอย่างที่ได้สังเคราะห์จะถูกตรวจวิเคราะห์และทดสอบคุณสมบัติโดยใช้เทคนิคต่างๆ ได้แก่ XRD, Raman, SEM, TEM, FT-IR, UV-vis, XPS และ TGA จากนั้นศึกษาคุณสมบัติทางไฟฟ้าไดอิเล็กทริก การนำความร้อน ความแข็งแรง ทางเคมีไฟฟ้า และการยับยั้งเชื้อแบคทีเรีย เป็นต้น ผลการวิจัยสรุปได้ดังนี้ คือ ผลจากการศึกษาลักษณะด้วยเทคนิคXRD ยืนยันว่านาโนซีเมนต์แสดงโครงสร้างของ C3AH6 และโครงสร้างขนาดนาโนของ C3AH6 ยืนยันได้จากเทคนิค TEM มีคุณสมบัติทางแสงซึ่งเป็นวัสดุโปร่งใสที่มองเห็นได้ ผลการตอบสนองความถี่ไฟฟ้าพบว่า วัสดุมีค่าคงที่ไดอิเล็กทริกสูง นอกจากนี้ซีเมนต์ C3AH6 ยังมีคุณสมบัติเป็นฉนวนไฟฟ้าที่สมบูรณ์แบบและซีเมนต์ฉนวนความร้อน ดังนั้นจึงสามารถสรุปได้ว่าซีเมนต์ C3AH6 โครงสร้างนาโนได้ถูกสังเคราะห์โดยกระบวนการไฮเดรชัน (hydration) สำหรับสมบัติเชิงแสง สมบัติการตอบสนองความถี่ไฟฟ้าสูงและการนำความร้อนต่ำที่เป็นสารประกอบซีเมนต์สำหรับฉนวนกันความร้อนที่โปร่งใสรวมทั้งวัสดุตัวเก็บประจุไฟฟ้าของซีเมนต์ C3AH6/rGO นาโนคอมโพสิต พบว่าอนุภาค C3AH6/x%rGO มีอนุภาคขนาดนาโนเมตร C3AH6/rGO แสดงค่าความแข็งด้วย micro-hardness มีค่ามากขึ้นเมื่อเพิ่มเปอร์เซ็นต์ของ rGO ค่าคงที่ไดอิเล็กทริกสูง และการนำไฟฟ้าเพิ่มขึ้นเมื่อมีการเติมนาโน rGO เพิ่มขึ้นอย่างไรก็ตาม ค่าการนำความร้อนมีแนวโน้มที่จะลดลง โดยวัสดุซีเมนต์ C3AH6/rGO นาโนคอมโพสิตจะมี

เอกสารนี้เป็นเอกสารที่สงวนไว้สำหรับการใช้งานเพื่อการศึกษาค้นคว้าเท่านั้น เมื่อนำไปใช้ประโยชน์ด้านการค้าไม่ว่ากรณีใดๆ ทั้งสิ้น อีกทั้งห้ามมิให้ตัดแปลงเนื้อหา และต้องอ้างอิงถึงเจ้าของเอกสารทุกครั้งที่มีการนำไปใช้

คุณสมบัติทางเคมีไฟฟ้าเพิ่มสูงขึ้นอีกด้วยและซีเมนต์C3AH6/rGO ยังแสดงฤทธิ์ต้านเชื้อแบคทีเรีย E.coli ได้ดีขึ้นเมื่อขนาดของอนุภาคเล็กลงจากการเติมrGO เพิ่มมากขึ้นสรุปได้ว่าซีเมนต์ C3AH6/rGO นาโนคอมโพสิต มีคุณสมบัติที่เหมาะสมสำหรับการใช้งาน เช่น วัสดุซีเมนต์ที่มีความแข็งแรงที่ดี ค่าคงที่ไดอิเล็กทริกสูง สมบัติทางเคมีไฟฟ้าสูง สมบัติการนำความร้อน ต้านเชื้อแบคทีเรียได้ และใช้เป็นวัสดุตัวเก็บประจุไฟฟ้าได้ต้นแบบของแผ่นคอนกรีตบล็อกผลิตพลังงานไฟฟ้าจากความร้อน (CGH) โดยต้นแบบ CGH สามารถทำงานที่อุณหภูมิสูงถึง 700 °C ต้นแบบ CGH โดยใช้หลักการของ Seebeck ด้วยการแปลงความร้อนเป็นไฟฟ้าได้โดยตรง ต้นแบบ CGH ประกอบด้วยแท่งโมดูลเทอร์โมอิเล็กทริกที่ได้สังเคราะห์ขึ้นเองในห้องปฏิบัติการ โดยใช้วัสดุเทอร์โมอิเล็กทริก CaMnO_3 จากการศึกษา พบว่าแท่งเทอร์โมอิเล็กทริกโมดูลเดียวจะมีค่าแรงดันไฟฟ้าเท่ากับ 155mV กระแส 11mA และกำลังไฟฟ้า 1.7 mW ในอุณหภูมิที่แตกต่างกัน 470 °C สำหรับโมดูลด้านร้อนอุณหภูมิที่ 700 °C พลังงานไฟฟ้าสามารถเพิ่มขึ้นได้ด้วยการเชื่อมต่อโดยโมดูลเทอร์โมอิเล็กทริกหลายตัวพร้อมกัน ผลการศึกษาแสดงให้เห็นว่าพลังงานไฟฟ้าเป็นสัดส่วนโดยตรงกับจำนวนของโมดูลเทอร์โมอิเล็กทริก นอกจากนี้ยังพบว่าต้นแบบ CGH ที่ประกอบด้วยโมดูลเทอร์โมอิเล็กทริก 50 ตัวเชื่อมต่อวงจรไฟฟ้าแบบผสมที่ความสูงของโมดูล 2 เซนติเมตร บนแผ่นความร้อนสำหรับทดสอบความต้านทานความร้อนและสร้างอุณหภูมิที่แตกต่างระหว่างด้านที่สัมผัสกับแผ่นความร้อนและด้านที่ไม่ได้สัมผัสกับแผ่นความร้อน จะมีค่าความต่างอุณหภูมิสูงสุดคือ 553.50 องศาเซลเซียส (ที่อุณหภูมิด้านร้อนที่ 700 องศาเซลเซียสและด้านเย็นเท่ากับ 146.50องศาเซลเซียส) ผลการทดสอบการวัดทางไฟฟ้าเปรียบเทียบกับความแตกต่างของอุณหภูมิพบว่าค่าสำหรับการศึกษาแสดงให้เห็นว่า ศักย์ไฟฟ้าสูงสุดคือ 702.44 mV กระแสไฟฟ้าคือ 55.06 mA จากข้อมูลที่ได้เครื่องต้นแบบ CGH ที่ได้พัฒนานี้จะสามารถนำไปใช้ในพลังงานความร้อนจากแหล่งความร้อนต่างๆ เช่น การเผาไหม้ชีวมวลโรงงานอุตสาหกรรมที่มีความร้อนสูญเสียและโรงไฟฟ้าโดยต้นแบบ CGH อาจจะสามารถปรับให้เป็นโรงไฟฟ้าพลังความร้อนขนาดใหญ่เพื่อส่งพลังงานไฟฟ้าให้กับอุตสาหกรรมได้

คำสำคัญ: สมาร์ทซีเมนต์, แคลเซียมอลูมิเนต (C12A7), แคลเซียมอลูมิเนตเอกซไฮเดรต (C3AH6), ริดิวซ์กราฟีนออกไซด์ (rGO), นาโนคอมโพสิต, แคลเซียมแมงกานีสออกไซด์ (CaMnO_3), วัสดุเทอร์โมอิเล็กทริก, เครื่องกำเนิดไฟฟ้าเทอร์โมอิเล็กทริก

Thesis Title	Study on the Synthesis and Properties of Smart Cement C3AH6/RGO Nano-composite and Development of Thermoelectric Generator Using CaMnO ₃
Student Name	Chaiwat Phrompet
Student ID	58605014
Degree	Doctor of Philosophy (Applied physics)
Department	Physics
Year	2020
Thesis Advisor	Associate Professor Dr. Chesta Ruttanapun
Thesis Co-advisor	Assistant Professor Dr. Chaval Sriwong

Abstract

The objectives of this thesis were to study on the synthesis, characterization, and properties of $3\text{CaO}\cdot\text{Al}_2\text{O}_3\cdot 6\text{H}_2\text{O}$ (C3AH6) nano-cement and the C3AH6 nano-cement incorporated with reduced graphene oxide (C3AH6/rGO) nanocomposites as smart cement materials. Development of the prototype of electrical power concrete block generation from heat by using CaMnO₃ as thermoelectric materials was also investigated. As-synthesized smart cement samples were characterized and analyzed by several techniques, such as, XRD, Raman, SEM, TEM, FT-IR, UV-vis, XPS and TGA. Moreover, the properties of synthesized cement samples, for the example, dielectric constant, optical, electrical, thermal conductivities, micro hardness, electrochemical properties, supercapacitor, and antibacterial activity were also studied. The results can be briefly concluded as follows: the nanostructured C3AH6 and C3AH6/rGO nanocomposite smart cements were successfully fabricated by adopting a conventional hydration process. C3AH6 nano-cement indicated a high dielectric response, large optical band gap and remained thermodynamically stable at below 350 °C with low thermal conductivity as thermal insulator. However, the C3AH6/rGO nanocomposite cements appeared to have good smart cements properties including high electrical conductivity, giant dielectric constants, greater Vickers micro-hardness values, high electrochemical and supercapacitor properties with high performance in antibacterial activities. These properties tend to increase along with an increase of

rGO content (wt.x%) loading. In contrast, thermal conductivity reduced as the contents of rGO in the C3AH6/rGO nanocomposites increased. These results indicated that nano-sized C3AH6 cement incorporated with rGO material exhibited suitable properties for multifunctional applications as smart cement materials. In addition, the prototype of concrete block electric power generation from heat (CGH) and its applications in municipal melting furnace or municipal incinerator are investigated. This CGH prototype consisted of thermoelectric modules containing thermoelectric material synthesized from CaMnO_3 thermoelectric material. It was found that a single thermoelectric module showed voltage as 155 mV current as 11 mA and the electrical power as 1.7 mW in temperature difference of 470°C for the high temperature side module at 700°C . The electrical power can be increased by connecting several thermoelectric modules together. Also, the prototype of CGH consisting of 50 thermoelectric modules are connected to the electrical circuit at the module's height at 2 cm on the hot plate. The results showed that electrical power is directly proportional to the number of thermoelectric modules. The difference in maximum heat temperature was 553.50°C (at the hot side, the temperature was at 700°C and at 146.50°C for the cold side). In addition, testing of electrical measurements, when compared to temperature differences, as showed that the maximum electric potential was at 702.44 mV and the current was at 55.06 mA. Thus, these results implied that CGH prototype can be applied to thermal energy from various heat sources, such as burning, biomass, waste, heat industrial and power plants. The CGH prototype may be scaled into large-scale thermal power plant to supply the electrical energy to different industries.

Keywords: Smart cement, $12\text{CaO}\cdot 7\text{Al}_2\text{O}_3$ (C12A7), $\text{Ca}_3\text{Al}_2(\text{OH})_{12}$ (C3AH6), Reduced graphene oxide (rGO), Nanocomposites, CaMnO_3 , Thermoelectric material, Thermoelectric generator.

Acknowledgements

(กิตติกรรมประกาศ)

วิทยานิพนธ์ฉบับนี้เกิดขึ้นได้โดยได้รับความกรุณา ความช่วยเหลือ การสนับสนุนจากแหล่งทุน และการสนับสนุนในด้านต่างๆ จากบุคคลหลายท่านด้วยกัน ทำให้ได้รับโอกาสและสร้างแรงบันดาลใจ นำมาสู่ความสำเร็จที่เกิดขึ้นในวิทยานิพนธ์ฉบับนี้ จึงขอขอบพระคุณเป็นอย่างสูงต่อท่านทั้งหลาย ดังนี้

สำหรับความสำเร็จของวิทยานิพนธ์ฉบับนี้ได้รับความกรุณาอาจารย์ที่ปรึกษาวิทยานิพนธ์หลัก รองศาสตราจารย์ ดร. เสรษฐา รัตนพันธ์ และอาจารย์ที่ปรึกษาวิทยานิพนธ์ร่วม ผู้ช่วยศาสตราจารย์ ดร. ขวาลย์ ศรีวงษ์ ที่กรุณาให้คำปรึกษาหัวข้อวิจัย ตลอดจน คำแนะนำ ข้อเสนอแนะ ในการทำวิจัย การเขียนบทความ ได้มีผลงานตีพิมพ์ในวารสารวิชาการระดับนานาชาติอันเป็นที่ยอมรับและการเขียน วิทยานิพนธ์ฉบับนี้สำเร็จลุล่วงไปได้ด้วยดี

ขอขอบพระคุณ ผู้ช่วยศาสตราจารย์ ดร. ประธาน บุณศิริ อาจารย์ ดร. วิฑูรย์ ยินดีสุ และ ผู้ช่วยศาสตราจารย์ ดร. เมตยา กิตติวรรณ ที่ร่วมเป็นคณะกรรมการสอบเค้าโครงและสอบวิทยานิพนธ์

ขอขอบพระคุณ รองศาสตราจารย์ ดร. สมศักดิ์ พิมานแพง ภาควิชาฟิสิกส์ คณะวิทยาศาสตร์ มหาวิทยาลัยศรีนครินทรวิโรฒ ที่เป็นประธานกรรมการสอบวิทยานิพนธ์และสอบวิทยานิพนธ์

ขอขอบคุณ นักวิจัยหลังปริญญาเอก และน้องๆ นักศึกษาปริญญาโท ปริญญาตรี ในศูนย์ความเป็นเลิศด้านวิจัยและนวัตกรรมวัสดุอัจฉริยะ ทุกๆ ท่าน ที่ได้ให้คำแนะนำที่เป็นประโยชน์และช่วยเหลือในการจัดเตรียมอุปกรณ์การทดลอง ขอขอบคุณ ศูนย์ความเป็นเลิศด้านวิจัยและนวัตกรรม วัสดุอัจฉริยะ ภาควิชาฟิสิกส์ คณะวิทยาศาสตร์ สถาบันเทคโนโลยีพระจอมเกล้าเจ้าคุณทหารลาดกระบัง ที่อำนวยความสะดวกด้านอุปกรณ์เครื่องมือในการทดลองและสถานที่ในการทำวิจัย

วิทยานิพนธ์นี้ ได้รับทุนสนับสนุนในการทำวิจัย จากสำนักงานคณะกรรมการส่งเสริมวิทยาศาสตร์ วิจัยและนวัตกรรม (สกสว.) โครงการทุนพัฒนานักวิจัยและงานวิจัยเพื่ออุตสาหกรรม (พวอ.) ระดับปริญญาเอก ที่สัญญาเลขที่ PHD6010046 และขอขอบคุณ บัณฑิตวิทยาลัยสถาบันเทคโนโลยีพระจอมเกล้าเจ้าคุณทหารลาดกระบัง

สุดท้ายต้องขอขอบคุณ ภรรยาของข้าพเจ้า คุณดวงเดือน พรหมดวง ที่คอยดูแลให้กำลังใจเป็นผู้ช่วยเหลืออยู่เบื้องหลังที่ดีตลอดมา สำหรับคุณงานความดีอันใดที่เกิดจากวิทยานิพนธ์ฉบับนี้ ข้าพเจ้า ขอมอบให้บิดาของข้าพเจ้า คุณพ่อไชยศ มารดาคุณแม่ชูลี พรหมเพชร และคุณแม่แก้ว พรหมดวง พี่ชาย พี่สาว น้องสาว เครือญาติ และครูอาจารย์ที่เคารพทุกท่านที่ได้ประสาทวิชาความรู้และถ่ายทอดประสบการณ์ที่ดีให้แก่ข้าพเจ้า ตลอดจนทุกท่านที่ไม่ได้กล่าวมา ณ ที่นี้

ชัยวัฒน์ พรหมเพชร

26 มีนาคม 2563

เอกสารนี้เป็นเอกสารที่สงวนไว้สำหรับการใช้งานเพื่อการศึกษาเท่านั้น ไม่อนุญาตให้นำไปใช้ประโยชน์ด้านการค้า ไม่ว่ากรณีใดๆ ทั้งสิ้น อีกทั้งห้ามมิให้ตัดแปลงเนื้อหา และต้องอ้างอิงถึงเจ้าของเอกสารทุกครั้งที่มีการนำไปใช้

Table of contents

	Page
Abstract in Thai.....	i
Abstract in English.....	iii
Acknowledgements.....	v
Table of contents.....	vi
List of tables.....	xi
List of figures.....	x
List of Abbreviations.....	xvii
Chapter 1 Introduction.....	1
1.1 Research motivation.....	1
1.2 Objectives of the study.....	6
1.3 Scope of the study.....	6
1.4 Benefits of the study.....	6
Chapter 2 Theory and literature reviews.....	7
2.1 Fundamental properties of $\text{Ca}_{12}\text{Al}_{14}\text{O}_{33}$ mayenite.....	7
2.2 Fundamental properties of $\text{Ca}_3\text{Al}_2(\text{OH})_{12}$ (C3AH6) katoite.....	8
2.3 Synthesis of Graphene.....	9
2.3.1 Introduction.....	9
2.3.2 Overview of graphene synthesis methodologies.....	11
2.3.3 Chemical Synthesis: Graphene from Reduced Graphene Oxide.....	12
2.4 Fundamental of thermoelectric.....	13
2.4.1 Introduction.....	13
2.4.2 Thermoelectric Effect.....	14
2.4.3 The Figure of Merit.....	17
2.4.4 New-Generation thermoelectric.....	17
2.5 Supercapacitors.....	19
2.5.1 Component and classification of supercapacitor.....	20
2.5.2 Supercapacitor Performance.....	23
2.6 Literature reviews.....	28
2.6.1 $\text{Ca}_{12}\text{Al}_{14}\text{O}_{33}$ (C12A7) cement.....	28
2.6.2 C3AH6 cement and C3AH6-rGO nanocomposites.....	28

เอกสารนี้เป็นเอกสารที่สงวนไว้สำหรับการใช้งานเพื่อการศึกษาเท่านั้น ไม่อนุญาตให้นำไปใช้ประโยชน์ด้านการค้า
ไม่ว่ากรณีใดๆ ทั้งสิ้น อีกทั้งห้ามมิให้ดัดแปลงเนื้อหา และตั้งviอ้างอิงถึงเจ้าของเอกสารทุกครั้งที่มีการนำไปใช้

2.6.3 Synthesis of Graphene.....	29
2.6.4 Thermoelectric generators.....	30
2.6.5 Smart nanocomposite cement-based materials.....	33
Chapter 3 Research methodology.....	34
3.1 Research materials and tools.....	34
3.1.1 Chemicals and materials.....	34
3.1.2 Experimental tools.....	35
3.2 Experimental procedure.....	40
3.2.1 Procedures for synthesis of C3AH6-rGO composite samples.....	40
3.2.2 Procedures for synthesis of CaMnO ₃ as thermoelectric materials....	45
3.2.3 Prototype of concrete block electric power generation from heat and applications in municipal melting furnace or municipal Incinerator.....	47
3.3 Characterizations and properties measurements.....	48
3.3.1 Characterizations.....	48
3.3.2 Properties measurements.....	49
Chapter 4 Results and discussion.....	50
4.1 Synthesis of nanostructure C3AH6 cements.....	50
4.1.1 Microstructural Characterizations.....	50
4.1.2 Optical Properties.....	56
4.1.3 Dielectric properties.....	59
4.1.4 Thermal properties.....	61
4.2 Synthesis of rGO-C3AH6 nanocomposites.....	65
4.2.1 GO and rGO characterizations.....	65
4.2.2 Nanometer sized C3AH6 cement and rGO-C3AH6 nanocomposites characterizations.....	68
4.2.3 The properties of rGO-C3AH6 nanocomposites.....	81
4.3 Prototype of concrete block electric power generation from heat and applications in municipal melting furnace or municipal incinerator.....	98
4.3.1 Synthesis of CaMnO ₃ as thermoelectric materials.....	98
4.3.2 The prototype of wall panel thermoelectric module for electricity production from high temperature heat from municipal waste incinerator prototype.....	101

4.3.3 Prototype of concrete block electric power generation from heat and applications in municipal melting furnace or municipal incinerator.....	104
4.3.4 Electrical Properties of Thermoelectric Modules.....	105
4.3.4.1 The result of a single thermoelectric module from CaMnO_3 at the diameter of 1 cm to connect series electrical circuit.....	105
4.3.4.2 The result of 2 thermoelectric module of CaMnO_3 at the diameter of 1 cm to connect parallel electrical circuit.....	110
4.3.4.3 The result of 50 thermoelectric module of CaMnO_3 at the diameter of 1 cm at the height 2 cm to connect compound electrical circuit.....	116
Chapter 5 Conclusions and suggestions.....	118
5.1 Conclusions.....	118
References.....	120
Appendix.....	126
Appendix A.....	127
A.1 : C3A6 PDF#03-0125.....	128
A.2 : C12A7 PDF#09-0413.....	132
Appendix B.....	134
B.1 : Academic Publications.....	135
B.2 : International conference.....	136
Author biography.....	208

เอกสารนี้เป็นเอกสารที่สงวนไว้สำหรับการใช้งานเพื่อการศึกษาเท่านั้น ไม่อนุญาตให้นำไปใช้ประโยชน์ด้านการค้า ไม่ว่าจะกรณีใดๆ ทั้งสิ้น อีกทั้งห้ามมิให้ดัดแปลงเนื้อหา และตั้ง **viii** ไปถึงเจ้าของเอกสารทุกครั้งที่มีการนำไปใช้

List of tables

Table	Page
2.1 Thermoelectric properties of single crystal and bulk nanocomposite Semiconductors.....	19
4.1 SEM and EDX of the prepared C12A7 cement powder (a and b), and SEM and EDX of the concocted C3AH6 cement hydrate powder (c and d).....	55
4.2 SEM images and EDX analysis of (a) pristine C3AH6, (b) 2%rGO-C3AH6 and (c) 4%rGO-C3AH6 samples.....	71
4.3 Csc value at different scan rates and current densities were calculated by CV and GCD test, and EIS analysis of C3AH6 and all rGO-C3AH6 electrodes.....	95
4.4 Summary of differences of preparation method and characteristic of 10%rGO-C3AH6 prepared at KMITL Lab and this Osaka Lab.....	96

List of figures

Figure	Page
1.1 The reaction schematic diagram on occurring the nanostructure C3AH6 cement hydrate.....	2
1.2 Synthesis and the differences between the two processes to produce nanometer sized C3AH6 and nanocomposited C3AH6-rGO.....	4
1.3 Prototype of concrete block electric power generation from heat and applications in municipal melting furnace or municipal incinerator.....	5
2.1 A cubic unit cell of the C12A7 mayenite structure.....	7
2.2 A cubic unit cell of C3AH6 structure: blue, green red and ping balls represent Ca, Al, O, and H atoms and C3AH6 1x1x1, 2x2x2 unit cell.....	8
2.3 The 2D hexagonal nanosheets of graphene (top) and relevant structures: fullerene (bottom left), carbon nanotubes (bottom centre) and graphite (bottom right).....	9
2.4 Scalability against cost and graphene quality trends for various synthesis graphene techniques.....	10
2.5 Classification of graphene synthesis processes.....	11
2.6 The process flow chart graphene synthesis derived from reduced graphene oxide.....	12
2.7 Electron concentrations in a thermoelectric material.....	14
2.8 Thermocouple.....	15
2.9 Schematic for the Peltier effect and the Thomson effect.....	15
2.10 Dimensionless figures of merit for various nanocomposite thermoelectric materials.....	18
2.11 Plotting of specific power against specific energy for different types of conventional capacitor, battery and fuel cell technologies.....	20
2.12 Three important parts of supercapacitor: the electrodes (anode and cathode), separator and electrolyte solution.....	21
2.13 Schematic representations of supercapacitor types.....	22

2.14 Schematic drawing of (a)three-electrode system and (b)two-electrode system: working electrode (W), reference electrode (R), and counter electrode (C).....	23
2.15 Cyclic voltammogram curves of (a) ideal capacitor, (b) EDLC, and (c) pseudocapacitive materials.....	24
2.16 Cyclic voltammograms of ordered graphitic mesoporous carbon at different scan rates.....	25
2.17 Galvanostatic charge–discharge plots of (a) EDLC and (b) pseudocapacitive material.....	26
3.1 The balance apparatus.....	35
3.2 The ball-milling equipment.....	35
3.3 The hot air oven apparatus.....	35
3.4 The furnace apparatus.....	36
3.5 The alumina crucible.....	36
3.6 The agate mortar.....	36
3.7 The Pelleting mould for pellet sample and bar sample.....	37
3.8 The hydraulic pressure machine.....	37
3.9 The hot-press sintering apparatus.....	37
3.10 The thermocouple equipment.....	38
3.11 The digital multimeter equipment.....	38
3.12 The thermal imaging camera equipment.....	38
3.13 The Lab-top.....	39
3.14 The High-press continuous automatic machine.....	39
3.15 Flow chart illustrating the synthesis of C3AH6 cement–reduced graphene oxide nanocomposite samples.....	40
3.16 Photograph showing all the overview procedures for synthesis of C3AH6 cement–reduced graphene oxide nanocomposite samples.....	41
3.17 Preparation of C12A7 cement powder.....	42

3.18 Preparation of C3AH6 nanocement powder.....	42
3.19 Preparation of reduced graphene oxide (rGO).....	43
3.20 Preparation of rGO-C3AH6 nanocomposite.....	44
3.21 Flow chart for the synthesis of CaMnO ₃ as thermoelectric modules materials..	46
3.22 Photograph showing the overview procedures for synthesis of CaMnO ₃ as thermoelectric modules materials.....	47
3.23 Photograph showing the prototype of concrete block electric power generation from heat and applications in municipal melting furnace or municipal incinerator.....	48
3.24 Flow chart of characterizations and properties measurements.....	49
4.1 XRD pattern for pristine C12A7 and C3AH6 samples comparison with C12A7 and C3AH6 reference.....	51
4.2 IR spectra of C3AH6 specimen and the concocted C12A7 precursor.....	52
4.3 (a) XPS survey spectrum of C3AH6 and XPS spectra of (b) Ca 2p, (c) Al 2p, and (d) O 1s for pristine C3AH6 samples.....	53
4.4 TGA curves of pristine C3AH6 cement hydrate samples.....	54
4.5 (a) Microscopy images of transmission of electron for the concocted C3AH6 powder (b) the SAED pattern.....	56
4.6 (a) absorbance, (b) direct energy gap and (c) indirect energy gap of the concocted C3AH6 specimen and C12A7 samples.....	58
4.7 (a) the capacitance, (b) the dielectric constant, (c) the dielectric loss, and (d) the AC electrical conductivity as function of the frequency of the C3AH6 and C12A7 specimens.....	61
4.8 (a) Thermal diffusivity, (b) Thermal conductivity as a function of the temperature (T) and (c) as a function of 1/T ³ of the concocted C3AH6 and C12A7sample.....	64
4.9 XRD pattern for pristine graphite and the synthesized GO and rGO samples.....	65
4.10 Raman spectra for pristine graphite and the synthesized GO and rGO samples..	66
4.11 UV-vis spectra of as-synthesized GO and rGO samples.....	67

4.12 FT-IR spectra of the synthesized GO and rGO samples.....	68
4.13 XRD pattern of pristine C3AH6, and 1%rGO-C3AH6, 2%rGO-C3AH6, 3%rGO-C3AH6, and 4%rGO-C3AH6 composite samples.....	69
4.14 An average of crystallite and particles sizes of C3AH6 and x%rGO-C3AH6 with various contents of rGO loading.....	70
4.15 EDX elemental mapping of C3AH6 samples.....	72
4.16 EDX elemental mapping of 2%rGO-C3AH6 samples.....	73
4.17 EDX elemental mapping of 4%rGO-C3AH6 samples.....	74
4.18 TEM images of synthesized (a) rGO nanosheets, (b) nanometer sized C3AH6, and (c) nanocomposited 2%rGO-C3AH6 and (d) 4%rGO-C3AH6 samples.....	76
4.19 Raman spectra of pristine C3AH6 and x%rGO-C3AH6 samples.....	77
4.20 FT-IR spectra of pristine C3AH6, 1%rGO-C3AH6, 2%rGO-C3AH6, 3%rGO-C3AH6 and 4%rGO-C3AH6 samples.....	78
4.21 (a) XPS survey spectra of C3AH6 and 2%rGO-C3AH6 samples and (b) XPS survey spectra of C(1s) of the synthesized C3AH6, 2%rGO- C3AH6 and 4%rGO-C3AH6 samples.....	79
4.22 (a) Absorption coefficient of C3AH6 and x%rGO-C3AH6 samples and (b) the relationship between an allowed direct optical gap of C3AH6 and x%rGO-C3AH6 samples.....	80
4.23 TGA diagram of C3AH6, 2%rGO-C3AH6, 3%rGO-C3AH6 and 4%rGO-C3AH6 samples.....	81
4.24 Diagonal length of the impression on surfaces of C3AH6, 1%rGO-C3AH6, 2%rGO-C3AH6, 3%rGO-C3AH6 and 4%rGO-C3AH6 composited samples.....	82
4.25 Micro-hardness of C3AH6, 1%rGO-C3AH6, 2%rGO-C3AH6, 3%rGO-C3AH6 and 4%rGO-C3AH6 composited samples.....	83
4.26 Antibacterial properties of (a) C3AH6, (b) 1%rGO-C3AH6, (c) 2%rGO-C3AH6, (d) 3%rGO-C3AH6 and (e) 4%rGO-C3AH6 composited samples.....	84

4.27 (a) Dielectric constant and (b) dielectric loss as a function of frequency, and (c) electrical conductivity of C3AH6, 1%rGO-C3AH6, 2%rGO-C3AH6, 3%rGO-C3AH6 and 4%rGO-C3AH6 nanocomposites samples.....	86
4.28 (a) thermal conductivity a function of temperature, (b) thermal conductivity a function of inverse of temperature, (c) Specific heat of C3AH6, 1%rGO-C3AH6, 2%rGO-C3AH6, 3%rGO-C3AH6 and 4%rGO-C3AH6 samples.....	88
4.29 (a) CV curves at a scan rate of 100 mV s^{-1} of C3AH6 and all rGO-C3AH6 electrodes. (b), (c), (d), (e), (f), (g) and (h) CV curves at different scan rates of C3AH6 and all rGO-C3AH6 electrodes.....	90
4.30 (a) shows GCD curves at a scan rate of 0.5 A g^{-1} of C3AH6 and all rGO-C3AH6 electrodes. (b), (c), (d), (e), (f), (g) and (h) show GCD curves at different currentdensities of C3AH6 and all rGO-C3AH6 electrodes.....	91
4.31 (a) and (b): specific capacitance plots of C3AH6 and all rGO-C3AH6 electrodes at different scan rates and current densities were calculated by CV and GCD test and (c): cycling stability of C3AH6 and all rGO-C3AH6 electrodes using GCD test at a current density of 5 A g^{-1}	92
4.32 (a) Niquist impedance plots of C3AH6 and all rGO-C3AH6 electrodes. (b), (c), (d), (e), (f), (g) and (h) the fitting Niquist impedance plots with inset the enlargement of the plots near origin and showing an equivalent circuit of C3AH6 and all rGO-C3AH6 electrodes.....	94
4.33 (a) The Resistivity (ρ), (b) Seebeck coefficient (S) and (c) Power factor (PF) of the 10%rGO-C3AH6 sample.....	97
4.34 XRD patterns of prepared CaMnO_3 precursor referencing the JCPDS#03-0830...98	
4.35 SEM images of CaMnO_3 with magnifications from (a) 500x, (b) 2000x, (c) 4000x, and (d) 6000x, respectively.....	99
4.36 SEM images with inset a high magnification view of selected area, and displayed the EDS-mapping images for C, O, Ca and Mn elements of CaMnO_3 samples..	100

4.37 Connection of conventional thermoelectric modules N-type and P-type.....	101
4.38 Connection of conventional thermoelectric modules N-type.....	102
4.39 (a) Stainless steel electrode materials (b) aluminum electrode materials after coated with silver.....	103
4.40 Prototype of thermoelectric module wall plate to generate electricity from heat.....	104
4.41 Prototype of concrete block electric power generation from heat and applications in municipal melting furnace or municipal incinerator.....	105
4.42 The temperature difference in the room temperature range to 700 °C For at the height of module 1.5 cm.....	106
4.43 Graph relation between temperature difference voltage (mV) and current (mA) for at the height of module 1.5 cm.....	106
4.44 The temperature difference in the room temperature range to 700 for at the height of module 2.0 cm.....	107
4.45 Graph relation between temperature difference voltage (mV) and current (mA) for at the height of module 2.0 cm.....	108
4.46 The temperature difference in the room temperature range to 700 °C for at the height of module 2.0 cm.....	109
4.47 Graph relation between temperature difference voltage (mV) and current (mA) for the module at a height of 2.5 cm.....	109
4.48 Graph relations between hot side temperature and voltage (mV) for 2 module of the thermoelectric module to connect series electrical circuit at the height of the module at 1.5, 2.0 and 2.5 cm.....	110
4.49 The temperature difference in the room temperature range to 700 °C for 2 module of the thermoelectric module to connect parallel electrical circuit at the height of the module at 1.5 cm.....	111

เอกสารนี้เป็นเอกสารที่สงวนไว้สำหรับการใช้งานเพื่อการศึกษาเท่านั้น ไม่อนุญาตให้นำไปใช้ประโยชน์ด้านการค้า
ไม่ว่ากรณีใดๆ ทั้งสิ้น อีกทั้งห้ามมิให้ตัดแปลงเนื้อหา และต้องอ้างอิงถึงเจ้าของเอกสารทุกครั้งที่มีการนำไปใช้

4.50 Graph relation between temperature difference voltage (mV) and current (mA) for 2 module of the thermoelectric module to connect parallel electrical circuit at the height of the module at 1.5 cm.....	112
4.51 The temperature difference in the room temperature range to 700 °C for 2 module of the thermoelectric module to connect parallel electrical circuit at the height of the module at 2.0 cm.....	113
4.52 Graph relation between temperature difference voltage (mV) and current (mA) for 2 module of the thermoelectric module to connect parallel electrical circuit at the height of the module at 2.0 cm.....	113
4.53 The temperature difference in the room temperature range to 700 °C For 2 module of the thermoelectric module to connect parallel electrical circuit at the height of the module at 2.5 cm.....	114
4.54 Graph relation between temperature difference voltage (mV) and current (mA) for 2 module of the thermoelectric module to connect parallel electrical circuit at the height of the module at 2.5 cm.....	115
4.55 Graph relation between hot side temperature and current (mA) for 2 module of the thermoelectric module to connect parallel electrical circuit at the height of the module at 1.5, 2.0 and 2.5 cm.....	116
4.56 The temperature difference in the room temperature range to 700 °C for 50 module of the thermoelectric module to connect compound electrical circuit at the height of the module at 2.0 cm.....	117
4.57 Graph relation between temperature difference voltage (mV) and current (mA) for 50 module of the thermoelectric module to connect compound electrical circuit at the height of the module at 2.0 cm.....	117

List of Abbreviations

A	Area of the sample
C_p	Specific Heat of the specimen
D	Bulk Density
D_{XRD}	Average Crystallite Sizes
E_g	Direct Optical gab
h_ν	Proton Energy
I	Current
T	Temperature
T_H	Temperature at hot site
T_C	Temperature at cold site
ΔT	Temperature gradient
L	Thickness of the specimen
Q	Heat absorption Energy
R	Resistance of the specimen
V	Electrical Potential
α	Seeback Coefficient
π	Peltier Coefficient.
τ	Thomson Coefficient.
ZT	Dimensionless Figure of merit
ρ	Electrical Resistivity
σ	Electrical Conductivity
κ	Thermal Conductivity
κ_e	Electronic Thermal Conductivity
κ_{ph}	Phonon Thermal Conductivity
λ	X-ray wavelength
β	Full-wide at half-maximum of the highest intensity peak
θ	Half of diffraction peak angle
ϵ_0	Permittivity of free space
ω	Phono angular Frequency

เอกสารนี้เป็นเอกสารที่สงวนไว้สำหรับการใช้งานเพื่อการศึกษาเท่านั้น ไม่อนุญาตให้นำไปใช้ประโยชน์ด้านการค้า
ไม่ว่ากรณีใดๆ ทั้งสิ้น อีกทั้งห้ามมิให้ดัดแปลงเนื้อหา และ **xvii** ไปถึงเจ้าของเอกสารทุกครั้งที่มีการนำไปใช้

Chapter 1

Introduction

1.1 Research motivation

Thailand has large amount of inexpensive raw materials for producing cement composites for constructions purposes such as buildings and roads. Therefore, if the cement composites could be improved to be smart materials, the cement's raw materials would provide more value. Smart cement composites that can generate electricity from heat is one promising route because heat can be generated by sunlight available throughout the year in Thailand [1-4]. Physical properties of Portland cement materials have been widely investigated for new finding in scientific applications and importance technology. The Portland cements are commonly used in construction industries which is based mainly upon calcium aluminate (CA) cements compounds [5]. There are several composite calcium aluminate (CA) used in Portland cement such as $3\text{CaO}\cdot\text{Al}_2\text{O}_3$ (abbreviated C3A in cement notation), $12\text{CaO}\cdot 7\text{Al}_2\text{O}_3$ (C12A7) [5,6,7]. The calcium aluminate cement can be presented by notation of $n\text{CaO}\cdot m\text{Al}_2\text{O}_3$ (C_nA_m). Cement hydration process occurs when anhydrous cement reacts with water, for example of $3\text{CaO}\cdot\text{Al}_2\text{O}_3\cdot 6\text{H}_2\text{O}$ (C3AH6), or also known as Tricalcium Aluminate Hexahydrate [8,9,10]. The cement hydrate is one of the cement hydrate composites that draw attention in terms of dielectric behavior as presented by having electrical response as a function of frequency for capacitors applications [5,11,12]. The pure C3AH6 cement hydrate, or katoite cement mineral and hydrogarnet group, contains a stoichiometric formula $\text{Ca}_3\text{Al}_2(\text{OH})_{12}$ [8] or a solid form of cement containing calcium aluminate cement hydrates which is kept at room temperature. The crystal-like structure exhibited in a cubic unit cell located in space group of $Ia\bar{3}d$ (230). Dilnesa et. al. [13] has explained in detail that the C3AH6 contains general formula $\text{Ca}_3\text{Al}_2(\text{OH}_4)_3$ of the Ca site as specified by divalent cations (Ca^{2+}), Al site occupied by trivalent cations (Al^{3+}) in an octahedral and a tetrahedral framework and the 4OH locating within the tetrahedral framework for charge balancing. The H^+ ions bonded with each of the four O atoms with surrounding space. The unit cell contains 6 of the $\text{Ca}_3\text{Al}_2(\text{OH})_{12}$ units which possesses 132 atoms

เอกสารนี้เป็นเอกสารที่สงวนไว้สำหรับการใช้งานเพื่อการศึกษาเท่านั้น ไม่อนุญาตให้นำไปใช้ประโยชน์ด้านการค้า
ไม่ว่ากรณีใดๆ ทั้งสิ้น อีกทั้งห้ามมิให้ตัดแปลงเนื้อหา และต้องอ้างอิงถึงเจ้าของเอกสารทุกครั้งที่มีการนำไปใช้

(24 Ca, 16 Al, 96 H and 96 O) and were essentially formed by a three dimensional framework containing the $\text{Ca}(\text{OH})_8$ dodecahedra sub-structure and the $\text{Al}(\text{OH})_6$ octahedra sub-structure [8,13]. The unit cell structure displays lattice parameters of a lattice constant $a=12.55695 \text{ \AA}$, and unit cell volume $V=1986 \text{ \AA}^3$. Naturally, the C3AH6 cement is constructed in a crystal phase at high temperatures. Furthermore, Barnes and Bensted [14] had explained that the C3AH6 cement hydrate can be formed by having C12A7 quickly reacted with water above 60°C . For physical properties, Smith, et. al. [12] have reported that the C3AH6 cement hydrate displayed the characteristic of high frequency in response with value of $1 \times 10^{12} \text{ F}$ to $2 \times 10^{12} \text{ F}$ for frequency ranging from 10^6 Hz to 10^9 Hz . However, there is no report yet on the preparation process for nanostructure of C3AH6 cement hydrate and its effects on optical, thermal and dielectric properties.

In this investigation, the nanostructure C3AH6 was prepared by applying hydration process of starting C12A7. Moreover, the nanostructure, optical, thermal and dielectric properties were observed in detail of the C3AH6 comparing to the precursor C12A7. Figure 1.1 illustrates schematic diagram of the reaction of nanostructure C3AH6 cement hydrate.

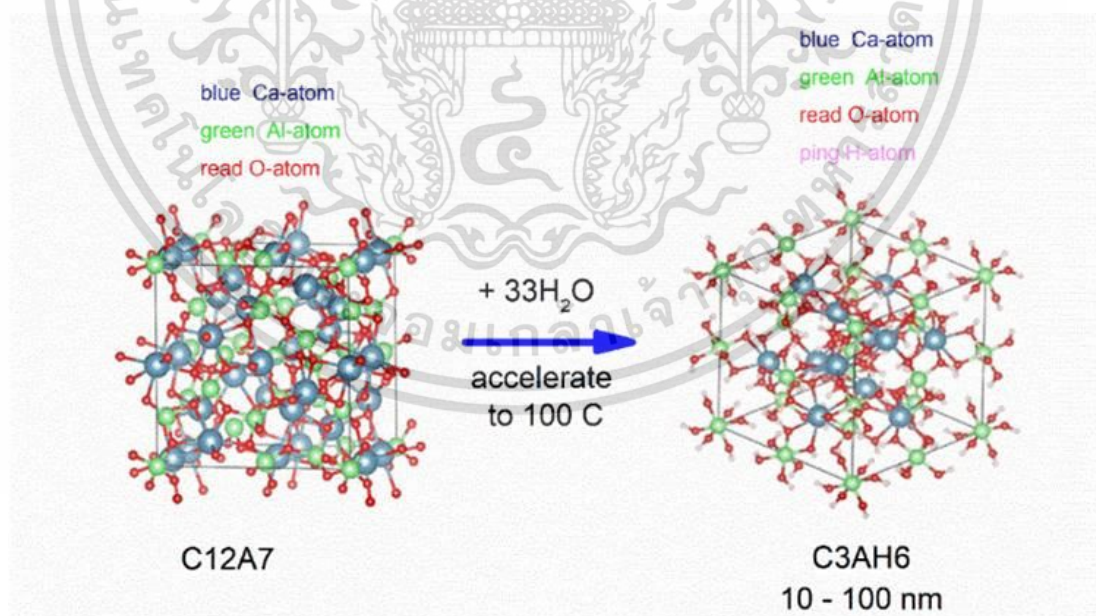


Figure 1.1 The reaction schematic diagram on occurring the nanostructure C3AH6 cement hydrate. [15].

เอกสารนี้เป็นเอกสารที่สงวนไว้สำหรับการใช้งานเพื่อการศึกษาเท่านั้น ไม่อนุญาตให้นำไปใช้ประโยชน์ด้านการค้า
ไม่ว่ากรณีใดๆ ทั้งสิ้น อีกทั้งห้ามมิให้ตัดแปลงเนื้อหา และต้องอ้างอิงถึงเจ้าของเอกสารทุกครั้งที่มีการนำไปใช้

The properties of C3AH6 hydrogarnet were better than those of materials containing complex nanosized structures. C3AH6 cement has the formula, $\text{Ca}_3\text{Al}_2(\text{OH})_{12}$ [8]. However, C3AH6 cement has poor dielectric and mechanical constant, thermal conductivity, electrochemical properties with no antibacterial properties. Thus, it should be improved by the incorporation of appropriate nanocomposite materials. Currently, many publications on the enhancement of cement-based compounds by using graphene oxide (GO) composites and reduced graphene oxide (rGO) composites are available. Among several, Sedaghat et al. [18] discovered the electrical conductivity and thermal diffusivity of cement/graphene composite structural applications were formed by partially replacing graphene with Portland cement. Similarly, Li and Kim [18] attempted graphene oxide composited with calcium aluminate cement to improve the strength of flexural and compressive materials for construction repairing field. Dimov et al. [16] additionally asserted that nanoengineered concrete composites with GO significantly provides more strength. Gholampour et al. [19] explained the consequences of GO and rGO composites in a cement mortar for axial tension and compression properties improvement. Khan et al. [17] succeeded in attempting the experiment on aconductive nanoscale calcium aluminate cement by applying rGO and GO components. Specifically, rGO, which is a two-dimensional (2D) carbon nanomaterial, has been acceptably applied in construction field because of its compatible electrical, thermal and mechanical properties which led to a high surface area [16,17]. Therefore, this 2D rGO material may have preferable performance in terms of enhancing the properties of nanosized C3AH6 hydrogarnet cement. Nanosized C3AH6 tend to utilize the 2D nanostructured rGO in various functions and applications that demand micro hardness, a stable dielectric constant, electrochemical properties, antibacterial activity and thermal conductivity.

For this research, the author proposed to attempt at a method on preparing 2D nanocomposites of minimized GO and nanosized C3AH6 by using a quick cement hydration process for investigating the mechanical, optical, dielectric, thermal, electrochemical and antibacterial properties. This approach utilizes the 2D nanostructured rGO incorporated in the nanosized C3AH6 cement-base, advancing its material properties. The improved properties of nanocomposited rGO/nanosized

C3AH6 cement, dielectric constant, electrochemical, thermal conductivity,
เอกสารนี้เป็นเอกสารที่สงวนไว้สำหรับการใช้งานเพื่อการศึกษาเท่านั้น ไม่อนุญาตให้นำไปใช้ประโยชน์ด้านการค้า
ไม่ว่ากรณีใดๆ ทั้งสิ้น อีกทั้งห้ามมิให้ตัดแปลงเนื้อหา และต้องอ้างอิงถึงเจ้าของเอกสารทุกครั้งที่มีการนำไปใช้

thermoelectric, micro hardness and antibacterial properties are shown in Figure 1.2 illustrating synthesis and differences between the two processes to produce nanometer sized C3AH6 and nanocomposited rGO-C3AH6 [15].

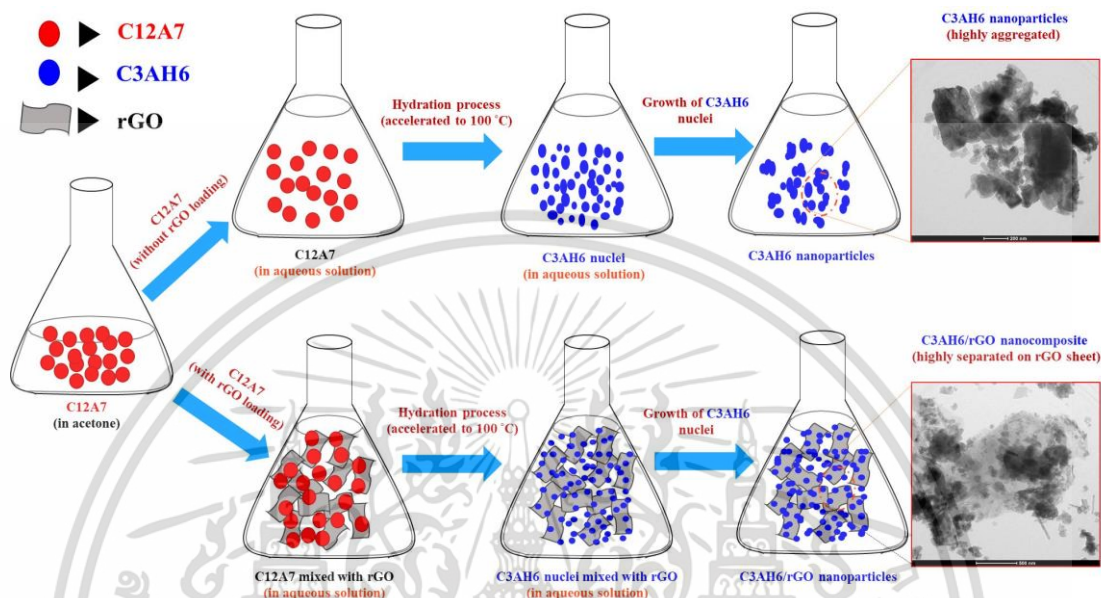


Figure 1.2 Synthesis and the differences between the two processes to produce nanometer sized C3AH6 and nanocomposited C3AH6-rGO.

This study concerned the development of a concrete block electric power generation from heat and applications in municipal melting furnace or municipal incinerator (CGH) prototype working at high temperature up to 800 °C. The CGH prototype was used with the Seebeck effect schematic by directly converting heat into electricity. The CGH prototype consisted of mechanical components: (1) steel structure with wheels, (2) gas fuel system, (3) waste burning system, (4) combustion chamber, (5) heat storage, (6) TEG and (7) hot exhaust vent. Thermoelectric modules have thermoelectric material synthesized from CaMnO_3 thermoelectric material in a laboratory. A single thermoelectric module showed voltage 155 mV, current 11 mA, and the electrical power 1.7 mW in temperature difference of 470 °C for the high temperature side at 650 °C. The electrical power can be increased by connecting several thermoelectric modules together. The experimental results indicated that the electrical power corresponds accordingly to the number of thermoelectric modules.

เอกสารนี้เป็นเอกสารที่สงวนไว้สำหรับการใช้งานเพื่อการศึกษาเท่านั้น ไม่อนุญาตให้นำไปใช้ประโยชน์ด้านการค้า
ไม่ว่ากรณีใดๆ ทั้งสิ้น อีกทั้งห้ามมิให้ตัดแปลงเนื้อหา และต้องอ้างอิงถึงเจ้าของเอกสารทุกครั้งที่มีการนำไปใช้

It was found that the CGH prototype consisted of 56 thermoelectric modules connected into series could immediately light up the 150 mW LED in temperature difference of $465\text{ }^{\circ}\text{C}$ for the high temperature side at $650\text{ }^{\circ}\text{C}$. The CGH prototype can be applied in thermal energy from various heat sources such as burning biomass, waste industrial heat and power plants. The CGH prototype may be scaled into large-scale thermal power plant to supply the electrical energy. Figure 1.3 showed prototype of concrete block electric power generation from heat and applications in municipal melting furnace or municipal incinerator.

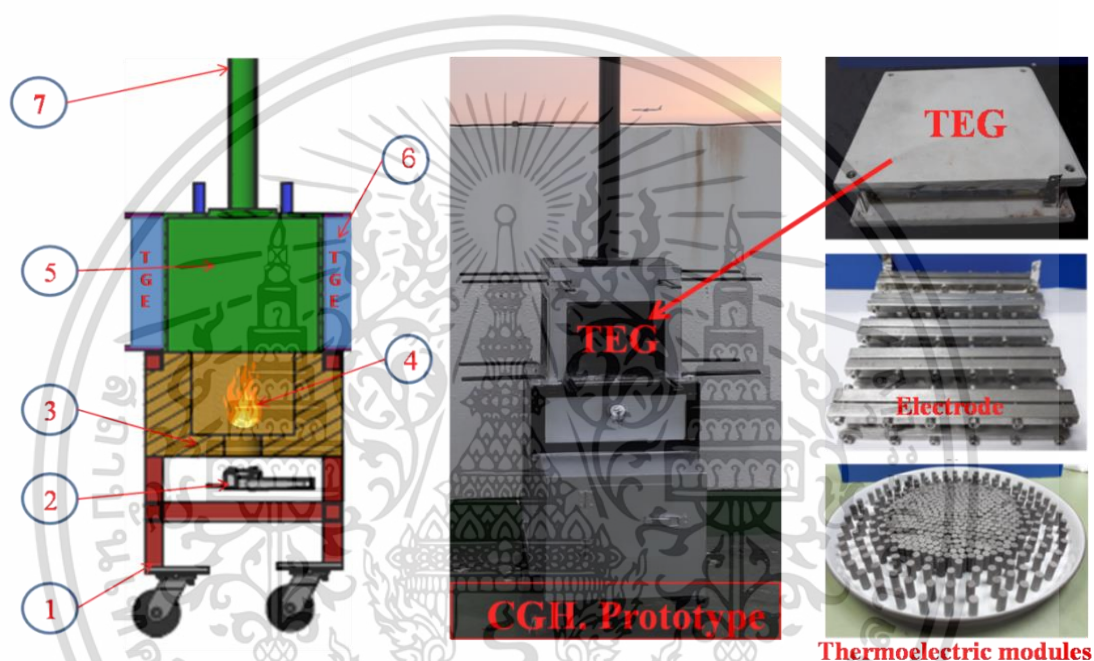


Figure 1.3 Prototype of concrete block electric power generation from heat and applications in municipal melting furnace or municipal incinerator.

This dissertation seeks to study as followed: first, to develop the electrical, thermal conductivity, mechanical, dielectric, and antibacterial properties in which pristine Nanostructure C_3AH_6 compounds were formed by applying hydration method through the use of C_12A_7 powder with a convenient solid-state reaction method. The electrical and thermal conductivity of the C_3AH_6 were developed by fabricating nanocomposites of nanosized C_3AH_6 -rGO by using a rapid cement hydration process in which water is quickly heated at $100\text{ }^{\circ}\text{C}$ in order to enhance the micro hardness, dielectric constant, thermal conductivity, thermoelectric, electrochemical and antibacterial properties. Second, the development of prototype

เอกสารนี้เป็นเอกสารที่สงวนไว้สำหรับการใช้งานเพื่อการศึกษาเท่านั้น ไม่อนุญาตให้นำไปใช้ประโยชน์ด้านการค้า
ไม่ว่ากรณีใดๆ ทั้งสิ้น อีกทั้งห้ามมิให้ตัดแปลงเนื้อหา และต้องอ้างอิงถึงเจ้าของเอกสารทุกครั้งที่มีการนำไปใช้

of concrete block electric power generation from heat and applications in municipal melting furnace or municipal incinerator (CGH) prototype working at high temperature up to 800 °C. The CGH prototype was used with the Seebeck effect schematic by directly converting heat into electricity from thermoelectric modules synthesizing from CaMnO_3 thermoelectric material in a laboratory. The experimental results indicated that the electrical power corresponds accordingly to the number of thermoelectric modules.

1.2 Objectives of the study

- 1) To synthesize and improve nanostructured tricalcium aluminate hexahydrate (C_3AH_6) cement and $\text{C}_3\text{AH}_6/\text{rGO}$ nanocomposites.
- 2) To study the potential use of the C_3AH_6 and $\text{C}_3\text{AH}_6/\text{rGO}$ on smart cement nanocomposites.
- 3) To develop the electrical power generated concrete blocks from heat by using CaMnO_3 as thermoelectric materials.

1.3 Scopes of the study

- 1) Synthesis of C_3AH_6 cements by using hydration method through the use of C_{12}A_7 powder as precursor.
- 2) Synthesis of $\text{C}_3\text{AH}_6/\text{rGO}$ nanocomposites based on cement materials.
- 3) Characterization and properties measurements of all the prepared cement samples.
- 4) Development of electrical power generated concrete blocks from heat using CaMnO_3 as the prototype of thermoelectric material modules.

1.4 Benefits of the study

- 1) Knowledge on the synthesis of C_3AH_6 nano-cements.
- 2) Understanding of the use of $\text{C}_3\text{AH}_6/\text{rGO}$ nanocomposite on smart cement material.
- 3) Understanding of the development of electrical power generated concrete blocks from heat by using CaMnO_3 as a prototype of thermoelectric materials module.

เอกสารนี้เป็นเอกสารที่สงวนไว้สำหรับการใช้งานเพื่อการศึกษาเท่านั้น ไม่อนุญาตให้นำไปใช้ประโยชน์ด้านการค้า ไม่ว่าจะกรณีใดๆ ทั้งสิ้น อีกทั้งห้ามมิให้ตัดแปลงเนื้อหา และต้องอ้างอิงถึงเจ้าของเอกสารทุกครั้งที่มีการนำไปใช้

Chapter 2

Theory and Literature Reviews

2.1 Fundamental properties of $\text{Ca}_{12}\text{Al}_{14}\text{O}_{33}$ mayenite

Chemical formula of mayenite can be written as follows: $12\text{CaO}\cdot 7\text{Al}_2\text{O}_3$ (C12A7), $\text{Ca}_{24}\text{Al}_{28}\text{O}_{66}$. C12A7 cement structure is connected by Ca, Al and O atoms conjoint cement configuration creating void nanometer-sized cages inside structures, while each cage shows a nanoporous with a size of 0.4 nm, as shown in Figure 2.1. A cubic unit cell of the C12A7 cement structure in different colors including red, blue and orange balls illustrating illustrate Al, Ca and O atoms. The grey sphere shows a cage-like shape of the structure. The crystal structure of C12A7 has nanocages with a set inner diameter. An insulating unit cell of C12A7 structure consists of 2 molecules with 1 occupied by crystallographic nanocage and existing 4^+ charged of a cage wall as expressed by $[\text{Ca}_{24}\text{Al}_{28}\text{O}_{66}]^{4+}$. By capturing 2 free oxygen ions (O^{2-}) in cages, or as called as extra framework, the 2 cages in a unit cell naturally fosters neutrality of the electricity. The C12A7 structure indicated that, as replaced by free oxygen anions: O^- , O^{2-} , free O^{2-} ions are flexibly bounded to the lattice framework as expressed by C12A7: O^{2-} . A change of anion in the cage dominates the band of energy structure as a result of a transition of the optical, thermal and electrical properties.

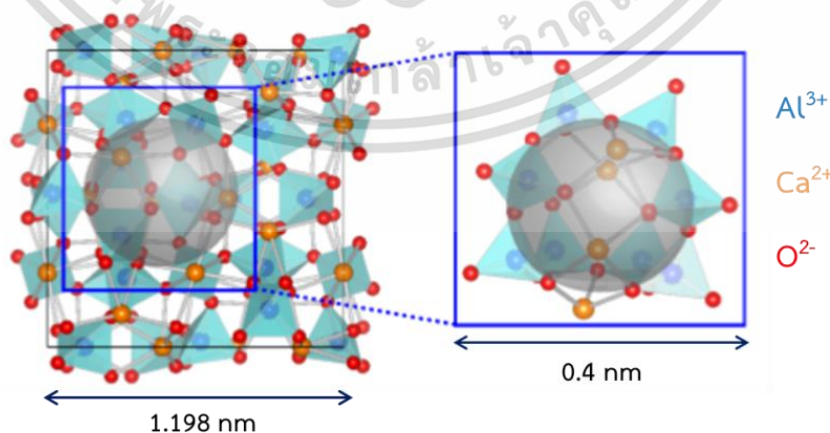


Figure 2.1 A cubic unit cell of the C12A7 mayenite structure [20].

เอกสารนี้เป็นเอกสารที่ลงวันไว้สำหรับการใช้งานเพื่อการศึกษาเท่านั้น ไม่อนุญาตให้นำไปใช้ประโยชน์ด้านการค้า
ไม่ว่ากรณีใดๆ ทั้งสิ้น อีกทั้งห้ามมิให้ตัดแปลงเนื้อหา และต้องอ้างอิงถึงเจ้าของเอกสารทุกครั้งที่มีการนำไปใช้

2.2 Fundamental properties of $\text{Ca}_3\text{Al}_2(\text{OH})_{12}$ (C3AH6) katoite

The chemical formula of katoite can be written as follows: Tricalcium Aluminate Hexahydrate, $\text{Ca}_3\text{Al}_2(\text{OH})_{12}$, $3\text{CaO}\cdot\text{Al}_2\text{O}_3\cdot 6\text{H}_2\text{O}$ and C3AH6. Cement hydration process occurs when the C3AH6 cement reacts to water. The pure C3AH6 cement hydrate, or also known as katoite cement mineral and in hydrogarnet group, contains the following stoichiometric formula C3AH6 [8]. At room temperature, this is the solid cement structure of the calcium aluminate cement hydrates. Crystal structure displayed in a cubic unit cell existing in the space group of $Ia\bar{3}d$ (230). The C3AH6 cement contained a $\text{Ca}_3\text{Al}_2(\text{OH})_3$ formula. A Ca site as assigned by divalent cations (Ca^{2+}), An Al site occupied by trivalent cations (Al^{3+}) in an octahedral and a tetrahedral framework and a 4OH^- situating within the tetrahedral framework. For charge balancing, a H^+ ions bonded with each of the four O atoms as surrounded by empty site. The unit cell contains 8 of the C3AH6 units with 132 atoms (24 Ca, 16 Al, 96 H and 96 O) created by a three dimensional framework with $\text{Ca}(\text{OH})_8$ dodecahedra sub-structure and the $\text{Al}(\text{OH})_6$ octahedra sub-structure. The unit cell structure indicates lattice parameters of a lattice constant $a=12.55695 \text{ \AA}$, and unit cell volume $V=1986 \text{ \AA}^3$. Naturally, C3AH6 cement can be created crystal phase at high ambient temperatures. The C3AH6 cement hydrate can exist by using C12A7 cement reacted rapidly with water at accelerated temperatures above 60°C . For physical properties, there is no report on preparing process for nanostructure of C3AH6 cement hydrate and its effect on optical, thermal, dielectric and thermoelectric properties.

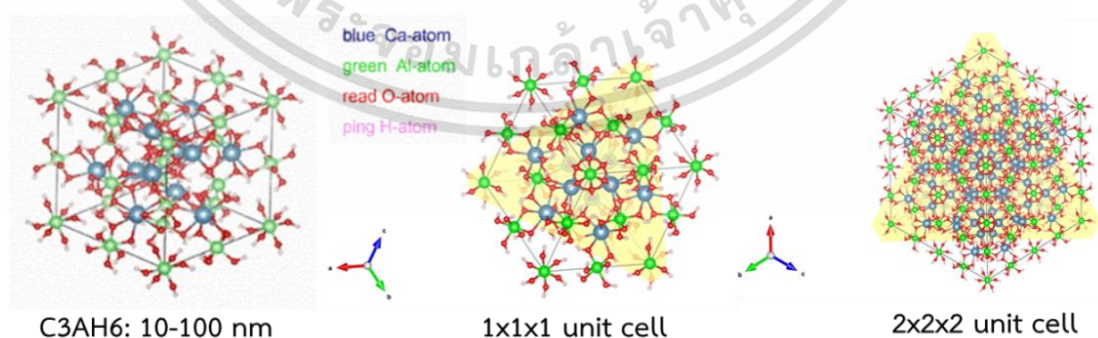


Figure 2.2 A cubic unit cell of C3AH6 structure: blue, green red and pink balls represent Ca, Al, O, and H atoms and C3AH6 1x1x1, 2x2x2 unit cell.

เอกสารนี้เป็นเอกสารที่สงวนไว้สำหรับการใช้งานเพื่อการศึกษาเท่านั้น ไม่อนุญาตให้นำไปใช้ประโยชน์ด้านการค้า ไม่ว่าจะกรณีใดๆ ทั้งสิ้น อีกทั้งห้ามมิให้ตัดแปลงเนื้อหา และต้องอ้างอิงถึงเจ้าของเอกสารทุกครั้งที่มีการนำไปใช้

2.3 Synthesis of Graphene

2.3.1 Introduction [21]

The current research in nanotechnology describes graphene as one of the most studied carbon nanomaterials. Due to its potential applications for future electronics, graphene drew utmost attention in terms of condensed-matter physics and materials science. Graphene is a hexagonal honeycomb lattice, which creates 3D bulk graphite, once layers of single honeycomb graphitic lattices are arranged and confined by a van der Waals force as illustrated on the right side of Figure 2.3. In addition, graphene can also create a sphere which is called 0-dimensional fullerene or rolled up because of its axis to create 1-dimensional cylindrical structure or known as carbon nanotube (CNT). Single graphitic layer is generally referred to as monolayer graphene, bilayer and trilayer graphene for and three graphitic layers and thick graphene-nanocrystalline thin graphite or multilayer graphene for those beyond 5 and up to 30 layers of graphene.



Figure 2.3 The 2D hexagonal nanosheets of graphene (top) and relevant structures: fullerene (bottom left), carbon nanotubes (bottom centre) and graphite (bottom right) [22].

เอกสารนี้เป็นเอกสารที่สงวนไว้สำหรับการใช้งานเพื่อการศึกษาเท่านั้น ไม่อนุญาตให้นำไปใช้ประโยชน์ด้านการค้า ไม่ว่าจะกรณีใดๆ ทั้งสิ้น อีกทั้งห้ามมิให้ตัดแปลงเนื้อหา และต้องอ้างอิงถึงเจ้าของเอกสารทุกครั้งที่มีการนำไปใช้

With high carrier density, high mobility, optical conductivity and mechanical properties, graphene illustrates outstanding electrical and thermal conductivity. In addition, in terms of electrical properties, room temperature, quantum Hall effect ballistic charge transport, high charge carrier density, and tunable band gap are similarly outstanding properties of graphene. Graphene properties also vary with stacked layers, therefore, creating possibility to apply to different devices. In the case of bilayer graphene shows gapless semiconductor pattern which takes place once parabolic bands of k and k' reach the single point at the Brillouin Zone. Due to graphene's outstanding electrical properties, it has drawn attentions to application to future electronics, for example, photonic devices, integrated circuit components, flexible displays, ballistic transistors, sensors and transparent conducting electrodes. These properties allow graphene to be used as a medium in a FET. High optical transparency and high electrical conductivity also prove graphene as a possible option for conducting transparent electrodes, necessary for applications in devices such as touch screen, organic photovoltaic cells, organic light-emitting diodes (OLEDs) and liquid crystal displays. Several devices that utilize graphene such as Li-ion battery, solar cells, supercapacitor, transistors and photonic devices, have illustrated its potential applications. Different reports explained graphene synthesis as stemming from chemical process, chemical exfoliation, mechanical exfoliation from graphite, chemical vapor deposition (CVD) and epitaxy on Si C surface. Accordingly, graphene brought about significant improvements to both industrial and scientific community as demonstrated in Figure 2.4 the scalability against cost and graphene quality trends that alter according to various synthesis techniques.

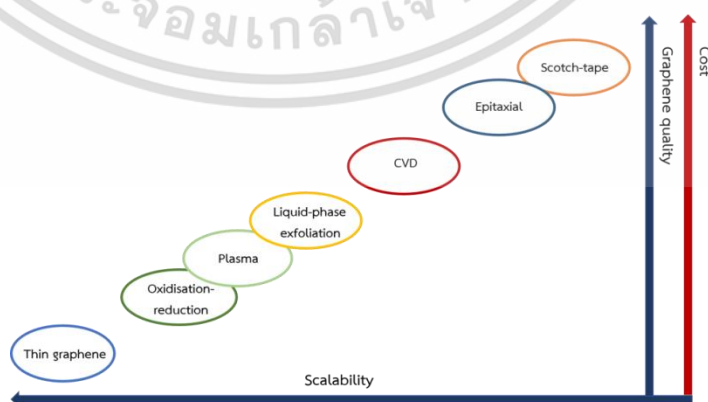


Figure 2.4 Scalability against cost and graphene quality trends for various synthesis graphene techniques. (Image reproduced from Ref. [21]).

เอกสารนี้เป็นเอกสารที่สงวนไว้สำหรับการใช้งานเพื่อการศึกษาเท่านั้น เมื่ออนุญาตให้นำไปใช้ประโยชน์ด้านการค้า ไม่ว่าจะกรณีใดๆ ทั้งสิ้น อีกทั้งห้ามมิให้ดัดแปลงเนื้อหา และต้องอ้างอิงถึงเจ้าของเอกสารทุกครั้งที่มีการนำไปใช้

2.3.2 An Overview of graphene synthesis methodologies [21]

Different methodologies, to date, have been developed to test graphene synthesis and graphene-derived materials namely: chemical synthesis, mechanical cleaving (exfoliation), thermal CVD synthesis, chemical exfoliation and epitaxial growth methods. Several other processes such as electrochemical exfoliation, unzipping of CNT, laser ablation were also developed. The methodologies of graphene synthesis can be categorized into top-down and bottom-up approach. The top-down approach describes nanoscale materials synthesis by minimizing its sizes from bulk. Meanwhile, the bottom-up approach describes the formation of a structure by atomic or molecular arrangements. For instance, all types of exfoliation process are considered top-down, while epitaxial processes, CVD and pyrolysis are bottom-up (Figure 2.5). In 1999, mechanical cleaving of highly ordered pyrolytic graphite by atomic force microscopy (AFM). Using AFM cantilever, the mechanical cleaving method was able to concoct ~10 nm thick of graphene. In 2004, the idea of singular atomic thick layer graphene fabrication was mentioned when a tape was used for exfoliating graphene layers to create bulk graphite. In the same way, chemical exfoliation is a technique that exfoliates a solution-dispersed graphite by injecting a sizable alkali ion between layers of graphite. Similar to CNT synthesis, catalytic thermal CVD is proven as the most appropriate technique.

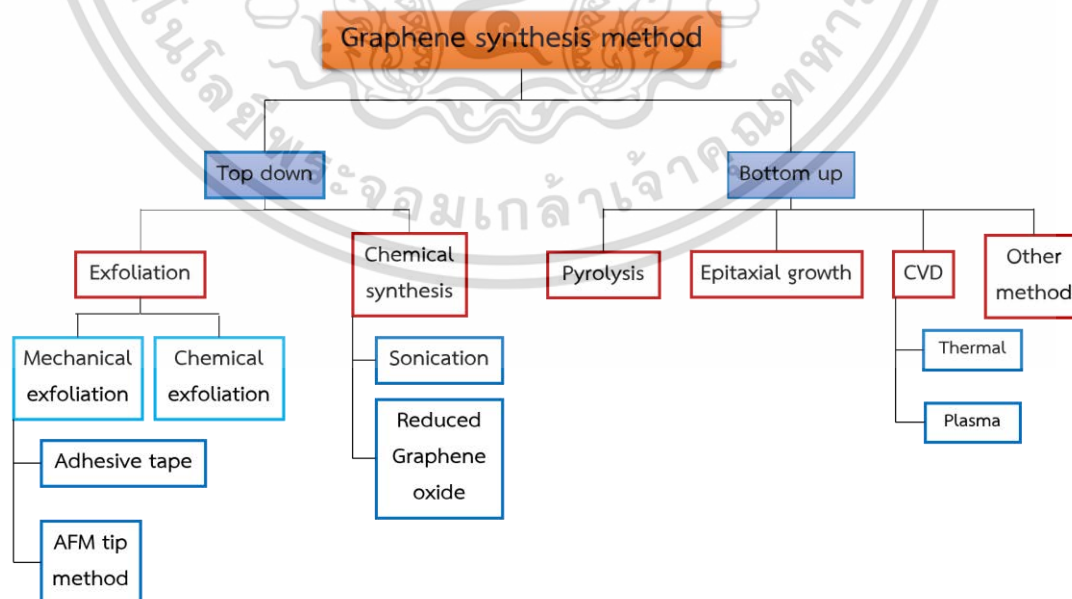
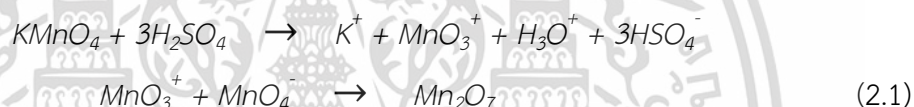


Figure 2.5 Classification of graphene synthesis processes.

เอกสารนี้เป็นเอกสารที่สงวนไว้สำหรับการใช้งานเพื่อการศึกษาเท่านั้น ไม่อนุญาตให้นำไปใช้ประโยชน์ด้านการค้า ไม่ว่าจะกรณีใดๆ ทั้งสิ้น อีกทั้งห้ามมิให้ตัดแปลงเนื้อหา และต้องอ้างอิงถึงเจ้าของเอกสารทุกครั้งที่มีการนำไปใช้

2.3.3 Chemical Synthesis: graphene from reduced graphene oxide [21]

Graphene's chemical synthesis is an indirect top-down technique. It is the first technique which indicated synthesis of graphene by chemical route. Boehm et al., in 1962, showed monolayer flakes of minimized GO. This technique was just recognized by the Nobel Prize. Three well-known GO synthesis techniques include the Brodie method, the Staudenmaier method, and the Hummers and Offeman method. These techniques involve graphite oxidation through effective oxidants and acids. The level of oxidation differ according to reactions of conditions such as temperature, pressure, stoichiometry, as well as the graphite type utilized as a starting material. Hummers proposed the Hummers method, or graphite oxidation by combining graphite with potassium permanganate, sulfuric acid and sodium nitrite. During this procedure, potassium permanganate and sulfuric acid react and form dimanganese heptoxide, which is an effective oxidizing agent as illustrated below:



Chemical reduction procedure was undergone by utilizing dimethylhydrazine or hydrazine with either surfactant or polymer to create uniformed colloidal suspensions of graphene. As reported in a few researches, the reduction of GO is performed by applying sodium borohydrate (NaBH_4) and hydroquinone. In Figure 2.6, the process chart is indicated in the schematic below.

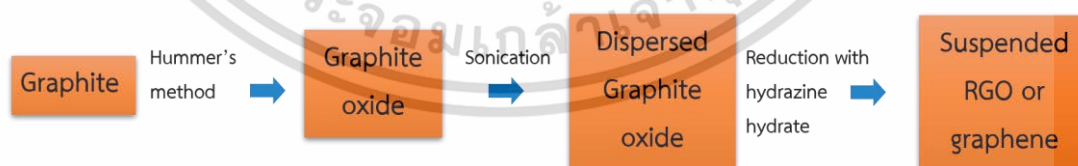


Figure 2.6 The process flow chart graphene synthesis derived from reduced graphene oxide.

2.4 Fundamental of thermoelectric

2.4.1 Introduction [23]

Thermoelectric is linked to thermal and electrical occurrences. Thermoelectric procedures has the ability to turn energy from thermal to electrical. Thermoelectric generators illustrate capacity heat recovery of waste from automotive vehicles and power plants. Today, study of thermoelectric is crucial with many useful applications. Introduced in the early nineteenth century, before that there have not been considerable improvements for thermoelectricity in terms of materials or efficiency until the recent work in nanotechnology, which resulted in a significant performance improvement. Therefore, it is essential to grasp the rudiments of thermo-electrics development and thermal design. Back in 1821, Thomas J. Seebeck found that a circuit consisted of two different wires, when one of the junctions was heated, it can generate an electromotive force or a potential difference. This is also known as the Seebeck effect. Thirteen years later, Jean Peltier discovered, in 1834, that depending on its direction, through a thermocouple, the passage of an electric current can produce heating or cooling effect. This is also known as the reverse process or the Peltier effect. In 1841, James P. Joule discovered Joule heating. Then William Thomson learned, in 1854, a difference in temperature between any two points of a current-carrying conductor, depending on the direction of current and material, leads to either heat absorbs or liberation. This discovery contributed to the Peltier heating or known as the Thomson effect. Mechanisms of thermoelectricity were not properly studied until the end of the nineteenth century with the introduction of electrons. Today, it is a common knowledge that, even at room temperature, an electric field, thermal energy or solar energy can liberate electrons from their atomic binding, moving them to where the electrons can move freely. This is why electrostatics exist everywhere. Nevertheless, as shown in Figure 2.7, once a difference in temperature across a conductor is detected, the hot region of the conductor generates more free electrons, then accelerates diffusion of these electrons which naturally resulted from the movement from the hot region to the cold region. In contrast, via Coulomb forces, the distribution of electron generates an electric field, which then leads the electrons to move from the hot region to the cold region. Thus, a heat flow takes place in the conversed direction of the current. This process is shown in Figure 2.7.

เอกสารนี้เป็นเอกสารที่สงวนไว้สำหรับการใช้งานเพื่อการศึกษาเท่านั้น ไม่อนุญาตให้นำไปใช้ประโยชน์ด้านการค้า
ไม่ว่ากรณีใดๆ ทั้งสิ้น อีกทั้งห้ามมิให้ตัดแปลงเนื้อหา และต้องอ้างอิงถึงเจ้าของเอกสารทุกครั้งที่มีการนำไปใช้

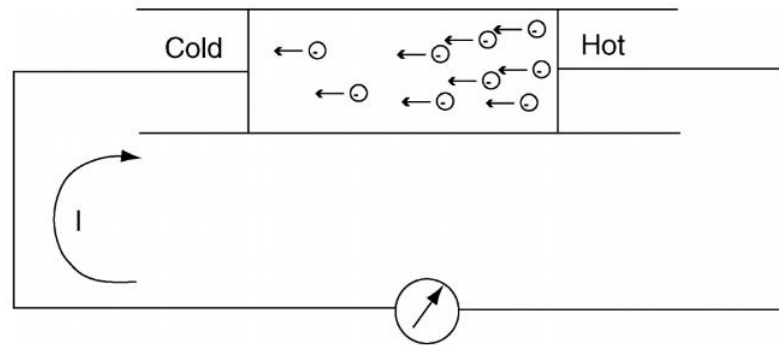


Figure 2.7 Electron concentrations in a thermoelectric material [23].

2.4.2 Thermoelectric Effect [24]

Seebeck Effect

The Seebeck effect refers to the conversion of a temperature difference into an electric current. Illustrated in Figure 2.8, wire A is connected at both ends to wire B and a voltmeter is put in wire B. With temperature difference being imposed between two junctions; it is learned that voltage V or potential difference will appear on the voltmeter. The potential difference V is:

$$V = \alpha_{AB} \Delta T \quad (2.2)$$

Where $\Delta T = T_h - T_c$ and α_{AB} is known as the Seebeck coefficient, which is measured in $\mu\text{V}/\text{K}$. As shown in Figure 2.8, if emf tends to drive an electric current through wire A from the hot junction to the cold junction, the sign of α is then positive. In practice, it is rare to measure the absolute Seebeck coefficient as the voltage meter usually reads relative Seebeck coefficient between wire A and B. The absolute Seebeck coefficient can be derived from calculating the Thomson coefficient.

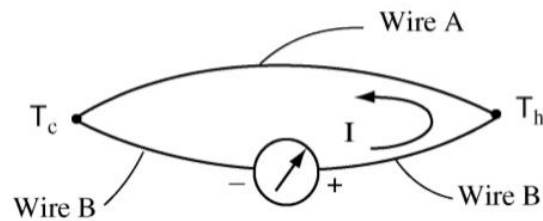


Figure 2.8 Thermocouple.

Peltier Effect

As outlined in Figure 2.9, when a current flows across a junction between two different wires, it is discovered, in order to keep its temperature constant, heat must be consistently added. Heat is commensurable to the current flow and altering the sign once the current is reversed. Therefore, the Peltier heat can be explained in the equation 2.3.

$$\dot{Q}_{Peltier} = \pi_{AB} I \quad (2.3)$$

Where π_{AB} is the Peltier coefficient and the sign of π_{AB} is positive if the junction at which the current enters wire A is heated, and the junction at which the current leaves wire A is cooled. The Peltier heating or cooling is reversible between heat and electricity. This implies that heating will generate electricity and electricity will generate heating without energy loss.

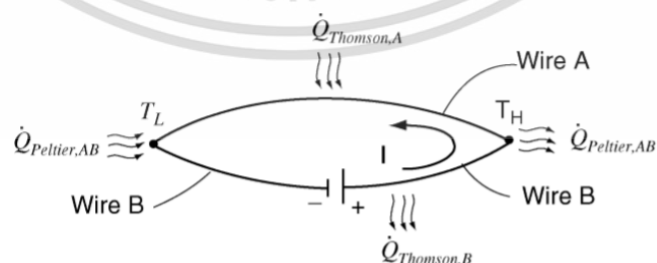


Figure 2.9 Schematic for the Peltier effect and the Thomson effect.

เอกสารนี้เป็นเอกสารที่สงวนไว้สำหรับการใช้งานเพื่อการศึกษาเท่านั้น ไม่อนุญาตให้นำไปใช้ประโยชน์ด้านการค้า ไม่ว่าจะกรณีใดๆ ทั้งสิ้น อีกทั้งห้ามมิให้ดัดแปลงเนื้อหา และต้องอ้างอิงถึงเจ้าของเอกสารทุกครั้งที่มีการนำไปใช้

Thomson Effect

As illustrated in Figure 2.9, which is an experimental observation depending on the material, when current flows, heat is absorbed into wire A with negative temperature gradient and liberated in wire B because of the positive temperature gradient [24]. The Thomson heat is commensurable to both electric currents, and is schematically displayed in Figure 2.9. Therefore, the Thomson heat can be explained in the equation 2.4.

$$\dot{Q}_{Thomson} = \tau_{AB} I \Delta T \quad (2.4)$$

Where τ is the Thomson coefficient. Among the three thermoelectric coefficients, the Thomson coefficient is the most unique as it is the only thermoelectric coefficient that is measurable for individual materials. There is also another form of heat, or Joule heating.

Thomson Relationships

1854, Thomson [25] thermodynamically observed the relationships as exhibited in Equations (2.5) and (2.6) by adopting the first and second laws of thermodynamics with assumptions that the reversible and irreversible processes in thermoelectricity are independent of one another. The assumption remained a challenge until the introduction of new thermodynamics. Compared to the Peltier effect, the Thomson effect is less significant. These relationships were later proven by experiments.

$$\pi_{AB} = \alpha_{AB} \Delta T \quad (2.5)$$

$$\tau_{AB} = \frac{d\alpha_{AB}}{dt} \quad (2.6)$$

Equation (2.5) leads to the very useful Peltier cooling in Equation (2.3) as

$$\dot{Q}_{Peltier} = \alpha_{AB} I \Delta T \quad (2.7)$$

เอกสารนี้เป็นเอกสารที่สงวนไว้สำหรับการใช้งานเพื่อการศึกษาเท่านั้น ไม่อนุญาตให้นำไปใช้ประโยชน์ด้านการค้า
ไม่ว่ากรณีใดๆ ทั้งสิ้น อีกทั้งห้ามมิให้ตัดแปลงเนื้อหา และต้องอ้างอิงถึงเจ้าของเอกสารทุกครั้งที่มีการนำไปใช้

Where T is the temperature at a junction between two different materials and the dot above the heat Q indicates the amount of heat transported per unit time.

2.4.3 The Figure of Merit

The performance of thermoelectric devices is assessed by equation 2.8.

$$ZT = \frac{\alpha^2}{\sigma k} = \frac{\alpha^2 \sigma}{k} \quad (2.8)$$

Where ZT = is the figure of merit (1/K)

α = is the seebeck coefficient ($\mu\text{V/K}$)

ρ = is the electrical resistivity (Ωcm)

$\sigma = 1/\rho =$ is the electrical conductivity (Ωcm)⁻¹

k = is the thermal conductivity (W/mK)

The figure of merit is defined as ZT , where T is an absolute temperature. There is no limitation on ZT . However, it has been defined to the values around $ZT \approx 1$ in existing devices. The larger ZT value, the greater the energy conversion efficiency. The quantity of $\alpha^2 \sigma$ is defined as the power factor. Thus, both the Seebeck coefficient α and electrical conductivity σ must be maximized, while the thermal conductivity k must be minimized.

2.4.4 New-Generation thermoelectric

Although, in 1821, Seebeck discovered thermoelectric phenomena and Altenkirch, in 1911, defined Equation (1.7), it took until 1950s and 1960s to develop the first functioning devices, which are known today as the first generation of thermoelectric averaging at $Z \sim 1.0$. Devices made of these can operate at $\sim 5\%$ conversion efficiency. After certain stagnant years, in 1990s, new theories on the size

เอกสารนี้เป็นเอกสารที่สงวนไว้สำหรับการใช้งานเพื่อการศึกษาเท่านั้น ไม่อนุญาตให้นำไปใช้ประโยชน์ด้านการค้า
ไม่ว่ากรณีใดๆ ทั้งสิ้น อีกทั้งห้ามมิให้ตัดแปลงเนื้อหา และต้องอ้างอิงถึงเจ้าของเอกสารทุกครั้งที่มีการนำไปใช้

effects of thermoelectric properties led to new experimental research which finally brought important developments in the later decades. Although the original theoretical ideas revolved around possibilities of increasing the power factor, experimental revolutions were accomplished mostly by minimizing the lattice thermal conductivity. Among various research methodologies, one has developed and has caused an almost doubling of ZT at high temperatures and has defined the second generation of bulk thermoelectric materials with ZT in the range of 1.3–1.7. This approach utilizes nanoscale precipitates and composition in homogeneities to significantly suppress the lattice thermal conductivity. Recently, the third-generation bulk thermoelectric are under development which simultaneously combines different innovative ZT -enhancing approaches including development of Seebeck coefficients through valence band convergence, and reduction of the lattice thermal conductivity through all length-scale lattice disorder. The third generation of bulk thermoelectric illustrates high ZT , ranging from 1.8 to 2.2, relating to the difference in temperature, with conversion efficiency estimated increase to ~15–20%. Are shown in Table 2.1 and by the in Figure 2.10.

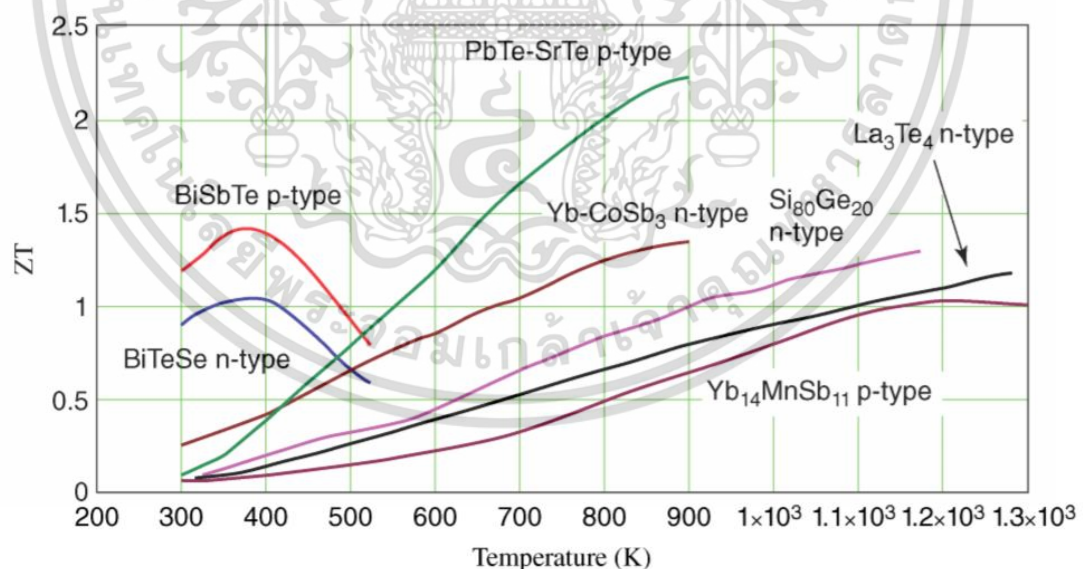


Figure 2.10 Dimensionless figures of merit for various nanocomposite thermoelectric materials.

เอกสารนี้เป็นเอกสารที่สงวนไว้สำหรับการใช้งานเพื่อการศึกษาเท่านั้น ไม่อนุญาตให้นำไปใช้ประโยชน์ด้านการค้า ไม่ว่าจะกรณีใดๆ ทั้งสิ้น อีกทั้งห้ามมิให้ดัดแปลงเนื้อหา และต้องอ้างอิงถึงเจ้าของเอกสารทุกครั้งที่มีการนำไปใช้

Table 2.1 Thermoelectric properties of single crystal and bulk nanocomposite semiconductors [23]

	Type	Temperature (K)	$ \alpha $ ($\mu\text{V/K}$)	σ (Ωcm) ⁻¹	k_e (W/mK)	k (W/mK)	ZT
Bi₂Te₃	p-type single crystals	300	230	500	0.6	2.0	0.5
BiSbTe	p-type, nanocomposites	400	220	700	0.6	1.0	1.4
Bi₂Te_{2.7}Se_{0.3}	n-type nanocomposites	400	210	700	0.6	1.2	1.0
PbTe-SrTe	p-type nanocomposites	900	270	300	0.4	1.1	2.2
Si₇₀Ge₃₀	n-type single crystals	1000	350	320	0.5	4.0	0.8
Si₈₀Ge₂₀	n-type nanocomposites	1200	250	400	0.5	2.8	1.3
CoSb₃	n-type single crystals	800	240	800	0.5	4.0	0.6
Yb-CoSb₃	n-type, Yb-filled skutterudites	800	200	1600	2.0	3.2	1.3
Yb₁₄MnSb₁₁	p-type, Zintl compound	1200	190	200		0.7	1.1
La₃Te₄	n-type single crystals	1200	280	80	0.3	0.7	1.1

2.5 Supercapacitors

The energy storage system is crucial for meeting a rapid growth of global energy demand and handling environment issues that may arise. It has become the focus of different studies with an interest to improve the efficiency of devices' energy storage. Supercapacitor has developed in the past decades and displayed great capability to support the advancements of energy storage [26]. As shown in Figure 2.11, as opposed to conventional devices such as capacitors, batteries and fuel cells, because of its increasingly high power, prolonged cycling ability and fast charge, discharge property, balanced energy density and rate capability, supercapacitor is one of the most preferred devices in terms of energy storage. Therefore, supercapacitor contains competitive advantages as promising energy storage devices suitable for applications, for example, satellites devices, telecommunication and powered electronics, standby power systems and electrical hybrid vehicles [27].

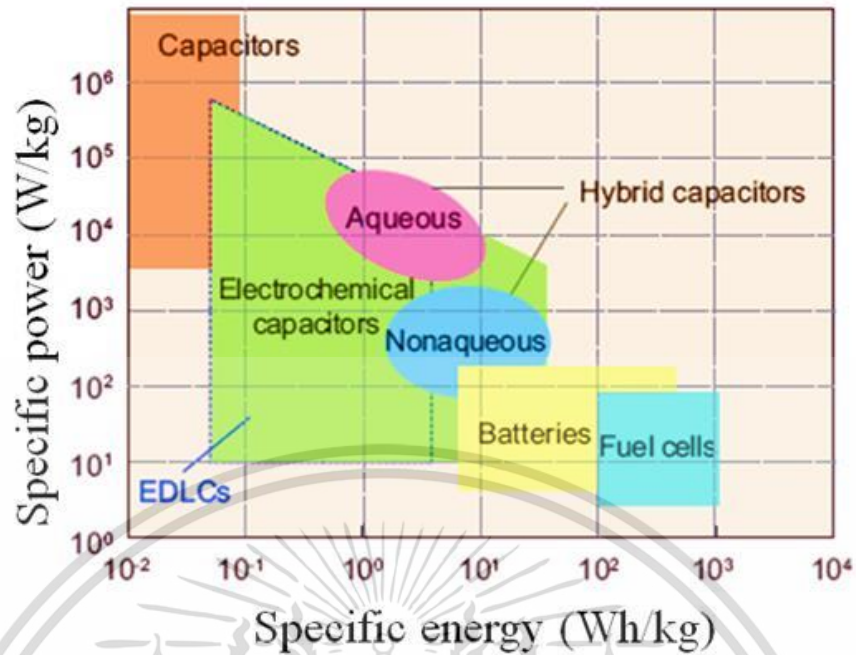


Figure 2.11 Plotting of specific power against specific energy for different types of conventional capacitor, battery and fuel cell technologies [27].

2.5.1 Component and classification of supercapacitor

In general, as shown in Figure 2.12, supercapacitor consists of 3 important parts including the electrodes which are comprised of anode and cathode with significant surface area electrode materials (high porous electrode materials), electrolyte solution and thin dielectrics (separator) to maintain capacitances in magnitude higher than conventional capacitors [27]. In addition, supercapacitor can be categorized into three sorts which are electrochemical double-layer capacitor, pseudocapacitor and hybrid capacitor [27].

เอกสารนี้เป็นเอกสารที่สงวนไว้สำหรับการใช้งานเพื่อการศึกษาเท่านั้น ไม่อนุญาตให้นำไปใช้ประโยชน์ด้านการค้า ไม่ว่าจะกรณีใดๆ ทั้งสิ้น อีกทั้งห้ามมิให้ดัดแปลงเนื้อหา และต้องอ้างอิงถึงเจ้าของเอกสารทุกครั้งที่มีการนำไปใช้

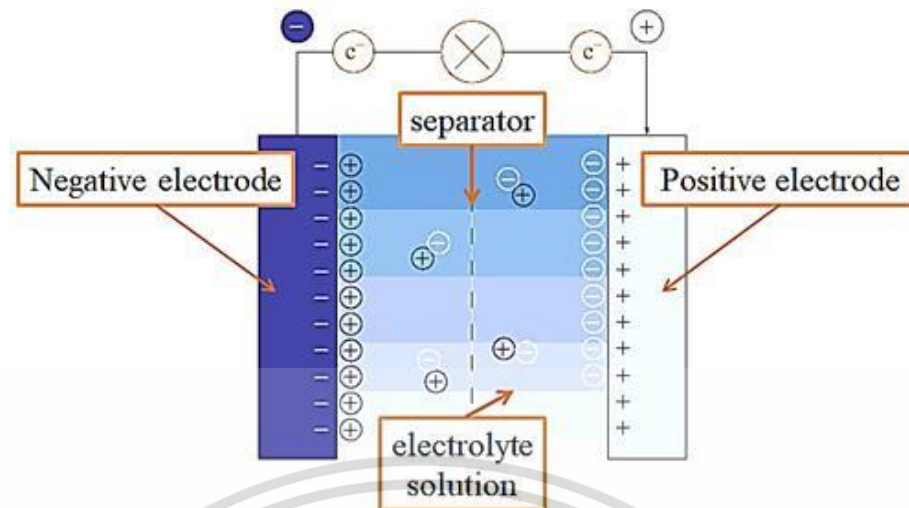


Figure 2.12 Three important parts of supercapacitor: the electrodes (anode and cathode), separator and electrolyte solution [27].

2.5.1.1 Electrochemical double-layer capacitors (EDLCs)

This type of superconductor is built from an electrolyte solution, and thin separator dielectrics which are two material-based electrodes. Figure 2.13 (a) indicates the schematic of general EDLC which are similar to conventional capacitor. The EDLC energy storage is a charge-discharge procedure depending on electrostatic on the electrode surfaces. Therefore, double-layer of charge state is formed at each electrode. These double-layers led to a decline in the distance between electrodes but an increase in surface area, allowing EDLCs to maintain higher energy densities when compared to regular capacitors. Since it does not transfer charge between electrolyte and electrode nor chemical or composition changes related to non-Faradaic procedures. Accordingly, EDLCs charge storage is highly reversible and cycling stable [27].

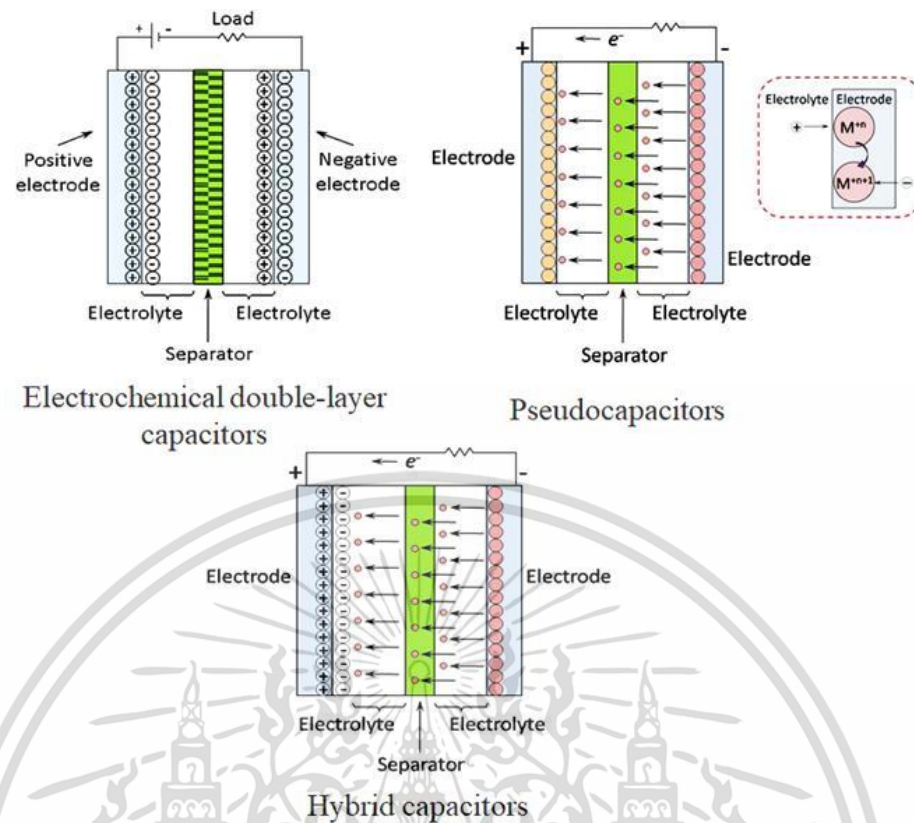


Figure 2.13 Schematic representations of supercapacitor types [28].

2.5.1.2 Pseudocapacitor

Pseudocapacitor differs from EDLCs because storage charge of the pseudocapacitor relies on Faradaic redox reaction through the transfer of anode and cathode electrode and electrolyte solution. This is also achieved through intercalation processes, reduction-oxidation reactions and electro sorption. Compared to EDLCs, the Faradaic procedures let pseudocapacitors increase capacitances and energy densities [28].

2.5.1.3 Hybrid capacitors

Hybrid capacitors sought to utilize its advantages while addressing drawbacks of EDLCs and pseudo capacitors to create improved qualities for better performance. Applying both Faradaic and non-Faradaic procedures in storage charge, hybrid capacitors maintained specific energy and specific power greater than that of EDLCs by not having to give up its affordability and cycling stability which conversely have held down the success of pseudo capacitors [28].

เอกสารนี้เป็นเอกสารที่สงวนไว้สำหรับการใช้งานเพื่อการศึกษาเท่านั้น ไม่อนุญาตให้นำไปใช้ประโยชน์ด้านการค้า ไม่ว่าจะกรณีใดๆ ทั้งสิ้น อีกทั้งห้ามมิให้ตัดแปลงเนื้อหา และต้องอ้างอิงถึงเจ้าของเอกสารทุกครั้งที่มีการนำไปใช้

2.5.2 Supercapacitor Performance [29]

Key parameters are applied to quantitatively assess the supercapacitor's performance include capacitance and cycle stability. All adopted techniques to derive these parameters are electrochemical ones.

2.5.2.1 Electrochemical cell design for performance testing

The assessment of supercapacitors are categorized into two-electrode and three-electrode systems. By screening electrode materials, the previous configuration concentrates on the estimation of electrode materials.

1) Three-electrode system

The three-electrode system composes of a reference electrode, a working electrode and counter electrode, which are all intermixed to a potentiostat as displayed in Figure 2.14 (a). where the working electrode is generally fabricated by coating active material onto the substrate of a stable electrode. The active material is dissolved in a selected solvent until a slurry with a uniformed dispersion is acquired. Carbon supplements are supplied into this slurry once the active material is highly conductive. There are various types of common reference electrodes with discrete fixed potentials such as normal hydrogen electrode, silver chloride electrode, and saturated calomel electrode.

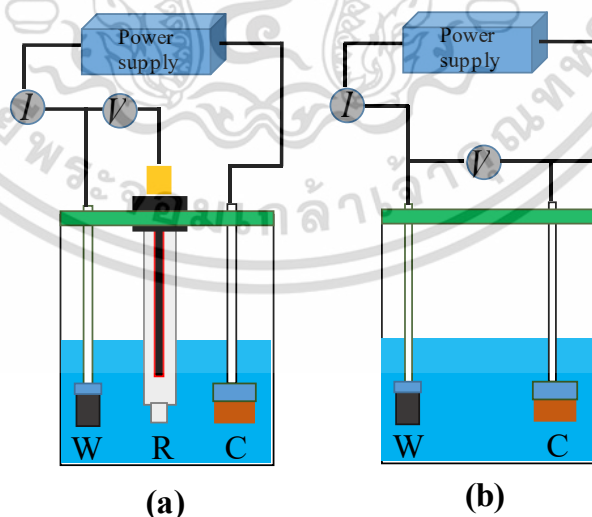


Figure 2.14 Schematic drawing of (a) three-electrode system and (b) two-electrode system: working electrode (W), reference electrode (R), and counter electrode (C) [30].

เอกสารนี้เป็นเอกสารที่สงวนลิขสิทธิ์ไว้สำหรับการใช้งานเพื่อการศึกษาเท่านั้น ไม่อนุญาตให้นำไปใช้ประโยชน์ด้านการค้า ไม่ว่าจะกรณีใดๆ ทั้งสิ้น อีกทั้งห้ามมิให้ตัดแปลงเนื้อหา และต้องอ้างอิงถึงเจ้าของเอกสารทุกครั้งที่มีการนำไปใช้

2) Two-electrode system

Figure 2.14 (b) shows a two-electrode system including a cathode and an anode. The anode and cathode are synthesized by creating slurry from active materials. The slurry is then sprayed or pasted onto the substrate electrode. To assess capability of each electrodes.

2.5.2.2 Specific capacitance (C_s)

Capacitance (C) is an important performance parameter derived from supercapacitors analysis. Specific capacitance (C_s) is calculated in order to compare the performance of electrodes. Cyclic voltammetry (CV) and galvanostatic charge-discharge (GCD) measurements are applied to calculate the capacitance of materials.

1) Measurement of (CV)

Cyclic voltammetry measurement examines the electrochemical phenomena occurred in active materials of the working electrode. This technique applies potential to the working electrode, referencing electrode's fixed potential, which move back and forth between the two predefined potentials in a linear formation. The potential range is confined by the electrolyte's operating stability. Scanning the potential range provides a time-dependent current and plotting this current (I) against the scanned potential (E) graphs a CV curve for capacitance diagnosis as shown in Figure 2.15.

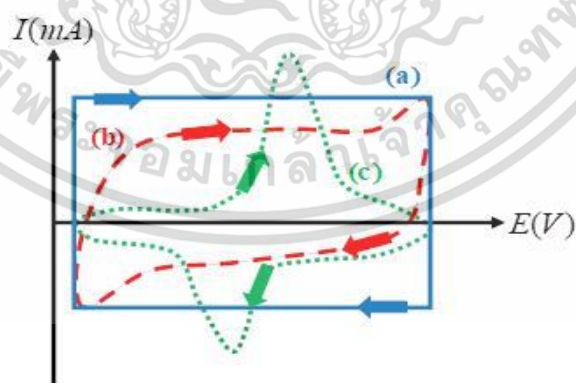


Figure 2.15 Cyclic voltammogram curves of (a) ideal capacitor, (b) EDLC, and (c) pseudocapacitive materials [29].

In theory, a rectangular CV as shown in Figure 2.15 (a) reveal an ideal capacitor. On the other hand, EDLC materials do not behave as expected, leading to a distorted rectangular shape as showed in Figure 2.15 (b). As seen in Figure 2.15 (c), Faradaic reactions from pseudocapacitors output redox peaks. These curves, specific capacitance can be assessed by the following equation;

$$C_{sc} = \frac{\int idV}{2mv\Delta V} \quad (2.9)$$

where $\int idV$ is the integral region of closed CV curve, v the potential scan rate, ΔV the potential range and m the mass of the active material. In addition, potential scan rates pertain crucial impacts of on the measured capacitances. As seen in Figure 2.16, at lower rates, CV curves displays a nearly ideal capacitive pattern with a rectangular shaped curve. Notwithstanding, increasing scan rates alters the ideal rectangular CV curve. At higher scan rates, the electrochemical kinetics cannot compete with an abrupt change in potential.

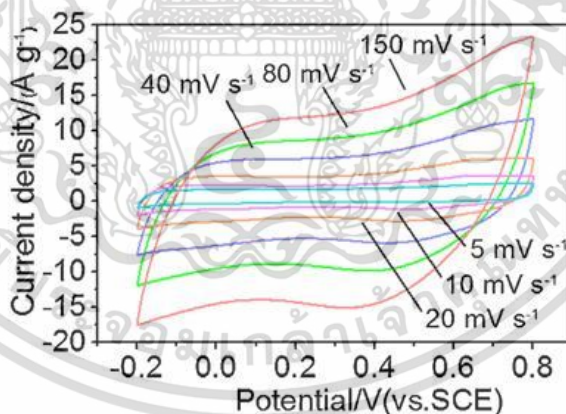


Figure 2.16 Cyclic voltammograms of ordered graphitic mesoporous carbon at different scan rates [30].

เอกสารนี้เป็นเอกสารที่สงวนไว้สำหรับการใช้งานเพื่อการศึกษาเท่านั้น ไม่อนุญาตให้นำไปใช้ประโยชน์ด้านการค้า
ไม่ว่ากรณีใดๆ ทั้งสิ้น อีกทั้งห้ามมิให้ตัดแปลงเนื้อหา และต้องอ้างอิงถึงเจ้าของเอกสารทุกครั้งที่มีการนำไปใช้

2) Galvanostatic charge–discharge (GCD)

The GCD technique utilizes a constant current density (Ag^{-1}) and assesses the possible response according to the duration as showed in Figure 2.11. It is clear that, similar to CV plots, the two materials illustrate different responses. EDLC materials charge and discharge in a linear pattern, while the nonlinearity of pseudo capacitive materials is a result of the redox reactions. In EDLC case, the slope of the discharging section is operated by the following equation;

$$C_{sc} = \frac{I}{(m)dV/dt} \quad (2.10)$$

where C = is the capacitance of the material.

I = is the applied current.

m = is the mass of the active material.

dV/dt = is the slope of the discharging GCD curve.

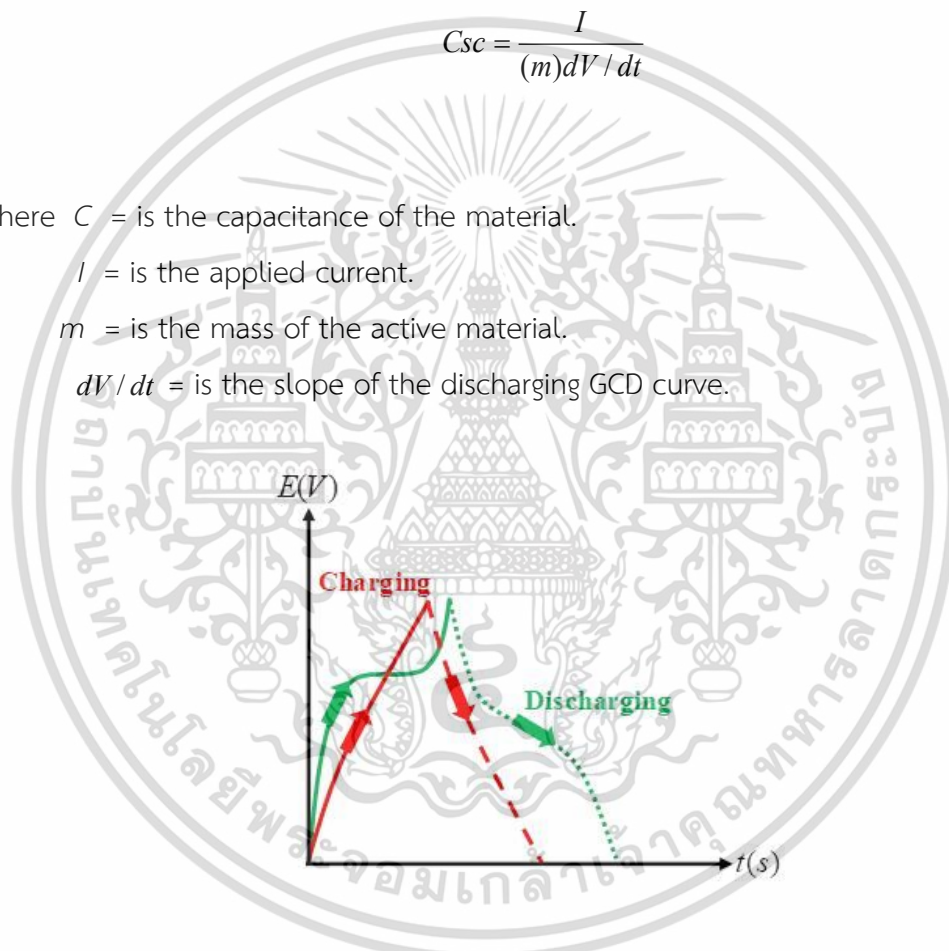


Figure 2.17 Galvanostatic charge–discharge plots of (a) EDLC and(b) pseudocapacitive material [29].

เอกสารนี้เป็นเอกสารที่สงวนไว้สำหรับการใช้งานเพื่อการศึกษาเท่านั้น ไม่อนุญาตให้นำไปใช้ประโยชน์ด้านการค้า
ไม่ว่ากรณีใดๆ ทั้งสิ้น อีกทั้งห้ามมิให้ดัดแปลงเนื้อหา และต้องอ้างอิงถึงเจ้าของเอกสารทุกครั้งที่มีการนำไปใช้

In pseudocapacitive material case, the changed of the equation without the slope is exhibited in the following equation;

$$C_{cs} = \frac{I(\Delta t)}{m\Delta V} \quad (2.11)$$

where Δt = is the total discharge time.

I = is the applied current.

m = is the mass of the active material.

ΔV = is the potential difference at the discharging phase.

In alignment with the dependence on scan rates, current density also impacts specific capacitance.

2.5.2.3 Energy and power densities

Energy and power densities of a supercapacitor are crucial for identifying its performance for actual applications. Both CV and GCD methods can assess densities of power and densities. Specific energy density is expressed by the following equation;

$$E = \frac{1}{2} C_{sc}(\Delta V)^2 \quad (2.12)$$

where C_s = is the specific capacitance from CV or GCD techniques.

ΔV = is the operating potential range.

The squared potential range illustrates operating voltage window that controls density of the energy. Therefore, the electrolyte determines the operating potential range. The specific power density is expressed by the following equation

$$P = \frac{E}{\Delta t} \quad (2.13)$$

where Δt is the rate of discharge of the cell.

เอกสารนี้เป็นเอกสารที่สงวนไว้สำหรับการใช้งานเพื่อการศึกษาเท่านั้น ไม่อนุญาตให้นำไปใช้ประโยชน์ด้านการค้า ไม่ว่าจะกรณีใดๆ ทั้งสิ้น อีกทั้งห้ามมิให้ดัดแปลงเนื้อหา และต้องอ้างอิงถึงเจ้าของเอกสารทุกครั้งที่มีการนำไปใช้

2.6 Literature reviews

2.6.1 $\text{Ca}_{12}\text{Al}_{14}\text{O}_{33}$ (C12A7) cement

Calcium, aluminum and oxygen atoms connect the C12A7 cement structure which contains vacant nano-sized cages with building in nanometer-sized cage within the structure [31-32], while each cage shows a nanoporous with a size of 0.4 nm. A unit cell of insulating C12A7 structure composts of 2 molecules with 1 occupying crystallographic nanocage with presenting 4^+ charged of cage wall as illustrated in $[\text{Ca}_{24}\text{Al}_{28}\text{O}_{66}]^{4+}$ [32]. The 2 cages in a unit cell supports neutrality of electricity by capturing 2 free oxygen ions (O^{2-}) in cages as called extra framework [35]. By previous works in the C12A7 structure have revealed that free O^{2-} ions are flexibly bounded to the lattice framework as expressed by C12A7: O^{2-} . Hayashi et.al. [34] explained that the C12A7 concoction process in dry oxygen atmosphere at temperature 1350°C can generate O^- , and O^{2-} . Furthermore, Lu et. al. [35] and Hayashi et.al. [34] have argued that the free O^- and O^{2-} can be replaced by free electron as conducting C12A7 as exhibited by C12A7 and have detailed its optical and electrical properties. Chaiwat et.al. [20] have also studied the effect of free oxygen radical anions and free electrons in C12A7 structure in optical, electronic and properties of antibacterial activity.

2.6.2 C3AH6 cement and C3AH6-rGO nanocomposites

The CA cement can create anhydrous cement when reacting to water or also known as cement hydration process such an example in $3\text{CaO}\cdot\text{Al}_2\text{O}_3\cdot 6\text{H}_2\text{O}$ (C3AH6), which is called tricalcium aluminate hexahydrate [8,9,10]. The cement hydrate is one of the cement hydrate composites that has been in focus because of its dielectric behavior as presented by electrical response as a function of frequency for capacitors applications [11,12]. The pure C3AH6 cement hydrate, which is called katoite cement mineral and in hydrogarnet group, containing a stoichiometric formula C3AH6 [8]. This solid cement structure of the calcium aluminate cement hydrates at room temperature. The crystal structure shows in a cubic unit cell existing in the space group of $Ia\bar{3}d$ (230). Dilnesa et. al. [13] has described that the C3AH6 cement contained with formula $\text{Ca}_3\text{Al}_2(\text{OH})_4$ of the Ca site assigning by

เอกสารนี้เป็นเอกสารที่สงวนไว้สำหรับการใช้งานเพื่อการศึกษาเท่านั้น ไม่อนุญาตให้นำไปใช้ประโยชน์ด้านการค้า
ไม่ว่ากรณีใดๆ ทั้งสิ้น อีกทั้งห้ามมิให้ตัดแปลงเนื้อหา และต้องอ้างอิงถึงเจ้าของเอกสารทุกครั้งที่มีการนำไปใช้

divalent cations (Ca^{2+}), the Al site occupying by trivalent cations (Al^{3+}) in an octahedral and a tetrahedral framework and the 4OH^- positioning within the tetrahedral framework. For charge balancing, The H^+ ions were bonding to each of the four O atoms as surrounded by empty site. The unit cell contains 6 of the C_3AH_6 units with 132 atoms and naturally formed by a three dimensional framework with the $\text{Ca}(\text{OH})_8$ dodecahedra sub-structure and the $\text{Al}(\text{OH})_6$ octahedra sub-structure [8,13]. The unit cell structure contains lattice parameters of a lattice constant $a=12.55695 \text{ \AA}$, and unit cell volume $V=1986 \text{ \AA}^3$. Generally, the C_3AH_6 cement can be formed crystal phase at higher ambient temperatures. The C_3AH_6 cement hydrate exits by using C_12A_7 reacted rapidly with water at accelerated temperatures above $60 \text{ }^\circ\text{C}$. For physical properties, there is no report on preparing process for nanostructure of C_3AH_6 cement hydrate and its effect on optical, thermal, dielectric and thermoelectric properties.

Today, different reports on enhanced properties of cement-based compounds by using GO composites and rGO composites have been published. Sedaghat et al. [18] by partially replacing graphene with Portland cement, has elaborated the thermal diffusivity and electrical conductivity of cement-graphene composite structural applications. By using rGO and GO components, Khan et al. [17] succeeded in concocting a conductive nanoscale calcium aluminate cement. Specifically, rGO, a two-dimensional carbon nanomaterial, has been acceptably utilized in terms of construction applications because of its suitable for electrical, thermal and mechanical properties resulted from a high surface area [16,36].

2.6.3 Synthesis of graphene

Graphene's chemical synthesis is considered an indirect top-down graphene synthesis. This is the first technique demonstrating graphene synthesis by chemical route. Boehm et al., In 1962, were the first to report monolayer flakes of rGO. The experiment was recently recognized by the Nobel Prize. The technique includes oxidation of graphite, reduction of graphene oxide and dissipation of the flakes by sonication. Today, there are three well-known GO synthesis methods available, namely, the Brodie method [37], the Staudenmaier method [38], and the Hummers and Offerman method [39]. These techniques involve oxidation of graphite utilizing

เอกสารนี้เป็นเอกสารที่สงวนไว้สำหรับการใช้งานเพื่อการศึกษาเท่านั้น ไม่อนุญาตให้นำไปใช้ประโยชน์ด้านการค้า
ไม่ว่ากรณีใดๆ ทั้งสิ้น อีกทั้งห้ามมิให้ตัดแปลงเนื้อหา และต้องอ้างอิงถึงเจ้าของเอกสารทุกครั้งที่มีการนำไปใช้

effective oxidants and acids. The level of oxidation differed according to stoichiometry, and the graphite type utilized as a starting material as well as to the reacting conditions (temperature, pressure, etc.). Brodie et al. [37] was the first to concoct GO by combining graphite with potassium chlorate and nitric acid. Nevertheless, several steps of the process consumed time and were hazardous. To tackle these challenges, by combining graphite with sodium nitrite, sulfuric acid, and potassium permanganate, Hummers [39] introduced the oxidation method for graphite or the Hummers method. For pristine graphite, after 1 hour of oxidative reaction, the interlayer distance is 3.34 \AA , which is enlarged up to 5.62 \AA , then at $7.0 \pm 0.35 \text{ \AA}$, further interlayer expansion has occurred upon a continued oxidation to 24 hour. Accordingly, the interlayer distance increased, which then led to a separation of a single layer from the GO bulk materials. Upon hydrazine hydrate treatment, GO reduced to graphene. In this manner, reduction of GO is also performed by utilizing sodium borohydrate (NaBH_4) and hydroquinone [39,40].

2.6.4 Thermoelectric generators

Introduced as an alternative solution, the thermoelectric power generation (TEG) technology seek to tackle the problem of emission reduction. Presented as an innovative pathway to improvements in terms of supplying the concentric shape adapted TEG modules and applying the heat pipe technologies. The analysis illustrates the sufficient power output for the limited space under the chassis of the passenger car. By correcting the heat pipes at the dual sides of the concentric TEG modules, efforts are also focused to derive enhanced convective heat transfer. Accordingly, temperature profile of TEG system depends on operational limitations and the durability of each component. Additionally, the results indicate a significance of heat transfer against the TEG power generation under two possible configurations in a passenger car. The highest power output per repeat unit is achieved at 29.8 W per 0.45 L with a ZT value 0.87 for a Bi_2Te_3 -based thermoelectric material in this studies [41]. Thermoelectric materials have continuously attracted attentions because its thermoelectric effects allow direct conversion between thermal and electrical energy. This literature review summaries the thermoelectric phenomena, applications and parameter relationships. Adopted techniques for thermoelectric

เอกสารนี้เป็นเอกสารที่สงวนไว้สำหรับการใช้งานเพื่อการศึกษาเท่านั้น ไม่อนุญาตให้นำไปใช้ประโยชน์ด้านการค้า
ไม่ว่ากรณีใดๆ ทั้งสิ้น อีกทั้งห้ามมิให้ตัดแปลงเนื้อหา และต้องอ้างอิงถึงเจ้าของเอกสารทุกครั้งที่มีการนำไปใช้

performance enhancement include modifications of electronic band structures and band convergence to enhance Seebeck coefficients, nanostructuring and all-scale hierarchical architecture to minimize the lattice thermal conductivity. A few thermoelectric materials with intrinsically low thermal conductivities are also explained [42]. Phase composition and microstructure analysis illustrate high density and pure CaMnO_3 phase which are achievable. The electric conductivity can be improved through Dy doping and resulting in a relative increase in thermal conductivity. The highest dimensionless figure of merit ZT of 0.15 derived at 973 K for $x = 0.02$ sample, which is about 4 times larger than that of the pure CaMnO_3 . This shows that CaMnO_3 is a convincing option for n-type thermoelectric material at high temperature [43].

The physical and numerical models are formed. The effects of certain important parameters, for example, thermoelectric element length, slag washing water temperature, packing factor of the thermoelectric module and heat exchanger flow passage length on the performance of the thermoelectric power generation device are examined. The results indicate that for blast furnace slag flushing water at 100°C , water temperature dropped 1.5°C per meter, about 0.93 kW electrical energy were generated per area and conversion efficiency of 2% was achievable. The cost recovery period of the equipment was about 8 years [44]. The rare earth Pr doped $\text{Ca}_{1-x}\text{Pr}_x\text{MnO}_3$ ($x=0, 0.06, 0.08, 0.1, 0.12, \text{ and } 0.14$) compound bulk samples were concocted to examine the effect of Pr doping on thermoelectric transport properties of CaMnO_3 compound system. The electrical performances of the doped samples illustrated by resistivity and Seebeck coefficient fluctuations were tuned with an optimized power factor value of $0.342 \text{ mW}/(\text{m}\cdot\text{K}^2)$ at 873 K for $x=0.08$ sample, which was more significant compared to that of the un-doped sample. The lattice thermal conduction was confined, resulting in a significantly repressed thermal conductivity. The thermoelectric performance was remarkably improved by Pr doping and the dimensionless figure of merit ZT for the $\text{Ca}_{0.92}\text{Pr}_{0.08}\text{MnO}_3$ compound was optimized with the maximum value 0.16 at 873 K [45]. The prototype that harvest thermoelectric energy from railway track. By utilizing the thermal energy existed in railway tracks, this technology encourages power rail-side sensors in off-grid and distanced areas without damaging natural resources. The proposed method utilizes thermal energy from the railway track and transfers it to the TEG prototype under

the bottom of rails. Assessment of the prototype is performed by finite volume analysis, field test, and laboratory experiment. The results showed that the TEG prototype can generate 5.8 -316.8 mW of power across a resistant load at thermal gradient from 8 °C to 29.2 °C. A DC-DC buck-booster circuit with lithium battery management is developed to charge batteries through the harvested thermal energy. The system is managed at a low voltage of 0.9 V and its conversion efficiency is higher than 60% [46]. The internal combustion engine (ICE) does not effectively turn chemical energy into mechanical energy. Most of the energy is dispersed as heat in the exhaust and coolant. With a waste heat recovery system, efforts are focused on indirectly enhancing the efficiency of the engine. Both TEGs and heat pipes are durable, stable, silent, passive and scalable. Heat pipes also present limitations such as maximum rates of temperatures limit and heat transfer. Once applied in conjunction, these methods create the possibility to generate a totally solid state and passive waste heat recovery system [47]. The nanostructured Bi_2Te_3 and Sb_2Te_3 were synthesized and deposited on both sides of a silk fabric to create TE columns. These TE columns were linked to silver foils to create a prototype by applying 12 thermocouples. Effectively, in the ΔT range of 5–35 K, the generator could turn thermal energy into electricity. The maximum voltage and power outputs were ~10 mV and ~15 nW, with no significant change during 100 cycles of bending and twisting. Various voltage output profiles were gathered from an arm-attached generator before and after 30 min of walking in order to showcase the possibility of a silk fabric-based TE generator [48]. A new set of road thermoelectric generator system (RTEGS), which can generate electricity when there is a temperature difference between road surface and ambient air, was developed. Further, to assess the capacity of energy generation based on indoor and outdoor tests, a RTEGS prototype was developed. Results indicated that in winter when the temperature difference between road surface and ambient air was at 15 °C, the output voltage of RTEGS was about 0.4 V by asphalt mixture slab (300 mm × 300 mm by size). In summer, with a temperature difference of 25–30 °C, the output voltage was about 0.6–0.7 V. This implies that some 160 kW h of energy can be derived in 8 h from a road of 1 km in length and 10 m in width. For asphalt pavement in tropical and subtropical regions, a significant variation in temperature is more appropriate for RTEGS [49].

เอกสารนี้เป็นเอกสารที่สงวนไว้สำหรับการใช้งานเพื่อการศึกษาเท่านั้น ไม่อนุญาตให้นำไปใช้ประโยชน์ด้านการค้า
ไม่ว่ากรณีใดๆ ทั้งสิ้น อีกทั้งห้ามมิให้ตัดแปลงเนื้อหา และต้องอ้างอิงถึงเจ้าของเอกสารทุกครั้งที่มีการนำไปใช้

2.6.5 Smart nanocomposite cement-based materials

New nanocomposite smart multifunctional materials, today, are deemed effective technological developments in construction field where thermal-energy efficiency should take into account mechanical performance requirements and environmental sustainability. Specifically, all carbon nanoinclusions are observed to be able to minimize the capability of solar reflectance, while generating difference in thermal emittance. Graphene nanoplatelets indicate the most capable nanoinclusion in terms of accelerating thermal conductivity and diffusivity. Accordingly, similar graphene samples generate the most significant capacitance and electrical conductivity. Notwithstanding, even though multi-walled carbon nanotubes seemed to be giving relatively less significant contributions to electrical conductivity, they are observed as the most appropriate nanoinclusions in terms of ensuring strain sensing capabilities to the cement-based composites [50].

The influence of rGO-C3AH6 nanocomposites on electrochemical properties. The rGO-C3AH6 nanocomposite samples with a varied degree of rGO loading. The maximum specific surface area and average pore size diameters were approximately at $74.20 \text{ m}^2/\text{g}$ and 11.72 nm for 20%rGO-C3AH6. The charge transferring in rGO-C3AH6 nanocomposites was explained by adopting band alignments model between C3AH6 and rGO. Moreover, the electrochemical properties of rGO-C3AH6 electrodes provided outstanding capacitive properties, illustrating the mechanism for storage charge of a hybrid supercapacitor behavior [51].

The C3AH6 cement hydrate-based nanocomposites were similarly assessed. Conductive Ag nanoparticles (Ag-NPs) were utilized as a filler. Pellet samples of AgNPs/C3AH6 nanocomposites with different filler volume fractions ($f_{\text{Ag-NPs}}$) were concocted by applying a hot-press sintering technique. Microstructural analysis indicated that C3AH6 nanoparticles were formed and Ag-NPs was evenly dispersed in the C3AH6 matrix. Here, dielectric permittivity (ϵ') of the nanocomposite with $f_{\text{Ag-NPs}}=0.15$ increased by a factor of 4 over the measured frequency range, while the dielectric loss tangent decreased. With an even further increases above $f_{\text{Ag-NPs}}=0.16$, the ϵ' values at 100Hz, 1kHz and 10MHz of the nanocomposite significantly enhanced by factors of 484, 47 and 16. This rapid change in ϵ' can be described by the percolation model. Nevertheless, the dielectric behavior still does not follow the percolation model even at 10 MHz. [52].

เอกสารนี้เป็นเอกสารที่สงวนไว้สำหรับการใช้งานเพื่อการศึกษาเท่านั้น ไม่อนุญาตให้นำไปใช้ประโยชน์ด้านการค้า
ไม่ว่ากรณีใดๆ ทั้งสิ้น อีกทั้งห้ามมิให้ดัดแปลงเนื้อหา และต้องอ้างอิงถึงเจ้าของเอกสารทุกครั้งที่มีการนำไปใช้

Chapter 3

Research methodology

This chapter presents materials and methods utilized in products synthesis including the characterizations, preparations and measurements of the products. This chapter consists of:

1. Research material and tools
2. Experimental procedure
3. Characterizations and preparation measurement

The detail of each section is described as follows:

3.1 Research materials and tools

3.1.1 Chemicals and materials

The chemicals for using in the experiment could be presented as follows:

- 1) Calcium carbonate (CaCO_3 , Sigma-Aldrich (USA), 99% purity)
- 2) Alumina powder (Al_2O_3 , Sigma-Aldrich (USA), 99.9% purity)
- 3) Manganese dioxide (MnO_2 , 99% purity)
- 4) Ethanol (95%)
- 5) Deionized Water (DI)
- 6) Acetone ($\text{C}_3\text{H}_6\text{O}$)
- 7) Graphite powder (Sigma-Aldrich (USA), 99% purity))
- 8) Sodium nitrite (NaNO_2)
- 9) Sulfuric acid: 92 ml (H_2SO_4 , 98%)
- 10) Ethyl acetoacetate ($\text{CH}_3\text{COCH}_2\text{COOC}_2\text{H}_5$)
- 11) Potassium permanganate (KMnO_4)
- 12) Hydrogen peroxide (H_2O_2 , 30%)
- 13) Hydrochloric acid (HCl, 37%)
- 14) An ammonia solution (NH_3 , 28-30%)

เอกสารนี้เป็นเอกสารที่สงวนไว้สำหรับการใช้งานเพื่อการศึกษาเท่านั้น ไม่อนุญาตให้นำไปใช้ประโยชน์ด้านการค้า
ไม่ว่ากรณีใดๆ ทั้งสิ้น อีกทั้งห้ามมิให้ตัดแปลงเนื้อหา และต้องอ้างอิงถึงเจ้าของเอกสารทุกครั้งที่มีการนำไปใช้

3.1.2 Experimental tools

The tools for using in the experiment could be presented as follows:

1) Balance



Figure 3.1 The balance apparatus.

2) Ball-milling



Figure 3.2 The ball-milling equipment.

3) Hot air oven (UN55, Memmert)



Figure 3.3 The hot air oven apparatus.

เอกสารนี้เป็นเอกสารที่สงวนไว้สำหรับการใช้งานเพื่อการศึกษาเท่านั้น ไม่อนุญาตให้นำไปใช้ประโยชน์ด้านการค้า ไม่ว่าจะกรณีใดๆ ทั้งสิ้น อีกทั้งห้ามมิให้ดัดแปลงเนื้อหา และต้องอ้างอิงถึงเจ้าของเอกสารทุกครั้งที่มีการนำไปใช้

4) Furnace (Nabertherm, GmbH TC03/14, Germany)



Figure 3.4 The furnace apparatus.

5) Alumina crucible



Figure 3.5 The alumina crucible.

6) Agate mortar



Figure 3.6 The agate mortar.

เอกสารนี้เป็นเอกสารที่สงวนไว้สำหรับการใช้งานเพื่อการศึกษาเท่านั้น เมื่ออนุญาตให้นำไปใช้ประโยชน์ด้านการค้าไม่ว่ากรณีใดๆ ทั้งสิ้น อีกทั้งห้ามมิให้ดัดแปลงเนื้อหา และต้องอ้างอิงถึงเจ้าของเอกสารทุกครั้งที่มีการนำไปใช้

7) Pelleting mould

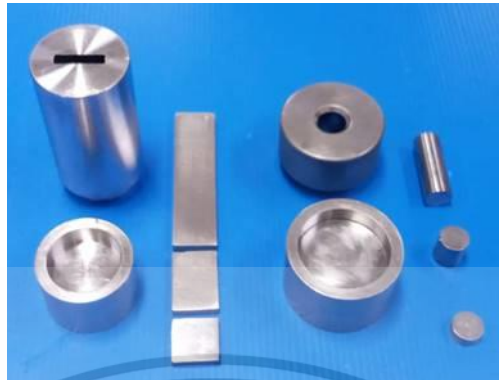


Figure 3.7 The Pelleting mould for pellet sample and bar sample.

8) Hydraulic pressure



Figure 3.8 The hydraulic pressure machine.

9) Hot-Press sintering



Figure 3.9 The hot-press sintering apparatus.

เอกสารนี้เป็นเอกสารที่สงวนไว้สำหรับการใช้งานเพื่อการศึกษาเท่านั้น ไม่อนุญาตให้นำไปใช้ประโยชน์ด้านการค้า
ไม่ว่ากรณีใดๆ ทั้งสิ้น อีกทั้งห้ามมิให้ตัดแปลงเนื้อหา และต้องอ้างอิงถึงเจ้าของเอกสารทุกครั้งที่มีการนำไปใช้

10) Thermocouple Type K (-200 - 1350 °C)



Figure 3.10 The thermocouple equipment.

11) Digital Multimeter (U1241 C/U1242C 4-Digital Handheld, Make in Malaysia, KEYSIGHT Technologie)



Figure 3.11 The digital multimeter equipment.

10) Thermal Imaging camera (Keysight Technologies U5856A, Range: -20-650°C)



Figure 3.12 The thermal imaging camera equipment.

เอกสารนี้เป็นเอกสารที่สงวนไว้สำหรับการใช้งานเพื่อการศึกษาเท่านั้น ไม่อนุญาตให้นำไปใช้ประโยชน์ด้านการค้า ไม่ว่าจะกรณีใดๆ ทั้งสิ้น อีกทั้งห้ามมิให้ดัดแปลงเนื้อหา และต้องอ้างอิงถึงเจ้าของเอกสารทุกครั้งที่มีการนำไปใช้

11) Computer (Lab-top Lenovo)



Figure 3.13 The Lab-top.

12) High-press continuous automatic machine



Figure 3.14 The high-press continuous automatic machine.

เอกสารนี้เป็นเอกสารที่สงวนไว้สำหรับการใช้งานเพื่อการศึกษาเท่านั้น ไม่อนุญาตให้นำไปใช้ประโยชน์ด้านการค้า ไม่ว่าจะกรณีใดๆ ทั้งสิ้น อีกทั้งห้ามมิให้ตัดแปลงเนื้อหา และต้องอ้างอิงถึงเจ้าของเอกสารทุกครั้งที่มีการนำไปใช้

3.2 Experimental procedure

3.2.1 Procedures for synthesis of C3AH6-rGO composite samples.

The procedure for the synthesis of C3AH6 cement-reduced graphene oxide hybrid composites are shown by the flow chart diagram in figure 3.15 and by the photograph in figure 3.16. From figure 3.15, the procedure of C3AH6-rGO sample could be performed into 4 parts. First, (1) Preparation of cements, the procedure consisted of two Step, Step1: Preparation of C12A7 cement and Step2: Preparation of C3AH6 cement hydrates. Second, (2) Preparation of rGO, the procedure consisted of three Step were explained in Step 1, Step 2 and Step 3, respectively. Third, (3) Preparation of C3AH6-rGO nanocomposite and finally, (4) Details of preparation of C3AH6 cement and C3AH6-rGO nanocomposite pallets are presented as follows:

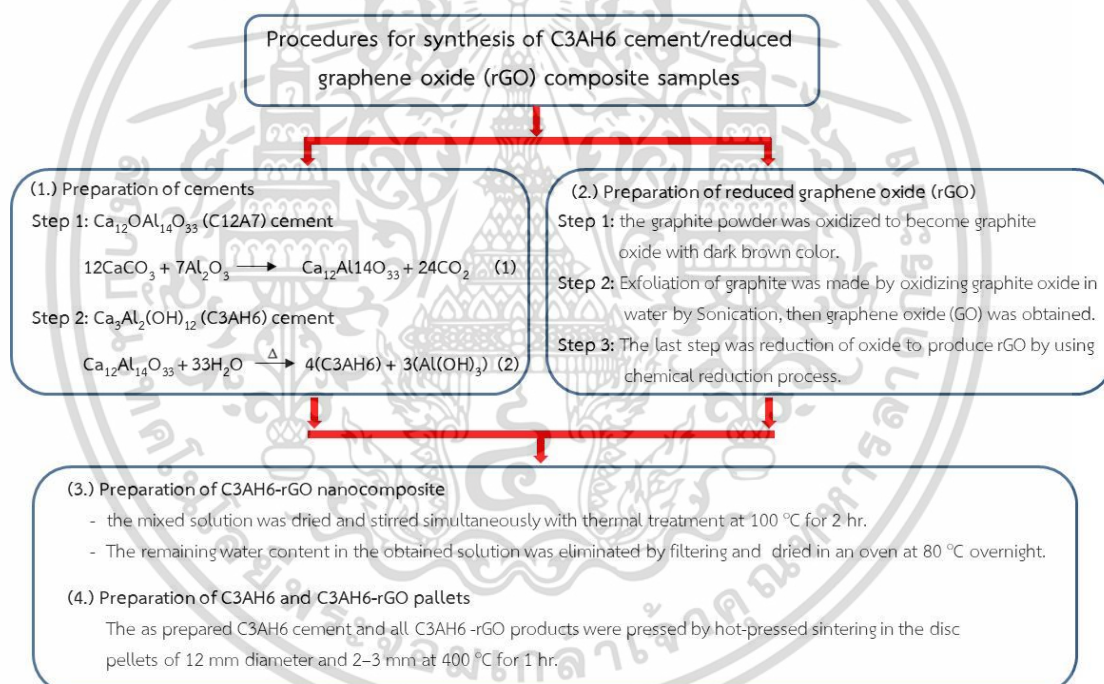


Figure 3.15 Flow chart illustrating the synthesis of C3AH6 cement–reduced graphene oxide nanocomposite samples.

เอกสารนี้เป็นเอกสารที่สงวนไว้สำหรับการใช้งานเพื่อการศึกษาเท่านั้น ไม่อนุญาตให้นำไปใช้ประโยชน์ด้านการค้า ไม่ว่าจะกรณีใดๆ ทั้งสิ้น อีกทั้งห้ามมิให้ดัดแปลงเนื้อหา และต้องอ้างอิงถึงเจ้าของเอกสารทุกครั้งที่มีการนำไปใช้

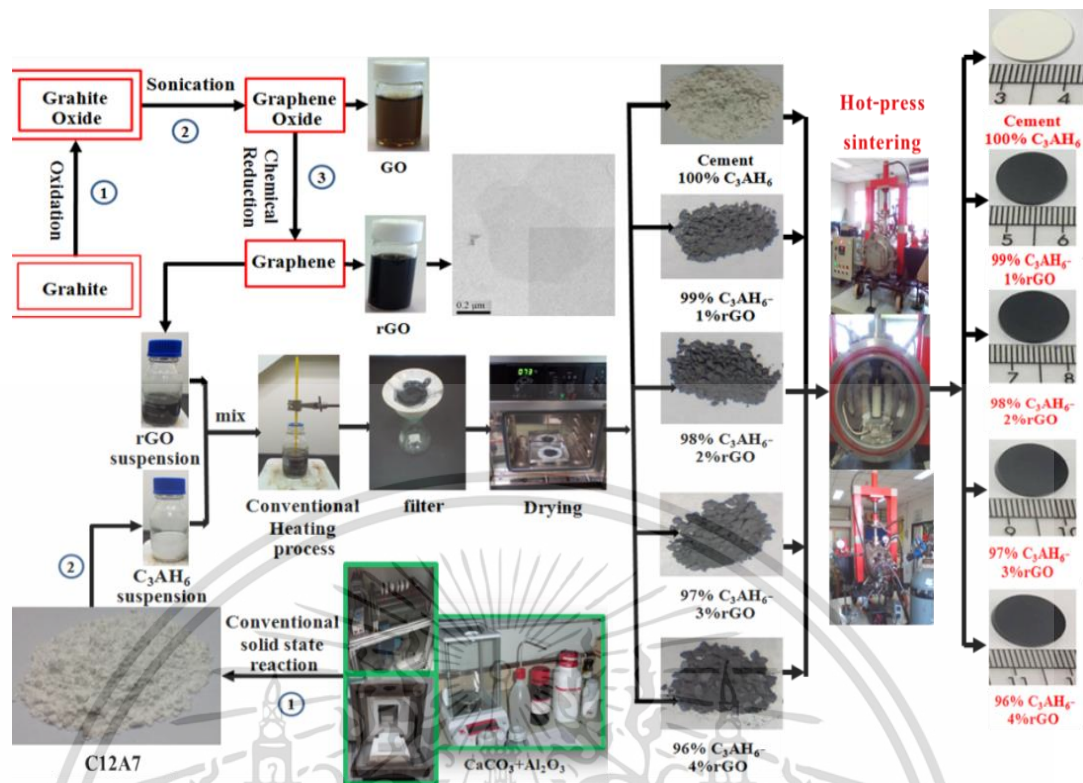
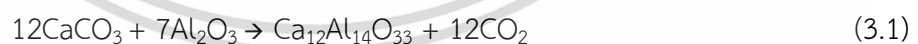


Figure 3.16 Photograph showing all the overview procedures for synthesis of C₃AH₆ cement–reduced graphene oxide nanocomposite samples.

(1) Synthesis of cements

Step1: Synthesis of C12A7 cement

For this step, C12A7 was synthesized by solid state reaction method. Starting materials composed Calcium carbonate (99%) and Alumina (99%) powders, which were weighted in a 12:7 ratio along a chemical formula, by equation 3.1 [31].



The powder was then blended by ball milling with ethanol at room temperature for 24 hours and dried at 100 °C in an oven for additional 24 hours. After that, sintered in an electric furnace at 1350 °C for 3 hours in an alumina crucible under an air atmosphere. The C12A7 sample was in the end disintegrated into powder as shown in Figure 3.17.

เอกสารนี้เป็นเอกสารที่สงวนไว้สำหรับการใช้งานเพื่อการศึกษาเท่านั้น ไม่อนุญาตให้นำไปใช้ประโยชน์ด้านการค้า ไม่ว่าจะกรณีใดๆ ทั้งสิ้น อีกทั้งห้ามมิให้ตัดแปลงเนื้อหา และต้องอ้างอิงถึงเจ้าของเอกสารทุกครั้งที่มีการนำไปใช้

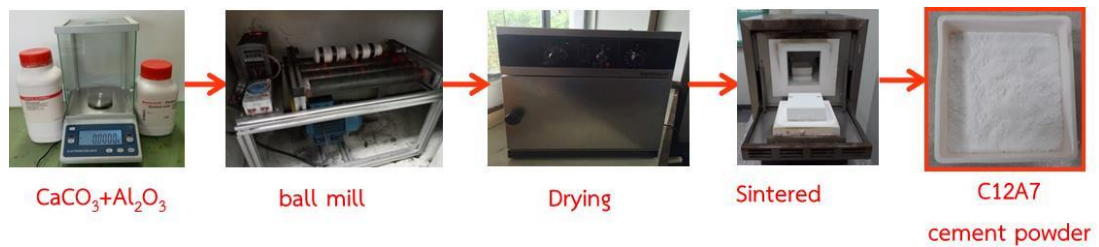


Figure 3.17 Preparation of C12A7 cement powder.

Step 2: Synthesis of C3AH6 cement hydrates

The C3AH6 cement were concocted by applying a hydration technique with the C12A7 powder as a starting material which aligns with the chemical reaction formula as expressed in equation 3.2 [32].



In a regular process, approximately 3 grams of C12A7 powder was introduced with 200 mL of the stirring DI water for 10 min at a room temperature. Then, the C12A7 suspension was heated at 100 °C for 2 hours over stirring. Consequently, the derived suspension, with DI water, was purified and rinsed then dried overnight in an oven at 80 °C. Finally, C3AH6 cement hydrates powder was derived as shown in Figure 3.18.



Figure 3.18 Preparation of C3AH6 nanocement powder.

เอกสารนี้เป็นเอกสารที่สงวนไว้สำหรับการใช้งานเพื่อการศึกษาเท่านั้น ไม่อนุญาตให้นำไปใช้ประโยชน์ด้านการค้า
ไม่ว่ากรณีใดๆ ทั้งสิ้น อีกทั้งห้ามมิให้ตัดแปลงเนื้อหา และต้องอ้างอิงถึงเจ้าของเอกสารทุกครั้งที่มีการนำไปใช้

(2) Synthesis of rGO

Step1: GO was synthesized by adopting the improved Hummers method using oxidizing graphite with a prominent acid and oxidizing agent. In a regular process, approximately 2 grams of graphite powder was combined with 6 grams of KMnO_4 in a beaker. Then the solid mixture was put into a 500 mL flask and cooled to 0°C in ice for 10 min. After that, while stirring and cooling, approximately 46 mL of H_2SO_4 was carefully introduced. At the same time, temperature of the obtained mixture was kept below 15°C . Consistently, for 30 min, the mixture was stirred at 40°C in water. After that, approximately 90 mL of distilled water was introduced, followed by heating of the mixture with stirring at 95°C in oil for an additional 60 min. Later, by adding 250 mL of distilled water, followed by 10 mL of a H_2O_2 solution, the reaction was put to a stop. As a result, this changed the color to the yellowish brown. By centrifugation, the byproduct was then isolated, rinsed with a 5% HCl solution in order to eliminate sulphate. It was purified and rinsed a couple times by with distilled water until pH of the purified solution was at about 7.

Step2: To put together an aqueous suspension of GO nanosheets, it was again distilled for 90 min under ultrasonication, followed by centrifugation. A dark-brown supernatant of an aqueous GO suspension was derived.

Step3: The rGO was synthesized by using a modified chemical reduction method [60] as explained. In short, 100 mL of the derived GO suspension was combined with 100 mL of distilled water in a beaker, followed by 0.1 mL of hydrazine hydrate solutions and 1 mL of an ammonia. The combined substance was then stirred and heated at 95°C in oil for 45 min. During this process, colour of the suspension changed from brown to black as shown in Figure 3.19.

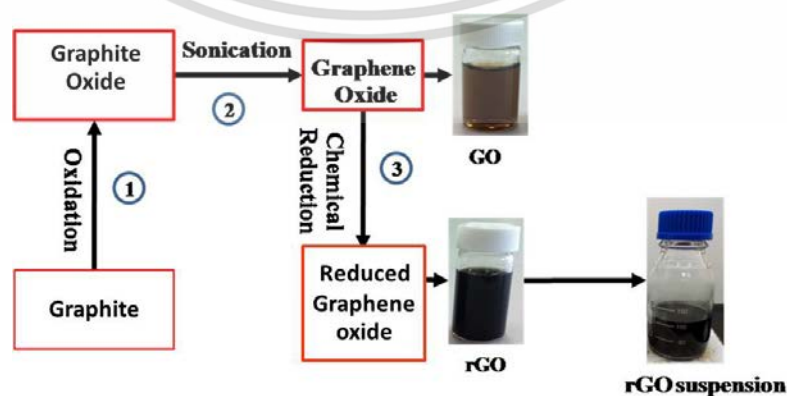


Figure 3.19 Preparation of reduced graphene oxide (rGO).

เอกสารนี้เป็นเอกสารที่สงวนลิขสิทธิ์สำหรับการใช้งานเพื่อการศึกษาเท่านั้น ไม่อนุญาตให้ทำซ้ำโดยไม่ได้รับอนุญาต
ไม่ว่ากรณีใดๆ ทั้งสิ้น อีกทั้งห้ามมิให้ตัดแปลงเนื้อหา และต้องอ้างอิงถึงเจ้าของเอกสารทุกครั้งที่มีการนำไปใช้

(3) Preparation of rGO-C3AH6 nanocomposite

The rGO-C3AH6 were concocted by applying a quick cement hydration process. This begins by rapidly heating water at 100 °C with the concocted C12A7 powder as a starting material. This process was executed with a variation of rGO loading, that are 1%, 2%, 3%, 5%, 7%, 10% and 20 wt% where the wt% of rGO to the C12A7 precursor. In a regular process to produce 1%rGO-C3AH6 cement, approximately 3 grams of C12A7 powder combined with 50 ml of acetone solution, 120 mL of stirring DI water maintained for 10 min at room temperature. Then, 30 mL of an rGO suspension was introduced and heated at 100 °C for 2 hours while stirred. After that, the byproduct of uniformed combination was purified, rinsed with DI water, and dried overnight in an 80 °C oven. Eventually, rGO-C3AH6 nanocomposite cement was derived. The same process was adopted to produce other 1%rGO-C3AH6 samples by deviating the degree of rGO loading. For this experiment, a purified C3AH6 sample was similarly concocted by using the abovementioned process, however without rGO loading as shown in Figure 3.20.

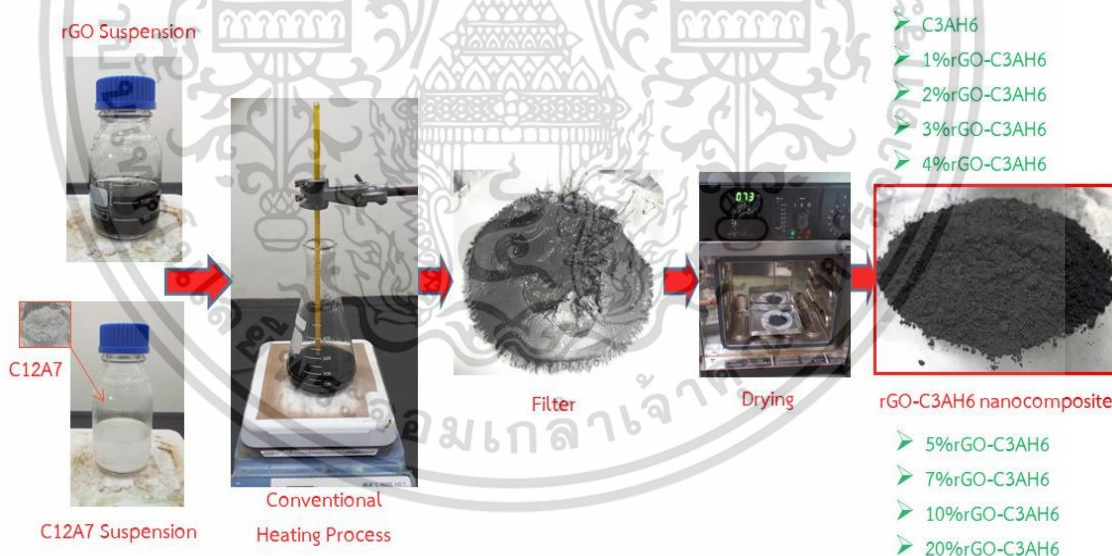


Figure 3.20 Preparation of rGO-C3AH6 nanocomposite.

เอกสารนี้เป็นเอกสารที่สงวนไว้สำหรับการใช้งานเพื่อการศึกษาเท่านั้น ไม่อนุญาตให้นำไปใช้ประโยชน์ด้านการค้า ไม่ว่าจะกรณีใดๆ ทั้งสิ้น อีกทั้งห้ามมิให้ตัดแปลงเนื้อหา และต้องอ้างอิงถึงเจ้าของเอกสารทุกครั้งที่มีการนำไปใช้

(4.) Preparation of C3AH6 and rGO-C3AH6 pallets

The powder of C3AH6 and all rGO-C3AH6 samples were pressed into pellets (without a binder) of $\approx 10\text{-}12$ mm in diameter and $\approx 1\text{-}3$ mm in thickness by uniaxial compression at ≈ 200 MPa. Then, the silver paste was painted on each pellet face of these samples. Next, all samples were kept in an oven at 150°C for 2 hours. Finally, the samples were measured the dielectric properties. For the measurements of thermal conductivity and thermoelectric the products were compressed by hot-pressed sintering into disc-shaped pellets that were 10 mm in diameter and 2–3 mm thick at 400°C for 1 hour.

3.2.2 Procedures for synthesis of CaMnO_3 as thermoelectric materials

The procedures for synthesis of CaMnO_3 was executed by applying a solid-state reaction method. Preceding materials composed of Calcium carbonate (CaCO_3 , 99% purity) and Manganese dioxide (MnO_2 , 99% purity) powders, which were used as starting materials that align with the chemical reaction formula,



The starting materials were crushed in a ball mill machine for 24 hour and then dried at 100°C . The mixed powder was calcined at 1200°C under air atmosphere for 12 hour. The product showed black powder showing the CaMnO_3 powder. To examine structural properties of the samples, XRD was used. Morphology was noted by utilizing SEM and EDS. The thermoelectric modules CaMnO_3 were compacted by High-press continuous automatic machine sintering into Cylindrical-shaped pellets at 8500 kPa that were 10 mm in diameter and 20 mm thick at room temperature. The modules CaMnO_3 Cylindrical-shaped pellets were sintered by performed inside alumina boat in furnace at 1200°C in air for 12 hour. The procedures for the synthesis of CaMnO_3 as thermoelectric materials are shown by the flow chart diagram in Figure 3.21 and by the photograph in Figure 3.22. The detail could be presented as follows:

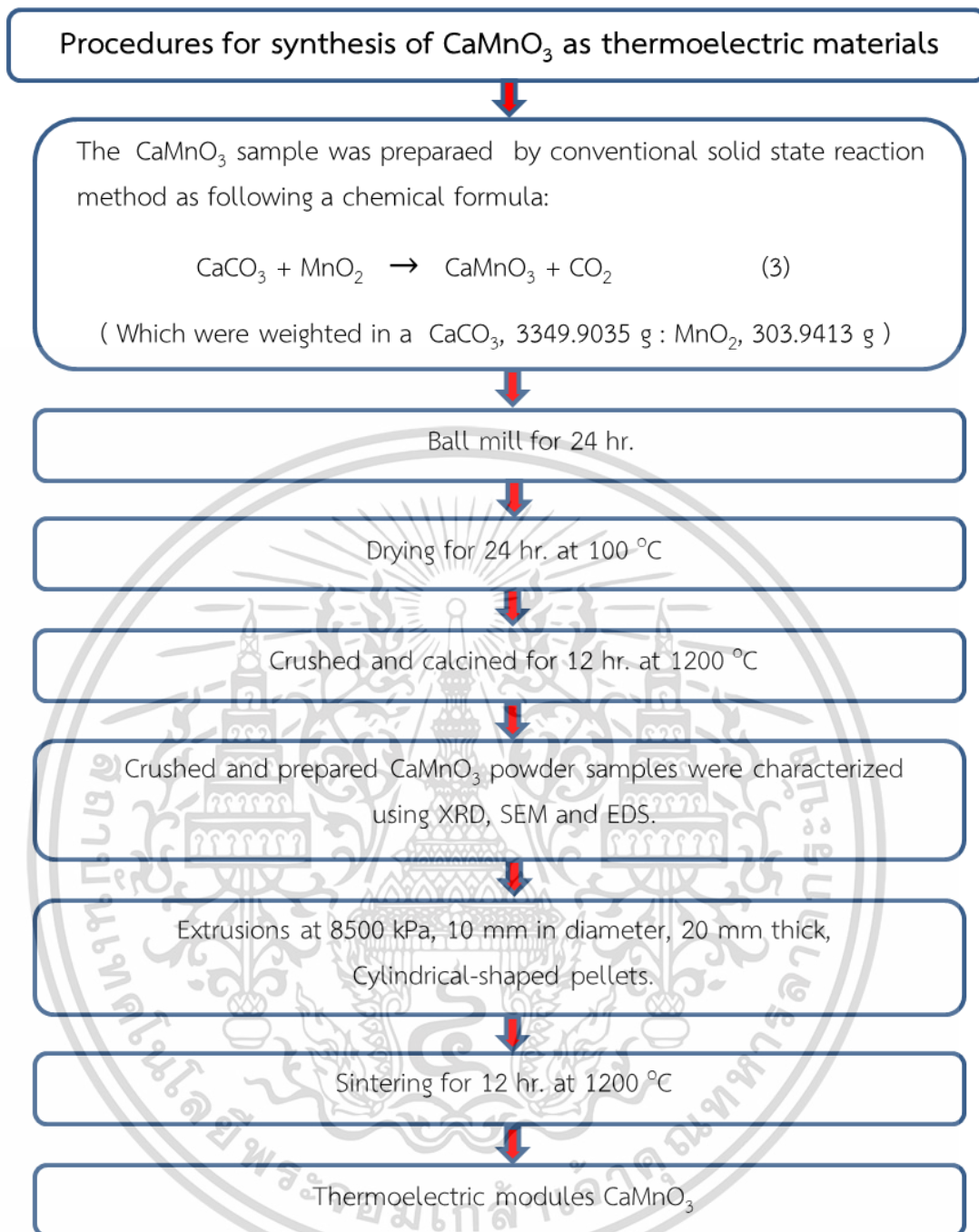


Figure 3.21 Flow chart for the synthesis of CaMnO_3 as thermoelectric modules materials.

เอกสารนี้เป็นเอกสารที่สงวนไว้สำหรับการใช้งานเพื่อการศึกษาเท่านั้น ไม่อนุญาตให้นำไปใช้ประโยชน์ด้านการค้า ไม่ว่าจะกรณีใดๆ ทั้งสิ้น อีกทั้งห้ามมิให้ดัดแปลงเนื้อหา และต้องอ้างอิงถึงเจ้าของเอกสารทุกครั้งที่มีการนำไปใช้

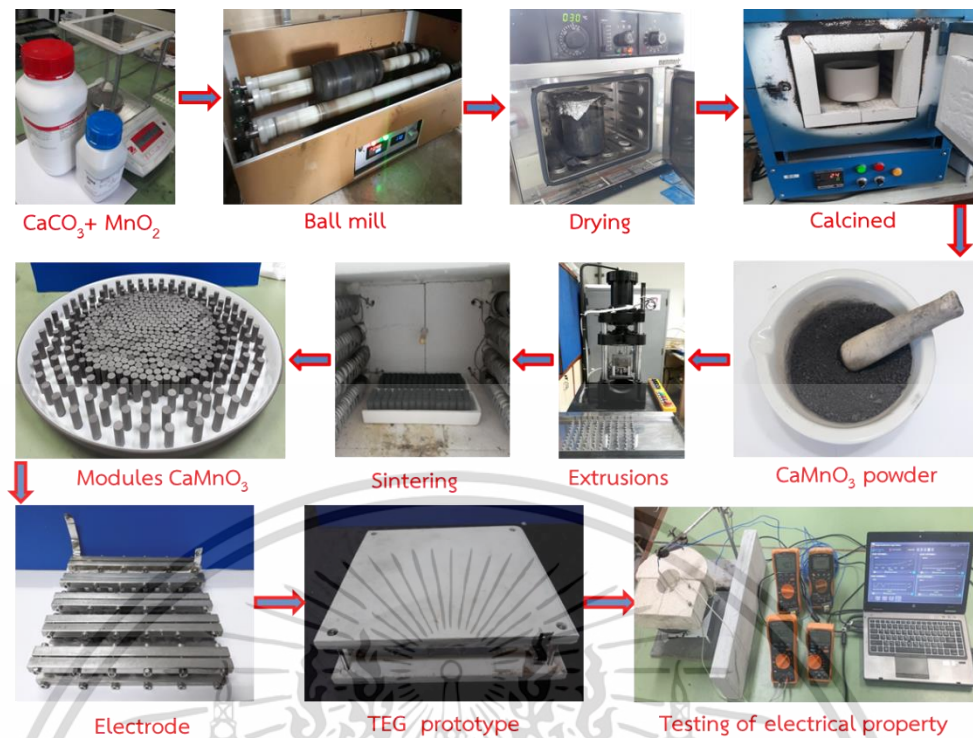


Figure 3.22 Photograph showing the overview procedures for synthesis of CaMnO_3 as thermoelectric modules materials.

3.2.3 Prototype of concrete block electric power generation from heat and applications in municipal melting furnace or municipal incinerator

The concrete block electric power generation from heat, and its applications in municipal melting furnace or municipal incinerator (CGH) prototype working at high temperature up to $800\text{ }^\circ\text{C}$. The CGH prototype was used the Seebeck effect schematic by directly convert heat into electricity. The CGH prototype was consisted of thermoelectric modules having thermoelectric material synthesized from CaMnO_3 thermoelectric material in our laboratory. The components of the machine: (1) Steel structure with wheels, (2) Gas fuel system, (3) Waste burning system, (4) Combustion chamber, (5) Heat storage, (6) TEG and (7) Hot exhaust vent. The Prototype of concrete block electric power generation from heat and applications in municipal melting furnace or municipal incinerator are shown by the photograph in figure 3.23.

เอกสารนี้เป็นเอกสารที่สงวนไว้สำหรับการใช้งานเพื่อการศึกษาเท่านั้น ไม่อนุญาตให้นำไปใช้ประโยชน์ด้านการค้า ไม่ว่าจะกรณีใดๆ ทั้งสิ้น อีกทั้งห้ามมิให้ตัดแปลงเนื้อหา และต้องอ้างอิงถึงเจ้าของเอกสารทุกครั้งที่มีการนำไปใช้

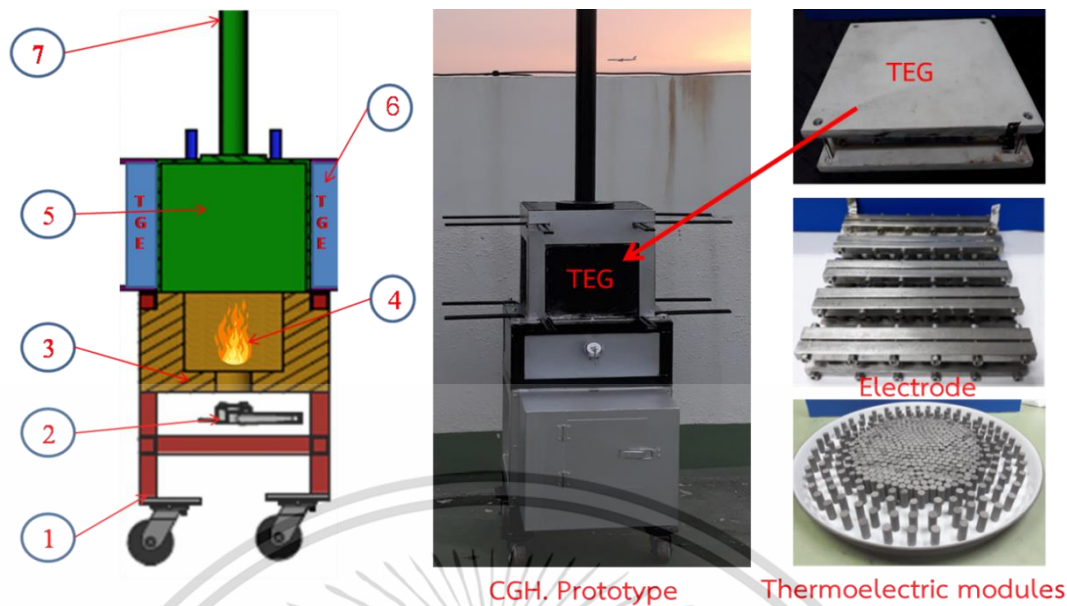


Figure 3.23 Photograph showing the prototype of concrete block electric power generation from heat and applications in municipal melting furnace or municipal incinerator.

3.3 Characterizations and properties measurements

3.3.1 Characterizations

Samples were investigated in structural properties and confirmed by several techniques such as X-ray Diffraction (XRD) with a 2θ scanning range from 10 to 80 degrees (Rigaku, Miniflex Cu K-alpha radiation). Raman Spectroscopy is a spectroscopic technique for observing vibrational, rotational and low frequency modes. Photons of the laser light are absorbed by the molecular and then emitted. Raman is an effective technique that was adopted to assess the structural configuration of graphene-based materials. Scanning Electron Microscope (SEM), were also employed to examine morphology of the surface and distribution. Transmission Electron Microscope (TEM), (HRTEM) (JEOL-2100 operating at 200 kV) Fourier-Transformed Infrared Spectroscopy (FT-IR), vibration function of the atomic bonding. UV-vis Diffuse Reflectance Spectroscopy (DRS), (Perkin Elmer, Lambda 950), the optical properties of cement powder samples were also evaluated. In addition, to assess weight loss of the samples, thermogravimetric analysis. Thermogravimetric Analysis (TGA), (Netzsch STA 449F3 Jupiter) was conducted over a temperature range of 50-1200 °C with under air.

เอกสารนี้เป็นเอกสารที่สงวนไว้สำหรับการใช้งานเพื่อการศึกษาเท่านั้น ไม่อนุญาตให้นำไปใช้ประโยชน์ด้านการค้า ไม่ว่าจะกรณีใดๆ ทั้งสิ้น อีกทั้งห้ามมิให้ตัดแปลงเนื้อหา และต้องอ้างอิงถึงเจ้าของเอกสารทุกครั้งที่มีการนำไปใช้

3.3.2 Properties measurements

With the Nano-Flash thermal diffusivity analyzer using a NETZSCH LFA 477, thermal properties of the samples were then studied on flat specimens that were 2 to 3 mm thick and 12 mm in diameter. By using an impedance analyzer (precision LCR meter Model: E 4980A), the dielectric measurements were performed. Similarly, electrical conductivity was assessed over a frequency range from 20 Hz to 10 MHz. at room temperature. In order to evaluate micro-hardness of the C3AH6 precursor and rGO-C3AH6 samples, a pyramid on square based method with a diamond indenter of the Vickers indenter hardness tester system (Shimadzu HMV-G21) was adopted. Electrochemical behavior, electrodes from all samples were then evaluated by using potentiostatic cyclic voltammetry (CV) measurements at constant current at potential windows of 0 to 1 V while remain conjoined to a Metrohm Autolab PGSTAT302N potentiostat-galvanostat system. To test samples, an agar disk-diffusion technique was applied against Gram-negative, Escherichia coli bacteria 1×10^8 CFU/mL concentration to conclude their antibacterial properties. The samples were put into disc shaped specimens with a diameter of 12 mm at approximate. After that, the disc samples were positioned on the E. coli seeded agar plates and incubated for 24 hours at 37 °C. Consequently, the developed inhibition zones surrounding the discs were recorded.

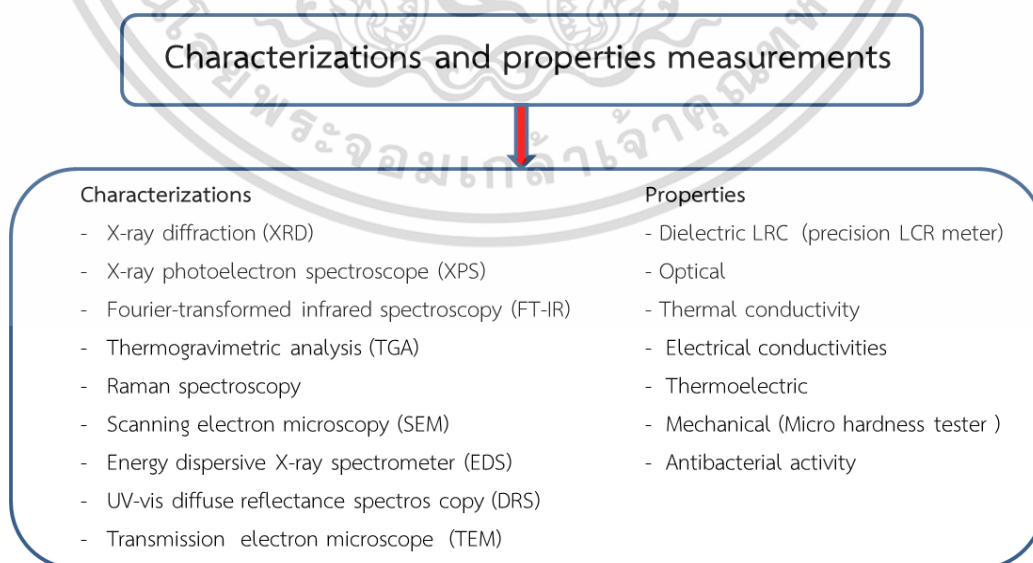


Figure 3.24 Flow chart of characterizations and properties measurements.

เอกสารนี้เป็นเอกสารลิขสิทธิ์ของงานเพื่อการศึกษาเท่านั้น อนุญาตให้นำไปใช้
 ไม่ว่ากรรมใดๆ ทั้งสิ้น อีกทั้งห้ามมิให้ตัดแปลงเนื้อหา และต้องอ้างอิงถึงเจ้าของเอกสารทุกครั้งที่มีการนำไปใช้

Chapter 4

Results and discussion

For this chapter, discussions of results are categorized into three sections in terms of improving C3AH6 technique and prototype of concrete block electric power generation from heat. Firstly, synthesis of nanostructure tricalcium aluminate hexahydrate (C3AH6) cements. Secondly, synthesis of C3AH6 cement-reduced graphene oxide (rGO) nanocomposites, and finally prototype of concrete block electric power generation from heat and applications in municipal melting furnace or municipal incinerator.

4.1 Synthesis of nanostructure C3AH6 cements

4.1.1 Microstructural characterizations

- X-ray diffraction (XRD)

The XRD pattern of the concocted C12A7 sample as a precursor and the C3AH6 sample. The diffraction patterns of C12A7 sample aligned with that of PDF#09-0413 file and in accordance with the formation of standard C12A7 phase with the space group, $\bar{1}43d$. The XRD pattern also illustrated diffraction of the concocted C3AH6 sample at diffraction angles 2θ on 17.26, 19.96, 26.51, 28.37, 33.41, 34.94, 36.41, 39.22, 40.56, 44.39, 45.60, 50.24, 52.45, 53.52, 54.59, 58.71, 59.71, 66.47, 70.18, 73.80 and 75.57° which supported the Miller index of the diffraction peaks at (211), (220), (321), (400), (332), (422), (431), (521), (440), (611), (444), (640), (552), (642), (651), (800), (741), (840), (664), (844), and (860) respectively as shown in Figure 4.1 implied that diffraction patterns of the C3AH6 sample aligned with the diffraction patterns peaks standard of the PDF#03-0125 file. Accordingly, the XRD pattern of the concocted C3AH6 indicated a significant emergence of phase at $2\theta = 18^\circ$ and 20.5° as suggested in the phasing of alumina trihydrate (aluminium hydroxide; $\text{Al}(\text{OH})_3$) (AH3) which was explained in the previous work in Ref. [11]. The C12A7 cement hydration process's reaction to water corresponded to the reaction $\text{C12A7} + 33\text{H}_2\text{O} \rightarrow 4(\text{C3AH6}) + 3(\text{AH3})$ and also supported in Ref. [10] led to such results. Similarly, the

AH3 phase appeared in a tiny amount by duration time of the C12A7 hydration process.

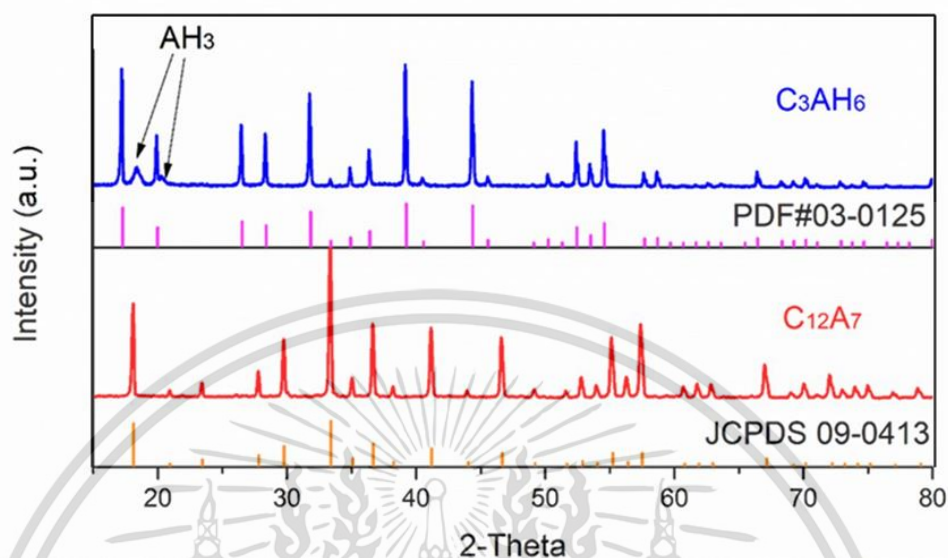


Figure 4.1 XRD pattern for pristine C12A7 and C3AH6 samples comparison with C12A7 and C3AH6 reference.

The average size of crystallite of the concocted C3AH6 sample can be studied by applying the following Scherrer's equation [12], by equation 4.1.

$$D_{XRD} = \frac{0.94\lambda}{\beta \cos \theta} \quad (4.1)$$

Where D_{XRD} is the average crystallite sizes

λ is the X-ray wavelength ($\lambda = 1.5406 \text{ \AA}$)

β is the full-width at half- maximum of the highest intensity peak

θ is the half of diffraction peak angle

The calculation indicated that the average size of crystallite of the concocted C3AH6 sample was roughly 61.53 nanometers. It can be inferred from the result that the C3AH6 had nanostructure in both crystalline and particles.

เอกสารนี้เป็นเอกสารที่สงวนไว้สำหรับการใช้งานเพื่อการศึกษาเท่านั้น ไม่อนุญาตให้นำไปใช้ประโยชน์ด้านการค้า ไม่ว่าจะกรณีใดๆ ทั้งสิ้น อีกทั้งห้ามมิให้ตัดแปลงเนื้อหา และต้องอ้างอิงถึงเจ้าของเอกสารทุกครั้งที่มีการนำไปใช้

- IR spectroscopy

To clarify the occurrence of the hydration process on synthesized C3AH6 cement, IR spectroscopy was performed. Figure 4.2 showed the IR spectra of the concocted C3AH6 in comparison to the results of the C12A7 precursor samples. In terms of the C3AH6 cement absorption band, the spectra illustrated three bands in a lower region of the wave-number area between 200 and 1000 cm^{-1} which was in alignment with the M-O (M=Ca, Al) stretching. Frequency of the absorption bands at 535 cm^{-1} and 760 cm^{-1} were initiated from AlO_6 octahedra and the absorption band in the frequency of 420 cm^{-1} given to CaO polyhedral. The frequency of bands at 760 cm^{-1} supported the stretching vibrations of Al-O bonds and the frequency of 530 cm^{-1} which aligned with the bending vibrations of Al-O-Al bonds. In addition, the band ranges from 700 to 500 cm^{-1} which were linked to the hydration with condensed AlO_6 octahedral [12]. The bands at 3460 cm^{-1} , again, supported the M-OH (M=Ca, Al) stretching vibrations as corresponding to the C12A7 preceding samples. In addition, the absorption band of the concocted C3AH6 indicated the vibration of O-H-bending at peak 1630 cm^{-1} and the vibration of O-H stretching at a peak at 3670 cm^{-1} as an indication of water molecules (H_2O) [13]. The appearing of the O-H-bending and O-H stretching absorptions as initiated by the $\text{Al}(\text{OH})_6$ octahedrons, while the O-H-bending and O-H stretching vanished from the C12A7 precursor sample. The results also corroborated the occurrence of the hydration process for fabrication C3AH6 cement hydrate.

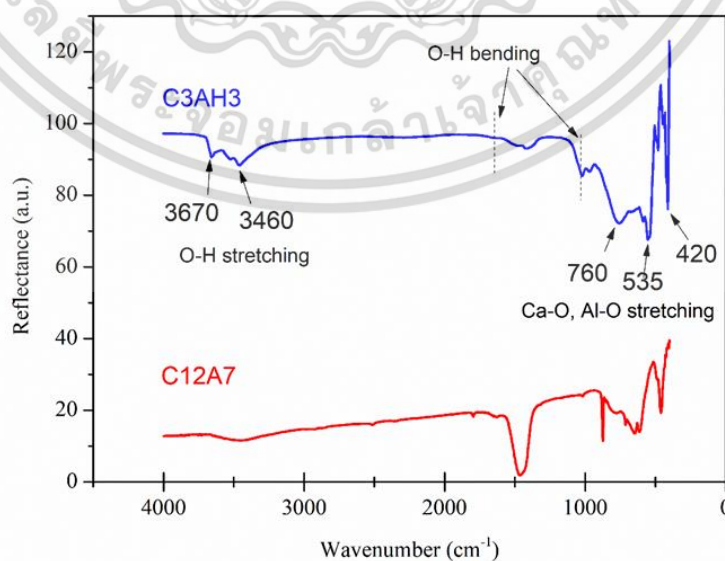


Figure 4.2 IR spectra of C3AH6 specimen and the concocted C12A7 precursor.

เอกสารนี้เป็นเอกสารที่สงวนไว้สำหรับการใช้งานเพื่อการศึกษาเท่านั้น เมื่ออนุญาตให้นำไปใช้ประโยชน์ด้านการค้า ไม่ว่าจะกรณีใดๆ ทั้งสิ้น อีกทั้งห้ามมิให้ตัดแปลงเนื้อหา และต้องอ้างอิงถึงเจ้าของเอกสารทุกครั้งที่มีการนำไปใช้

- X-ray Photoelectron Microscopy (XPS)

Figure 4.3(a) illustrated the wide scan XPS survey spectra of the concocted C3AH6 specimen. The spectra detailed the existence of the XPS spectrum for compiling Ca, Al and O 1s energies peaks with regards to the C 1s peak [16]. Figure 4.3(b) indicated the XPS spectra of Ca 2p of the concocted C3AH6 specimen. The XPS spectra outlined 2 peaks references which situated approximately at 347.3 eV and 350.8 eV. The peak at 347.3 eV was designated to the Ca 2p_{3/2} and the peak at while 350.8 eV was assigned to Ca 2p_{1/2} core levels of Ca²⁺ ions. Two different peaks of Ca 2p XPS spectrum were a result of the spin orbit splitting [14]. Figure 4.3(c) clarified the XPS core-level spectra of Al 2p for the concocted C3AH6 specimen. The Al 2s XPS spectra was placed around 74 eV, which corresponded to the previous reports [16]. The peak at 74.25 eV was an illustration of the Al³⁺ in the concocted C3AH6 specimen. The state of Al valence ascertained the existence of the Ca-O bonds and Al-O bonds in the C3AH6 specimen structure. Figure 4.3(d) illustrated the O 1s spectrum, which was assigned approximately at 531.5 eV. These indicated the existence of the O bonding in the C3AH6 specimen structure.

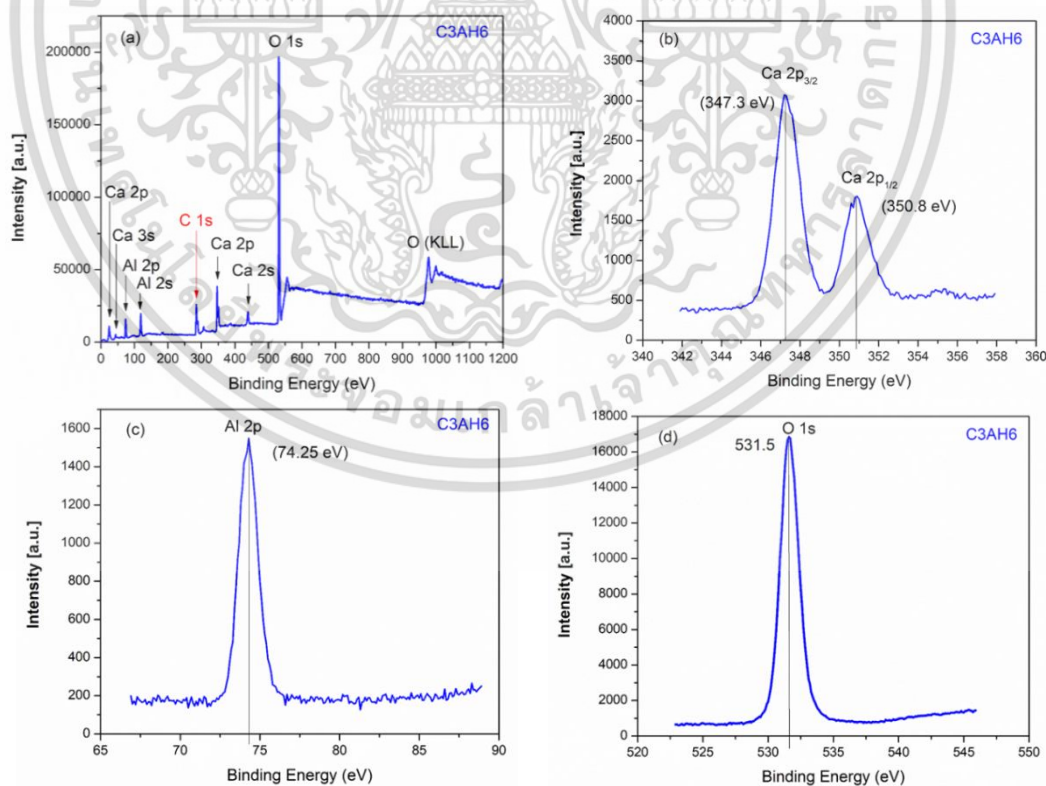


Figure 4.3 (a) XPS survey spectrum of C3AH6 and XPS spectra of (b) Ca 2p, (c) Al 2p, and (d) O 1s for pristine C3AH6 samples.

เอกสารนี้เป็นเอกสารที่สงวนไว้สำหรับการใช้งานเพื่อการศึกษาเท่านั้น ไม่อนุญาตให้นำไปใช้ประโยชน์ด้านการค้า
ไม่ว่ากรณีใดๆ ทั้งสิ้น อีกทั้งห้ามมิให้ตัดแปลงเนื้อหา และต้องอ้างอิงถึงเจ้าของเอกสารทุกครั้งที่มีการนำไปใช้

- Thermogravimetric analysis (TGA)

Analysis of the concocted C3AH6 specimen in thermal terms. The TG-DTA curves presented four exothermic in the temperature range from 100 to 900 °C by 65 % weight loss. The C3AH6 specimen dissolved slowly to amorphous anhydrous and to water vaporization between 100-550 °C. The significant loss was observed at 200-300 °C. Meanwhile, a less significant loss was observed between 400-550 °C [32]. At dehydrations between 300 and 350°C, the C3AH6 dissolved to create C3AH 1.5 at around 550 °C [16]. The diagram below displayed complete dehydrations to form C12A7 phase at temperature over 740 °C. The outcome showed C3AH6 as a solid material appropriate for application in ranging lower than 300 °C.

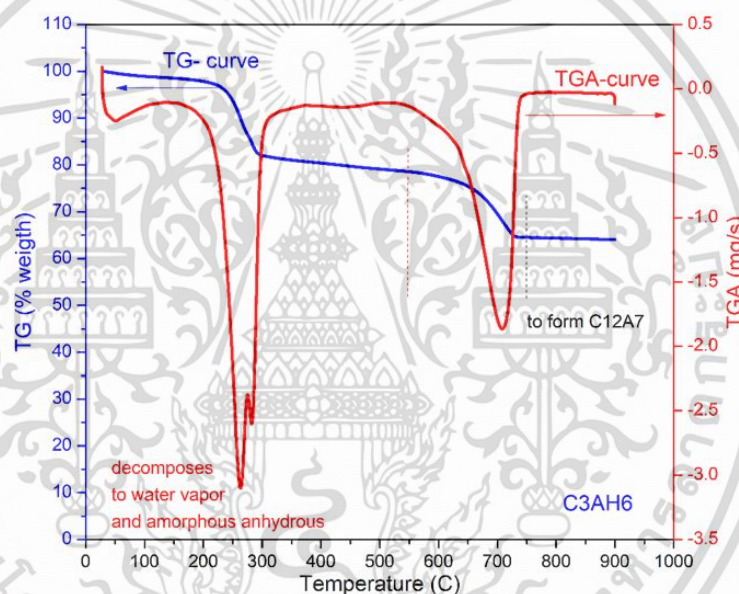


Figure 4.4 TGA curves of pristine C3AH6 cement hydrate samples.

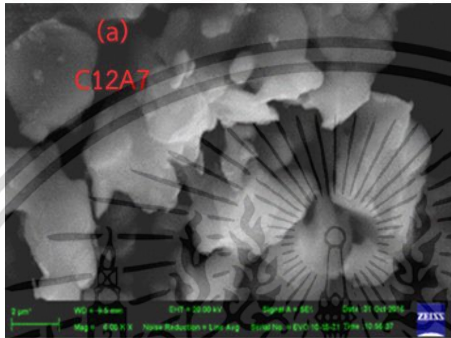
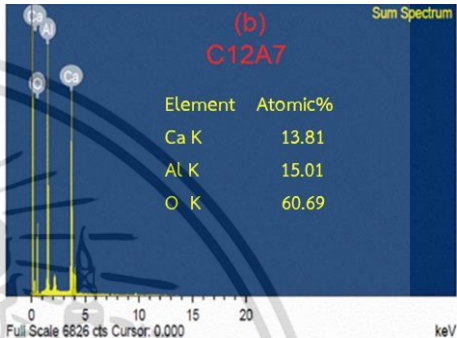
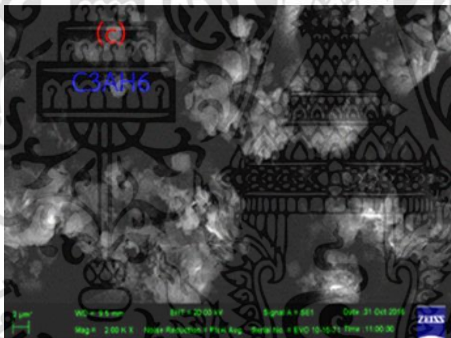
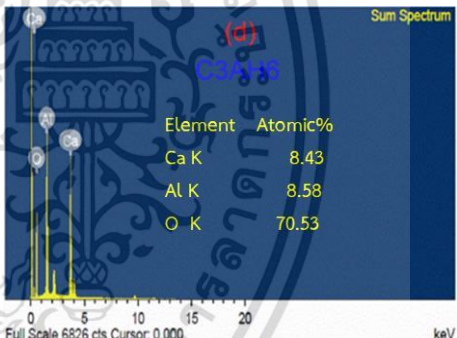
- Scanning electron microscopy (SEM)

The SEM image and EDX spectrographs of chemical compositions for the concocted C12A7 and C3AH6 specimens. Table 4.1 (a) illustrated the SEM image of the concocted C12A7 specimen magnified at 6,000x. Table 4.1 (b) showed the appetite of Ca, Al, and O atom of the C12A7 specimen. The chemical structure of the C12A7 specimen were accordingly derived from the EDS with atomic percentages for Ca, Al and O atom. For the concocted C3AH6 specimen, Table 4.1 (c) displayed the SEM image of the C3AH6 specimen in the magnifications 6,000x. Table 4.1 (d) displayed the appetite of Ca, Al, and O atom of the C3AH6 specimen. Clearly, the

เอกสารนี้เป็นเอกสารที่สงวนไว้สำหรับการใช้งานเพื่อการศึกษาเท่านั้น ไม่อนุญาตให้นำไปใช้ประโยชน์ด้านการค้า
ไม่ว่ากรณีใดๆ ทั้งสิ้น อีกทั้งห้ามมิให้ตัดแปลงเนื้อหา และต้องอ้างอิงถึงเจ้าของเอกสารทุกครั้งที่มีการนำไปใช้

EDS spectrographs did not show the atomic percentages of H atom because it was not observed by the EDS technique. Results above confirmed that the phasing of the fabricated C3AH6 structure was formed.

Table 4.1 SEM and EDX of the prepared C12A7 cement powder (a and b), and SEM and EDX of the concocted C3AH6 cement hydrate powder (c and d).

Samples	SEM	EDX								
C12A7 cements		 <table border="1"> <thead> <tr> <th>Element</th> <th>Atomic%</th> </tr> </thead> <tbody> <tr> <td>Ca K</td> <td>13.81</td> </tr> <tr> <td>Al K</td> <td>15.01</td> </tr> <tr> <td>O K</td> <td>60.69</td> </tr> </tbody> </table>	Element	Atomic%	Ca K	13.81	Al K	15.01	O K	60.69
Element	Atomic%									
Ca K	13.81									
Al K	15.01									
O K	60.69									
C3AH6 cements		 <table border="1"> <thead> <tr> <th>Element</th> <th>Atomic%</th> </tr> </thead> <tbody> <tr> <td>Ca K</td> <td>8.43</td> </tr> <tr> <td>Al K</td> <td>8.58</td> </tr> <tr> <td>O K</td> <td>70.53</td> </tr> </tbody> </table>	Element	Atomic%	Ca K	8.43	Al K	8.58	O K	70.53
Element	Atomic%									
Ca K	8.43									
Al K	8.58									
O K	70.53									

- Transmission electron microscopy TEM

Using TEM, the surface morphological was illustrated in Figure 4.5. Figure 4.5(a) displayed layered nanostructure of the particles varied in size approximately equivalent of 10 to 50 nanometre, as small nano-size particles which was close to the average crystallite size by calculation resulted from the XRD results. The yield of nanostructures was possibly an outcome of the concoction of C3AH6 cement hydrate by mixing C12A7 with water in an accelerated duration for heating temperature to 100 °C. The amount of AH3 structure was characterized by the building up of the nanosheet-like structure as exhibited in Figure 4.5(a). Additionally,

เอกสารนี้เป็นเอกสารที่สงวนไว้สำหรับการใช้งานเพื่อการศึกษาเท่านั้น ไม่อนุญาตให้นำไปใช้ประโยชน์ด้านการค้า ไม่ว่าจะกรณีใดๆ ทั้งสิ้น อีกทั้งห้ามมิให้ตัดแปลงเนื้อหา และต้องอ้างอิงถึงเจ้าของเอกสารทุกครั้งที่มีการนำไปใช้

Figure 4.5(b) explained the diffraction rings of the SAED pattern, illustrating a high poly-crystalline. The building up of C3AH6 with nanostructures implied further industrial applications.

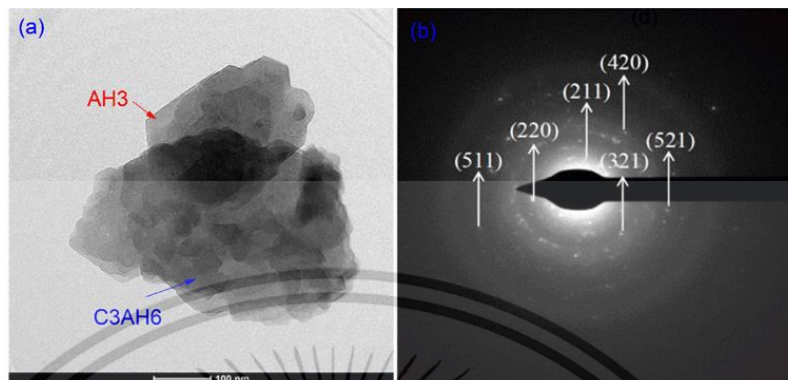


Figure 4.5 (a) Microscopy images of transmission of electron for the concocted C3AH6 powder (b) the SAED pattern.

4.1.2 Optical Properties

Optical properties were measured to definition of excitation energy using UV-visible spectra and optical property of the concocted C3AH6 specimen and the concocted C12A7 precursor. Absorption coefficient spectra (α) of the C3AH6 and the C12A7 specimens were measured at room temperature. Figure 4.6(a) displayed absorbance spectra of the C3AH6 and the C12A7 samples. The results showed that the higher peak for absorption spectra of the C3AH6 and C12A7 samples presented under the wavelength 400 nm. For C3AH6 sample, the absorption spectra was lower than that of the C12A7 sample in terms of wave length ranging from 200 nm to 700 nm. As for the absorption coefficient spectra, the correlation between photon energy and energy gap can be explained in equation 4.2.

$$\alpha(h\nu) \propto \frac{(h\nu - E_g)^m}{h\nu} \quad (4.2)$$

where E_g is the direct optical gap

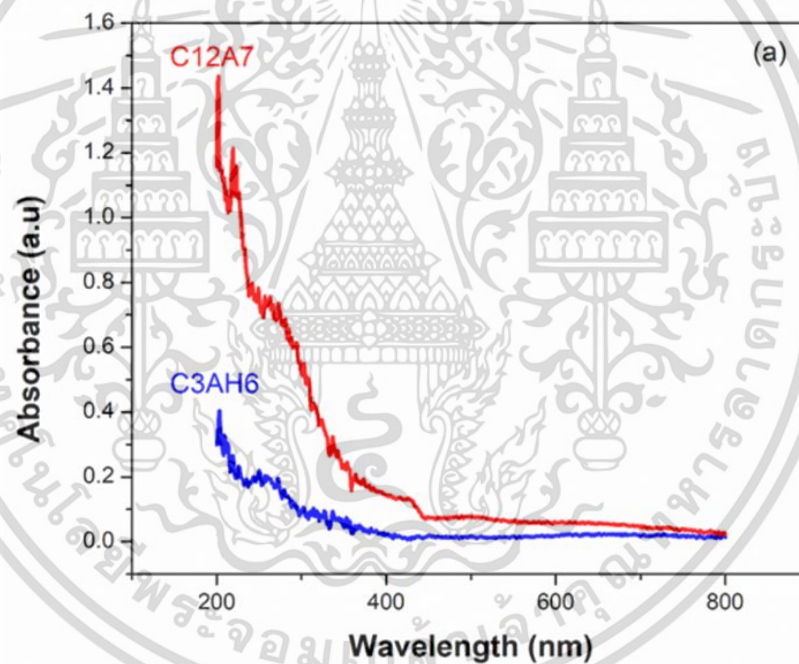
$h\nu$ is the photon energy

$m = 1/2$ is the value of allowed direct transition

$m = 2$ is the value of allowed indirect transition [17].

เอกสารนี้เป็นเอกสารที่สงวนไว้สำหรับการใช้งานเพื่อการศึกษาเท่านั้น ไม่อนุญาตให้นำไปใช้ประโยชน์ด้านการค้า ไม่ว่าจะกรณีใดๆ ทั้งสิ้น อีกทั้งห้ามมิให้ตัดแปลงเนื้อหา และต้องอ้างอิงถึงเจ้าของเอกสารทุกครั้งที่มีการนำไปใช้

The value of E_g can be derived by fit curve of $(\alpha h\nu)^2$ versus $h\nu$ in the linear line to the interception of photon energy ($h\nu$) axis. Figure 4.6(b) displayed the E_g of the concocted C3AH6 cement hydrate sample and the prepared C12A7 sample at room temperature. The value of E_g for the C3AH6 sample was at 4.1 eV and for the C12A7 sample was at 3.9 eV [18] as presenting transparent materials ($E_g > 3.0$ eV). The results revealed direct energy gap of the C3AH6 sample which was more significant than that of C12A7 sample. Figure 4.6(c) presented the indirect energy gap of the concocted C3AH6 sample and the prepared C12A7 sample at room temperature. The results indicated that the value of indirect energy gap of the C3AH6 sample was at 2.5 eV. While, the indirect energy gap of the C12A7 sample was at 2.45 eV for the first transitional level, and at 4.0 eV for the second transitional level.



เอกสารนี้เป็นเอกสารที่สงวนไว้สำหรับการใช้งานเพื่อการศึกษาเท่านั้น ไม่อนุญาตให้นำไปใช้ประโยชน์ด้านการค้า
ไม่ว่ากรณีใดๆ ทั้งสิ้น อีกทั้งห้ามมิให้ตัดแปลงเนื้อหา และต้องอ้างอิงถึงเจ้าของเอกสารทุกครั้งที่มีการนำไปใช้

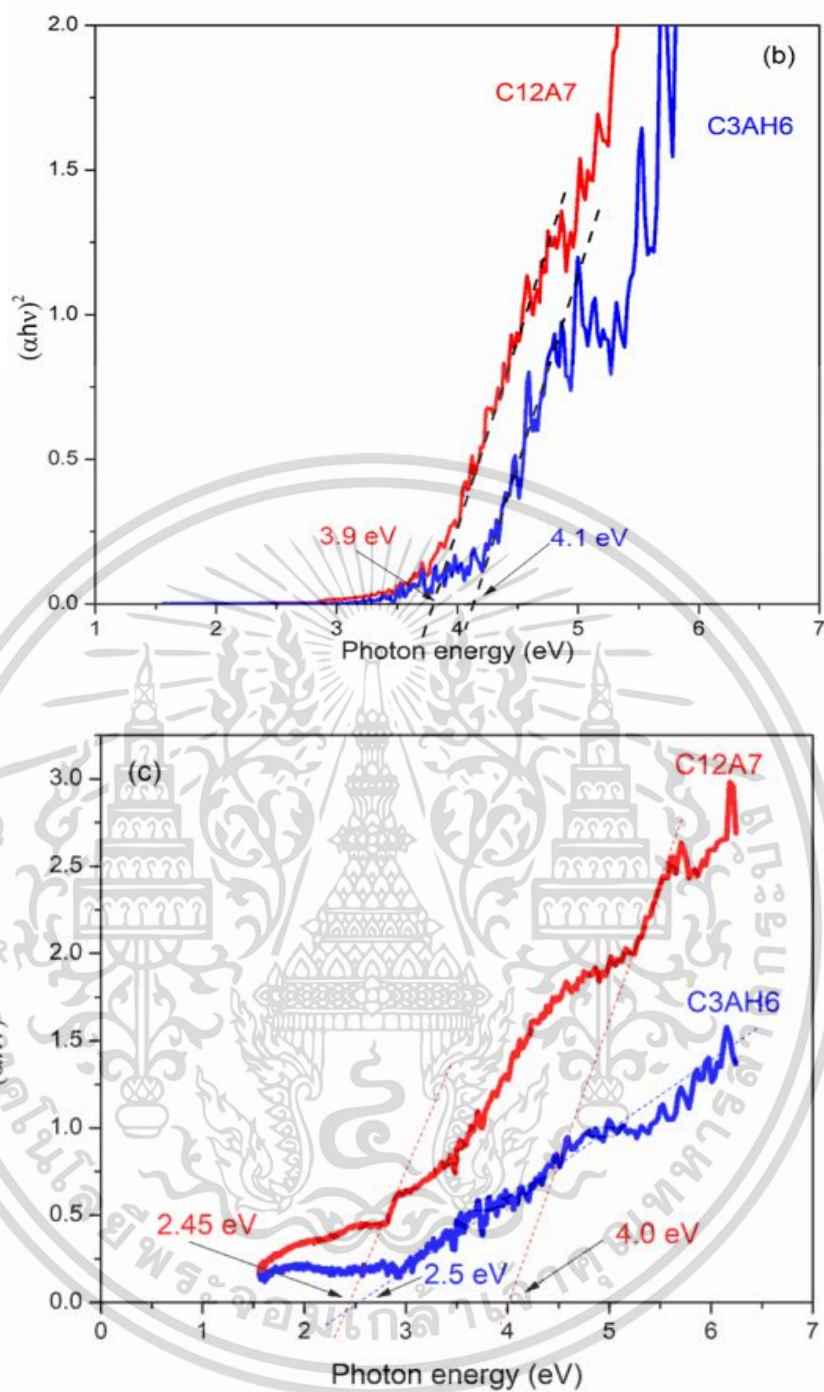


Figure 4.6 (a) absorbance, (b) direct energy gap and (c) indirect energy gap of the concocted C3AH6 specimen and C12A7 samples.

เอกสารนี้เป็นเอกสารที่สงวนไว้สำหรับการใช้งานเพื่อการศึกษาเท่านั้น ไม่อนุญาตให้นำไปใช้ประโยชน์ด้านการค้า ไม่ว่าจะกรณีใดๆ ทั้งสิ้น อีกทั้งห้ามมิให้ตัดแปลงเนื้อหา และต้องอ้างอิงถึงเจ้าของเอกสารทุกครั้งที่มีการนำไปใช้

4.1.3 Dielectric properties

In terms of dielectric properties measurement, the concocted C3AH6 power and the C12A7 precursor powder were hot-pressed in disc shape of graphite molds at 400 °C for 1 hour. The specimens in size of 12 mm diameter and 3 mm thickness for disc shape pellet were obtained. Both sides of the C3AH6 and the C12A7 discs were cleaned and coated with Ag electrodes in order to support an Ohmic contact. The dielectric properties as the relation to electrical nature on the samples were investigated. In the experiment, the electrical impedance response with frequency was recorded from 20 Hz to 2 MHz and the C and the dissipation factor (as loss tangent = $\tan\delta$) values were measured. Figure 4.7(a) indicated the C behavior of the C3AH6 and C12A7 specimens as a function of frequency. The C measurements of the two samples were conducted with the frequency range from 40 Hz to 2 MHz at room temperature. The results illustrated that the C of the C3AH6 specimen were above the C of the C12A7 specimen in all frequency range. The C of C3AH6 specimen was rapidly rose from 10^{-10} F to 10^{-11} F from frequency 40 Hz to 2 MHz. While, the C of the C12A7 specimen was totally unrelated to the frequency of the constant at 6×10^{-12} F. The ϵ' value can be obtained by equation 4.3. [53]

$$\epsilon' = \frac{C l}{\epsilon_0 A} \quad (4.3)$$

where l is the thickness of the sample

A is the area of the sample

ϵ_0 is the Permittivity of free space (8.85×10^{-12} F/m)

The assessments of both specimens were performed with the frequency ranging from 40 Hz to 2 MHz at room temperature. Figure 4.7(b) outlined dielectric constant of the C3AH6 and C12A7 specimens as a function of the frequency. The results indicated that ϵ' of the C3AH6 specimen was higher than that of the C12A7 specimen in all frequency ranges. For the frequency of 20 Hz to 10 kHz, and constant value at 20 for frequency of 10 Hz to 2 MHz, the ϵ' value of C3AH6 specimen has quickly subsided from 150 to 20 while, the ϵ' value of the C12A7 specimen remained constant at 10 in all frequency ranges. The dielectric loss (ϵ'') as imaginary part was

obtained by a formula $\epsilon'' = \epsilon' \tan \delta$ Figure 4.7(c) displayed the ϵ'' values of the C3AH6 and C12A7 specimens as function of the frequency. The results indicated that, with an increased frequency, the ϵ'' values of the C3AH6 specimen has quickly subsided from 2 to 0.8. At the same time, ϵ'' values of the C12A7 specimen remained constant at 0.05 all frequency ranges. Equation 4.4 explained the electrical conductivity as function of the frequency.

$$\sigma = \frac{1}{\rho} = \left(\frac{L}{AR} \right) \quad (4.4)$$

where σ is the electrical conductivity

ρ is the electrical resistivity

L is the thickness of the specimen

A is the cross section area of the specimen

R is the resistance of the specimen

Figure 4.7(d) indicated AC electrical conductivity of the C3AH6 and C12A7 specimens. The results illustrated that the σ value of the C3AH6 specimen was close to the results of the C12A7 specimen in all frequency range. Similarly, C3AH6 and C12A7 samples both contained the value lower than 10^{-7} S/m. This implied an ideal electric insulator for both samples. The abovementioned results explained the electrical impedance of the C12A7 which was not in alignment with the frequency in ranging from 20 Hz to 2 MHz. In addition, the electrical conductivity of the C12A7 showed an ideal electric insulator. Also, dielectric constant, dielectric loss and capacitance contained small value as displaying non-dielectric materials. In contrast, the abovementioned results displayed the value of dielectric constant, dielectric loss and capacitance of the fabricated C3AH6 as higher than that of the C12A7 specimen in the frequency in ranging from 20 Hz to 2 MHz. This implied that the C3AH6 responded to the frequency and vice versa. The C3AH6 frequency response was a result of the dielectric polarization in the compounds because of the deformational and relaxed polarization of materials under ac-electric field. Also, the high value of the dielectric constant and dielectric loss of the C3AH6 were a byproduct of the dielectric polarization of cement hydration component in the nanostructures. This

pointed out that the C3AH6 cement materials may be display application of smart wall capacitor from low cost cement materials.

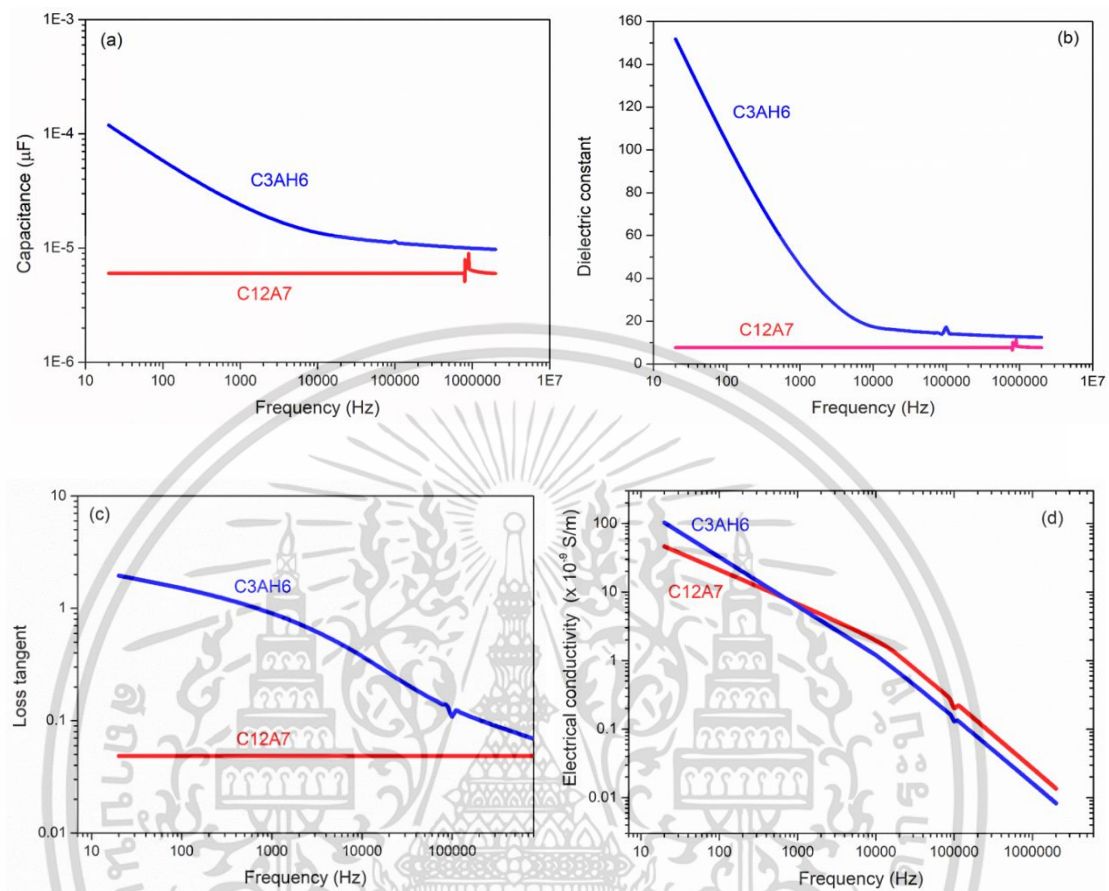


Figure 4.7 (a) the capacitance, (b) the dielectric constant, (c) the dielectric loss, and (d) the AC electrical conductivity as function of the frequency of the C3AH6 and C12A7 specimens.

4.1.4 Thermal properties

For thermal conductivity assessment of the concocted C3AH6 and the concocted C12A7 precursor, the samples were hot-pressed in the disc shape pellet of 12 mm diameter and 3 mm thickness. The thermal conductivity (κ) was conducted by applying the relation by equation 4.5. [54]

$$\kappa = aDC_p \quad (4.5)$$

where a is the thermal diffusivity

เอกสารนี้เป็นเอกสารที่สงวนไว้สำหรับการใช้งานเพื่อการศึกษาเท่านั้น ไม่อนุญาตให้นำไปใช้ประโยชน์ด้านการค้า
ไม่ว่ากรณีใดๆ ทั้งสิ้น อีกทั้งห้ามมิให้ตัดแปลงเนื้อหา และต้องอ้างอิงถึงเจ้าของเอกสารทุกครั้งที่มีการนำไปใช้

D is the bulk density

C_p is the specific heat of the specimen

Applying the Archimedes method, D of samples were assessed. Using the thermal diffusivity measurements over a temperature range of 298 to 573 K by laser Flash technique, the values of the a and C_p were derived. Thermal diffusivity for the samples was assessed by applying the Parker's formula as by equation 4.6. [55]

$$a = 0.139d^2 / t_{(1/2)} \quad (4.6)$$

Where $t_{(1/2)}$ is the time to reach half of the maximum temperature amplitude

d is the thickness of the bulk samples across the direction of heat flow

Figure 4.8(a) indicated the thermal diffusivity of the C3AH6 and the C12A7 specimens. The results showed the thermal diffusivity of the C3AH6 was lower than that of the C12A7 specimens in all temperature range. Figure 4.8(b) presented thermal conductivity as function of the temperature of the C3AH6 and C12A7 specimen. The results showed the κ values of the C3AH6 specimen lower than that of the C12A7 specimen. The range of thermal conductivity of the C3AH6 specimen was around 0.5 W/mK. For the thermal conductivity relation, the κ can be expressed in equation 4.7

$$\kappa = \kappa_e + \kappa_{ph} \quad (4.7)$$

Where κ is the total thermal conductivity ($\text{W m}^{-1} \text{K}^{-1}$)

κ_e is the electronic thermal conductivity ($\text{W m}^{-1} \text{K}^{-1}$)

κ_{ph} is the phonon thermal conductivity ($\text{W m}^{-1} \text{K}^{-1}$)

By AC electrical conductivity as in Figure 4.8(b), the κ_e value by above relation of both the C3AH6 and C12A7 specimen displayed small value. This implied that the κ values of the both materials were mainly controlled by the κ_{ph} part. By neglecting κ_e part, the equation for describing the thermal conductivity of κ_{ph} part can be explained by equation 4.8 [56].

เอกสารนี้เป็นเอกสารที่สงวนไว้สำหรับการใช้งานเพื่อการศึกษาเท่านั้น ไม่อนุญาตให้นำไปใช้ประโยชน์ด้านการค้า
ไม่ว่ากรณีใดๆ ทั้งสิ้น อีกทั้งห้ามมิให้ดัดแปลงเนื้อหา และต้องอ้างอิงถึงเจ้าของเอกสารทุกครั้งที่มีการนำไปใช้

$$\kappa_{phonon} = \frac{k_B}{2\pi^2\nu} \left(\frac{k_B T}{\hbar} \right)^3 \int_0^{\frac{\theta_D}{T}} (\tau_{ph}) \frac{x^4 e^x}{(e^x - 1)^2} dx \quad (4.8)$$

Where $x = \hbar\omega/k_B T$;

\hbar is the reduced Planck constant

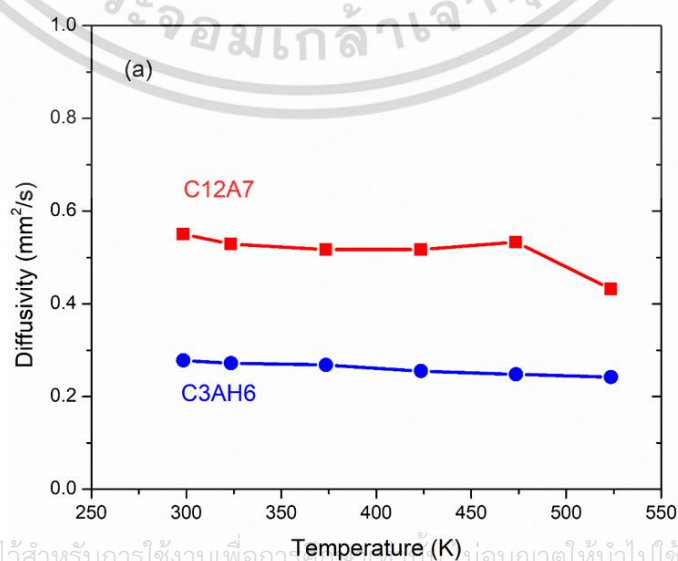
ω is the phonon angular frequency

ν is the phonon velocity

T is the absolute temperature

τ_{ph} is the phonon relaxation time

Figure 4.8(c) showed the curve of κ_{phonon} versus $1/T^3$ for the C3AH6 and C12A7 specimens. The results illustrated that the values of the C12A7 specimens were directly proportional to invert of temperature, while, the C3AH6 was small and proportional to invert of temperature. This implied that the low thermal conductivity of C3AH6 was mainly controlled by the point defect term due to complexed structure of the O-H functional group as occurrence from the hydration process and the grain boundary term by the small gran size of nanostructure. With the above results, the lower value of the thermal diffusivity and thermal conductivity of the C3AH6 specimen than that of the C12A7 specimens was caused by the cement hydration in the concrete nanostructures. The results pointed out that the reduction the thermal diffusivity of the C3AH6 was advantageous for reducing thermal conductivity as affecting a decrease in thermal cracking and improving thermal integrity with durability in concrete structures.



เอกสารนี้เป็นเอกสารที่สงวนไว้สำหรับการใช้งานเพื่อการวิจัยเท่านั้น มิอนุญาตให้นำไปใช้ประโยชน์ด้านการค้า
ไม่ว่ากรณีใดๆ ทั้งสิ้น อีกทั้งห้ามมิให้ตัดแปลงเนื้อหา และต้องอ้างอิงถึงเจ้าของเอกสารทุกครั้งที่มีการนำไปใช้

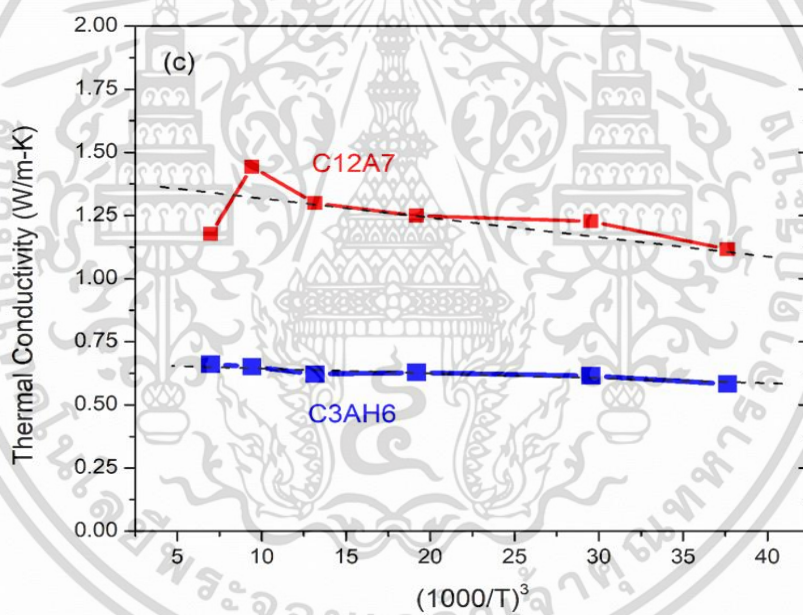
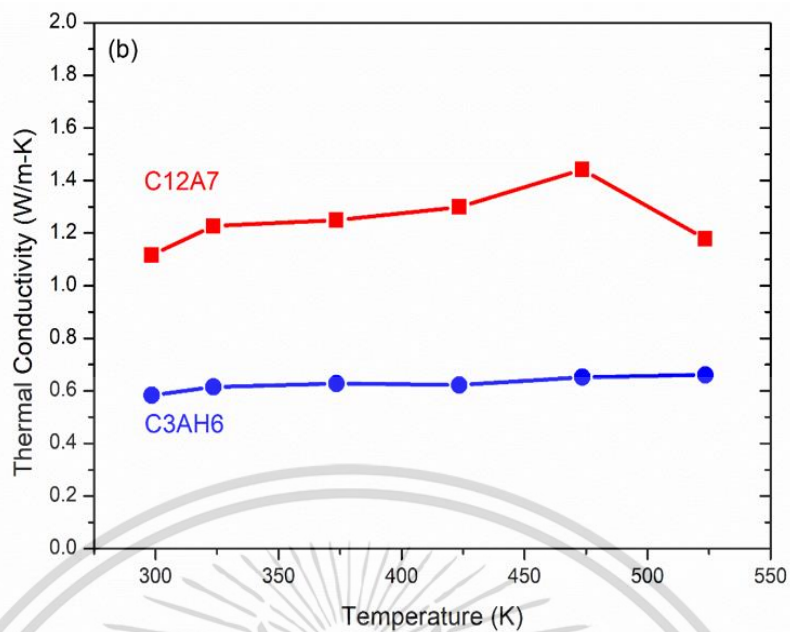


Figure 4.8 (a) Thermal diffusivity, (b) Thermal conductivity as a function of the temperature (T) and (c) as a function of $1/T^3$ of the concocted C3AH6 and C12A7 sample.

เอกสารนี้เป็นเอกสารที่สงวนไว้สำหรับการใช้งานเพื่อการศึกษาเท่านั้น ไม่อนุญาตให้นำไปใช้ประโยชน์ด้านการค้า ไม่ว่าจะกรณีใดๆ ทั้งสิ้น อีกทั้งห้ามมิให้ตัดแปลงเนื้อหา และต้องอ้างอิงถึงเจ้าของเอกสารทุกครั้งที่มีการนำไปใช้

4.2 Synthesis of rGO-C3AH6 nanocomposites

4.2.1 GO and rGO characterizations

Different spectroscopic techniques were applied to examine the crystalline phases and chemical structure. The applied techniques include:

- X-ray diffraction (XRD)

The XRD results confirmed the crystal structures of pristine graphite (as starting materials), as-synthesized graphene oxide (GO), and reduced graphene oxide (rGO), which all the results are illustrated in Figure 4.9. It was implied that XRD pattern of GO appeared around at $2\theta = 10.2^\circ$ only (has the thickness of the sheet as 0.866 nanometer). However, the characteristic peak of pristine graphite was not found. This finding implied that the starting materials of graphite was successfully reacted to different chemicals. At the same time, the XRD pattern of the synthesized rGO exhibited peak around at $2\theta = 24.5^\circ$ with had the thickness of the sheet as 0.363 nanometer, but no characteristics peak of GO was found. This finding confirmed that GO successfully reacted to different chemicals using this reaction, yielding products with purified rGO product.

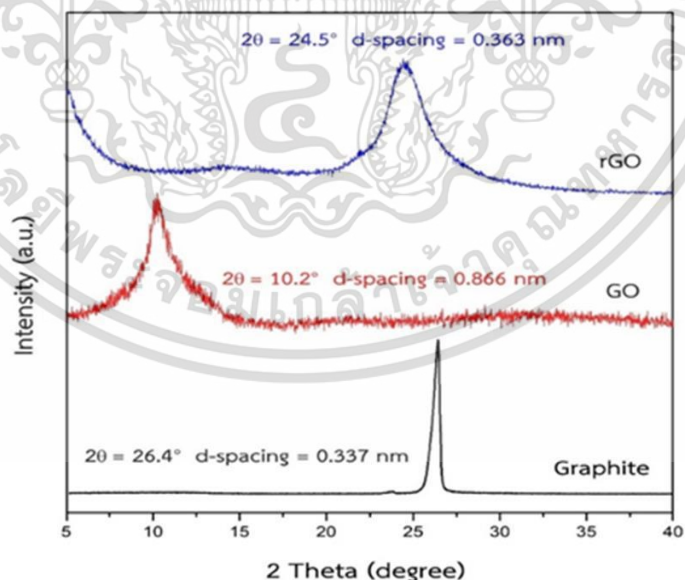


Figure 4.9 XRD pattern for pristine graphite and the synthesized GO and rGO samples.

เอกสารนี้เป็นเอกสารที่สงวนไว้สำหรับการใช้งานเพื่อการศึกษาเท่านั้น ไม่อนุญาตให้นำไปใช้ประโยชน์ด้านการค้า ไม่ว่าจะกรณีใดๆ ทั้งสิ้น อีกทั้งห้ามมิให้ตัดแปลงเนื้อหา และต้องอ้างอิงถึงเจ้าของเอกสารทุกครั้งที่มีการนำไปใช้

- Raman spectrum

Figure 4.10 displayed the resulted from Raman spectroscopy (Raman) of starting graphite materials, GO and rGO samples. It was observed that the absorption peaks of both GO and rGO samples exhibited two characteristic at approximate wave range of 1350 cm^{-1} (D band) and 1600 cm^{-1} (G band) as showing the functions of sp^3 carbon, and graphitic carbon sp^2 (-C=C-), respectively. After the graphite oxidization with the modified Hummers method, the proportion of GO intensity peak of D band against G band (I_D/I_G) was increased from 0.06 to 0.96. At the same time, after the chemical reduction process of GO the proportion of intensity of peak D band against G band (I_D/I_G) was also increased from 0.96 to 1.23. These findings illustrated the change of functions group on the structure of graphite as a starting material to GO and rGO products through these both reactions. These results corresponded to the data on crystallite and chemical structures by XRD, UV-vis and FT-IR techniques.

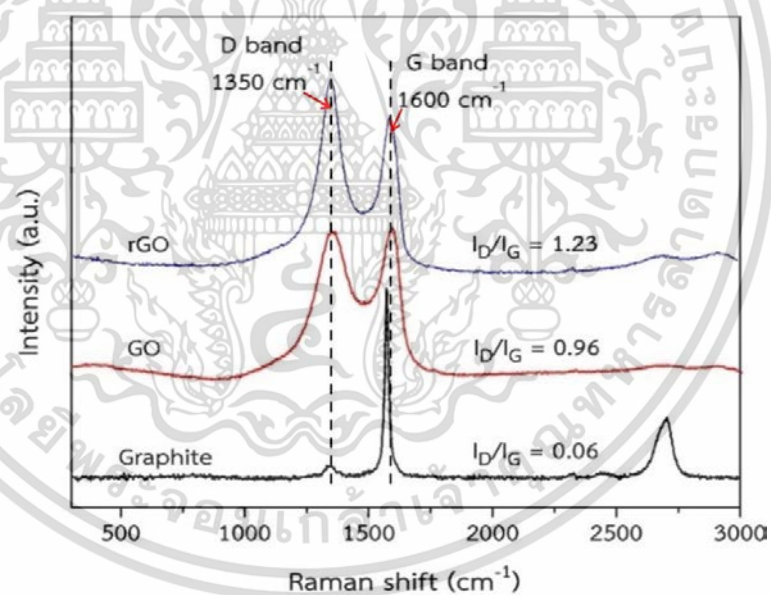


Figure 4.10 Raman spectra for pristine graphite and the synthesized GO and rGO samples.

- UV visible spectrometer

Figure 4.11 showed UV-Vis spectra (UV-Vis) of GO and rGO suspension samples. It can be seen that the absorption band on the wavelength range at 230 nm confirmed the characteristics structure (-C=C-) of GO of ($\pi-\pi^*$) and on the wave

เอกสารนี้เป็นเอกสารที่สงวนไว้สำหรับการใช้งานเพื่อการศึกษาเท่านั้น ไม่อนุญาตให้นำไปใช้ประโยชน์ด้านการค้า
ไม่ว่ากรณีใดๆ ทั้งสิ้น อีกทั้งห้ามมิให้ตัดแปลงเนื้อหา และต้องอ้างอิงถึงเจ้าของเอกสารทุกครั้งที่มีการนำไปใช้

length range of 300 nm due to characteristic band ($-C=O$) of GO ($n-\pi^*$). However, after the reduction process of GO through this reaction, it was found that the characteristic band of ($n-\pi^*$) due to $-C=O$ group of GO structure disappeared and were not found on UV-vis spectrum of rGO product. Meanwhile shifted peak of $\pi-\pi^*$ of rGO appeared at wavelength at around 267 nm. These findings indicated that the functional groups on the GO structure were eliminated through the chemical reduction process, yielding of purified rGO product.

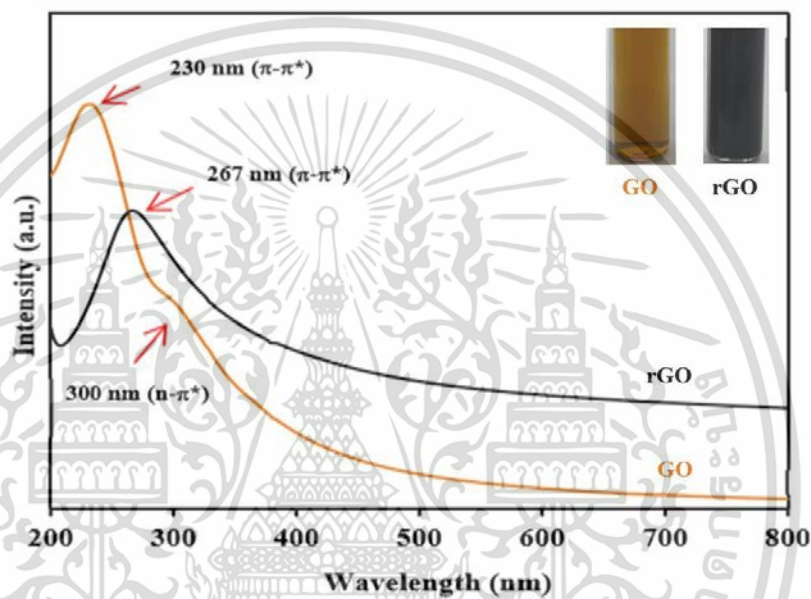


Figure 4.11 UV-vis spectra of as-synthesized GO and rGO samples.

- FT-IR spectra

Figure 4.12 illustrated the FT-IR spectra of as-synthesized GO and rGO samples. From the figure it can be observed that the vibration peaks of the oxygen functional groups, such as hydroxyl, carbonyl/carboxyl, and epoxy groups exhibited for the GO sample, which appeared at approximately 3410 cm^{-1} , 1740 cm^{-1} , and 1050 cm^{-1} , respectively. The peak was observed at approximately 1630 cm^{-1} due to the skeleton of sp^2 aromatic carbon [18-19]. With after the chemical reduction of GO, the intensity peaks of the oxygen functional groups were decreased, and some peak was disappeared. These results implied that during such processes, GO was reduced to rGO owing to the oxygen containing groups were mainly removed from the skeleton of GO.

เอกสารนี้เป็นเอกสารที่สงวนไว้สำหรับการใช้งานเพื่อการศึกษาเท่านั้น ไม่อนุญาตให้นำไปใช้ประโยชน์ด้านการค้า ไม่ว่าจะกรณีใดๆ ทั้งสิ้น อีกทั้งห้ามมิให้ตัดแปลงเนื้อหา และต้องอ้างอิงถึงเจ้าของเอกสารทุกครั้งที่มีการนำไปใช้

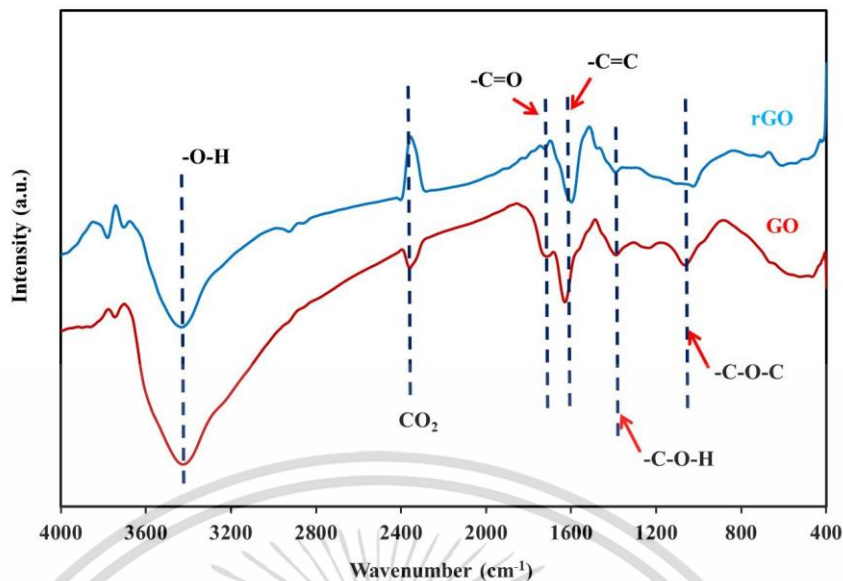


Figure 4.12 FT-IR spectra of the synthesized GO and rGO samples.

4.2.2 Nanometer sized C3AH6 cement and rGO-C3AH6 nanocomposite characterizations

- X-ray diffraction (XRD)

Figure 4.13 showed the XRD peaks of the synthesized C3AH6 and x%rGO-C3AH6 composites with different rGO contents. The results indicated that the diffraction patterns of all C3AH6 and x%rGO-C3AH6 samples corresponded with the diffraction patterns of the pristine C3AH6 peak, indicating the formation of C3AH6 phase in all samples. The lattice constant of C3AH6 was $a = 12.583 \text{ \AA}$, and for 4%rGO-C3AH6, $a = 12.581 \text{ \AA}$. However, the presence of an excessive $\text{Al}(\text{OH})_3$ phase at $2\theta = 18^\circ$ and 23.5° can be appeared in all samples. In addition, however, the characteristic peaked at $2\theta = 25.2^\circ$ of rGO [15,32], were not observed in all the x%rGO-C3AH6 samples because of an amorphous phase and a low content of the rGO composite in the C3AH6 specimen.

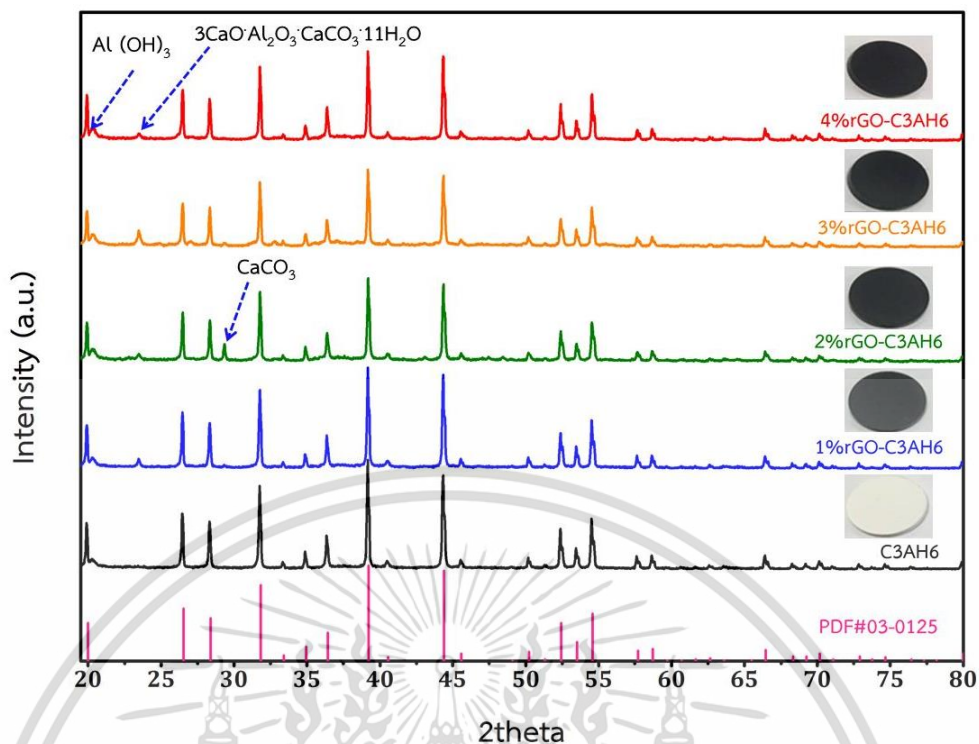


Figure 4.13 XRD pattern of pristine C3AH6, and 1%rGO-C3AH6, 2%rGO-C3AH6, 3%rGO-C3AH6, and 4%rGO-C3AH6 composite samples.

Moreover, the average crystallite sizes of the pristine C3AH6 and x%rGO-C3AH6 samples were evaluated by adopting the Scherrer's [13] equation as shown in equation 4.1. Figure 4.14 showed the average size of C3AH6 which was around 61.53 nm, and while those of x%rGO-C3AH6 were 75.73, 66.15, 65.40, and 69.59 nm for x=1, 2, 3 and 4, respectively. The results indicated that both C3AH6 and x%rGO-C3AH6 exhibited nanometer crystalline sizes. The average size of crystallite x%rGO-C3AH6 was similar to that of C3AH6. This explained that no changes in an average size of crystallite x%rGO-C3AH6 was due to the rGO loading in the C3AH6 cement.

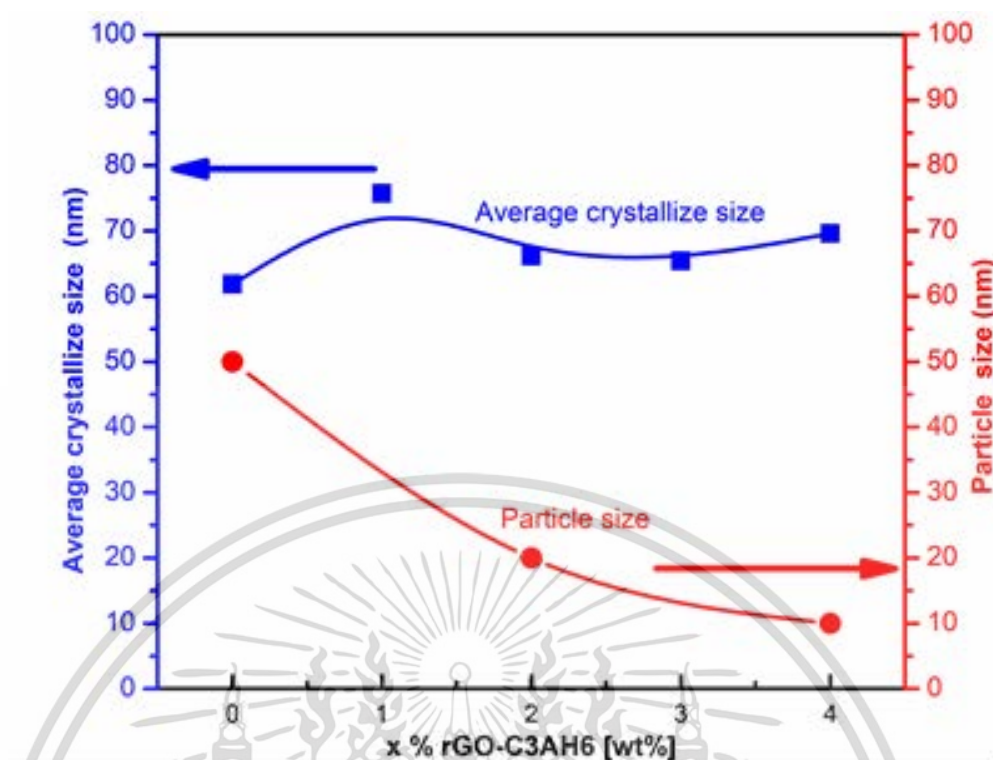
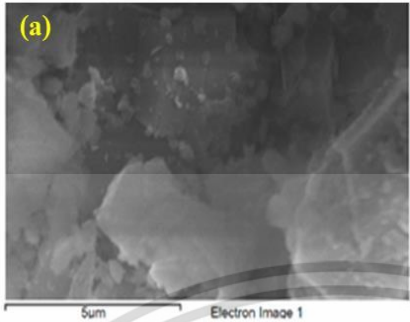
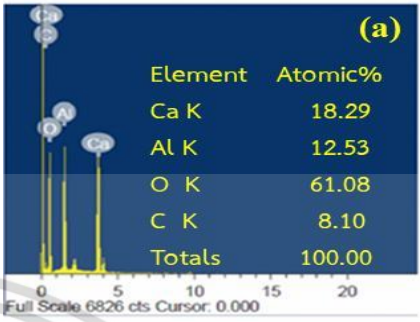

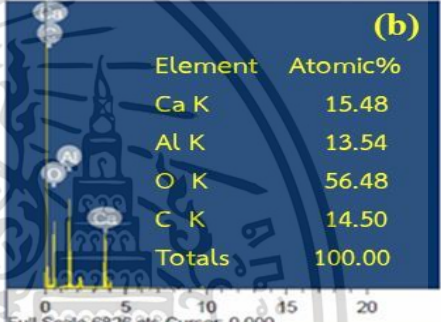

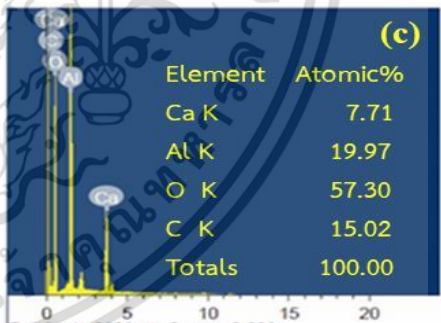


Figure 4.14 An average of crystallite and particles sizes of C3AH6 and x%rGO-C3AH6 with various contents of rGO loading.

- Scanning electron microscopy (SEM)

The morphology and element composition for all samples were carried out using SEM and EDX techniques, and the result is shown in Table 4.2. It was found that the edge shaped particles can be observed with all samples, whereas, amount of carbon in the 2% and 4%rGO-C3AH6 samples as the rGO in the composite has elevated to a level about 2 times greater than that of the C3AH6 sample. This indicated that by incorporating of the C3AH6 and rGO to form composite materials.

Table 4.2 SEM images and EDX analysis of (a) pristine C3AH6, (b) 2%rGO-C3AH6 and (c) 4%rGO-C3AH6 samples.

Samples	SEM	EDX
pristine C3AH6		
2%rGO-C3AH6		
4%rGO-C3AH6		

- EDS mapping

The EDS mapping of the C3AH6 sample exhibited a uniformed distribution of the powder surface as illustrated in Figure 4.15 that by applying a hydration process colloid with rapid heating, C3AH6 can be obtained from a C12A7 precursor. The results revealed elements of Ca, Al, O, and C on the surface Interestingly, the appearance of compound formed in the C3AH6 sample also confirmed the finding.

เอกสารนี้เป็นเอกสารที่สงวนไว้สำหรับการใช้งานเพื่อการศึกษาเท่านั้น ไม่อนุญาตให้นำไปใช้ประโยชน์ด้านการค้า ไม่ว่าจะกรณีใดๆ ทั้งสิ้น อีกทั้งห้ามมิให้ตัดแปลงเนื้อหา และต้องอ้างอิงถึงเจ้าของเอกสารทุกครั้งที่มีการนำไปใช้

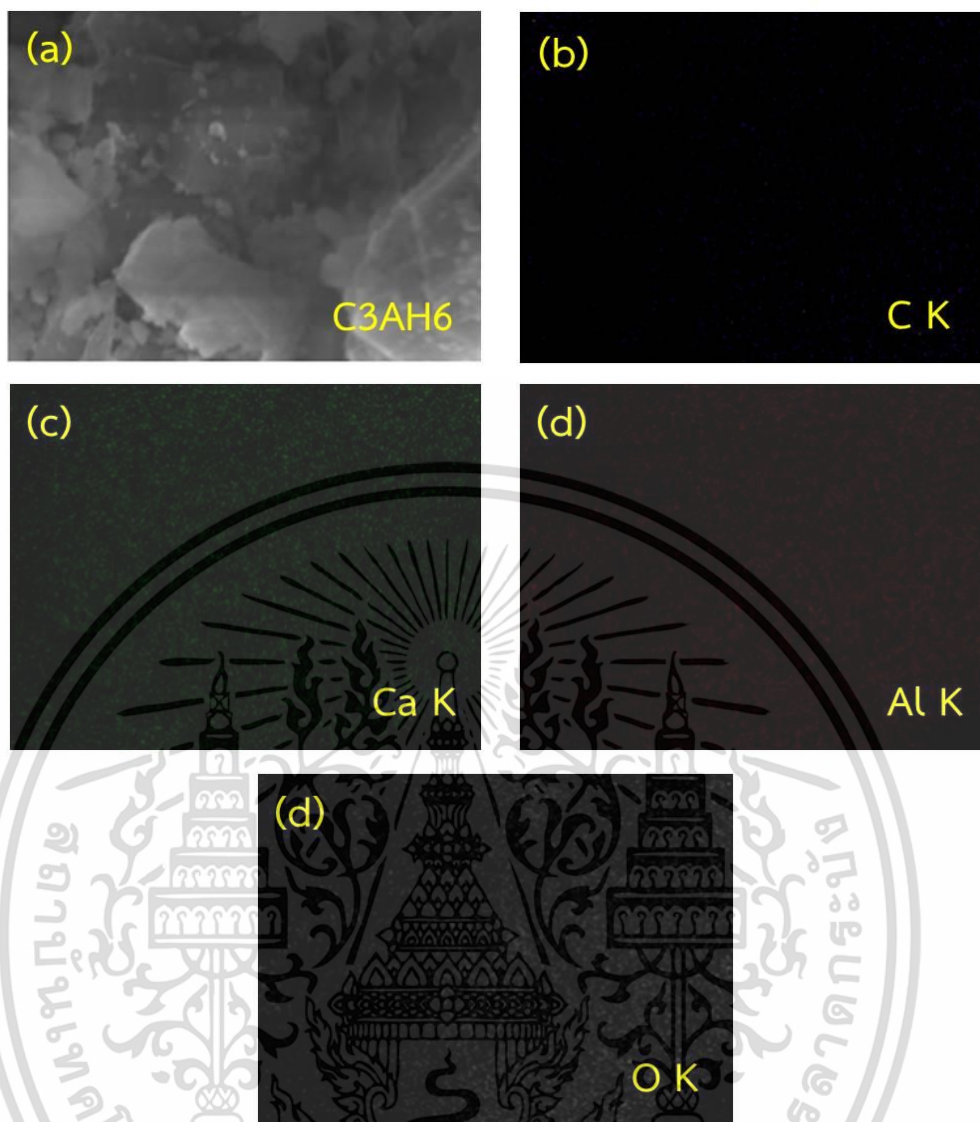


Figure 4.15 EDX elemental mapping of C3AH6 samples

As indicated in Figure 4.16, the EDX elemental mapping of 2%rGO-C3AH6 samples illustrated a uniformed distribution of carbon on the powder surface. By applying a hydration process with rGO colloid with rapid heating, the rGO and C3AH6 composite can be obtained from a C12A7 precursor. The results indicated the elements of Ca, Al, O, and C on the surface.

เอกสารนี้เป็นเอกสารที่สงวนไว้สำหรับการใช้งานเพื่อการศึกษาเท่านั้น ไม่อนุญาตให้นำไปใช้ประโยชน์ด้านการค้า
ไม่ว่ากรณีใดๆ ทั้งสิ้น อีกทั้งห้ามมิให้ตัดแปลงเนื้อหา และต้องอ้างอิงถึงเจ้าของเอกสารทุกครั้งที่มีการนำไปใช้

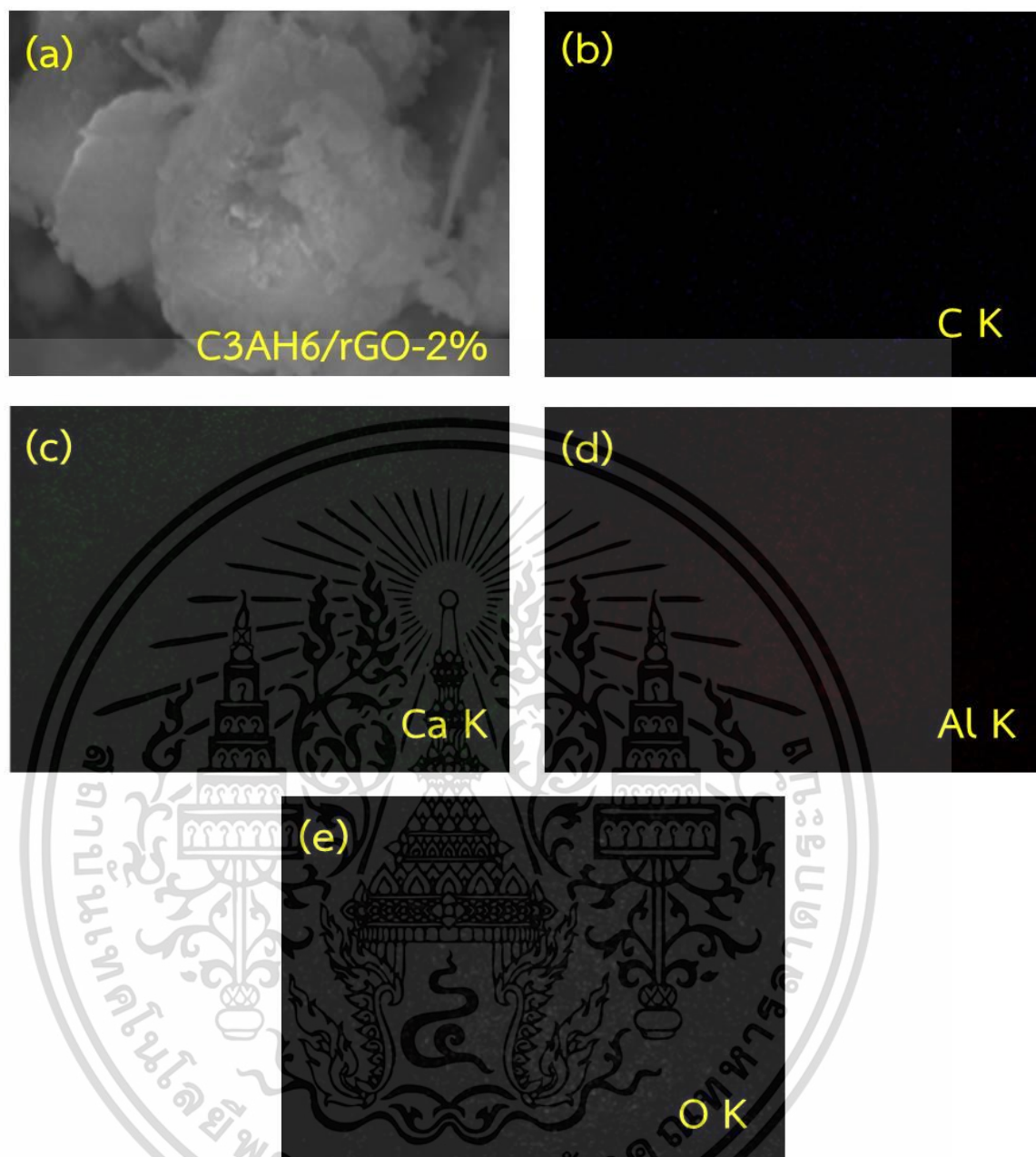


Figure 4.16 EDX elemental mapping of 2%rGO-C3AH6 samples.

As illustrated in Figure 4.17, the EDX elemental mapping of 4%rGO-C3AH6 sample indicated a uniformed distribution of carbon on the powder surface. By applying hydration process with rGO colloid with rapid heating, the rGO and C3AH6 composite can be obtained from a C12A7 precursor. The results indicated elements of Ca, Al, O, and C on the surface.

เอกสารนี้เป็นเอกสารที่สงวนไว้สำหรับการใช้งานเพื่อการศึกษาเท่านั้น ไม่อนุญาตให้นำไปใช้ประโยชน์ด้านการค้า ไม่ว่าจะกรณีใดๆ ทั้งสิ้น อีกทั้งห้ามมิให้ดัดแปลงเนื้อหา และต้องอ้างอิงถึงเจ้าของเอกสารทุกครั้งที่มีการนำไปใช้

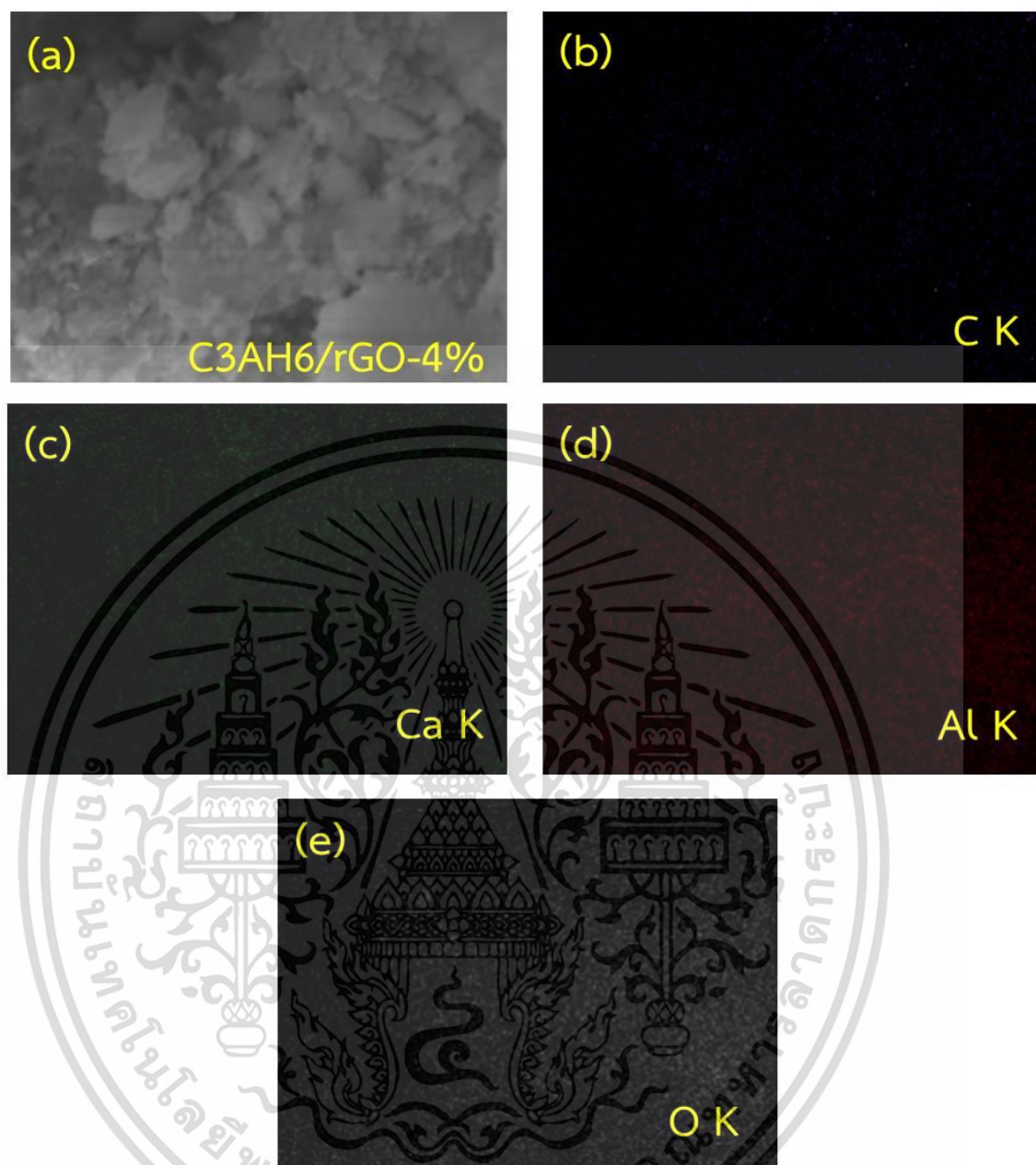


Figure 4.17 EDX elemental mapping of 4%rGO-C3AH6 samples.

- Transmission electron microscopy TEM

Figure 4.18 (a) showed TEM images of synthesized rGO. The results exhibited layers of nano sheeted and nano flaked material in the synthesized rGO, corroborating that the synthesized rGO had a nanosheet morphology. Figure 4.18(b) illustrated TEM images of synthesized C3AH6 sample. The results outlined the particle sizes of the C3AH6 sample in a layered nanostructure. The smallest

เอกสารนี้เป็นเอกสารที่สงวนไว้สำหรับการใช้งานเพื่อการศึกษาเท่านั้น ไม่อนุญาตให้นำไปใช้ประโยชน์ด้านการค้า ไม่ว่าจะกรณีใดๆ ทั้งสิ้น อีกทั้งห้ามมิให้ดัดแปลงเนื้อหา และต้องอ้างอิงถึงเจ้าของเอกสารทุกครั้งที่มีการนำไปใช้

nanosized particles were around 40 to 50 nanometer. The nanosized particles of C3AH6 sample were roughly around 50 nanometer in diameter, like the calculated average crystallite size of C3AH6 (61 nanometer). Figure 4.18(c) and (d) similarly indicated the surface morphology, particles size and shape of the x%rGO-C3AH6 composite samples for x=2 and 4. The displayed dark areas implied that a higher resolution of TEM imaging technique could elaborate the x%rGO-C3AH6 composite [23]. The rGO and C3AH6 particles were observed as nanosheets and dark nanoparticles. This indicated the occurrence of nanocomposited rGO-C3AH6 with nano flaked rGO and nanometer sized C3AH6 cement. The images exhibited small x%rGO-C3AH6 nanocomposite particles with sizes of 10 to 20 nanometers. The particle sizes ascertained that the synthesized x%rGO-C3AH6 nanocomposites contained nanometer sized particles. The smallest particle size of the 2%rGO-C3AH6, as illustrated in Figure 4.18(c), was ~20 nanometer, while the smallest particle size of the 4%rGO-C3AH6, as displayed in Figure 4.18(d), was 10 nanometer. The results indicated that the nanometer sized particles of the 4%rGO-C3AH6 sample were smaller than that of those the 2%rGO-C3AH6 sample. The rGO content majorly impacted the grain sizes of the rGO-C3AH6 composite samples. It was implied that the grain sizes relates to the amount of rGO in the composites. Selective Area Electron Diffraction (SAED) has been utilized to identify the crystal forms of single, double and multilayer rGO. TEM images, SAED patterns and EDX of the rGO nanosheets, nanometer sized C3AH6, and x%rGO-C3AH6 nanocomposite samples indicated diffraction rings implying a high poly-crystalline content as explained in Figure 4.18. The results illustrated ring patterns of the rGO sample. This was the attributes of poly-crystalline rGO deriving from its stacked multilayer orientation. Figure 4.18(b) exhibited the SAED pattern of the C3AH6 sample. This SAED pattern illustrated diffraction rings similarly suggesting high poly-crystalline content, subsequently, ascertaining the presence of nanometer sized C3AH6 particles. Figure 4.18(c) and (d) illustrated the SAED patterns of the synthesized nanocomposited x%rGO-C3AH6 samples. This SAED pattern was an attribute of combined diffraction rings resulted from a mixture of polycrystalline rGO and nanometer sized C3AH6 and x%rGO-C3AH6 cements, ascertaining the production of nanocomposited.

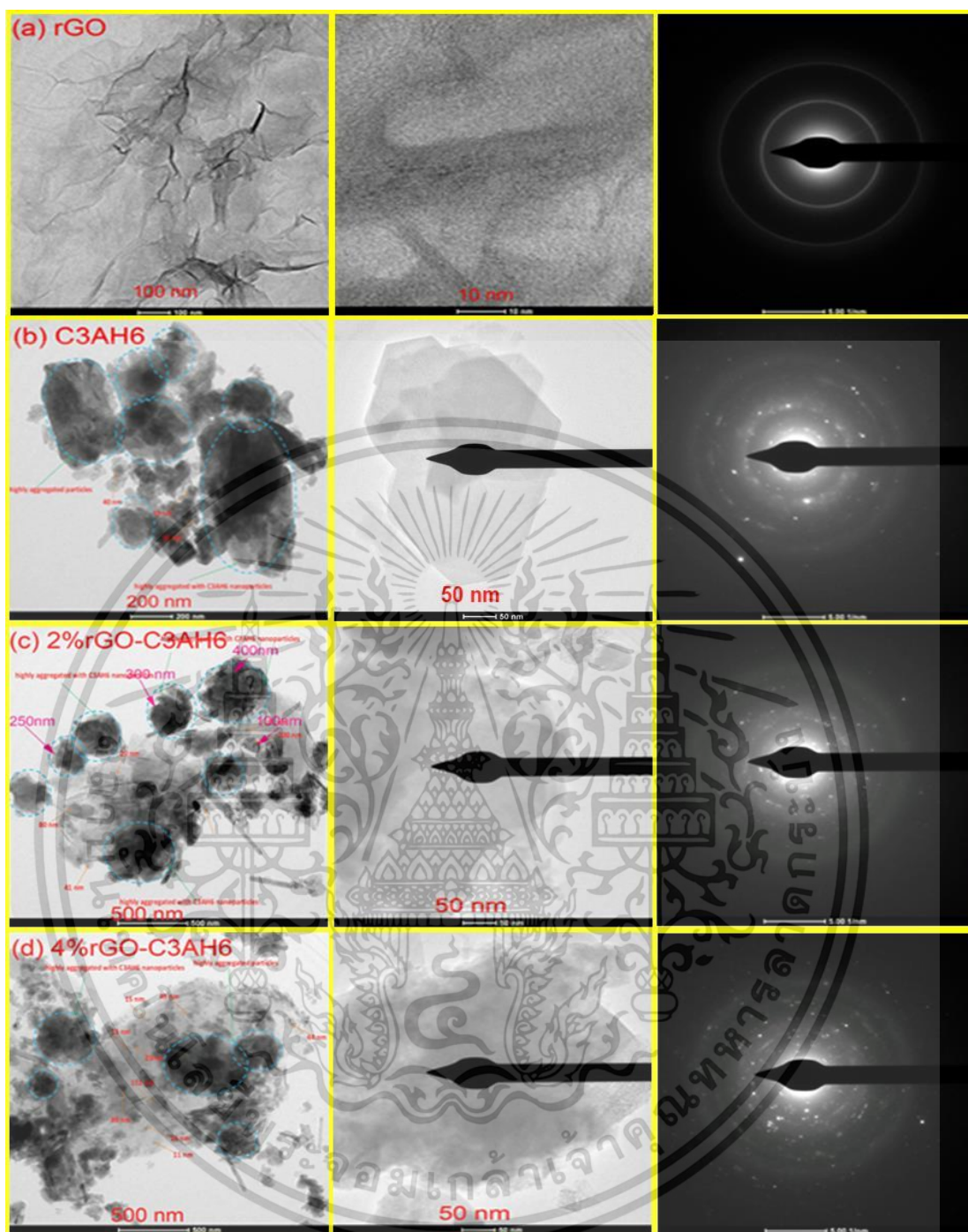


Figure 4.18 TEM images of synthesized (a) rGO nanosheets, (b) nanometer sized C3AH6, and (c) nano composited 2%rGO-C3AH6 and (d) 4%rGO-C3AH6 samples.

เอกสารนี้เป็นเอกสารที่สงวนไว้สำหรับการใช้งานเพื่อการศึกษาเท่านั้น ไม่อนุญาตให้นำไปใช้ประโยชน์ด้านการค้า ไม่ว่าจะกรณีใดๆ ทั้งสิ้น อีกทั้งห้ามมิให้ดัดแปลงเนื้อหา และต้องอ้างอิงถึงเจ้าของเอกสารทุกครั้งที่มีการนำไปใช้

- Raman spectra analysis

The Raman spectra of the lattice structure of the C3AH6, the Raman bands situated at 100-1200 cm^{-1} . The synthesized of C3AH6 at 533 cm^{-1} and 1050 cm^{-1} caused two peaks as illustrated in all synthesized samples. The attribute of C3AH6 bands sample appeared at 533 cm^{-1} and was marked to $[\text{AlO}_4^{5-}]$ stretching. The peak situated at 1050 cm^{-1} which is a characteristic of the C3AH6 structure. This was available in all samples of the x%rGO-C3AH6 since they contained a C3AH6 component. It was noted that the D (1348 cm^{-1}) and G (1576 cm^{-1}) band peaks of the rGO structure were found in all x%rGO-C3AH6 samples. However, these were not found in the C3AH6 sample. This implied that the disappearance of rGO contributed to a successful synthesis of C3AH6. The x%rGO-C3AH6 composites samples illustrated in both D and G band peaks of the rGO structure and peaks at 533 cm^{-1} and 1050 cm^{-1} of the C3AH6 structure. This ascertained that the nanometer sized rGO sheets were converted to a nanocomposite with nanometer sized C3AH6 particles to produce x% rGO-C3AH6 nanocomposites.

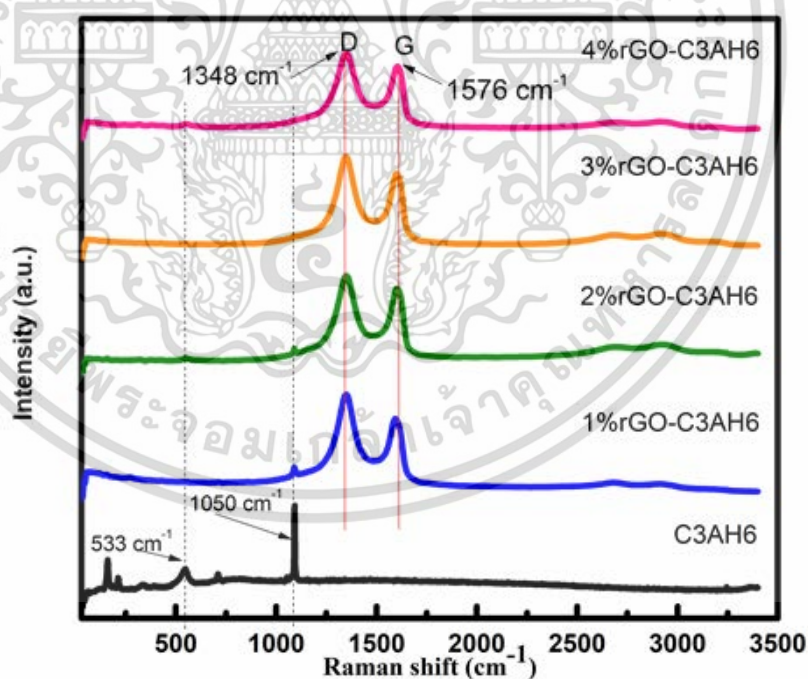


Figure 4.19 Raman spectra of pristine C3AH6 and x%rGO-C3AH6 samples.

เอกสารนี้เป็นเอกสารที่สงวนไว้สำหรับการใช้งานเพื่อการศึกษาเท่านั้น ไม่อนุญาตให้นำไปใช้ประโยชน์ด้านการค้า
ไม่ว่ากรณีใดๆ ทั้งสิ้น อีกทั้งห้ามมิให้ตัดแปลงเนื้อหา และต้องอ้างอิงถึงเจ้าของเอกสารทุกครั้งที่มีการนำไปใช้

- FT-IR spectra analysis

In addition, to confirm the rGO composite in the C3AH6 matrix, the FT-IR spectroscopy was used. Figure 4.20 illustrated the FT-IR spectra of C3AH6 cement-based and the x%rGO-C3AH6 nanocomposite in different of x weigh % contents. The FT-IR spectra of all x%rGO-C3AH6 specimens showed reflection dips close to the energy of the functional group -C=C- of rGO at 1626 cm^{-1} as indicated in the inset. The weak reflection dips was also seen at the energy position of functional group -C=O of GO at 993 cm^{-1} all samples. The reflectance decreases at the dip position by increasing the amount of rGO as expected.

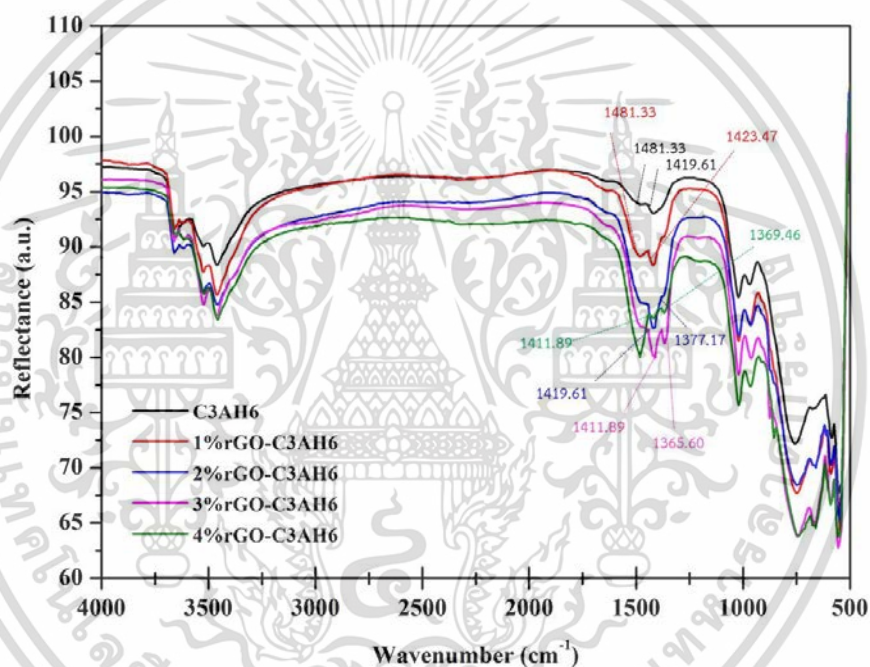


Figure 4.20 FT-IR spectra of pristine C3AH6, 1%rGO-C3AH6, 2%rGO-C3AH6, 3%rGO-C3AH6 and 4%rGO-C3AH6 samples.

- X-ray photoelectron spectroscopy (XPS)

Figure 4.21(a) outlined a wide scan XPS survey spectra of the synthesized C3AH6, and 2%rGO-C3AH6 samples. The XPS survey exhibited the spectra of O (1s), Ca (2p), Ca (2s), Al (2p) and C (1s) of the C3AH6 and 2%rGO-C3AH6 samples respectively. The spectral results indicated synergies of Ca, Al, O (1s) and C (1s) peaks. Figure 4.21(b) illustrated the XPS spectra of C1s from the synthesized C3AH6, 2%rGO-

เอกสารนี้เป็นเอกสารที่สงวนไว้สำหรับการใช้งานเพื่อการศึกษาเท่านั้น ไม่อนุญาตให้นำไปใช้ประโยชน์ด้านการค้า
ไม่ว่ากรณีใดๆ ทั้งสิ้น อีกทั้งห้ามมิให้ตัดแปลงเนื้อหา และต้องอ้างอิงถึงเจ้าของเอกสารทุกครั้งที่มีการนำไปใช้

C3AH6 and 4%rGO-C3AH6 samples. The XPS spectra exhibited a peak at 285 eV as indications of the C3AH6 sample and three peak positions situated at 284.42 eV, 285.39 eV, and 288.92 eV, as evident in all of the 2%rGO-C3AH6 and 4%rGO-C3AH6 samples. Two peaks of 2%rGO-C3AH6 and 4%rGO-C3AH6 samples situated at 288.92 eV and 285.39 indicated C=O and C-O bonds [12] for carbon atoms in these samples. The peak situated at 284.42 eV [12], which represented the C-C bond of sp² carbon atoms in a conjugated honeycomb lattice rGO, appeared in the synthesized 2%rGO-C3AH6 and 4%rGO-C3AH6 samples.

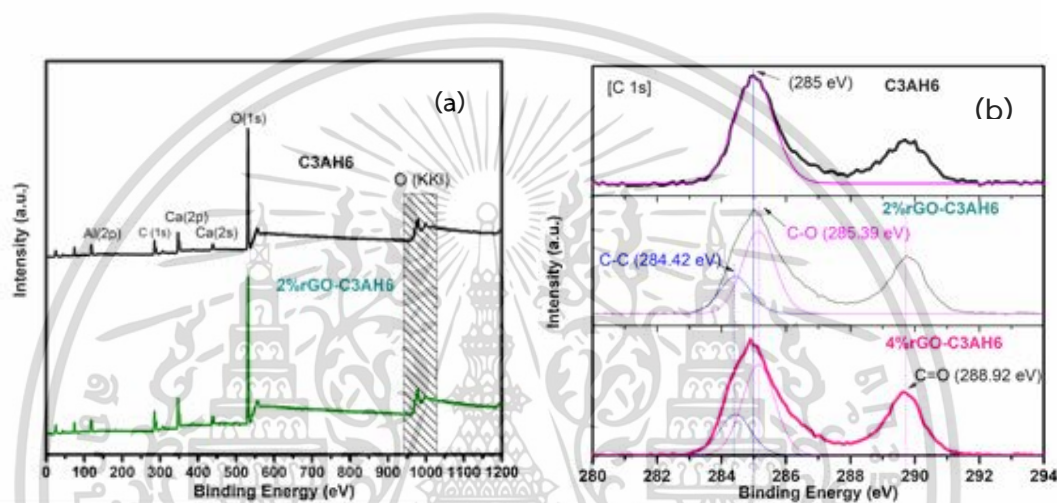


Figure 4.21 (a) XPS survey spectra of C3AH6 and 2%rGO-C3AH6 samples and (b) XPS survey spectra of C(1s) of the synthesized C3AH6, 2%rGO-C3AH6 and 4%rGO-C3AH6 samples.

- UV-visible spectroscopy

Figure 4.22(a) The UV-visible spectra of x%rGO-C3AH6 varied from the spectra of the C3AH6. The x%rGO-C3AH6 samples illustrated a low absorption over the visible range, however, a high absorption in a lower energy range. The UV-absorption band of rGO at 270 nanometer, indicated that the inset [25], was missing from the spectra of the x%rGO-C3AH6 samples. Nevertheless, the rGO absorption peak was observed in the spectra of x%rGO-C3AH6 nanocomposites with rGO at 1, 2, 3 and 4 wt% levels. The absorption of the x%rGO-C3AH6 nanocomposite was higher at elevated levels of rGO, which corresponded to the dark brown color of the powder samples. Figure 4.22(b) illustrated direct optical gaps (E_g) of the sintered C3AH6 and

x%rGO-C3AH6 nanocomposited samples at room temperature. The E_g of C3AH6 was

เอกสารนี้เป็นเอกสารที่สงวนไว้สำหรับการใช้งานเพื่อการศึกษาเท่านั้น ไม่อนุญาตให้นำไปใช้ประโยชน์ทางการค้า
ไม่ว่ากรณีใดๆ ทั้งสิ้น อีกทั้งห้ามมิให้ตัดแปลงเนื้อหา และต้องอ้างอิงถึงเจ้าของเอกสารทุกครั้งที่มีการนำไปใช้

4.2 eV, while those of the x%rGO-C3AH6 were 3.0, 2.5, 2.0 and 1.5 eV for rGO contents where x=1, 2, 3, and 4 wt%, accordingly. These implied that the E_g of the x%rGO-C3AH6 decreased as rGO content increased. Furthermore, C3AH6 had a high E_g value of 5.55 eV, while the E_g values of x%rGO-C3AH6 had a constant value of 6.05 eV.

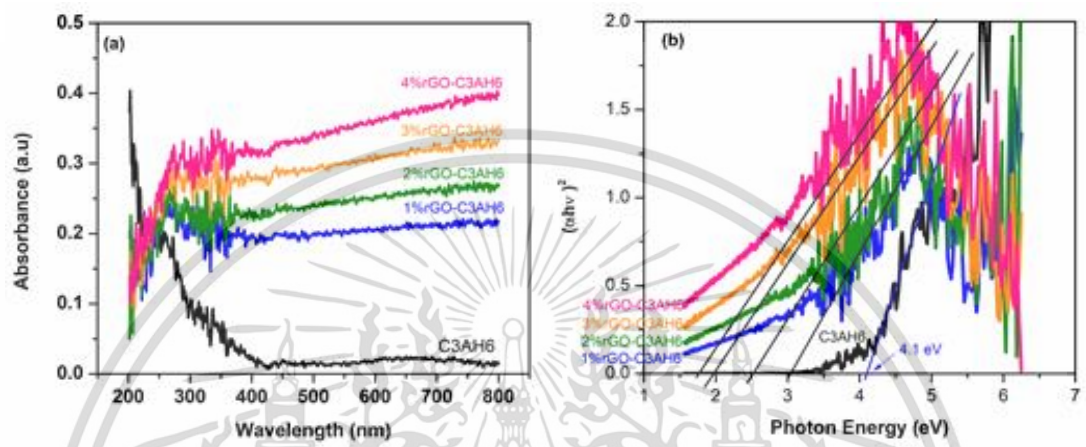


Figure 4.22 (a) Absorption coefficient of C3AH6 and x%rGO-C3AH6 samples and (b) the relationship between an allowed direct optical gap of C3AH6 and x%rGO-C3AH6 samples.

- TGA analysis

Figure 4.23 explained a TGA diagram of the C3AH6 specimen and the x%rGO-C3AH6 nanocomposited specimens. The diagram showed mass loss at from water decomposed from the C3AH6 specimen and the x%rGO-C3AH6 nanocomposited specimens at around 100 °C. The C3AH6 specimen and the x%rGO-C3AH6 nanocomposited specimens gradually dissolves with amorphous anhydrous and water vaporization at between 100-550 °C. The major mass loss was at 200-300 °C and a smaller loss was at between 400-550 °C. For the dehydrations between 300 and 350 °C, the C3AH6 decomposed and formed C3AH1.5 and at around 320-550 °C completely dehydrates to form C12A7 compound. The results pointed out that the x%rGO-C3AH6 nanocomposited suit table using to application in ranging lower than 300 °C.

เอกสารนี้เป็นเอกสารที่สงวนไว้สำหรับการใช้งานเพื่อการศึกษาเท่านั้น ไม่อนุญาตให้นำไปใช้ประโยชน์ด้านการค้า ไม่ว่าจะกรณีใดๆ ทั้งสิ้น อีกทั้งห้ามมิให้ตัดแปลงเนื้อหา และต้องอ้างอิงถึงเจ้าของเอกสารทุกครั้งที่มีการนำไปใช้

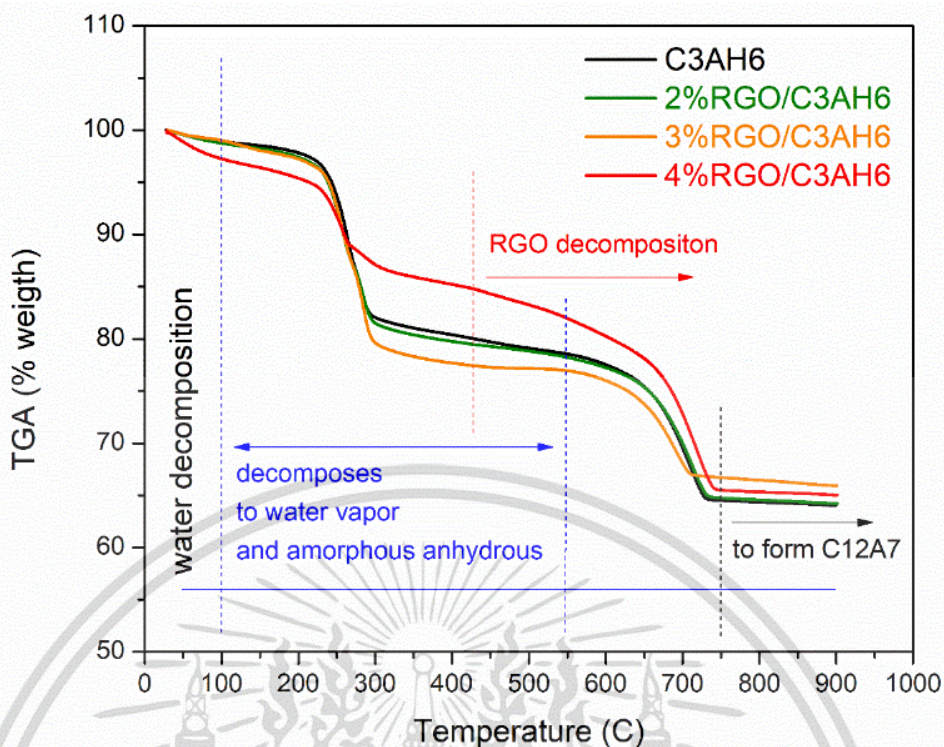


Figure 4.23 TGA diagram of C3AH6, 2%rGO-C3AH6, 3%rGO-C3AH6 and 4%rGO-C3AH6 samples.

4.2.3 The properties of rGO-C3AH6 nanocomposites

- Micro hardness properties

Micro hardness of the concocted nanometer sized C3AH6 and synthesized x%rGO-C3AH6 samples were assessed by adopting the pyramid on a square base method as explained by the Vickers indenter hardness (HV) technique. This technique evaluate micro hardness by defining the ratio of the load applied to the projected area of the indentation as shown in equation 4.9 [57]

$$HV = 1854(P/d^2) \quad (4.9)$$

where HV is the Vickers micro hardness value

P is the applied load (kg)

d is the average diagonal length (mm)

Figure 4.24. The image was enlarged by a factor of 10 from the machine. The derived d values were 0.225, 0.216, 0.202, 0.1827 and 0.167 mm for the nanometer sized C3AH6 and nano-composited 1%, 2%, 3%, and 4% rGO-C3AH6 samples, respectively. It was discovered that shading of the dark brown colour on the surface of the C3AH6 and x%rGO-C3AH6 nanocomposited samples intensified as the percentage weight of rGO increased.

Figure 4.25 these HV values were 74, 80, 90, 111, and 132 HV/2kg, respectively. It was illustrated that the HV values increased by a power of two with elevating weight percent of rGO. An improvement of rGO-C3AH6 composites shown in the HV value as observed in the nanometer sized rGO-C3AH6 nanocomposites. For the TEM results, the decreased sizes of the nanocomposited rGO-C3AH6 specimens were altered because of an accelerating percent weight of rGO that intensified the HV value.

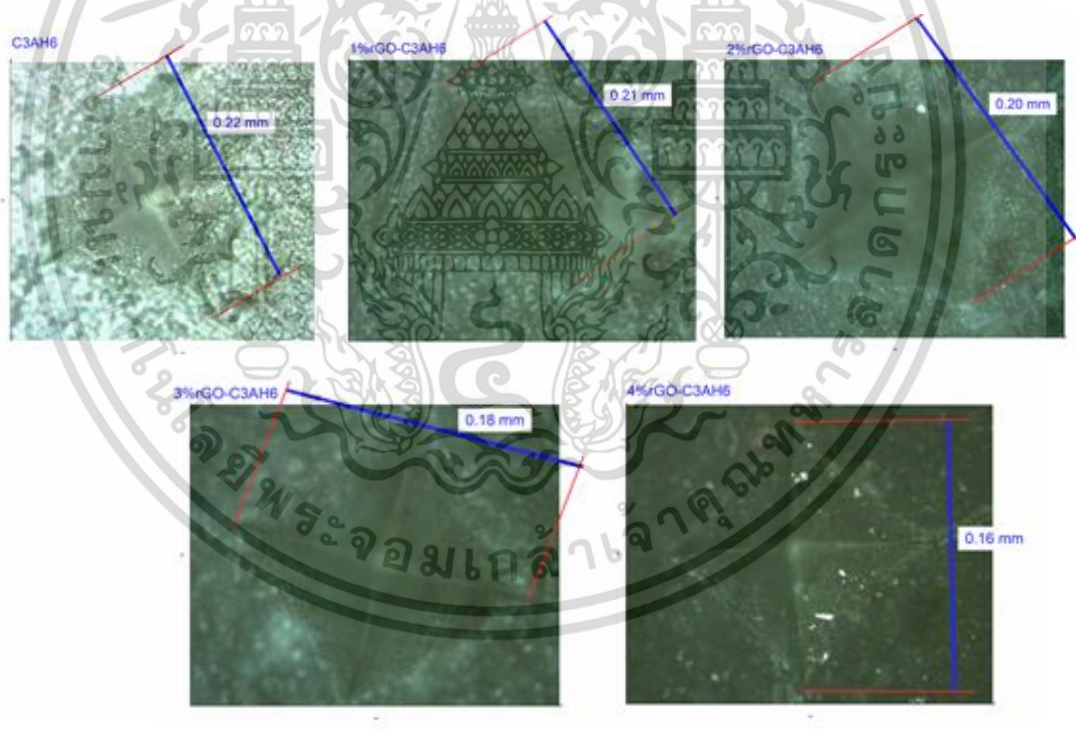


Figure 4.24 Diagonal length of the impression on surfaces of C3AH6, 1%rGO-C3AH6, 2%rGO-C3AH6, 3%rGO-C3AH6 and 4%rGO-C3AH6 composited samples.

เอกสารนี้เป็นเอกสารที่สงวนไว้สำหรับการใช้งานเพื่อการศึกษาเท่านั้น ไม่อนุญาตให้นำไปใช้ประโยชน์ด้านการค้า ไม่ว่าจะกรณีใดๆ ทั้งสิ้น อีกทั้งห้ามมิให้ตัดแปลงเนื้อหา และต้องอ้างอิงถึงเจ้าของเอกสารทุกครั้งที่มีการนำไปใช้

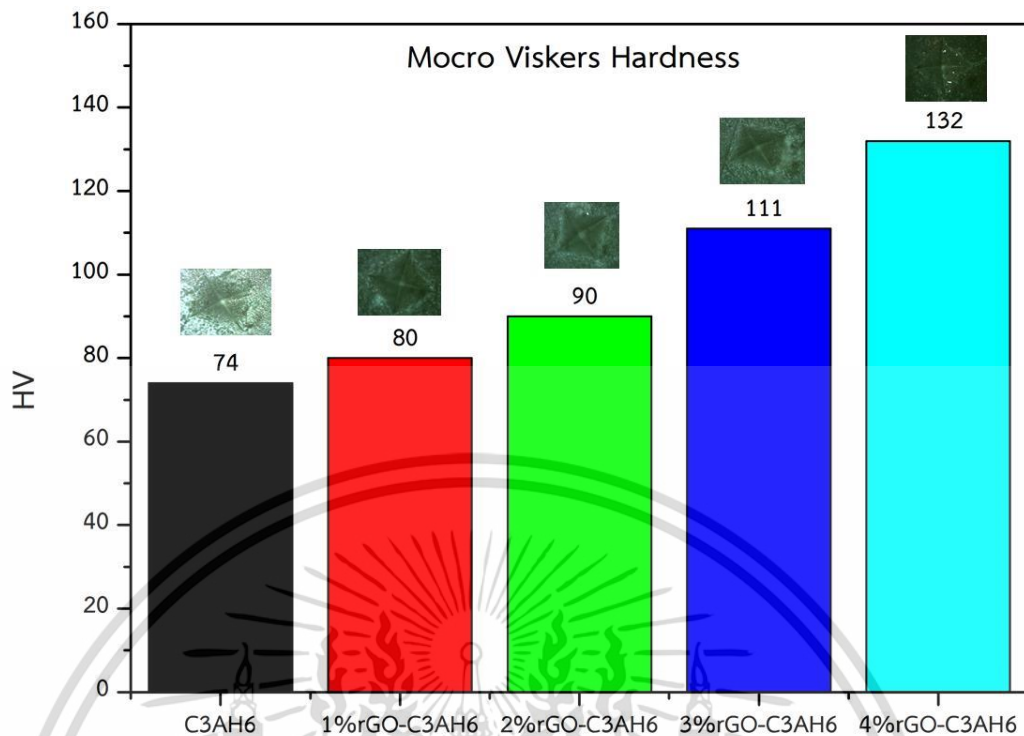


Figure 4.25 Micro-hardness of C3AH6, 1%rGO-C3AH6, 2%rGO-C3AH6, 3%rGO-C3AH6 and 4%rGO-C3AH6 composited samples.

- Antibacterial properties

The results were explained in Figure 4.26. It was noted that nanometer sized C3AH6 generated no clear zone implying that the substance was unable to kill bacteria. The 12 mm red line in the figure represented the diameter of a C3AH6 pellet. The x%rGO-C3AH6 nanocomposited indicated clear zones revealing antibacterial activity against E. coli. The width of clear zones resulted from the 1%rGO-C3AH6, 2%rGO-C3AH6 and 3%rGO-C3AH6 nanocomposite samples enlarged as the increasing level of rGO loading. 4%rGO-C3AH6 cement produced the highest degree of antibacterial activity against E. coli. This implied that the antibacterial property of the x%rGO-C3AH6 cement is interlinked with the level of rGO in the nanocomposited cement and with the smaller particle sizes, 10 to 20 nanometer, of x%rGO-C3AH6. The antibacterial action of the nanocomposited x%rGO-C3AH6 was a result of the extraction of phospholipids from lipid membranes [58], generating strong interactions with these molecules in bacterial cell membranes. These results corroborated the importance of minimized particle size to generate increased rGO

เอกสารนี้เป็นเอกสารที่สงวนไว้สำหรับการใช้งานเพื่อการศึกษาเท่านั้น ไม่อนุญาตให้นำไปใช้ประโยชน์ด้านการค้า
ไม่ว่ากรณีใดๆ ทั้งสิ้น อีกทั้งห้ามมิให้ตัดแปลงเนื้อหา และต้องอ้างอิงถึงเจ้าของเอกสารทุกครั้งที่มีการนำไปใช้

content within the nanocomposited x%rGO-C3AH6 and concurrently accelerated antibacterial activity.

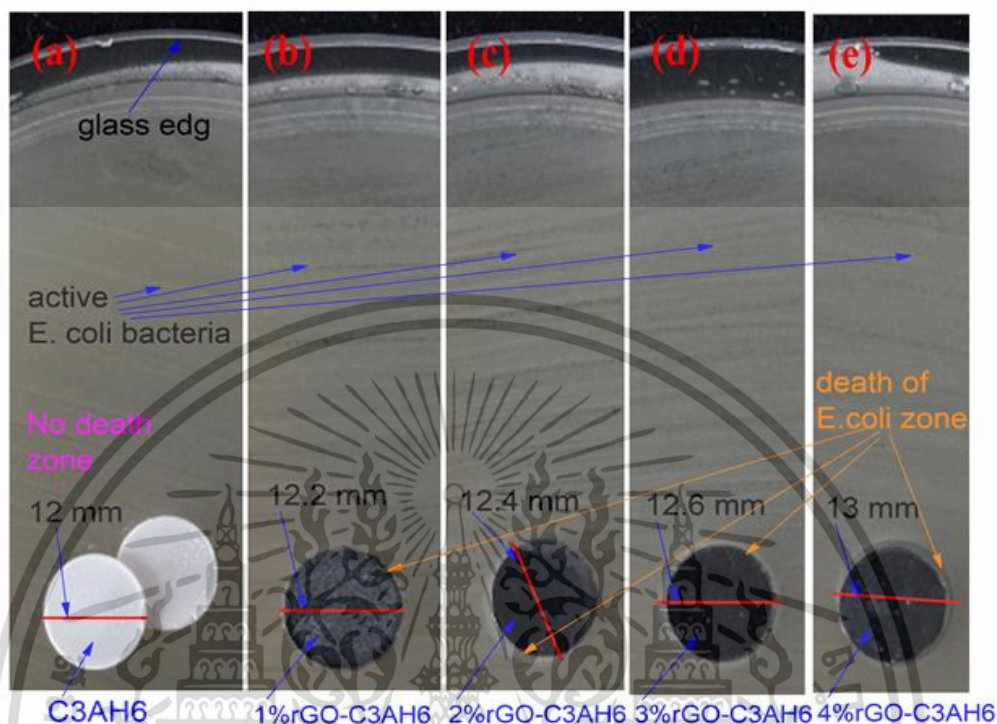


Figure 4.26 Antibacterial properties of (a) C3AH6, (b) 1%rGO-C3AH6, (c) 2%rGO-C3AH6, (d) 3%rGO-C3AH6 and (e) 4%rGO-C3AH6 composited samples.

- Dielectric properties

Utilizing an impedance analyzer to evaluate dielectric properties of the x%rGO-C3AH6 nanocomposites, the values of electric capacitance (C) and resistance (R) of the specimens were assessed. These measurements were conducted over the frequency range of 20 Hz - 2 MHz. Figure 4.27(a) the results indicated that the dielectric response of the C3AH6 and x%rGO-C3AH6 samples exhibited strong frequency dependence. The real dielectric constant of all samples decreased as frequency increased. The ϵ' values of the samples at low frequency were greater than that at high frequency. The ϵ' value of C3AH6 was 1.52×10^2 at 20 Hz, and those of x%rGO-C3AH6, at 20 Hz, were 4.45×10^2 , 6.86×10^2 , 1.010×10^3 and 3.2×10^3 for x=1, 2, 3 and 4, accordingly. It was noted that the ϵ' values of x%rGO-C3AH6 samples were higher than that of C3AH6. The dielectric constant of the 4%rGO-C3AH6 sample

เอกสารนี้เป็นเอกสารที่สงวนไว้สำหรับการใช้งานเพื่อการศึกษาเท่านั้น ไม่อนุญาตให้นำไปใช้ประโยชน์ด้านการค้า ไม่ว่าจะกรณีใดๆ ทั้งสิ้น อีกทั้งห้ามมิให้ตัดแปลงเนื้อหา และต้องอ้างอิงถึงเจ้าของเอกสารทุกครั้งที่มีการนำไปใช้

was roughly 10 times greater than that of the nanometer sized C3AH6 sample. The ϵ' value of 4%rGO-C3AH6 (3.2×10^3) exhibited nearly significant dielectric magnitude. The dielectric constant of x%rGO-C3AH6 increased with the percentage weight of rGO composite, which aligned with the decreased size of particle of the x%rGO-C3AH6 nanocomposites. This illustrated that the decreasing particle sizes of the x%rGO-C3AH6 specimens accelerated dielectric constants of the nanocomposited rGO-C3AH6 samples. The results above indicated that the dielectric constant values of x%rGO-C3AH6 were greater than that of C3AH6 over the entire frequency range and the values increased as the particle sizes reduced in the samples. The x%rGO-C3AH6 samples exhibited a uniformed distribution of nanometer sized particle. The nanometer sized particles of the x%rGO-C3AH6 nanocomposites created a large dielectric constant. The dielectric constant increased as with the percentage weight of rGO. The results indicated that the surfaces of rGO nanocomposites affected the acceleration of the dielectric constant by controlling the dispersion of rGO sheets. Figure 4.27(b) illustrated the tangent loss of the C3AH6 and x%rGO-C3AH6 samples. It was noted that the loss tangents of C3AH6 and x%rGO-C3AH6 decreased with increasing frequency. The loss tangents of x%rGO-C3AH6 nanocomposites were greater than that of C3AH6 over the entire frequency range studied. The 4%rGO-C3AH6 nanocomposite pertained the highest loss tangent. These results indicated that the loss tangent of x%rGO-C3AH6 increased with the amount of rGO. The trend of loss tangent for x%rGO-C3AH6 nanocomposite accordingly increased with the rGO content. This pattern was explained at high frequency and was linked to dipolar relaxation. At lower frequencies, it was linked to interfacial polarization and conductivity. This effect related to the surface morphology of rGO nanocomposites with C3AH6 arising from the diffusion of rGO sheets and the surface interface between the conducting grains and insulating grain boundaries. Figure 4.27(c) illustrated the AC electrical conductivity (σ_{ac}) of nanometer sized C3AH6 and x%rGO-C3AH6 nanocomposited specimens vs. the percentage weight of rGO at 20, 10^4 , 10^5 , 10^6 MHz. The AC conductivity of these specimens increased with the rGO content. The σ_{ac} values of the x%rGO-C3AH6 nanocomposites were larger than that of C3AH6 over the entire frequency range under the study. The 4%rGO-C3AH6 nanocomposite illustrated the highest σ_{ac} values. The σ_{ac} of x%rGO-C3AH6 increased with the rGO content.

เอกสารนี้เป็นเอกสารที่สงวนไว้สำหรับการใช้งานเพื่อการศึกษาเท่านั้น ไม่อนุญาตให้นำไปใช้ประโยชน์ด้านการค้า
ไม่ว่ากรณีใดๆ ทั้งสิ้น อีกทั้งห้ามมิให้ตัดแปลงเนื้อหา และต้องอ้างอิงถึงเจ้าของเอกสารทุกครั้งที่มีการนำไปใช้

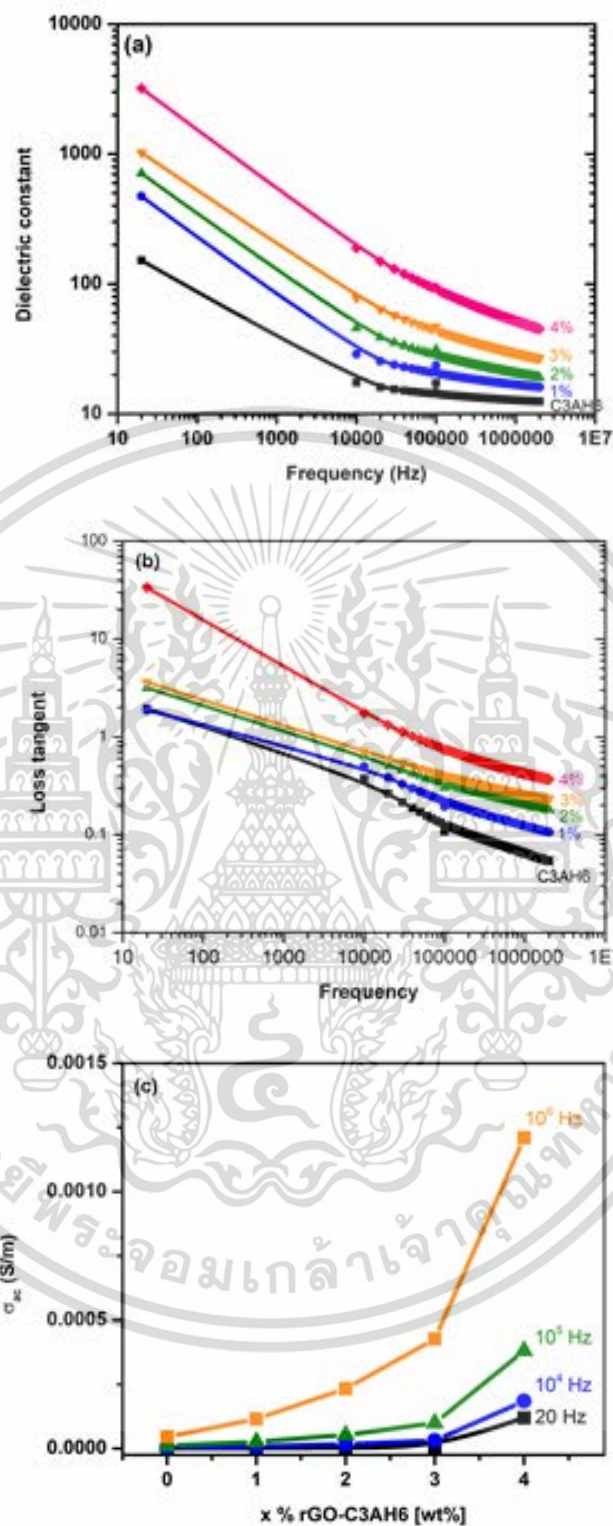


Figure 4.27 (a) Dielectric constant and (b) dielectric loss as a function of frequency, and (c) electrical conductivity of C3AH6, 1%rGO-C3AH6, 2%rGO-C3AH6, 3%rGO-C3AH6 and 4%rGO-C3AH6 nanocomposites samples.

เอกสารนี้เป็นเอกสารที่สงวนไว้สำหรับการใช้งานเพื่อการศึกษาเท่านั้น ไม่อนุญาตให้นำไปใช้ประโยชน์ด้านการค้า ไม่ว่าจะกรณีใดๆ ทั้งสิ้น อีกทั้งห้ามมิให้ตัดแปลงเนื้อหา และต้องอ้างอิงถึงเจ้าของเอกสารทุกครั้งที่มีการนำไปใช้

- Thermal properties

Figure 4.28(a) illustrated thermal conductivity as a function of the temperature for the C3AH6 and x%rGO-C3AH6 samples. The κ values of all samples insignificantly altered according to temperature. These values for the x%rGO-C3AH6 samples were greater than that of the C3AH6 sample and decreased with the amount of rGO. High rGO contents in x%rGO-C3AH6 nanocomposites increased, resulting in reduced κ values. The thermal conductivity. Based on the AC electrical conductivity exhibited in Figure 4.28(b), the κ_e values of the x%rGO-C3AH6 and C3AH6 were small. Magnitude of κ values of all samples was mainly influenced by κ_{phonon} . If the κ_e value is neglected, the thermal conductivity of κ_{phonon} . Figure 4.28(b) indicated the relationship, κ_{phonon} versus $1/T^3$, for the x%rGO-C3AH6 and C3AH6 samples. The results revealed that only C3AH6 had an inverse relationship with temperature, suggesting that phonon processes (τ_U) mainly influenced the thermal conductivity of C3AH6. The x%rGO-C3AH6 samples did not illustrate similar pattern. Definitely, the grain boundary ($\frac{1}{\tau_B} = v/L$) term influenced the effect of nanocomposite of the x%rGO-C3AH6 specimens. L , the characteristic grain size of the x%rGO-C3AH6 nanocomposites, was nanometer sized. Similarly, the nanometer sized grain characteristic reacted to reduce the κ_{phonon} value of the x%rGO-C3AH6 nanocomposites. The reduction of thermal conductivity of the x%rGO-C3AH6 samples was a result of a smaller particle size at the boundary. They were reduced from 20 nm to 10 nm as the percentage volume of the rGO nanoflakes increased during the preparation process. The rGO nanocomposite content in C3AH6 influenced the development of the thermal conductivity of x%rGO-C3AH6 nanocomposites. The specific heat (C_p) values of the C3AH6 and x%rGO-C3AH6 samples were derived from the thermal diffusivity measurements over a temperature range of 298 to 573 K by a laser flash technique. Figure 4.28(c) explained C_p as a function of the temperature of the x%rGO-C3AH6 and C3AH6 samples. The results illustrated that the C_p value of all samples increased according to the temperature. The C_p of 1%rGO-C3AH6 and 2%rGO-C3AH6 was greater than the C3AH6 cement, while 3%rGO-C3AH6 and 4%rGO-C3AH6 pertained lower C_p values. The lower rGO content in x%rGO-C3AH6 composites led to higher C_p values. This trend of x%rGO-C3AH6 indicated a decrease in C_p with increasing amounts of rGO. The high rGO content in x%rGO-C3AH6 composites reduced the C_p values.

เอกสารนี้เป็นเอกสารที่สงวนไว้สำหรับการใช้งานเพื่อการศึกษาเท่านั้น ไม่อนุญาตให้นำไปใช้ประโยชน์ด้านการค้า
ไม่ว่ากรณีใดๆ ทั้งสิ้น อีกทั้งห้ามมิให้ตัดแปลงเนื้อหา และต้องอ้างอิงถึงเจ้าของเอกสารทุกครั้งที่มีการนำไปใช้

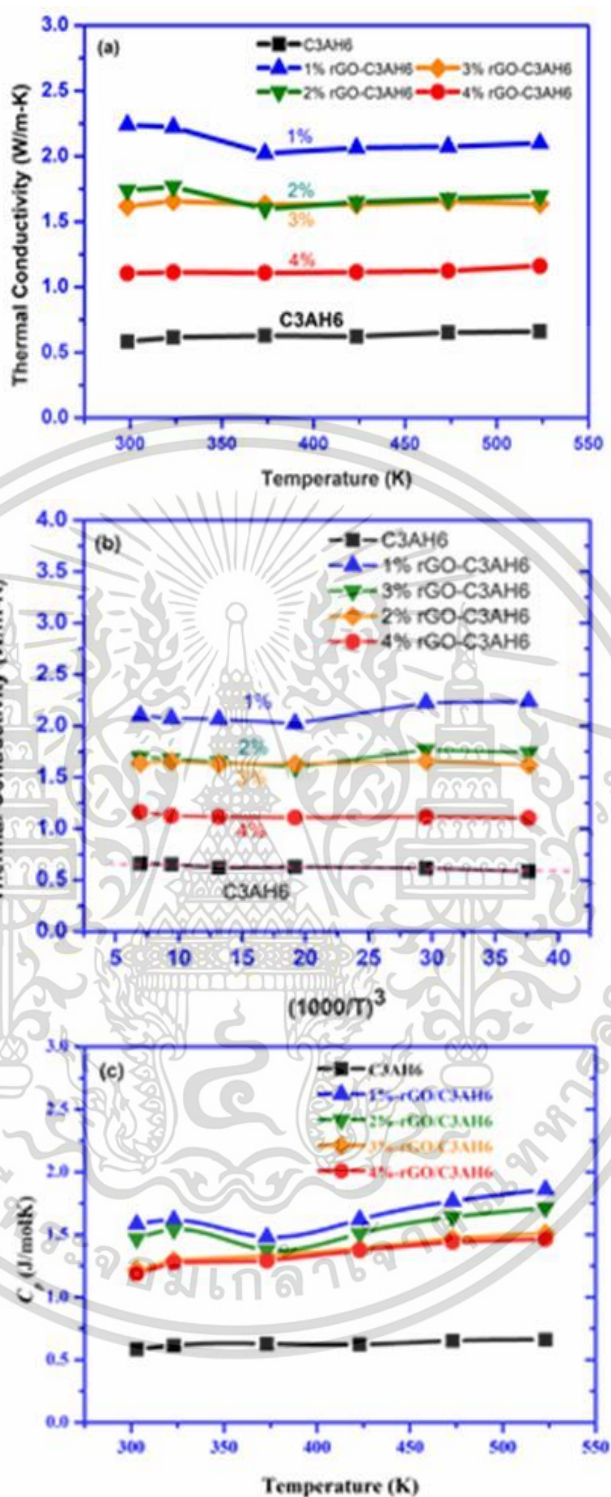


Figure 4.28 (a) thermal conductivity a function of temperature, (b) thermal conductivity a function of inverse of temperature, (c) Specific heat of C3AH6, 1%rGO-C3AH6, 2%rGO-C3AH6, 3%rGO-C3AH6 and 4%rGO-C3AH6 samples.

เอกสารนี้เป็นเอกสารที่สงวนไว้สำหรับการใช้งานเพื่อการศึกษาเท่านั้น ไม่อนุญาตให้นำไปใช้ประโยชน์ด้านการค้า ไม่ว่าจะกรณีใดๆ ทั้งสิ้น อีกทั้งห้ามมิให้ตัดแปลงเนื้อหา และต้องอ้างอิงถึงเจ้าของเอกสารทุกครั้งที่มีการนำไปใช้

- Electrochemical properties

The fabricated a slurry for working active electrodes, each obtained at a ratio of 80: 10: 10 wt% of all material samples (C3AH6 and all x%rGO-C3AH6), PVDF and acetylene black were well mixed with a slurry of N-methyl-2-pyrrolidone (NMP) 0.5 ml using by ball milling method at room temperature for 24 hours. Then, a slurry was coated onto a nickel foam sheet within a coating area of $1 \times 1 \text{ cm}^2$ and kept dried for 3 hours in an oven at $80 \text{ }^\circ\text{C}$. Finally, these active electrodes were pressed at 1.5 tons for 1 min by using uniaxial compression and soaked into 1.0 M KOH aqueous solution for 3 hours before performing an electrochemical test. Figure 4.29(a) shows CV curves of all electrodes at a scan rate of 100 mV s^{-1} in a potential window of -0.1-0.0 V. The CV curves of C3AH6 and all rGO-C3AH6 electrodes show a clear reversible reaction of a capacitive behavior occurring at the interface of electrode and electrolyte, suggesting the storage charge mechanism of electrical double layer capacitors (EDLCs) behavior. As shown in Figure 4.29 (b)–(h), the CV curves of C3AH6 and all rGO-C3AH6 electrodes at scan ranges from 10 to 200 mV s^{-1} , illustrated intensity and area of these CV curves gradually increase with an increasing scan rate because of the efficient migration of OH^- ions through the porous structure and oxygen containing functional groups at electrode surface of rGO Figure 4.30 (a)–(h) presents the GCD curves of C3AH6 and all rGO-C3AH6 electrodes conducted within a potential window of -0.1 - 0.0 V at a scan rate of 0.5 A g^{-1} and different current densities ranges from 0.2 to 10 A g^{-1} . All GCD curves exhibited a symmetric shape, which represents characteristics of EDLCs behavior. It was noted that the discharge curves of C3AH6 and all rGO-C3AH6 electrodes indicated low internal resistance (R_i), implying high conductivity of electrode material. Specific capacitances (C_{sc}) of C3AH6 and all rGO-C3AH6 electrodes were assessed based on the CV curve and discharge curves as illustrated in Figure 4.31 (a)–(b) and the derived values are explained in Table 4.3. Figure 4.31 (a)–(b) showed that the C_{sc} values decreased with an increasing current density due to the imperfection of electrodes that prevent the diffusion and penetration of electrolyte ions into the active sites of electrode materials. Furthermore, small particles could lead to high surface area and large mesopore of active redox sites for more OH^- ions to be accessible in electrolyte. Notwithstanding, it was found that all rGO-C3AH6 electrodes provided excellent cycling stability as shown in Figure 4.29(c).

เอกสารนี้เป็นเอกสารที่สงวนไว้สำหรับการใช้งานเพื่อการศึกษาเท่านั้น ไม่อนุญาตให้นำไปใช้ประโยชน์ด้านการค้า
ไม่ว่ากรณีใดๆ ทั้งสิ้น อีกทั้งห้ามมิให้ดัดแปลงเนื้อหา และต้องอ้างอิงถึงเจ้าของเอกสารทุกครั้งที่มีการนำไปใช้

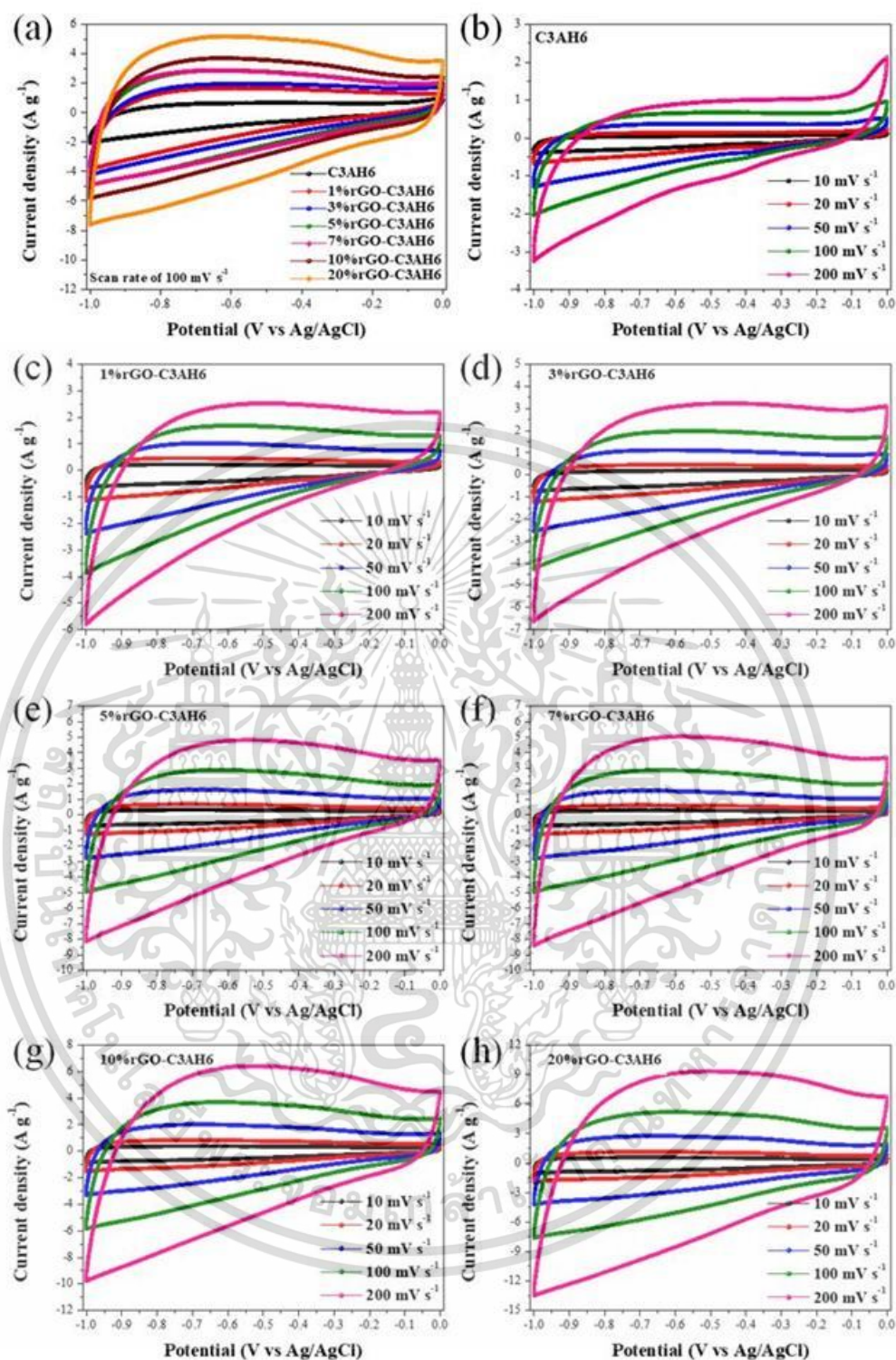


Figure 4.29 (a) CV curves at a scan rate of 100 mV s^{-1} of C3AH6 and all rGO-C3AH6 electrodes. (b), (c), (d), (e), (f), (g) and (h) CV curves at different scan rates of C3AH6 and all rGO-C3AH6 electrodes.

เอกสารนี้เป็นเอกสารที่สงวนไว้สำหรับการใช้งานเพื่อการศึกษาเท่านั้น ไม่อนุญาตให้นำไปใช้ประโยชน์ด้านการค้า ไม่ว่าจะกรณีใดๆ ทั้งสิ้น อีกทั้งห้ามมิให้ตัดแปลงเนื้อหา และต้องอ้างอิงถึงเจ้าของเอกสารทุกครั้งที่มีการนำไปใช้

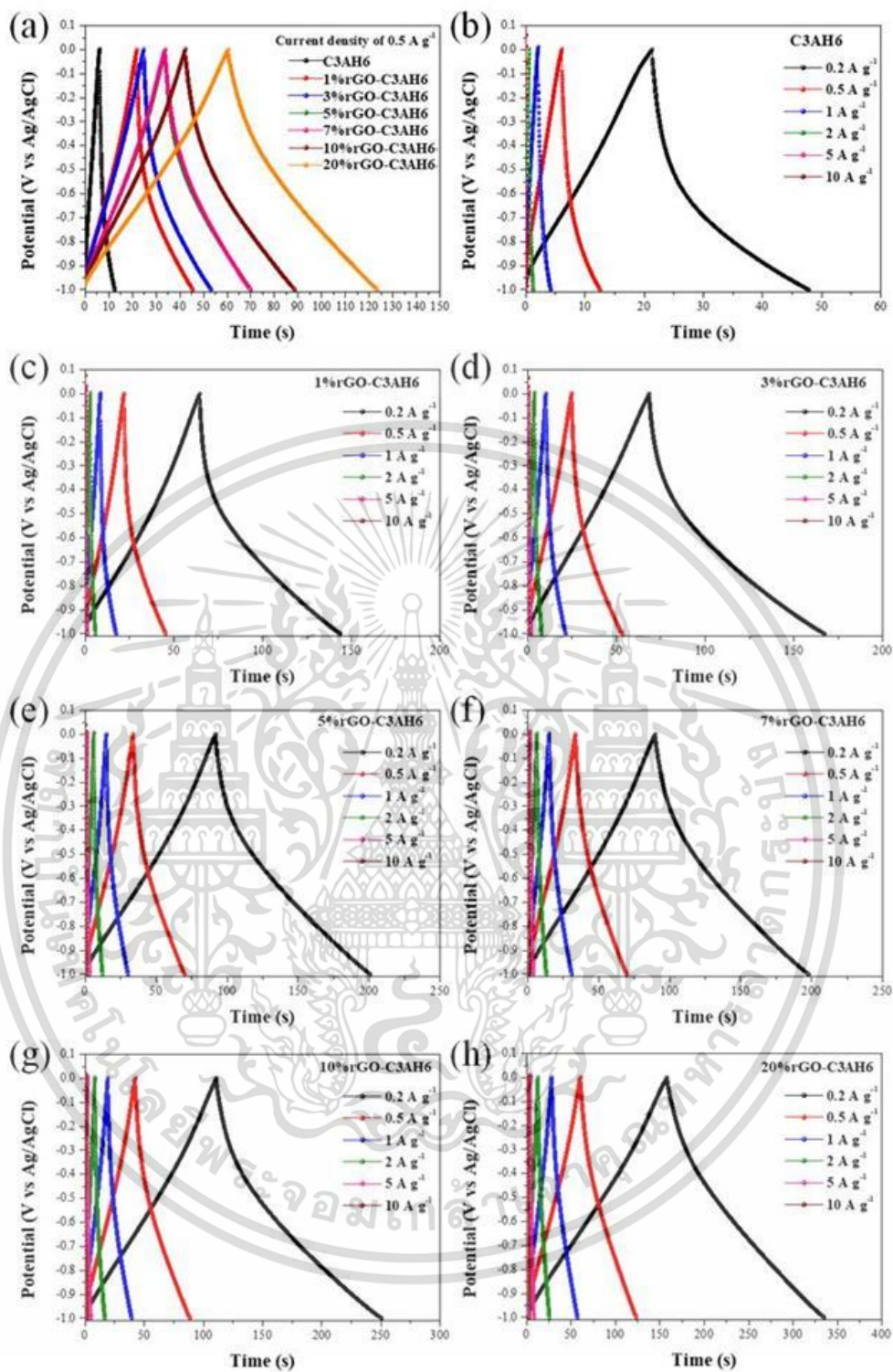


Figure 4.30 (a) shows GCD curves at a scan rate of 0.5 A g^{-1} of C3AH6 and all rGO-C3AH6 electrodes. (b), (c), (d), (e), (f), (g) and (h) show GCD curves at different current densities of C3AH6 and all rGO-C3AH6 electrodes.

เอกสารนี้เป็นเอกสารที่สงวนไว้สำหรับการใช้งานเพื่อการศึกษาเท่านั้น ไม่อนุญาตให้นำไปใช้ประโยชน์ด้านการค้า ไม่ว่าจะกรณีใดๆ ทั้งสิ้น อีกทั้งห้ามมิให้ตัดแปลงเนื้อหา และต้องอ้างอิงถึงเจ้าของเอกสารทุกครั้งที่มีการนำไปใช้

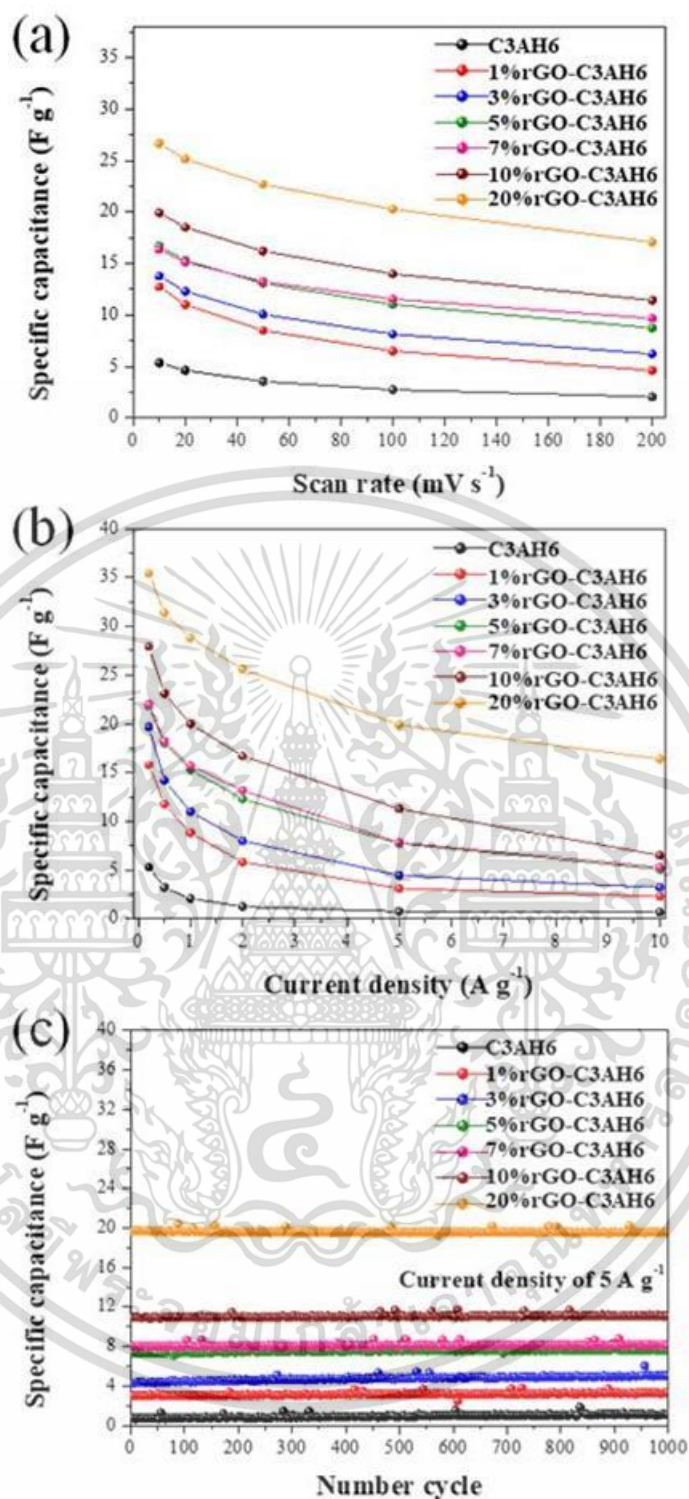


Figure 4.31 (a) and (b): specific capacitance plots of C3AH6 and all rGO-C3AH6 electrodes at different scan rates and current densities were calculated by CV and GCD test and (c): cycling stability of C3AH6 and all rGO-C3AH6 electrodes using GCD test at a current density of 5 $A g^{-1}$.

เอกสารนี้เป็นเอกสารที่สงวนไว้สำหรับการใช้งานเพื่อการศึกษาเท่านั้น ไม่อนุญาตให้นำไปใช้ประโยชน์ด้านการค้า ไม่ว่าจะกรณีใดๆ ทั้งสิ้น อีกทั้งห้ามมิให้ดัดแปลงเนื้อหา และต้องอ้างอิงถึงเจ้าของเอกสารทุกครั้งที่มีการนำไปใช้

Figure 4.32(a) explained the Nyquist plots of C3AH6 and all rGO-C3AH6 electrodes. The intercepts on Z' axis in a high frequency region usually links to a series resistance (R_s) of solution at the interface of electrode/electrolyte. A semicircular curve is mainly assigned to the charge transfer resistance (R_{ct}), which aligns with the charge transfer mechanism arises at the interface of electrode/electrolyte. As illustrated in Figure 4.32(a), all electrodes illustrated a semicircle in a high frequency region and a straight line in a low frequency region. These EIS spectra of all electrodes were examined in detail by inputting the experimental data with the equivalent circuit model through Z View software, as shown in Figure 4.32(b)–(h) and the obtained values are explained in Table 4.3. These results indicated the low R_{ct} values, implying a faster charge transfer mechanism at the electrode/electrolyte surface. Furthermore, in a low frequency region of Nyquist plots, the slopes of all rGO-C3AH6 electrodes were higher than that of C3AH6 electrode, implying a proper electrical conductivity because of the influence of rGO and the low diffusion resistance (DE_{diff}) of electrolyte ions. This result implied that a composite of C3AH6 with rGO NSs can improve the electrochemical performance of C3AH6 electrode.

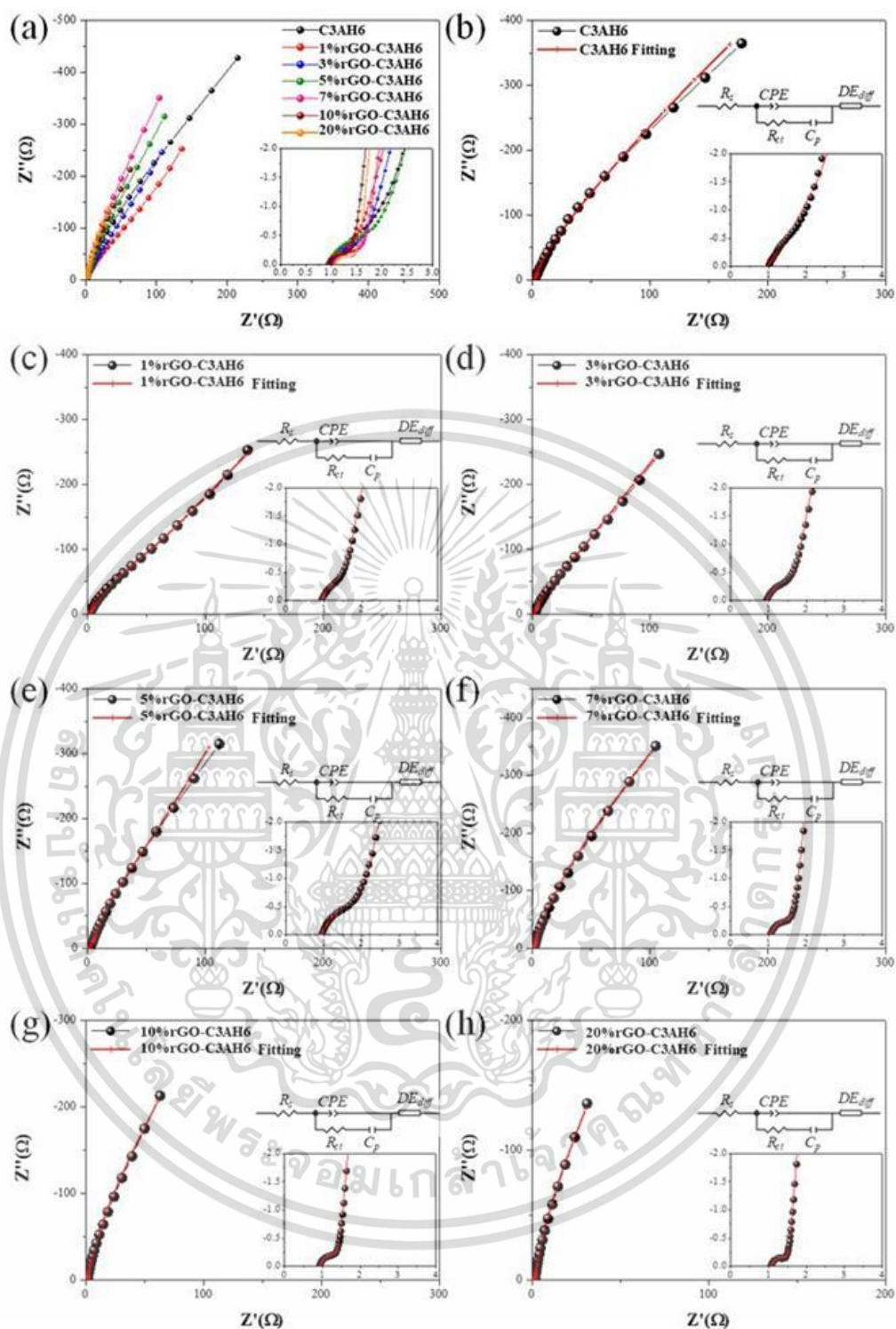


Figure 4.32 (a) Nyquist impedance plots of C3AH6 and all rGO-C3AH6 electrodes. (b), (c), (d), (e), (f), (g) and (h) the fitting niquist impedance plots with inset the enlargement of the plots near origin and showing an equivalent circuit of C3AH6 and all rGO-C3AH6 electrodes.

เอกสารนี้เป็นเอกสารที่สงวนไว้สำหรับการใช้งานเพื่อการศึกษาเท่านั้น ไม่อนุญาตให้นำไปใช้ประโยชน์ด้านการค้า ไม่ว่าจะกรณีใดๆ ทั้งสิ้น อีกทั้งห้ามมิให้ตัดแปลงเนื้อหา และต้องอ้างอิงถึงเจ้าของเอกสารทุกครั้งที่มีการนำไปใช้

Table 4.3 Csc value at different scan rates and current densities were calculated by CV and GCD test, and EIS analysis of C3AH6 and all rGO-C3AH6 electrodes

Parameters	Electrodes						
	C3AH6	1%rGO -C3AH6	3%rGO -C3AH6	5%rGO -C3AH6	7%rGO -C3AH6	10%rGO -C3AH6	20%rGO -C3AH6
Csc (F g⁻¹) by CV							
10 mVs ⁻¹	5.348	12.740	13.775	16.685	16.352	19.927	26.650
20 mVs ⁻¹	4.614	11.013	12.299	15.316	15.126	18.511	25.140
50 mVs ⁻¹	3.545	8.499	10.058	13.069	13.237	16.200	22.699
100 mVs ⁻¹	2.747	6.495	8.142	11.029	11.549	14.005	20.279
200 mVs ⁻¹	2.042	4.607	6.216	8.723	9.674	11.413	17.084
Csc (F g⁻¹) by GCD							
0.2 A g ⁻¹	5.290	15.800	19.700	21.800	22.000	27.900	35.400
0.5 A g ⁻¹	3.230	11.800	14.200	18.000	18.200	23.100	31.400
1 A g ⁻¹	2.120	8.830	11.000	15.300	15.700	20.000	28.800
2 A g ⁻¹	1.270	5.850	8.020	12.300	13.200	16.700	25.600
5 A g ⁻¹	0.772	3.140	4.460	7.740	7.840	11.300	19.900
10 A g ⁻¹	0.686	2.330	3.250	5.100	5.320	6.540	16.400
EIS analysis							
Rs (Ω) (%error)	1.003 (1.3017)	0.93215 (1.366)	0.94597 (1.4679)	0.93441 (1.4352)	1.051 (1.3108)	0.92941 (1.4364)	1.06 (1.3846)
CPE-T (%error)	0.008707 (4.5899)	0.020318 (4.6502)	0.017097 (5.563)	0.012761 (7.793)	0.011238 (12.083)	0.018427 (14.955)	0.01958 (23.69)
CPE-P (%error)	0.71507 (1.3251)	0.67337 (1.6964)	0.66357 (1.6508)	0.70711 (1.9237)	0.7097 (2.4747)	0.70428 (3.1401)	0.67395 (5.0391)
Rct (Ω) (%error)	1.642 (16.635)	1.021 (21.665)	0.7612 (15.775)	1.001 (14.164)	0.61836 (11.043)	0.5397 (13.421)	0.44839 (10.888)
Cp (F) (%error)	0.003940 (7.7826)	0.008577 (11.401)	0.01989 (8.6576)	0.0237 (7.4599)	0.024722 (5.7807)	0.040222 (7.1391)	0.08097 (6.0448)
DE-R (Ω) (%error)	3.064 (27.011)	1.38 (44.401)	4.693 (31.807)	8.713 (27.076)	1.279 (31.61)	0.78066 (48.185)	0.94206 (60.441)

เอกสารนี้เป็นเอกสารที่สงวนไว้สำหรับการใช้งานเพื่อการศึกษาเท่านั้น ไม่อนุญาตให้นำไปใช้ประโยชน์ด้านการค้า
ไม่ว่ากรณีใดๆ ทั้งสิ้น อีกทั้งห้ามมิให้ตัดแปลงเนื้อหา และต้องอ้างอิงถึงเจ้าของเอกสารทุกครั้งที่มีการนำไปใช้

- Thermoelectric properties

Measurement methods S and ρ were measured simultaneously in the range of 300 to 523 K using a commercial apparatus (Ulvac ZEM-3) under a reduced He atmosphere. The value of density d was calculated from the measured weight and dimensions from Division of Sustainable Energy and Environmental Engineering, Graduate School of Engineering, Osaka University, Japan (Osaka Lab). Table 4.4 shows the summary of differences of preparation method and characteristic of 10%rGO-C3AH6, prepared at KMITL and this lab.

Table 4.4 Summary of differences of preparation method and characteristic of 10%rGO- C3AH6 prepared at KMITL Lab and this Osaka Lab.

10%rGO-C3AH6	KMITL Lab	Osaka Lab
Production method	Cold pressing	Spark plasma sintering (SPS)
Conditions	6 MPa, 300 K for 10 min	60 MPa, 600 K for 10 min
Sample	Cuboid (5x5x20 mm)	Pellet (\varnothing 12.7 mm, $h \sim 1.8$ mm)
Measured density	2.01 g cm ⁻³	1.40 cm ⁻³
Resistivity (ρ) at 300 K	1.16 Ω	0.35 m Ω

Figure 4.33(a) shows the Resistivity (ρ) as a function of temperature of differences of preparation method and characteristic of 10%rGO-C3AH6, prepared at KMITL lab and Osaka lab. The ρ value of 10%rGO-C3AH6 sample was approximately 1.16 Ω and 0.35 m Ω , respectively. Figure 4.33(b) shows temperature dependence of Seebeck coefficient (S) of the 10%rGO-C3AH6, prepared at KMITL lab and Osaka lab in temperature 300K to 550K. The bulk rGO-C3AH6 sample showed negative of Seebeck coefficient value as presenting n-type thermoelectric materials. The Seebeck coefficient values of bulk rGO-C3AH6 sample was decreased from -9.30 μ V/K to -7.76 μ V/K and 9.41 μ V/K to 2.10 μ V/K, respectively, prepared at KMITL lab and Osaka lab for temperature increased from 300 K to 550 K. Figure 4.33(c) shows the comparison of the power factor (PF) of bulk rGO-C3AH6 samples.

เอกสารนี้เป็นเอกสารที่สงวนไว้สำหรับการใช้งานเพื่อการศึกษาเท่านั้น ไม่อนุญาตให้นำไปใช้ประโยชน์ด้านการค้า
ไม่ว่ากรณีใดๆ ทั้งสิ้น อีกทั้งห้ามมิให้ตัดแปลงเนื้อหา และต้องอ้างอิงถึงเจ้าของเอกสารทุกครั้งที่มีการนำไปใช้

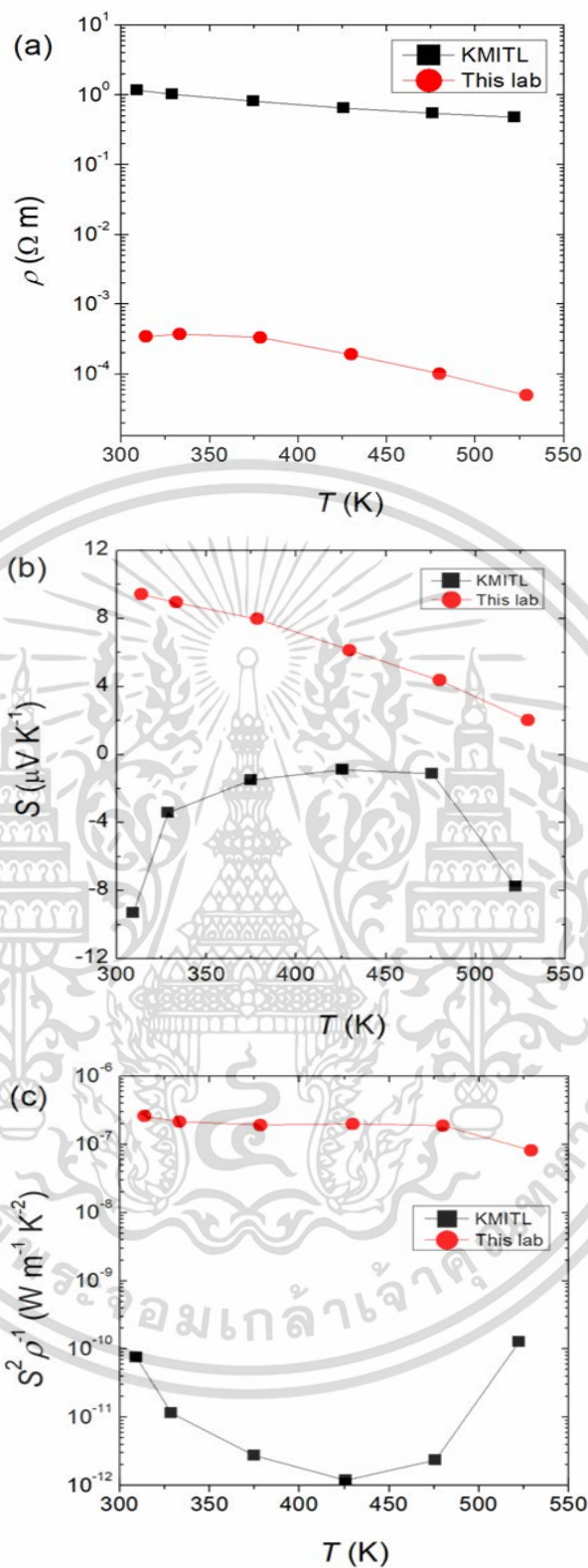


Figure 4.33 (a) The Resistivity (ρ), (b) Seebeck coefficient (S) and (c) Power factor (PF) of the 10%rGO-C3AH6 sample.

เอกสารนี้เป็นเอกสารที่สงวนไว้สำหรับการใช้งานเพื่อการศึกษาเท่านั้น ไม่อนุญาตให้นำไปใช้ประโยชน์ด้านการค้า ไม่ว่าจะกรณีใดๆ ทั้งสิ้น อีกทั้งห้ามมิให้ตัดแปลงเนื้อหา และต้องอ้างอิงถึงเจ้าของเอกสารทุกครั้งที่มีการนำไปใช้

4.3 Prototype of concrete block electric power generation from heat and applications in municipal melting furnace or municipal incinerator

4.3.1 Synthesis of CaMnO_3 as thermoelectric materials

The CaMnO_3 oxide compound, which was synthesized in the previous laboratory for analysis. The characteristic of CaMnO_3 compounds its reproducibility was also confirmed by XRD SEM and EDS. The measurement results will show as follows.

- X-ray diffraction (XRD)

Figure 34 showed the XRD diffraction patterns of the CaMnO_3 after calcining the sample at 1200°C for 12 hours. It was found that crystalline powder with CaMnO_3 diffraction pattern appeared at diffraction angle at 2θ ($^\circ$) = 23.836° , 33.928° , 36.190° , 38.268° , 40.040° , 42.193° , 44.141° , 45.545° , 48.929° , 50.373° , 53.886° , 54.935° , 56.402° and 62.258° . The samples showed major phase of CaMnO_3 structure, corresponding to JCPDS file no. 03-0830.

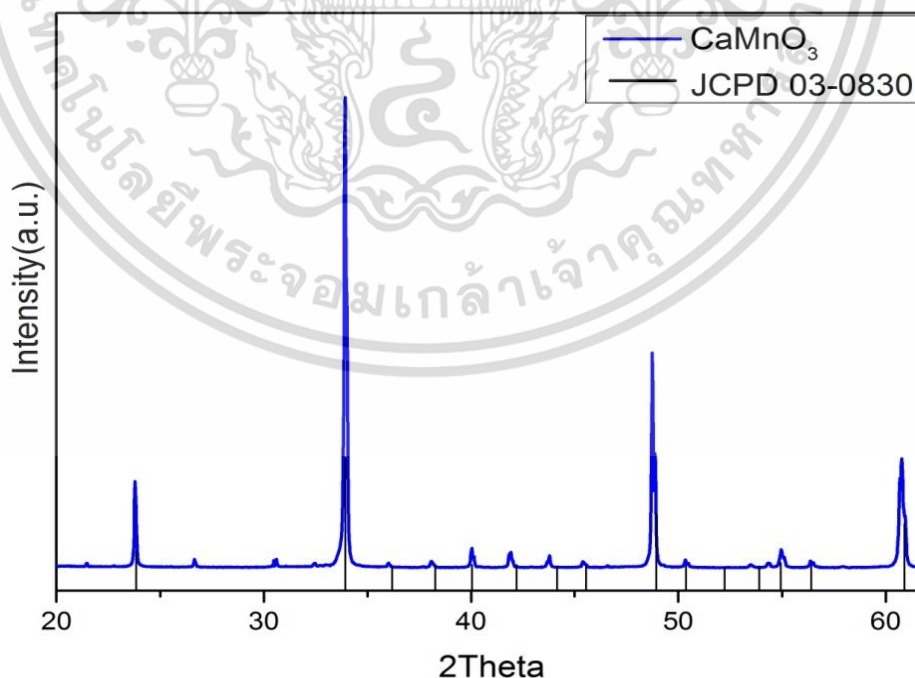


Figure 4.34 XRD patterns of prepared CaMnO_3 precursor referencing the

JCPDS#03-0830 file.

เอกสารนี้เป็นเอกสารที่สงวนไว้สำหรับการใช้งานเพื่อการศึกษาเท่านั้น ไม่อนุญาตให้นำไปใช้ประโยชน์ด้านการค้า ไม่ว่าจะกรณีใดๆ ทั้งสิ้น อีกทั้งห้ามมิให้ดัดแปลงเนื้อหา และต้องอ้างอิงถึงเจ้าของเอกสารทุกครั้งที่มีการนำไปใช้

- Scanning Electron Microscope (SEM)

The SEM is a test process that scans a sample with an electron beam to produce a magnified image for analysis. The CaMnO_3 oxide compound was synthesized in the previous lab for analysis by SEM with magnifications from (a) 500x, (b) 2000x, (c) 4000x and (d) 6000x, respectively. It was found that the SEM images obtained CaMnO_3 oxide compound can be prepared to homogeneous and has a rough porous surface. Which has a good effect on low thermal conductivity is a good property of thermoelectric materials was shown in Figure 4.35.

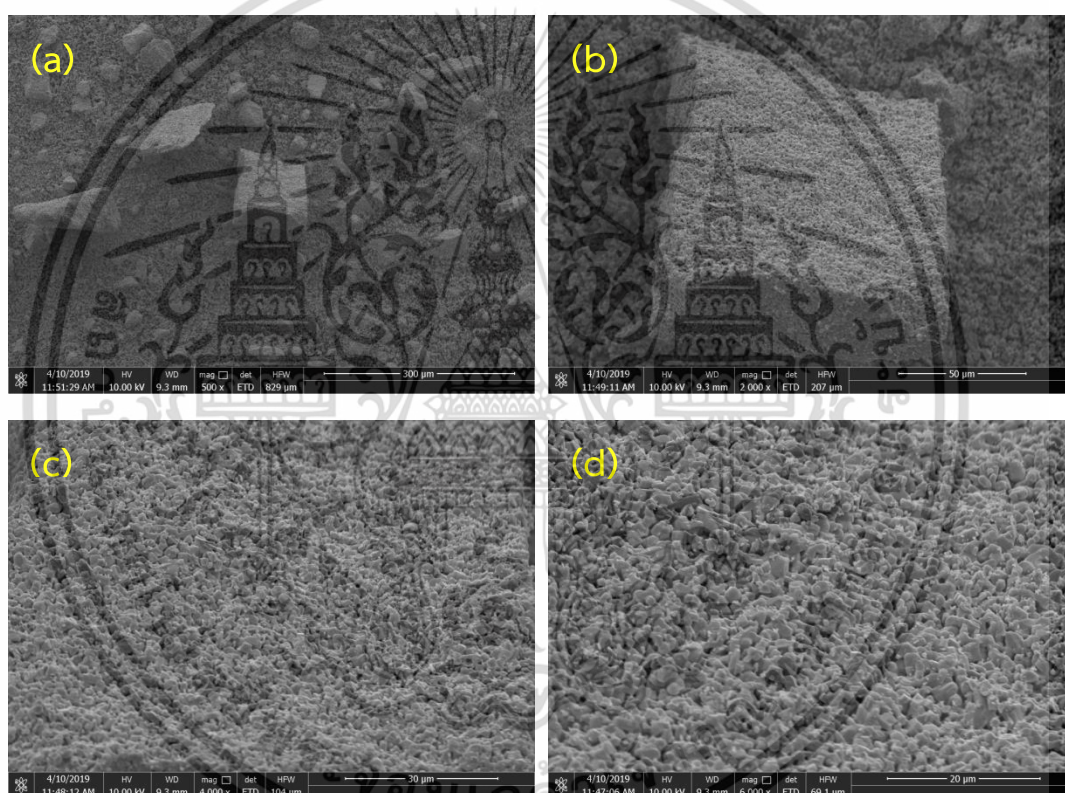


Figure 4.35 SEM images of CaMnO_3 with magnifications from (a) 500x, (b) 2000x, (c) 4000x, and (d) 6000x, respectively.

เอกสารนี้เป็นเอกสารที่สงวนไว้สำหรับการใช้งานเพื่อการศึกษาเท่านั้น ไม่อนุญาตให้นำไปใช้ประโยชน์ด้านการค้า
ไม่ว่ากรณีใดๆ ทั้งสิ้น อีกทั้งห้ามมิให้ตัดแปลงเนื้อหา และต้องอ้างอิงถึงเจ้าของเอกสารทุกครั้งที่มีการนำไปใช้

- Energy Dispersive X-Ray Spectrometer (EDS)

The EDS is a measurement and analysis of energy elements to analyze various elements which is a mixed proportion of each element. And the distribution of the elements is separated into various colors. Figure 4.36 showed the results of EDS identify the elements in the CaMnO_3 oxide compound by the weight ratio of the elements C: O: Ca: Mn will be 7.38% : 39.41% : 22.77% : 30.45%. It was found that each element is well distributed.

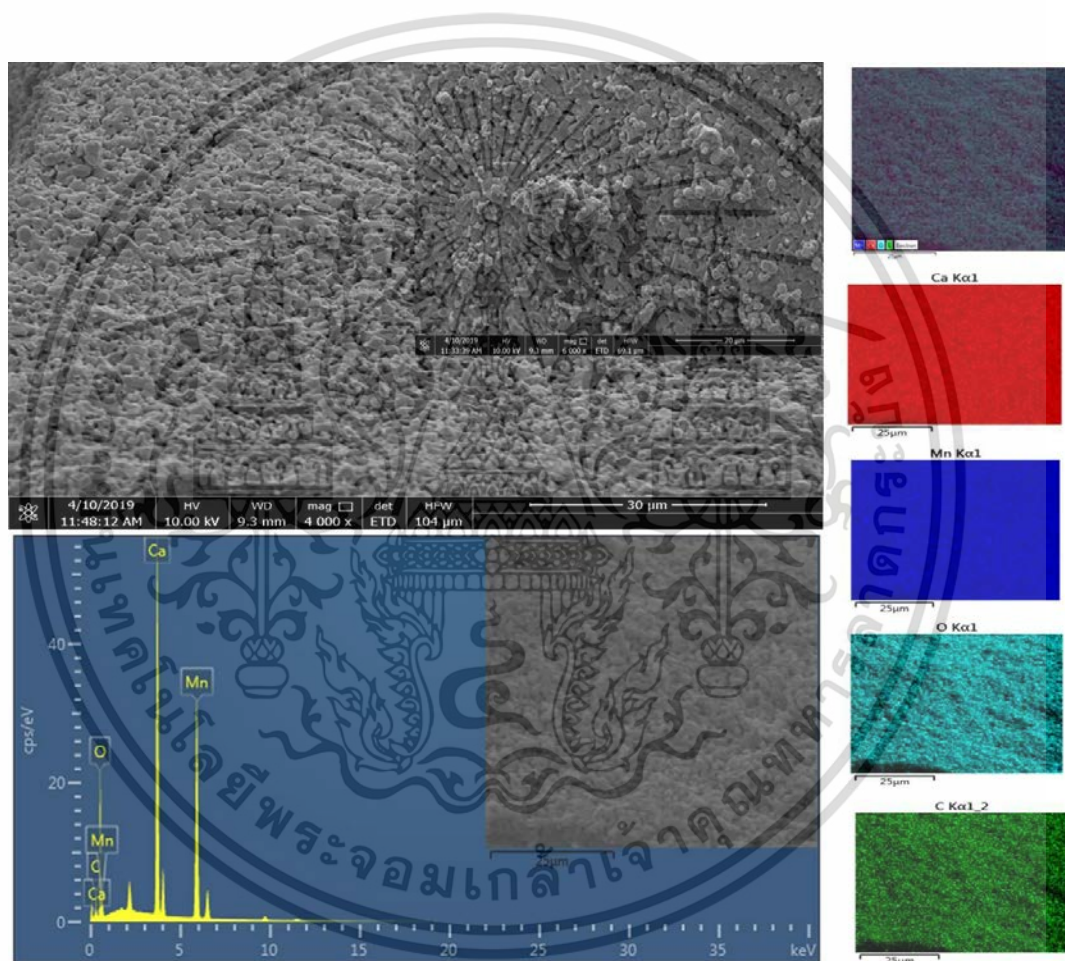


Figure 4.36 SEM images with inset a high magnification view of selected area, and displayed the EDS-mapping images for C, O, Ca and Mn elements of CaMnO_3 samples.

เอกสารนี้เป็นเอกสารที่สงวนไว้สำหรับการใช้งานเพื่อการศึกษาเท่านั้น ไม่อนุญาตให้นำไปใช้ประโยชน์ด้านการค้า ไม่ว่าจะกรณีใดๆ ทั้งสิ้น อีกทั้งห้ามมิให้ตัดแปลงเนื้อหา และต้องอ้างอิงถึงเจ้าของเอกสารทุกครั้งที่มีการนำไปใช้

4.3.2 The prototype of wall panel thermoelectric module for electricity production from high temperature heat from municipal waste incinerator prototype

- Electrical connector new thermoelectric cell module rods

Generally, there are 2 types of electrical connection thermoelectric cell module rods such as N-type and P-type connected in series. The other side provides heat from the heat source and the other side is cool. Must have a cooling system helps to cooling with the heat sink to make a difference in temperature as shown in Figure 4.37.

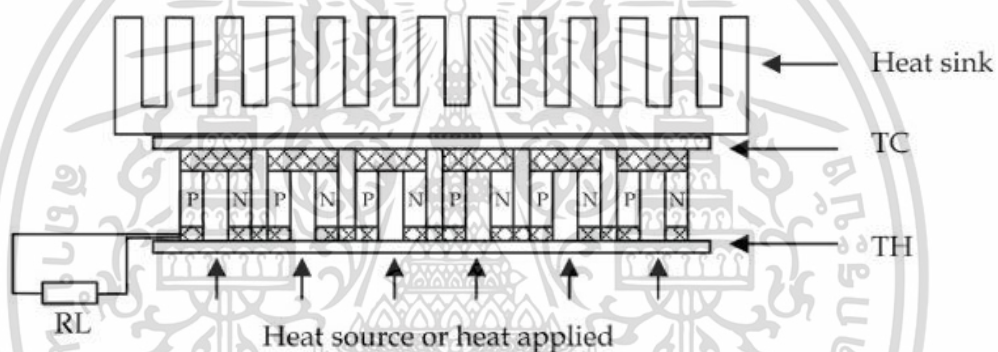


Figure 4.37 Connection of conventional thermoelectric modules N-type and P-type.

The connection of new thermoelectric modules with single type of N-type. Is a preparation of N-type thermoelectric materials that are connected in pairs were as shown in Figure 4.38(a) and can expand the number of series circuit thermoelectric modules as shown in Figure 4.38(b) and can expand the number of parallel circuit thermoelectric modules as shown in Figure 4.38(c). The other side provides heat from the heat source and the other side is cool without cooling fan but can be to make a difference temperature which the new type of thermoelectric modules connector.

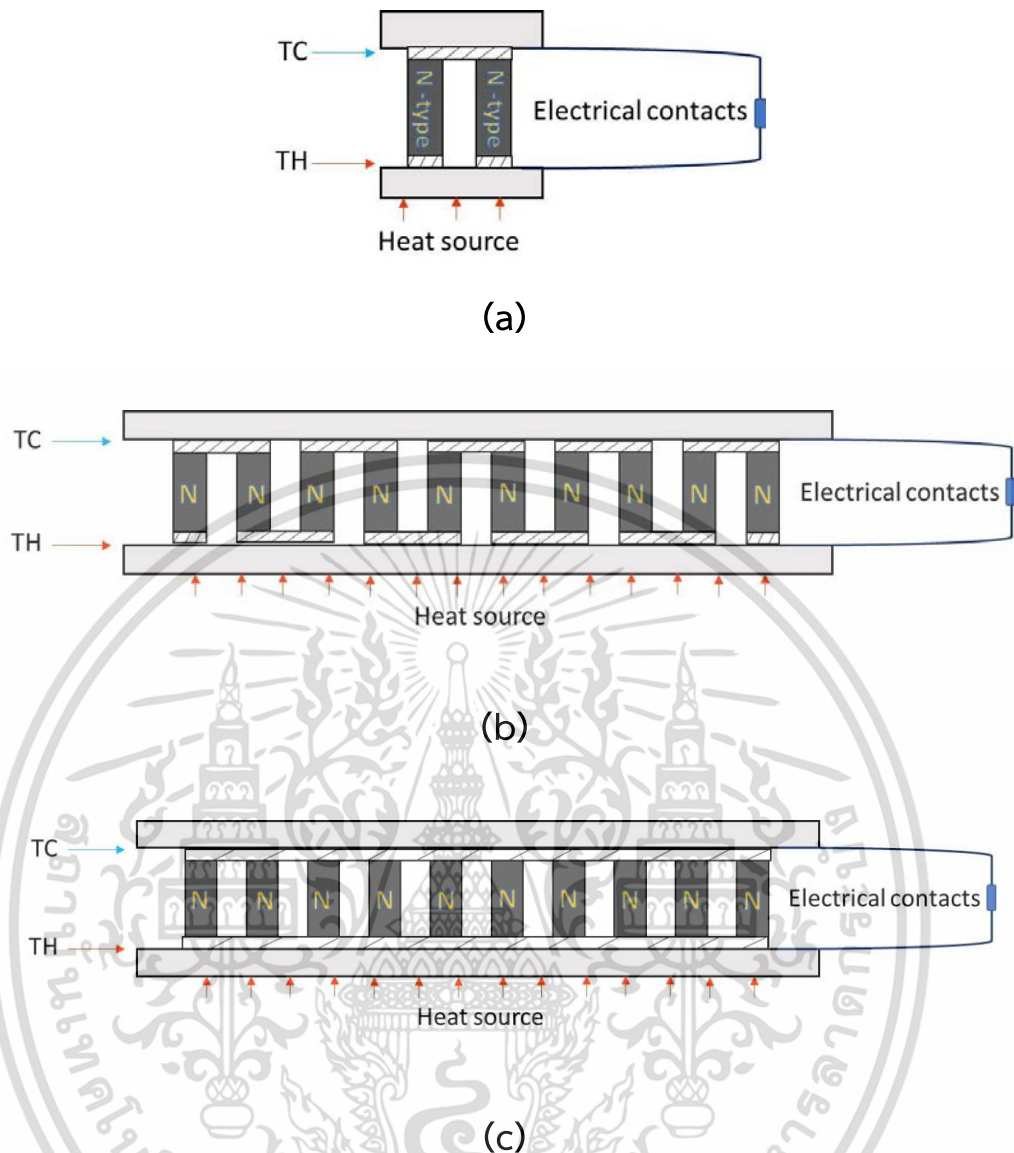


Figure 4.38 Connection of conventional thermoelectric modules N-type.

- The using of new electrode materials

Using stainless steel materials to be used as electrodes for connecting to self-prepared thermoelectric modules in the laboratory as shown in Figure 4.39(a) which can actually be used in the temperature range of 700°C but there was disadvantage that the process of forming the electrode is difficult and heavy weight. Therefore choose new materials using materials made of aluminum. The advantages are cheaper and lightweight compared to materials made of stainless steel. After that coated with silver to improve electrical conductivity and reduce the adhesion of the

เอกสารนี้เป็นเอกสารที่สงวนไว้สำหรับการใช้งานเพื่อการศึกษาเท่านั้น ไม่อนุญาตให้นำไปใช้ประโยชน์ด้านการค้า
 ไม่ว่าจะกรณีใดๆ ทั้งสิ้น อีกทั้งห้ามมิให้ดัดแปลงเนื้อหา และต้องอ้างอิงถึงเจ้าของเอกสารทุกครั้งที่มีการนำไปใช้

oxides that occur which can actually be used in the temperature range not more than of 600 °C as shown in Figure 4.39(b).

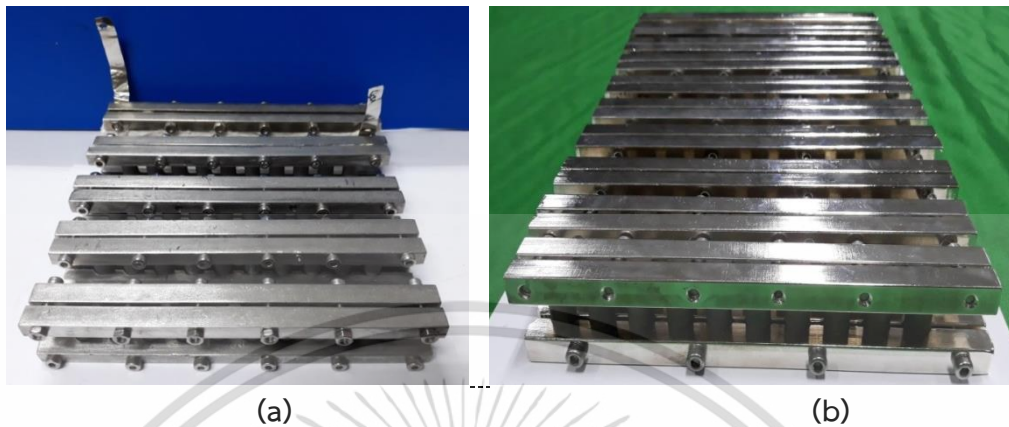


Figure 4.39 (a) Stainless steel electrode materials (b) aluminum electrode materials after coated with silver

- Connect the thermoelectric module wall plate to generate electricity from heat.

The prototype of the thermoelectric module wall plate to generate electricity from heat include of 50 thermoelectric rods with compound electric circuit connected by heat resistant wires. After that, the calcium silica plates are splice on both sides to short circuits protection. The hot side has been drilled to allow radiant heat to pass directly to the module which is a new design. As a result, the heat distribution to the prototype of the wall thermoelectric module produces electricity very well as shown Figure 4.40.

เอกสารนี้เป็นเอกสารที่สงวนไว้สำหรับการใช้งานเพื่อการศึกษาเท่านั้น ไม่อนุญาตให้นำไปใช้ประโยชน์ด้านการค้า ไม่ว่าจะกรณีใดๆ ทั้งสิ้น อีกทั้งห้ามมิให้ตัดแปลงเนื้อหา และต้องอ้างอิงถึงเจ้าของเอกสารทุกครั้งที่มีการนำไปใช้

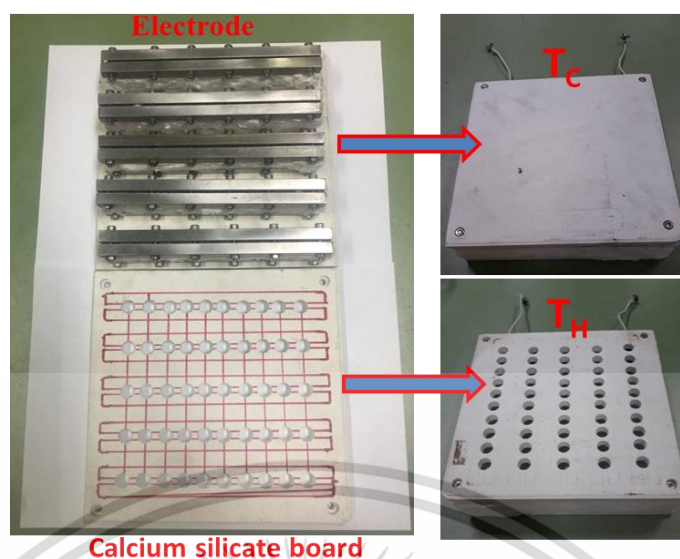


Figure 4.40 Prototype of thermoelectric module wall plate to generate electricity from heat.

4.3.3 Prototype of concrete block electric power generation from heat and applications in municipal melting furnace or municipal incinerator

The construction of a municipal hybrid electricity waste stove system consisting of heat-resistant wall panels and embedded thermoelectric modules. The detailed designs are in the appendix and the municipal waste stove system components are hybrid power generation models. The basic principle is to use gas fuel to warm up and burn waste, will be able to burn wet waste. After that, when the complete combustion occurs, the fuel gas system will be cut off from the combustion system to use a general combustion aeration system. The components are as follows (1) Steel structure with wheels (2) Gas fuel system (3) Waste combustion system (4) Combustion chamber (5) Heat storage room (6) Heat resistant wall power generation (7) Hot air vent. The prototype of the incinerator can be installed prototypes of thermoelectric module panels to generate electricity directly from heat is a total of four sides. Which has been designed on each side are size 25x25x5 cm equal to the prototype of the wall panel, the thermoelectric module produces electricity that can be splice installed as shown in Figure 4.41.

เอกสารนี้เป็นเอกสารที่สงวนไว้สำหรับการใช้งานเพื่อการศึกษาเท่านั้น ไม่อนุญาตให้นำไปใช้ประโยชน์ด้านการค้า ไม่ว่าจะกรณีใดๆ ทั้งสิ้น อีกทั้งห้ามมิให้ตัดแปลงเนื้อหา และต้องอ้างอิงถึงเจ้าของเอกสารทุกครั้งที่มีการนำไปใช้

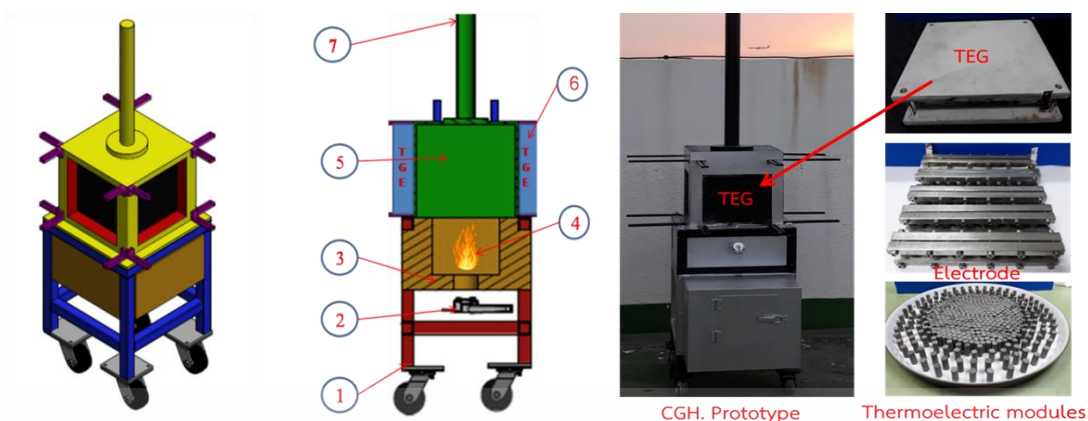


Figure 4.41 Prototype of concrete block electric power generation from heat and applications in municipal melting furnace or municipal incinerator.

4.3.4 Electrical Properties of Thermoelectric Modules

4.3.4.1 The result of a single thermoelectric module from CaMnO_3 at the diameter of 1 cm to connect series electrical circuit

- At the height of the module 1.5 cm

The results of the thermoelectric module test in the laboratory. Bring 2 module of the thermoelectric module of the above size to test on the hot plate for test the heat resistance and create different temperature between the side that touches the hot plate and the side that does not touch the hot plate. The results showed that the difference of the maximum heat temperature was $552.8\text{ }^\circ\text{C}$ (at the hot side temperature of $700\text{ }^\circ\text{C}$ and the cold side was $148.2\text{ }^\circ\text{C}$) as shown in Figure 4.42. The results of testing of electrical measurements compared to temperature differences as showed that the maximum electric potential is 95.30 mV , the current is 2.29 mA and the electric potential can be constant as time changes as shown in Figure 4.43. Shows as electricity measurement results show that the fabricated thermoelectric modules can directly convert heat into electricity. Which corresponds to the Seebeck effect and the electrical value increases according to the temperature difference with has tendency to be increase.

เอกสารนี้เป็นเอกสารที่สงวนไว้สำหรับการใช้งานเพื่อการศึกษาเท่านั้น ไม่อนุญาตให้นำไปใช้ประโยชน์ด้านการค้า
ไม่ว่ากรณีใดๆ ทั้งสิ้น อีกทั้งห้ามมิให้ดัดแปลงเนื้อหา และต้องอ้างอิงถึงเจ้าของเอกสารทุกครั้งที่มีการนำไปใช้

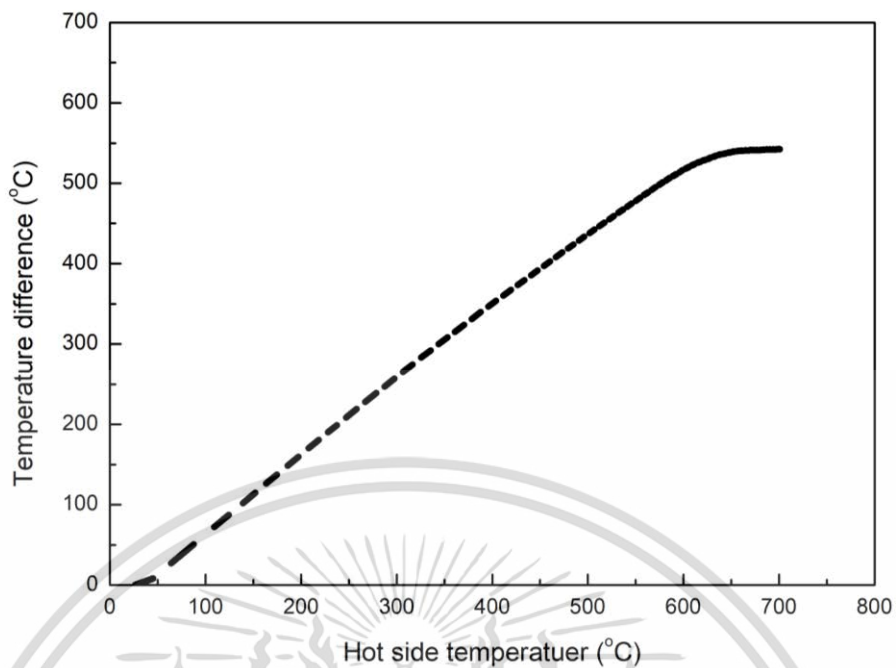


Figure 4.42 The temperature difference in the room temperature range to 700 °C for at the height of module 1.5 cm.

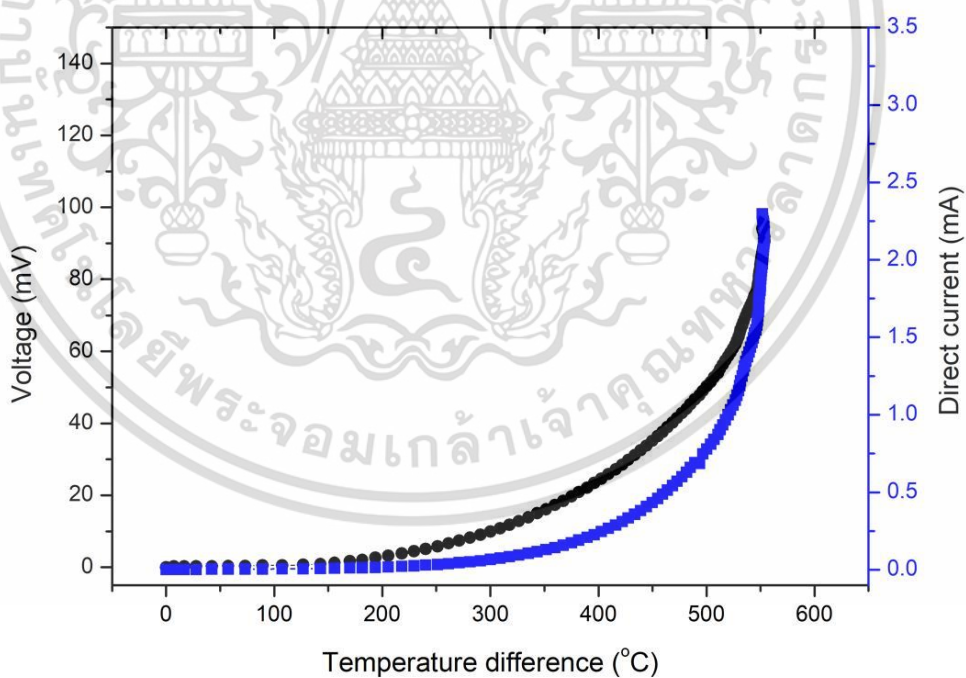


Figure 4.43 Graph relation between temperature difference voltage (mV) and current (mA) for at the height of module 1.5 cm.

เอกสารนี้เป็นเอกสารที่สงวนไว้สำหรับการใช้งานเพื่อการศึกษาเท่านั้น ไม่อนุญาตให้นำไปใช้ประโยชน์ด้านการค้า ไม่ว่าจะกรณีใดๆ ทั้งสิ้น อีกทั้งห้ามมิให้ดัดแปลงเนื้อหา และต้องอ้างอิงถึงเจ้าของเอกสารทุกครั้งที่มีการนำไปใช้

- At the height of the module 2.0 cm

The results showed that the difference of the maximum heat temperature was $574.3\text{ }^{\circ}\text{C}$ (at the hot side temperature of $701.1\text{ }^{\circ}\text{C}$ and the cold side was $123.8\text{ }^{\circ}\text{C}$) as shown in Figure 4.44. Figure 4.45 showed the results of testing of electrical measurements compared to temperature differences as showed that the maximum electric potential is 126.20 mV , the current is 1.68 mA and the electric potential can be constant as time changes. The results electrical value increases according to the temperature difference with has tendency to be increase.

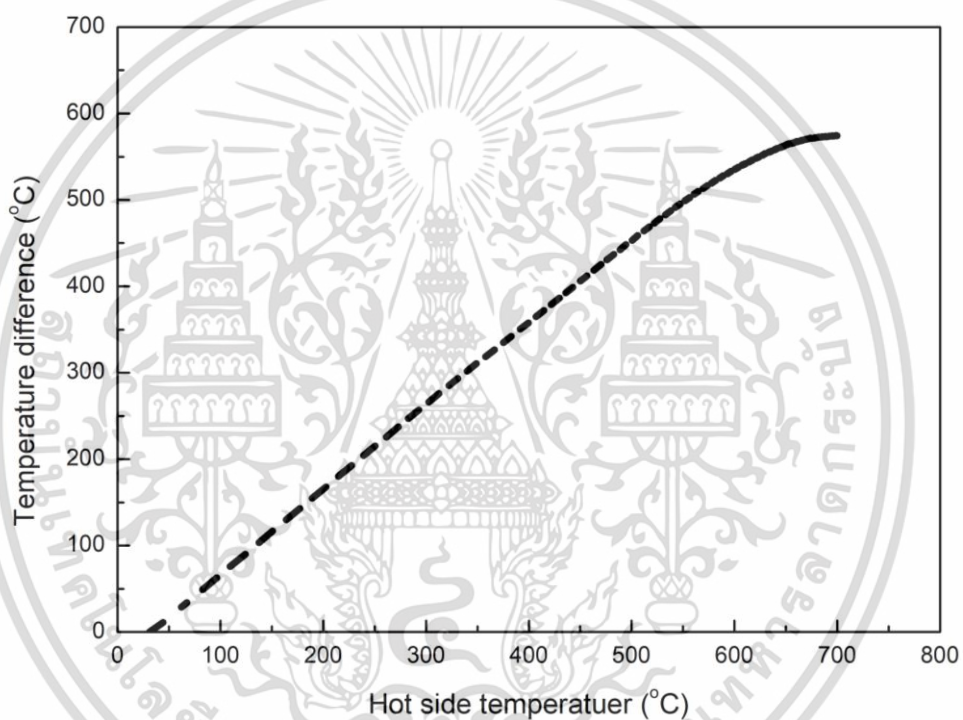


Figure 4.44 The temperature difference in the room temperature range to 700 for at the height of module 2.0 cm.

เอกสารนี้เป็นเอกสารที่สงวนไว้สำหรับการใช้งานเพื่อการศึกษาเท่านั้น ไม่อนุญาตให้นำไปใช้ประโยชน์ด้านการค้า
ไม่ว่ากรณีใดๆ ทั้งสิ้น อีกทั้งห้ามมิให้ตัดแปลงเนื้อหา และต้องอ้างอิงถึงเจ้าของเอกสารทุกครั้งที่มีการนำไปใช้

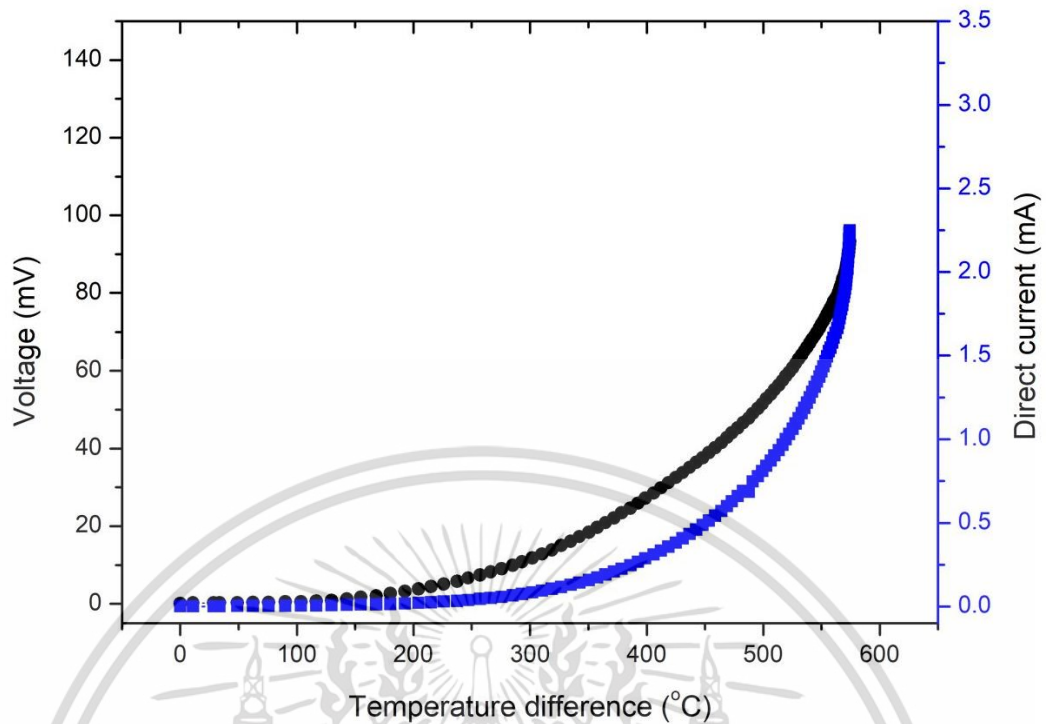


Figure 4.45 Graph relation between temperature difference voltage (mV) and current (mA) for at the height of module 2.0 cm.

- At the height of the module 2.5 cm

The results showed that the difference of the maximum heat temperature was 615.6°C (at the hot side temperature of 701.1°C and the cold side was 85.5°C) as shown in Figure 4.46. Figure 4.47 showed the results of testing of electrical measurements compared to temperature differences as showed that the maximum electric potential is 125.20 mV, the current is 2.38 mA and the electric potential can be constant as time changes. The results electrical value increases according to the temperature difference with has tendency to be increase.

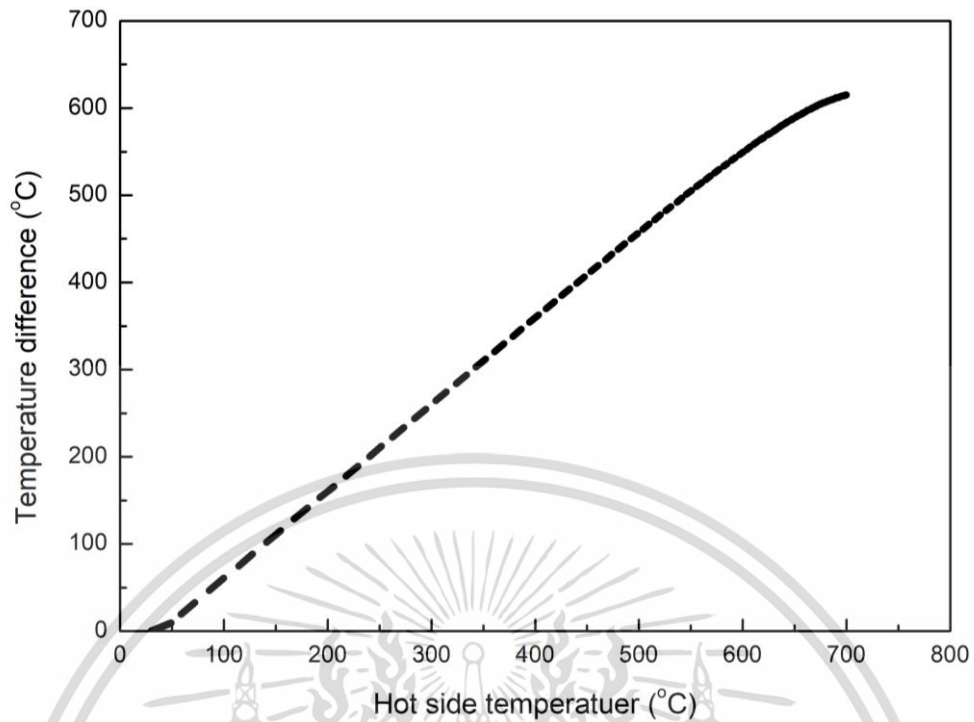


Figure 4.46 The temperature difference in the room temperature range to 700 °C for at the height of module 2.0 cm.

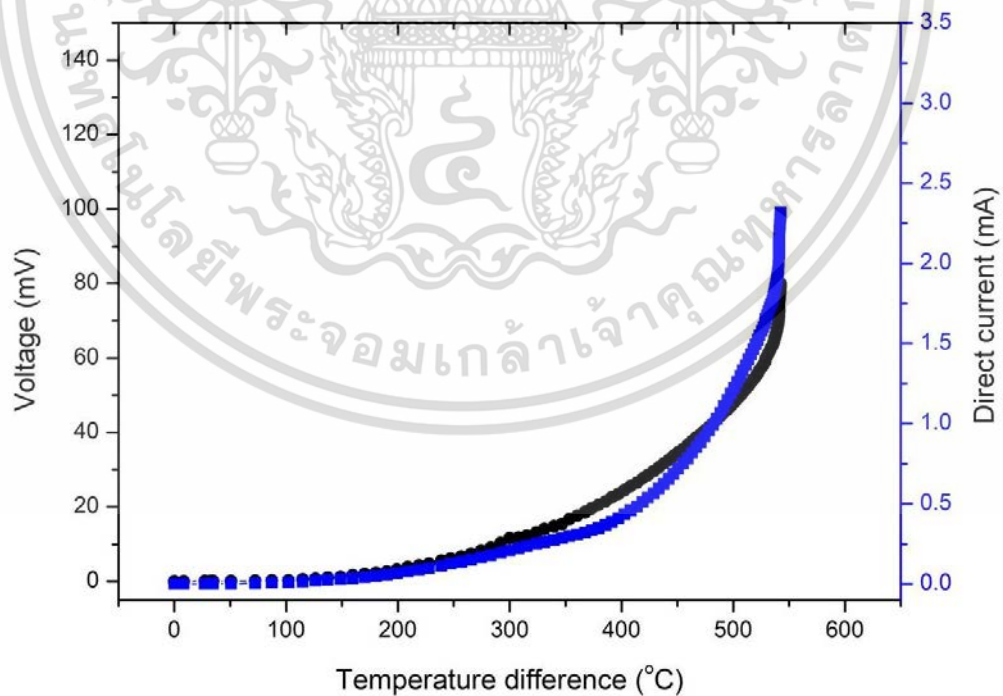


Figure 4.47 Graph relation between temperature difference voltage (mV) and current (mA) for the module at a height of 2.5 cm.

เอกสารนี้เป็นเอกสารที่สงวนไว้สำหรับการใช้งานเพื่อการศึกษาเท่านั้น ไม่อนุญาตให้นำไปใช้ประโยชน์ด้านการค้า ไม่ว่าจะกรณีใดๆ ทั้งสิ้น อีกทั้งห้ามมิให้ตัดแปลงเนื้อหา และต้องอ้างอิงถึงเจ้าของเอกสารทุกครั้งที่มีการนำไปใช้

The results of the production of thermoelectric modules for a single thermoelectric module to connected in series electric circuits at various heights. It can found that at height of 1.5 cm provides a minimum voltage compared to an increase in height of 2.0 cm and at height of 2.5 cm provides similar electric potential. We could see that too much height is not good because it will increase the number of masses. Therefore, should design the optimum of height as shown in Figure 4.48.

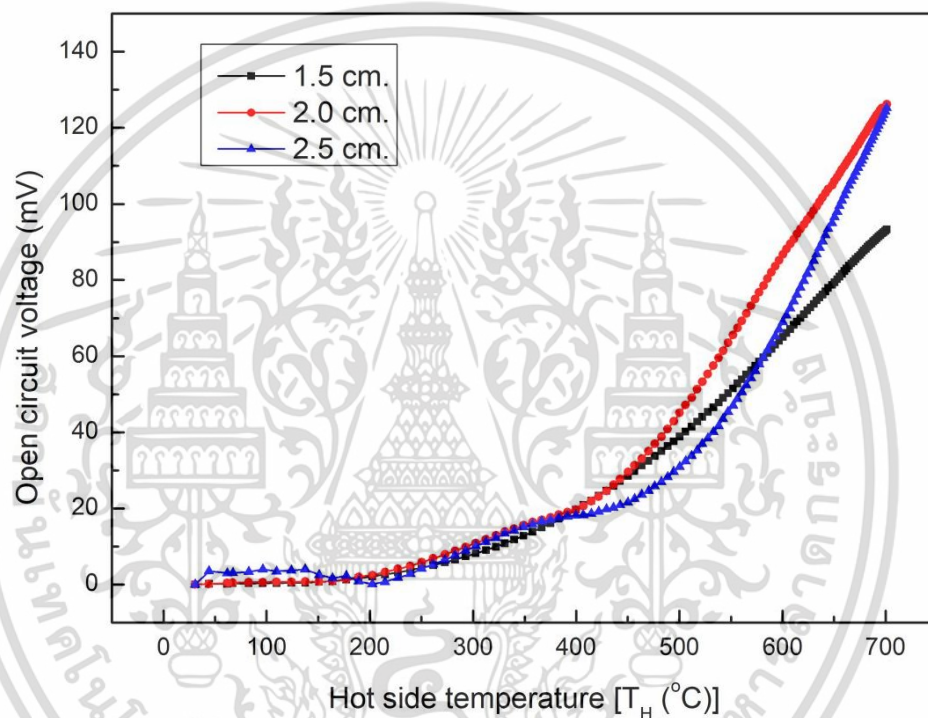


Figure 4.48 Graph relations between hot side temperature and voltage (mV) for 2 module of the thermoelectric module to connect series electrical circuit at the height of the module at 1.5, 2.0 and 2.5 cm.

4.3.4.2 The result of 2 thermoelectric module of CaMnO_3 at the diameter of 1 cm to connect parallel electrical circuit - At the height of the module 1.5 cm

The results of the thermoelectric module test in the laboratory. Bring 2 module of the thermoelectric module are connect parallel electrical circuit of the above size to test on the hot plate for test the heat resistance and create different

เอกสารนี้เป็นเอกสารที่สงวนไว้สำหรับการใช้งานเพื่อการศึกษาเท่านั้น ไม่อนุญาตให้นำไปใช้ประโยชน์ด้านการค้า ไม่ว่าจะกรณีใดๆ ทั้งสิ้น อีกทั้งห้ามมิให้ดัดแปลงเนื้อหา และต้องอ้างอิงถึงเจ้าของเอกสารทุกครั้งที่มีการนำไปใช้

temperature between the side that touches the hot plate and the side that does not touch the hot plate. The results showed that the difference of the maximum heat temperature was $542.6\text{ }^{\circ}\text{C}$ (at the hot side temperature of $700.7\text{ }^{\circ}\text{C}$ and the cold side was $165.4\text{ }^{\circ}\text{C}$) as shown in Figure 4.49. The results of testing of electrical measurements compared to temperature differences as showed that the maximum electric potential is 80.00 mV , the current is 2.32 mA and the electric potential can be constant as time changes as shown in Figure 4.50. Shows as electricity measurement results and the electrical value increases according to the temperature difference with has tendency to be increase.

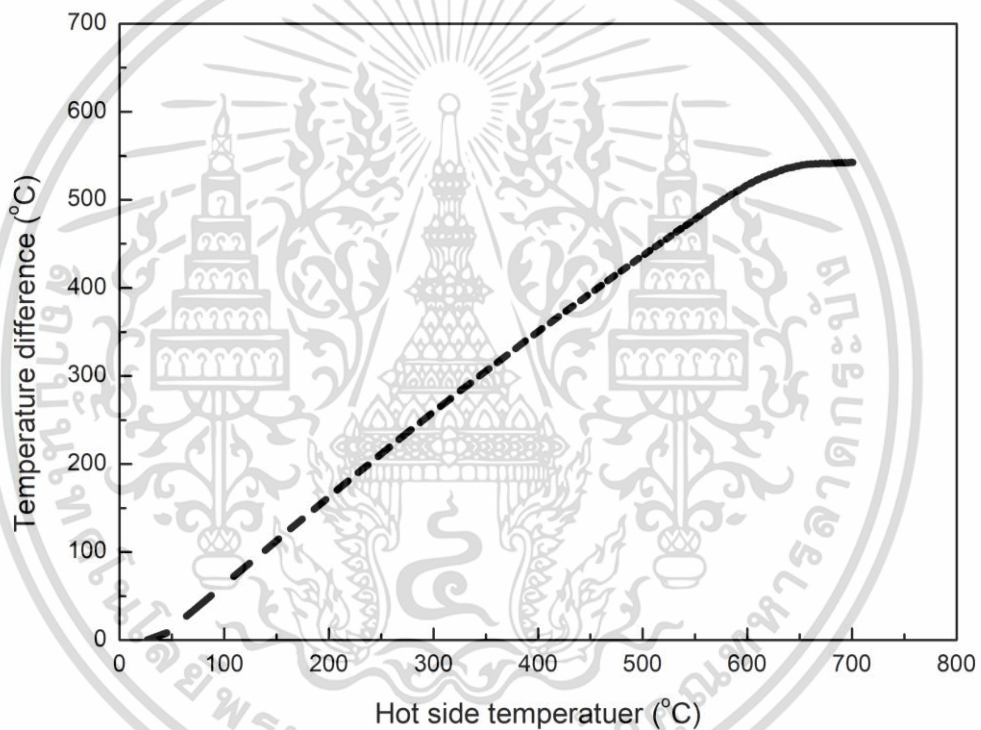


Figure 4.49 The temperature difference in the room temperature range to $700\text{ }^{\circ}\text{C}$ for 2 module of the thermoelectric module to connect parallel electrical circuit at the height of the module at 1.5 cm .

เอกสารนี้เป็นเอกสารที่สงวนไว้สำหรับการใช้งานเพื่อการศึกษาเท่านั้น ไม่อนุญาตให้นำไปใช้ประโยชน์ด้านการค้า
ไม่ว่ากรณีใดๆ ทั้งสิ้น อีกทั้งห้ามมิให้ดัดแปลงเนื้อหา และต้องอ้างอิงถึงเจ้าของเอกสารทุกครั้งที่มีการนำไปใช้

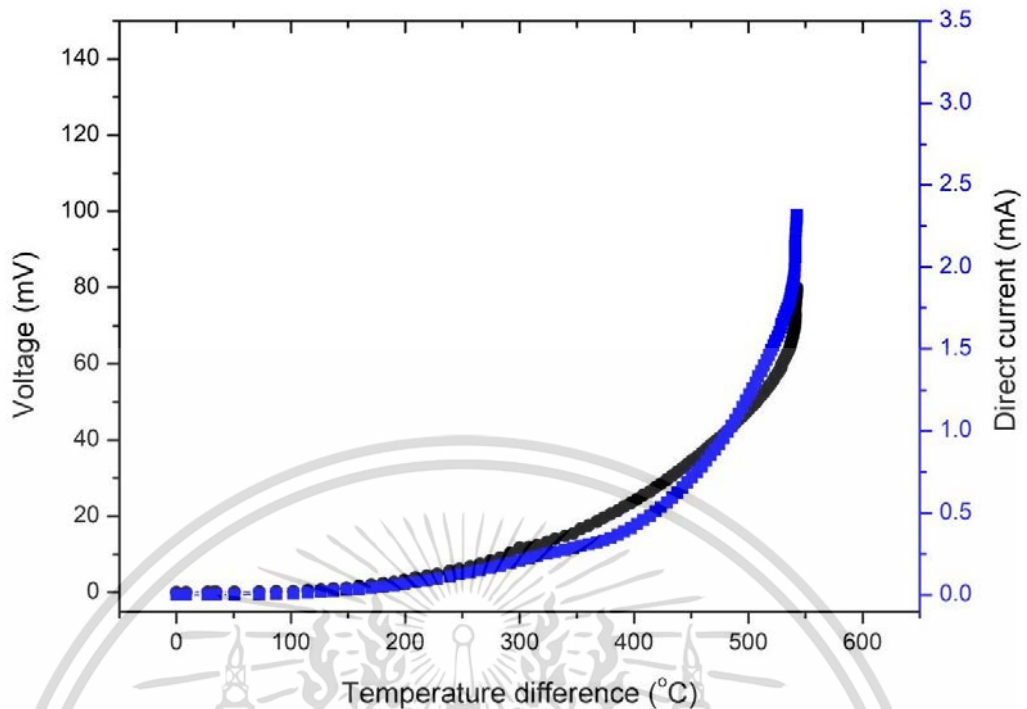


Figure 4.50 Graph relation between temperature difference voltage (mV) and current (mA) for 2 module of the thermoelectric module to connect parallel electrical circuit at the height of the module at 1.5 cm.

- At the height of the module 2.0 cm

The results showed that the difference of the maximum heat temperature was 602.20°C (at the hot side temperature of 700.80°C and the cold side was 98.60°C) as shown in Figure 4.51. Figure 4.52 showed the results of testing of electrical measurements compared to temperature differences as showed that the maximum electric potential is 94.20 mV , the current is 2.43 mA and the electric potential can be constant as time changes. The results electrical value increases according to the temperature difference with has tendency to be increase.

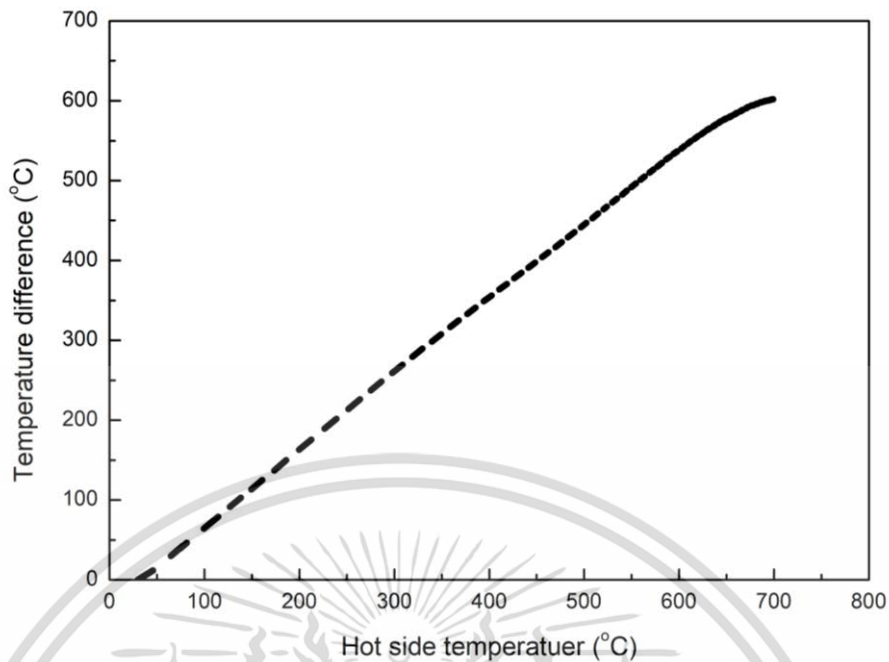


Figure 4.51 The temperature difference in the room temperature range to 700 °C for 2 module of the thermoelectric module to connect parallel electrical circuit at the height of the module at 2.0 cm.

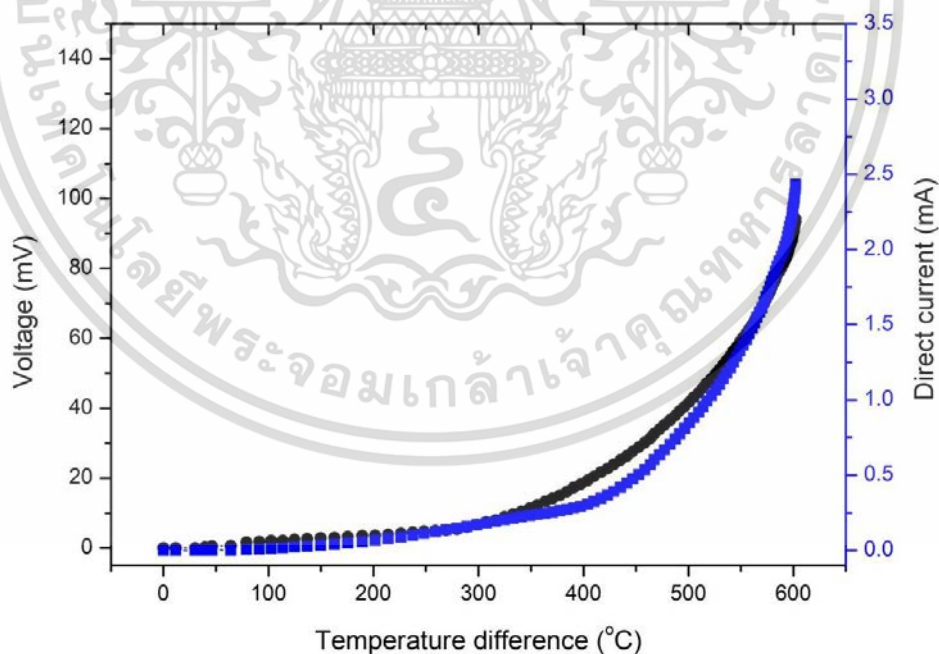


Figure 4.52 Graph relation between temperature difference voltage (mV) and current (mA) for 2 module of the thermoelectric module to connect parallel electrical circuit at the height of the module at 2.0 cm.

เอกสารนี้เป็นเอกสารที่สงวนไว้สำหรับการใช้งานเพื่อการศึกษาเท่านั้น ไม่อนุญาตให้นำไปใช้ประโยชน์ด้านการค้า ไม่ว่าจะกรณีใดๆ ทั้งสิ้น อีกทั้งห้ามมิให้ดัดแปลงเนื้อหา และต้องอ้างอิงถึงเจ้าของเอกสารทุกครั้งที่มีการนำไปใช้

- At the height of the module 2.5 cm

The results showed that the difference of the maximum heat temperature was $617.90\text{ }^{\circ}\text{C}$ (at the hot side temperature of $700.50\text{ }^{\circ}\text{C}$ and the cold side was $82.60\text{ }^{\circ}\text{C}$) as shown in Figure 4.53. Figure 4.54 showed the results of testing of electrical measurements compared to temperature differences as showed that the maximum electric potential is 119.80 mV , the current is 3.73 mA and the electric potential can be constant as time changes. The results electrical value increases according to the temperature difference with has tendency to be increase.

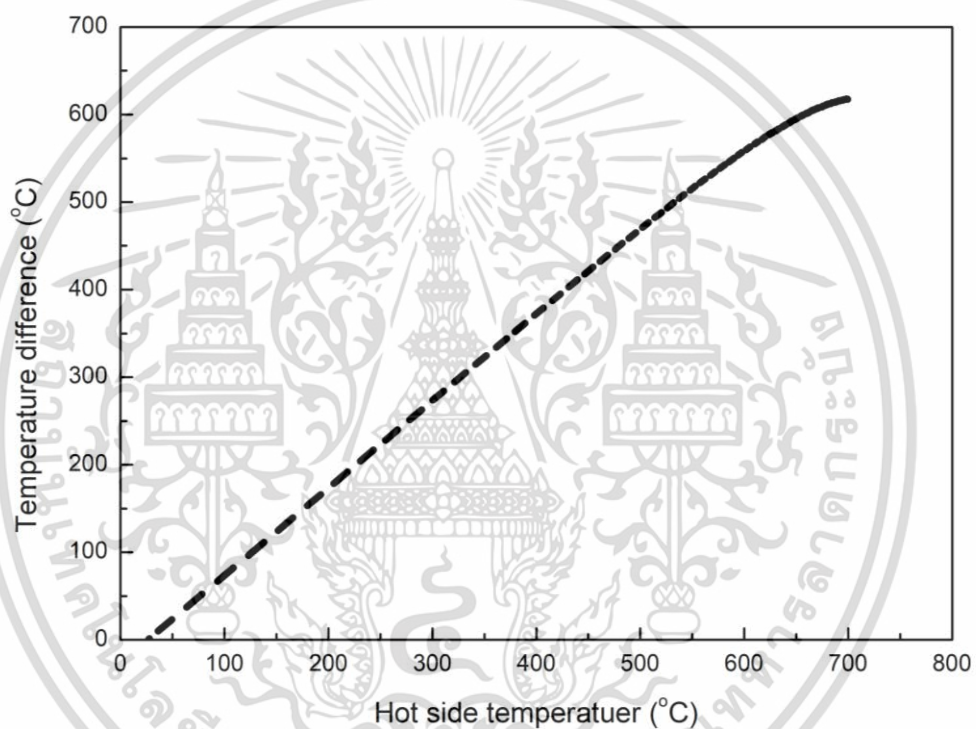


Figure 4.53 The temperature difference in the room temperature range to $700\text{ }^{\circ}\text{C}$ for 2 module of the thermoelectric module to connect parallel electrical circuit at the height of the module at 2.5 cm.

เอกสารนี้เป็นเอกสารที่สงวนไว้สำหรับการใช้งานเพื่อการศึกษาเท่านั้น ไม่อนุญาตให้นำไปใช้ประโยชน์ด้านการค้า
ไม่ว่ากรณีใดๆ ทั้งสิ้น อีกทั้งห้ามมิให้ตัดแปลงเนื้อหา และต้องอ้างอิงถึงเจ้าของเอกสารทุกครั้งที่มีการนำไปใช้

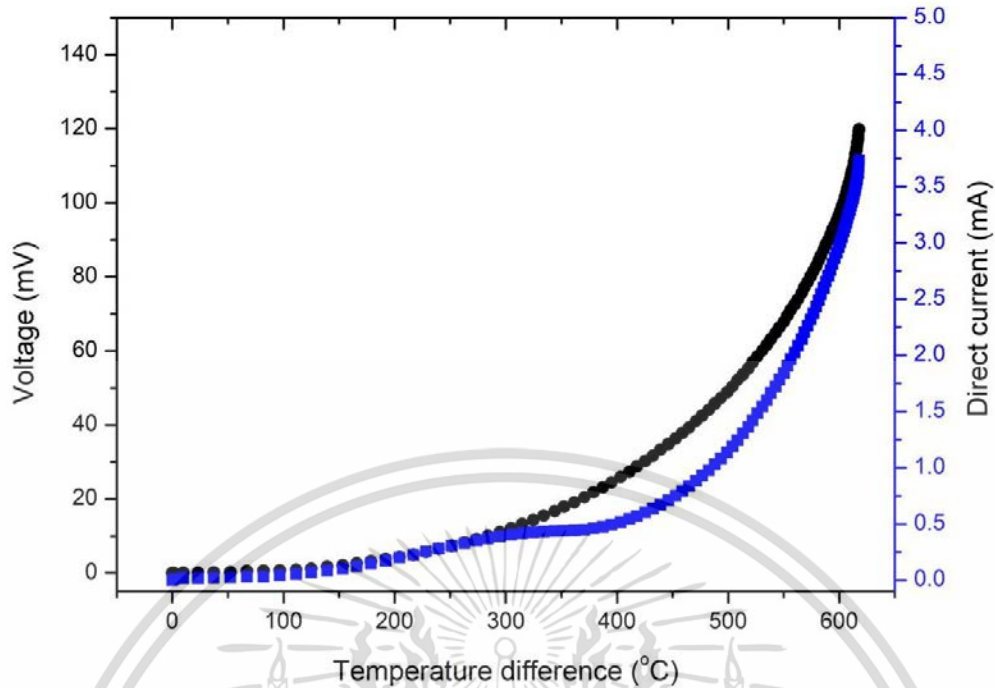


Figure 4.54 Graph relation between temperature difference voltage (mV) and current (mA) for 2 module of the thermoelectric module to connect parallel electrical circuit at the height of the module at 2.5 cm.

The results of the production of thermoelectric modules for 2 modules are connected in parallel electric circuits at various heights. It can be found that at height of 1.5 cm provides a minimum current of 2.32 mA compared to an increase in height of 2.0 cm the current is 2.43 mA and at height of 2.5 cm provides the current is 3.73 mA. We could see that the height of the module affects the production of the electric current which the current will increase according to the height. Therefore, should design the height suitable for the actual be use as shown in Figure 4.55.

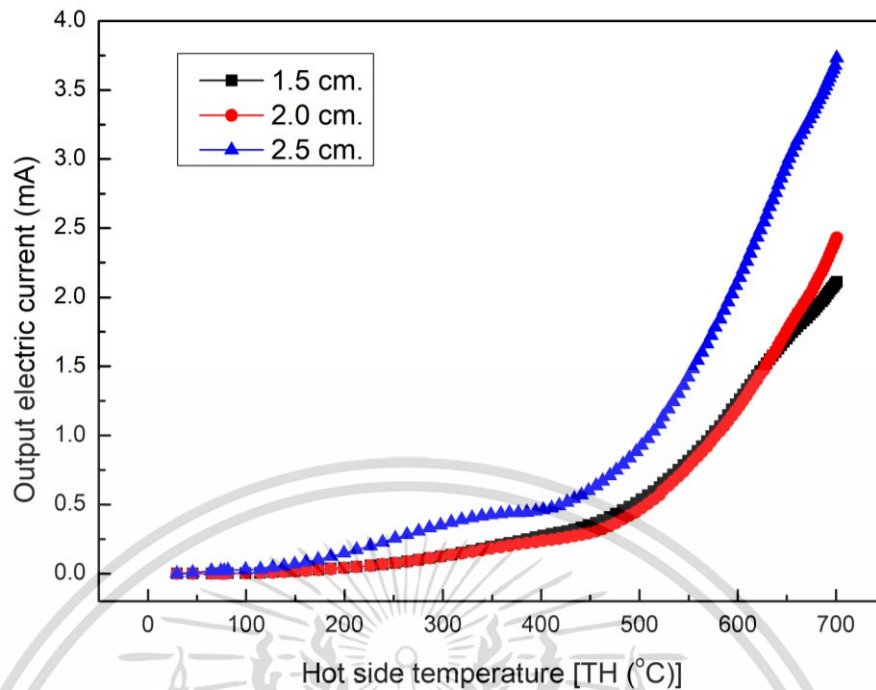


Figure 4.55 Graph relation between hot side temperature and current (mA) for 2 module of the thermoelectric module to connect parallel electrical circuit at the height of the module at 1.5, 2.0 and 2.5 cm.

4.3.4.3 The result of 50 thermoelectric module of CaMnO_3 at the diameter of 1 cm at the height 2 cm to connect compound electrical circuit

The results of the thermoelectric module test in the laboratory. Bring 50 module of the thermoelectric module are connect compound electrical circuit at the height of the module 2 cm test on the hot plate for test the heat resistance and create different temperature between the side that touches the hot plate and other side that does not touch the hot plate. The results showed that the difference of the maximum heat temperature was $553.50\text{ }^{\circ}\text{C}$ (at the hot side temperature of $700\text{ }^{\circ}\text{C}$ and the cold side was $146.50\text{ }^{\circ}\text{C}$) as shown in Figure 4.56. The results of testing of electrical measurements compared to temperature differences as showed that the maximum electric potential is 702.44 mV , the current is 55.06 mA and the electric potential can be constant as time changes as shown in Figure 4.57. Shows as electricity measurement results and the electrical value increases according to the temperature difference with has tendency to be increase

เอกสารนี้เป็นเอกสารที่สงวนไว้สำหรับการใช้งานเพื่อการศึกษาเท่านั้น ไม่อนุญาตให้นำไปใช้ประโยชน์ด้านการค้า ไม่ว่าจะกรณีใดๆ ทั้งสิ้น อีกทั้งห้ามมิให้ตัดแปลงเนื้อหา และต้องอ้างอิงถึงเจ้าของเอกสารทุกครั้งที่มีการนำไปใช้

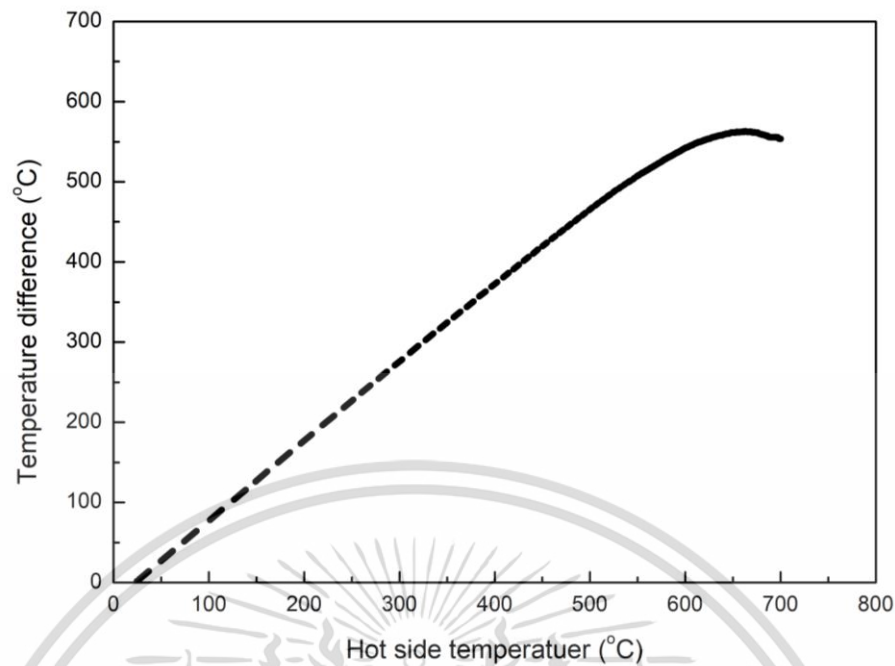


Figure 4.56 The temperature difference in the room temperature range to 700 °C for 50 module of the thermoelectric module to connect compound electrical circuit at the height of the module at 2.0 cm.

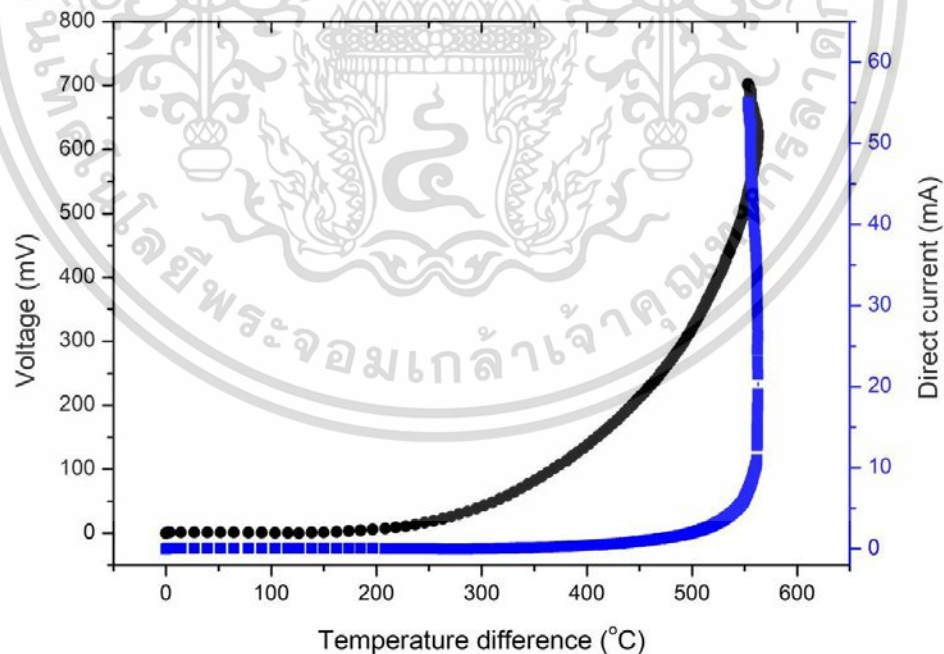


Figure 4.57 Graph relation between temperature difference voltage (mV) and current (mA) for 50 module of the thermoelectric module to connect compound electrical circuit at the height of the module at 2.0 cm.

เอกสารนี้เป็นเอกสารที่สงวนไว้สำหรับการใช้งานเพื่อการศึกษาเท่านั้น ไม่อนุญาตให้นำไปใช้ประโยชน์ด้านการค้า ไม่ว่าจะกรณีใดๆ ทั้งสิ้น อีกทั้งห้ามมิให้ตัดแปลงเนื้อหา และต้องอ้างอิงถึงเจ้าของเอกสารทุกครั้งที่มีการนำไปใช้

Chapter 5

Conclusions and Suggestions

5.1 Conclusions

This dissertation seeks to study the synthesis and properties of smart cement C3AH6-rGO nanocomposite and the development of thermoelectric generator by using CaMnO₃ as follows:

1. Synthesis of nanostructure tricalcium aluminate hexahydrate (C3AH6) cements.
2. Synthesis of C3AH6 cement/reduced graphene oxide (C3AH6-rGO) smart cement nanocomposites.
3. Development of thermoelectric generator from heat using CaMnO₃ and applications in municipal melting furnace or municipal incinerator.

Samples were investigated in structural properties using X-ray Diffraction (XRD), Raman Spectroscopy, Scanning Electron Microscope (SEM), Transmission Electron Microscope (TEM), Fourier-Transformed Infrared Spectroscopy (FT-IR), UV-vis Diffuse Reflectance Spectroscopy (DRS), X-ray Photoelectron Spectroscopy (XPS), Thermogravimetric Analysis (TGA), and the properties measurements dielectric LRC, electrochemical properties, optical, electrical conductivities, thermoelectric, thermal conductivity, supercapacitor, antibacterial activity and micro hardness. The result can be concluded as follows:

Samples of smart cement were characterized and confirmed by several techniques such as, XRD, Raman, SEM, TEM, FT-IR, UV-vis, XPS, TGA. Moreover, the properties of as-synthesized cement samples, for example, dielectric constant, electrochemical properties, optical, electrical, thermal conductivities, thermoelectric, micro hardness, supercapacitor, and antibacterial activity were also studied. The results can be concluded as follows, the nanostructured C3AH6 and C3AH6-rGO nanocomposite smart cements were successfully fabricated by a conventional hydration process. C3AH6 nanocement displayed a high dielectric response, large optical band gap, thermodynamically stable at below 350 °C and low thermal

เอกสารนี้เป็นเอกสารที่สงวนไว้สำหรับการใช้งานเพื่อการศึกษาเท่านั้น ไม่อนุญาตให้นำไปใช้ประโยชน์ด้านการค้า
ไม่ว่ากรณีใดๆ ทั้งสิ้น อีกทั้งห้ามมิให้ตัดแปลงเนื้อหา และต้องอ้างอิงถึงเจ้าของเอกสารทุกครั้งที่มีการนำไปใช้

conductivity as thermal insulator. However, the C3AH6-rGO nanocomposite cements appeared to have good smart cements properties including high electrical conductivity, giant dielectric constants, greater Vickers micro hardness values, high electrochemical and supercapacitor properties and high performance in antibacterial activities. These interested properties tend to increase as the rGO content (wt.x%) loading increases. In contrast, thermal conductivity reduced against an increase in contents of rGO in the C3AH6-rGO nanocomposites. These results indicated that nanosized C3AH6 cement incorporated with rGO material exhibited in suitable properties for multifunctional applications as smart cement materials.

In addition, the prototype of concrete block electric power generation from heat (CGH) and its applications in municipal melting furnace or municipal incinerator are investigated. This CGH prototype consisted of thermoelectric modules having thermoelectric material synthesized derived from CaMnO_3 thermoelectric material. It was found that a single thermoelectric module indicated voltage as 155 mV, current as 11 mA, and the electrical power as 1.7 mW in a difference in temperature of 470°C for the high temperature side module at 700°C . The electrical power can be increased by connecting several thermoelectric modules together. Also, the CGH prototype consisted of 50 thermoelectric modules, were connected to the electrical circuit at the height of the module as 2 cm on the hot plate. The results showed that the electrical power was directly proportional to the number of thermoelectric modules. The difference in the maximum heat temperature was at 553.50°C (the hot side temperature was at 700°C and the cold side was at 146.50°C). In addition, testing of electrical measurements, when compared to temperature differences, showed that the maximum electric potential was at 702.44 mV and the current was 55.06 mA. Thus, these results implied that CGH prototype can be applied to thermal energy from various heat sources such as burning, biomass, waste, industrial heat and power plants. The CGH prototype may be scaled into a large-scale thermal power plant in order to supply the electrical energy to industries.

References

- [1] R. Lourenço, R. Angelicab, J. Rodriguesa. 2013. "Preparation of Refractory Calcium Aluminate Cement using the Sonochemical Process." *Materials Research*. 16(4) : 731-739.
- [2] A. M. Fogg, A. J. Freij, A. L. Rohl, M. I. Ogden, and G. M. Parkinson. 2002. "Toward a Fundamental Understanding of Molecular Recognition: A Synthetic and Computational Study of Morphological Control of $\text{Ca}_3\text{Al}_2(\text{OH})_{12}$." *J. Phys. Chem. B*. 106: 5820-5826.
- [3] Nilforoushan, M. Reza, Talebiaan, and Nasrien. 2007. "The Hydration Products of a Refractory calcium aluminate cement at Low Temperatures." *Iran. J. Chem. Chem. Eng.* 26: 2.
- [4] V. Antonovica, J. Kerieneb, R. Borisa, and M. Aleknevicius. 2013. "The Effect of Temperature on the Formation of the Hydrated Calcium Aluminate Cement Structure." *Procedia Engineering*. 57: 99-106.
- [5] G. Goracci, M. Monasterio, H. Jansson and S. Cervený. 2017. "Dynamics of nano-confined water in Portland cement-comparison with synthetic C-S-H gel and other silicate materials." *Scientific Reports*. 7 : 8258.
- [6] L. Fernández-Carrasco, J. Rius and C. Miravittles. 2008. "Supercritical carbonation of calcium aluminate cement." *Cement and Concrete Research*. 38 : 1033–1037.
- [7] W.J. Wei, S.D. Tze and H.C. Liaw. 2005 "Calcium aluminate composites with controlled duplex structures! Hydration reaction and densification." *Journal of Ceramic Processing Research*. 6 (3) : 223-229.
- [8] M. U. Okoronkwo, F. P. Glasser. 2016. "Compatibility of hydrogarnet, $\text{Ca}_3\text{Al}_2(\text{SiO}_4)_x(\text{OH})_4(3-x)$, with sulfate and carbonate-bearing cement phases: 5–85 °C." *Cement and Concrete Research*. 83 : 86–96.
- [9] V. Antonovica, J. Kerieneb, R. Borisa, M. Aleknevicius. 2013. "The Effect of Temperature on the Formation of the Hydrated Calcium Aluminate Cement Structure." *Procedia Engineering*. 57 : 99–106.

[10] J. Plank, M. Zhang-Preße, N.P. Ivleva, R. Niessner. 2016. “Stability of single phase C3A hydrates against pressurized CO₂” *Construction and Building Materials*. 122 : 426–434.

[11] M. Torres-Luque, J. F. Osma, M. Sánchez-Silva, E. Bastidas-Arteaga and F. Schoefs. 2017. “Chlordetect: Commercial Calcium Aluminate Based Conductimetric Sensor for Chloride Presence Detection.” *Sensors*. 17 : 2099.

[12] A. Smith, P. Abelard, F. Thummen, A. Allemand. 2004. “Electrical characterisation as a function of frequency: application to aluminous cement during ear hydration.” *Cement & Concrete Composites*. 14 : 477-484.

[13] B. Z. Dilnesa, B. Lothenbach, G. Renaudin, A. Wichser, D. Kulik. 2014. “Synthesis and characterization of hydrogarnet Ca₃(Al_xFe_{1-x})₂(SiO₄)_y(OH)₄(3-y).” *Cement and Concrete Research*. 59 : 96–111.

[14] P. Barnes and J. Bensted. 2019. “Structure and Performance of cements” Second edition. CRC Press : 584.

[15] Chaiwat Phrompet, Chaval Sriwong, Chesta Ruttanapun. 2019. “Mechanical, dielectric, thermal and antibacterial properties of reduced graphene oxide (rGO)-nanosized C3AH6 cement nanocomposites for smart cement-based materials.” *Composites Part B: Engineering*. 175 : 107-128.

[16] Dimitar Dimov, Iddo Amit, Olivier Gorrie, Matthew D. Barnes, Nicola J. Townsend, Ana I. S. Neves, Freddie Withers, Saverio Russo, and Monica Felicia Craciun. 2018. “Ultra-high Performance Nanoengineered Graphene–Concrete Composites for Multifunctional Applications.” *Adv. Funct. Mater.* 28 (170) : 51-83.

[17] Karim Khan, Ayesha Khan Tareen, Sayed Elshahat, Ashish Yadav, Usman Khan, Minghui Yang, Luigi Bibbo, Zhengbiao Ouyang. 2018. “Facile synthesis of cationic doped [Ca₂₄Al₂₈O₆₄]⁴⁺ (4e-) composite via rapid citrate sol-gel method.” *Dalton Transactions*. 47 : 3819-3830.

[18] Ahmadreza Sedaghat, Manoj K. Ram, A. Zayed, Rajeev Kamal, Natallia Shanahan. 2014. “Investigation of Physical Properties of Graphene-Cement Composite for Structural Applications.” *Journal of Composite Materials*. 4 : 12-21.

[19] Aliakbar Gholampour, Meisam Valizadeh Kiamahalleh, Diana N. H. Tran, Togay Ozbakkaloglu, and Dusan Losic. 2017. “From Graphene Oxide to Reduced Graphene Oxide: Impact on the Physiochemical and Mechanical Properties of Graphene-Cement Composites.” *ACS Appl. Mater. Interfaces*. 9 : 43275-43286.

[20] Chaiwat Phrompet, Chaval Sriwong, Pornjuk Srepusharawoot, Santi Maensiri, Prinya Chindaprasirt, Chesta Ruttanapun. 2019. "Effect of free oxygen radical anions and free electrons in a $\text{Ca}_{12}\text{Al}_{14}\text{O}_{33}$ cement structure on its optical, electronic and antibacterial properties." *Heliyon*. 5 : e01808.

[21] Wen Lu, Jong-Beom Baek and Liming Dai. 2015. "Carbon Nanomaterials for Advanced Energy Systems." Canada. John Wiley & Sons.

[22] E. P. Randviir, D. Brownson and C. E. Banks. 2014. "A decade of graphene research: production, applications and outlook." *Materials Today*. 17(9) : 426-432.

[23] HoSung Lee. 2017. "THERMOELECTRICS DESIGN AND MATERIALS." Western Michigan University. USA. John Wiley & Sons.

[24] Nettleton, H.R. 1922. "The Thomson effect." *Proceedings of the Physical Society of London*.

[25] Thomson, W. 1854. "Account of researches in thermo-electricity." *Proceedings of the Royal Society of London*. 7: 49–58.

[26] V. Augustyn, P. Simon, B. Dunn. 2014. "Pseudocapacitive oxide materials for high-rate electrochemical energy storage." *Energy Environ. Sci.* 7 : 1597–1614.

[27] Y. Wang, Y. Song and Yongyao Xia. 2016. "Electrochemical capacitors: mechanism, materials, systems, characterization and applications." *Chem Soc Rev*. 45 : 5925-5950.

[28] M. Vangari, T. Pryor and L. Jiang. 2013. "Supercapacitors : Review of materials and fabrication methods." *Journal of Energy Engineering*. 139(2) : 72-79.

[29] B. K. Kim, S.Sy, A. Yu and J. Zhang.2015. "Electrochemical Supercapacitors for Energy Storage and Conversion." *Handbook of Clean Energy Systems Online*. John Wiley & Sons, Ltd.

[30] Guo, X. L., Kuang, M., Li, F., Liu, X. Y., Zhang, Y. X., Dong, F., & Losic, D. 2016. "Engineering of three dimensional (3-D) diatom@ TiO_2 @ MnO_2 composites with enhanced supercapacitor performance." *Electrochimica Acta*. 190 : 159–167.

[31] C. Ruttanapun, P. Srepusharawoot, and S. Maensiri. 2018. "Effect of Fe^{3+} -doped $\text{Ca}_{12}\text{Al}_{14}\text{O}_{33}$ cement on optical and thermal properties", *Chinese Journal of Physics*. 56 : 252–260.

[32] Chaiwat Phrompet, Chaval Sriwong, Santi Maensiri, Prinya Chindaprasirt, Chesta Ruttanapun. 2018. "Optical and dielectric properties of nano-sized tricalcium aluminate hexahydrate (C3AH6) cement." *Construction and Building Materials*. 179 : 57-65.

[33] E. Feizi and A. K. Ray. 2016. "12CaO·7Al₂O₃ Ceramic: A Review of the Electronic and Optoelectronic Applications in Display Devices." *J Disp Technol*. 12 : 451-459.

[34] Katsuro Hayashi, Masahiro Hirano, Satoru Matsuishi, and Hideo Hosono. 2004. "Microporous Crystal 12CaO·7Al₂O₃ Encaging Abundant O-Radicals." *J. Am. Chem. Soc.* 5 : 738-739.

[35] GONG Lu, SHEN Jing, LI Quan-Xin. 2010. "Investigation on the Antibacterial Activity and Mechanism of CAO-O Particles." *Journal of Inorganic Materials*. 25 : 943-946.

[36] Mao Li, Jin-man Kim. 2017. "Strength Properties and Micro-structure of Steel Slag Based Hardened Cementitious Composite with Graphene Oxide." *MATEC Web of Conferences*. 138 : 03012.

[37] B.C. Brodie. 1860. "Sur le poids atomique du graphite" *Annales de Chimie Physique*. 59 : 466.

[38] L. Staudenmaier. 1898. "Verfahren zur Darstellung der Graphitsaure." *Berichte Der Deutschen Botanischen Gesejjschaft*. 31 : 14-81.

[39] W.S. Hummer, R.E. Offeman. 1985. "Perparation of graphitic oxide" *Journal of American Chemical Society*. 80 : 13-39.

[40] A.B. Bourlinos, D. Gournis, D. Petridis, T. Szabo, A. Szeri, I. Dekany. 2003. "Chemical reduction to graphite and surface modification with primary aliphatic amines and amino acids." *Langmuir*. 19 : 233-305.

[41] Li B, Huang K, Yan Y, Li Y, Twaha S, Zhu J. 2017. "Heat transfer enhancement of a modularised thermoelectric power generator for passenger vehicles." *Apple Energy*. 205 : 868-879.

[42] Zhang X, Zhao LD. 2015. "Thermoelectric materials: Energy conversion between heat and electricity." *Journal Materiomics*. 1 : 92-105.

[43] Bin Zhan, Jinle Lan, Yaochun Liu, Yang Shen, Cewen Nan. 2014. “High Temperature Thermoelectric Properties of Dy-doped CaMnO_3 Ceramics.” *Journal of Materials Science & Technology*. 30 : 821-825.

[44] Meng F, Chen L, Sun F, Yang B. Thermoelectric power generation driven by blast furnace slag flushing water. *Energy* 2014, 66, 965-972.

[45] Feipeng Z, Baocheng N, Kunshu Z, Xin Z, Qingmei L, Jiuxing Z. 2013. “Effects of praseodymium doping on thermoelectric transport properties of CaMnO_3 compound system.” *J Rare Earth Sci*. 31: 88.

[46] Gao M, Su C, Cong J, Yang F, Wang Y, Wang P. 2019. “Harvesting thermoelectric energy from railway track.” *Energy*. 180 : 315-329.

[47] Orr B, Akbarzadeh A, Mochizuki M, Singh R. 2016. “A review of car waste heat recovery systems utilizing thermoelectric generators and heat pipes.” *Applied Thermal Engineering*. 101 : 490-495.

[48] Lu Z, Zhang H, Mao C, Li CM. 2016. “Silk fabric-based wearable thermoelectric generator for energy harvesting from the human body.” *Appl energy*. 164 : 57-63.

[49] Jing W, Yuan D, Xu S, Hu H, Xiao J, Sha A, Huang Y. 2017 “Energy harvesting from asphalt pavement using thermoelectric technology.” *Appl energy*. 205 : 941-950.

[50] Anna Laura Pisello, Antonella D’Alessandro, Sara Sambuco, Marco Rallini, Filippo Ubertini, Francesco Asdrubali, Annibale Luigi Materazzi, Franco Cotana. 2017 “Multipurpose experimental characterization of smart nanocomposite cement-based materials for thermal-energy efficiency and strain-sensing capability.” *Solar Energy Materials and Solar Cells*. 161 : 77-88.

[51] Chaiwat Phrompet, Keerati Maneesai, Wattan Tuichai, Attaphol Karaphun, Chaval Sriwong and Chesta Ruttanapun. 2020. “Electrochemical properties of tricalcium aluminate hexahydrate-reduced graphene oxide nanocomposites for supercapacitor device.” *Journal of Energy Storage*. 30 : 101-474.

[52] Nutthakritta Phromviyo, Prasit Thongbal, Kunthaya Ratchaphonsaenwong, Narong Chanlek, Prinya Chindapasirt. 2019. “Dielectric and electrical properties of nano-Ag/C3AH6 nanocomposites.” *Applied Surface Science*. 483 : 294-301

[53] J. Eufinger, A.Schmidt, M. Lerch and J. Janek. 2015. “Novel anion conductors-conductivity, thermodynamic stability and hydration of anion substituted mayenite-type cage compounds C12A7 : X (X = O, OH, Cl, F, CN, S, N).” *Phys. Chem. Chem. Phys.* 17: 6844.

[54] A.P. Grosvenor, B.A. Kobe, M.C. Biesinger, N.S. McIntyre, Surf. 2004. *Interface Anal.* 36 : 1564–1574

[55] A. Sedaghat, M. K. Ram, A. Zayed, R. Kamal, N. Shanahan.2014 “Investigation of Physical Properties of Graphene-Cement Composite for Structural Applications.” *Journal of Composite Materials.* 4 :12-21.

[56] L. Guo, X. Xu, J. R. Salvador, and G. P. Meisner. 2013. “Coupled vibrational modes in multiple-filled skutterudites and the effects on lattice thermal conductivity reduction.” *APPLIED PHYSICS LETTERS.* 905 : 102-111.

[57] Kamalak H, Erdem M, Altin E, Demirel S, Oz E, Altin S .2016. “Giant Dielectric Constant and Mechanical, Heat Conducting and Structural Properties of Dental Composites by Adding Ca Ions.” *J Dent Oro Surg.* 1(3) : 112.

[58] Karthika Prasad, G. S. Lekshmi, Kola Ostrikov, Vanessa Lussini, James Blinco, Mandhakini Mohandas, Krasimir Vasilev, Steven Bottle, Kateryna Bazaka and Kostya Ostrikov. 2017. “Synergic bactericidal effects of reduced graphene oxide and silver nanoparticles against Gram- positive and Gram-negative bacteria.” *Scientific Reports.* 7 : 15-91.



Appendix

เอกสารนี้เป็นเอกสารที่สงวนไว้สำหรับการใช้งานเพื่อการศึกษาเท่านั้น ไม่อนุญาตให้นำไปใช้ประโยชน์ด้านการค้า
ไม่ว่ากรณีใดๆ ทั้งสิ้น อีกทั้งห้ามมิให้ดัดแปลงเนื้อหา และต้องอ้างอิงถึงเจ้าของเอกสารทุกครั้งที่มีการนำไปใช้



Appendix A

เอกสารนี้เป็นเอกสารที่สงวนไว้สำหรับการใช้งานเพื่อการศึกษาเท่านั้น ไม่อนุญาตให้นำไปใช้ประโยชน์ด้านการค้า
ไม่ว่ากรณีใดๆ ทั้งสิ้น อีกทั้งห้ามมิให้ดัดแปลงเนื้อหา และต้องอ้างอิงถึงเจ้าของเอกสารทุกครั้งที่มีการนำไปใช้

Crystallographic reference

A.1 : C3AH6 PDF#03-0125

00-024-0217

Nov 15, 2016 11:00 AM (User)

PDF Card Report

Status: Primary **QM:** Star (S) **Pressure/Temperature:** Ambient
Chemical Formula: Ca₃Al₂(OH)₁₂ **Empirical Formula:** Al₂Ca₃H₁₂O₁₂
Weight %: Al14.27 Ca31.79 H3.20 O50.75 **Atomic %:** Al6.90 Ca10.34 H41.38 O41.38
Compound Name: Calcium Aluminum Hydroxide **Mineral Name:** Katoite, syn

Experimental

Author's Reported Data

Radiation: CuK α 1 : 1.5406Å **Intensity:** Diffractometer

Physical

SYS: Cubic **SPGR:** Ia-3d (230)

Author's Cell

AuthCell a: 12.5727(2)Å	AuthCell Vol: 1987.40Å ³	AuthCell Z: 8.00
AuthCell MolVol: 248.43		

Dcalc: 2.520g/cm³ **SS/FOM:** F(30) = 91.0(0.0106, 31)

Crystal

ICDD Calculated Parameters

Space Group: Ia-3d (230) **Molecular Weight:** 378.29

Crystal Data

XtlCell a: 12.573Å	XtlCell b: 12.573Å	XtlCell c: 12.573Å
XtlCell : 90.00°	XtlCell : 90.00°	XtlCell : 90.00°
XtlCell Vol: 1987.40Å ³	XtlCell Z: 8.00	

Crystal Data Axial Ratio

XtlCell a/b: 1.000	XtlCell c/b: 1.000
---------------------------	---------------------------

Reduced Cell

RedCell a: 10.888Å	RedCell b: 10.888Å	RedCell c: 10.888Å
RedCell : 109.47°	RedCell : 109.47°	RedCell : 109.47°
RedCell Vol: 993.70Å ³		

เอกสารนี้เป็นเอกสารที่สงวนไว้สำหรับการใช้งานเพื่อการศึกษาเท่านั้น ไม่อนุญาตให้นำไปใช้ประโยชน์ด้านการค้า
 ไม่ว่าจะกรณีใดๆ ทั้งสิ้น อีกทั้งห้ามมิให้ตัดแปลงเนื้อหา และต้องอ้างอิงถึงเจ้าของเอกสารทุกครั้งที่มีการนำไปใช้

00-024-0217

Nov 15, 2016 11:00 AM (User)

PDF Card Report

Status: Primary **QM:** Star (S) **Pressure/Temperature:** Ambient
Chemical Formula: Ca₃Al₂(OH)₁₂ **Empirical Formula:** Al₂Ca₃H₁₂O₁₂
Weight %: Al14.27 Ca31.79 H3.20 O50.75 **Atomic %:** Al6.90 Ca10.34 H41.38 O41.38
Compound Name: Calcium Aluminum Hydroxide **Mineral Name:** Katoite, syn

Experimental

Author's Reported Data

Radiation: CuK α 1 : 1.5406Å **Intensity:** Diffractometer

Physical

SYS: Cubic **SPGR:** Ia-3d (230)

Author's Cell		
AuthCell a: 12.5727(2)Å	AuthCell Vol: 1987.40Å ³	AuthCell Z: 8.00
AuthCell MolVol: 248.43		

Dcalc: 2.529g/cm³ **SS/FOM:** F(30) = 91.0(0.0106, 31)

Crystal

ICDD Calculated Parameters

Space Group: Ia-3d (230) **Molecular Weight:** 378.29

Crystal Data		
XtlCell a: 12.573Å	XtlCell b: 12.573Å	XtlCell c: 12.573Å
XtlCell : 90.00°	XtlCell : 90.00°	XtlCell : 90.00°
XtlCell Vol: 1987.40Å ³	XtlCell Z: 8.00	

Crystal Data Axial Ratio	
XtlCell a/b: 1.000	XtlCell c/b: 1.000

Reduced Cell		
RedCell a: 10.888Å	RedCell b: 10.888Å	RedCell c: 10.888Å
RedCell : 109.47°	RedCell : 109.47°	RedCell : 109.47°
RedCell Vol: 993.70Å ³		

เอกสารนี้เป็นเอกสารที่สงวนไว้สำหรับการใช้งานเพื่อการศึกษาเท่านั้น ไม่อนุญาตให้นำไปใช้ประโยชน์ด้านการค้า
 ไม่ว่ากรณีใดๆ ทั้งสิ้น อีกทั้งห้ามมิให้ตัดแปลงเนื้อหา และต้องอ้างอิงถึงเจ้าของเอกสารทุกครั้งที่มีการนำไปใช้

00-024-0217

Nov 15, 2016 11:00 AM (User)

Optical

: =1.605

Structure**Crystal (Symmetry Allowed):** Centrosymmetric**Miscellaneous****Pearson:** cI232.00 **Pearson w/o H:** cI136**Mineral Classification:** Garnet (Group), hydroxide (Subgroup)**Subfile(s):** Cement and Hydration Product, Inorganic, Mineral Related (Mineral , Synthetic), NBS Pattern, Common Phase, Educational Pattern, Primary Pattern**Entry Date:** 08/20/1982 **Last Modification Date:** 01/14/2012**Cross-Ref PDF #'s:** 00-003-0125 (Deleted), 00-061-0329 (Primary), 04-007-2666, 04-008-4297, 04-008-8979, 04-008-8343**References**

Type	Reference
Primary Reference	Natl. Bur. Stand. (U. S.) Monogr. 25 11-16 (1974).

Comments

Database Comments: Additional Patterns: To replace 00-003-0125. See PDF 00-061-0329. Color: Colorless. General Comments: Forms solid solution with hibschite, hydrogrossular, and grossular. Sample Preparation: Prepared by treating a saturated solution of CaO and 6% phenol. Al metal dissolved in KOH was added. Compound was dried at 110 C for 2 hours. Temperature of Data Collection: Pattern taken at 298 K.

d-Spacings (71) - 00-024-0217 (Fixed Slit Intensity) - Cu K1 1.54056Å

2	d(Å)	I	h	k	l	*	2	d(Å)	I	h	k	l	*
17.2715	5.130900	90	2	1	1		62.6413	1.461900	3	6	6	0	
19.9721	4.442000	40	2	2	0		63.6075	1.461600	1	8	3	1	
26.5219	3.358000	55	3	2	1		65.4780	1.424300	1	7	5	2	
28.3821	3.142000	45	4	0	0		66.4502	1.405800	12	8	4	0	
31.8193	2.810000	80	4	2	0		68.3329	1.371600	5	8	4	2	
33.4069	2.690000	6	3	3	2		69.2583	1.355500	5	7	6	1	
34.9377	2.586000	15	4	2	2		70.1703	1.340100	8	6	6	4	
36.4183	2.465000	30	4	3	1		71.0716	1.325300	2	6	5	1	
39.2222	2.296000	100	5	2	1		72.9002	1.296500	5	9	3	2	
40.5664	2.222000	4	4	4	0		73.7599	1.283900	2	8	4	4	
44.3917	2.039000	95	6	1	1		74.6697	1.270100	4	9	4	1	
45.5695	1.990000	8	6	2	0		76.4496	1.244900	2	10	1	1	
49.1090	1.853800	1	6	3	1		77.3233	1.233000	1	10	2	0	
50.2309	1.814800	10	4	4	4		78.1814	1.221600	1	9	4	3	
51.3297	1.778500	2	5	4	3		79.9794	1.198600	8	10	3	1	
52.4312	1.743700	40	6	4	0		81.7212	1.177400	1	8	7	1	
53.5087	1.711100	20	7	2	1		82.5617	1.167300	8	10	4	0	
54.5807	1.680000	50	6	4	2		83.4454	1.157400	4	10	3	3	
57.6990	1.596400	11	6	5	1		84.3029	1.147800	10	10	4	2	
58.7017	1.571500	13	8	0	0		85.1806	1.138200	1	8	7	3	
59.6908	1.547800	1	7	4	1		86.8851	1.120200	8	11	2	1	
60.6806	1.524900	1	8	2	0		87.7574	1.111300	4	8	8	0	
61.6603	1.503000	2	6	5	3		90.3212	1.086300	4	11	3	2	

© 2016 International Centre for Diffraction Data. All rights reserved.

Page 2 / 3

เอกสารนี้เป็นเอกสารที่สงวนไว้สำหรับการใช้งานเพื่อการศึกษาเท่านั้น ไม่อนุญาตให้นำไปใช้ประโยชน์ด้านการค้า
ไม่ว่ากรณีใดๆ ทั้งสิ้น อีกทั้งห้ามมิให้ดัดแปลงเนื้อหา และต้องอ้างอิงถึงเจ้าของเอกสารทุกครั้งที่มีการนำไปใช้

00-024-0217

Nov 15, 2016 11:00 AM (User)

2	d(Å)	I	h	k	l	*	2	d(Å)	I	h	k	l	*
92.9440	1.062400	1	10	6	2		112.4275	0.826800	3	12	6	2	
93.7818	1.055100	2	9	6	5		113.3243	0.822000	1	13	4	1	
94.6391	1.047800	2	12	0	0		116.2019	0.807300	1	8	8	8	
95.5015	1.040600	1	11	4	3		119.1048	0.893500	1	13	5	2	
96.3470	1.033700	2	12	2	0		120.0989	0.889000	1	14	2	0	
97.2365	1.026600	2	11	5	2		121.0957	0.884600	1	12	7	3	
98.1204	1.019700	5	12	2	2		123.1197	0.876000	3	14	3	1	
98.9716	1.013200	1	12	3	1		124.1475	0.871800	2	12	8	0	
104.2558	0.975800	5	11	6	3		125.2288	0.867500	<1	13	5	4	
107.8212	0.953200	2	13	2	1		126.2625	0.863500	3	14	4	0	
108.7386	0.947700	1	12	4	4		127.3787	0.859300	<1	14	3	3	
110.5675	0.937100	5	12	6	0		128.4454	0.855400	8	14	4	2	
111.4778	0.932000	3	13	3	2								



เอกสารนี้เป็นเอกสารที่สงวนไว้สำหรับการใช้งานเพื่อการศึกษาเท่านั้น ไม่อนุญาตให้นำไปใช้ประโยชน์ด้านการค้า
ไม่ว่ากรณีใดๆ ทั้งสิ้น อีกทั้งห้ามมิให้ดัดแปลงเนื้อหา และต้องอ้างอิงถึงเจ้าของเอกสารทุกครั้งที่มีการนำไปใช้

A.2 : C12A7 PDF#09-0413

00-009-0413

Oct 25, 2016 10:50 AM (User)

PDF Card Report

Status: Primary **QM:** Star (S) **Pressure/Temperature:** Ambient
Chemical Formula: Ca₁₂ Al₁₄ O₃₃ **Empirical Formula:** Al₁₄ Ca₁₂ O₃₃
Weight %: Al27.24 Ca34.68 O38.07 **Atomic %:** Al23.73 Ca20.34 O55.93
Compound Name: Calcium Aluminum Oxide **Mineral Name:** Mayenite, syn

Experimental

Author's Reported Data

Radiation: CuK α 1 : 1.5406Å **Filter:** Ni Beta **Intensity:** Diffractometer

Physical

SYS: Cubic **SPGR:** I-43d (220)

Author's Cell		
AuthCell a: 11.982Å	AuthCell Vol: 1720.24Å ³	AuthCell Z: 2.00
AuthCell MolVol: 860.12		

Dcalc: 2.877g/cm³ **SS/FOM:** F(30) = 50.9(0.0159, 37)

Crystal

ICDD Calculated Parameters

Space Group: I-43d (220) **Molecular Weight:** 1386.68

Crystal Data		
XtlCell a: 11.982Å	XtlCell b: 11.982Å	XtlCell c: 11.982Å
XtlCell : 90.00°	XtlCell : 90.00°	XtlCell : 90.00°
XtlCell Vol: 1720.24Å ³	XtlCell Z: 2.00	

Crystal Data Axial Ratio	
XtlCell a/b: 1.000	XtlCell c/b: 1.000

Reduced Cell		
RedCell a: 10.377Å	RedCell b: 10.377Å	RedCell c: 10.377Å
RedCell : 109.47°	RedCell : 109.47°	RedCell : 109.47°
RedCell Vol: 860.12Å ³		

เอกสารนี้เป็นเอกสารที่สงวนไว้สำหรับการใช้งานเพื่อการศึกษาเท่านั้น ไม่อนุญาตให้นำไปใช้ประโยชน์ด้านการค้า
 ไม่ว่าจะกรณีใดๆ ทั้งสิ้น อีกทั้งห้ามมิให้ตัดแปลงเนื้อหา และต้องอ้างอิงถึงเจ้าของเอกสารทุกครั้งที่มีการนำไปใช้

00-009-0413

Oct 25, 2016 10:50 AM (User)

Structure

Crystal (Symmetry Allowed): Non-centrosymmetric, Piezo (2nd Harm.)

Miscellaneous

Pearson: cI118.00

Subfile(s): Cement and Hydration Product, Common Phase, Ionic Conductors, Mineral Related (Mineral, Synthetic), NBS Pattern, Inorganic, Primary Pattern

Last Modification Date: 01/14/2012

Cross-Ref PDF #'s: 00-060-0718 (Primary), 01-070-2144 (Alternate), 01-078-0910 (Primary), 04-014-8824, 04-015-0818, 04-015-0821

References

Type Reference

Primary Reference: Natl. Bur. Stand. (U. S.), Circ. 539 9, 20 (1960)

Comments

Database Comments: Additional Patterns: See PDF 01-070-2144, 01-078-0910 and 00-060-0718.
Analysis: Spectrographic analysis showed the following impurities: 0.1-1.0% each of Na, Si, Sr; 0.01-0.1% Fe, Mg; 0.001-0.01% each of Cu, Mn, Mo.
Color: Colorless. Sample Source or Locality: Sample prepared by Portland Cement Association Fellowship at NBS, Gaithersburg, Maryland, USA.
Temperature of Data Collection: Pattern taken at 295 K. Unit Cell Data Source: Powder Diffraction.

d-Spacings (36) - 00-009-0413 (Fixed Slit Intensity) - Cu K1 1.54056Å

2	d(Å)	I	h	k	l	*	2	d(Å)	I	h	k	l	*
18.1261	4.890000	95	2	1	1		57.5177	1.601000	30	6	4	2	
20.9341	4.240000	8	2	2	0		60.8084	1.522000	6	7	3	2	
23.4530	3.790000	16	3	1	0		61.8887	1.498000	6	8	0	0	
27.8217	3.204000	25	3	2	1		62.9631	1.475000	8	7	4	1	
29.7781	2.998000	45	4	0	0		67.1413	1.393000	16	8	3	1	
33.4089	2.680000	100	4	2	0		89.2291	1.356000	4	7	5	2	
35.0788	2.556000	18	3	3	2		70.1763	1.340000	8	8	4	0	
36.6957	2.447000	50	4	2	2		72.2217	1.307000	8	8	4	2	
38.2680	2.350000	10	5	1	0		73.1953	1.292000	6	9	2	1	
41.2055	2.189000	40	5	2	1		74.1981	1.277000	6	8	6	4	
44.0504	2.054000	10	5	3	0		75.1616	1.263000	6	9	3	0	
46.6806	1.945000	30	6	1	1		77.1010	1.238000	4	9	3	2	
49.2109	1.850000	8	5	4	1		79.0768	1.210000	8	9	4	1	
51.6884	1.767000	6	6	3	1		81.9239	1.175000	2	10	2	0	
52.8785	1.730000	12	4	4	4		84.7392	1.143000	4	10	3	1	
54.0581	1.695000	8	7	1	0		87.6883	1.112000	8	10	4	0	
55.2219	1.662000	30	6	4	0		89.5130	1.094000	6	10	4	2	
56.4018	1.630000	10	7	2	1		90.4593	1.085000	4	11	1	0	

เอกสารนี้เป็นเอกสารที่สงวนไว้สำหรับการใช้งานเพื่อการศึกษาเท่านั้น ไม่อนุญาตให้นำไปใช้ประโยชน์ด้านการค้า
ไม่ว่ากรณีใดๆ ทั้งสิ้น อีกทั้งห้ามมิให้ตัดแปลงเนื้อหา และต้องอ้างอิงถึงเจ้าของเอกสารทุกครั้งที่มีการนำไปใช้



Appendix B

เอกสารนี้เป็นเอกสารที่สงวนไว้สำหรับการใช้งานเพื่อการศึกษาเท่านั้น ไม่อนุญาตให้นำไปใช้ประโยชน์ด้านการค้า
ไม่ว่ากรณีใดๆ ทั้งสิ้น อีกทั้งห้ามมิให้ดัดแปลงเนื้อหา และต้องอ้างอิงถึงเจ้าของเอกสารทุกครั้งที่มีการนำไปใช้

B.1 : Academic Publications

- 1.* Chaiwat Phrompet, Chaval Sriwong, Santi Maensiri, Prinya Chindaprasirt, Chesta Ruttanapun, “Optical and dielectric properties of nano-sized tricalcium aluminate hexahydrate (C3AH6) cement”, Construction and Building Materials, 179 (2018) 57–65. (ISI, IF: 4.046) (Scimago Q1) (Web of Science Q1)
- 2.* Chaiwat Phrompet, Chaval Sriwong, Chesta Ruttanapun, “Mechanical, dielectric, thermal and antibacterial properties of reduced graphene oxide (rGO)-nanosized C3AH6 cement nanocomposites for smart cement-based materials”, Composites Part B : Engineering, 175 (2019) 107-128 (ISI, IF : 6.864) (Scimago Q1) (Web of Science Q1)
3. Chaiwat Phrompet, Chaval Sriwong, Pornjuk Srepusharawoot, Santi Maensiri, Prinya Chindaprasirt, Chesta Ruttanapun, “Effect of free oxygen radical anions and free electrons in a $\text{Ca}_{12}\text{Al}_{14}\text{O}_{33}$ cement structure on its optical, electronic and antibacterial properties”, Heliyon, 5 (2019) e01808. (ISI) (Scimago Q1)
4. Wannisa Thongsamrit, Chaiwat Phrompet, Keerati Maneesai, Attaphol Karaphun, Wattan Tuichai, Chaval Sriwong and Chesta Ruttanapun, “Effect of grain boundary interfaces on electrochemical and thermoelectric properties of a Bi_2Te_3 /reduced graphene oxide composites”, Materials Chemistry and Physics Volume 250, 1 August 2020, 123196. (ISI, IF: 2.781) (Scimago Q2)
5. Chaiwat Phrompet, Keerati Maneesai, Wattan Tuichai, Attaphol Karaphun, Chaval Sriwong and Chesta Ruttanapun, “Electrochemical properties of tricalcium aluminate hexahydrate/reduced graphene oxide nanocomposites for supercapacitor device”, Journal of Energy Storage Volume 30, August 2020, 101-474. (ISI, IF: 3.517) (Scimago Q1)

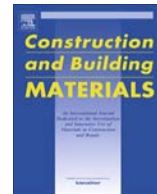
***Notification:** The published papers in number 1 and number 2 only were used to claim for graduation in Ph.D. of Acting Sub Lt. Chaiwat Phrompet.

เอกสารนี้เป็นเอกสารที่สงวนไว้สำหรับการใช้งานเพื่อการศึกษาเท่านั้น ไม่อนุญาตให้นำไปใช้ประโยชน์ด้านการค้า ไม่ว่ากรณีใดๆ ทั้งสิ้น อีกทั้งห้ามมิให้ตัดแปลงเนื้อหา และต้องอ้างอิงถึงเจ้าของเอกสารทุกครั้งที่มีการนำไปใช้

B.2 : International conference

Poster Presentations

1. Chaiwat Phrompet, Chaval Sriwong, Worawat Meevasana, Santi Maensiri, and Chesta Ruttanapun, “Prototype of Graphene Oxide and reduced Graphene Oxide Fabrications Machine for Small Industrials”, The Second Materials Research Society of Thailand International Conference (2nd MRS Thailand International Conference) 10-12 July 2019 The Zign Hotel, Pattaya, Thailand.
2. Chaiwat Phrompet, Chaval Sriwong and Chesta Ruttanapun, “Supercapacitor Properties of $3\text{CaO}\cdot\text{Al}_2\text{O}_3\cdot 6\text{H}_2\text{O}$ cement/reduced graphene oxide nanocomposite for Energy Storage Applications”, The Second Materials Research Society of Thailand International Conference (2nd MRS Thailand International Conference) 10-12 July 2019 The Zign Hotel, Pattaya, Thailand.
3. Chaiwat Phrompet and Chesta Ruttanapun, “Prototype of concrete blocks electric power generation from heat and applications in municipal melting furnaces or municipal incinerators” the 5th Southeast Asia Conference on Thermoelectrics 2018, 14-17 December 2018, Sokha Siem Reap Resort & Convention Center, Siem Reap, Cambodia. Sokha Siem Reap Resort & Convention Center, Siem Reap, Cambodia.
4. Chaiwat Phrompet, Chaval Sriwong, Santi Maensiri, and Chesta Ruttanapun, “Thermoelectric properties of $3\text{CaAl}_2\text{O}_3\cdot 6\text{H}_2\text{O}$ /reduce graphene oxide hybrid base on cement composite fabrication by hot press sintering”, The first materials research society of Thailand international conference, Convention center, The empress hotel, Chiang Mai, Thailand, October 31- November 3, 2017.
5. Chaiwat Phrompeta, Chaval Sriwongb, Chesta Ruttanapuna, and Santi Maensiric, Preparation and characterization of cement $12\text{CaO}\cdot 7\text{Al}_2\text{O}_3$ /reduced graphene oxide hybrid composites and their electrical properties, Nano Thailand 2016, 27-29 November 2016, THE GREENERY RESORT KHAO YAI.



Optical and dielectric properties of nano-sized tricalcium aluminate hexahydrate (C3AH6) cement

Chaiwat Phrompet^a, Chaval Sriwong^{b,c,e}, Santi Maensiri^{d,e}, Prinya Chindaprasit^{f,g}, Chesta Ruttanapun^{a,b,e,*}

^a Department of Physics, Faculty of Science, King Mongkut's Institute of Technology Ladkrabang, Chalongkrung Road, Ladkrabang, Bangkok 10520, Thailand

^b Smart Materials Research and Innovation Unit (AMRIU), Faculty of Science, King Mongkut's Institute of Technology Ladkrabang, Chalongkrung Road, Ladkrabang, Bangkok 10520, Thailand

^c Department of Chemistry, Faculty of Science, King Mongkut's Institute of Technology Ladkrabang, Chalongkrung Road, Ladkrabang, Bangkok 10520, Thailand

^d School of Physics, Institute of Science, Suranaree University of Technology, Nakhon Ratchasima 30000, Thailand

^e Thailand Center of Excellence in Physics, Commission on Higher Education, 328 Si Ayutthaya Road, Bangkok 10400, Thailand

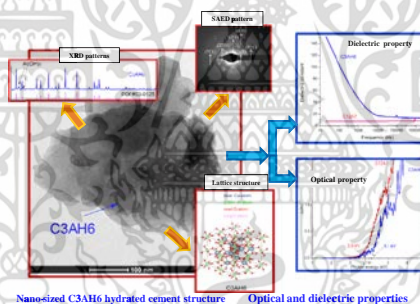
^f Sustainable Infrastructure Research and Development Center, Department of Civil Engineering, Faculty of Engineering, Khon Kaen University, Thailand

^g Academy of Science, The Royal Society of Thailand, Dusit, Bangkok 10300, Thailand

HIGHLIGHTS

- Nano-sized C3AH6 was fabricated by simple hydration process from C12A7 precursor.
- Nano-sized C3AH6 cement showed high capacitance and dielectric constant.
- C3AH6 was visible transparent materials with a direct energy gap of 4.1 eV.

GRAPHICAL ABSTRACT



ARTICLE INFO

Article history:

Received 6 March 2018

Received in revised form 12 May 2018

Accepted 23 May 2018

Available online 29 May 2018

Keywords:

C3AH6

Cement hydrates

Optical property

Dielectric constant

C12A7

ABSTRACT

The present study investigates the optical and dielectric properties of nano-sized C3AH6 cement hydrates. A cement product was fabricated via a simple hydration process using a derivative of a C12A7 cement precursor reacting with de-ionized water while raising the reaction temperature to 100 °C. A crystalline phase of the C3AH6 cement product was characterized and confirmed using an XRD technique. Its morphology was also evaluated using TEM and SEM techniques. It was found that nano-sized C3AH6 (in size 10–50 nm) was successfully derived via this process. This cement product was thermodynamically stable over the range of room temperature to 300 °C. The optical direct gap was 4.1 eV and the indirect energy gap was 2.45 eV. Over the range of 20 Hz to 2 MHz, the observed capacitance was 10^{-10} F– 10^{-11} F and the dielectric constant varied from 20 to 150. The dielectric properties were enhanced over those of general cement compounds. This effect was due to its complex structure in which –O–H bonding appeared in the structure and the formation of nano-sized structures from this process. These results suggested that the nano-C3AH6 hydrated particles were transparent to visible light and exhibited a high frequency electrical response. This implies an important role for these cement-based materials as potential

* Corresponding author at: Department of Physics, Faculty of Science, King Mongkut's Institute of Technology Ladkrabang, Bangkok 10520, Thailand.

E-mail address: chesta.ru@kmitl.ac.th (C. Ruttanapun).

candidates having optical and dielectric properties appropriate for applications such as smart building materials in the form of transparent electrode windows, smart wall capacitors, triboelectric devices and supercapacitors.

© 2018 Elsevier Ltd. All rights reserved.

1. Introduction

Recently, cement-based materials [1] have attracted significant attention owing to their very interesting optical and dielectric properties for applications as smart building materials including transparent electrode windows, smart wall capacitors, triboelectric devices, and supercapacitors. These cement-based materials are composed of Portland and calcium aluminate cements. They are abundant, low cost and easily fabricated materials. Portland cements, which are composed of phases of lime-silica minerals, are commonly used in structures, agro-industrial infrastructure and transport infrastructure [2]. Calcium aluminate cements, which consist of reactive phases of lime-alumina compounds with various geometric structures, represented by the notation, $n\text{CaO}\cdot m\text{Al}_2\text{O}_3$ (CnAm in cement notation), are used in construction and optical devices, among other applications [3–6]. Calcium aluminate cements, such as monocalcium aluminate [$\text{CaO}\cdot\text{Al}_2\text{O}_3$ (CA)] [4] and monocalcium dialuminate [$\text{CaO}\cdot 2\text{Al}_2\text{O}_3$ (CA2)] are used for refractory castable and structural materials [3]. It is notable that dodeca-calcium hepta-aluminate [$12\text{CaO}\cdot 7\text{Al}_2\text{O}_3$ (C12A7)] cement offers high performance in optical smart materials such as transparent electrodes [7], transparent conducting oxides [8], emitters [9], and electrides [10]. Hussain et al. [11], Lobo et al. [12] and Ruttanapun et al. [13] reported a direct optical energy gap for the C12A7 insulator phase of approximately 3.5 eV [12], 3.64 eV [11], and 4.2 eV [13] by computer simulation and 3.9 eV [13] by calculation. For calcium aluminate cements (CA, CA2, CA6, CA3), Hussain et al. [11] reported a direct optical energy gap of 3.85–4.62 eV using a first principles approach. Dielectric properties are related to the electrical nature of a material. Cabeza et al. [2] reported a dielectric constant for Portland cement of approximately 13 for frequencies ranging from 100 kHz to 15 MHz. Torres-Luque et al. [14] and Hussain et al. [11] reported that calcium aluminate cements (CA, CA2, C12A7) displayed dielectric constants of approximately 2–4 over a frequency range of 100 Hz–5 MHz. In another study, Smith et al. [13] worked with hydrated alumina cements and observed dielectric constants for calcium aluminate decahydrate [$\text{CaO}\cdot\text{Al}_2\text{O}_3\cdot 10\text{H}_2\text{O}$ (CAH10)] and tricalcium aluminate hexahydrate [$3\text{CaO}\cdot\text{Al}_2\text{O}_3\cdot 6\text{H}_2\text{O}$ (C3AH6)] cement hydrate in the range of 15–35 at a frequency of 1 GHz. From this, it can be concluded that the hydrated alumina cements of this type displayed dielectric constants that were higher than those of calcium aluminate cements. Using the Kramers-Kroing approach [3], the dielectric and optical properties (AC conductivity and absorption coefficient) can be related via the dielectric function consisting of the real and imaginary parts of dielectric constant. Consequently, hydrated alumina cements are promising candidates to improve optical and dielectric properties for smart building materials in applications such as smart wall capacitors, triboelectric devices and transparent electrode devices [4,15,16].

Moreover, C3AH6 cement hydrate is the focus for investigation of the optical and dielectric properties because it is a thermodynamically stable cement structure derived from calcium aluminate cement hydrate compounds at room temperature [16]. Pure C3AH6 is called katoite cement and it is a mineral in the hydrogarnet group. It has a stoichiometric formula of $\text{Ca}_3\text{Al}_2(\text{OH})_{12}$ [17]. Its crystal structure displays a cubic unit cell in the Ia3d (2 3 0) space group. Dilnesa et al. [18] found that C3AH6 can be described by a

general formula, $\text{Ca}_3\text{Al}_2(\text{OH})_3$, with the Ca site occupied by divalent cations (Ca^{2+}), the Al site by trivalent cations (Al^{3+}) in an octahedral and a tetrahedral framework, and the 4OH^- positioned inside the tetrahedral framework. The H^+ ions were bonded to each of the four O atoms surrounding the vacant site for charge balancing. The unit cell contained six $\text{Ca}_3\text{Al}_2(\text{OH})_{12}$ units, comprising 132 atoms (24 Ca, 16 Al, 96H and 96O). It basically formed a tree framework consisting of $\text{Ca}(\text{OH})_8$ dodecahedra and $\text{Al}(\text{OH})_6$ octahedral sub-structures [17,18]. The unit cell structure had a lattice constant of $a = 12.55695 \text{ \AA}$, and a unit cell volume $V = 1986 \text{ \AA}^3$. In nature, C3AH6 can form a crystalline phase at high temperatures. Literature reports [17,19,20] detailed that C3AH6 can exist as an anhydrous cement when CA reacts with water in a cement hydration process [17,19,20]. Additionally, Barnes and Bensted [21] reported that C3AH6 can be prepared using C12A7 cement as starting material that can be rapidly reacted with water at elevated temperatures above $60 \text{ }^\circ\text{C}$. However, to best of our knowledge, there are no reports of an investigation into the optical and dielectric properties of C_3AH_6 cement hydrate.

This work therefore aims to investigate the optical and dielectric properties of C3AH6 cement hydrate. A C3AH6 product was synthesized via a simple hydration process using a C12A7 cement precursor reacting with water at $100 \text{ }^\circ\text{C}$. The C12A7 precursor and the resulting products were characterized using X-ray diffraction (XRD), transmission electron microscopy (TEM), and a high-resolution TEM (HRTEM), IR spectroscopy, X-ray photoelectron spectroscopy (XPS), thermogravimetric analysis (TGA), and differential thermogravimetric analysis. Ultraviolet/visible/near-infrared (UV-VIS-NIR) spectroscopy and impedance analysis of optical and dielectric properties were done. Their optical and dielectric properties were investigated. Surface nano-scale morphology and thermodynamic stability were evaluated. The effect of nano-C3AH6 particles on dielectric properties are reported.

2. Experimental details

2.1. Chemicals

Calcium carbonate (CaCO_3 , 99% purity), alumina powder (Al_2O_3 , 99.9% purity), and ethanol (95%) were purchased from Sigma-Aldrich (USA). All chemicals were used as received without further purification.

2.2. Preparation of C12A7 cement

In this work, C12A7 cement powder was first prepared via a solid state reaction using CaCO_3 and Al_2O_3 as starting materials. In brief, CaCO_3 and Al_2O_3 powders were stoichiometrically mixed following the reaction, $12\text{CaCO}_3 + 7\text{Al}_2\text{O}_3 \rightarrow \text{Ca}_{12}\text{Al}_{14}\text{O}_{33}$ (C12A7) + 12CO_2 . The powder was mixed during ball milling with ethanol for 24 h at room temperature. This was followed by drying in an oven at $80 \text{ }^\circ\text{C}$ for 24 h. Then, the resulting powder was placed in an alumina crucible and sintered in an electric furnace at $1200 \text{ }^\circ\text{C}$ in an air atmosphere for 24 h. Finally, the obtained C12A7 cement sample was crushed into a powder for use as a precursor material to prepare C3AH6 cement-hydrates.

2.3. Preparation of C3AH6 cement hydrate

C3AH6 cement hydrate was prepared via a simple hydration method using the prepared C12A7 powder as a precursor. This reaction was according to $C_{12}A_7 + 33(H_2O) \rightarrow 4(C_3AH_6) + 3(Al(OH)_3)$ [22]. In a typical process, about 3 g of C12A7 powder was mixed with 200 mL of de-ionized (DI) water. DI water was used in preparation process since it contained no ions. A volume of 200 mL of DI water was used in this process to enable a facile hydration reaction process. First, C12A7 powder (3g) and DI water (200 mL) were blended in a beaker by magnetic stirring at room temperature for 10 min. Then, the C12A7 suspension was stirred and heated from room temperature to 100 °C. Next, the suspension was stirred at 100 °C for 2 h. After that, the obtained suspension was filtered, washed with DI water several times, and then dried overnight in an oven at 80 °C. The resulting product was a C3AH6 cement hydrate powder.

2.4. Preparation of C3AH6 and C12A7 pellets

The fabricated C3AH6 cement and prepared C12A7 precursor sample powders were prepared by hot-pressed sintering in graphite molds into disc pellets of 12 mm diameter and 2–3 mm thickness at 400 °C for 1 h for dielectric property measurements. Then, these pellets were polished on both sides, and coated with Ag electrodes for supporting Ohmic contact.

2.5. Characterization

The lattice parameters were investigated using an X-ray diffractometer (XRD), (Rigaku, Miniflex Cu K-alpha radiation), with a 2θ scanning range from 10 to 80° and stepping interval of 0.02°. The vibration mode of atomic bonding was evaluated using a Fourier-transform infrared spectroscopy (FTIR), (Bruker, Senterra). An X-ray photoelectron spectroscopy (XPS), (Kratos, AXIS Ultra DLD) was employed for determining the charge states of each element in the sample with Al K α radiation ($h\nu = 1486.6$ eV). A transmission electron microscope (TEM), and a high-resolution TEM (HRTEM) (JEOL-2100) operating at 200 kV) were used to measure nano particles size, crystallite size of the samples. Thermogravimetric analysis (TGA, Netzsch STA 449F3 Jupiter) was performed over a temperature range of 25 °C–900 °C with a heating rate of 10 °C/min in air to measure the weight loss of the samples.

2.6. Properties measurement

The optical properties of the samples were investigated using a UV Visible Near Infrared Spectrometer, (Perkin Elmer, Lambda 950). The optical measurements determined the absorption coefficient spectra of the specimens at room temperature. The dielectric properties were determined using an impedance analyzer (Precision LCR Meter; Model: E4980A). The dielectric measurements were used to determine the capacitance, resistance and dissipation factor (loss tangent) values of the samples at room temperature and over various frequencies in the range of 20 Hz to 2 MHz.

3. Results and discussion

3.1. XRD characterization

Fig. 1 shows the XRD patterns of the prepared C12A7 sample that was used as a precursor and the fabricated C3AH6 cement hydrate sample. The XRD patterns of the diffraction file pattern of the Joint Commission for Powder Diffraction Standards File PDF#09-0413 and PDF#03-0125 were inserted into the figure for

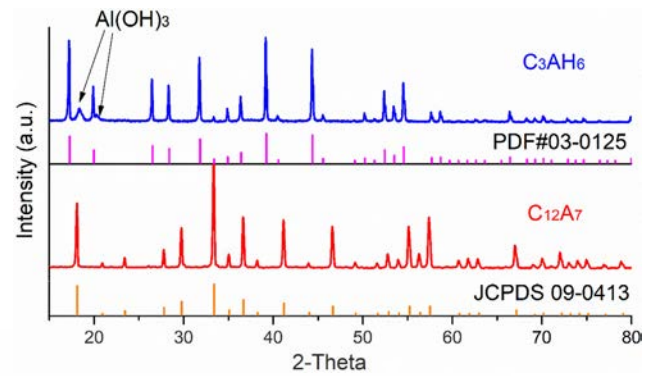


Fig. 1. XRD patterns of the fabricated C3AH6 cement hydrate and the prepared C12A7 precursor samples.

referencing the peak positions. The diffraction patterns of the prepared C12A7 sample were in good agreement with the PDF#09-0413 file, confirming its conformance to the standard C12A7 phase within space group, I43d. Additionally, the XRD pattern for the diffraction of the fabricated C3AH6 sample at 2θ diffraction angles corresponded to the Miller index of the diffraction peaks as is shown in Table 1. The results demonstrate that the diffraction patterns of the C3AH6 sample corresponded well to those of the PDF#03-0125 file. Obviously, the XRD pattern of the prepared C3AH6 showed an excessive phase at $2\theta = 18^\circ$ and 20.5° , indicating a phase of aluminium hydroxide ($Al(OH)_3$), as reported in previous work [22]. The appearance of shorter and fewer peaks of the AH3 sample corresponded to the diffraction patterns peaks of the standard in the PDF#76-1782 file. This result was due to a hydration process of the C12A7 cement reaction with DI water corresponding to the reaction, $C_{12}A_7 + 33H_2O \rightarrow 4(C_3AH_6) + 3(Al(OH)_3)$ as discussed in the literature [21,22]. However, the AH3 phase appeared for a very small duration during the process, when the derivative C12A7 underwent a hydration process. The average crystallite sizes of the fabricated C3AH6 sample were examined using Scherrer's equation as follows [23]:

$$D_{XRD} = \frac{0.94\lambda}{\beta \cos\theta}$$

Table 1

The XRD diffraction angles corresponding to the Miller index of the diffraction peaks of the fabricated C3AH6 sample.

Diffraction angles (2θ)	Miller index
17.26	(2 1 1)
19.96	(2 2 0)
26.51	(3 2 1)
28.37	(4 0 0)
33.41	(3 3 2)
34.94	(4 2 2)
36.41	(4 3 1)
39.22	(5 2 1)
40.56	(4 4 0)
44.39	(6 1 1)
45.60	(4 4 4)
50.24	(6 4 0)
52.45	(5 5 2)
53.52	(6 4 2)
54.59	(6 5 1)
58.71	(8 0 0)
59.71	(7 4 1)
66.47	(8 4 0)
70.18	(6 6 4)
73.80	(8 4 4)
75.57	(8 6 0)

where D_{XRD} is the average crystallite size, λ is the X-ray wavelength ($\lambda = 1.5406 \text{ \AA}$), β is the full-width at half-maximum of the highest intensity peak, and θ is half of the diffraction peak angle. The calculation showed that the average crystallite size of the fabricated C3AH6 sample was approximately 61.53 nm. This result implied that the C3AH6 cement hydrate crystal structure was nano-crystalline.

3.2. TEM analysis

Surface nano-scale morphology, nano-particle sizes and shapes of nano-particles of the resulting C3AH6 specimens were studied using TEM. The surface morphology is presented in Fig. 2. Fig. 2 (a) displays layered nano-particles of the C3AH6 specimen that vary in size from approximately 10–50 nm. The yield of nano-particles resulted from the preparation of C3AH6 cement-hydrate using a derivative C12A7 cement with DI water at an elevated temperature of 100 °C. Moreover, the degree of the AH3 structure was also represented by the formation of nano-sheet-like structures as shown in Fig. 2(a). Furthermore, Fig. 2(b) shows diffraction rings of the SAED pattern indicating a high poly-crystalline content. Also, the formation of nano-C3AH6 cement hydrate particles revealed optical and dielectric properties that suggest further industrial applications.

3.3. IR spectroscopy analysis

IR spectroscopy was performed to elucidate the hydration process of synthesized C3AH6 cement. Fig. 3 displays the IR spectra of the fabricated C3AH6 cement compared to those of the C12A7 precursor samples. The spectra showed three bands in the low part of the wave-number region between 200 and 1000 cm^{-1} corresponding to M–O (M = Ca, Al) stretching. The absorption bands at frequencies of 535 cm^{-1} and 760 cm^{-1} originated from the AlO6 octahedral framework, and the absorption band at the frequency of 420 cm^{-1} was assigned to the CaO polyhedral framework. The bands at 760 cm^{-1} corresponded to stretching vibrations of Al–O bonds while those at a frequency of 530 cm^{-1} corresponded to bending vibrations of Al–O–Al bonds. Also, the bands in the region ranging from 700 to 500 cm^{-1} were associated with the hydration of the condensed AlO6 octahedral framework [23]. The bands at 3460 cm^{-1} corresponded to M–OH (M = Ca, Al) stretching vibrations in the C12A7 precursor. Additionally, the absorption band of the fabricated C3AH6 cement displayed a vibration mode of O–H bending

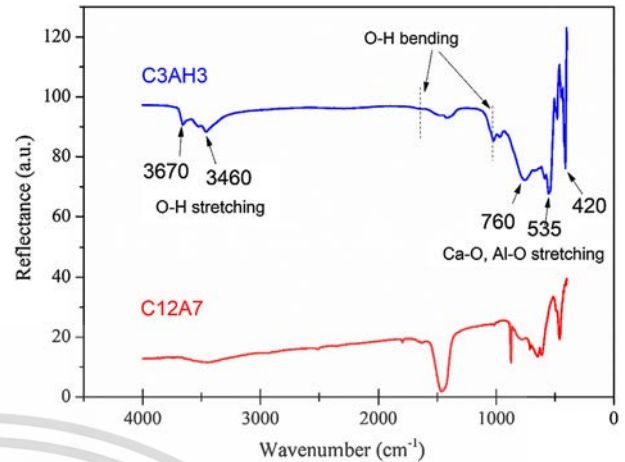


Fig. 3. IR spectroscopy spectra of the fabricated C3AH6 cement hydrate and the prepared C12A7 cement precursor samples.

at the 1630 cm^{-1} peak and the vibration of O–H stretching at a peak at around 3200–3670 cm^{-1} , indicating the presence of water molecules (H_2O) [24]. The appearance of the absorptions for O–H bending and O–H stretching originated from the Al(OH)6 octahedral framework. O–H bending and stretching disappeared from the C12A7 precursor. These results confirmed a hydration process in the fabrication of C3AH6 cement hydrate.

3.4. Schematic diagram

A schematic depicting the hydrate reaction is shown in Fig. 4. The schematic is supported by the results. A nano-particle morphology in the fabricated C3AH6 sample was produced from a derivative C12A7 cement reacting with DI water at temperatures 100 °C. The C12A7 cement structure can be described by a unit cell occupying 12 crystallographic nano-cages with 4⁺ charged ions at the cage wall, as denoted by [C12A7]⁴⁺ [25]. Trapping of free O²⁻ inside two of the 12 cages in a unit cell occurred for charge balance. This C12A7 phase was a C12A7 insulator. The C3AH6 structure can be described as an octahedral and tetrahedral framework of connected by Ca²⁺ divalent cations and Al³⁺ trivalent cations with 4OH⁻ positioned inside the tetrahedral framework [18]. H⁺ ions bonded to each of the four O atoms for charge balancing. Fig. 4

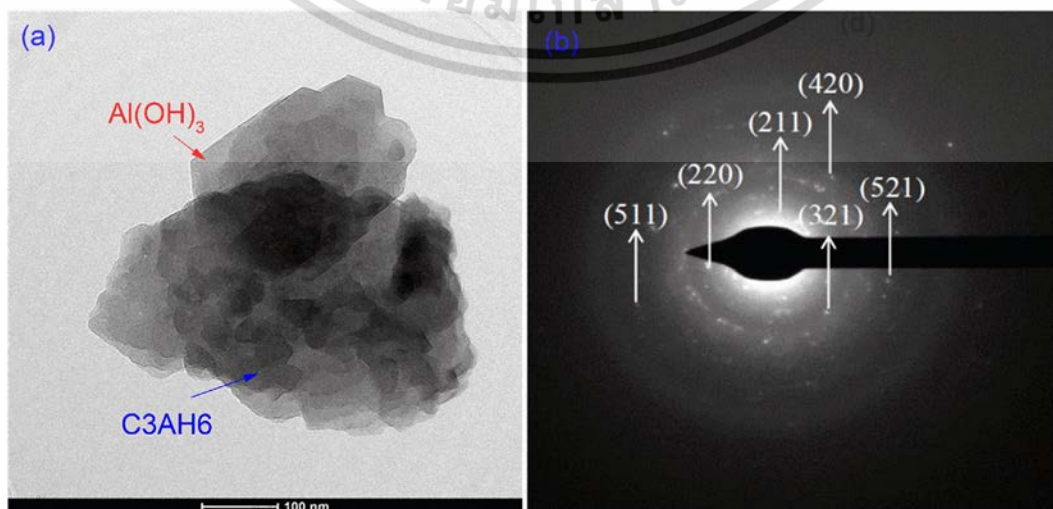


Fig. 2. (a) Transmission electron microscopy (TEM) images of the fabricated C3AH6 cement hydrate powder and (b) its SAED pattern.

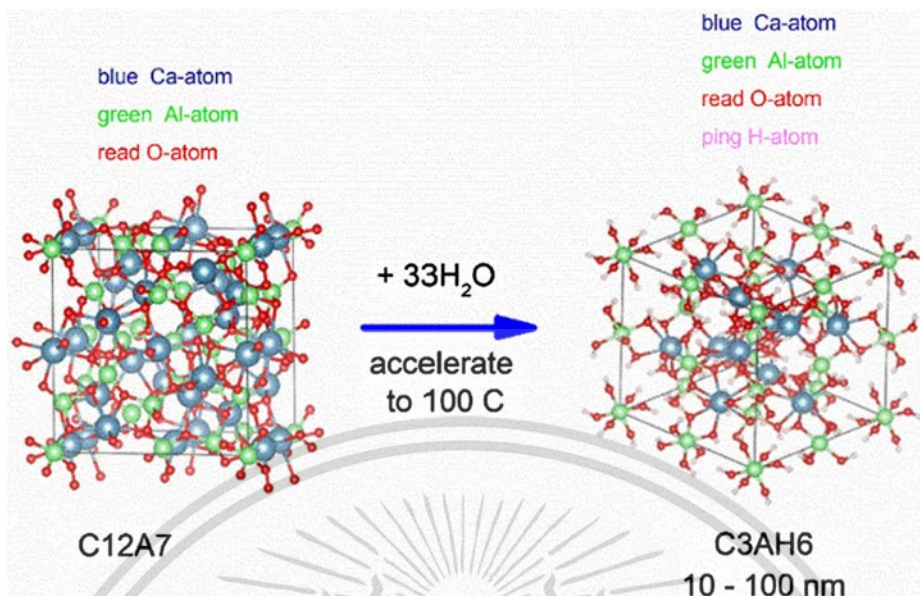


Fig. 4. Suggested reaction schematic diagram for the nano-sized C3AH6 cement hydrate.

describes the production of the nano-sized C3AH6 cement. The reaction fully succeeded using a derivative C12A7 with DI water at an elevated temperature of 100 °C over a short time. This reaction was a hydration process according to reaction, $C12A7 + 33(H_2O) \rightarrow 4(C3AH6) + 3(Al(OH)_3)$ [22]. The XRD results revealed that this cement hydration produced yielded a tiny amount of a AH3 nano-sheet structure.

3.5. TGA characterization

Fig. 5 shows the thermal analysis of the nano-C3AH6 cement hydrate particles. The TG-DTA curves present four exothermic events in the temperature range of 100 °C–900 °C as weight losses (65%). The first weight loss was due to the physically absorbed water evaporating from the C3AH6 specimen at around 100 °C. The C3AH6 specimen gradually decomposed to water vapor and an amorphous anhydrous material at 100–550 °C. The major mass loss was at 200–300 °C and a smaller loss occurred between 400 and 550 °C [26]. After the dehydration between 300 and 350 °C,

the C3AH6 decomposed to form $C_3AH_{1.5}$ at around 550 °C [27]. Finally, the sample was completely dehydrated to form a C12A7 phase at a temperature greater than 740 °C. The results show that the nano-C3AH6 particles were thermodynamically stable in over the range of room temperature to 300 °C.

3.6. XPS analysis

Fig. 6 shows the XPS survey spectrum and XPS spectra of O 1s, Ca 2p, Al 2s and Al 2p of the nano-C3AH6 cement hydrate particles. XPS measurements were done calibrating all peaks using a carbon deposit C 1s binding energy of 284.8 eV. Fig. 6(a) presents a wide scan XPS survey spectra of the fabricated C3AH6 specimen. The spectra showed XPS spectrum evidence for the binding energies of Ca, Al and O 1s peaks with reference to the C 1s peak [27]. Fig. 6(b) presents the XPS spectra of Ca 2p of the fabricated C3AH6 specimen. The XPS spectra showed two peak positions located at around 347.3 eV and 350.8 eV. The peak at 347.3 eV was assigned to the Ca 2p_{3/2} and the peak at 350.8 eV was due to Ca 2p_{1/2} core levels of Ca²⁺ ions. The two distinguishable peaks of Ca 2p in the XPS spectrum were due to spin orbit splitting [25]. Fig. 6(c) presents the XPS core-level spectra of Al 2p for the fabricated C3AH6 specimen. The Al 2s XPS spectra were positioned at around 74 eV, which is consistent with literature reports [27]. The peak at 74.25 eV indicated Al³⁺ in the fabricated C3AH6 specimen. The valence state of Al confirmed the existing of Ca-O and Al-O bonds in the C3AH6 specimen. Fig. 6(d) presents the O 1s spectrum, which occurred at around 531.5 eV. This showed the presence of O bonding in the nano-C3AH6 particles.

3.7. Optical properties

Fig. 7 shows the UV–visible spectra and optical properties of the fabricated C3AH6 cement hydrate and the prepared C12A7 precursor specimens. In the measurements of the C3AH6 and the C12A7 specimens, the absorption coefficient spectra (α) were obtained at room temperature. By the absorption coefficient spectra, the relation of the energy gap to photon energy can be presented by $\alpha(h\nu) \propto \frac{(h\nu - E_g)^m}{h\nu}$, where E_g is the optical energy gap, $h\nu$ is the photon energy and $m = 1/2$ is the value of the allowed direct transition and

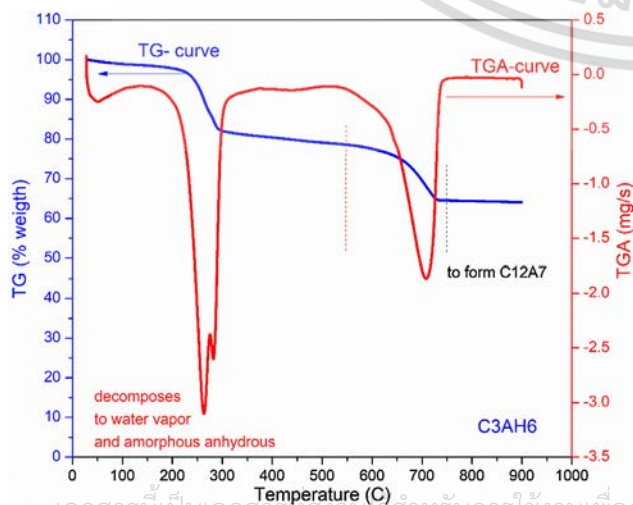


Fig. 5. Thermal analysis of the fabricated C3AH6 cement hydrate specimen.

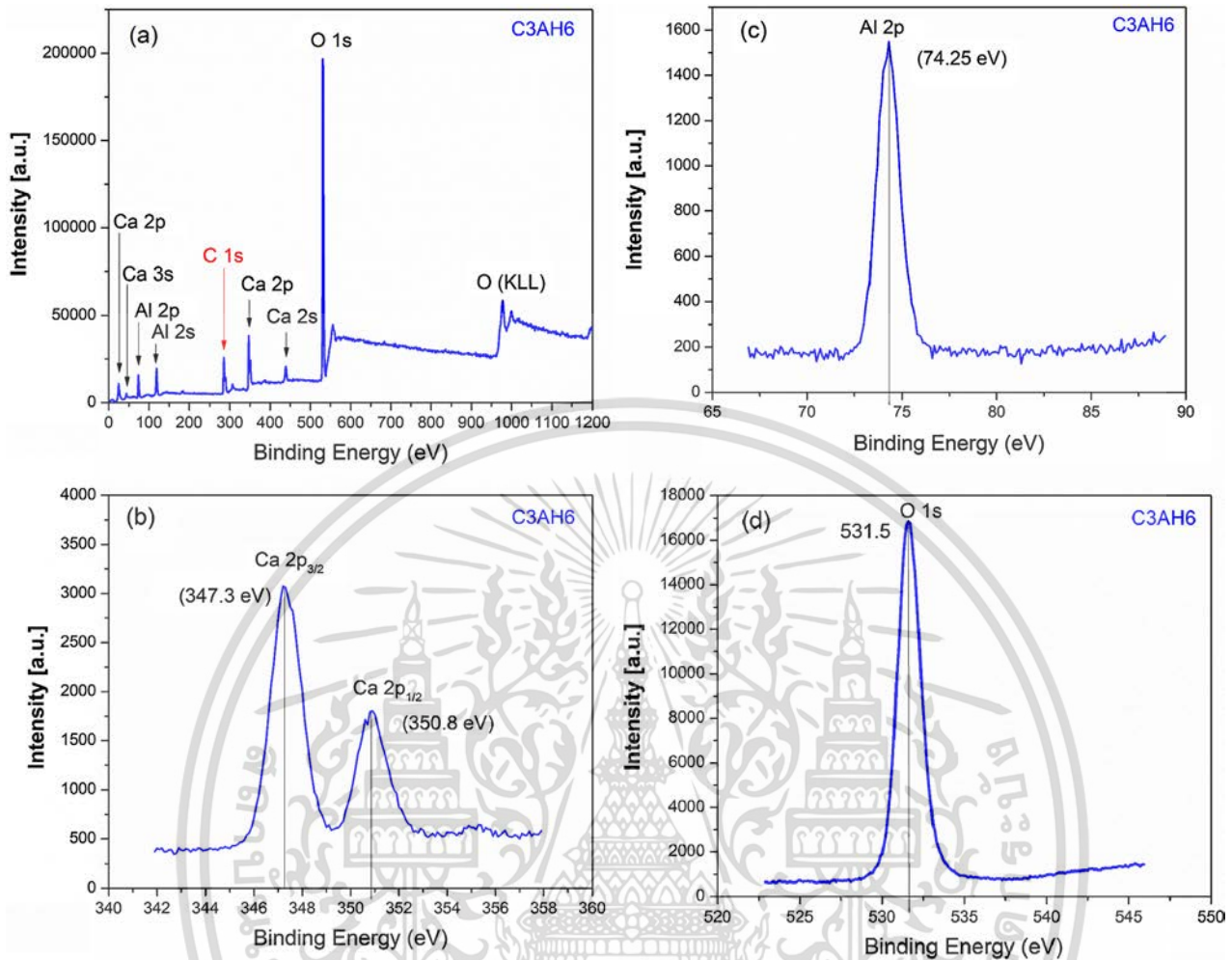


Fig. 6. (a) XPS survey spectrum and XPS spectra of Ca 2p (b), and Al 2p (c) and O 1s (d), of the fabricated C3AH6 samples.

$m = 2$ is the value of allowed indirect transition [28]. The E_g value can be evaluated using the formula [13], $(\alpha h\nu)^2 = A(h\nu - E_g)$, where A is a constant that is independent of $h\nu$. The value of E_g can be obtained by a linear fitting of $(\alpha h\nu)^2$ versus $h\nu$ to determine the intercept of the photon energy ($h\nu$) axis. For the indirect energy gap, the formula used $m = 2$ and the indirect E_g value can be determined by fitting a curve of $(\alpha h\nu)^{1/2}$ versus $h\nu$ to determine the intercept of the $h\nu$ axis.

Fig. 7(a) shows absorbance spectra of the C3AH6 and the C12A7 samples from wavelengths of 200 nm–800 nm. The results showed that spectra line of the C3AH6 sample was lower than that of the C12A7 sample at all measured wavelengths. The results highlight that the C3AH6 sample absorbed less light than the C12A7 sample. The absorption spectra of both samples displayed lower spectra curves at wavelengths greater than 400 nm. So, both samples absorbed less light at wavelengths over 400 nm.

Fig. 7(b) displays the direct E_g value of the C3AH6 and C12A7 samples at room temperature. The results showed that direct E_g value of the C3AH6 sample was 4.1 eV and that of the C12A7 sample was 3.9 eV. This shows that both samples were transparent materials since their E_g values were greater the 3.0 eV [28]. The results revealed that the direct E_g value of the C3AH6 sample was larger than that of the C12A7 sample.

Fig. 7(c) presents the indirect energy gap of the C3AH6 and the C12A7 samples at room temperature. The indirect energy gap of the C3AH6 sample was 2.5 eV, and that of the C12A7 sample was

2.45 eV for first transition level and 4.0 eV for second transition level. The results revealed that the indirect energy gap of the C3AH6 sample (2.5 eV) was similar to the indirect energy gap of the C12A7 sample (2.45 eV) for the first transition.

The above results indicated that the C3AH6 cement hydrate was a transparent material. It had a direct optical energy gap of 4.1 eV. Its optical energy gap was higher than that of the reported direct optical energy gap of the C12A7 insulator (3.5 eV [12], 3.64 eV [11], and 3.9 eV [13]). Additionally, the optical gap value of the C3AH6 occurred in the energy gap region of calcium aluminate cement (CA, CA2, CA6, CA3) materials (3.85 eV–4.62 eV [11]). This strongly indicated that C3AH6 cement hydrate materials displayed an optical gap similar to calcium aluminate cement materials. Due to the limited values of the optical energy gap of the C3AH6 cement materials, the optical properties were considered using their dielectric constant values by the Clausius-Mosotti equation [29] following $\alpha = f \left[\frac{\epsilon' - 1}{\epsilon' + 2} \right]$, where ϵ' is the real dielectric constant, f is a constant value, as discussed in the next section.

3.8. Dielectric properties

Fig. 8 shows the dielectric properties of the fabricated C3AH6 cement hydrate specimen and the prepared C12A7 precursor. The values for capacitance (C), resistance (R) and loss tangent ($\tan \delta$) were obtained for these materials. The complex dielectric constant (ϵ^*) of the materials consisted of a relative dielectric constant (ϵ')

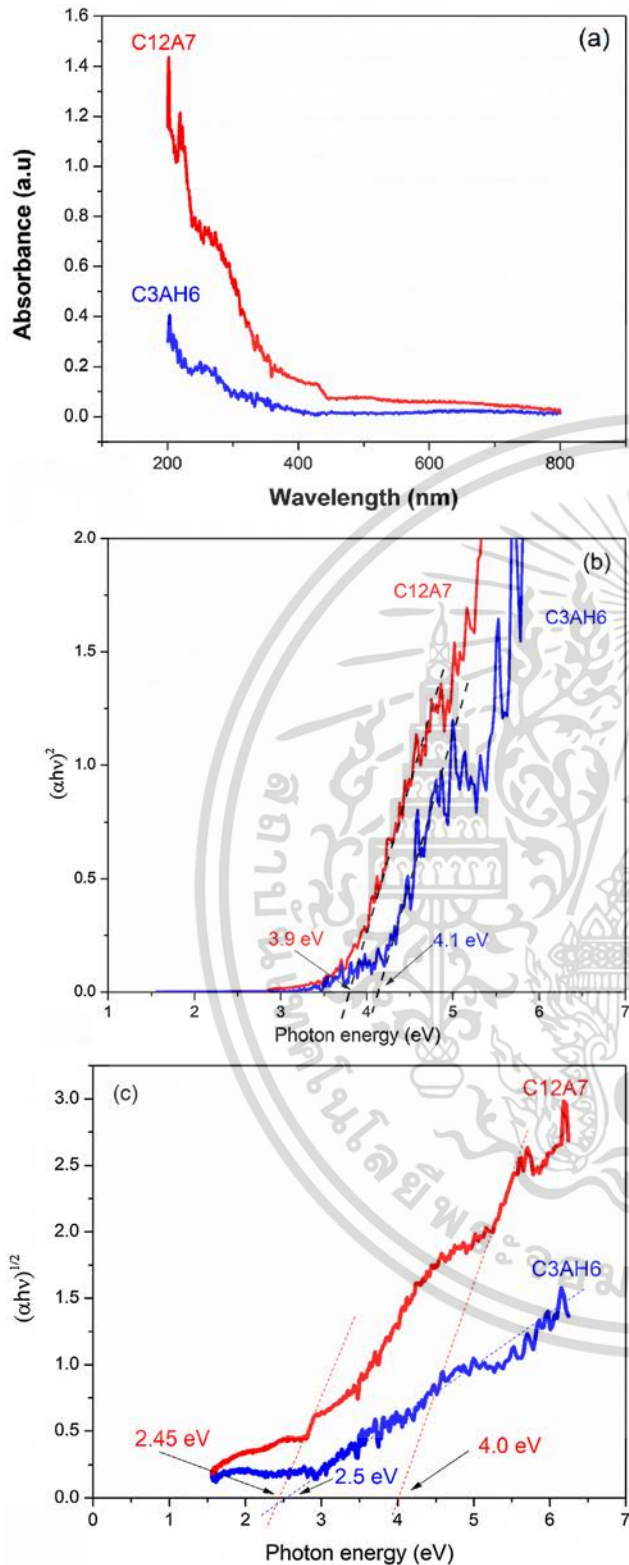


Fig. 7. (a) Absorbance, (b) direct energy gap and (c) indirect energy gap of the fabricated C3AH6 cement hydrate and C12A7 cement samples.

as the real part and the dielectric loss (ϵ'') as an imaginary term following the relation $\epsilon^* = \epsilon' + i\epsilon''$ [30]. The ϵ' value can be determined from the equation, $\epsilon' = (Cl)/(\epsilon_0 a)$ [31], where l is the thickness of the sample, a is the area of the sample and ϵ_0 is the permittivity of free space (8.85×10^{-12} F/m). The dielectric loss (ϵ'') was calculated from the relation, $\epsilon'' = \epsilon' \tan \delta$.

Fig. 8(a) displays the C behavior of the C3AH6 and C12A7 specimens as a function of frequency from 20 Hz to 2 MHz. The results showed that the C value of the C12A7 precursor sample was virtually independent of frequency. This value was constant at 6×10^{-12} F. The C value of C3AH6 cement sample rapidly increased from 10^{-10} F to 10^{-11} F over the frequency range of 40 Hz to 2 MHz. The results showed that the C value of the C3AH6 specimen was higher than that of the C12A7 specimen at all measured frequencies. This confirmed that hydrated alumina cement materials presented a larger C value than calcium aluminate cement materials. The result might have been due to the presence of H^+ bonding to each of the O atoms to produce $Ca(OH)_8$ and $Al(OH)_6$ substructures in the C3AH6. Additionally, the C value for the C3AH6 specimen in the current work was larger than that reported by Smith et al. [16] of around 10^{-12} F to 2×10^{-12} F in the frequency range of 10^6 Hz– 10^9 Hz. This result might have been due to the formation of nano-size particles in the C3AH6 compound.

Fig. 8(b) shows the dielectric constant (ϵ') of the C3AH6 and C12A7 specimens as a function of frequency from 20 Hz to 2 MHz. The results show that the ϵ' value of the C3AH6 specimen was greater than the ϵ' value of the C12A7 specimen at all measured frequencies. The ϵ' value of the C12A7 precursor sample was a constant value of 0.05 at all measured frequencies. The ϵ' value of the C3AH6 sample rapidly decreased from 150 to 20 over the frequency range of 20 Hz to 10 kHz, and was a constant value of 20 at frequencies ranging from 10 Hz to 2 MHz. These results were greater in magnitude than those of previous reports for Portland cement (~ 13 at frequencies from 100 kHz to 15 MHz) by Cabeza et al. [2], and for calcium aluminate cements (~ 2 – 4 at frequencies from 100 Hz to 5 MHz) by Torres-Luque et al. [14]. Additionally, the ϵ' value of the C3AH6 specimen at frequencies from 10^6 Hz to 10^9 Hz was larger than that of a previous report for calcium aluminate cement hydrate by Smith et al. [16]. This confirmed that the nano-sized particles of C3AH6 hydrated cement compound displayed a higher ϵ' value than that of general cement-based compounds.

Fig. 8(b) shows the dielectric loss (ϵ'') of the C3AH6 and C12A7 specimens as a function of frequency from 20 Hz to 2 MHz. The results showed that the ϵ'' value of the C3AH6 specimen rapidly decreased from 2 to 0.8 as frequency was increased, while the ϵ'' value of the C12A7 specimen was constant at 0.05 at all measured frequencies. This showed that the ϵ'' of the C3AH6 specimen was slightly smaller than for the C12A7 cement.

The electrical equivalent circuit of the materials with their frequency response was evaluated via a parallel RC-circuit, where R is the sample resistance and C is the sample capacitance. The alternating-current (AC) conductivity as a function of frequency can be expressed by the relation, $\sigma = l/aR$, where σ is the AC electrical conductivity as a function of frequency of the specimen. Fig. 8 (d) shows the AC electrical conductivity of the C3AH6 and C12A7 specimens as a function of frequency from 20 Hz to 2 MHz. The results showed that the σ value of the C3AH6 specimen was similar to that of the C12A7 specimen at all measured frequencies. Also, both samples showed σ values lower than 10^{-7} S/m, indicating that both samples acted as perfect electric insulators.

The above results revealed that the electrical impedance of the C12A7 cement remained unchanged over the frequency range of 20 Hz to 2 MHz and the electrical conductivity of the C12A7 cement displayed the behavior of a perfect electric insulator. The dielectric properties (capacitance, dielectric constant and dielectric loss value) of the C12A7 cement were very small, as would be expected for non-dielectric materials. The results showed that the dielectric properties of the C3AH6 cement hydrate were higher than those of the C12A7 specimen at all measured frequencies. The results were affected by dielectric polarization in the C3AH6 structure due to deformational and relaxation polarization of the mate-

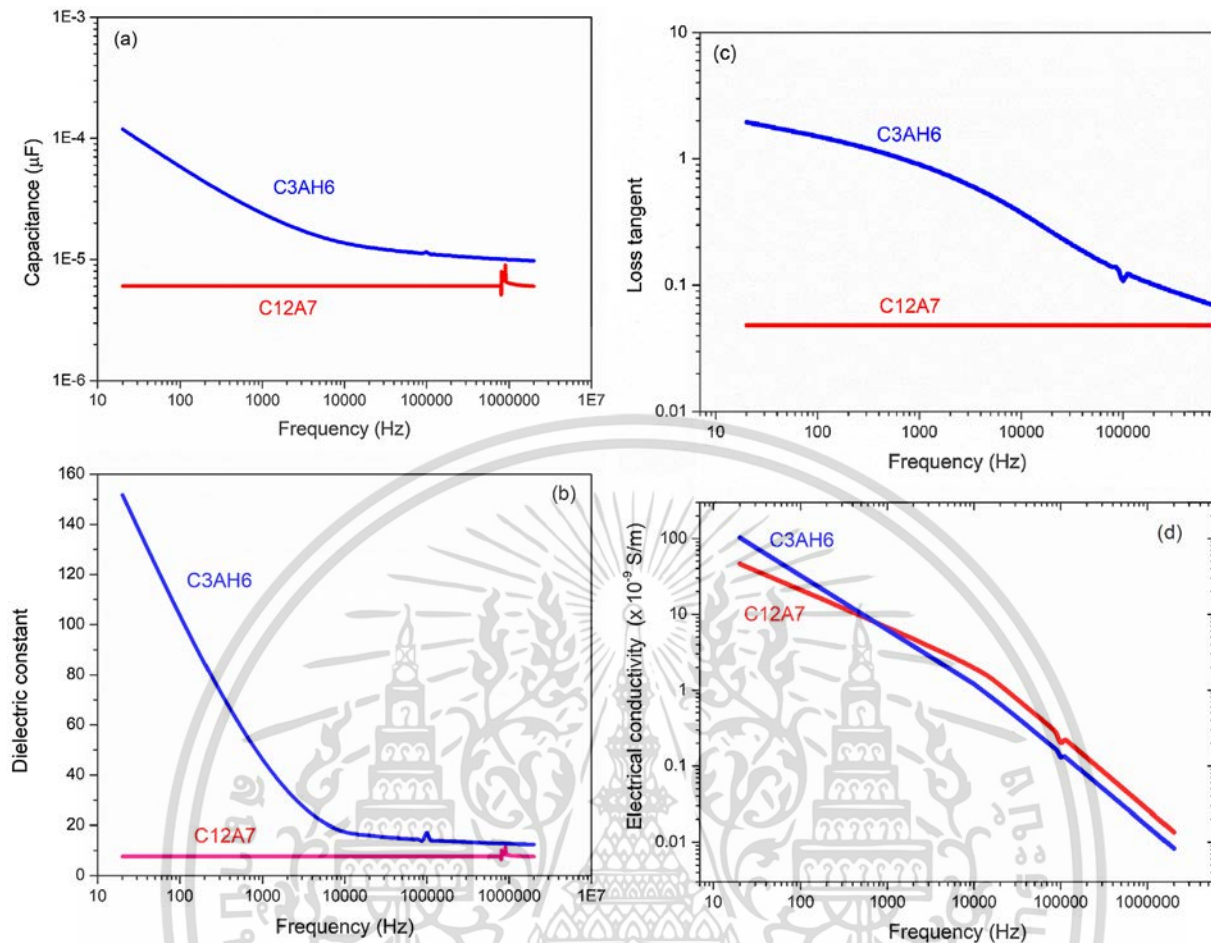


Fig. 8. (a) Capacitance, (b) dielectric constant, (c) dielectric loss, and (d) AC electrical conductivity as a function of frequency of the C3AH6 and C12A7 specimens.

rial under an AC electric field. This effect was caused by the complex structure of the C3AH6 cement, i.e., O–H bonding to produce H^+ bonding with each the O atoms occurring in the $Ca(OH)_8$ and $Al(OH)_6$ sub-structures as shown in Fig. 4. Furthermore, the results revealed that the effect of nano-sized particles on the dielectric properties was higher than that of the C3AH6 hydrated cement. This implied that nano-sized particles played a key role to enhance dielectric properties. Thus, the effect of nano-sized particles on dielectric properties might affect the optical energy gap of the C3AH6 cement as described by the Clausius-Mosotti equation.

4. Conclusions

Nano-sized C3AH6 cement hydrate was successfully fabricated via a hydration reaction of a C12A7 precursor in DI water as its temperature was rapidly increased to 100 °C. The optical and dielectric properties of the resulting cement product were investigated. Characterization by XRD techniques confirmed that the crystallization of a C3AH6 phase structure was a hydrogarnet cement hydrate structure. TEM techniques confirmed the existence of nano-sized structures as in size of 10 nm–50 nm. XPS and EDX revealed Ca, Al, and O components. The TG-DTA results indicated thermodynamically stable materials in the range of room temperature to 300 °C. The C3AH6 cement displayed a direct energy gap of 4.1 eV and an indirect energy gap of 2.45 eV, indicating that it is a transparent material. Impedance analysis showed the C3AH6 cement response at frequencies ranging from 20 Hz to 2 MHz. The C3AH6 cement structure had a large capacitance value, in

the range of 10^{-10} F– 10^{-11} F. The dielectric constant was in the range of 20–150, whereas a smaller value of the dielectric loss was in the range 2–0.8. The large values were due to the complex structure of the C3AH6 cement with –O–H bonding where H^+ bonding occurred with each O atom in the structure. Moreover, enhancement of the dielectric properties was due to the nano-sized particles of C3AH6 hydrate cement. It can be concluded that nano-sized C3AH6 hydrate cement particles were visibly transparent and had a high electrical frequency response. Thus, nano-sized C3AH6 cement products are potential candidates for applications as smart building materials, such as transparent electrode windows, smart wall capacitors, triboelectric devices, and supercapacitors.

Acknowledgements

C. Ruttanapun would like to thank the Thailand Research Fund (TRF) (Contract Number: MRG6080236) for financial support. C. Phrompet, C. Sriwong, and C. Ruttanapun would like to thank the Thailand Research Fund (TRF) (Contract Number: PHD6010046) for financial support. Moreover, we would like to thank the King Mongkut's Institute of Technology Ladkrabang (KMITL) and the Faculty of Science, King Mongkut's Institute of Technology Ladkrabang (KMITL) for funding our research grant. S. Maensiri would like to acknowledge the SUT-COE on Advanced Functional Materials, Suranaree University of Technology, Thailand for financial support. Lastly, P. Chindaprasirt and C. Ruttanapun would like to acknowledge the financial support of the Thailand Research Fund (TRF)

under the TRF Distinguished Research Professor Grant No. DPG6180002.

References

- [1] Y.L. Yaphary, Z. Yu, R.H.W. Lam, D. Lau, Effect of triethanolamine on cement hydration toward initial setting time, *Constr. Build. Mater.* 141 (2017) 94–103.
- [2] M. Cabeza, P. Merino, A. Miranda, X.R. Nóvoa, I. Sancheza, Impedance spectroscopy study of hardened portland cement paste, *Cem. Concr. Res.* 881–891 (2002).
- [3] H. Mei, Y. Zhong, P. Wang, Z. Jia, C. Li, N. Cheng, Electronic, optical, and lattice dynamical properties of tetracalcium trialuminate ($\text{Ca}_4\text{Al}_6\text{O}_{13}$), *Materials* 11 (2018) 49.
- [4] G. Goracci, M. Monasterio, H. Jansson, S. Cervený, Dynamics of nano-confined water in Portland cement-comparison with synthetic C-S-H gel and other silicate materials, *Sci. Rep.* 7 (2017) 8258.
- [5] L. Fernández-Carrasco, J. Rius, C. Miravittles, Supercritical carbonation of calcium aluminate cement, *Cem. Concr. Res.* 38 (2008) 1033–1037.
- [6] W.J. Wei, S.D. Tze, H.C. Liaw, Calcium aluminate composites “with controlled duplex structures: I. Hydration reaction and densification”, *J. Ceram. Process. Res.* 6 (3) (2005) 223–229.
- [7] C.H. Jung, I.R. Hwang, B.H. Park, D.H. Yoon, Characterization of $12\text{CaO}\cdot 7\text{Al}_2\text{O}_3$ doped indium tin oxide films for transparent cathode in top-emission organic light-emitting diodes, *J. Nanosci. Nanotechnol.* 13 (2013) 7556–7560.
- [8] H. Hosono, S.W. Kim, M. Miyakawa, S. Matsuishi, T. Kamiya, Thin film and bulk fabrication of room-temperature-stable electride C12A7:e utilizing reduced amorphous $12\text{CaO}\cdot 7\text{Al}_2\text{O}_3$ (C12A7), *J. Non-Cryst. Solids.* 354 (2008) 2772–2776.
- [9] L.P. Rand, J.D. Williams, R.A. Martinez, Colorado State University Research Foundation, $12\text{CaO}\cdot 7\text{Al}_2\text{O}_3$ electride hollow cathode, United States Patent US 9305733 B2, 2016 Apr 5.
- [10] S.W. Kim, Y. Toda, K. Hayashi, M. Hirano, H. Hosono, Synthesis of a room temperature stable $12\text{CaO}\cdot 7\text{Al}_2\text{O}_3$ electride from the melt and its application as an electron field emitter, *Chem. Mater.* 18 (2006) 1938–1944.
- [11] A. Hussain, S. Mehmood, M.N. Rasool, S. Aryal, P. Rulis, W.Y. Ching, Electronic structure, mechanical, and optical properties of $\text{CaO}\cdot\text{Al}_2\text{O}_3$ system: a first principles approach, *Indian J. Phys.* (2016) 917–929.
- [12] R.P.S.M. Lobo, N. Bontemps, M.I. Berton, T.O. Mason, K.R. Poeppelmeier, A.J. Freeman, M.S. Park, J.E. Medvedeva, Optical conductivity of mayenite: from insulator to metal, *J. Phys. Chem. C* 119 (16) (2015) 8849–8856.
- [13] C. Ruttanapun, P. Srepusharawoot, S. Maensiri, Effect of Fe^{3+} -doped $\text{Ca}_{12}\text{Al}_{14}\text{O}_{33}$ cement on optical and thermal properties, *Chin. J. Phys.* 56 (2018) 252–260.
- [14] M. Torres-Luque, J.F. Osma, M. Sánchez-Silva, E. Bastidas-Arteaga, F. Schoefs, Chloridetect: commercial calcium aluminate based conductimetric sensor for chloride presence detection, *Sensors* 17 (2017) 2099.
- [15] M. Torres-Luque, J.F. Osma, M. Sánchez-Silva, E. Bastidas-Arteaga, F. Schoefs, Chloridetect: commercial calcium aluminate based conductimetric sensor for chloride presence detection, *Sensors* 17 (2017) 2099.
- [16] A. Smith, P. Abeland, F. Thummen, A. Allemand, Electrical characterisation as a function of frequency: application to aluminous cement during ear hydration, *Cem. Concr. Compos.* 14 (2004) 477–484.
- [17] M.U. Okoronkwo, F.P. Glasser, Compatibility of hydrogarnet, $\text{Ca}_3\text{Al}_2(\text{SiO}_4)_x(\text{OH})_{4(3-x)}$, with sulfate and carbonate-bearing cement phases: 5–85 °C, *Cem. Concr. Res.* 83 (2016) 86–96.
- [18] B.Z. Dilnesa, B. Lothenbach, G. Renaudin, A. Wichser, D. Kulik, Synthesis and characterization of hydrogarnet $\text{Ca}_3(\text{Al}_x\text{Fe}_{1-x})_2(\text{SiO}_4)_y(\text{OH})_{4(3-y)}$, *Cem. Concr. Res.* 59 (2014) 96–111.
- [19] V. Antonoviča, J. Kerienė, R. Borisa, M. Aleknevičius, The effect of temperature on the formation of the hydrated calcium aluminate cement structure, *Proc. Eng.* 57 (2013) 99–106.
- [20] J. Plank, M. Zhang-Preße, N.P. Ivleva, R. Niessner, Stability of single phase C_3A hydrates against pressurized CO_2 , *Constr. Build. Mater.* 122 (2016) 426–434.
- [21] P. Barnes, J. Bensted, *Structure and Performance of Cements*, second ed., CRC Press, 2001.
- [22] Y. Wang, B. Zhu, X. Li, P. Chen, Effect of dispersants on the hydrate morphologies of spinel-containing calcium aluminate cement and on the properties of refractory castables, *Ceram. Int.* 42 (2016) 711–720.
- [23] K.V. Baiju, S. Shukla, K.S. Sandhya, J. James, K.G.K. Warriar, Photocatalytic activity of sol-gel-derived nanocrystalline titania, *J. Phys. Chem.* 111 (2007) 7612–7622.
- [24] R.K. Mishra, L. Fernández-Carrasco, R.J. Flatt, H. Heinz, A force field for tricalcium aluminate to characterize surface properties, initial hydration, and organically modified interfaces in atomic resolution, *Dalton Trans.* 43 (2014) 10602–10616.
- [25] P.V. Sushko, A.L. Shluger, M. Hirano, H. Hosono, From insulator to electride: a theoretical model of nanoporous oxide $12\text{CaO}\cdot 7\text{Al}_2\text{O}_3$, *J. Am. Chem. Soc.* 129 (2007) 942–951.
- [26] J.M. Rivas Mercury, A.H. De Aza, X. Turrillas, P. Pena, The synthesis mechanism of $\text{Ca}_3\text{Al}_2\text{O}_6$ from soft mechanochemically activated precursors studied by time-resolved neutron diffraction up to 1000 °C, *J. Solid State Chem.* 177 (2004) 866–874.
- [27] R.K. Pan, S. Feng, H.Z. Tao, XPS and NMR analysis on $12\text{CaO}\cdot 7\text{Al}_2\text{O}_3$, *IOP Conf Series, Mater. Sci. Eng.* 167 (2017) 012017.
- [28] C. Ruttanapun, S. Maensiri, Effects of spin entropy and lattice strain from mixed-trivalent $\text{Fe}^{3+}/\text{Cr}^{3+}$ on the electronic, thermoelectric and optical properties of delafossite $\text{CuFe}_{1-x}\text{Cr}_x\text{O}_2$ ($x = 0.25, 0.5, 0.75$), *J. Phys. D Appl. Phys.* 48 (2015) 495103.
- [29] S. Kalyanaraman, P.M. Shajinshinu, S. Vijayalakshmi, Refractive index, band gap energy, dielectric constant and polarizability calculations of ferroelectric Ethylenediaminium Tetrachlorozincate crystal, *J. Phys. Chem. Solids* 86 (2015) 108–113.
- [30] H. Kamalak, M. Erdem, E. Altin, S. Demirel, E. Oz, S. Altin, Giant dielectric constant and mechanical, heat conducting and structural properties of dental composites by adding Ca ions, *J. Dent Oro Surg.* 1 (3) (2016) 112.
- [31] J. Eufinger, A. Schmidt, M. Lerch, J. Janek, Novel anion conductors - conductivity, thermodynamic stability and hydration of anion substituted mayenite-type cage compounds $\text{C12A7}: \text{X}$ ($\text{X} = \text{O}, \text{OH}, \text{Cl}, \text{F}, \text{CN}, \text{S}, \text{N}$), *PCCP* 17 (2015) 6844.

เอกสารนี้เป็นเอกสารที่สงวนไว้สำหรับการใช้งานเพื่อการศึกษาเท่านั้น ไม่อนุญาตให้นำไปใช้ประโยชน์ด้านการค้า
ไม่ว่ากรณีใดๆ ทั้งสิ้น อีกทั้งห้ามมิให้ตัดแปลงเนื้อหา และต้องอ้างอิงถึงเจ้าของเอกสารทุกครั้งที่มีการนำไปใช้



Mechanical, dielectric, thermal and antibacterial properties of reduced graphene oxide (rGO)-nanosized C3AH6 cement nanocomposites for smart cement-based materials

Chaiwat Phrompet^{a,b}, Chaval Sriwong^{a,c,d}, Chesta Ruttanapun^{a,b,d,*}

^a Smart Materials Research and Innovation Unit (SM-RIU), Faculty of Science, King Mongkut's Institute of Technology Ladkrabang, Chalongkrung Road, Ladkrabang, Bangkok, 10520, Thailand

^b Department of Physics, Faculty of Science, King Mongkut's Institute of Technology Ladkrabang, Chalongkrung Road, Ladkrabang, Bangkok, 10520, Thailand

^c Department of Chemistry, Faculty of Science, King Mongkut's Institute of Technology Ladkrabang, Chalongkrung Road, Ladkrabang, Bangkok, 10520, Thailand

^d Thailand Center of Excellence in Physics, Commission on Higher Education, 328 Si Ayuthaya Road, Bangkok, 10400, Thailand

ARTICLE INFO

Keywords:

Nanocomposites
C3AH6 cement
Reduced graphene oxide (rGO)
Dielectric property
Thermal property
Antibacterial activity

ABSTRACT

This work aimed to fabricate nanocomposites of reduced graphene oxide (rGO)-nanosized C3AH6 cement via a rapid cement hydration for enhancing its micro-hardness, dielectric constant, thermal conductivity, electrochemical and antibacterial properties. rGO-nanosized C3AH6 nanocomposites (~10–20 nm in diameter) with 1, 2, 3, and 4% weight of rGO, were successfully synthesized from a Ca12Al14O33 and rGO colloid that was rapidly heated with water to a temperature of 100 °C. Nanocomposites of x%rGO-C3AH6 (x = 1, 2, 3, and 4) were characterized using XRD, UV-vis spectroscopy, Raman spectroscopy, X-ray photoelectron spectroscopy and TGA techniques. The chemical composition was confirmed using SEM and EDX characterization. The results revealed a nanocomposited rGO-C3AH6 material with nanosheet and nanoflaked rGO, as well as nanosized C3AH6 particles. The results presented rGO-C3AH6 with high performance multifunctional properties that included enhanced mechanical, dielectric, and thermal properties. The vickers micro-hardness and dielectric constant were enhanced by the effect of rGO-C3AH6 nanocomposites. The thermal conductivity of rGO-C3AH6 was higher than that of C3AH6. The electrical conductivity and electrochemical properties were effectively increased with greater levels of rGO in the material. Its antibacterial activity was confirmed by the formation of clearing zones on a Petri plate seeded with *Escherichia coli* (*E. coli*). The diameter of these zones increased with the rGO content. These results confirmed that nanocomposited rGO-C3AH6 was effective in enhancing mechanical, dielectric and thermal properties while serving as a high performance multifunctional cement-based material.

1. Introduction

The new urban civil works, smart buildings, are a combination of modern engineering, architecture and technology requiring multifunctional cement-based construction materials. They provide modern infrastructure for consumers that is friendly, safe and healthy, built with energy efficient and low cost materials [1]. Conventional cement materials can be modified with enhanced properties to improve their performance with multifunctional properties. These outstanding properties consist of high mechanical strength, low thermal conductivity, energy storage capability and antibacterial action. Smart building infrastructure require highly unique properties including resistance to heat conduction, the ability to producing energy by converting thermal energy

into electricity. They employ a thermoelectric effect [2]) storing energy as super-capacitors or batteries [3] and their structural members can resist bacterial growth [4]. In general, conventional cement-based compounds [5] use large amounts of raw materials that consist of four mineral phases, alite, betite, aluminate and ferrite. Alite is referred to as tricalcium silicate (Ca_3SiO_5) or C3S. Betite is dicacium silicate (Ca_2SiO_4) or C2S, while aluminate is tricalcium aluminate ($\text{Ca}_3\text{Al}_2\text{O}_6$) or C3A. Ferrite is tetracalcium aluminoferrite phase ($\text{Ca}_4\text{Al}_n\text{Fe}_{2-n}\text{O}_7$) or C4AF. Main products of cement hydration, which are products of the reaction between cement and water, consist of ettringite ($\text{Ca}_3\text{Al}(\text{OH})_6\text{-}12\text{H}_2\text{O}]_2\text{-}2\text{H}_2\text{O}$), calcium silicate hydrate ($3\text{CaO}\text{-}3\text{SiO}_2\text{-}4\text{H}_2\text{O}$), and calcium hydroxide ($\text{Ca}(\text{OH})_2$) [6]. In hydrated Portland cement, aluminate cement (C3A) hydration can occur very rapidly to form

* Corresponding author. Department of Physics, Faculty of Science, King Mongkut's Institute of Technology Ladkrabang, Bangkok, 10520, Thailand.
E-mail addresses: chesta.ru@kmitl.ac.th, chesta.ruttanapun@gmail.com (C. Ruttanapun).

<https://doi.org/10.1016/j.compositesb.2019.107128>

Received 30 March 2019; Received in revised form 14 June 2019; Accepted 5 July 2019

Available online 6 July 2019

1359-8368/© 2019 Elsevier Ltd. All rights reserved.

C2AH8 ($\text{CaO-Al}_2\text{O}_3\cdot 8\text{H}_2\text{O}$) and C4AH13 ($4\text{CaO-Al}_2\text{O}_3\cdot 8\text{H}_2\text{O}$) phases, and to finally form C3AH6 ($3\text{CaO-Al}_2\text{O}_3\cdot 6\text{H}_2\text{O}$). The C3AH6, which is a stable phase in room temperature [6,7], is the primary hydrate of Portland cement. Additionally, the C3AH6 product is easily produced via a rapid reaction of Ca12Al14O33 cement with water, elevating its temperature to above 60°C [8,9]. Also, anhydrous cement, C3AH6, can be used as a multifunctional cement-based material due to its thermodynamic stability at room temperature and easy preparation via a conventional hydration process using low-cost starting materials. C3AH6 cement is a mineral in the hydrogarnet group with the general formula, $\text{Ca}_3(\text{Al}_x\text{Fe}_{1-x})_2(\text{SiO}_4)_y(\text{OH})_{4(3-y)}$, where $x = 1$, and $y = 0$ [6]. Previous work [8] has reported that C3AH6 has poor dielectric properties as its dielectric constant varies from 20 to 150 over the range of 20 Hz to 2 MHz. There have limited reports on its mechanical and electrochemical properties as well as its antibacterial nature. Also in the Portland cement group, a calcium aluminate cement can be used in unique and innovative multi-functional ways, such as transparent electrodes [10], transparent conducting oxides [11], and conducting electrode [12] devices. It may have antibacterial properties to assist in keeping the environment clean [14]. Similarly, C3AH6 cement may display other high performance multi-functional properties. For example, Ref. [13] has revealed that the value of the dielectric constant of C3AH6 can be improved by three orders of magnitude by incorporating nano-Ag and nano-sized C3AH6 in to a composite material. This shows that nano-composites can improve C3AH6 cement for use as smart cement-based materials.

In addition, there have many reports that the conventional cement-based compounds have been enhanced properties by compositing with modifying graphene based (graphene oxide (GO) and reduced graphene oxide (rGO) [1]. Particularly, GO and rGO, which are a two-dimensional (2D) carbon nanomaterial, has been widely used for construction applications due to its favorable mechanical, thermal and electrical properties resulting from a high surface area [1]. There have several modifying cement hydrate for high performance cement materials. The nanoparticle Ca12Al14O33 electrides have been successfully prepared via a carbon nanoreaction process [15,16] with reduced graphene oxide composite (rGO) coated by nanocaged Ca12Al14O33 particles for enhancing electrical conductivity. Khan et al. [16] succeed in fabricating a conductive nanoscale calcium aluminate cement using rGO and GO components. Sedaghat et al. [17] reported on the thermal diffusivity and electrical conductivity of cement/graphene composite structural applications prepared by partial replacement of graphene with Portland cement. Li and Kim [18] used graphene oxide composited with calcium aluminate cement for improving the flexural and compressive strength of materials used for repair in the construction field. Dimov et al. [1] presented nano-engineered concrete composites incorporating GO that provided ultrahigh strength. Gholampour et al. [19] reported the effect of GO and rGO composites in a cement mortar for improving its axial tension and compression properties. Thus, this 2-D rGO material may have excellent performance for improving the properties of nanosized C3AH6 hydrogarnet cement. However, to the best of our knowledge, there are no reports of an improvement mechanical, dielectric constant, thermal conductivity properties to high performance and reveals of electrochemical, antibacterial properties of C3AH6 cement hydrate by co-operating with 2-D nanostructured rGO for smart cement-based materials. Moreover, Phrompet et al. [8]. have reported that nanostructured C3AH6 hydrogarnet cement was derived from a Ca12Al14O33 cement precursor reacting with water at an elevated temperature in a simple hydration process [20,21]. Also, the smart cement materials should be improved by incorporation between nanosized C3AH6 with using 2-D nanostructured GO or rGO in multifunctional applications requiring micro-hardness, an appropriate dielectric constant, thermal conductivity, electrochemical properties and antibacterial activity.

Herein, this work is proposed a method for preparing 2-D nanocomposites of reduced graphene oxide (rGO) and nanosized C3AH6

cement via a rapid cement hydration process for investigation of its mechanical, optical, dielectric, thermal, electrochemical, and antibacterial properties. This mechanism employs 2-D nanostructured rGO inserted into a nanosized C3AH6 cement-base enhancing its material properties. The Ca12Al14O33 cement precursor and the resulting products were characterized using X-ray diffraction (XRD), transmission electron microscopy (TEM), high-resolution TEM (HRTEM), IR spectroscopy, X-ray photoelectron spectroscopy (XPS), the thermogravimetric (TG) and the derivative thermogravimetry (DTG) analysis and UV-vis spectrometry. The micro-hardness, dielectric constant, thermal conductivity, and electrochemical properties of these materials were investigated. Surface nanoscale morphology and thermodynamic stability of these materials were evaluated. The enhanced properties of nanocomposited reduced graphene oxide-nanosized C3AH6 cement, micro-hardness, dielectric constant, electrochemical, thermal conductivity and antibacterial properties are reported.

2. Experimental details

2.1. Chemicals and materials

Calcium carbonate (CaCO_3 , 99% purity), alumina powder (Al_2O_3 , 99.9% purity), graphite powder (99% purity), and hydrogen peroxide (H_2O_2 , 30%) were purchased from Sigma-Aldrich (USA). Sulfuric acid (H_2SO_4 , 98%), hydrochloric acid (HCl, 37%), and potassium permanganate (KMnO_4) were obtained from Merck (Germany). An ammonia solution (NH_3 , 28–30%) was supplied from Baker (USA). All chemicals were used as received without further purification.

2.2. Preparation of reduced graphene oxide (rGO)

First, graphite oxide was synthesized via a modified Hummers' method by oxidizing graphite with a strong acid and oxidizing agent. In a typical procedure, about 2 g of graphite powder was mixed with 6 g of KMnO_4 in a beaker, and then the solid mixture was poured into a 500 mL round bottom flask and cooled to 0°C in an ice bath for 10 min. After that, about 46 mL of H_2SO_4 was gradually added under stirring and cooling, so that the temperature of mixture was maintained below 15°C . Then, the mixture was stirred at 40°C in water bath for 30 min. Next, about 90 mL of distilled water was slowly added, followed by heating the mixture under stirring at 95°C in an oil bath for another 60 min. Subsequently, the reaction was stopped by adding 250 mL of distilled water, followed by 10 mL of a H_2O_2 solution, changing the colour of the mixture to a yellowish-brown. The resulting product was separated by centrifugation, washed with a 5% HCl solution to remove sulphate. It was filtered and washed several times using distilled water until the pH of filtered solution was about 7. After that, the resulting solid paste product was dried in an oven at 65°C overnight, resulting in a graphite oxide product. Next, to prepare an aqueous suspension of GO nanosheets, the synthesized graphite oxide powder (800 mg) was re-dispersed in distilled water (120 mL) under ultrasonication for 90 min, followed by centrifugation. Finally, a dark-brown supernatant of an aqueous GO suspension was obtained.

Second, reduced graphene oxide (rGO) was synthesized via a previously described modified chemical reduction method [2]. In brief, 100 mL of the obtained GO (2 mg/mL) suspension was mixed with 100 mL of distilled water in a beaker, followed by addition of 1 mL of an ammonia and 0.1 mL of hydrazine hydrate solutions. Then, the mixture was heated and stirred at 95°C in oil bath for 45 min. During the reduction, the suspension colour changed from brown to black. Finally, a stable aqueous suspension of rGO nanosheets was obtained.

2.3. Preparation of Ca12Al14O33 cement

In this work, Ca12Al14O33 cement powder was first prepared via a solid state reaction using CaCO_3 and Al_2O_3 as starting materials. In a

typical procedure, CaCO_3 and Al_2O_3 powders were stoichiometrically weighed following the reaction, $12\text{CaCO}_3 + 7\text{Al}_2\text{O}_3 \rightarrow \text{Ca}_{12}\text{Al}_{14}\text{O}_{33} + 12\text{CO}_2$ [8,20]. The powder was mixed by ball milling with ethanol for 24 h at room temperature, and dried in an oven at 100°C for another 24 h. The obtained powder was placed in an alumina crucible, and then sintered in an electric furnace at 1200°C under an air atmosphere for 24 h. Finally, the obtained $\text{Ca}_{12}\text{Al}_{14}\text{O}_{33}$ sample was crushed into a powder to be used as a precursor material to prepare C3AH6 cement-hydrate.

2.4. Preparation of rGO-C3AH6 nanocomposite

The nanocomposite composed of rGO and C3AH6 cement, which produces a cement of the formula, $\text{Ca}_3\text{Al}_2(\text{OH})_{12}$ [9], with rGO-C3AH6 nanocomposite were prepared via a rapid cement hydration process by rapid heating with water at 100°C using the prepared $\text{Ca}_{12}\text{Al}_{14}\text{O}_{33}$ powder as a starting material according to the chemical reaction, $\text{Ca}_{12}\text{Al}_{14}\text{O}_{33} + 33\text{H}_2\text{O} \rightarrow 4(\text{C}_3\text{AH}_6) + 3(\text{Al}(\text{OH})_3)$ [8]. This was done with varying degrees of rGO loading, i.e., 1%, 2%, 3% and 4 wt%. The nanocomposite cements were referenced as x%rGO-C3AH6, where x is the weight percentage (wt%) of rGO to the $\text{Ca}_{12}\text{Al}_{14}\text{O}_{33}$ precursor. In a typical procedure to make 1%rGO-C3AH6 cement, about 3 g of $\text{Ca}_{12}\text{Al}_{14}\text{O}_{33}$ powder was mixed with 120 mL of de-ionized (DI) water and 50 mL of an acetone solution with stirring at room temperature for 10 min. After that, 30 mL of a rGO (1 mg/mL) suspension was added and heated at 100°C for 1 h with stirring. Then, the resulting homogeneous mixture was filtered, washed with DI water, and dried in an oven at 60°C overnight. Finally, 1%rGO-C3AH6 nanocomposite cement was obtained. Similar procedures were used to prepare the other x%rGO-C3AH6 cement samples by varying the rGO loading. To make the total volume of all mixtures equal to 200 mL, the amounts of DI water were varied as 90 mL, 60 mL, and 30 mL for preparation of the 2%rGO-C3AH6, 3%rGO-C3AH6 and 4%rGO-C3AH6 samples, respectively. For an experimental control, a pure C3AH6 cement sample was prepared using the procedure described above, but with no rGO loading.

2.5. Preparation of C3AH6 and rGO-C3AH6 pellets

In thermal conductivity and dielectric constant measurements, the C3AH6 cement and all rGO-C3AH6 products were compacted by hot-pressed sintering into disc-shaped pellets that were 12 mm in diameter and 2–3-mm thick at 400°C for 1 h. For electrical frequency response measurements, the both sides of the discs were polished and coated with gold for Ohmic contact by Sputter coating.

3. Characterizations

The lattice parameters were investigated using X-ray diffractometry (XRD), (Rigaku, Miniflex Cu K-alpha radiation), with a 2θ scanning range from 10 to 80° and stepping interval of 0.02° . The vibration mode of the atomic bonding was evaluated using FTIR, (Bruker, Senterra). An X-ray photoelectron spectroscope (XPS), (Kratos, AXIS Ultra DLD) was employed to determine the charge states of each element in the sample. Transmission electron microscopy (TEM), and a high-resolution TEM (HRTEM) (JEOL-2100 operating at 200 kV) were used to determine the surface morphology. The optical properties of cement powder samples were investigated using a UV-visible spectrometer, (PerkinElmer, Lambda 950). Thermogravimetric analysis (TGA, Netzsch STA 449F3 Jupiter) was performed over a temperature range of 35 – 900°C with a heating rate of $10^\circ\text{C}/\text{min}$ in nitrogen gas for measuring the weight loss of the cement samples.

4. Property measurements

The dried materials were ground into fine powders. The fine powders were sintered into a disc shape, 12 mm in diameter and 2 mm thick in

alumina molds at a pressure of 8 MPa and temperature of 200°C for 1 h. Stoichiometrically mixed powders were ball milled in ethanol (95%) for 18 h and dried for 24 h at room temperature. The mixed powders were pressed into pellets confined in an alumina crucible, and sintered in an electric furnace at 1200°C in air for 24 h. The thermal properties of the samples were determined on flat specimens that were 2–3 mm thick using a NETZSCH LFA 477 Nano-Flash thermal diffusivity analyzer.

The dielectric measurements were done using an impedance analyzer (precision LCR meter Model: E 4980A). Electrical conductivity was measured at room temperature over a frequency range from 20 Hz to 10 MHz.

The micro-hardness of the C3AH6 precursor and x%-rGO/C3AH6 samples was evaluated using a pyramid on square base method with a diamond indenter of the Vickers indenter hardness tester system [Shimadzu HMV-G21].

Electrodes made from the C3AH6 precursor and x%-rGO/C3AH6 samples were used to measure their electrochemical behavior. A 2 mg mass of powder from each sample was sandwiched between nickel foam plates and compressed at 10 kPa for 1 min after soaking in electrolyte for 12 h. Electrodes from all samples were evaluated by potentiostatic cyclic voltammetry (CV) measurements at constant current within potential windows of 0–1 V while connected to a Metrohm Autolab PGSTAT302 N potentiostat-galvanostat system.

Neat C3AH6 sample and the obtained x%rGO-C3AH6 cement composite samples were tested using an agar disk-diffusion method against Gram-negative, *Escherichia coli* (*E. coli*) bacteria at concentration of 1×10^8 CFU/mL to determine their antibacterial properties. The x% rGO-C3AH6 samples were hot-pressed into disc shaped specimens with a diameter of approximately 12 mm. Then, the disc samples were placed on the *E. coli* seeded agar plates and incubated at 37°C for 24 h, after which the inhibition zones that had developed around the discs were photographed and diameters of clear zones reported.

5. Simulation of XRD peaks

Calculation XRD structures was done using the Powder Diffraction function in Visualization for Electronics and Structural Analysis (VESTA) software. VESTA is a module for simulation and analysis of X-ray diffraction pattern data. The crystal structure parameters of $\text{Ca}_{12}\text{Al}_{14}\text{O}_{33}$ cement referenced to 09–0413 of the JCPDS standard database were used.

6. Results and discussion

6.1. $\text{Ca}_{12}\text{Al}_{14}\text{O}_{33}$ cement characterization

Fig. 1(a) shows XRD pattern of a prepared $\text{Ca}_{12}\text{Al}_{14}\text{O}_{33}$ [8] sample as a precursor using the JCPDS#09–0413 file as a standard reference peak and the XRD pattern from the simulation $\text{Ca}_{12}\text{Al}_{14}\text{O}_{33}$ peaks. This confirmed that the prepared $\text{Ca}_{12}\text{Al}_{14}\text{O}_{33}$ sample formed a phase consisting of the resulting cement structure. The $\text{Ca}_{12}\text{Al}_{14}\text{O}_{33}$ sample was used as a precursor for synthesis of a nanosized C3AH6 cement hydrate sample and nanocomposite between 2-D sheets of rGO and nanosized C3AH6 specimens.

Fig. 1(b) shows an SEM image and Electron Dispersion Spectroscopy (EDS) of the chemical composition of the fabricated $\text{Ca}_{12}\text{Al}_{14}\text{O}_{33}$ and an SEM image of the prepared $\text{Ca}_{12}\text{Al}_{14}\text{O}_{33}$ specimen at a magnification of $6000\times$. The image displays the morphology of a micrometer sized edge shaped crystal. The inset of Fig. 1(b) depicts the appearance of Ca, Al, and O atoms in the prepared $\text{Ca}_{12}\text{Al}_{14}\text{O}_{33}$ specimen. The chemical composition of the $\text{Ca}_{12}\text{Al}_{14}\text{O}_{33}$ specimen was obtained from the EDS showing atomic percentages of 13.81%, 15.01%, and 60.69% for Ca, Al and O atoms, respectively. This result of EDS confirmed the formation of the prepared $\text{Ca}_{12}\text{Al}_{14}\text{O}_{33}$ specimen.

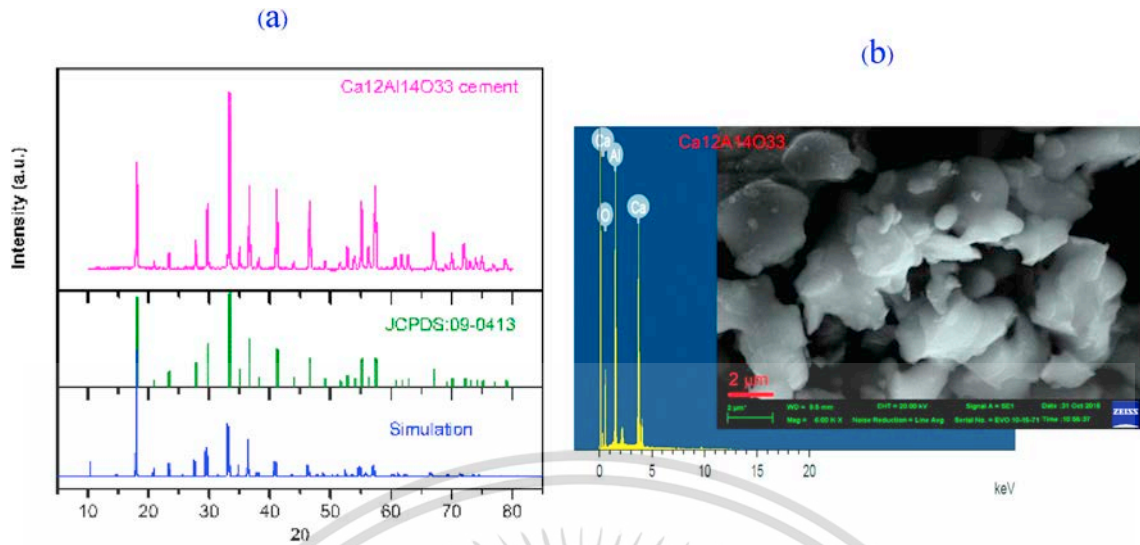


Fig. 1. (a) XRD patterns of prepared Ca12Al14O33 precursor referencing the JCPDS#09-0413 file [8] and the simulation Ca12Al14O33 peaks and (b) SEM and insert of EDS elemental spectrum of the prepared Ca12Al14O33 cement powder.

6.2. GO and rGO characterizations

The chemical structure, crystalline phases and identity of the functional groups of synthesized GO and rGO samples were investigated and confirmed using several spectroscopic techniques. Fig. 2 shows the characterization of synthesized GO and rGO samples. Fig. 2(a) shows the

UV-vis absorption of synthesized GO and rGO samples. The results show an absorption peak at 230 nm due to a $\pi-\pi^*$ transition ($-C=C-$) of GO that was red-shifted to a longer wavelength (at around 268 nm) during the chemical reduction. This indicated that the electronic conjugation inside the rGO structure was restored after the reduction of GO [2,5,16], which is the possible reaction mechanism for the chemical reduction of GO to

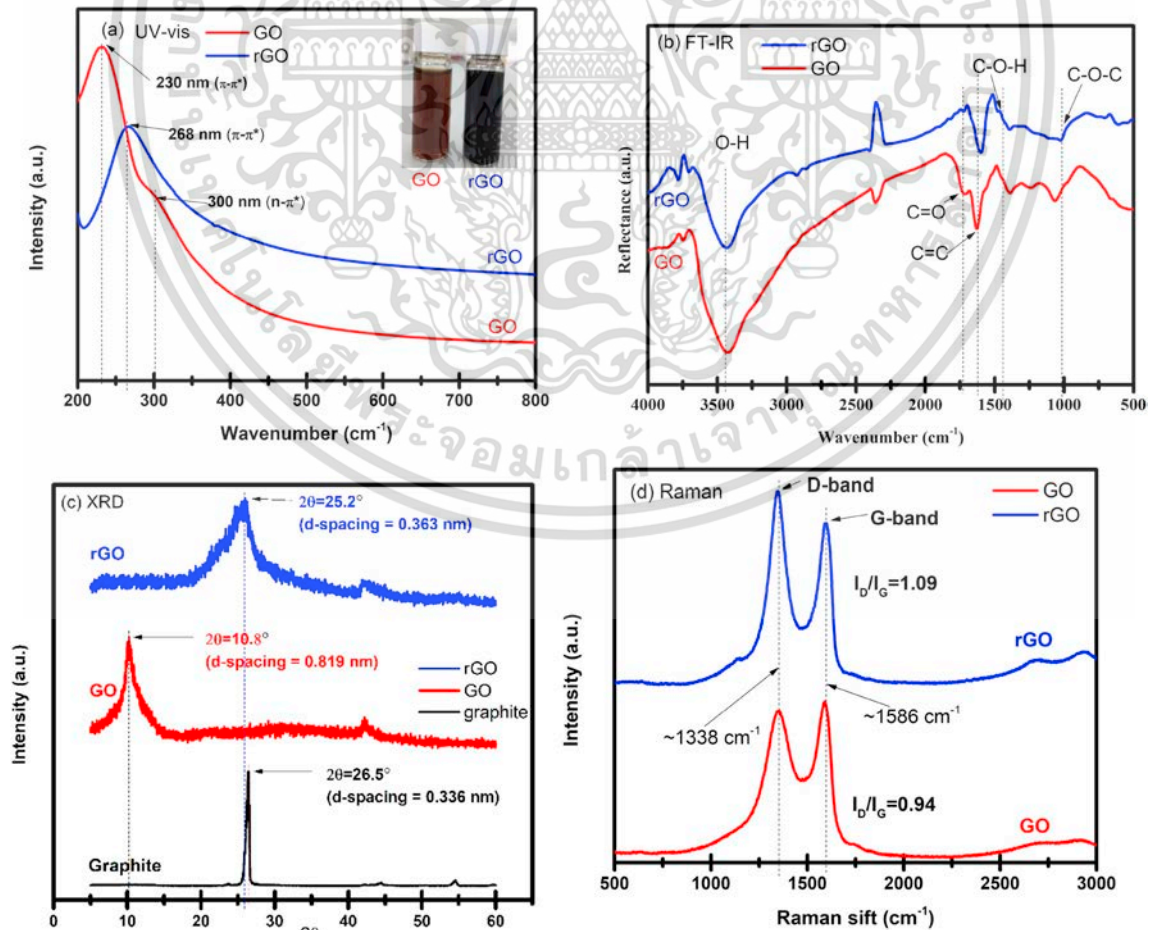


Fig. 2. (a) UV-Vis (GO and rGO aqueous dispersion as insert), (b) FT-IR, (c) XRD and (d) Raman spectra of synthesized GO and rGO samples.

ไม่ว่ากรณีใดๆ ทั้งสิ้น อีกทั้งห้ามมิให้ตัดแปลงเนื้อหา และต้องอ้างอิงถึงเจ้าของเอกสารทุกครั้งที่มีการนำไปใช้

produce rGO as previously described [16,19]. Furthermore, the colour of the GO aqueous dispersion changed from a light brown to black during the chemical reduction using hydrazine as a reducing agent (see the inset of Fig. 2(a)). The colour change of the GO suspension after reduction was confirmed to result from the reduction of GO to rGO [16, 19].

Fig. 2(b) illustrates the FT-IR spectra of the obtained GO and rGO samples. As can be seen from this figure, the vibration bands for the GO sample appeared at around 3410 cm^{-1} , 1740 cm^{-1} , and 1050 cm^{-1} , which correspond to the presence of hydroxyl (-O-H stretching), carbonyl/carboxyl (-C=O stretching), and epoxy (-C-O-C- stretching) groups, respectively. The peak at around 1630 cm^{-1} is attributed to the skeleton of sp^2 aromatic carbon (-C=C- stretching) [16,19]. After the chemical reduction of GO, it was observed that the peaks due to oxygen containing groups decreased in intensity and sometimes vanished, suggesting that GO was completely reduced to rGO during such processes. This result implies that the oxygen containing groups were mostly removed from the skeleton of GO along with some carboxyl groups to form rGO [16,19].

An XRD technique was used to determine the crystal structure phase and interlayer d-spacing of graphite in the synthesized GO and rGO samples, and the results are presented in Fig. 2(c). It can be observed that graphite exhibits a sharp diffraction peak at $2\theta = 26.5^\circ$, corresponding to a typical diffraction of the (002) graphitic carbon plane [9, 22]. The interlayer d-spacing of pristine graphite was calculated according to Bragg's law and determined to be 0.336 nm. The synthesized GO appears as a broad peak at $2\theta = 10.8^\circ$ with an interlayer d-spacing of 0.819 nm. This implies that as graphite is transformed to GO, most of the oxygen containing functional groups are bonded to the graphite surface and that the interlayers of graphite are expanded by chemical oxidation, which results an increased interlayer value for GO [23]. After the reduction of GO, a very broad characteristic peak of rGO appeared at around $2\theta = 25.2^\circ$ with an interlayer d-spacing of 0.382 nm. This result indicates that as GO was converted to rGO, most of the oxygen containing functional groups were removed from the skeleton and basal plane of each GO sheet. Overall, the interlayer d-spacing of the obtained rGO nanosheets was greatly decreased [16,19].

Raman spectroscopy is a powerful technique that can be used to characterize the structural configuration of graphene-based materials. In general, the Raman spectrum of graphitic carbon displays three bands, a D band and a G band with a weak 2D band [16,19]. The D band is associated with the breathing mode of the K point phonons of A_{1g} symmetry. It mainly indicates the surface disorder and defects of graphene. The G band is the result of first order scattering of E_{2g} phonons from sp^2 carbon. It expresses the graphitic composition of the materials [16,19]. Fig. 2(d) displays the Raman spectra of pristine graphite and of the synthesized GO and rGO samples. It can be clearly observed that all graphite, GO and rGO samples exhibited two main peaks at around 1338 cm^{-1} and 1586 cm^{-1} , which correspond to disordered carbon (D band) and graphitic sp^2 carbon (G band), respectively [23]. Moreover, the evolution of disorder is usually quantified by the intensity ratio of the D band to the G band (I_D/I_G). After chemical reduction, the rGO nanosheets showed an increased I_D/I_G intensity ratio compared to that of both the pristine graphite and GO. This is attributed to the formation of a large sp^2 domain with smaller average sizes [16,19].

7. Nanometer sized C3AH6 and rGO-C3AH6 nanocomposite cements

7.1. XRD characterization

Fig. 3 shows X-Ray diffraction patterns of the obtained C3AH6 cement-hydrate sample and x%rGO-C3AH6 composite samples with $x = 1\%$, 2% , 3% and 4% weight of rGO. The XRD peaks of the synthesized C3AH6 sample and x%rGO-C3AH6 composites with various rGO contents and the Joint Commission for Powder Diffraction Standards

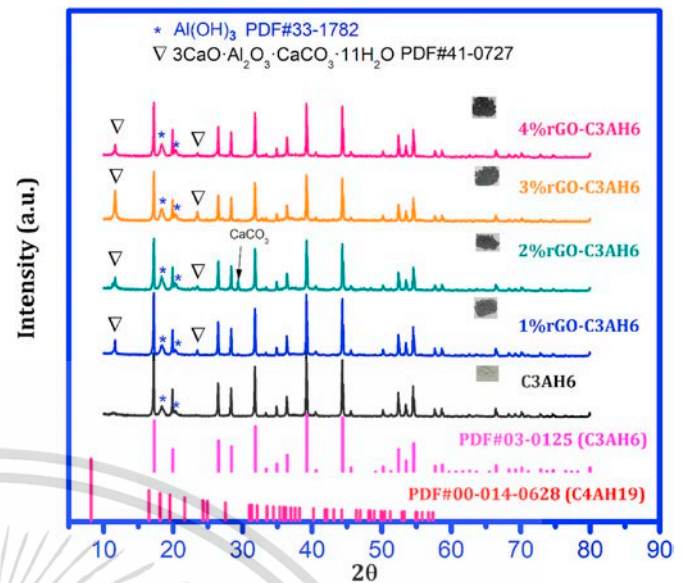


Fig. 3. XRD patterns the fabricated C3AH6 and x%rGO-C3AH6 ($x = 1, 2, 3$ and 4) samples and the standard PDF#03-0125 file of the C3AH6 hydrate cement and PDF#00-014-0628 file of the Calcium Aluminum Oxide Hydrate (C4AH19).

(JCPDS) File (PDF#03-0125) as cubic within space group Ia-3d are illustrated. The peak data of the C3AH6 cement, referenced to the CCD standard JCPDS No. 03-0125, was included with that of the x%rGO-C3AH6 composites. The results show that the observed diffraction patterns of all the C3AH6 and x%rGO-C3AH6 samples correspond well to the diffraction patterns of the C3AH6 peak standard, indicating the formation of a C3AH6 cement-hydrate phase in all samples. The lattice constant of C3AH6 cement was $a = 12.583\text{ \AA}$, and for 4%rGO-C3AH6, $a = 12.581\text{ \AA}$. The lattice constant of 4%rGO-C3AH6 did not change with the rGO content. The presence of an excess aluminum hydroxide (Al(OH)₃) phase at $2\theta = 18^\circ$ and 23.5° in all samples was consistent with the diffraction pattern peak standard of the PDF#76-1782 file and with previous findings [17]. A small amount of an Al(OH)₃ phase appeared during the hydration process of the Ca₁₂Al₁₄O₃₃ cement according to the reaction, $\text{Ca}_{12}\text{Al}_{14}\text{O}_{33} + 33\text{H}_2\text{O} \rightarrow 4(\text{C3AH6}) + 3(\text{Al(OH)}_3)$ [15]. Another small CaCO₃ precursor phase was observed at $2\theta = 28.5^\circ$ only for the 2%rGO-C3AH6 sample. Additionally, a characteristic small $3\text{CaO}\cdot\text{Al}_2\text{O}_3\cdot\text{CaCO}_3\cdot 11\text{H}_2\text{O}$ phase for the x%rGO-C3AH6 composite samples was found, but did not appear in the C3AH6 sample. This revealed that nanosheet rGO reacted with the nanosized C3AH6 cement to form a $3\text{CaO}\cdot\text{Al}_2\text{O}_3\cdot\text{CaCO}_3\cdot 11\text{H}_2\text{O}$ phase following the reaction, $\text{Ca}_3\text{Al}_2(\text{OH})_{12} + \text{rGO} + \text{CO}_2 \rightarrow 3\text{CaO}\cdot\text{Al}_2\text{O}_3\cdot\text{CaCO}_3\cdot 11\text{H}_2\text{O}$. The XRD peak at $2\theta = 25.2^\circ$, characteristic of rGO [19,23,24], was not observed in the x%rGO-C3AH6 samples due to an amorphous phase and very low content of the rGO composite in the C3AH6 specimen. The XRD results of all samples absented the Calcium Aluminum Oxide Hydrate which is chemical formula: $\text{Ca}_4\text{Al}_2\text{O}_7\cdot 19\text{H}_2\text{O}$ (C4AH19) phase as referencing to diffraction pattern peak standard of the PDF#00-014-0628 file.

The average crystallite sizes of the fabricated C3AH6 and x%rGO-C3AH6 samples were calculated via Scherrer's [8] equation as $D_{\text{XRD}} = \frac{0.94\lambda}{\beta \cos \theta}$ where D_{XRD} denotes the average crystallite size, λ denotes the X-ray wavelength ($\lambda = 1.5406\text{ \AA}$), β denotes the full-width at half-maximum of the highest intensity peak, and θ denotes half of the diffraction peak angle. Fig. 4 displays the average crystallite size of C3AH6 and x%rGO-C3AH6 vs. rGO content (wt%). The average crystallite size of C3AH6 was approximately 61.53 nm and those of x%rGO-C3AH6 were 75.73, 66.15, 65.40, and 69.59 nm for $x = 1, 2, 3$ and 4 , respectively. The results show that both C3AH6 and x%rGO-C3AH6 display nanometer crystalline sizes. The average crystallite size of x%rGO-C3AH6 was close to that of C3AH6. This implies that the rGO

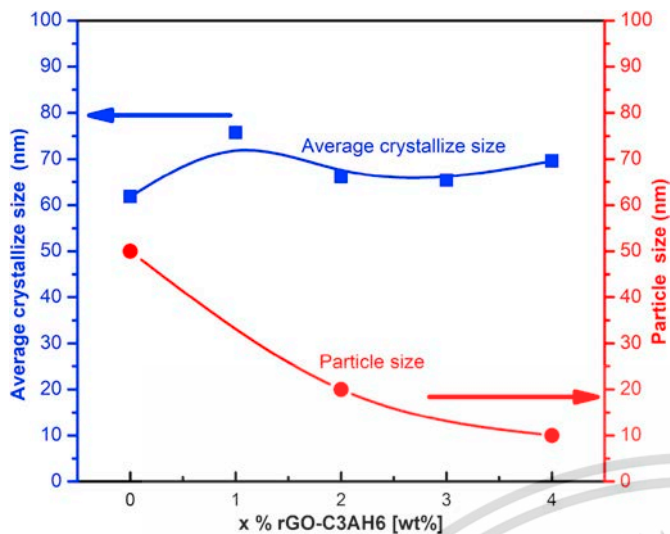


Fig. 4. Average crystallite and particles sizes of C3AH6 and x%rGO-C3AH6 vs. rGO % weight.

loading in the C3AH6 cement at 1, 2, 3 and 4% weight resulted in very small changes in average crystallite size of x%rGO-C3AH6.

7.2. SEM analysis

Fig. 5 shows SEM images and EDS of the synthesized C3AH6, 2% rGO-C3AH6 and 4%rGO-C3AH6 samples. The SEM analysis displays morphology of edge shaped particles for all samples and a coating with a carbon compound, confirming a rGO composite in the synthesized x% rGO-C3AH6 samples. The EDS spectrum of the synthesized C3AH6 sample had phases where Ca = 18.29 wt%, Al = 12.53 wt%, O = 61.08 wt% and C = 8.10 wt%, the synthesized 2%rGO-C3AH6 showed phases where Ca = 14.48 wt%, Al = 14.53 wt%, O = 56.48 wt% and C = 14.50 wt%, and the 4%rGO-C3AH6 displayed the phases with Ca = 7.70 %wt, Al = 19.97 %wt, O = 57.30 wt% and C = 15.02 wt%. It can be observed that the amount of C in the 2% and 4%rGO-C3AH6 samples as the rGO in the composite was increased to a level about 2 times greater than that of the C3AH6 sample. This implies that a composite of rGO and C3AH6 can be successfully derived from a Ca12Al14O33 precursor via a hydration process with a rGO colloid and rapid heated. The EDS mapping of the 4%rGO-C3AH6 sample displayed a homogeneous distribution of carbon on the powder surface. This confirmed the presence of a carbon compound in the rGO composite of the 4%rGO-C3AH6 sample.

7.3. TEM, SAED and EDX characterizations

Surface morphology, particle size and shape at a nanoscale of the synthesized rGO, C3AH6 cement and x%rGO-C3AH6 composite samples are shown in Fig. 6. This figure shows small grains and pores with nanometer sized grains. Fig. 6(a) illustrates TEM images of synthesized rGO. The results display layers of nanosheeted and nanoflaked material in the synthesized rGO, confirming that the synthesized rGO had a nanosheet morphology.

Fig. 6(b) displays TEM images of synthesized C3AH6 sample. The results show the particle sizes of the C3AH6 sample in a layered nanostructure. The smallest nanosized particles were approximately 40–50 nm. The nanosized particles of C3AH6 sample were approximately 50 nm in diameter, close to the calculated average crystallite size of C3AH6 (61 nm) as shown in Fig. 4, confirming the presence of nanometer sized particles. The nanostructure of the C3AH6 cement was produced using Ca12Al14O33 cement with water. The reaction time was accelerated by heating to a temperature of 100 °C as previous described

[15]. This method can be used to grow nanoscale C3AH6 cement-hydrate particles.

Fig. 6 (c) and (d) show the surface morphology, particles size and shape of the x%rGO-C3AH6 composite samples for x = 2 and 4, respectively. Dark regions in the figures suggest that the higher resolution TEM imaging technique may provide more details of the x%rGO-C3AH6 composite [17]. The rGO and C3AH6 particles are seen as nanosheets and dark nanoparticles, respectively. This shows occurrence of nanocomposited rGO-C3AH6 with nanoflaked rGO and nanometer sized C3AH6 cement. The images show small x%rGO-C3AH6 nanocomposite particles with sizes of 10 nm–20 nm. The particle sizes of x% rGO-C3AH6 were smaller than the calculated average crystallite size shown in Fig. 4. The particle sizes confirmed that the synthesized x% rGO-C3AH6 nanocomposites contained nanometer sized particles. The smallest particle size of the 2%rGO-C3AH6, as shown in Fig. 6(c), was ~20 nm, while the smallest particle size of the 4%rGO-C3AH6, as shown in Fig. 4(d), was 10 nm. Fig. 4 shows particle sizes of C3AH6 and x% rGO-C3AH6 vs. rGO content (wt%). The particle sizes of C3AH6 and x% rGO-C3AH6 decreased with increasing rGO percent weight. The results indicate that the nanometer sized particles of the 4%rGO-C3AH6 sample were smaller than that of those the 2%rGO-C3AH6 sample. The rGO content significantly affected the grain sizes of the rGO-C3AH6 composite samples. This implies that the grain sizes were dependent on the amount of rGO in the composites. Nanoparticle rGO-C3AH6 was successfully prepared from the nanometer sized C3AH6 and Ca12Al14O33 cement reacted with water at a temperature of 100 °C. The size of C3AH6 cement particles was limited by pore sizes and density of rGO nanosheets. Thus, the size of the 4%rGO-C3AH6 sample was smaller than that of 2%rGO-C3AH6 sample due to the higher density of the rGO nanosheets, leading to a smaller pore size of C3AH6 particles. Following Shenghua et al. [24], the regulatory mechanism of rGO-C3AH6 formation during rGO cement hydration involves the rGO surface providing nucleation sites for the C3AH6 hydration products during growth. The size of the nanocomposited x%rGO-C3AH6 samples can be controlled by varying the percent weight of the nanoflaked rGO in the preparation process.

Selective Area Electron Diffraction (SAED) has been used for identifying the crystal forms of single, double and multilayer rGO. TEM images, SAED patterns and EDX of the rGO nanosheets, nanometer sized C3AH6, and 2%rGO-C3AH6 and 4%rGO-C3AH6 nanocomposite samples show diffraction rings indicating a high poly-crystalline content as presented in Fig. 6. Fig. 6(a) shows the SAED pattern of the synthesized rGO. The results present ring patterns of the rGO sample. This is characteristic of poly-crystalline rGO resulting from its stacked multilayer orientation. Fig. 6(b) shows the SAED pattern of the C3AH6 sample. This SAED pattern shows diffraction rings also indicating a high poly-crystalline content, confirming the presence of nanometer sized C3AH6 cement particles. Fig. 6(c) and (d) show the SAED patterns of the synthesized nanocomposited 2%rGO-C3AH6 and 4%rGO-C3AH6 samples, respectively. This SAED pattern is characteristic of mixed diffraction rings resulting from a combination of polycrystalline rGO and nanometer sized C3AH6 cement, confirming of the production of nanocomposited x%rGO-C3AH6 cements.

7.4. Raman spectra analysis

Fig. 7 shows the Raman spectra of the synthesized C3AH6 cement sample and the x%rGO-C3AH6 nanocomposited samples (x = 1%, 2%, 3% and 4%). The Raman bands located at 100–1200 cm^{-1} arose from the lattice structure of the C3AH6 cement. There were two peaks caused by the synthesized of C3AH6 at 533 cm^{-1} and 1050 cm^{-1} . These peaks were present in all synthesized samples. The characteristic bands of the C3AH6 sample appearing at 533 cm^{-1} can be attributed to $[\text{AlO}_4]^-$ stretching. The peak located at 1050 cm^{-1} is characteristic of the structure of C3AH6 cement. This was present in all samples of the x% rGO-C3AH6 since they contained a C3AH6 hydrated cement component.

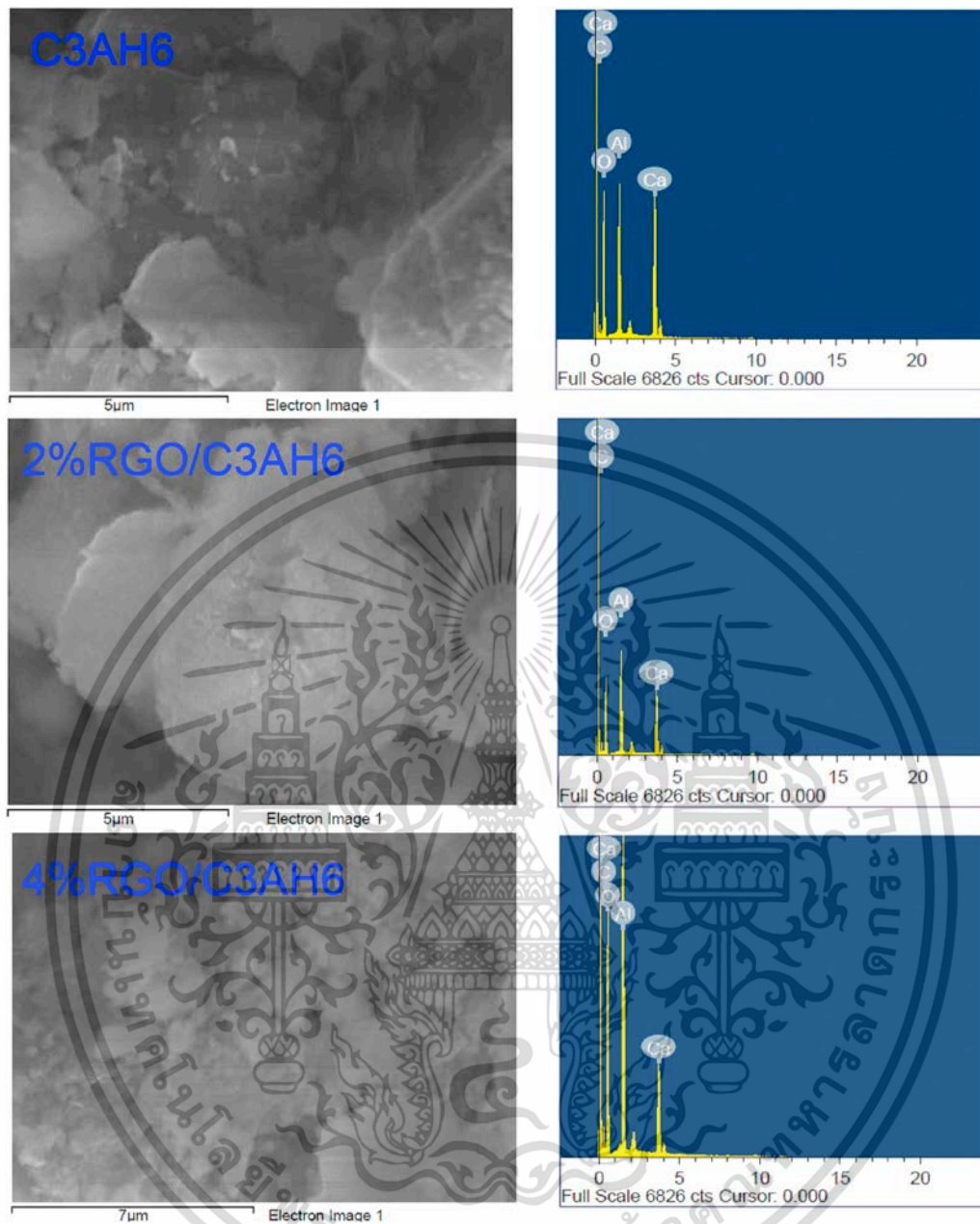


Fig. 5. SEM images and EDX spectra of synthesized C3AH6, 2%rGO-C3AH6 and 4%rGO-C3AH6 samples.

It was observed that the D (1348 cm^{-1}) and G (1576 cm^{-1}) band peaks of the rGO structure were found in all x%rGO-C3AH6 samples, but were not found in the C3AH6 sample. This indicated that the synthesis of C3AH6 cement was successful due to the disappearance of rGO. The x% rGO-C3AH6 composites samples exhibited both D and G band peaks of the rGO structure and peaks at 533 cm^{-1} and 1050 cm^{-1} of the C3AH6 cement structure. This confirmed that the nanometer sized rGO sheets were converted to a nanocomposite with nanometer sized C3AH6 cement particles to produced x% rGO-C3AH6 nanocomposites. Additionally, the intensity of the D and G band peaks was strongly increased with greater amounts of rGO, indicating formation of a composite between the rGO and the C3AH6 cement with increasing rGO content.

7.5. EDS mapping analysis

The EDS mapping of the composited 4%rGO-C3AH6 sample displayed a homogeneous distribution of carbon on the powder surface as

shown in Fig. 8. The rGO and C3AH6 composite can be derived from a $\text{Ca}_{12}\text{Al}_{14}\text{O}_{33}$ precursor via a hydration process with rGO colloid with rapid heating. This was confirmed by the appearance of a carbon compound from the rGO composite in the 4%rGO-C3AH6 sample.

7.6. X-ray photoelectron spectroscopy

X-ray photoelectron spectroscopy (XPS), which is a surface sensitive analytical technique, was used for determining of the chemical composition and bonding in the rGO and C3AH6 components. These measurements were made on the surfaces of the powder materials. Fig. 9 shows the XPS survey spectrum and XPS spectra of C(1s) of the C3AH6, 2%rGO-C3AH6 and 4%rGO-C3AH6 samples. Fig. 9(a) shows a wide scan XPS survey spectra of the synthesized C3AH6, and 2%rGO-C3AH6 samples. The XPS survey displayed the spectra of O (1s), Ca (2p), Ca (2s), Al (2p) and C(1s) of the C3AH6 and 2%rGO-C3AH6 samples. The spectral results show the binding energies of Ca, Al, O(1s) and C(1s)

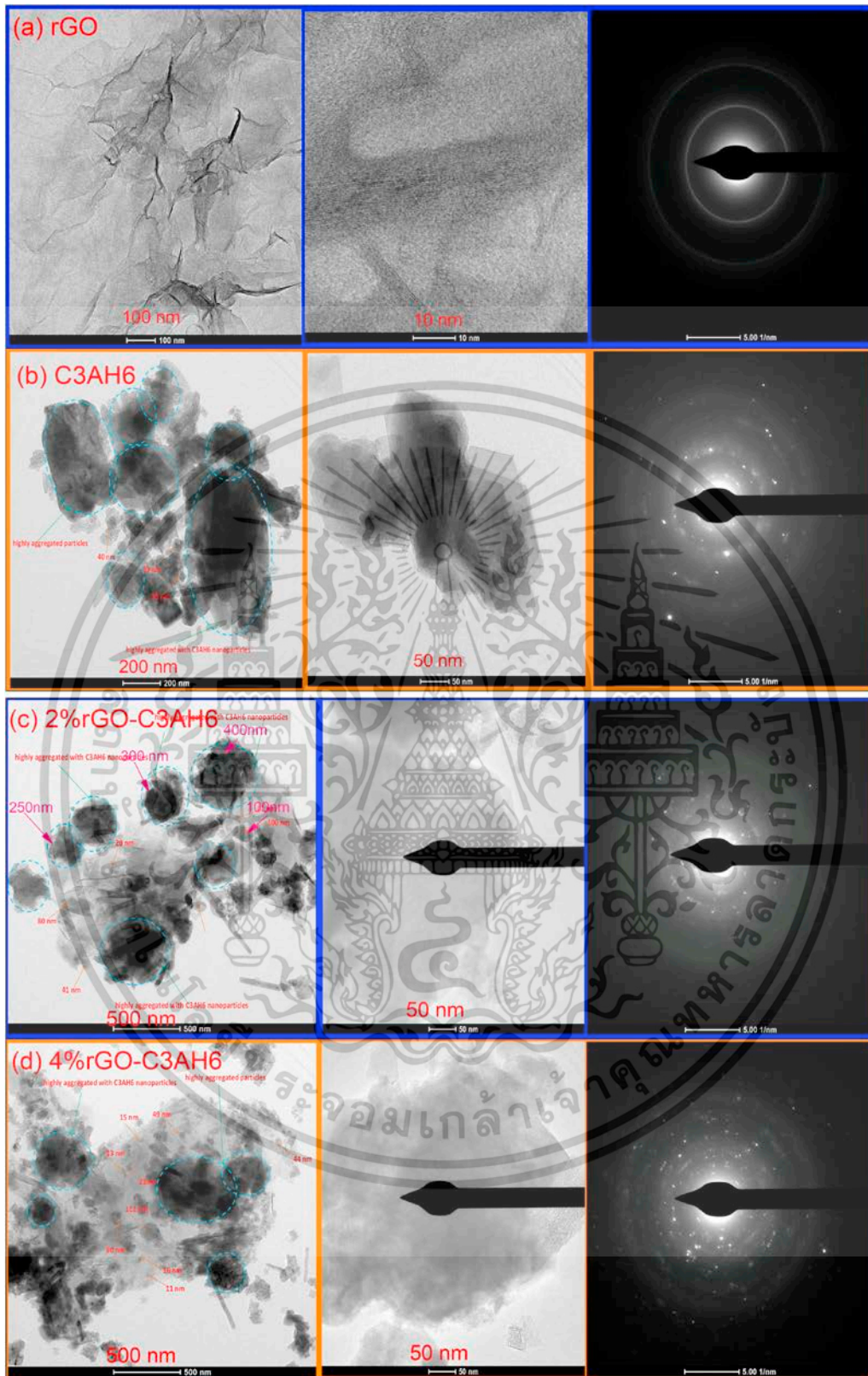


Fig. 6. TEM images of synthesized (a) rGO nanosheets, (b) nanometer sized C3AH6, and (c) nanocomposited 2%rGO-C3AH6 and (d) 4%rGO-C3AH6 samples.

peaks. Fig. 9(b) presents the XPS spectra of C1s from the synthesized C3AH6, 2%rGO-C3AH6 and 4%rGO-C3AH6 samples. The XPS spectra show a peak at 285 eV as indication of the C3AH6 sample and three peak positions located at 284.42 eV, 285.39 eV, and 288.92 eV, as indications of the 2%rGO-C3AH6 and 4%rGO-C3AH6 samples. Two peaks of 2%

rGO-C3AH6 and 4%rGO-C3AH6 samples located at 288.92 eV and 285.39 indicated C=O and C-O bonds [16], respectively, for carbon atoms in these samples. The peak located at 284.42 eV [16], which represent the C-C bond of sp² carbon atoms in a conjugated honeycomb lattice rGO, appeared in the synthesized 2%rGO-C3AH6 and 4%

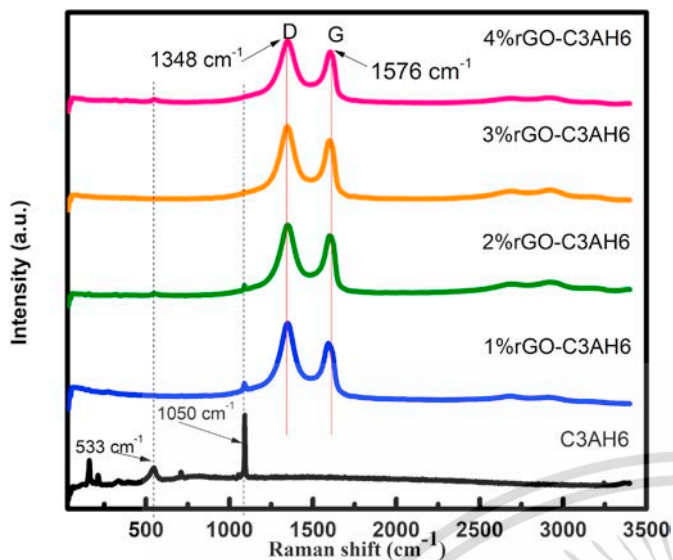


Fig. 7. Raman spectra of synthesized C3AH6 and x%-rGO-C3AH6 samples (as nanocomposited cements with various rGO contents) (x = 1%, 2%, 3% and 4 wt%).

rGO-C3AH6 samples, but was not seen in the C3AH6 sample. This confirms that a nanocomposite between rGO nanosheets and nanometer sized C3AH6 was present in the 2% and 4%rGO-C3AH6 nanocomposites.

7.7. UV-visible spectroscopy

Fig. 10(a) shows UV-visible diffuse reflectance spectroscopy spectra of the C3AH6 cement and x%rGO-C3AH6 (1%, 2%, 3%, and 4 wt%) nanocomposites with various rGO contents. The UV-visible spectra of x%rGO-C3AH6 were different from the spectra of the C3AH6 cement. The x%rGO-C3AH6 samples exhibited low absorption over the visible range,

and higher absorption in a lower energy range. The UV-absorption band of rGO at 270 nm, shown in the inset [25], was not found in the spectra of the x%rGO-C3AH6 samples. However, the rGO absorption peak was seen in the spectra of x%rGO-C3AH6 nanocomposites with rGO at 1, 2, 3 and 4 wt% levels. The absorption of the x%rGO-C3AH6 nanocomposite was higher at increased levels of rGO, which is consistent with the dark brown colour of the powder samples, shown in the right-side of Fig. 3.

The relationship between the absorption coefficient and the optical energy gap is given by Tauc's law as: $\alpha(h\nu) \propto \frac{(h\nu - E_g)^{1/2}}{h\nu}$, where $h\nu$ and E_g are the photon energy and direct optical gap, respectively. The exponent, $1/2$, represents the allowed direct transition type. The relationship of an allowed direct optical gap is expressed by $(ah\nu)^2 = A(h\nu - E_g)$, where A is a constant (independent from $h\nu$). The value of E_g was obtained as the intercept of a straight line on the photon energy axis of a plot of $(ah\nu)^2$ vs. $h\nu$. Fig. 10(b) displays the direct optical gaps (E_g) of the sintered C3AH6 cement and x%rGO-C3AH6 (1%, 2%, 3%, and 4 wt%) nanocomposited samples at room temperature. The E_g of C3AH6 was 4.2 eV, whereas those of the x%rGO-C3AH6 were 3.0, 2.5, 2.0 and 1.5 eV for rGO contents where x = 1, 2, 3, and 4 wt%, respectively. These revealed that the E_g of the x%rGO-C3AH6 decreased with increasing rGO content. Additionally, C3AH6 had a high E_g value of 5.55 eV, whereas the E_g values of x%rGO-C3AH6 (where x = 1, 2, 3, and 4) had a constant value of 6.05 eV.

7.8. Schematic diagram

The fabrication strategy for synthesis the rGO-C3AH6 nanocomposite samples is schematically shown in Fig. 11. The figure presents of the procedure for synthesis of rGO-C3AH6 nanocomposites via a hydration process with rGO colloid and rapid heating. First, the Ca12Al14O33 cement suspension was mixed with the rGO suspension in the same container. Then, the mixed suspension was rapidly heated from room temperature to 100 °C for 2 h with stirring. During this time, the nanostructure C3AH6 hydrogarnet cement developed in the presence of the rGO suspension via a cement hydration process according the chemical reaction, $Ca_{12}Al_{14}O_{33} + 33(H_2O) \rightarrow 4(C_3AH_6) + 3(Al(OH)_3)$.

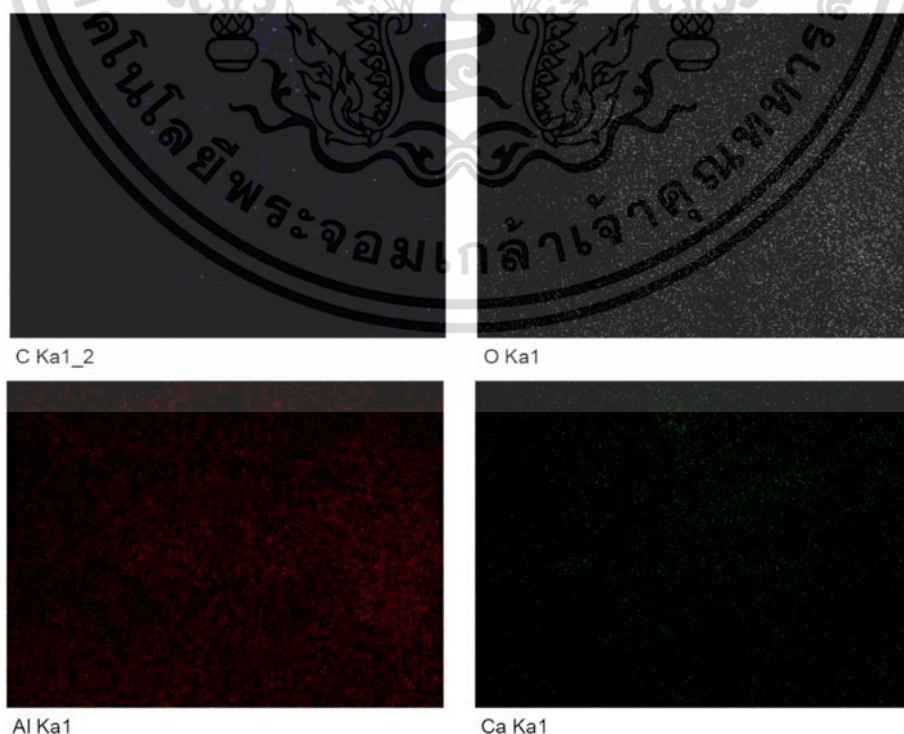


Fig. 8. Element distribution map of the synthesized 4%rGO-C3AH6 samples.

เอกสารนี้เป็นเอกสารที่สงวนลิขสิทธิ์ของมหาวิทยาลัยเทคโนโลยีพระจอมเกล้าเจ้าคุณทหารลาดกระบัง. การนำเอกสารนี้ไปใช้โดยไม่ได้รับอนุญาตถือว่าผิดกฎหมาย. กรุณาแจ้งเจ้าของเอกสารทุกครั้งที่มีการนำไปใช้

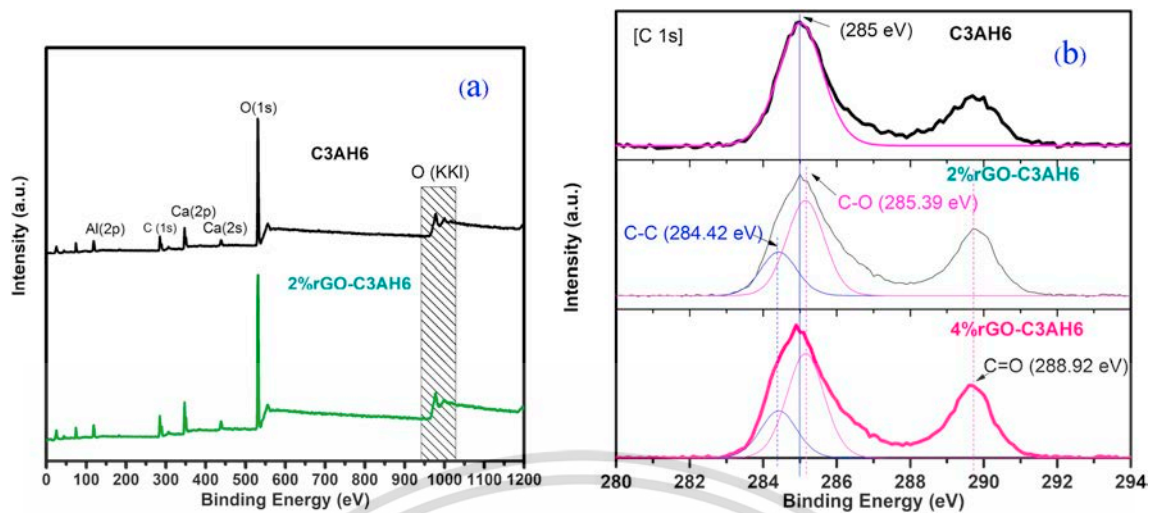


Fig. 9. (a) XPS survey spectra of the synthesized C3AH6 and 2%rGO-C3AH6 samples and (b) XPS survey spectra of C(1s) of the synthesized C3AH6, 2%rGO-C3AH6 and 4%rGO-C3AH6 samples.

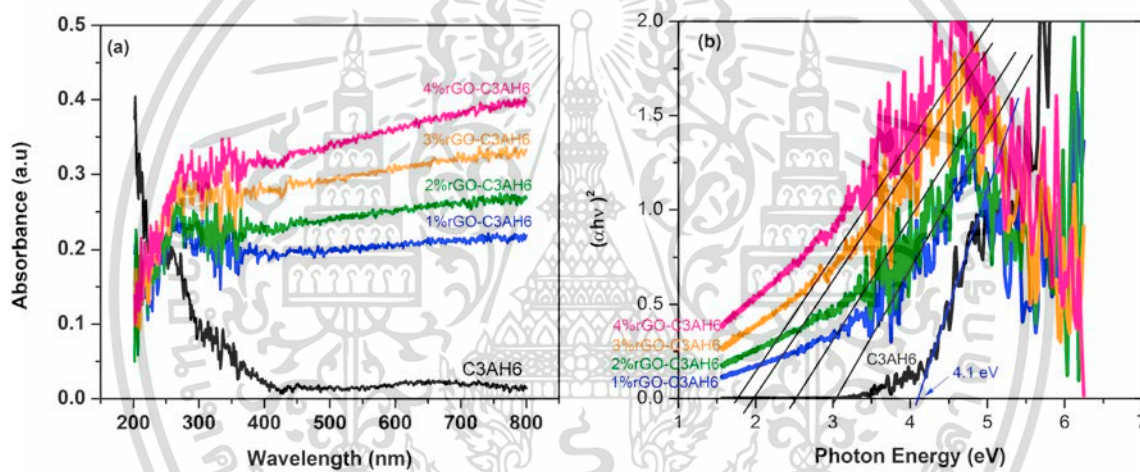


Fig. 10. (a) Absorption coefficient of synthesized C3AH6 and x%rGO-C3AH6 nanocomposites with various rGO contents (1%, 2%, 3% and 4 wt%) and (b) the relationship between an allowed direct optical gap of C3AH6 and x%rGO-C3AH6 nanocomposites.

Fig. 11 displays a suggested scheme illustrating the nanometer sized C3AH6 undergoing rapid heating from room temperature to 100 °C and formation of nanocomposited rGO-C3AH6 via a hydration process with rGO colloid rapid heated for 1 h. The schematic presents the Ca12A14O33 structure reacting with water to form a new nanostructural C3AH6 hydrogarnet cement via a hydration process. In same way, nanostructural C3AH6 was grown on the surface of rGO nanosheets to form a nanocomposited rGO-C3AH6. Consequently, the nanostructure of C3AH6 hydrogarnet cement was successfully loaded onto the surface of rGO nanosheets and formed a nanocomposited rGO-C3AH6 structure. The reaction implies that the volume fraction of rGO significantly affected the grain sizes of the nanocomposites. The grain sizes increased as the percent volume of rGO was increased. The size of C3AH6 hydrogarnet cement particles was limited them by pore size resulting from the density of rGO nanosheets. The regulating mechanism of the C3AH6 nanocomposite formation was affected by the rGO surface providing nucleation sites for C3AH6 hydration. The particle size of the x%rGO-C3AH6 nanocomposite can be controlled by varying the percent volume of rGO nanoflakes in the preparation process during the reaction of the Ca12A14O33 cement precursor with rGO colloid, as depicted in Fig. 11.

8. The properties of rGO-C3AH6 nanocomposites

8.1. Micro-hardness properties

In investigating the improvement of the mechanical properties of the nanocomposited rGO-C3AH6 cement, the x%rGO-C3AH6 nanocomposites samples were tested using a micro-hardness determination method. The micro-hardness of the prepared nanometer sized C3AH6 and synthesized x%rGO-C3AH6 ($x = 1, 2, 3$ and 4) samples were evaluated using the method of a pyramid on a square base according to the Vickers indenter hardness (HV) technique. This technique determines micro-hardness by defining of the ratio of the load applied to the projected area of the indentation following the relationship [26], $HV = 1854(P/d^2)$, where HV is the Vickers micro-hardness value, P is the applied load in kg and d is the average diagonal length of the impression in mm. In testing, a load of 2 kg was applied for 5 s during mechanical tests. The tests were repeated in five different regions on the surface for each sample and average values calculated. Fig. 12 shows an image of the diagonal length of the impression on the surface of C3AH6 and x% rGO-C3AH6 nanocomposited ($x = 1, 2, 3$ and 4 wt%) samples. The image was magnified by a factor of 10 from the machine. The obtained d values were 0.225, 0.216, 0.202, 0.1827 and 0.167 mm for the

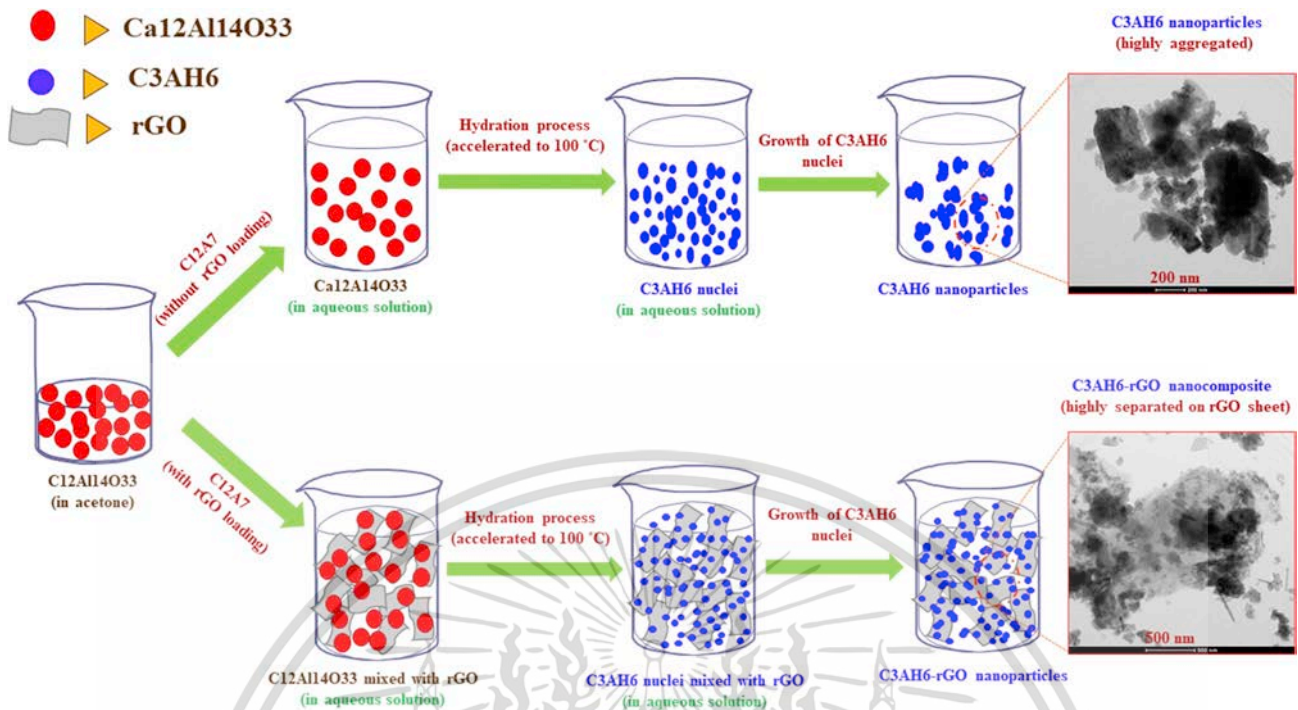


Fig. 11. Schematic illustration of the procedure for synthesis of rGO-C3AH6 nanocomposites and the differences between the two processes to procedure nanometer sized C3AH6 and nanocomposited rGO-C3AH6.

nanometer sized C3AH6 and nanocomposited 1%, 2%, 3%, and 4% rGO-C3AH6 samples, respectively. It was observed that the dark brown colour of the surface of the C3AH6 and x%rGO-C3AH6 nanocomposited (x = 1%, 2%, 3% and 4 wt%) samples increased with the weight percent of rGO.

The HV values of nanometer sized C3AH6 sample and nanocomposited 1%, 2%, 3%, and 4% rGO-C3AH6 samples are shown in Fig. 13. These HV values were 73.8, 80.2, 90.2, 1101, and 132.4 HV/2 kg, respectively. It can be seen that the HV values increased by a power of two with increased weight percent of rGO. The results revealed that improvement of rGO-C3AH6 cement composites reflected by the HV value was seen in the nanometer sized rGO-C3AH6 nanocomposites. In the TEM results, the decreased sizes of the nanocomposited rGO-C3AH6 specimens were affected by an increasing weight percent of rGO that enhanced the HV value. The micro-hardness of nanocomposited rGO-C3AH6 cement specimens was affected by the amount of nanocomposite in the samples.

8.2. Dielectric properties

To evaluate dielectric properties of the x%rGO-C3AH6 nanocomposites (x = 1, 2, 3 and 4), the values of electric capacitance (C) and resistance (R) of the specimens were measured using an impedance analyzer. Specimens of C3AH6 cement and x%rGO-C3AH6 nanocomposites were hot-pressed into disc shapes using ceramic molds with side areas of 128 mm² with an inter-electrode distance of 1.3 mm. The two parallel surfaces of each specimen were sputter coated with gold for Ohmic contact. These measurements were done over the frequency range of 20 Hz–2 MHz.

The complex dielectric constant (κ), which is the relative complex permittivity (ϵ_r) describing the interaction of a material within an electric field E , consists of a real part (ϵ') that represents energy storage and an imaginary part (ϵ'') representing energy loss. The real part of complex permittivity (dielectric constant, ϵ') is defined as the energy stored inside as material in an applied external electric field. The imaginary part of complex permittivity (ϵ'') represents a loss factor of

dissipated energy for a material in an external electric field. The relative complex permittivity (ϵ_r) is a combination of the real (ϵ') and imaginary complex permittivity (ϵ'') terms expressed as [27,28]:

$$\epsilon_r = \epsilon' + i\epsilon'' = \epsilon_\infty + \frac{\epsilon_s - \epsilon_\infty}{1 + i2\pi f\tau_0} \quad (1)$$

where f is frequency, τ_0 is the polarization relaxation time, ϵ_s is the stationary permittivity and ϵ_∞ is the optical dielectric constant at a high frequency limit. The real complex permittivity (ϵ') can be expressed as:

$$\epsilon' = \epsilon_\infty + \frac{\epsilon_s - \epsilon_\infty}{1 + (2\pi f\tau_0)^2} \quad (2)$$

The imaginary complex permittivity (ϵ''), i.e., loss factor, can be expressed as:

$$\epsilon'' = \frac{2\pi f\tau_0(\epsilon_s - \epsilon_\infty)}{1 + (2\pi f\tau_0)^2} + \frac{\sigma(T)}{2\pi f\epsilon_0} \quad (3)$$

The loss factor relation (ϵ'') is a summation of the effects of the dielectric loss (first term) and the effects of conductivity (second term). In the above equation, the relationship between ϵ' and ϵ'' can be expressed as:

$$\left(\epsilon' - \frac{\epsilon_s + \epsilon_\infty}{2}\right)^2 + (\epsilon'')^2 = \left(\frac{\epsilon_s - \epsilon_\infty}{2}\right)^2 \quad (4)$$

Additionally, the ratio of the imaginary part of complex permittivity to the real part defines a loss tangent ($\tan \delta$), expressed as $\tan \delta = \epsilon''/\epsilon'$. Furthermore, the AC conductivity of dielectric materials can be expressed as a summation of two terms, $\sigma_{ac}(T) = \sigma_0(T) + \sigma(\omega, T)$, where $\sigma_0(T)$ denotes the frequency that is independent of the DC conductivity term associated with the drifting of charge carriers. $\sigma(\omega, T)$ represents the frequency dependence of the AC conductivity term associated with dielectric relaxation affected by the localized electric charge carriers (with a value of less than 1 at room temperature). AC conductivity (σ_{ac}) can be expressed as:

$$\sigma_{ac} = \epsilon' \epsilon_0 (2\pi f) \tan \delta$$

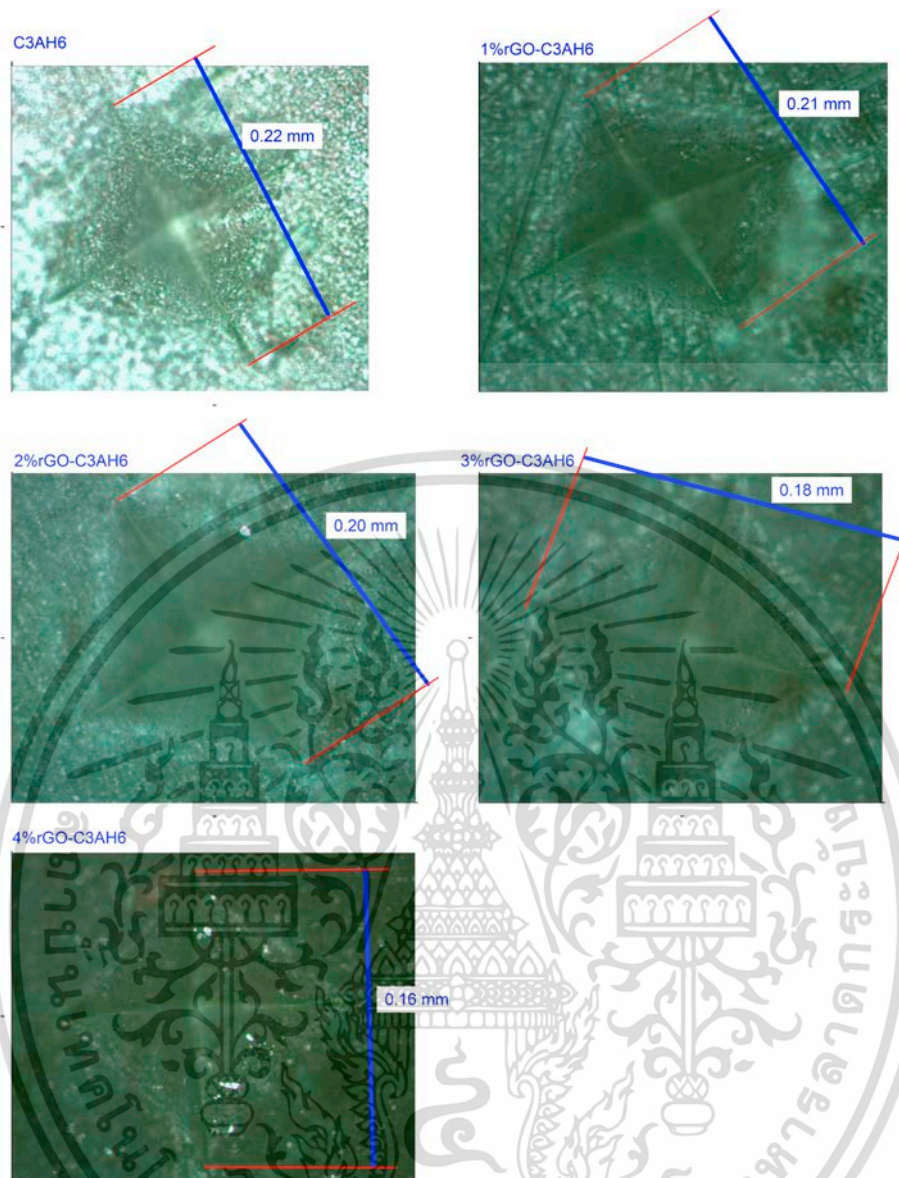


Fig. 12. Diagonal length of the impression on surfaces of synthesized C3AH6 and x%rGO-C3AH6 nanocomposite cements with various rGO contents (x = 1%, 2%, 3% and 4 wt%).

Experimentally, the values of capacitance (C) and resistance (R) were used to calculate the real (ϵ') and imaginary complex permittivities (ϵ''). The ϵ' value was calculated from the equation, $\epsilon' = (Ct)/(\epsilon_0 A)$ [29], where t is the thickness of the pellet sample, C is the capacitance of the specimen, A is the area of the circular pellet sample and ϵ_0 is the permittivity of free space (8.85×10^{-12} F/m). The ϵ'' value was determined from the equation, $\epsilon'' = \epsilon' / 2\pi fRC$.

Fig. 14 shows the frequency response of the dielectric constant, dielectric loss and AC electrical conductivity of the C3AH6 cement and x%rGO-C3AH6 nanocomposites. Fig. 14 (a) shows the frequency dependence of the real complex permittivity (ϵ') or real part of the dielectric constant of C3AH6 and x%rGO-C3AH6 (x = 1, 2, 3 and 4) over the frequency range of 20 Hz to 2 MHz. The results show that the dielectric response of the C3AH6 and x%rGO-C3AH6 samples had strong frequency dependence. The real complex permittivity (dielectric constant) of all samples decreased with increasing frequency. The ϵ' values of the samples at low frequency were greater than that at high frequency. The ϵ' value of C3AH6 was 1.52×10^2 at 20 Hz, and those of x%rGO-C3AH6 were 4.45×10^2 , 6.86×10^2 , 1.010×10^3 and 3.2×10^3 for x = 1, 2, 3

and 4, respectively, at 20 Hz. It was found that the ϵ' values of x%rGO-C3AH6 (x = 1, 2, 3 and 4) samples were higher than that of C3AH6. The dielectric constant of the 4%rGO-C3AH6 sample was approximately 10 times greater than that of the nanometer sized C3AH6 sample. The ϵ' value of 4%rGO-C3AH6 (3.2×10^3) displayed nearly giant dielectric magnitude. The dielectric constant of x%rGO-C3AH6 was increased with the weight percent of rGO composite, corresponding to the decreased particle size of the x%rGO-C3AH6 nanocomposites. This implies that dielectric constants of the nanocomposited rGO-C3AH6 samples were enhanced by the decreasing particle sizes of the x%rGO-C3AH6 specimens.

The above results showed that the dielectric constant values of x%rGO-C3AH6 were greater than that of C3AH6 over the entire frequency range and the values increased with the reduced particle sizes in the samples. The x%rGO-C3AH6 samples displayed a homogeneous nanometer sized particle distribution. The enhanced ϵ' values of x%rGO-C3AH6 can be described by the Maxwell-Weigner model, which relates interfacial polarizations at a conductor-insulator interface. The model describes a dielectric medium containing linked boundaries between

เอกสารนี้เป็นเอกสารที่สงวนไว้สำหรับการใช้งานเพื่อการศึกษาเท่านั้น ไม่อนุญาตให้เผยแพร่โดยไม่ได้รับอนุญาต

ไม่ว่ากรณีใดๆ ทั้งสิ้น อีกทั้งห้ามมิให้คัดลอกเนื้อหา และต้องอ้างอิงถึงเจ้าของเอกสารทุกครั้งที่มีการนำไปใช้

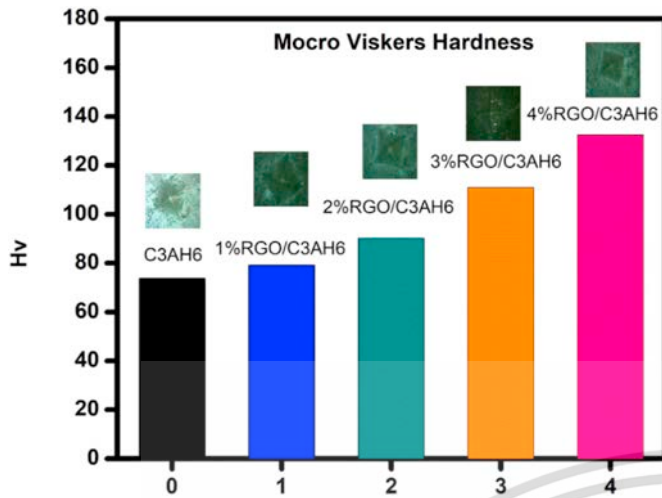


Fig. 13. Micro-hardness of synthesized C3AH6 and x%rGO-C3AH6 nanocomposited cements.

conducting grains and poorly conducting grain boundaries acting as insulators. Since dielectric materials are influenced by external electric fields, the charge carriers stayed at the grain boundaries to generate large degrees of polarization and the dielectric constant. The appearance of a polarization effect in x%rGO-C3AH6 was due to the large number of oxygen vacancies or small pores at the grain boundaries. The polarization process in dielectric materials resulted from the presence of a large

number of defects in the form of oxygen vacancies, micro-pores and dangling bonds. The particle size of nanocomposited x%rGO-C3AH6 was reduced by an increasing amount of nanoflaked rGO in the composite. This implied that the enhancement of ϵ' values at low frequencies in x%rGO-C3AH6 was affected by the nanograin boundary size, which was reduced with increasing amounts of rGO. The nanometer sized particles of the x%rGO-C3AH6 nanocomposites caused a large dielectric constant. The dielectric constant increased with the weigh percent of rGO. The results show that the surfaces of rGO nanocomposites played an important role in enhancing the dielectric constant by controlling the dispersion of rGO sheets and the surface interface between the conducting grains and poorly conducting grain boundaries.

The loss tangent ($\tan \delta$) represents energy dissipation in a dielectric material. Fig. 14 (b) shows the tangent loss of the C3AH6 and x%rGO-C3AH6 samples. The loss tangents of C3AH6 and x%rGO-C3AH6 were found to decrease with increasing frequency. The loss tangents of x% rGO-C3AH6 nanocomposites were greater than that of C3AH6 over the entire frequency range studied. The 4%rGO-C3AH6 nanocomposite had the highest loss tangent. These results showed that the loss tangent of x% rGO-C3AH6 increased with the amount of rGO. The loss tangent trend for x%rGO-C3AH6 nanocomposite linearly increased with the rGO content. This behavior was described at high frequency and is related to dipolar relaxation. At lower frequencies, it is related to interfacial polarization and conductivity. This effect was correlated to the surface morphology of rGO nanocomposites with C3AH6 arising from the dispersion of rGO sheets and the surface interface between the conducting grains and insulating grain boundaries. Fig. 14 (c) shows the AC electrical conductivity (σ_{ac}) of nanometer sized C3AH5 cement and x% rGO-C3AH6 nanocomposited specimens vs. the weight percent of rGO at

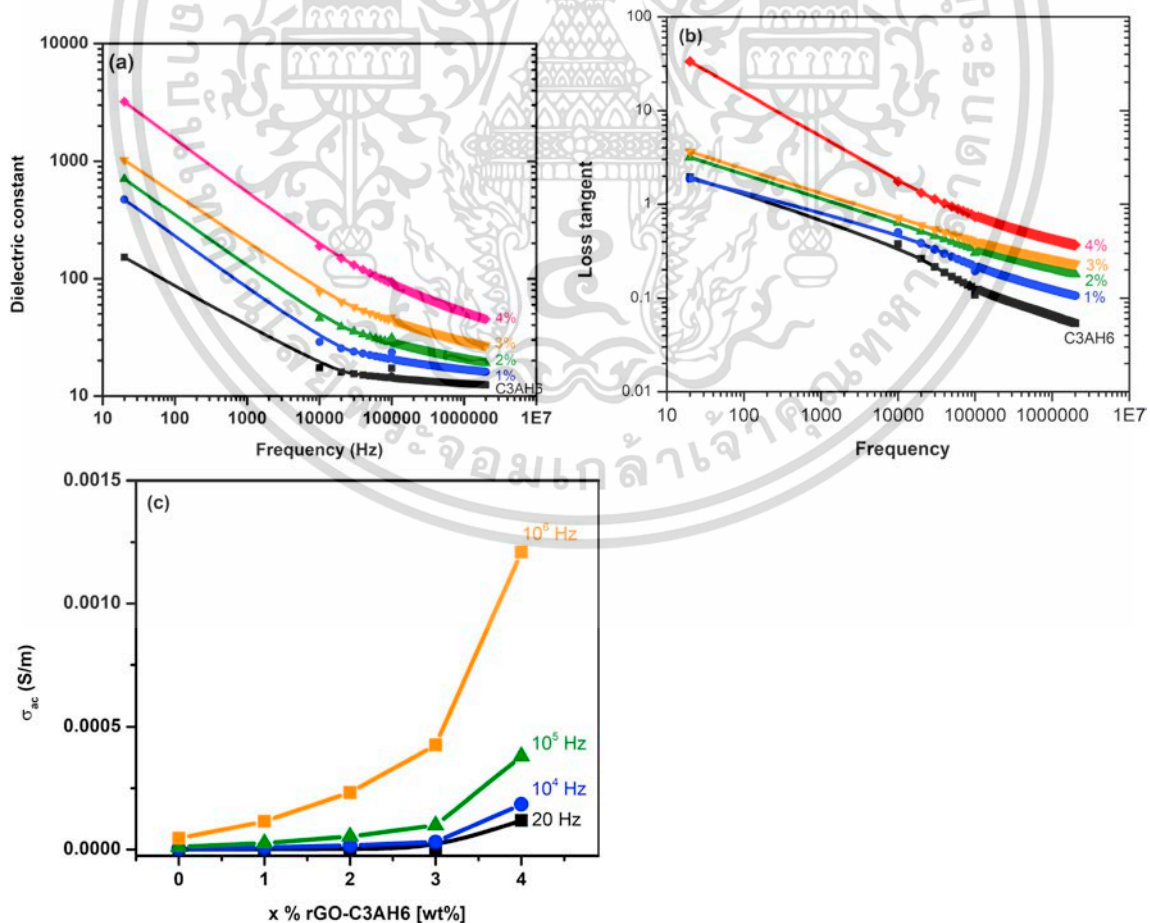


Fig. 14. (a) Dielectric constant and (b) dielectric loss as a function of frequency, and (c) electrical conductivity of C3AH6 and rGO-C3AH6 nanocomposites vs. rGO content (1%, 2%, 3% and 4 wt%).

20, 10^4 , 10^5 , 10^6 MHz. The AC conductivity of these specimens was found to increase with the rGO content. The σ_{ac} values of the x%rGO-C3AH6 nanocomposites were larger than that of C3AH6 over the entire frequency range under study. The 4%rGO-C3AH6 nanocomposite displayed the highest σ_{ac} values. The σ_{ac} of x%rGO-C3AH6 increased with the rGO content. The electric conductivity of x%rGO-C3AH6 nanocomposites arose from the homogenous dispersion of rGO sheets in the material promoting the conductivity of the materials.

From the above results, the synthesized nanometer sized C3AH6 and nanocomposited x%rGO-C3AH6 samples were evaluated electrochemically for applications in energy storage as supercapacitors [3]. The electrochemical properties were measured using cyclic voltammetry and the galvanostatic charge–discharge method. Fig. 15 shows the CV response obtained for the synthesized nanometer sized C3AH6, nanocomposited 2%rGO-C3AH6 and 4%rGO-C3AH6 modified electrodes at a scan rate of 50 mV/s. These observations showed a weak oxidation peak current response of the nanometer sized C12AH6, nanocomposited 2% rGO-C3AH6 and 4%rGO-C3AH6 modified electrodes of 0.001, 0.005, and 0.045 V, respectively.

This result indicates that all sample displayed the behavior of supercapacitors. The 4%rGO-C3AH6 modified electrode had enhanced performance that was greater than that of the nanometer sized C3AH6 due to the effect of rGO nanosheets composited with C3AH6 cement. While, the performance of the 4%rGO-C3AH6 modified electrodes was more enhanced than that of 2%rGO-C3AH6 due to its smaller particle sizes, ~ 40 nm for 4%rGO-C3AH6 vs. ~ 100 nm for 2%rGO-C3AH6. The 4%rGO-C3AH6 nanocomposite showed an oxidation peak current response at 0.045 that was 45 and 9 fold higher, respectively, than those of nanometer sized C3AH6 cement and 2%rGO-C3AH6. This shows that the particle size of nanocomposited rGO-C3AH6 played a significant role in the enhancement of the oxidation peak for its electrochemical properties. The enhanced activity of the 4%rGO-C3AH6 nanocomposite may have been due to an enrichment effect via diffusion within the modified electrode and the high useful surface area of rGO. Free electron charge transfer between the material and electrode surface was increased by the presence of rGO nanosheets composited with the cement. The bulk electrode served as an adsorption matrix for its surface with a strong π - π effect from the rGO composite and cement media interaction within the material. This indicated that the rGO-C3AH6 nanocomposites were effective for supercapacitor applications.

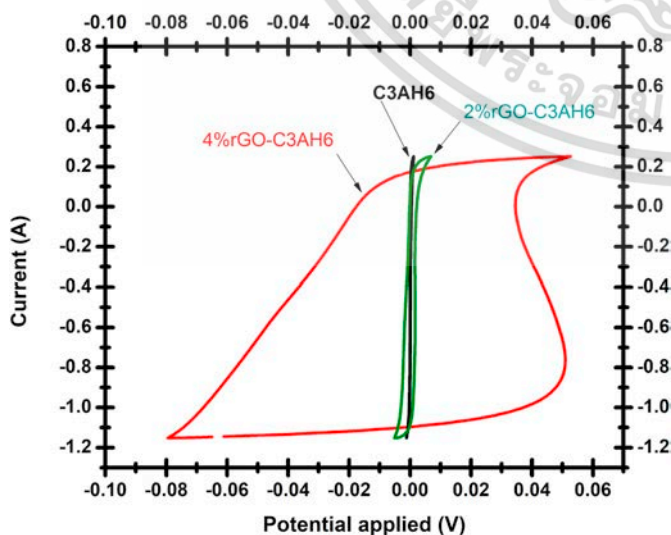


Fig. 15. Cyclic voltammetry (CV) of synthesized nanometer sized C3AH6, nanocomposited 2%rGO-C3AH6 and 4%rGO-C3AH6 modified electrodes at a scan rate of 50 mV/s.

8.3. Thermal (TG) properties

To understand the thermal stability and phase transformation of nanometer sized C3AH6 cement hydrate and the nanocomposited x% rGO-C3AH6 samples, thermogravimetric (TG) and the derivative thermogravimetry (DTG) techniques were carried out. The TG and DTG analyses of the thermal stability of nanosized C3AH6 and the x%rGO-C3AH6 nanocomposite, where $x = 2\%$ and 4% , are shown in Fig. 16. Fig. 16 (a) and (b) show results of TG and DTG analyses of the 2%rGO-C3AH6 and 4%rGO-C3AH6 nanocomposited samples. There is similarity to the nanosized C3AH6 cement hydrate, its four stages of weight loss (%) and endothermic peaks in the range of 35°C – 900°C . In the first stage, at around 35°C – 200°C , an endothermic peak was due to the removal of physically absorbed water from the cement surfaces [30,31], while the second stage at around 200°C – 320°C was due to the decomposition of water (in crystals), aluminium hydroxide ($\text{Al}(\text{OH})_3$) and amorphous anhydrous [32,33]. In the next stage, decomposition of nanosized C3AH6 cement occurred with an accompanying phase transformation to C3AH1.5 at temperatures of around 320°C – 550°C [8]. Finally, in the fourth stage of the weight loss, an endothermic peak at around 550°C – 740°C was observed that can be attributed to the decomposition of C3AH1.5 cement as well as its phase transformation to a stable $\text{Ca}_{12}\text{Al}_{14}\text{O}_{33}$ structure.

For comparison with the nanometer sized C3AH6 cement, the residual weight % at above 740°C of the nanocomposited x%rGO-C3AH6 samples was slightly increased with rGO loading. The x%rGO-C3AH6 samples had a higher decomposition temperature than those of nanosized C3AH6 cement in both the second and fourth stages in the DTG curve, as shown in Fig. 16(b). The maximum decomposition and the phase transformation temperatures of the nanocomposited C3AH6, the 2%rGO-C3AH6 and the 4%rGO-C3AH6 samples shifted to the higher temperatures, from 707°C to 718°C , as can be seen in Fig. 16(b). This result shows that enhancement of the thermal and phase stability of the nanocomposited x%rGO-C3AH6 cements was affected by incorporation of C3AH6 nanoparticles with rGO nanosheets. Based on a previous study [34], the loaded rGO in materials have high thermal stability. Thus, beneficial heat transfer properties (high thermal resistance) result without increasing the material temperature which contributes to the increased activation energy of these composite cements [35]. For this reason, nanocomposited rGO-C3AH6 cements are more thermodynamically stable than nanometer sized C3AH6 cement. There are many potential applications for these materials in the field of smart cements due to their thermal resistance, among other useful properties.

The thermal conductivity of nanocomposited x%-rGO-C3AH6 ($x = 1\%$, 2% , 3% and 4%) and C3AH6 samples were measured over the temperature range from 300 K to 550 K using a laser flash technique. The samples were hot-pressed into disc shaped pellets, 12 mm in diameter and 3 mm thick. The thermal conductivity (κ) was determined using the relationship, $\kappa = aD C_p$ [29], where a , D and C_p are the thermal diffusivity, the bulk density, and the specific heat of the sample materials, respectively. The density of the samples was evaluated by the Archimedes method yielding 1.584 g/cm^3 for the C3AH6 sample and 1.712 g/cm^3 , 1.764 g/cm^3 , 1.782 g/cm^3 and 1.860 g/cm^3 for the 1%, 2%, 3% and 4% rGO-C3AH6 samples, respectively. The thermal diffusivity for the samples was evaluated using Parker's formula as $a = 0.139d_T^2/t_{(1/2)}$ [17], where, $t_{(1/2)}$ is the time to reach half of the maximum temperature amplitude, and d_T is the thickness of the bulk samples in the direction of heat flow.

Fig. 17(a) shows thermal conductivity as a function of the temperature for the 1%, 2%, 3%, 4%rGO-C3AH6 and C3AH6 samples. The κ values of all samples changed little with temperature. These values for the x%rGO-C3AH6 samples were greater than that of the C3AH6 sample and decreased with increasing amounts of rGO. High rGO contents in x% rGO-C3AH6 nanocomposites caused reduced κ values.

The thermal conductivity, κ , can be expressed as $\kappa = \kappa_e + \kappa_{\text{phonon}}$,

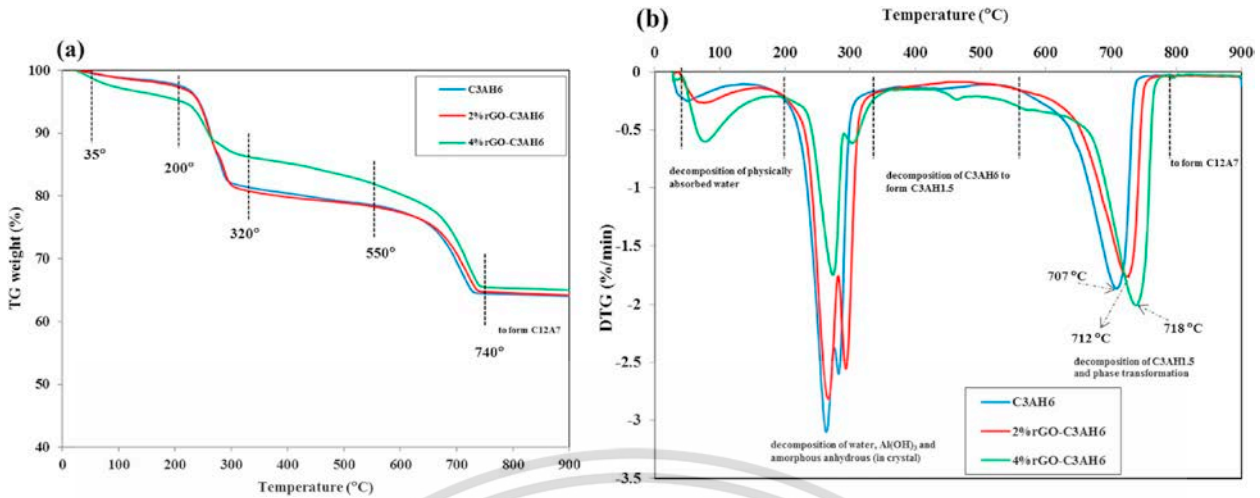


Fig. 16. (a) The thermogravimetric (TG) analysis and (b) the derivative thermogravimetry (DTG) curve of synthesized nanometer sized C3AH6 and nanocomposited x%rGO-C3AH6 samples with various rGO contents (x = 2, and 3 wt%).

where κ_e is the thermal conductivity of electronic part and κ_{phonon} is the thermal conductivity of phonon part. The κ_e value can be obtained from the relationship, $\kappa_{el} = L_0 T \sigma$, where L_0 is the Lorenz factor ($L_0 = 2.45 \times 10^{-8} \text{ W}\Omega/\text{K}^2$), T is the absolute temperature, and σ is electrical conductivity.

From the AC electrical conductivity shown in Fig. 17 (b), the κ_e values of the x%rGO-C3AH6 (x = 1%, 2%, 3% and 4%) and C3AH6 were

small. The magnitude of κ values of all samples was primarily influenced by κ_{phonon} . If the κ_e value is neglected, the thermal conductivity of κ_{phonon} part can be expressed as:

$$\kappa_{phonon} = \frac{k_B}{2\pi^2\nu} \left(\frac{k_B T}{\hbar}\right)^3 \int_0^{\omega_p} (\tau_{ph}) \frac{x^4 e^x}{(e^x - 1)^2} dx \quad [36], \text{ where } x = \hbar\omega/k_B T. \text{ The } \hbar, \omega, \nu \text{ and } \tau_{ph} \text{ values are the reduced Planck constant, the phonon}$$

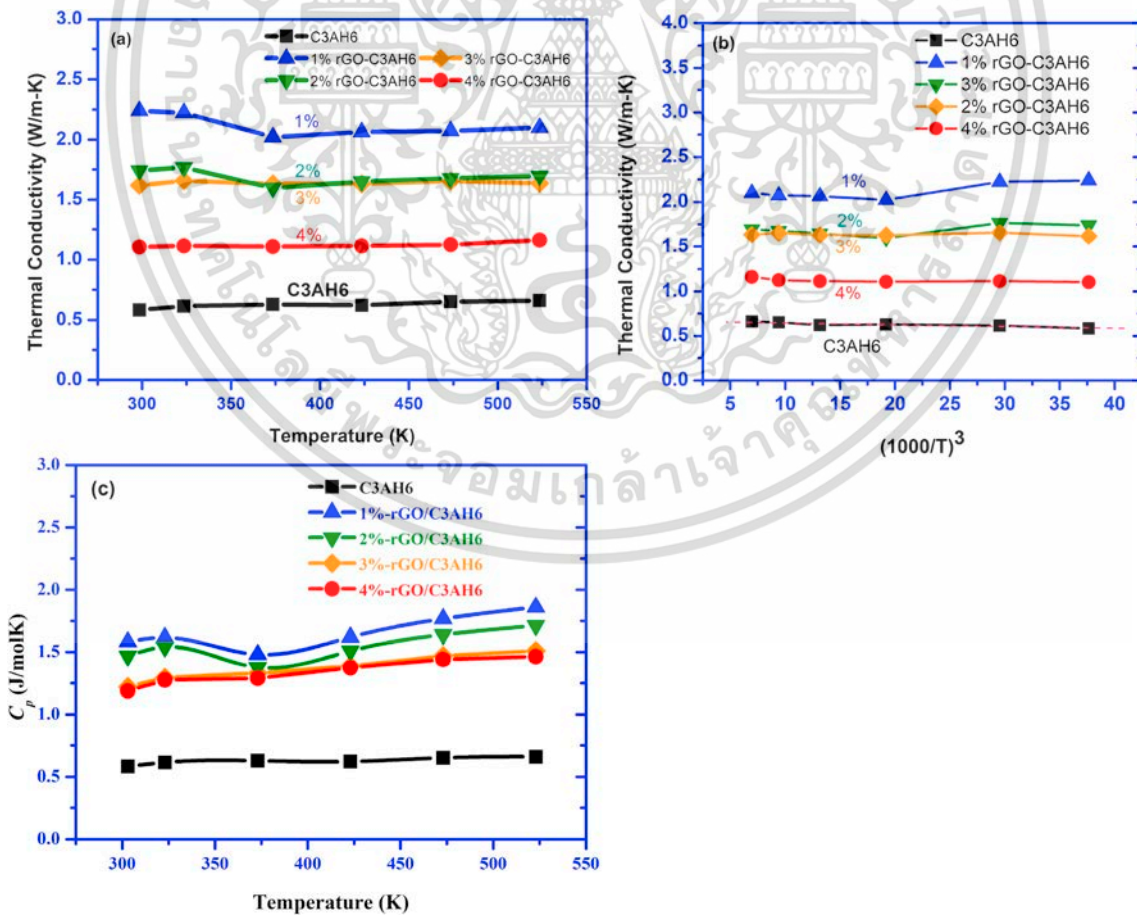


Fig. 17. (a) Thermal conductivity of synthesized C3AH6 and xrGO-C3AH6 nanocomposite samples with various rGO contents (1%, 2%, 3% and 4 wt%) as a function of temperature, (b) thermal conductivity of C3AH6 and xrGO-C3AH6 samples as a function of inverse of temperature, and (c) Specific heat of synthesized C3AH6 and xrGO-C3AH6 nanocomposite samples.

angular frequency, the velocity of sound and the phonon relaxation time, respectively. The τ_{ph} value can be expressed as, $\frac{1}{\tau_{ph}} = \frac{1}{\tau_B} + \frac{1}{\tau_U} + \frac{1}{\tau_P}$, where, τ_U is the phonon-phonon processes, τ_P is a point defect, and τ_B is the grain boundary. The τ_U , τ_P and τ_B values are given by $\frac{1}{\tau_U} = (B)\omega^2 T^3$, $\frac{1}{\tau_P} = A\omega^4$ and $\frac{1}{\tau_B} = v/L$, respectively, where ω is the phonon angular frequency, A and B are parameters independent of temperature, v is the phonon group velocity and L is the characteristic grain size.

Fig. 17 (a) shows the relationship, κ_{phonon} versus $1/T^3$, for the x%rGO-C3AH6 (x = 1%, 2%, 3% and 4%) and C3AH6 samples. The results indicated that only C3AH6 had an inverse relationship with temperature, implying that the thermal conductivity of only C3AH6 was primarily influenced by phonon-phonon processes (τ_U). The x%rGO-C3AH6 (x = 1, 2, 3 and 4) samples did not display this behavior.

Clearly, the nanocomposite effect of the x%rGO-C3AH6 specimens was affected by the grain boundary ($\frac{1}{\tau_B} = v/L$) term. L , the characteristic grain size of the x%rGO-C3AH6 nanocomposites, was nanometer sized. Also, the nanometer sized grain characteristic acted to reduce the κ_{phonon} value of the x%rGO-C3AH6 nanocomposites. The reduction of thermal conductivity of the x%rGO-C3AH6 samples resulted from the smaller particle sizes at the boundary. They were reduced from 20 nm to 10 nm as the volume percent of the rGO nanoflakes was increased during the preparation process. The rGO nanocomposite content in C3AH6 played an important role in development of the thermal conductivity of x%rGO-C3AH6 nanocomposites.

The specific heat (C_p) values of the C3AH6 and x%rGO-C3AH6 samples were obtained by thermal diffusivity measurements over a temperature range of 298–573 K by a laser flash technique. Fig. 17(c) shows C_p as a function of the temperature of the x%rGO-C3AH6 and C3AH6 samples. The results reveal that the C_p value of all samples increased with temperature. The C_p of 1%rGO-C3AH6 and 2%rGO-C3AH6 was greater than the C3AH6 cement, while 3%rGO-C3AH6 and 4%rGO-C3AH6 had lower C_p values. The lower rGO content in x%rGO-C3AH6 composites caused higher C_p values. This trend for x%rGO-C3AH6 showed a decrease in C_p with increasing amounts of rGO. The high rGO content in x%rGO-C3AH6 composites reduced the C_p values.

8.4. Antibacterial properties

The anti-bacterial activities of nanocomposited rGO-C3AH6 samples were measured. These properties of the prepared C3AH6 and x%rGO-C3AH6 nanocomposite cements were tested using an agar disk-diffusion method against a Gram negative bacterium, *Escherichia coli* (*E. coli*) and the results are shown in Fig. 18. It was observed that nanometer sized C3AH6 cement produced no clear zone indicating that it was ineffective in killing bacteria. The 12 mm red line in the figure represents the diameter of a C3AH6 pellet. The x%rGO-C3AH6 nanocomposited cements showed clear zones indicating antibacterial activity against *E. coli*. The width of clear zones produced by the x%rGO-C3AH6 (1%rGO-C3AH6, 2%rGO-C3AH6 and 3%rGO-C3AH6) nanocomposite samples increased with the level of rGO loading. 4%rGO-C3AH6 cement produced the greatest degree of antibacterial activity against *E. coli*. This indicates that the antibacterial property of the x%rGO-C3AH6 cement is correlated with the level of rGO in the nanocomposited cement and with the smaller particle sizes, 10–20 nm, of x%rGO-C3AH6. The antibacterial action of the nanocomposited x%rGO-C3AH6 was due to the extraction of phospholipids from lipid membranes [37], producing strong interactions with these molecules in bacterial cell membranes. These results confirmed the importance of reduced particle size to produce increased rGO content within the nanocomposited x%rGO-C3AH6 cements and concurrent increased antibacterial activity.

Clearly, the experimental results from the nanocomposited x%rGO-C3AH6 cements confirmed that these specimens produced multifunctional material properties, including enhanced micro-hardness and dielectric constant, as well as improved electrochemical properties and antibacterial activity. Thermal conductivity and electrical resistance were lowered with nanometer sized particles and rGO loading.

9. Conclusions

Nanocomposited rGO – C3AH6 cements, with particle size diameters of 10–20 nm, were successfully synthesized from a Ca12A114O33 precursor and rGO colloid by rapid heating with water at 100 °C. The properties of nanocomposited x%rGO-C3AH6 materials was confirmed

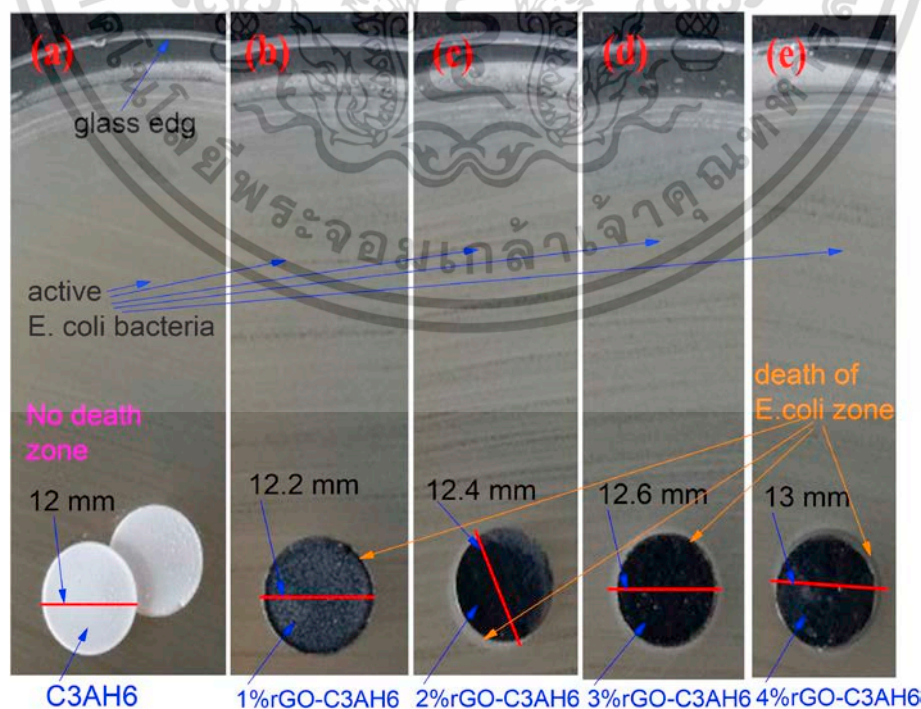


Fig. 18. Antibacterial properties of (a) the synthesized nanometer sized C3AH6 and x%rGO-C3AH6 nanocomposite samples with various rGO contents of (b) 1%, (c) 2%, (d) 3% and (e) 4 wt% against Gram negative *Escherichia coli* (*E. coli*).

by the XRD peaks corresponding to the standard C3AH6 hydrate cement. The presence of nanocomposited x%rGO-C3AH6 was confirmed by Raman spectra peaks, FT-IR spectra, UV-visible spectra, XPS spectra, TGA analysis and TEM surface morphology images. The experimental results revealed nanometer sized x%rGO-C3AH6 particles with small pore sizes and dense rGO nanosheets. Nanocomposited x%rGO-C3AH6 was produced at various rGO weight percentages. The mechanism of action of C3AH6 on the 2-D rGO composite was to present nucleation sites on the surfaces of the growing C3AH6 hydration products. The nanocomposited rGO-C3AH6 specimens showed greater Vickers micro-hardness values with increasing rGO content. They displayed high dielectric constants, close to those of giant dielectric materials and increased electric conductivity as the rGO content was increased. Thermal conductivity tended to be reduced with increasing levels of rGO-C3AH6 in the nanocomposites. The electrochemical properties of nanocomposited rGO-C3AH6 cement compounds were improved by nanometer sized particles playing a significant role in the enhancement of oxidation peaks. Additionally, nanocomposited rGO-C3AH6 cements displayed greater antibacterial activity against *E. coli* as the particle size was decreased and rGO loading increased. Nanocomposited rGO-C3AH6 displayed properties suitable for high performance multifunctional applications as cement materials, including improved micro-hardness, dielectric constant, electrochemical properties, thermal conductivity and antibacterial activity.

Acknowledgements

C. Ruttanapun would like to thank the Thailand Research Fund (TRF) (Contract Number: MRG6080236) for financial support. C. Phrompet, C. Sriwong, and C. Ruttanapun thank the Thailand Research Fund (TRF) (Contract Number: PHD60I0046) for financial support. Moreover, we express our sincere appreciation to King Mongkut's Institute of Technology Ladkrabang (KMITL) and the Faculty of Science, King Mongkut's Institute of Technology Ladkrabang (KMITL) for funding our research.

Appendix A. Supplementary data

Supplementary data to this article can be found online at <https://doi.org/10.1016/j.compositesb.2019.107128>.

References

- Dimov Dimitar, Amit Iddo, Gorrie Olivier, Barnes Matthew D, Townsend Nicola J, Neves Ana IS, Withers Freddie, Russo Saverio, Graciu Monica Felicia. Ultrahigh performance nanoengineered graphene-concrete composites for multifunctional applications. *Adv Funct Mater* 2018;28:1705183.
- Lee Myoung-Jae, Ahn Ji-Hoon, Sung Ji Ho, Heo Hoseok, Gi Jeon Seong, Woo Lee Jae, Song Yong, Hong Ki-Ha, Choi Byeongdae, Lee Sung-Hoon, Jo Moon-Ho. Thermoelectric materials by using two-dimensional materials with negative correlation between electrical and thermal conductivity. *Nat Commun* 2016;7:12011.
- Purkait Taniya, Singh Guneet, Kumar Dinesh, Singh Mandeep, Sundar Dey Ramendra. High-performance flexible supercapacitors based on electrochemically tailored three-dimensional reduced graphene oxide networks. *Sci Rep* 2018;8:640.
- Phrompet Chaiwat, Sriwong Chaval, Srepusharawoot Pornjuk, Maensiri Santi, Chindaprasirt Prinya, Ruttanapun Chesta. Effect of free oxygen radical anions and free electrons in a $\text{Ca}_{12}\text{Al}_4\text{O}_{33}$ cement structure on its optical, electronic and antibacterial properties. *Heliyon* 2019;5:e01808.
- Imbabi Mohammed S, Carrigan Collette, McKenna Sean. Trends and developments in green cement and concrete technology. *International Journal of Sustainable Built Environment* 2012;1:194-216.
- Dilnesa Belay Zeleke, Lothenbach Barbara, Renaudin Guillaume, Wichser Adrian, Kulik Dmitrii. Synthesis and characterization of hydrogarnet $\text{Ca}_3(\text{Al}_x\text{Fe}_{1-x})_2(\text{SiO}_4)_y(\text{OH})_{4(3-y)}$. *Cement Concr Res* 2014;59:96-111.
- Geng Guoqing, Li Jiaqi, Young-Sang Yu, Shapiro David A, Kilcoyne David AL, Monteiro Paulo JM. Nanometer-resolved spectroscopic study reveals the conversion mechanism of $\text{CaO}\cdot\text{Al}_2\text{O}_3\cdot 10\text{H}_2\text{O}$ to $2\text{CaO}\cdot\text{Al}_2\text{O}_3\cdot 8\text{H}_2\text{O}$ and $3\text{CaO}\cdot\text{Al}_2\text{O}_3\cdot 6\text{H}_2\text{O}$ at an elevated temperature. *Cryst Growth Des* 2017;17:4246-53.
- Phrompet Chaiwat, Sriwong Chaval, Maensiri Santi, Chindaprasirt Prinya, Ruttanapun Chesta. Optical and dielectric properties of nano-sized tricalcium aluminate hexahydrate(C3AH6) cement. *Constr Build Mater* 2018;179:57-65.
- Rong D, Qiu F, Zhang C, Fu L, Wang Y, Yang D. *Ceram Int* 2015;41:2502.
- Jung CH, Hwang IR, Park BH, Yoon DH. Characterization of $12\text{CaO}\cdot 7\text{Al}_2\text{O}_3\cdot \text{O}_3\text{doped}$ indium tin oxide films for transparent cathode in top-emission organic light-emitting diodes. *J Nanosci Nanotechnol* 2013;13:7556-60.
- Hosono H, Kim SW, Miyakawa M, Matsuishi S, Kamiya T. Thin film and bulk fabrication of room-temperature-stable electrode C12A7:e- utilizing reduced amorphous $12\text{CaO}\cdot 7\text{Al}_2\text{O}_3$ (C12A7). *J Non-Cryst Solids* 2008;354:2772-6.
- Kim SW, Toda Y, Hayashi K, Hirano M, Hosono H. Synthesis of a room temperature stable $12\text{CaO}\cdot 7\text{Al}_2\text{O}_3$ electrode from the melt and its application as an electron field emitter. *Chem Mater* 2006;18(7):1938-44.
- Phromviyo Nutthakritta, Thongbai Prasit, Ratchaphonsaenwong Kunthaya, Chanlek Narong, Chindaprasirt Prinya. Dielectric and electrical properties of nano-Ag/C3AH6 nanocomposites. *Appl Surf Sci* 2019;483:294-301.
- Lu GONG, SHEN Jing, Quan-Xin LI. Investigation on the antibacterial activity and mechanism of C12A7-O particles. *J Inorg Mater* 2010;25:943-6.
- Yakovlev Ilya V, Volodin Alexander M, Papulovskiy Evgeniy S, Andreev Andrey S, Lapina Olga B. Structure of carbon-coated C12A7 electrode via solid-state NMR and DFT calculations. *J Phys Chem C* 2017;121(40):22268-73.
- Khan Karim, Tareen Ayesha Khan, Elshahat Sayed, Yadav Ashish, Khan Usman, Yang Minghui, Bibbo Luigi, Ouyang Zhengbiao. Facile synthesis of cationic doped $[\text{Ca}_{24}\text{Al}_{128}\text{O}_{64}]^{4+}$ ($4e^-$) composite via rapid citrate sol-gel method. *Dalton Trans* 2018;47:3819-30. <https://doi.org/10.1039/C7DT04543C>.
- Sedaghat Ahmadreza, Manoj K, Ram, Zayed A, Kamal Rajeev, Shanahan Natallia. Investigation of physical properties of graphene-cement composite for Structural Applications. *J Compos Mater* 2014;4:12-21.
- Li Mao, Kim Jin-man. Strength properties and micro-structure of steel slag based hardened cementitious composite with graphene oxide. In: MATEC web of conferences 138, vol. 03012: 2017.
- Gholampour Aliakbar, Kiamahalleh Meisam Valizadeh, Tran Diana NH, Ozbakkaloglu Togay, Losic Dusan. From graphene oxide to reduced graphene oxide: impact on the physicochemical and mechanical properties of graphene-cement composites. *ACS Appl Mater Interfaces* 2017;9:43275-86.
- Ruttanapun C, Srepusharawoot P, Maensiri S. Effect of Fe³⁺-doped $\text{Ca}_{12}\text{Al}_{14}\text{O}_{33}$ cement on optical and thermal Properties. *Chin J Phys* 2018;56:252-60.
- Okoronkwo MU, Glasser FP. Compatibility of hydrogarnet, $\text{Ca}_3\text{Al}_2(\text{SiO}_4)_x(\text{OH})_{4(3-x)}$, with sulfate and carbonate-bearing cement phases: 5-85 °C. *Cement Concr Res* 2016;83:86-96.
- Nilforoushan Reza M, Talebiaan, Nasrien, Iran J Chem Chem Eng 2007;26:2.
- Zhang W, Li Y, Peng S, Cai X. Beilstein J Nanotechnol 2010;5:801.
- Ly Shenghua, Liu Jingjing, Yujuan TingSun, Zhou MaQingfang. Effect of GO nanosheets on shapes of cement hydration crystals and their formation process. *Constr Build Mater* 2014;64:231-9.
- Fang M, Long J, Zhao W, Wang L, Chen G. pH-Responsive chitosan-mediated graphene dispersions. *Langmuir* 2010;26(22):16771-4.
- Kamalak H, Erdem M, Altin E, Demirel S, Oz E, Altin S. Giant dielectric constant and mechanical, heat conducting and structural properties of dental composites by adding Ca ions. *J Dent Oro Surg* 2016;1(3):112.
- Eufinger J, Schmidt A, Lerch M, Janek J. *Phys Chem Chem Phys* 2015;17:6844.
- Liang B, Song Z, Wang M, Wang L, Jiang W. Fabrication and thermoelectric properties of graphene/ Bi_2Te_3 composite materials. *J. Nanomater.* 2013;2013. p. 6.
- Grosvenor AP, Kobe BA, Biesinger MC, McIntyre NS. *Surf Interface Anal* 2004;36:1564-74.
- Pineda-Aguilar Nayely, Gallegos-Sánchez Víctor J, Sánchez Eduardo M, Torres-González LUIS Carlos, Garza-Tovar Lorena L. Aluminum doped $\text{Na}_3\text{V}_2(\text{PO}_4)_2\text{F}_3$ via sol-gel Pechini method as a cathode material for lithium ion batteries. *J Sol Gel Sci Technol* 2017;83:405-12.
- Rakshit Soumyadipta, Ghosh Srabanti, Chall Sayantani, Mati Soumya Sundar, Moulikak SP, Bhattacharya Subhash Chandra. Controlled synthesis of spin glass nickel oxide nanoparticles and evaluation of their potential antimicrobial activity: a cost effective and ecofriendly approach. *RSC Adv* 2013;3:9348-19356.
- Tchamba AB, Sofack JC, Yongue R, Melo UC. Formulation of calcium dialuminate ($\text{CaO}\cdot 2\text{Al}_2\text{O}_3$) refractory cement from local bauxite. *Journal of Asian Ceramic Societies* 2015;3:164-72.
- Souza Adriane DV, Arruda Cezar C, Fernandes Leandro, Maria L, Antunes P, Kiyohara Pedro K, Salomao Rafael. Characterization of aluminium hydroxide (Al(OH)₃) for use as a porogenic agent in castable ceramics. *J Eur Ceram Soc* 2015;35:803-12.
- George Gejo, Simon Sanu Mathew, Prakashan VP, Sajna MS, Faisal Muhammad, Wilson Runcy, Chandran Anoop, Biju PR, Joseph Cyriac, Unnikrishnan NV. Green and facile approach to prepare polypropylene/in situ reduced graphene oxide nanocomposites with excellent electromagnetic interference shielding properties. *RCS Advances* 2018;8:30412-28.
- Zhang Lin, Li Hongqiang, Lai Xuejun, Su Xiaojing, Liang Tao, Zeng Xingrong. Thiolated graphene-based superhydrophobic sponges for oil-water separation. *Chem Eng J* 2017;316:736-43.
- Guo L, Xu X, Salvador JR, Meisner GP. Coupled vibrational modes in multiple-filled skutterudites and the effects on lattice thermal conductivity reduction. *Appl Phys Lett* 2013;102:111905.
- Prasad Karthika, Lekshmi GS, Ostrikov Kola, Lussini Vanessa, Blinco James, Mohandas Mandhakini, Vasilev Krasimir, Bottle Steven, Bazaka Kateryna, Ostrikov Kostya. Synergic bactericidal effects of reduced graphene oxide and silver nanoparticles against Gram-positive and Gram-negative bacteria. *Sci Rep* 2017;7:1591.

เอกสารนี้เป็นเอกสารที่สงวนไว้สำหรับการใช้งานเพื่อการศึกษาเท่านั้น ไม่อนุญาตให้นำไปใช้ประโยชน์ด้านการค้า

ไม่ว่ากรณีใดๆ ทั้งสิ้น อีกทั้งห้ามมิให้ดัดแปลงเนื้อหา และต้องอ้างอิงถึงเจ้าของเอกสารทุกครั้งที่มีการนำไปใช้



Effect of free oxygen radical anions and free electrons in a $\text{Ca}_{12}\text{Al}_{14}\text{O}_{33}$ cement structure on its optical, electronic and antibacterial properties



Chaiwat Phrompet^{a,b}, Chaval Sriwong^{a,c,f}, Pornjuk Srepusharawoot^{d,f}, Santi Maensiri^{e,f}, Prinya Chindaprasirt^{g,h}, Chesta Ruttanapun^{a,b,f,*}

^a Smart Materials Research and Innovation Unit (SMRIU), Faculty of Science, King Mongkut's Institute of Technology Ladkrabang, Chalokkrung Road, Ladkrabang, Bangkok 10520, Thailand

^b Department of Physics, Faculty of Science, King Mongkut's Institute of Technology Ladkrabang, Chalokkrung Road, Ladkrabang, Bangkok 10520, Thailand

^c Department of Chemistry, Faculty of Science, King Mongkut's Institute of Technology Ladkrabang, Chalokkrung Road, Ladkrabang, Bangkok 10520, Thailand

^d Institute of Nanomaterials Research and Innovation for Energy (IN-RIE), Department of Physics, Faculty of Science, Khon Kaen University, Khon Kaen 40002, Thailand

^e School of Physics, Institute of Science, Suranaree University of Technology, Nakhon Ratchasima 30000, Thailand

^f Thailand Center of Excellence in Physics, Commission on Higher Education, 328 Si Ayuthaya Road, Bangkok 10400, Thailand

^g Sustainable Infrastructure Research and Development Center, Department of Civil Engineering, Faculty of Engineering, Khon Kaen University, Khon Kaen 40002, Thailand

^h Academy of Science, The Royal Society of Thailand, Dusit, Bangkok 10300, Thailand

ARTICLE INFO

Keywords:

Materials science
Civil engineering
Condensed matter physics
Materials chemistry
Bioengineering
Free oxygen radical anions
Optical property
Electronic property
Antibacterial property
 $\text{Ca}_{12}\text{Al}_{14}\text{O}_{33}$ cement

ABSTRACT

The aim of this work was to investigate the effect of free oxygen radicals and free electrons in a $\text{Ca}_{12}\text{Al}_{14}\text{O}_{33}$ (C12A7) cement structure on the optical, electronic and antibacterial activity of this material. $\text{Ca}_{12}\text{Al}_{14}\text{O}_{33}$ was successfully fabricated via rapid heating to high temperatures by high frequency electromagnetic induction. $\text{Ca}_{12}\text{Al}_{14}\text{O}_{33}$ cement samples were characterized using XRD and UV-Vis-DRS spectroscopy. The morphology and chemical composition of the samples were also investigated using SEM and EDS techniques. The presence of free oxygen radicals (O_2^- ions) in the insulating structure of $\text{Ca}_{12}\text{Al}_{14}\text{O}_{33}$ was confirmed using Raman spectroscopy showing a spectrum peak at 1067 cm^{-1} . The excitation of free electrons in the $\text{Ca}_{12}\text{Al}_{14}\text{O}_{33}$ cement was indicated by UV-Vis absorption spectra at 2.8 eV and an optical energy gap of 3.5 eV, which is consistent with the first-principles calculations for the band energy level. The effects of free oxygen radicals and free electrons in the $\text{Ca}_{12}\text{Al}_{14}\text{O}_{33}$ structure as antibacterial agents against *Escherichia Coli* (*E. coli*) and *Staphylococcus Aureus* (*S. aureus*) were investigated using an agar disk-diffusion method. The presence of O_2^- anions as a reactive oxygen species (ROS) at the surface of $\text{Ca}_{12}\text{Al}_{14}\text{O}_{33}$ caused inhibition of *E. coli* and *S. aureus* cells. The free electrons in the conducting C12A7 reacted with O_2 gas to produce ROS, specifically super oxides (O_2^-), superoxide radicals (O_2^{\bullet}), hydroxyl radicals (OH^{\bullet}) and hydrogen peroxide (H_2O_2), which exhibited antibacterial properties. Both mechanisms were active against bacteria without effects from nano-particle sized materials and photocatalytic activity. The experimental results showed that the production of ROS from free electrons was greater than that of the free O_2^- anions in the structure of $\text{Ca}_{12}\text{Al}_{14}\text{O}_{33}$. The antibacterial actions for insulating and conducting $\text{Ca}_{12}\text{Al}_{14}\text{O}_{33}$ were different for *E. coli* and *S. aureus*. Thus, $\text{Ca}_{12}\text{Al}_{14}\text{O}_{33}$ cement has antibacterial properties that do not require the presence of nano-particle sizes materials or photocatalysis.

1. Introduction

Currently, the use of antimicrobials to promote public health is a research topic with much attention [1, 2, 3, 4]. The goal of such research is to identify materials with antibacterial properties capable of inhibiting or killing various bacteria through mechanisms not limited to photocatalytic and nano-particle effects [4,5]. Antibacterial materials have

attracted significant attention due to their very interesting application in preventing bacterial growth on smart building bathroom and kitchen walls [4]. There are four types of antibacterial activity: (1) cation elution, (2) pH effects, (3) electrostatic interactions between the surfaces of bacteria with nano-size particles, and (4) the effects of active oxygen species [4,6,7]. In addition to these, photocatalytic activity, electrostatic interaction, cellular internalization of nanoparticles and production of

* Corresponding author.

E-mail address: chesta.ruttanapun@gmail.com (C. Ruttanapun).

<https://doi.org/10.1016/j.heliyon.2019.e01808>

Received 10 December 2018; Received in revised form 21 April 2019; Accepted 21 May 2019

2405-8440/© 2019 The Authors. Published by Elsevier Ltd. This is an open access article under the CC BY license (<http://creativecommons.org/licenses/by/4.0/>).

เอกสารนี้เป็นเอกสารที่สงวนไว้สำหรับการใช้งานเพื่อการศึกษาเท่านั้น ไม่อนุญาตให้นำไปใช้ประโยชน์ด้านการค้า
ไม่ว่ากรณีใดๆ ทั้งสิ้น อีกทั้งห้ามมิให้ดัดแปลงเนื้อหา และต้องอ้างอิงถึงเจ้าของเอกสารทุกครั้งที่มีการนำไปใช้

reactive oxygen species (ROS) also have antimicrobial activity [4, 7, 8, 9]. ROS effects are predominantly used for antibacterial activity since it is an easy mechanism to employ [7,8]. ROS are comprised of hydroxyl radicals (OH^\bullet), hydrogen peroxide (H_2O_2) and superoxide ions (O_2^-) [4, 8]. These materials cause death by contacting bacterial membranes and directly damaging their surfaces [4,7]. ROS species can be generated from the reaction of free particles (free electrons and holes) in the course of photocatalytic activities [9, 10, 11]. The photocatalytic effect causes generation of free electrons and holes in materials using phonon energy corresponding to energy gap of the materials. There have been many reports that titanium dioxide (TiO_2) [12] and zinc oxide (ZnO) [10] can generate ROS through photocatalysis. Practically, TiO_2 and ZnO used phonon energy at 3.1 eV [13] and 3.2 eV [7], respectively, to photocatalytically produce ROS. They are produced from O_2 and H_2O adsorption promoting a reaction of free electrons and holes at the surfaces of materials to produce OH^- , H_2O_2 and O_2^- . Alternatively, ZnO [7, 8, 9,14] nanoparticles cause death of bacterial cells through electrostatic interactions between bacterial surfaces with nanoparticles in the absence of light, thereby damaging cell membranes. TiO_2 and ZnO act through photocatalysis and nanoparticle effects to produced antibacterial activity.

Recently, it has been reported that $\text{Ca}_{12}\text{Al}_{14}\text{O}_{33}$ cement exhibits free oxygen radical O^- ions in a vacant cage structure [15, 16, 17,18]. The $\text{Ca}_{12}\text{Al}_{14}\text{O}_{33}$ cement structure is linked by calcium, aluminum and oxygen atoms forming empty nanometer-sized cages within the structure [19,20], as shown in Fig. 1. A unit cell of insulating $\text{Ca}_{12}\text{Al}_{14}\text{O}_{33}$ is comprised of two molecules occupying 12 crystallographic nano-cages while presenting a 4^+ charge at the cage wall, represented as $[\text{Ca}_{24}\text{Al}_{28}\text{O}_{66}]^{4+}$ [21]. The two cages in this unit cell support electrical neutrality by entrapping two free oxygen ions (O^-) in cages referred to as an extra-framework [21]. The $\text{Ca}_{12}\text{Al}_{14}\text{O}_{33}$ structure was revealed to contain free O^- ions (as replaced by free oxygen radicals, O^\bullet , O_2^\bullet or $\text{O}_2^{\bullet-}$) loosely bound to a lattice framework, represented as $\text{Ca}_{12}\text{Al}_{14}\text{O}_{33}:\text{O}^-$ [21,22]. Hayashi et al. [23] showed that the process of preparing $\text{Ca}_{12}\text{Al}_{14}\text{O}_{33}$ cement in a dry oxygen atmosphere at temperature 1350°C could produce both O^- and O_2^- (as ROS species). Lu et al. [24] reported that the present of O^- and O_2^- resulted in antibacterial activity. Nevertheless, antimicrobial materials should be effective under various conditions and not limited to photocatalytic activity or nano-particle effects. Furthermore, Hayashi et al. [23] reported that free O^- and O_2^- could be replaced by free electrons in a conducting $\text{Ca}_{12}\text{Al}_{14}\text{O}_{33}$ cement, represented as $\text{Ca}_{12}\text{Al}_{14}\text{O}_{33}:\text{e}^-$. It has been reported that this material has distinct optical and electrical properties. However, to best of our knowledge, there are no reports of the effect and mechanisms of free electrons in the nano-cage structure of $\text{Ca}_{12}\text{Al}_{14}\text{O}_{33}$ cement on

antibacterial activity.

This work aims to investigate the effect of free electrons in the nano-cage structure of $\text{Ca}_{12}\text{Al}_{14}\text{O}_{33}$ cement on the optical, electronic and antibacterial activities of these materials. The developed material presenting free electrons in a nano-cage structure was characterized. Conducting $\text{Ca}_{12}\text{Al}_{14}\text{O}_{33}$ cement with free electrons was rapidly prepared by heating insulator cement inside a carbon crucible at high temperatures using high frequency electromagnetic induction. The mechanism and effect of free electrons and free oxygen radicals in the nano-cage structure of these materials on its optical, electronic and antibacterial properties were also investigated. Their antibacterial activities against gram-negative *E. coli* and gram-positive *S. aureus* are reported. Moreover, the mechanism of the antibacterial action of free electrons and free oxygen radicals in the nano-cage structure of $\text{Ca}_{12}\text{Al}_{14}\text{O}_{33}$ cement is described.

2. Experimental

2.1. Chemicals

Calcium carbonate (CaCO_3 , 99% Sigma-Aldrich), alumina powder (Al_2O_3 , 99.9% Sigma-Aldrich) and ethanol (95%) were used as the starting raw materials. All chemicals were used as received with no further purification.

2.1.1. Preparation of $\text{Ca}_{12}\text{Al}_{14}\text{O}_{33}$ cement as starting materials

$\text{Ca}_{12}\text{Al}_{14}\text{O}_{33}$ cement powder was first prepared via a solid-state reaction using CaCO_3 and Al_2O_3 as starting materials. In brief, CaCO_3 and Al_2O_3 powders were stoichiometrically prepared following the reaction, $12\text{CaCO}_3 + 7\text{Al}_2\text{O}_3 \rightarrow \text{Ca}_{12}\text{Al}_{14}\text{O}_{33} + 12\text{CO}_2$. The powders were mixed by ball milling in ethanol for 24 h at room temperature, and oven-drying at 100°C for 24 h. After that, the obtained powder was placed in an alumina crucible, and then sintered in an electric furnace at 1200°C under air atmosphere for 24 h. Finally, the obtained $\text{Ca}_{12}\text{Al}_{14}\text{O}_{33}$ sample, referenced as CAO@1200C, was crushed into a powder and used as a starting material to synthesize a conducting $\text{Ca}_{12}\text{Al}_{14}\text{O}_{33}$ cement sample.

2.1.2. Preparation of conducting $\text{Ca}_{12}\text{Al}_{14}\text{O}_{33}$ cement

The as-prepared CAO@1200C powder was used as a starting material for fabrication of conducting $\text{Ca}_{12}\text{Al}_{14}\text{O}_{33}$ cement. A mass of 100 g of CAO@1200C powder was placed in a carbon crucible with a carbon cap. Then, the carbon crucible was transferred into the middle of a Cu induction coil. High frequency electromagnetic induction heating was done using an induction coil (Model: TH-60AB (90 A, 3 phase, 380 V, 50–60 kHz)). The temperature was determined using an IR detector (Model: SENTEST (NS50PH1FF), accuracy class:2.0) focused on the surface of the

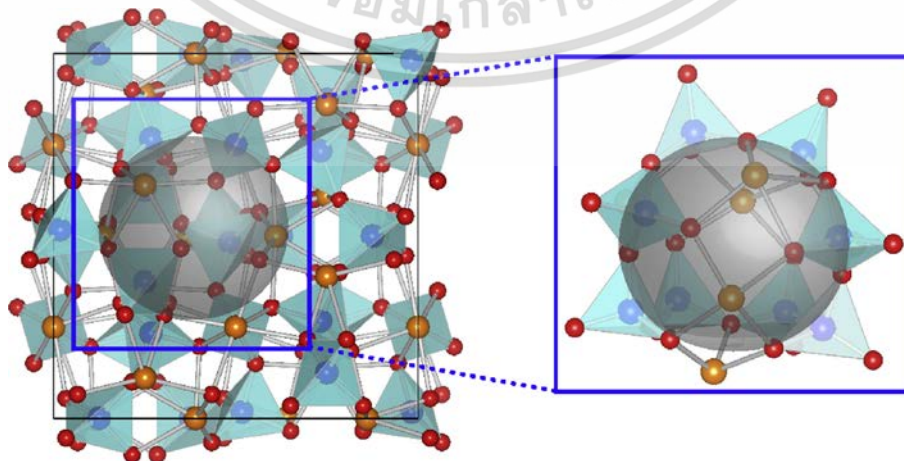


Fig. 1. A unit cell of the $\text{Ca}_{12}\text{Al}_{14}\text{O}_{33}$ cement structure: blue, orange and red balls denote Al, Ca and O atoms, respectively. The grey sphere represents the cage of this structure. The crystal structure of $\text{Ca}_{12}\text{Al}_{14}\text{O}_{33}$ contains nano-cages with a set inner diameter

ไม่ว่ากรณีใดๆ ทั้งสิ้น อีกทั้งห้ามมิให้ตัดแปลงเนื้อหา และต้องอ้างอิงถึงเจ้าของเอกสารทุกครั้งที่มีการนำไปใช้

carbon crucible. The CAO@1200C powder was rapidly heated from room temperature to sintering temperatures of 1350 °C, 1450 °C and 1550 °C with a 40 sec holding time (referenced as the CAO@1350C, CAO@1450C and CAO@1550C samples, respectively). Finally, the samples were cooled by natural convection to room temperature.

2.1.3. Preparation of the cement pellets

For pellet fabrication, the obtained CAO@1350C, CAO@1450C and CAO@1550C powders were subjected to uniaxial compression and pressed into disc-shaped pellets that were 10 mm in diameter and 2–3 mm thick. Then, the antibacterial activity of these pellets was tested.

2.2. Characterization

The lattice parameters were determined using an X-ray diffractometer (XRD), (Rigaku, Miniflex Cu K-alpha radiation), with a 2θ scanning range from 10 to 80° and step interval of 0.02°. Absorption spectroscopy was also done using a UV-Vis Spectrometer (Perkin Elmer, Lambda 950). A scanning electron microscope (SEM), JSM5800LV, JEOL, Japan with energy dispersive X-ray spectroscopy (EDX) (Oxford ISIS 300) was used to measure and confirm the morphologies of all the cement particles and bacteria, along with the elemental composition of the cement samples.

2.3. First-principles calculations

A first-principles approach was employed with the density of states of $\text{Ca}_{12}\text{Al}_{14}\text{O}_{33}:2\text{O}^{2-}$ cement and $\text{Ca}_{12}\text{Al}_{14}\text{O}_{33}:4\text{e}^{-}$ cement using the Vienna *Ab initio* Simulation Package (VASP) [25]. The pseudopotential used in this work was based on the Projector Augmented Wave (PAW) approach [26]. The PAW valence states were 3s and 3p, 4s, 3s and 3p, and 2s and 2p for Ca, Al and O, respectively. In this work, the Ceperley-Alder form of the exchange-correlation functional [27], which is the local density approximation (LDA), was used to determine the electronic density of states of both the $\text{Ca}_{12}\text{Al}_{14}\text{O}_{33}:2\text{O}^{2-}$ and $\text{Ca}_{12}\text{Al}_{14}\text{O}_{33}:4\text{e}^{-}$ cements. A 600 eV plane-wave cutoff energy and $5 \times 5 \times 5$ K-point sampling of the Brillouin zone were used for all calculations. The HSE06 hybrid functional was chosen to determine the density of the $\text{Ca}_{12}\text{Al}_{14}\text{O}_{33}:4\text{e}^{-}$ states.

2.4. Property measurements

The vibration mode of atomic bonding was evaluated using Fourier-transform infrared spectroscopy (FTIR), (Bruker, Senterra). The optical properties of the samples were investigated using a diffused reflectance UV-Visible spectrometer, (DRS) (Perkin Elmer, Lambda 950). Optical measurements were used to determine the absorption coefficient spectra of the specimens at room temperature.

2.5. Antibacterial property testing

The antibacterial properties of the CAO@1350C, CAO@1450C and CAO@1550C samples were tested using an agar disk-diffusion method against a gram-negative bacterium, *Escherichia coli* (*E. coli*) (ATCC 25922) and a gram-positive bacterium, *Staphylococcus aureus* (*S. aureus*) (ATCC 25923). All samples were pellet shaped with diameter of 10 mm. *E. coli* and *S. aureus* were cultivated on Muller Hinton agar at 37 °C for 24 h. Then, cells of *E. coli* and *S. aureus* were suspended in a 0.85% NaCl solution and the cell suspension was adjusted to 0.5 McFarland (1×10^8 CFU/mL). Subsequently, the *E. coli* and *S. aureus* cell suspensions were swabbed onto Muller Hinton agar. After drying, CAO@1350C, CAO@1450C and CAO@1550C sample pellets were placed on the agar surfaces. Then, the agar plates were incubated (Contherm, Scientific Ltd., New Zealand) at 37 °C for 24 h in a dark incubation chamber. Finally, the inhibition zones on the agar plates were photographed and the widths of inhibition zones reported. Inhibition of *E. coli* and *S. aureus* was confirmed using scanning electron microscopy (SEM), JSM5800LV, JEOL, Japan. สารนี้เป็นเอกสารที่สงวนไว้สำหรับการใช้งานเพื่อการวิจัย

3. Results and discussion

3.1. Characterization of $\text{Ca}_{12}\text{Al}_{14}\text{O}_{33}$ cement as a starting material

The CAO@1200C sample was prepared via a solid-state reaction at 1200 °C for use as a starting material for fabrication of conducting $\text{Ca}_{12}\text{Al}_{14}\text{O}_{33}$ cement. Fig. 2 displays the XRD patterns of the CAO@1200C sample. These XRD results show a pattern corresponding to the JCPDS#09–0413 file (a standard $\text{Ca}_{12}\text{Al}_{14}\text{O}_{33}$ cement phase). The results confirmed that the prepared CAO@1200C sample formed a phase of $\text{Ca}_{12}\text{Al}_{14}\text{O}_{33}$ cement.

3.2. Characterization of conducting $\text{Ca}_{12}\text{Al}_{14}\text{O}_{33}$

3.2.1. Sintering process

Fig. 3 (a) presents a schematic of an electromagnetic induction heating system for synthesizing the samples fabricated in the course of this work. The starting CAO@1200C powder was loaded into a carbon crucible. The carbon crucible was wrapped with a Cu induction coil. Cooling water was circulated in a Cu coiled tube to protect against overheating on operation of the magnetic induction heating. An IR detector was used to measure the temperature of the carbon crucible and this information used as feedback to control the power of the induction heater. The carbon crucible was rapidly heated from room temperature to 1350 °C, 1450 °C and 1550 °C, with a holding time of 40 seconds for sintering. Then, the samples were rapidly cooled to room temperature. Fig. 3 (b) shows an electromagnetic induction heating time of approximately 1 minute for sintering.

3.2.2. XRD characterization

Fig. 4 shows the XRD patterns of the synthesized CAO@1350C, CAO@1450C and CAO@1550C samples prepared by heating in a carbon crucible by high frequency electromagnetic induction. The XRD results showed that the patterns of the sintered CAO@1350C and CAO@1550C samples matched the JCPDS#09–0413 file as $\text{Ca}_{12}\text{Al}_{14}\text{O}_{33}$ cement phase [28, 29, 30, 31, 32]. These results confirmed the synthesis of a $\text{Ca}_{12}\text{Al}_{14}\text{O}_{33}$ cement phase in the CAO@1350C and CAO@1550C samples. In contrast, the XRD patterns of the synthesized CAO@1450C sample exhibited a different XRD pattern pattern that matched the JCPDS#09–0413 file. This result was due to formation of a glass $\text{Ca}_{12}\text{Al}_{14}\text{O}_{33}$ cement phase as corresponding to that observed in a previously published XRD pattern [33]. This implied that the preparation process produced a glass phase of $\text{Ca}_{12}\text{Al}_{14}\text{O}_{33}$ cement at a temperature of 1350 °C. Thus, this confirmed that all samples formed phases of $\text{Ca}_{12}\text{Al}_{14}\text{O}_{33}$ cement during high frequency induction heating. However, the CAO@1350C, CAO@1450C and CAO@1550C samples did not

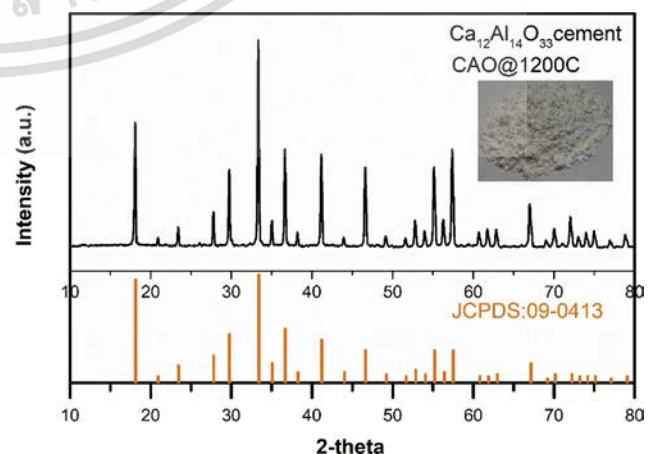


Fig. 2. XRD patterns of the CAO@1200C cement sample referencing the JCPDS#09–0413 file of the standard $\text{Ca}_{12}\text{Al}_{14}\text{O}_{33}$ cement phase. ราคา

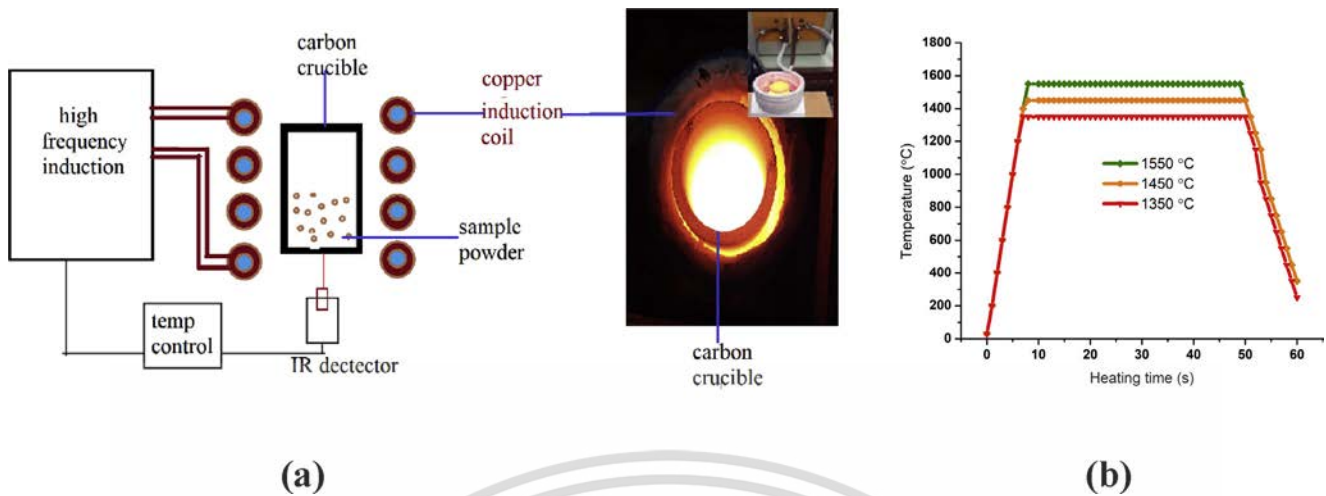


Fig. 3. (a) Schematic structure of the high frequency induction heating system with an image of material undergoing induction heating and (b) the temperature and heating time in the sintering process.

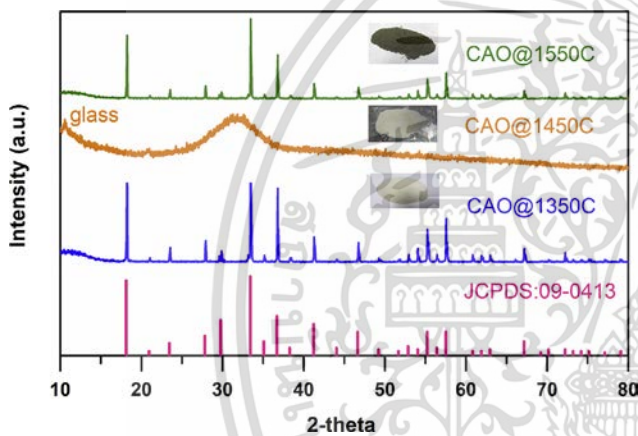


Fig. 4. XRD patterns of the synthesized CAO@1350C, CAO@1450C and CAO@1550C samples referencing the JCPDS#09-0413 file.

exhibit 20 XRD peaks at 26.5° , 10.8° and 25.2° . These reference graphite, graphene oxide, and reduced graphene oxide, respectively. These results confirmed that graphite from the crucible did not dissolve into the samples [34].

3.2.3. Photographic and electric resistance measurements

Fig. 5(a-k) presents images CAO@1350C, CAO@1450C and CAO@1550C samples fabricated at 1350°C , 1450°C and 1550°C , respectively, and measurement of their electric resistances using a multimeter. Fig. 5 (a) shows a white colored powder sample. This result reveals that the sample did not form a single crystal phase at this temperature. The resistance of the sample was very high as shown in Fig. 5 (b) and (c). Fig. 5 (d) presents a yellow colored sample that formed from a single crystal in the crushed powder sample (Fig. 5 (e)). A single crystal phase was produced that had a very high resistance as shown in Figs. 5 (f) and (g). Fig. 5 (h) shows a greenish-black colored sample with a cement from a single crystal type forming a green colored crushed powder (Fig. 5 (i)). This sample, sintered at 1550°C , was electrically conductive as shown in Figs. 5 (j) and (k), leading to the observation that sintering at temperatures higher than 1450°C produced a single crystal form of $\text{Ca}_{12}\text{Al}_{14}\text{O}_{33}$ cement. Only the CAO@1550C sample displayed electrical conductivity after its formation at 1550°C . The green color of this sample was not the same as the CAO@1350C and CAO@1450C samples implying a different mechanism for fabrication of the CAO@1550C sample than the CAO@1350C and CAO@1450C samples.

3.2.4. Absorption coefficients

The differences between the CAO@1550C, CAO@1350C and CAO@1450C cement phases were investigated from their optical absorption coefficients measured using UV Visible Spectrometry. Fig. 6 shows absorption coefficients in the UV spectrum of the prepared CAO@1200C starting powder, and the synthesized CAO@1350C, CAO@1450C and CAO@1550C samples at room temperature over the range of 1.6 eV–6 eV. The absorption spectra of the prepared CAO@1200C sample had the highest absorption peak at 4.1 eV. This was characteristic of the electrically insulating $\text{Ca}_{12}\text{Al}_{14}\text{O}_{33}$ cement phase with an extra-framework O_2^- (superoxide radical) and O^- (oxygen anion radical). They were inside the cavity-cages of the structure, denoted as $\text{Ca}_{12}\text{Al}_{14}\text{O}_{33}:\text{O}$ cement. The absorption spectra of the CAO@1350C and CAO@1450C samples showed their two highest absorption peak positions at 3.2 eV and 4.7 eV for the CAO@1350C sample, and 3.2 eV and 4.7 eV for the CAO@1450C sample. The absorption edge value of 3.2 eV for the CAO@1450C sample was attributed to the excitation between the energy level of encaged free oxygen O^- ions and the cage conduction band (CCB) as previously reported [19]. These implied the presence of extra-framework O^- ions in a nano-cavity cage within the structure of the insulating $\text{Ca}_{12}\text{Al}_{14}\text{O}_{33}:\text{O}$ cement, similar to the CAO@1200C sample. Additionally, the absorption spectra of the CAO@1550C sample displayed its two highest absorption peak positions at 2.8 eV and 1.5 eV. The first peak at 2.8 eV presented electrons transitioning from the occupied cage level (an F^+ -like center level due to a relaxation time) to the framework conduction band (FCB), as previously reported [28,29]. The energy at 2.8 eV was due to the inter-cage transition energy for the free electrons in cavity-cage structure. The second peak at 1.5 eV displayed an energy level from the F^+ -like center level to the cage-conduction band (CCB). A second peak energy level was reported in range of 0.4–1.5 eV [28, 29, 30, 31]. This energy level was too large for the empty cage and an electron with less energy to occupy the cage. The two peak positions at 2.8 and 1.5 eV were characteristic of conducting $\text{Ca}_{12}\text{Al}_{14}\text{O}_{33}:\text{e}^-$ cement. These results confirmed that the conducting $\text{Ca}_{12}\text{Al}_{14}\text{O}_{33}:\text{e}^-$ cement was completely converted from insulating $\text{Ca}_{12}\text{Al}_{14}\text{O}_{33}:\text{O}$ cement when heated inside the carbon crucible to a temperature of 1550°C . Obviously, this method can replace free oxygen in the cavity-cage with a free electron to form conducting $\text{Ca}_{12}\text{Al}_{14}\text{O}_{33}:\text{e}^-$ cement. The absorption peaks at 1.5–2.8 eV of the CAO@1550C sample were correlated to the greenish-black color of the sample shown Fig. 5. The powder color changed from white to green comparing the CAO@1200C to CAO@1550C samples. The sample color was caused by the free electron concentration in the structure. The white and green color samples presented free electron concentrations of 0 cm^{-3} and around $1 \times 10^{20}\text{ cm}^{-3}$,

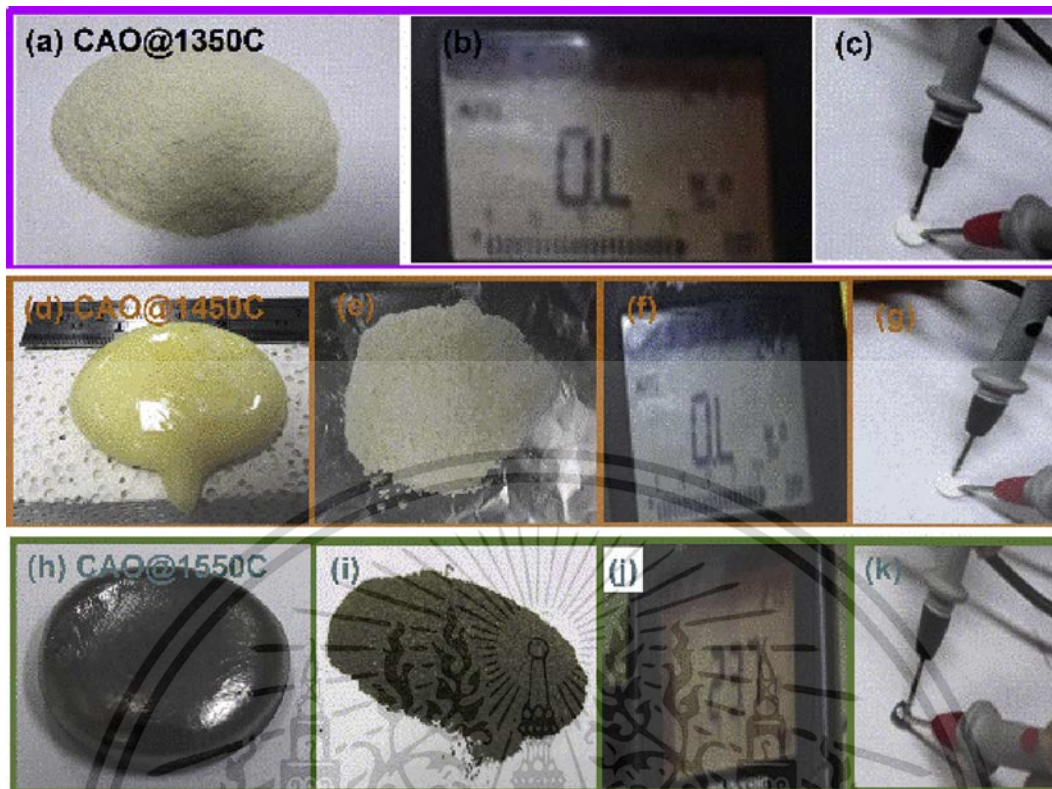


Fig. 5. Images of synthesized CAO@1350C, CAO@1450C and CAO@1550C samples fabricated at 1350 °C, 1450 °C and 1550 °C, respectively, (a) white colored of CAO@1350C powder, (b) and (c) measurement of the electric resistances of CAO@1350C sample as presenting electric insulator using a multi-meter, (d) yellow colored of CAO@1450C sample that formed a single crystal, (e) yellow colored crushed powder of CAO@1450C sample, (f) and (g) measurement of the electric resistances of CAO@1450C sample as presenting electric insulator, (h) greenish-black colored of CAO@1550C sample with a cement from a single crystal, (i) green colored crushed of CAO@1550C powder, and (j) and (k) measurement of the electric resistances of CAO@1550C sample as presenting electric conductor.

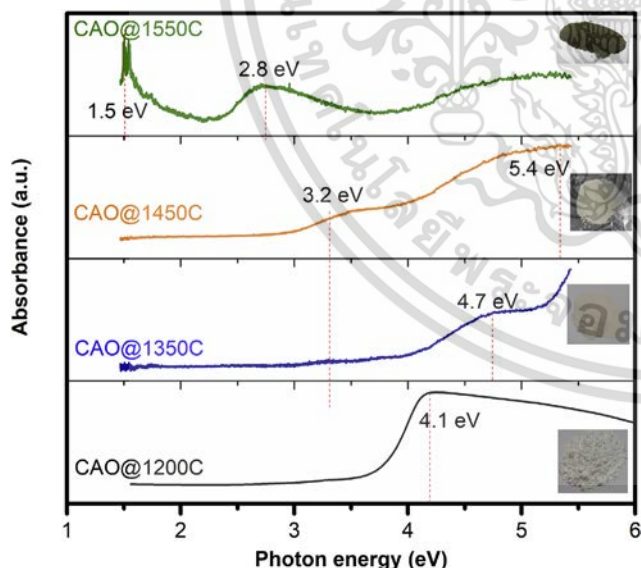


Fig. 6. Absorption coefficient as function of photon energy of CAO@1200C, CAO@1350C, CAO@1450C and CAO@1550C samples.

respectively, which is good agreement with earlier reports [32]. The CAO@1200C sample, i.e., starting powder, as well as the CAO@1350C and CAO@1450C samples, displayed a light color without free electrons in the structure. The CAO@1550C powder had a green color, with approximately $2 \times 10^{20} \text{ cm}^{-3}$ of free electrons. Additionally, the CAO@1200C, CAO@1350C, and CAO@1450C samples were electric

insulators while the CAO@1550C sample was electrically conductive.

The CAO@1200C starting powder, as well as the CAO@1350C and CAO@1450C samples, were white colored, indicating that they were transparent in the visible light region (1.6–3.2 eV), as well as acting as electrical insulators. These results illustrated that the CAO@1200C, CAO@1350C and CAO@1450C samples were electric insulators as the insulating $\text{Ca}_{12}\text{Al}_{14}\text{O}_{33}:\text{O}$ cement owing to free oxygen radicals in their cavity-cages. The greenish-black color of the CAO@1550C sample indicated light absorption in the region of 1.5–2.8 eV. This confirmed that sintering at 1550 °C by rapid induction heating could convert electrically insulating $\text{Ca}_{12}\text{Al}_{14}\text{O}_{33}:\text{O}$ cement to conducting $\text{Ca}_{12}\text{Al}_{14}\text{O}_{33}:\text{e}^-$ cement. This process can replace free oxygen radicals with free electrons in an electron-doped process inside a nano-cage $\text{Ca}_{12}\text{Al}_{14}\text{O}_{33}$ cement structure.

3.2.5. SEM and EDS analysis

The imagery in Fig. 7 (a), (c), (e) and (g) show SEM analysis and Figs. 7 (b), (d), (f) and (h) show EDS mapping of the synthesized CAO@1200C, CAO@1350C, CAO@1450C and CAO@1550C samples, respectively. All of the samples presented micrometer grain sizes. The EDS results show the presence of Ca, Al, O and C atoms, indicating that the samples formed a CAO phase structure. There was a homogeneous distribution of carbon atoms on the powder surfaces. Additionally, the percentage of C atoms was similar in all samples.

Thus, the results imply that the carbon remaining component of the synthesized process did not alter the percentage of carbon in the obtained CAO@1200C, CAO@1350C, CAO@1450C and CAO@1550C samples. EDS mapping of the CAO@1200C, CAO@1350C, CAO@1450C and CAO@1550C samples showed a homogeneous distribution of the Ca, Al, O and C atoms on the powder surfaces in Fig. 8 (a), (b), (c) and (d), respectively.

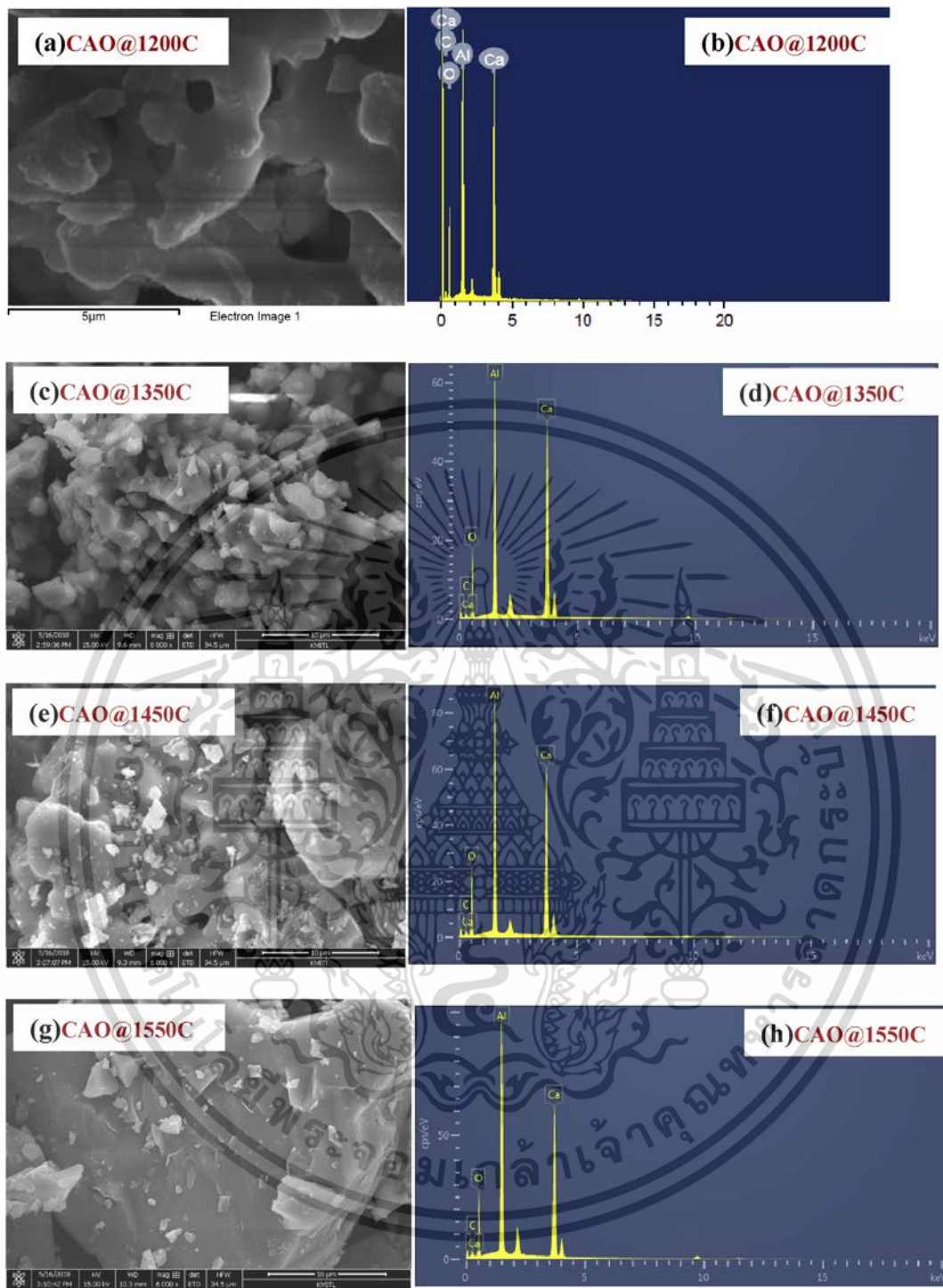


Fig. 7. SEM (a), (c), (e) and (g), and EDX (b), (d), (f) and (h) of the synthesized CAO@1200C, CAO@1350C, CAO@1450C and CAO@1550C samples, respectively.

3.3. Properties of conducting $\text{Ca}_{12}\text{Al}_{14}\text{O}_{33}$

3.3.1. Raman spectroscopy analysis

Raman spectroscopy [34, 35, 36, 37] was used to characterize the molecular structure and bonding of the fabricated materials. Fig. 9 shows Raman spectra of the prepared CAO@1200C sample as well as the synthesized CAO@1350C, CAO@1450C and CAO@1550C samples. The absorption bands for the $\text{Ca}_{12}\text{Al}_{14}\text{O}_{33}$ cement structure have normal lattice properties due to vibrations of Al^{3+} , Ca^{2+} and oxygen ions in the region from 50 to 3000 cm^{-1} [37]. In previous work [37], Raman peaks between 200 and 1000 cm^{-1} were ascribed to the lattice framework of

the $\text{Ca}_{12}\text{Al}_{14}\text{O}_{33}$ cement structure resulting from Al^{3+} ions in a tetrahedral structure. The Raman spectra peaks at 330, 510, and 773 cm^{-1} of the CAO@1350C, CAO@1450C and CAO@1550C samples corresponded to peaks of the CAO@1200C sample. The Raman peak at 330 cm^{-1} was caused by the oxygen (O^{2-}) framework due to vibrations of $\text{Ca}[\text{AlO}_4]$ and Ca–O bonding. The two bands at 510 cm^{-1} and 773 cm^{-1} indicated bending vibrations the Al–O–Al linkages and Al–O stretching vibrations, respectively, for a lattice structure with the oxygen and aluminum atoms in a symmetric framework with an Al–O $[\text{AlO}_4]^{5-}$ sub-structure [38]. The band at 178 cm^{-1} appeared on the CAO@1200C and CAO@1350C sample and was identified as characteristic of the lattice framework

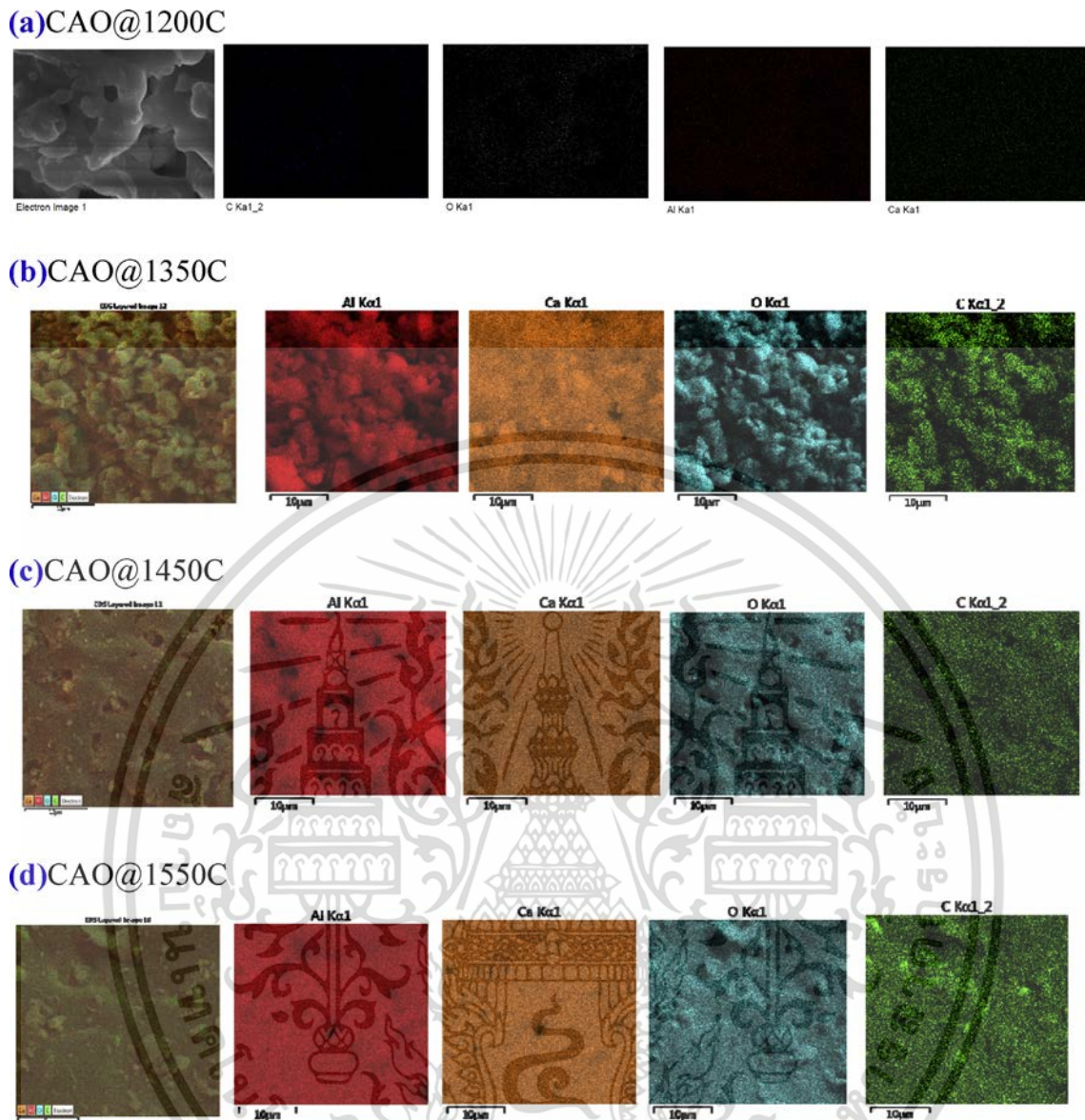
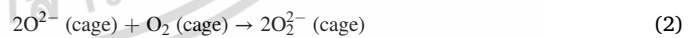
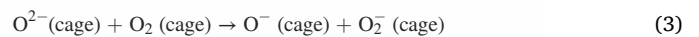


Fig. 8. Elemental distribution (SEM-EDS) of the synthesized (a) CAO@1200C, (b) CAO@1350C, (c) CAO@1450C and (d) CAO@1550C samples with a homogeneous distribution of the Ca, Al, O and C atoms on the powder surfaces.

caused by Al³⁺ ion coordination. This peak may be characteristic of insulating Ca₁₂Al₁₄O₃₃ cement prepared at temperatures lower than 1350 °C. The band at 885 cm⁻¹ appeared only in the CAO@1200C sample resulting from bending and stretching vibrations of the Al and O framework. This peak was characteristic of insulating Ca₁₂Al₁₄O₃₃ cement prepared at 1200 °C. The CAO@1200C sample exhibited two band peaks at around 1338 cm⁻¹ and 1586 cm⁻¹ that appeared only in the CAO@1500C sample resulting from a small amount of graphite from the carbon crucible that was not observed in the XRD results of Fig. 4. Additionally, a peak at 727 cm⁻¹ was observed in the CAO@1200C and CAO@1350C samples. In previous work [37], a band located at 727 cm⁻¹ indicated O₂²⁻-stretching of the extra-framework O₂²⁻ ion in electrically insulating Ca₁₂Al₁₄O₃₃ cement. The peak at 1067 cm⁻¹ represents the stretching mode of the extra-framework O₂⁻ ions of the CAO structure [37]. A peak at 1067 cm⁻¹ was presented by the CAO@1200C, CAO@1350C and CAO@1450C samples, indicating the presence of extra-framework O₂⁻ ions. The formation process of the O₂²⁻ ions can be described by Eqs. (1) and (2) [39]:



Additionally, the formation of superoxide (O₂⁻) ions occurred via the following chemical reaction in Eq. (3) [33]:



Formation of O₂²⁻ ions can be described by Eq. (4) [39]:



These reactions indicated that the extra-framework O₂²⁻ ions in the nano-cage cavity of the structure were present in the Ca₁₂Al₁₄O₃₃ cement prepared in the temperature range of 1200–1350 °C. Extra-framework O₂⁻ and O⁻ ions were present in the samples prepared at temperatures of 1200–1450 °C. Oxygen radical O₂⁻ and O⁻ ions were successfully replaced by extra-framework O₂²⁻ ions in a caged structure at 1350 °C.

Moreover, the Raman spectra bands at 725 and 1065 cm⁻¹ were not observed in the CAO@1550C sample, indicating a reduction of insulating Ca₁₂Al₁₄O₃₃ cement into a conductive form. Extra-framework O₂²⁻, O₂⁻

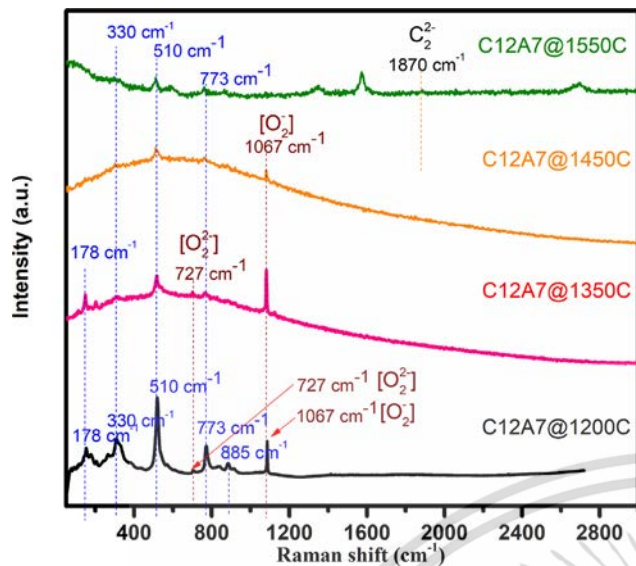
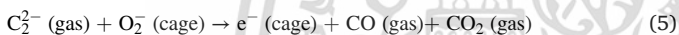


Fig. 9. Raman spectra of the CAO@1200C sample and synthesized CAO@1350C, CAO@1450C and CAO@1550C samples.

and O^- ions were not observed in the nano-cage cavity of the CAO@1550C sample. This implied that the CAO@1550C sample was completely converted from insulating $Ca_{12}Al_{14}O_{33}$ cement to its conducting form. This mechanism successfully replaced free oxygen ions in a cavity-cage with free electrons via the reaction in Eq. (5):



This mechanism required free radical carbon ions (C_2^{2-}) at a reaction temperature of 1550 °C. In this process, the C_2^{2-} ions were generated from the carbon crucible that reacted with O_2^- ions when it was heated to 1550 °C. Then, the reaction removed free oxygen O_2^- ions and injected free electrons (e^-) into the nano-cage structure. No peaks at 1870 cm^{-1} were observed for the CAO@1550C sample. Kim et al. [33] reported Raman band spectra at 1870 cm^{-1} , ascribing them to C_2^{2-} ions. C_2^{2-} ions were dissolved into the CAO@1550C sample from the C_2^{2-} atmosphere of the carbon crucible and were released out of the nano-cages during cooling. In summary, the extra-framework O_2^{2-} and O_2^- ions present in the CAO@1200C, CAO@1350C and CAO@1450C samples were responsible for producing an insulating $Ca_{12}Al_{14}O_{33}$ cement. The CAO@1550C sample, i.e., $Ca_{12}Al_{14}O_{33}:e^-$ cement, had free electrons in a nano-cage structure that allowed for electrical conduction.

3.3.2. Optical properties

The absorption coefficients shown in Fig. 6 present the optical properties of the CAO@1200C, CAO@1350C, CAO@1450C and CAO@1550C samples. They were used to calculate to optical energy gap (E_g) following the relationship in Eq. (6) [20]:

$$\alpha(h\nu) \propto \frac{(h\nu - E_g)^{1/2}}{h\nu} \quad (6)$$

where $h\nu$ denotes the photon energy, E_g represents the direct optical gap, and 1/2 is a value for the allowed direct transition type. Thus, the allowed direct optical gap can be calculated from Eq. (7):

$$(ah\nu)^2 = A(h\nu - E_g) \quad (7)$$

where A is a constant. The optical energy gap (E_g) was fitted to a straight line to intercept the photon energy ($h\nu$) axis. Fig. 10 shows the optical gap of the prepared CAO@1200C sample, as well as the sintered CAO@1350C, CAO@1450C and CAO@1550C samples at room temperature. Their energy gap values were 3.9 eV, 4.1 eV, 4.0 eV and 3.5 eV,

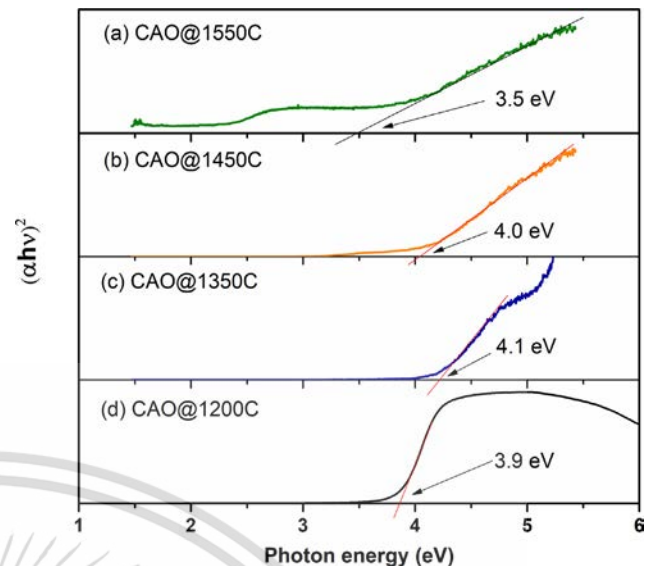


Fig. 10. Absorption coefficient of the CAO@1200C sample, and sintered CAO@1350C, CAO@1450C and CAO@1550C samples at room temperature in range of 1.6 eV–6 eV measured by UV-Vis spectroscopy.

respectively. The results showed that the CAO@1200C, CAO@1350C, and CAO@1450C energy gap values were close to 4.0 eV, indicating the insulating nature of this $Ca_{12}Al_{14}O_{33}$ cement. This value (4.0 eV) represents the energy gap for the allowed direct optical gap of the electronic transition from an occupied electronic state of the upper part of the framework conduction band (FCB) to the cage conduction band (CCB). Moreover, the energy gap of the CAO@1550C sample was 3.5 eV as indicating a conductive $Ca_{12}Al_{14}O_{33}$ cement phase structure. This value (3.5 eV) represents the energy of the electronic transition from the occupied framework valence band (FCB) to the cage conduction band (CCB).

3.3.3. First-principles calculations

First-principles calculations for evaluating the optical properties of $Ca_{12}Al_{14}O_{33}$ were performed as previously outlined [40,41]. The electronic properties of insulating $Ca_{12}Al_{14}O_{33}:2O^{2-}$ cement and conducting $Ca_{12}Al_{14}O_{33}:4e^-$ cement structures were determined in this manner. In the present study, the unit cell of the $Ca_{12}Al_{14}O_{33}:2O^{2-}$ structure contained 12 lattice framework cages $[Ca_{24}Al_{28}O_{64}]^{4+}$ and two O^{2-} anions (extra-framework) trapped at the center of a cage. The determination of the unit cell of $Ca_{12}Al_{14}O_{33}:e^-$ used $Ca_{12}Al_{14}O_{33}:2O^{2-}$ as an initial configuration and two O^{2-} anions were removed followed by the addition of four extra electrons inside the unit cell. The results showed that the lattice constants of the optimized structures were 11.8576 and 12.0256 Å for insulating $Ca_{12}Al_{14}O_{33}:2O^{2-}$ cement and conducting CAO: e^- cement, respectively.

For $Ca_{12}Al_{14}O_{33}:2O^{2-}$, Fig. 11 (a) clearly shows a peak located at 0.3 eV below the Fermi level corresponding to the 2p states of extra-framework $2O^{2-}$ ions. Additionally, the energy gap in this case is the difference between the energies of the highest states of the framework valence band (FVB) and the lowest states of the CCB. In this case, we found that the energy gap is approximately 4.1 eV. This result was close to the energy gap of the experimental results for CAO@1200C (3.9 eV), CAO@1350C (4.1 eV) and CAO@1450C (4.0 eV) as shown Fig. 10. The implication of this is that the CAO@1200C, CAO@1350C and CAO@1450C samples have a $Ca_{12}Al_{14}O_{33}:2O^{2-}$ structure. The 4.1 eV energy gap for the $Ca_{12}Al_{14}O_{33}:2O^{2-}$ represents the minimum energy required for the transition from the FVB to CCB. It was found that at least 2.3 eV is required for the electronic transition from the extra-framework O^{2-} ions to the CCB. The above results confirm that the CAO@1200C, CAO@1350C and CAO@1450C samples are electrically insulating

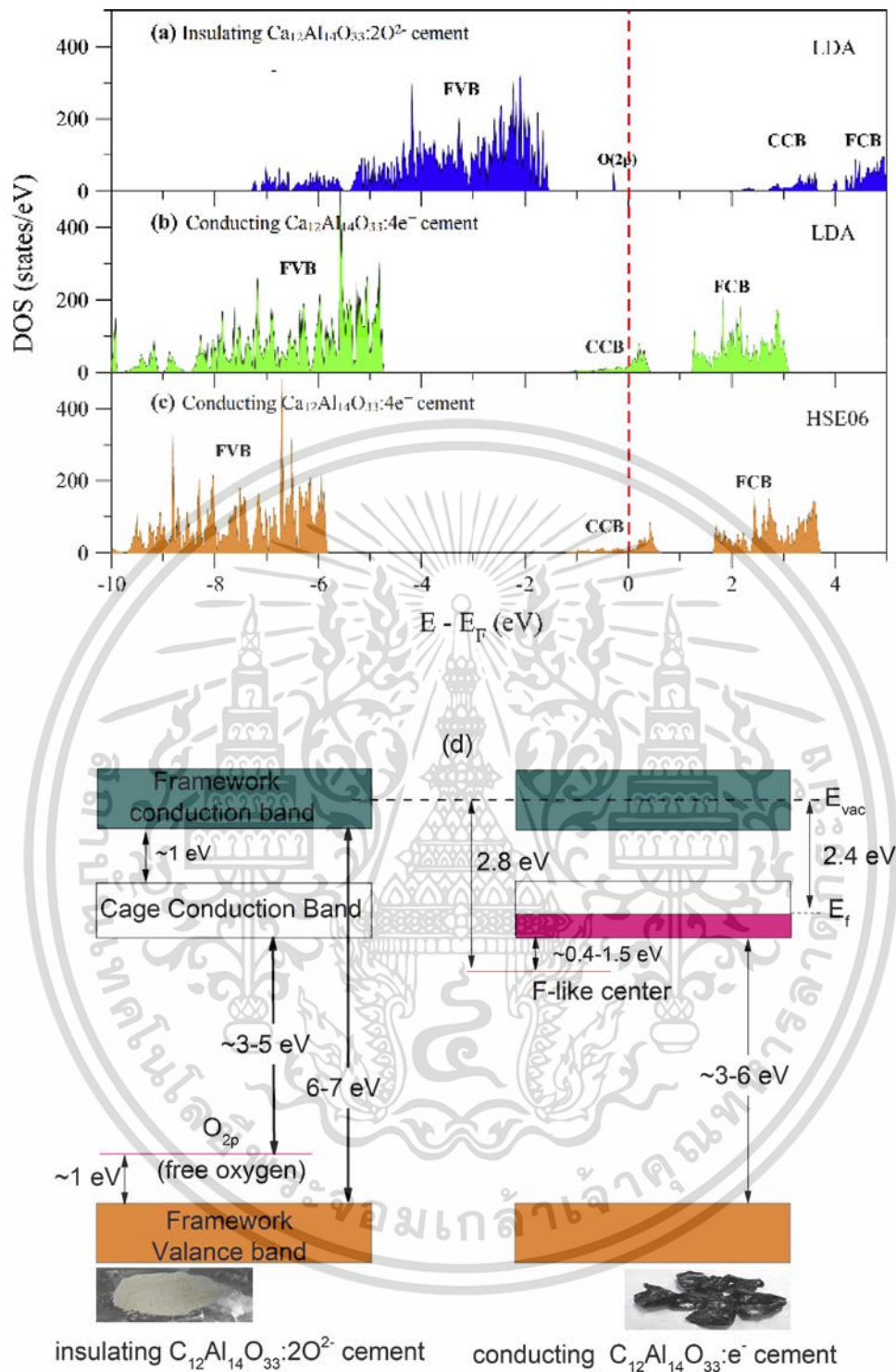


Fig. 11. The electronic density of states of (a) $\text{Ca}_{12}\text{Al}_{14}\text{O}_{33}:2\text{O}^{2-}$, (b) $\text{Ca}_{12}\text{Al}_{14}\text{O}_{33}:4e^-$ calculated using the LDA functional and (c) the electronic density of states of $\text{Ca}_{12}\text{Al}_{14}\text{O}_{33}:e^-$ computed using the HSE06 functional for the framework valence band (FVB), framework conduction band (FCB) and cage conduction band (CCB), respectively, (d) energy diagram of insulating $\text{Ca}_{12}\text{Al}_{14}\text{O}_{33}:2\text{O}^{2-}$ mayenite and conducting $\text{Ca}_{12}\text{Al}_{14}\text{O}_{33}:4e^-$ electride, respectively.

cement materials.

The electronic density of states of $\text{Ca}_{12}\text{Al}_{14}\text{O}_{33}:e^-$ was determined using the local density approximation (LDA) scheme shown in Fig. 11 (b). It is well established that electrical conductivity is directly related to the electron states at the Fermi level. A large number of electron states at the Fermi level energy, E_f (the highest occupied state), which is at 0 eV, results in high electrical conductivity.

According to the density of states of $\text{Ca}_{12}\text{Al}_{14}\text{O}_{33}:e^-$, it can easily be seen that there are CCB states at the Fermi level. This result implies that electron conduction comes from the CCB, in this case. Hence, $\text{Ca}_{12}\text{Al}_{14}\text{O}_{33}:e^-$ can be electrically conductive. However, the energy gap obtained from LDA functional analysis was always smaller than the experimentally derived energy gap. To improve the accuracy of our calculations, a hybrid functional was used. For $\text{Ca}_{12}\text{Al}_{14}\text{O}_{33}:4e^-$, we

determined the electronic density of states using the Heyd-Scuseria-Ernzerh of 06 (HSE06) hybrid functional shown in Fig. 11 (c). The electronic density of states calculated from the HSE06 hybrid functional looks similar to that determined from the LDA functional. Moreover, we found that the FVB states shifted to slightly lower energy levels relative to the FVB of LDA. Hence, the energy gap increased in this case. The energy difference between the highest FVB state and the lowest CCB state was approximately 4.7 eV. Additionally, the energy required for the electronic transition from FVB to FCB was rather high, 7.4 eV. Thus, it is impossible for electrons to be excited from the FVB to the FCB.

The energy difference between the highest FVB state and the lowest CCB state was approximately 3.7 eV–4.7 eV. This result was close to the experimentally derived energy gap for CAO@1550C (3.5 eV). The energy gap between FCB and CCB was about 0.42 eV, representing the metallic bands of $\text{Ca}_{12}\text{Al}_{14}\text{O}_{33}:\text{e}^-$ that are characteristic of the cage-like structures with no extra-framework oxygen species. According to Fig. 11 (b) and (c), only electron states of the CCB exist at the Fermi level. Consequently, electronic conduction was observed in this material because of the free electrons in the cage. The above results are consistent with previous work [42,43]. From Figs. 6, 10, and 11, the energy diagram for insulating $\text{Ca}_{12}\text{Al}_{14}\text{O}_{33}:\text{O}^{2-}$ and conducting $\text{Ca}_{12}\text{Al}_{14}\text{O}_{33}:\text{e}^-$ cements obtained from both experiments and calculations [28,30,43] is summarized in Fig. 11(d).

Moreover, the experimental and calculation results showed that the insulating $\text{Ca}_{12}\text{Al}_{14}\text{O}_{33}:\text{O}^{2-}$ cement had a direct optical gap of approximately 4.0 eV for the electronic transition from the FVB to the CCB. For conducting $\text{Ca}_{12}\text{Al}_{14}\text{O}_{33}:\text{e}^-$, the experimental and calculational results showed the direct transition gap from FVB to CCB was around 3.5–3.7 eV. This information indicated that it is impossible for electron excitations to occur between the FVB to FCB due to a rather large energy gap (3.5 eV). The conducting $\text{Ca}_{12}\text{Al}_{14}\text{O}_{33}:\text{e}^-$ cement displayed metallic behavior when it absorbs external energy at around 2.8 eV, corresponding to the energy level from CCB to FCB for free electron movement between cages. This energy (2.8 eV) corresponds to the absorption peak position at 2.8 eV that results in the greenish-black color of the sintered CAO@1550C sample shown in Fig. 5. Additionally, electrons become free electrons when their energy becomes greater than the work function (E_{vac}), which is 2.4 eV [31,44]. The broad absorption band at 2.8 eV for the CAO@1550C sample is attributed to the transition to intra-cage s-to-p forms of electrons trapped in the cages. The absorption band at 1.5 eV was due to the transition of inter-cage s-to-s charge transfer from an electron trapped in a cage to a vacant neighboring cage [38]. The transition of free electron movement of the CAO@1550C sample

($\text{Ca}_{12}\text{Al}_{14}\text{O}_{33}:\text{e}^-$ cement) was supported by oxygen gas adsorbed at the surfaces of the materials to produce free radicals [45] according to the reaction Eq. (8):



3.4. Schematic diagram for fabrication of conducting $\text{Ca}_{12}\text{Al}_{14}\text{O}_{33}$

A conducting $\text{Ca}_{12}\text{Al}_{14}\text{O}_{33}:\text{e}^-$ cement was successfully fabricated via a sintering process starting with insulating $\text{Ca}_{12}\text{Al}_{14}\text{O}_{33}:\text{O}^{2-}$ cement inside a carbon crucible using high frequency induction heating to 1550 °C. A schematic presenting the mechanism for converting insulating $\text{Ca}_{12}\text{Al}_{14}\text{O}_{33}:\text{O}^{2-}$ cement to conducting $\text{Ca}_{12}\text{Al}_{14}\text{O}_{33}:\text{e}^-$ cement via this process is shown in Fig. 12. Fig. 12(a) shows the starting $\text{Ca}_{12}\text{Al}_{14}\text{O}_{33}:\text{O}^{2-}$ cement powder loaded inside a carbon crucible. The $\text{Ca}_{12}\text{Al}_{14}\text{O}_{33}:\text{O}^{2-}$ structure is a linkage of calcium, aluminum and oxygen atoms consisting of empty nano-sized cages containing of free oxygen ions (O^{2-}), loosely bound to a lattice framework, inside cages as an extra-framework. Fig. 12(b) presents the process for producing conducting $\text{Ca}_{12}\text{Al}_{14}\text{O}_{33}:\text{e}^-$ cement by rapid heating carbon via electromagnetic induction heating to 1550 °C in a carbon crucible. The thermal energy (Q) in the carbon crucible was obtained from eddy currents and induced electromagnetic power [46] via the relationship Eq. (9):

$$Q = \sigma(T) \omega^2 B^2 \tag{9}$$

where $\sigma(T)$ is electrical conductivity as a function of temperature(S/m), ω is angular frequency (rad/sec), and B is the magnetic vector potential. At 1550 °C, an active carbon radical (C_2^-) species was generated from the heated carbon for producing a C_2^- atmosphere inside the crucible [31,33,34]. Then, the C_2^- ions reacted with free oxygen ions in the cavity-cages of the $\text{Ca}_{12}\text{Al}_{14}\text{O}_{33}:\text{O}^{2-}$ cement powder to produce CO or CO_2 gas, leaving an electron in the cavity-cage [34].

This process replaced free oxygen ions with free electrons by reacting active carbon C_2^- ions with free oxygen ions. First, carbon C_2^- ions were produced inside the crucible. Then, the C_2^- gas reacted with free oxygen species (O^{2-}) in cavity-cage at the surface layer of the insulating $\text{Ca}_{12}\text{Al}_{14}\text{O}_{33}:\text{O}^{2-}$ cement powder to produce CO or CO_2 gas and ejected free electrons into the cavity-cages via the reaction in Eq. (10),



This resulted in formation of two free electrons in the cage obtained from O^{2-} ions. Finally, the reaction ran to completion when the insulating

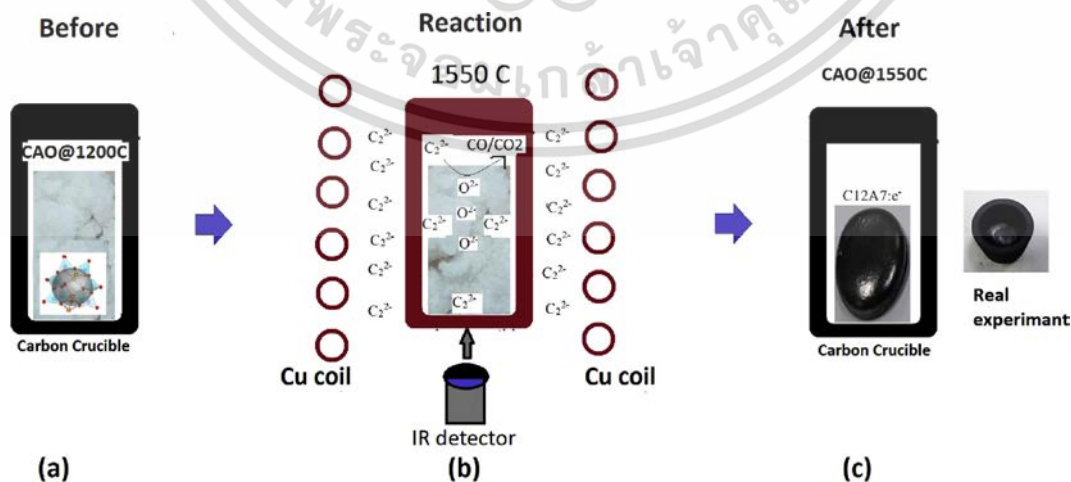


Fig. 12. Schematic diagram of the synthesized conducting $\text{Ca}_{12}\text{Al}_{14}\text{O}_{33}:\text{e}^-$ cement fabricated from insulating $\text{Ca}_{12}\text{Al}_{14}\text{O}_{33}:\text{O}^{2-}$ cement using a carbon crucible heated by a Cu induction coil via high frequency electromagnetic induction heating, (a) $\text{Ca}_{12}\text{Al}_{14}\text{O}_{33}:\text{O}^{2-}$ (CAO@1200C) cement powder in a carbon crucible, (b) the process of replacing of free oxygen ions by free electrons at powder surfaces via a reaction of active carbon (C_2^-) with free oxygen ions in a cavity-cage to produce CO/ CO_2 gas at 1550 °C and (c) the formation of conducting $\text{Ca}_{12}\text{Al}_{14}\text{O}_{33}:\text{e}^-$ cement.

$\text{Ca}_{12}\text{Al}_{14}\text{O}_{33}:\text{O}^{2-}$ cement was entirely converted to conducting $\text{Ca}_{12}\text{Al}_{14}\text{O}_{33}:\text{e}^-$. Fig. 12 (c) illustrates the formation of conducting $\text{Ca}_{12}\text{Al}_{14}\text{O}_{33}:\text{e}^-$ cement. A key to the production of the $\text{Ca}_{12}\text{Al}_{14}\text{O}_{33}:\text{e}^-$ cement at 1550 °C was the active carbon (C_2^-) atmosphere inside the carbon crucible at high temperature [34].

3.5. Anti-bacterial activities of $\text{Ca}_{12}\text{Al}_{14}\text{O}_{33}$ cements

Anti-bacterial activities of the as-fabricated CAO@1350C, CAO@1450C and CAO@1550C samples were investigated using two different bacterial species: (1) gram-negative *E. coli* and (2) gram-positive *S. Aureus* as shown in Figs. 13 and 14, respectively. The antibacterial properties of the samples were tested using an agar disk-diffusion method. Agar plates were first seeded with the test bacteria, followed by placed on the agar surfaces in a dark incubation chamber at 37 °C for 24 h. Both the insulating $\text{Ca}_{12}\text{Al}_{14}\text{O}_{33}:\text{O}^{2-}$ (CAO@1350C and CAO@1450C) and the conducting $\text{Ca}_{12}\text{Al}_{14}\text{O}_{33}:\text{e}^-$ (CAO@1550C) cement group materials were tested for antibacterial activity. Inhibition of bacterial growth was indicated by zones of clearing around the samples after they were placed on agar plates seeded with *E. coli* and *S. aureus* cells. SEM was used to show *E. coli* and *S. aureus* grown near the CAO@1350C, CAO@1450C and CAO@1550C samples in Figs. 13 (a) and

(b), and Figs. 14 (a) and (b), respectively. The results of these tests are shown in Figs. 13 (c), (d) and (e), and Figs. 14 (c), (d) and (e), for the CAO@1350C, CAO@1450C and CAO@1550C samples, respectively. SEM images of transition regions between areas with bacterial growth and inhibition of *E. coli* and *S. aureus* cells near the CAO@1350C, and CAO@1550C samples are shown Figs. 13 (f), (g) and (h), and Figs. 14 (f), (g) and (h), respectively.

The results from Figs. 13 and 14 demonstrate zones of inhibitions in the red-circled regions around the cement pellets. The inhibition zone widths are an index of *E. coli* inhibition. These zone widths were 12.8 mm, 11.1 mm and 15.5 mm for CAO@1350C, CAO@1450C and CAO@1550C samples, respectively. For *S. aureus*, the zones of inhibition were 22.7 mm, 13.9 mm and 36.2 mm wide for CAO@1350C, CAO@1450C and CAO@1550C samples, respectively. The histogram in Fig. 15 presents this data graphically. The results show that conducting $\text{Ca}_{12}\text{Al}_{14}\text{O}_{33}:\text{e}^-$ (CAO@1550C) exhibited much greater inhibition against both *E. coli* and *S. aureus* than the insulating $\text{Ca}_{12}\text{Al}_{14}\text{O}_{33}:\text{O}^{2-}$ (CAO@1350C, CAO@1450C) cement samples. The CAO@1450C cement displayed the smallest zone of inhibition resulting from its glass crystal phase (as shown in XRD results causing low antibacterial activity and few active sites on the sample surfaces. Moreover, it can be observed that the inhibition zones of *S. aureus* were larger than for *E. coli* due to the

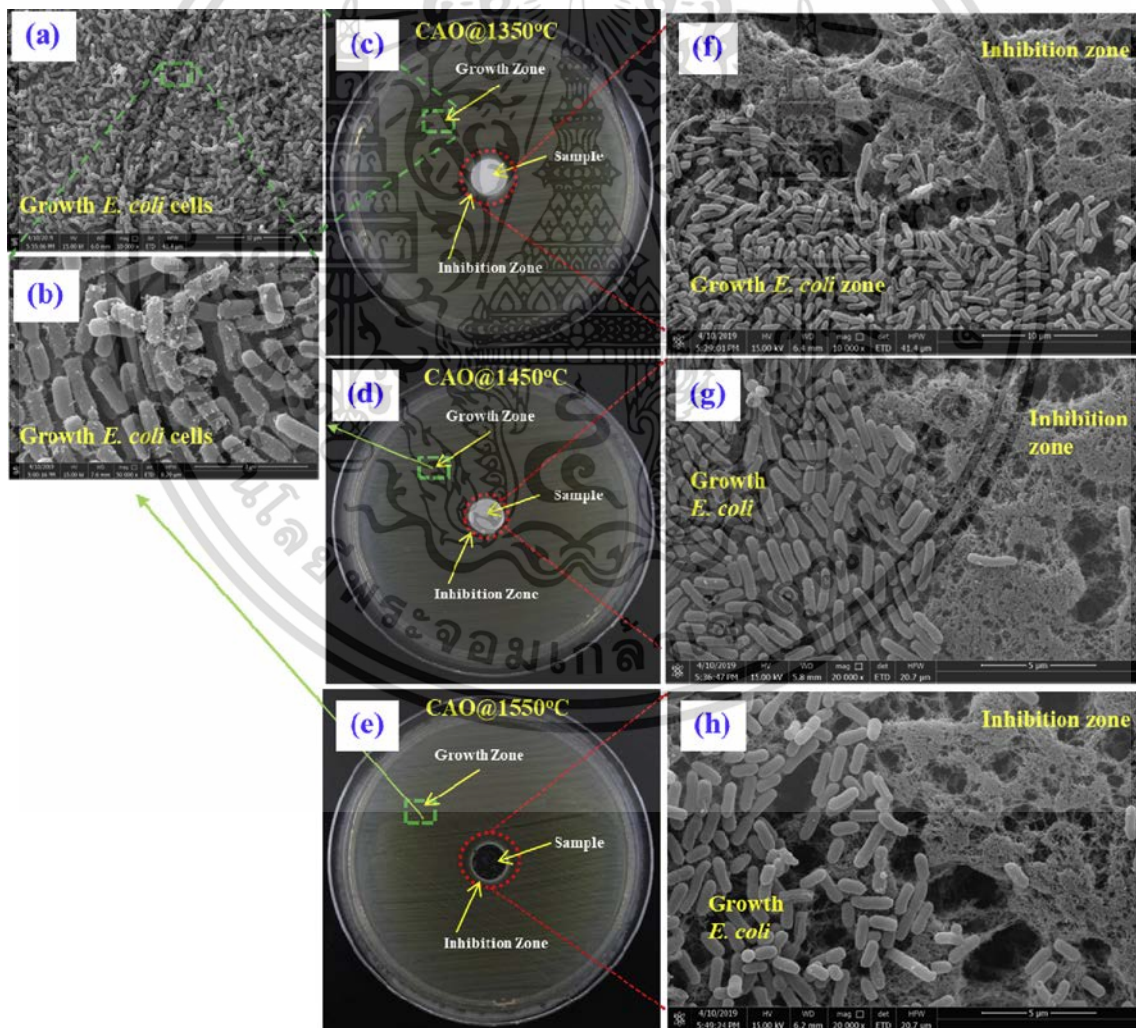


Fig. 13. Anti-bacterial activity testing of *E. coli* (ATCC 25922) using an agar disk-diffusion method producing zones of inhibition and SEM images showing zones of growth and inhibition of *E. coli*. (a) and (b) SEM of *E. coli* cell grown near the CAO@1350C, CAO@1450C and CAO@1550C samples, (c), (d) and (e) inhibition of bacterial growth zones of clearing around the samples after placed on agar plates seeded with *E. coli* cells of the CAO@1350C, CAO@1450C and CAO@1550C, respectively, and (f), (g) and (h) SEM images of transition regions between areas with bacterial growth and inhibition of *E. coli* cell near the CAO@1350C, and CAO@1550C samples, respectively.

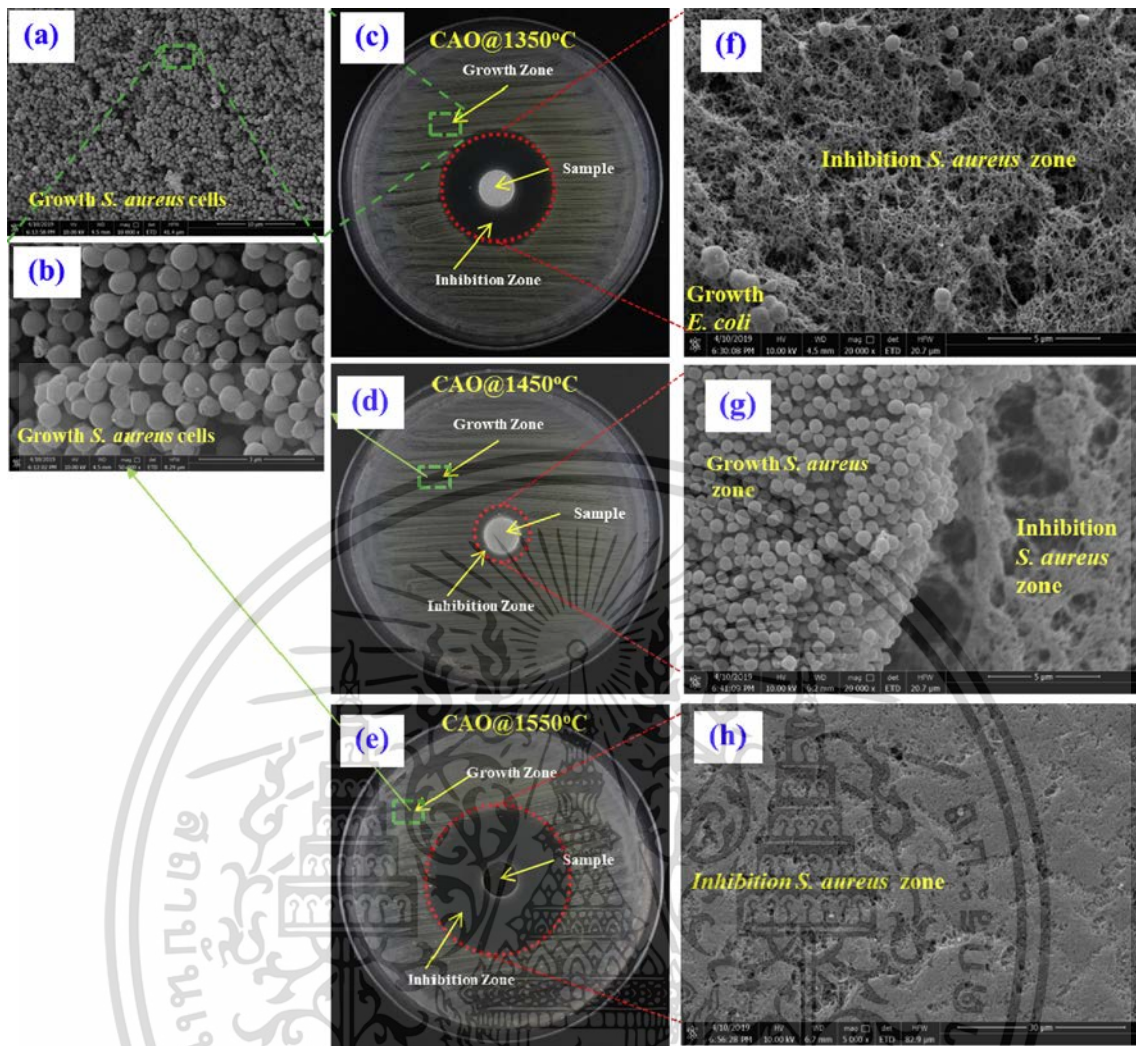


Fig. 14. Anti-bacterial activity testing of *S. aureus* (ATCC 25923) using an agar disk-diffusion method producing zones of inhibition and SEM images showing zones of growth and inhibition of *S. Aureus*, (a) and (b) SEM of *S. aureus* cell grown near the CAO@1350C, CAO@1450C and CAO@1550C samples, (c), (d) and (e) inhibition of bacterial growth zones of clearing around the samples after placed on agar plates seeded with *S. aureus* cell of the CAO@1350C, CAO@1450C and CAO@1550C, respectively, and (f), (g) and (h), SEM images of transition regions between areas with bacterial growth and inhibition of *S. aureus* cells near the CAO@1350C, and CAO@1550C samples, respectively.

structural differences in the bacterial cell walls. *E. coli* and other gram-negative bacteria have an outer cell membrane [47,48]. This provides *E. coli* with more resistance to reactive oxygen species (ROS). The SEM results show rod and spherical-shaped cells in the growth zones of *E. coli* and *S. aureus* in Figs. 13 (a) and (b), and Figs. 14 (a) and (b), respectively. Neither *E. coli* nor *S. aureus* grew in the inhibition zones shown in the SEM images (Figs. 13 (f), (g), (h), and Figs. 14 (f), (g) and (h), respectively). These results confirm that both bacterial species were inhibited to varying degrees by the CAO@1350C, CAO@1450C and CAO@1550C cements.

The mechanism to inactivate these bacteria was likely due to the effect of reactive oxygen species (ROS) such as super oxides (O_2^-), superoxide radicals ($O_2^{\cdot-}$), hydroxyl radicals (OH^{\cdot}) and hydrogen peroxide (H_2O_2). Several studies reported that reactive ROS interacting with bacterial cell components (proteins, lipids and DNA) cause cell death [4, 7–11]. The experimental results indicate that insulating $Ca_{12}Al_{14}O_{33}:O^{2-}$ cement material contained oxygen radicals (O_2^- and $O^{\cdot-}$ ions), while the conducting $Ca_{12}Al_{14}O_{33}:e^-$ cement material had a high concentration of the free electrons in its structure. It follows that these two material groups had different mechanisms for bacterial inactivation.

In case of the insulating $Ca_{12}Al_{14}O_{33}:O^{2-}$ material, the Raman spectroscopy in Fig. 9 for the insulating $Ca_{12}Al_{14}O_{33}:O^{2-}$ samples

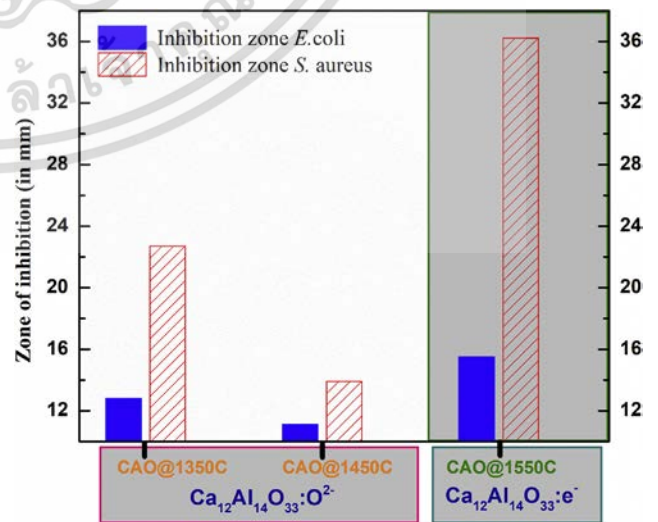


Fig. 15. Histogram depicting inhibition zone width for insulating $Ca_{12}Al_{14}O_{33}:O^{2-}$ cements (CAO@1350C and CAO@1450C), and $Ca_{12}Al_{14}O_{33}:e^-$ cement (CAO@1550C) against *E. coli* and *S. aureus*.

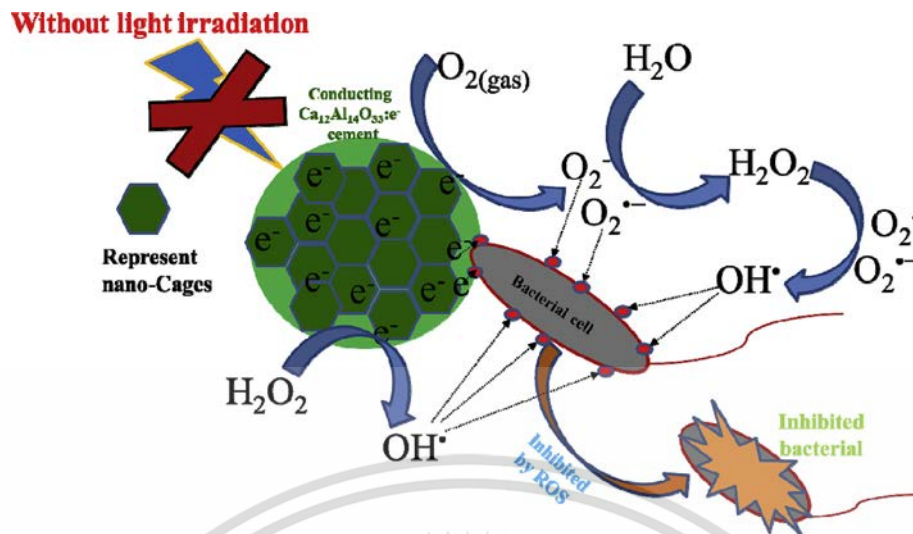


Fig. 16. Schematic diagram of the mechanism of anti-bacterial activity of the conducting $\text{Ca}_{12}\text{Al}_{14}\text{O}_{33}:\text{e}^-$ cement.

(CAO@1350C and CAO1450C) displayed a band of the ROS O_2^- species at 727 cm^{-1} , indicating an extra-framework for oxygen radicals (O_2^- and O^- ions) with concentrations up to $2 \times 10^{20}\text{ cm}^{-1}$ [24]. Clearly, the presence O_2^- species at the surface of the samples can cause inactivation of *E. coli* and *S. aureus* cells, as reported earlier [24], and this mechanism requires no photocatalytic effect.

In the case of conducting $\text{Ca}_{12}\text{Al}_{14}\text{O}_{33}:\text{e}^-$, as shown in Fig. 9, the CAO@1550C sample did not exhibit Raman bands of the ROS, O_2^- and O^- ions, species. The experimental results revealed that the CAO@1550C samples presented conducting materials with free electrons in its structure. This implies that the mechanism of bacterial inhibition of the conducting $\text{Ca}_{12}\text{Al}_{14}\text{O}_{33}:\text{e}^-$ cement was different than that of insulating $\text{Ca}_{12}\text{Al}_{14}\text{O}_{33}:\text{O}^{2-}$ cement. Additionally, due to the high free electron concentration ($1 \times 10^{20}\text{ cm}^{-1}$) in the conducting $\text{Ca}_{12}\text{Al}_{14}\text{O}_{33}:\text{e}^-$ structure with no photocatalytic effect, free electrons at surface of the material actively reacted with atmospheric oxygen, forming superoxide anions (O_2^-). Then, the O_2^- anions generated ROS species, i.e., H_2O_2 , O_2 , O_2^- and OH^\bullet as depicted in Fig. 16. These active oxygen species are extremely reactive, oxidizing and decomposing the organic substances of the bacteria. This implied that the conducting $\text{Ca}_{12}\text{Al}_{14}\text{O}_{33}:\text{e}^-$ cement displayed antibacterial activity with no photocatalytic effect. The reaction generating the ROS species occurred via redox reactions [8] as follows Eqs. (11), (12), (13), (14) and (15):



Superoxide anions (O_2^-) were first generated from O_2 gas in the atmosphere reacting with caged free electrons ($\text{Ca}_{12}\text{Al}_{14}\text{O}_{33}:\text{e}^-$ (cage)) at the surface of conducting $\text{Ca}_{12}\text{Al}_{14}\text{O}_{33}:\text{e}^-$ cement following Eq. (11). Then, H_2O_2 was generated as depicted in Eq. (12). H_2O_2 reacted with caged free electrons in conducting $\text{Ca}_{12}\text{Al}_{14}\text{O}_{33}:\text{e}^-$ cement, along with O_2^- , and O_2^- to generate OH^\bullet radicals according to the reactions in Eqs. (13), (14), and (15). In this manner, conducting $\text{Ca}_{12}\text{Al}_{14}\text{O}_{33}:\text{e}^-$ cement inhibited both *E. coli* and *S. aureus* through the action of nano-caged free electrons in ($\text{Ca}_{12}\text{Al}_{14}\text{O}_{33}:\text{e}^-$ (cage)). Fig. 16 schematically shows a proposed mechanism for the conducting $\text{Ca}_{12}\text{Al}_{14}\text{O}_{33}:\text{e}^-$ cement's antibacterial activity. In summary, in the first mechanism of antibacterial activity, bacteria near the surface of this material were inactivated by

ROS adsorbed on the surface of the $\text{Ca}_{12}\text{Al}_{14}\text{O}_{33}$ cement. The second mechanism of antibacterial activity involved bacterial inactivation by ROS species that diffused from the $\text{Ca}_{12}\text{Al}_{14}\text{O}_{33}$ cement surfaces into the agar. In this way, bacteria not in contact with $\text{Ca}_{12}\text{Al}_{14}\text{O}_{33}$ cement surfaces were inactivated.

Bacterial inhibition consisted of two modes, 1) the effects of ROS in the insulating cement samples, and 2) the effect of caged free electrons in the conduction cement sample. $\text{Ca}_{12}\text{Al}_{14}\text{O}_{33}:\text{O}^{2-}$ material displayed O_2^- species at the surface of the samples causing inactivation of *E. coli* and *S. aureus* cells. $\text{Ca}_{12}\text{Al}_{14}\text{O}_{33}:\text{e}^-$ cement displayed free electrons in cavity-cages with easily movement to the surface of the material. Thus, the free electrons at surface produced ROS species, i.e., H_2O_2 , O_2 , O_2^- and OH^\bullet at the surfaces of cement materials. Testing confirmed that the $\text{Ca}_{12}\text{Al}_{14}\text{O}_{33}:\text{e}^-$ cement displayed antibacterial action against *E. coli* and *S. aureus*. Neither effect involved photocatalytic activity. These cement materials can be used in smart antibacterial walls for operation rooms and hospital wards, restaurants, nurseries, and in homes. There are also applications in HVAC and food processing.

4. Conclusions

Antibacterial $\text{Ca}_{12}\text{Al}_{14}\text{O}_{33}$ material was successfully prepared by a rapid heating of insulating $\text{Ca}_{12}\text{Al}_{14}\text{O}_{33}$ powder in a carbon crucible to a high temperature by high frequency electromagnetic induction heating. The CAO@1550C ($\text{Ca}_{12}\text{Al}_{14}\text{O}_{33}:\text{e}^-$) cement sample formed a conducting phase in the $\text{Ca}_{12}\text{Al}_{14}\text{O}_{33}$ material that was confirmed by XRD results. EDX results presented the chemical composition of the $\text{Ca}_{12}\text{Al}_{14}\text{O}_3$ cement and the UV-Vis spectroscopy showed an absorption energy at 2.8 eV, characteristic of conducting $\text{Ca}_{12}\text{Al}_{14}\text{O}_{33}:\text{e}^-$ cement. Raman spectroscopy revealed that ROS of O_2^- species did not appear in the CAO@1550C sample, but was present in the CAO@1200C, CAO@1350C and the CAO@1450C samples. First principles calculations confirmed experimental results for the CAO@1550C sample. It formed a phase of conducting $\text{Ca}_{12}\text{Al}_{14}\text{O}_{33}:\text{e}^-$ cement with free electrons in a nano-cage structure of the conducting $\text{Ca}_{12}\text{Al}_{14}\text{O}_{33}$ cement. The conducting $\text{Ca}_{12}\text{Al}_{14}\text{O}_{33}:\text{e}^-$ cement displayed the highest antibacterial activity against both *E. coli* and *S. aureus* with no photocatalytic activity. The antibacterial mechanism of conducting $\text{Ca}_{12}\text{Al}_{14}\text{O}_{33}$ (from free electrons in a nano-caged structure) was higher for both *E. coli* and *S. aureus* than that of the insulating $\text{Ca}_{12}\text{Al}_{14}\text{O}_{33}$ cement (from presence of ROS species in the structure). The inhibition of *E. coli* and *S. aureus* was due to the presence free electrons reacting with O_2 at the surface of the materials to produce to produce ROS such as H_2O_2 , O_2 , O_2^- and OH^\bullet with no nano-sized particle interaction or photocatalytic effects. This investigation

revealed that $\text{Ca}_{12}\text{Al}_{14}\text{O}_{33}$ cement has antibacterial properties that can inactivate *E. coli* and *S. aureus*.

Declarations

Author contribution statement

Chaiwat Phrompet: Performed the experiments; Analyzed and interpreted the data.

Chaval Sriwong: Performed the experiments.

Pornjuk Srepusharawoot: Analyzed and interpreted the data.

Santi Maensiri, Prinya Chindaprasirt: Conceived and designed the experiments.

Chesta Ruttanapun: Conceived and designed the experiments; Performed the experiments; Wrote the paper.

Funding statement

C. Ruttanapun was supported by the Thailand Research Fund (Contract Number: MRG6080236). C. Phrompet, C. Sriwong, and C. Ruttanapun were supported by the Thailand Research Fund (Contract Number: PHD60I0046). S. Maensiri was supported by the SUT-COE on Advanced Functional Materials, Suranaree University of Technology, Thailand. C. Ruttanapun and P. Chindaprasirt were supported by the Thailand Research Fund (TRF Distinguished Research Professor Grant No. DPG6180002).

Competing interest statement

The authors declare no conflict of interest.

Additional information

No additional information is available for this paper.

References

- Stuart B. Levy, Bonnie Marshall, Antibacterial resistance worldwide: causes, challenges and responses, *Nat. Med.* 10 (2004) S122–S129.
- Kate E. Jones, Nikkita G. Patel, Marc A. Levy, Adam Storeygard, Deborah Balk, John L. Gittleman, Daszak Peter, Global trends in emerging infectious diseases, *Nature* 451 (21 February 2008) 990–993.
- Krasimir Vasilev, Alex Cavallaro, Peter Zilm, Special issue: antibacterial materials and coatings, *Molecules* 23 (2018) 585.
- Shanshan Liu, Huanxiang Yuan, Haotian Bai, Pengbo Zhang, Fengting Lv, Libing Liu, Zhihui Dai, Jianchun Bao, Shu Wang, Electrochemiluminescence for electric-driven antibacterial therapeutics, *J. Am. Chem. Soc.* 140 (2018) 2284–2291.
- Rui Liu, Kaveh Memarzadeh, Bei Chang, Yumei Zhang, Zheng Ma, P. Allaker Robert, Ling Ren, Ke Yang, Antibacterial effect of copper-bearing titanium alloy (Ti-Cu) against *Streptococcus mutans* and *Porphyromonas gingivalis*, *Sci. Rep.* 6 (2016) 29985.
- Jing Shen, Lu Gong, Quan-Xin Li, Structure and antibacterial property of Na2O doped CAO, *Chin. J. Inorg. Chem.* (2011) 353–360.
- G. Poongodi, P. Anandan, R. Mohan, Kumar, R. Jayavel, Studies on visible light photocatalytic and antibacterial activities of nanostructured cobalt doped ZnO thin films prepared by sol-gel spin coating method, *Spectrochim. Acta Mol. Biomol. Spectrosc.* 148 (2015) 237–243.
- Amna Sirelkhathim, Shahrom Mahmud, Azman Seeni, Noor Haida Mohamad Kaus, Ling Chuo Ann, Siti Khadijah Mohd Bakhori, Habsah Hasan, Dasmawati Mohamad, Review on zinc oxide nanoparticles: antibacterial activity and toxicity mechanism, *Nano-Micro Lett.* 7 (3) (2015) 219–242.
- Paula Judith Perez Espitia, Nilda de Fátima Ferreira Soares, Jane Sélia dos Reis Coimbra, Nélio José de Andrade, Renato Souza Cruz, Eber Antonio Alves Medeiros, Zinc oxide nanoparticles: synthesis, antimicrobial activity and food packaging applications, *Food Bioprocess Technol.* 5 (2012) 1447–1464.
- Waseem Raza Syed Mohammad Faisal, Mohammad Owais, D. Bahnemann, M. Muneer, Facile fabrication of highly efficient modified ZnO photocatalyst with enhanced photocatalytic, antibacterial and anticancer activity, *RSC Adv.* 6 (2016) 78335–78350.
- Sangeeta Adhikari, Aditi Banerjee, Neerugatti Krishna Rao Eswar, Debasish Sarkar, Giridhar Madras, Photocatalytic inactivation of *E. coli* by ZnO–Ag nanoparticles under solar radiation, *RSC Adv.* 5 (2015) 51067–51077.
- Saji George, Suman Pokhrel, Zhaoxia Ji, Bryana L. Henderson, Tian Xia, Linjiang Li, Jeffrey I. Zink, André E. Nel, Lutz Mädler, Role of Fe doping in tuning the band gap of TiO₂ for the photo-oxidation-induced cytotoxicity paradigm, *J. Am. Chem. Soc.* 133 (29) (2011) 11270–11278.
- M. Sandhyarani, K. Venkateswarlu, T.A. Nellaippan, N. Ramesh Babu, M. Harikishore, Effect of Ag doping on antibacterial and photocatalytic activity of nanocrystalline TiO₂, *Procedia Mater. Sci.* 6 (2014) 557–566.
- Weiwei He, Hyun-Kyung Kim, Wayne G. Wamer, David Melka, John H. Callahan, Jun-Jie Yin, Photogenerated charge carriers and reactive oxygen species in ZnO/Au hybrid nanostructures with enhanced photocatalytic and antibacterial activity, *J. Am. Chem. Soc.* 136 (2) (2014) 750–757.
- K. Hayashi, S. Matsuishi, T. Kamiya, M. Hirano, H. Hosono, Light-induced conversion of an insulating refractory oxide into a persistent electronic conductor, *Nature* 419 (2002) 462–465.
- S.W. Kim, K. Hayashi, M. Hirano, H. Hosono, Electron carrier generation in a refractory oxide $12\text{CaO}\cdot 7\text{Al}_2\text{O}_3$ by heating in reducing atmosphere: conversion from an insulator to a persistent conductor, *J. Am. Chem. Soc.* 89 (2006) 3294–3298.
- S.W. Kim, et al., Metallic state in a lime-alumina compound with manoporous structure, *Nano Lett.* 7 (2007) 1138–1143.
- Peter P. Edwards, Electrons in cement, *Science* 333 (2011) 49.
- C. Ruttanapun, P. Srepusharawoot, S. Maensiri, Effect of Fe³⁺-doped $\text{Ca}_{12}\text{Al}_{14}\text{O}_{33}$ cement on optical and thermal properties, *Chin. J. Phys.* 56 (2018) 252–260.
- Chaiwat Phrompet, Chaval Sriwong, Santi Maensiri, Prinya Chindaprasirt, Chesta Ruttanapun, Optical and dielectric properties of nano-sized tricalcium aluminate hexahydrate (C3AH6) cement, *Constr. Build. Mater.* 179 (2018) 57–65.
- E. Feizi, A.K. Ray, $12\text{CaO}\cdot 7\text{Al}_2\text{O}_3$ ceramic: a review of the electronic and optoelectronic applications in display devices, *J. Disp. Technol.* 12 (2016) 451–459.
- Q.X. Li, M. Nishioka, H. Kashiwagi, et al., High-intensity atomic oxygen radical anion emission mechanism from $12\text{CaO}\cdot 7\text{Al}_2\text{O}_3$ crystal surface, *Surf. Sci.* 527 (1/2/3) (2003) 100–112.
- Katsuro Hayashi, Masahiro Hirano, Satoru Matsuishi, Hideo Hosono, Microporous crystal $12\text{CaO}\cdot 7\text{Al}_2\text{O}_3$ encaging abundant O⁻ radicals, *J. Am. Chem. Soc.* 124 (5) (2002) 738–739.
- Gong Lu, Shen Jing, Li Quan-Xin, Investigation on the antibacterial activity and mechanism of CAO-O particles, *J. Inorg. Mater.* 25 (2010) 943–946.
- G. Kresse, J. Furthmuller, Efficiency of ab-initio total energy calculations for metals and semiconductors using a plane-wave basis set, *Comput. Mater. Sci.* 6 (1996) 15–50.
- P. Blochl, Projector augmented-wave method, *Phys. Rev. B* 50 (1994) 17953–17979.
- D.M. Ceperley, B.J. Alder, Ground state of the electron gas by a stochastic method, *Phys. Rev. Lett.* 45 (1980) 566–569.
- W. Kerrou, A. Kabir, G. Scherber, B. Boudjema, S. Zerkout, A. Bouabellou, C. Sedrati, Characterization of CAO thin films deposited by spray pyrolysis, *J. Mater. Sci. Mater. Electron.* 27 (2016) 10106–10112.
- H. Hosono, K. Hayashi, M. Hirano, Active anion manipulation for emergence of active functions in the nanoporous crystal $12\text{CaO}\cdot 7\text{Al}_2\text{O}_3$: a case study of abundant element strategy, *J. Mater. Sci.* 42 (2007) 1872.
- Dong Jiang, Zeyu Zhao, Shenglong Mu, Vincent Phaneuf, Jianhua Tong, Simple and efficient fabrication of mayenite electrides from a solution-derived precursor, *Inorg. Chem.* 56 (2017) 11702–11709.
- Sung Wng Kim, Hideo Hosono, Synthesis and properties of $12\text{CaO}\cdot 7\text{Al}_2\text{O}_3$ electride: review of single crystal and thin film growth, *Phil. Mag.* 92 (19-21) (2012) 2596–2628.
- Tian-Nan Ye, Jiang Li, Masaaki Kitano, Masato Sasase, Hideo Hosono, Electronic interactions between a stable electride and a nano-alloy control the chemoselective reduction reaction, *Chem. Sci.* 7 (2016) 5969–5975.
- SungWng Kim, Masashi Miyakawa, Katsuro Hayashi, Takashi Sakai, Masahiro Hirano, Hideo Hosono, Simple and efficient fabrication of room temperature stable electride: melt-solidification and glass ceramics, *J. Am. Chem. Soc.* 127 (2005) 1370–1371.
- Karim Khana, Ayesha Khan Tareenb, Sayed Elshahata, Ashish Yadava, Usman Khanc, Minghui Yangb, Luigi Bibboa, Zhengbiao Ouyanga, Facile synthesis of cationic doped $[\text{Ca}_{24}\text{Al}_{28}\text{O}_{64}]^{4+}(4e^-)$ composite via rapid citrate sol-gel method, *Dalton Trans.* 47 (11) (2018) 3819–3830.
- K. Hayashi, S. Matsuishi, N. Ueda, M. Hirano, H. Hosono, Maximum incorporation of oxygen radicals, O⁻ and O₂⁻ into $12\text{CaO}\cdot 7\text{Al}_2\text{O}_3$ with a nanoporous structure, *Chem. Mater.* 15 (2003) 1851–1854.
- Y. Dong, H. Hosono, K. Hayashi, Formation and quantification of peroxide anion in nanocage of $12\text{CaO}\cdot 7\text{Al}_2\text{O}_3$, *RSC Adv.* 3 (2013) 18311–18316.
- Koichi Kajihara, Satoru Matsuishi, Katsuro Hayashi, Masahiro Hirano, Hideo Hosono, Vibrational dynamics and oxygen diffusion in a nanoporous oxide ion conductor $12\text{CaO}\cdot 7\text{Al}_2\text{O}_3$ studied by ¹⁸O labeling and micro-Raman spectroscopy, *J. Phys. Chem. C* 111 (2007) 14855–14861.
- M. Ruzsaki, S. Witkowski, P. Pietrzyk, A. Kotarba, Z. Sojka, The role of intermediate calcium aluminate phases in solid state synthesis of mayenite $\text{Ca}_{12}\text{Al}_{14}\text{O}_{33}$, *Funct. Mater. Lett.* 4 (2) (2011) 183–186.
- Shuwu Yang, Junko N. Kondo, Satoru Hayashi, Mashiro Hirano, Kazunari Domen, Hideo Hosono, Formation and decomposition of oxygen species in nanoporous crystal $12\text{CaO}\cdot 7\text{Al}_2\text{O}_3$, *Chem. Mater.* 16 (2004) 104–110.
- Miriding Mutailipu, Min Zhang, Hongping Wu, Zhihua Yang, Yihan Shen, Junliang Sun, Shilie Pan, Ba₃Mg₃(BO₃)₃F₃ polymorphs with reversible phase transition and high performances as ultraviolet nonlinear optical materials, *Nat. Commun.* 9 (2018) 3089.
- M. Mutailipu, M. Zhang, B. Zhang, L. Wang, Z. Yang, X. Zhou, S. Pan, SrB₅O₇F₃ functionalized with [B₅O₉F₃]¹⁶⁻ chromophores: accelerating the rational design of

- deep-ultraviolet nonlinear optical materials, *Angew Chem. Int. Ed. Engl.* 57 (2018) 6095–6099.
- [42] A. Hussain, S. Mehmood, M.N. Rasool, S. Aryal, P. Rulis, W.Y. Ching, Electronic structure, mechanical, and optical properties of CaO-Al₂O₃ system: a first principles approach, *Indian J. Phys.* 90 (8) (2016) 917–929.
- [43] Jian Huang, Loredana Valenzano, Gaurav Sant, Framework and channel modifications in mayenite (12CaO·7Al₂O₃) nanocages by cationic doping, *Chem. Mater.* 27 (2015) 4731–4741.
- [44] M.I. Kitano, Y. Inoue, Y. Yamazaki, F. Hayashi, S. Kanbara, S. Matsuishi, T. Yokoyama, S.W. Kim, M. Hara, H. Hosono, Ammonia synthesis using a stable electride as an electron donor and reversible hydrogen store, *Nat. Chem.* 4 (11) (2012 Nov) 934–940.
- [45] Michikazu Hara, Masaaki Kitano, Hideo Hosono, Ru-Loaded CaO:e⁻ Electride as a Catalyst for Ammonia Synthesis, *ACS Catal.* 7 (4) (2017) 2313–2324.
- [46] B. Patidar, M.M. Hussain, A. Sharma, A.P. Tiwari, Transient numerical analysis of induction heating of graphite crucible at different frequency, *Int. J. Electromagn. (IJEL)* 1 (No 1) (August 2016) 35.
- [47] Moumita Khamrai, Sovan Lal Banerjee, Patit P. Kundu, Modified bacterial cellulose based self-healable polyelectrolyte film for wound dressing application, *Carbohydr. Polym.* 174 (2017) 580–590.
- [48] Kun Yu, Fei Lu, Qing Li, Honglei Chen, Bitao Lu, Jiawei Liu, Zhiqun Li, Fangying Dai, Dayang Wu, Guangqian Lan, In situ assembly of Ag nanoparticles (AgNPs) on porous silk cocoon-based wound film: enhanced antimicrobial and wound healing activity, *Sci. Rep.* 7 (2017) 2107.



เอกสารนี้เป็นเอกสารที่สงวนไว้สำหรับการใช้งานเพื่อการศึกษาเท่านั้น ไม่อนุญาตให้นำไปใช้ประโยชน์ด้านการค้า
ไม่ว่ากรณีใดๆ ทั้งสิ้น อีกทั้งห้ามมิให้ตัดแปลงเนื้อหา และต้องอ้างอิงถึงเจ้าของเอกสารทุกครั้งที่มีการนำไปใช้



Effect of grain boundary interfaces on electrochemical and thermoelectric properties of a Bi_2Te_3 /reduced graphene oxide composites

Wannisa Thongsamrit^{a,c,d,e}, Chaiwat Phrompet^{a,c,d,e}, Keerati Maneesai^{a,c,d,e},
Attaphol Karaphun^{a,c,d,e}, Wattana Tuichai^{a,c,d,e}, Chaval Sriwong^{b,c,d,e},
Chesta Ruttanapun^{a,c,d,e,*}

^a Department of Physics, Faculty of Science, King Mongkut's Institute of Technology Ladkrabang, Chalokkrung Road, Ladkrabang, Bangkok, 10520, Thailand

^b Department of Chemistry, Faculty of Science, King Mongkut's Institute of Technology Ladkrabang, Chalokkrung Road, Ladkrabang, Bangkok, 10520, Thailand

^c Smart Materials Research and Innovation Unit, Faculty of Science, King Mongkut's Institute of Technology Ladkrabang, Chalokkrung Road, Ladkrabang, Bangkok, 10520, Thailand

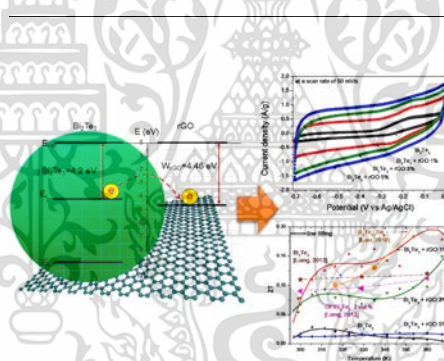
^d Center of Excellence in Smart Materials Research and Innovation, King Mongkut's Institute of Technology Ladkrabang, Chalokkrung Road, Ladkrabang, Bangkok, 10520, Thailand

^e Thailand Center of Excellence in Physics, Ministry of Higher Education, Science, Research and Innovation, 328 Si Ayutthaya Road, Bangkok, 10400, Thailand

HIGHLIGHTS

- The ultrasonic mixing of rGO nanosheets/ Bi_2Te_3 composites forming grain boundary interfaces.
- The conversion of p-type Bi_2Te_3 to n-type from rGO composites to supply electric charge carriers.
- Bi_2Te_3 + rGO composites increase storage charges with rGO contents.
- The highest ZT value at the bulk 1% Bi_2Te_3 + rGO composites.
- Improving of electrochemical and thermoelectric properties resulting from band alignment between Bi_2Te_3 and rGO nanosheets.

GRAPHICAL ABSTRACT



ARTICLE INFO

Keywords:

Thermoelectric
Electrochemical properties
 Bi_2Te_3
Reduced graphene oxide
Composite material
Grain boundary interface

ABSTRACT

The electrochemical and enhanced thermoelectric properties of pristine Bi_2Te_3 and Bi_2Te_3 /reduced graphene oxide (Bi_2Te_3 + rGO) composites at 1%, 3% and 5% levels of rGO were synthesized via a simple ultrasonic method. The X-ray diffraction (XRD), Raman spectroscopy, scanning electron microscopy (SEM), UV-vis spectrometry (UV-vis) and their electrochemical and thermoelectric properties were measured. The ultrasonic method succeeded in producing rGO nanosheets composited with Bi_2Te_3 forming grain boundary interfaces of rGO with Bi_2Te_3 . The resulting samples displayed a continuous network structure of rGO nanosheets in Bi_2Te_3 + rGO composites for electrons in the conduction band of the Bi_2Te_3 structure. Electrons were transferred to rGO nanosheets at the interface, contributing electron charge carriers in Bi_2Te_3 + rGO composites. This indicates band alignment between Bi_2Te_3 and rGO nanosheets. The Bi_2Te_3 + rGO composites exhibited an increasing storage charge mechanism of electrical double layer capacitors with greater rGO contents. The Bi_2Te_3 + rGO composites displayed negative a Seebeck coefficient for thermoelectric materials. The highest ZT value was 0.17 in the bulk 1% Bi_2Te_3 + rGO composite. Improved electrochemical and thermoelectric properties of the Bi_2Te_3 +

* Corresponding author. Department of Physics, Faculty of Science, King Mongkut's Institute of Technology, Ladkrabang, Bangkok, 10520, Thailand.
E-mail addresses: chesta.ruttanapun@gmail.com, chesta.ru@kmitl.ac.th (C. Ruttanapun).

<https://doi.org/10.1016/j.matchemphys.2020.123196>

Received 27 November 2019; Received in revised form 1 April 2020; Accepted 9 May 2020

Available online 14 May 2020

0254-0584/© 2020 Elsevier B.V. All rights reserved.

เอกสารนี้เป็นเอกสารที่สงวนไว้สำหรับการใช้งานเพื่อการศึกษาเท่านั้น ไม่อนุญาตให้นำไปใช้ประโยชน์ด้านการค้า
ไม่ว่ากรณีใดๆ ทั้งสิ้น อีกทั้งห้ามมิให้ดัดแปลงเนื้อหา และต้องอ้างอิงถึงเจ้าของเอกสารทุกครั้งที่มีการนำไปใช้

rGO 1% composite resulted from the interaction of the grain boundary interfaces of rGO nanosheets with pristine Bi_2Te_3 following the model of band alignment between Bi_2Te_3 and rGO nanosheets.

1. Introduction

Alternative energy technologies are emerging with many challenges. Numerous researchers seek green solutions to meet sustainable energy challenges while recovering waste heat from the environment as well as various other sources, such as sun light and a multitude of industrial processes, to produce electricity [1,2]. Thermoelectric (TE) materials are solid-state materials that can generate electricity from temperature gradients to produce electricity [1–3]. Efficient conversion is related to an energy balance of the system as a function of ZT , where T is absolute temperature in Kelvin and the Z value is expressed as the following:

$$Z = \frac{S^2 \sigma}{\kappa}, \quad (1)$$

where S is the Seebeck coefficient, σ is electrical conductivity, and κ is thermal conductivity. Bi_2Te_3 [4] and Bi_2Se_3 [5] based TE materials with large ZT values have successfully been used for TE devices. Particularly, Bi_2Te_3 is a high performance and low-temperature stable TE material [3]. Thus, there many methods to synthesize and enhance the properties of Bi_2Te_3 materials. These include doping and band engineering via Cu- and Se-doped atoms of n-type $\text{Cu}_{0.008}\text{Bi}_2\text{Te}_{2.7}\text{Se}_{0.3}$ [6] and CuI-doped $\text{Bi}_2\text{Te}_{2.7}\text{Se}_{0.3}$ [7].

Recently, there have many reports of composited TE materials with enhanced properties employing a modifying graphene base. They are referred to as reduced graphene oxides (rGO) [8]. The rGO materials are two-dimensional (2D) carbon nanomaterials with high surface area and are free electron charge carriers. They are widely used for improving the mechanical, thermal and electrical properties of materials [9–13]. Nam et al. [3] reported enhanced TE properties of TiO_2/rGO nanocomposites derived by increasing the ratio of electrical to thermal conductivity as an interface-controlled effect. An enhanced Bi_2Te_3 was reported by Ahmad et al. [8] using a simple and effective strategy employing the quantum confined structures of 2D graphene dispersed in a nanostructured Bi_2Te_3 powder for evaluating thermoelectric properties. Du et al. [12] reported rGO/ Bi_2Te_3 nanocomposite powders that were synthesized via a one-step *in-situ* reductive method.

However, there are no reports of improved electrochemical and thermoelectric properties of Bi_2Te_3 doped with rGO via a mixing/ultrasonic route. Moreover, Rahman et al. [9] reported incorporation of rGO into $\text{SrTiO}_{3-\delta}$ (STO) that weakly affected grain boundary interfaces causing enhanced TE properties. Xu et al. [14] reported that an ultrasonication treatment with stirring produced strong π - π interactions between the rGO and polymer molecules of poly (3, 4 ethylenedioxythiophene) for enhanced TE performance. Also, ultrasonication can be used to improve the TE properties of $\text{Bi}_2\text{Te}_3/\text{rGO}$ composites.

Herein, this work proposes an ultrasonication method for preparing a 2D rGO nanosheet composite with p-type pristine Bi_2Te_3 to improve the electrochemical and thermoelectric properties of such materials. An rGO precursor was prepared and characterized using X-ray diffraction (XRD), Raman spectroscopy, scanning electron microscopy (SEM), transmission electron microscopy (TEM), high-resolution TEM (HR-TEM), and UV–vis spectrometry. 2D rGO nanosheets and pristine Bi_2Te_3 with various rGO contents were synthesized using an ultrasonication method. Then, the bulk materials were fabricated by hot press sintering them. The electrochemical properties of all powders and their thermoelectric properties were characterized. The Seebeck coefficient, electrical conductivity and thermal conductivity of bulk samples were investigated. Morphology and thermodynamic stability of these samples were evaluated. The enhanced properties of rGO nanosheets and pristine Bi_2Te_3 composites were examined to determine the effects of grain boundary

interfaces by rGO incorporation with pristine Bi_2Te_3 on the thermo-electric and electrochemical properties of these materials. These results are reported. The effects of the ultrasonication method on grain boundary interfaces by rGO nanosheets and pristine Bi_2Te_3 behavior are discussed.

2. Experimental details

2.1. Chemicals and materials

Commercial grade p-type pristine Bi_2Te_3 powder was purchased from SANTECH™. Graphite powder (99% purity) and hydrogen peroxide (H_2O_2 , 30%) were purchased from Sigma-Aldrich (USA). Sulfuric acid (H_2SO_4 , 98%), hydrochloric acid (HCl, 37%), and potassium permanganate (KMnO_4) were obtained from Merck (Germany). An ammonia solution (NH_3 , 28–30%) was supplied by Baker (USA). All chemicals were used as received without further purification.

2.2. Preparation of reduced graphene oxide (rGO)

Reduced graphene oxide, rGO, was firstly synthesized via a modified Hummers method by oxidizing graphite with a strong acid and followed by chemical reduction method according to Phrompet et al. [15]. Briefly, graphite powder (2 g) was mixed with KMnO_4 (6 g) in a beaker. Then the mixed powder was poured into a 500 mL round bottom flask and cooled to 0 °C. After that, H_2SO_4 (46 mL) was gradually added under stirring and cooling, maintaining its temperature below 15 °C. Then, the mixture was stirred at 40 °C for 30 min. Next, distilled water (90 mL) was slowly added and the mixture was heated under stirring to 95 °C for 60 min. Subsequently, the reaction was stopped by adding distilled water (250 mL) and a H_2O_2 solution (10 mL). The obtained product was separated by centrifugation and washed with a 5% HCl solution to reduce sulphate. After that, it was filtered and washed several times with distilled water until the pH of filtered solution was about 7. The resulting solid paste product was dried in an oven overnight at 65 °C. The synthesized graphite oxide powder (800 mg) was re-dispersed in distilled water (120 mL) under ultrasonication for 90 min, followed by centrifugation. Finally, the supernatant of an aqueous graphene oxide (GO) suspension was obtained. Thus, reduced graphene oxide (rGO) was obtained from a GO (2 mg/mL) suspension in 100 mL mixed with distilled (100 mL), ammonia (1 mL) and hydrazine hydrate solutions (0.1 mL). Then, the obtained mixture was heated to 95 °C and stirred for 45 min. Finally, a stable aqueous suspension of rGO was obtained.

2.3. The preparation of $\text{Bi}_2\text{Te}_3 + \text{rGO}$ composites

The p-type Bi_2Te_3 pristine powder was crushed and dissolved in an aqueous acetone solution. The composite powders of Bi_2Te_3 and rGO nanosheets at various levels, 1%, 3% and 5 wt%, were mixed using an ultrasonication method as shown in Fig. 1(a). In a typical procedure to make $\text{Bi}_2\text{Te}_3 + \text{rGO}$ samples, first, about 5 g of Bi_2Te_3 powder was dispersed in 170, 110 and 50 mL of acetone to prepare 1%, 3% and 5% levels of rGO, respectively. Then, various rGO solutions (2 mg/mL) were mixed using a sonication method at room temperature for 1 h. After that, the mixture suspensions were further stirred at room temperature for 1 h. Then, the resulting homogeneous mixtures were filtered and washed using acetone, and then dried in an oven at 100 °C for 24 h. Finally, 1%, 3% and 5% $\text{Bi}_2\text{Te}_3 + \text{rGO}$ powder samples were obtained.

2.4. The fabrication of pristine Bi_2Te_3 and $\text{Bi}_2\text{Te}_3 + \text{rGO}$ composite electrodes

Working electrodes were made at 85 wt percent of pristine Bi_2Te_3 or as-prepared $\text{Bi}_2\text{Te}_3 + \text{rGO}$ samples, PVDF (10%) and acetylene black (5%) with 0.5 ml of NMP using ball milling at room temperature for 24 h to form a slurry. Then, the slurry was coated on a $1 \times 1 \text{ cm}^2$ area of a nickel foam substrate. The thickness of the nickel foam was $\sim 1.5 \text{ mm}$. It was oven dried at $80 \text{ }^\circ\text{C}$ for 3 h. Next, the active electrodes were pressed with a force of 1.5 tonnes for 1 min producing active electrodes with a thickness of $\sim 0.07 \text{ mm}$. The masses of active material in pristine Bi_2Te_3 and 1%, 3% and 5% $\text{Bi}_2\text{Te}_3 + \text{rGO}$ electrodes were 3.22, 3.49, 3.41, and 3.78 g, respectively. Finally, these active electrodes were soaked in an aqueous 6.0 M KOH solution for 3 h before performing electrochemical testing.

2.5. Fabrication of the pristine Bi_2Te_3 and $\text{Bi}_2\text{Te}_3 + \text{rGO}$ composite pellets

For pellets prepared as shown in Fig. 1(b), pristine Bi_2Te_3 and 1%, 3% and 5% $\text{Bi}_2\text{Te}_3 + \text{rGO}$ samples were subjected to uniaxial compression into disc-shaped pellets that were 10 mm in diameter with a thickness of 3 mm. They were hot-press sintered at $450 \text{ }^\circ\text{C}$ for 1 h under a hydraulic pressure of $\sim 12.7 \text{ MPa}$. Finally, 1%, 3% and 5% $\text{Bi}_2\text{Te}_3 + \text{rGO}$ pellets were obtained.

2.6. Characterization

The XRD phase of the rGO, pristine Bi_2Te_3 and 1%, 3%, and 5% $\text{Bi}_2\text{Te}_3 + \text{rGO}$ samples were analyzed using powder X-ray diffraction (XRD) in a PHILIPS X'Pert (X-ray source $\lambda \text{ CuK}\alpha = 1.5406 \text{ \AA}$). Raman spectroscopy was performed using a DXR Smart (Thermo Scientific) at a 532 nm excitation wavelength. The morphology of the samples was observed using SEM. A TEM and a high-resolution TEM (HRTEM) (JEOL-2100) operating at 200 kV) were used for measuring the nano particle sizes of the samples. Density (D) was measured using the Archimedes's principle. Thermogravimetric analysis (TGA, Netzsch STA 449F3 Jupiter) was performed over a temperature of $35 \text{ }^\circ\text{C}$ to $900 \text{ }^\circ\text{C}$ with a heating rate of $10 \text{ }^\circ\text{C}/\text{min}$ in nitrogen gas to measure the weight loss of the samples. The optical absorption spectra were measured using a UV-VIS-NIR spectrophotometer (Shimadzu UV-3101PC) at room temperature. For electrochemical properties, cyclic voltammetry (CV) and galvanostatic charge-discharge GCD tests were performed in a three-electrode cell system in an aqueous 6.0 M KOH solution, using Ag/AgCl in 3.0 M HCl and platinum wire as reference and counter electrodes, respectively. Thermal conductivity values were measured using a NETZSCH LFA 477 Nano-Flash thermal diffusivity analyzer on flat samples that were 12-mm in diameter and 2–3 mm thick. The Seebeck coefficient and electric conductivity were measured using an in-house testing apparatus described by Wongjom et al. [16] connected to a 34461a KEYSIGHT™ bench digital multi-meter, a 34420a KEYSIGHT™ nano voltmeter and a constant DC-current passed through the sample

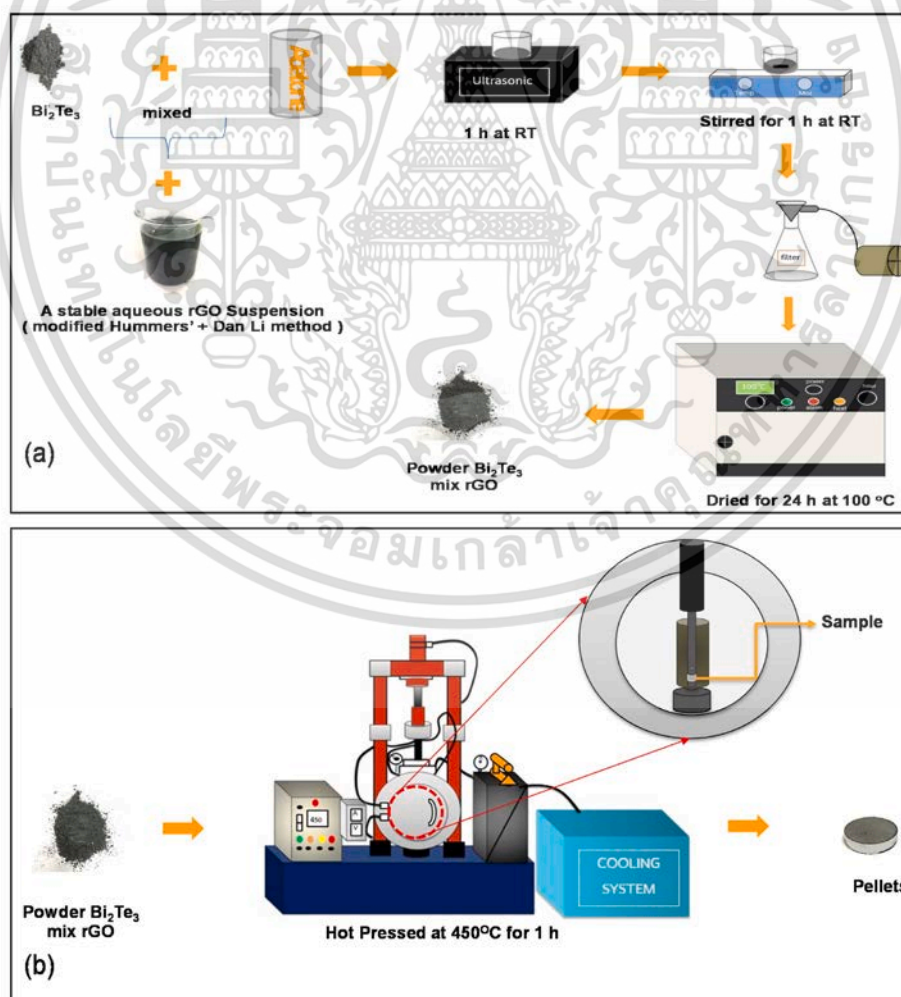


Fig. 1. (a) Schematic of the preparation of $\text{Bi}_2\text{Te}_3 + \text{rGO}$ 1%, 3% and 5% composites via a simple ultrasonication method, and (b) schematic of the fabrication of pristine Bi_2Te_3 and $\text{Bi}_2\text{Te}_3 + \text{rGO}$ 1%, 3% and 5% pellets by hot-press sintering.

ไม่ว่าการณ์ใดๆ ทั้งสิ้น อีกทั้งห้ามมิให้ตัดแปลงเนื้อหา และต้องอ้างอิงถึงเจ้าของเอกสารทุกครั้งที่มีการนำไปใช้

using a KEITHLEY™ source meter.

3. Results and discussion

3.1. The analysis of rGO nanosheet

Fig. 2(a) shows Raman spectroscopy of the prepared rGO nanosheets. The Raman spectra displayed two main peaks at around 1353 cm^{-1} and 1592 cm^{-1} , which correspond to disordered carbon (D band) and graphitic sp^2 carbon (G band) characteristic of rGO. The D band was associated with the breathing mode of the K point phonons of A_{1g} symmetry. It mainly indicated the surface disorder and defects of graphene. The G band is the result of first order scattering of E_{2g} phonons from sp^2 carbon. The evolution of disorder is usually quantified by the intensity ratio of the D to G bands (I_D/I_G). The I_D/I_G values were 1.031 as presented by reduced graphene oxide. A 2D peak at around 2700 cm^{-1} was observed for the rGO sample. This confirmed the complete sintering of rGO. Additionally, the morphology of rGO nanosheets was analyzed using bright field TEM images as shown in Fig. 2(b), indicated by the translucent thin sheets, creases and wrinkles. Fig. 2(c) demonstrates that

the composite $\text{Bi}_2\text{Te}_3 + \text{rGO}$ by using the pristine Bi_2Te_3 was grown onto the rGO suspension with dispersed in surfactant-assisted solvent (Acetone solvent). According to inset in Fig. 2(c), the newly formed interface at the surface might be the ionic interaction between pristine Bi_2Te_3 ($+$) and rGO (e^-). It was corresponded to the oxygen atoms existing at the rGO surface by providing tight ionic bonding with Bi^{3+} or Te^{4+} ions in the surface of Bi_2Te_3 as previously reported of a CNT/ Bi_2Te_3 interface [17]. Also, the $\text{Bi}_2\text{Te}_3 + \text{rGO}$ composite was caused to the pristine Bi_2Te_3 implanted into the rGO matrix. The characteristic microstructures of the $\text{Bi}_2\text{Te}_3 + \text{rGO}$ composite displayed similar flake-like shapes with comprised a contained rGO network structure as embedded by the Bi_2Te_3 grain as shown in Fig. 5(a) – (d).

3.2. Raman of rGO, Bi_2Te_3 pristine and $\text{Bi}_2\text{Te}_3 + \text{rGO}$ composite powders

To confirm the characteristic structures of rGO, pristine Bi_2Te_3 and the interaction interface between rGO and pristine Bi_2Te_3 of as-prepared $\text{Bi}_2\text{Te}_3 + \text{rGO}$ samples, Raman spectroscopy was carried out. Fig. 3(a) shows the Raman spectra of rGO, pristine Bi_2Te_3 and $\text{Bi}_2\text{Te}_3 + \text{rGO}$ composite samples at various rGO levels, 1%, 3% and 5%, in the spectral

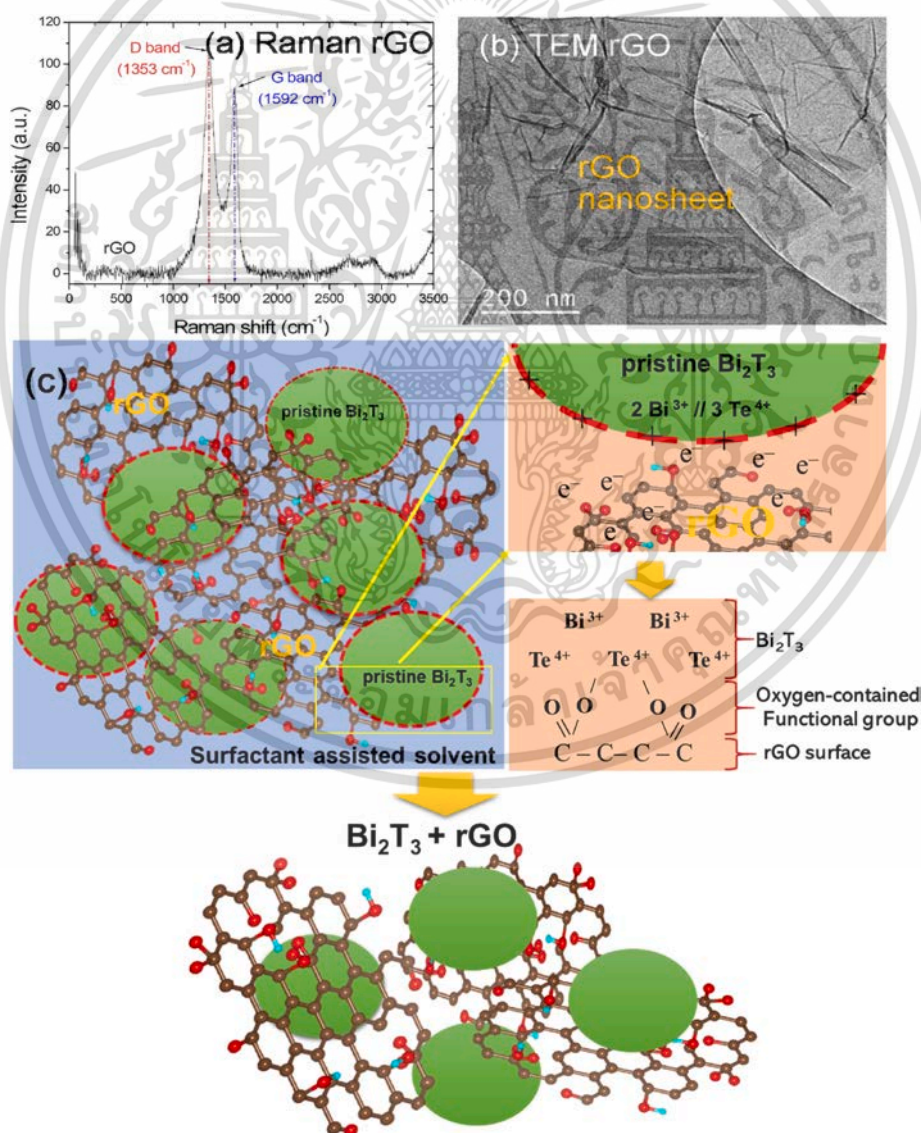


Fig. 2. (a) Dispersive Raman spectra, (b) bright field TEM images of rGO nanosheet and (c) the schematics of rGO suspension with the pristine Bi_2Te_3 to be reduced in the surface assisted solvent with inset the newly formed interface at the surface between pristine Bi_2Te_3 and rGO, and focus on the ionic bonding of $\text{Bi}_2\text{Te}_3 + \text{rGO}$ composite where pristine Bi_2Te_3 are implanted into the rGO matrix.

ไม่ว่ากรณีใดๆ ทั้งสิ้น อีกทั้งห้ามมิให้ตัดแปลงเนื้อหา และต้องอ้างอิงถึงเจ้าของเอกสารทุกครั้งที่มีการนำไปใช้

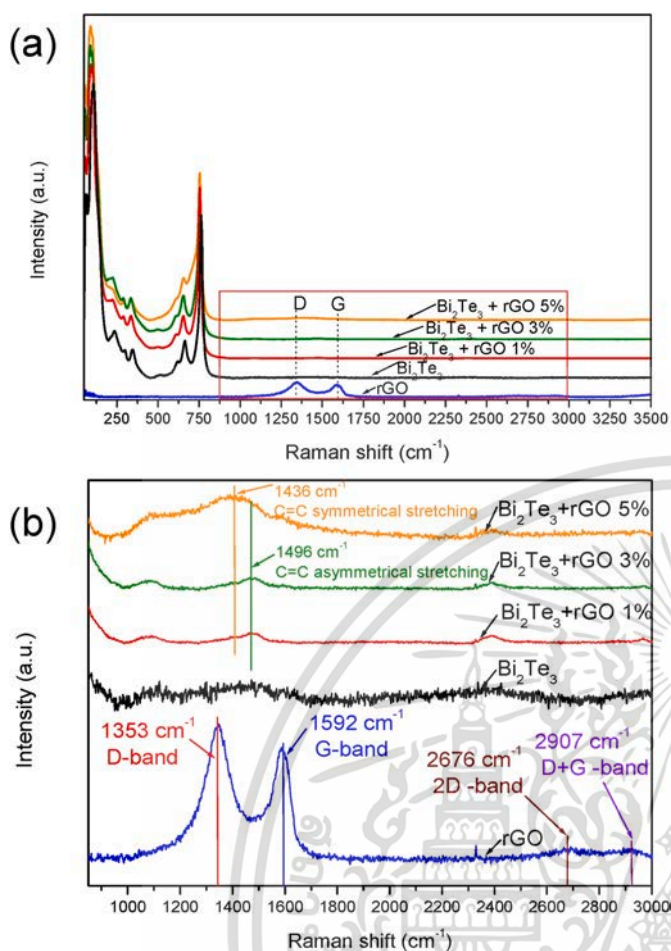


Fig. 3. (a) Dispersive Raman spectra of rGO, pristine Bi_2Te_3 and 1%, 3% and 5% $\text{Bi}_2\text{Te}_3 + \text{rGO}$ composite powders and (b) enlarged of D and G band in the Raman shift range of $800\text{--}3000\text{ cm}^{-1}$.

range from 100 cm^{-1} to 3500 cm^{-1} . Fig. 3(b) shows the Raman spectra of these samples in the spectral range from 1000 cm^{-1} to 3000 cm^{-1} . In these figure, two main peaks were observed in the spectral range from 200 cm^{-1} to 800 cm^{-1} in pristine Bi_2Te_3 , as shown in Fig. 3(a). The two peaks observed at 120 cm^{-1} and 750 cm^{-1} correspond to results reported in the literature [12]. The Raman spectra of all 1%, 3% and 5% $\text{Bi}_2\text{Te}_3 + \text{rGO}$ samples showed these two main peaks which are related are the spectral peaks of pristine Bi_2Te_3 . The position of these peaks in the spectra confirms the presence of the Bi_2Te_3 structure of the $\text{Bi}_2\text{Te}_3 + \text{rGO}$ composite powders. It can be clearly observed that the two main peaks at 1353 cm^{-1} and contributed to the D- and G-bands of the prepared rGO nanosheets. Moreover, the presences of Raman shifts in the D-band (at 1353 cm^{-1}) result from the vibration of sp^3 (-C-C-) hybridized carbon atoms, and G-band (at 1592 cm^{-1}) represents the vibration of sp^2 (-C=C-) hybridized carbon atoms of rGO structure were observed in the $\text{Bi}_2\text{Te}_3 + \text{rGO}$ composite samples. The ratio of the I_D/I_G values were 1.031 for successfully prepared rGO nanosheets. This elucidates the presence of an rGO composite in the 1%, 3% and 5% $\text{Bi}_2\text{Te}_3 + \text{rGO}$ samples. Moreover, a high intensity of Raman spectra peak at 1496 cm^{-1} for the 1% and 3% $\text{Bi}_2\text{Te}_3 + \text{rGO}$ samples and at 1436 cm^{-1} for the 5% $\text{Bi}_2\text{Te}_3 + \text{rGO}$ sample was observed. The Raman spectra peaks at 1255 cm^{-1} , 1365 cm^{-1} , 1436 cm^{-1} , and 1496 cm^{-1} were present due to -C-C- inter-ring stretching, -C-C- stretching, -C=C- symmetrical stretching, and -C=C- asymmetrical stretching [12,14,15], respectively. This indicates -C-C- and -C=C- symmetrical stretching in rGO nanosheets in the 1%, 3% and 5% $\text{Bi}_2\text{Te}_3 + \text{rGO}$ samples. The position of these peaks shows that a strong π -free electron induced interaction existed between

the interfaces of π - π conjugation of rGO molecules and free electrons of Bi_2Te_3 conductor. Similarly, the Raman result of these peaks was reported in previous study due to free electrons on the π - π conjugation of carbon nanotubes (CNT) structure interacted with Bi_2Te_3 structure by Kim et al. [17]. The schematic proposed on the interaction of Bi_2Te_3 particles and rGO nanosheets, as illustrated in Fig. 3(b). From this figure, a strong π -free electron from rGO nanosheets induced the grain boundary surface of Bi_2Te_3 particles to produce the ionic interaction between pristine Bi_2Te_3 (+) and rGO (e^-), correspondingly the free electrons exists at the rGO surface might provide tight ionic bonding with Bi^{3+} or Te^{4+} ions in the surface of Bi_2Te_3 particles. This result was due to the high sonication power used during the mixing process. It enhanced Bi_2Te_3 molecular adsorption and improved interaction with the rGO surfaces. The Bi_2Te_3 surfaces easily adsorbed material and was covered by the 2D templates of rGO nanosheets causing a strong π -free electron induced interaction. This effect occurred by exfoliation of rGO nanosheets in an aqueous dispersion with suspended Bi_2Te_3 during ultrasonic preparation. From this result, pristine Bi_2Te_3 could enhance both the thermoelectric and electrochemical properties of these materials owing to the effect of the rGO nanosheets of $\text{Bi}_2\text{Te}_3 + \text{rGO}$ materials.

3.3. XRD spectra of rGO, pristine Bi_2Te_3 and $\text{Bi}_2\text{Te}_3 + \text{rGO}$ composite powders

The XRD patterns and an enlargement of the (015) plane in the 2θ range of $27\text{--}30^\circ$ of prepared rGO, pristine Bi_2Te_3 and 1%, 3% and 5% $\text{Bi}_2\text{Te}_3 + \text{rGO}$ composite powders are shown in Fig. 4(a). XRD results of all samples showed the most dominant diffraction peaks at 2θ values of 17.46 , 27.61 , 34.60 , 40.04 , 41.26 , 44.61 , 50.18 , 53.82 , and 57.06° that can be attributed to the (006), (015), (1010), (0111), (110), (0015), (205), (1016), and (0210) planes of a rhombohedral structure of Bi_2Te_3 (R-3m as indexed by the standard data of JCPDF, No. 15-0863) [12,18]. The average crystalline sizes (D) of pristine Bi_2Te_3 and all $\text{Bi}_2\text{Te}_3 + \text{rGO}$ samples were calculated from the (006), (015), (1010), (0015), (1016), and (0210) reflection planes using Scherrer's equation, $D = k\lambda/\beta\cos\theta$, where D is the average crystalline size, k is a constant taken as 0.9, λ is the wavelength of incident X-rays, β is the full width at half maximum, and θ is the Bragg angle [19]. The calculated D values can be obtained from Fig. 4(b). As can be clearly seen in Fig. 4(b), the D value of Bi_2Te_3 sample at $39.395 \pm 2.827\text{ nm}$ was different from those of samples with increased rGO concentrations, 43.894 ± 2.911 , 42.439 ± 4.094 and $38.797 \pm 4.503\text{ nm}$ for 1%, 3% and 5% $\text{Bi}_2\text{Te}_3 + \text{rGO}$ composites, respectively. The decrease of D value corresponded to XRD results with greater intensity for the (015) plane, showing a shift to higher 2θ values that resulted from a decreased crystallite size of these samples. Similarly, the lattice parameters (a, b, c) of pristine Bi_2Te_3 and all $\text{Bi}_2\text{Te}_3 + \text{rGO}$ samples were obtained using a refinement employing a rhombohedral Bi_2Te_3 structure having the standard data of JCPDF, No. 15-0863, as depicted in Fig. 4(b). As can be seen in this figure, the lattice parameters (a, b, c) also decreased with increasing rGO content in agreement with previous literature reports [12,18,19].

3.4. SEM and EDS mapping of prepared rGO, pristine Bi_2Te_3 and $\text{Bi}_2\text{Te}_3 + \text{rGO}$ composite powders

The morphology of pristine Bi_2Te_3 and $\text{Bi}_2\text{Te}_3 + 1\%$, 3% and 5% rGO composite powders were analyzed from the SEM images shown in Fig. 5 (a) – (d). As seen in Fig. 5(a), the pristine Bi_2Te_3 sample consisted of agglomerated irregular flake-like shapes with a micrometer grain size. Additionally, the 1%, 3% and 5% $\text{Bi}_2\text{Te}_3 + \text{rGO}$ composites displayed similar flake-like shapes corresponding to the pristine Bi_2Te_3 sample with a uniform shape that comprised a continuous rGO network structure of nanosheets presenting Bi_2Te_3 materials, as shown in the high magnification views of Fig. 5(b) – (d). To confirm the components and dispersion of elements of both pristine Bi_2Te_3 and 1%, 3% and 5% $\text{Bi}_2\text{Te}_3 + \text{rGO}$ composite powders, the EDS spectra and EDS mapping

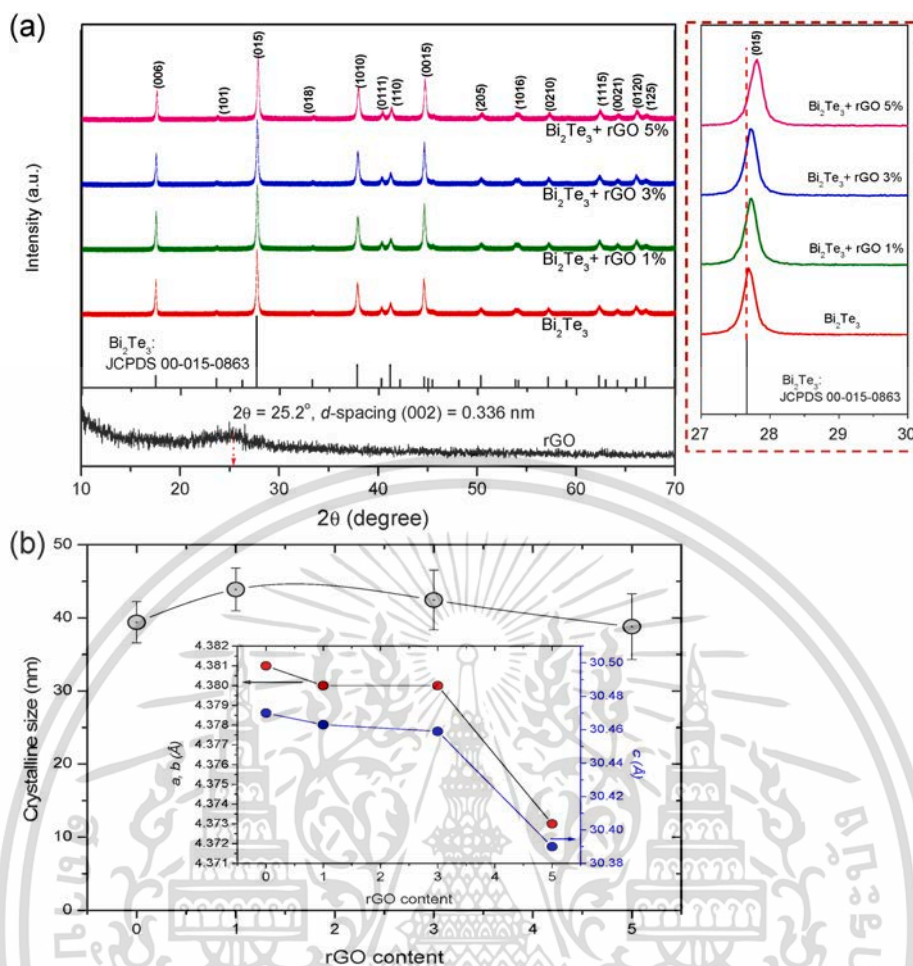


Fig. 4. (a) XRD patterns of prepared rGO, pristine Bi₂Te₃ and 1%, 3% and 5% Bi₂Te₃ + rGO composite powders and an inset showing enlargement of the (015) plane in the 2θ range of 27–30°, and (b) reveals the crystalline sizes and its inset shows lattice parameters (*a*, *b*, *c*).

were investigated. The results were shown in Fig. 6(b) – (d). It can be seen that only two elements, Bi (Bismuth) and Te (Tellurium), appeared on the pristine Bi₂Te₃ surfaces (Fig. 6(b)), whereas, the presence of three elements, Bi, Te and C (carbon) can be observed in all the Bi₂Te₃ + rGO composite samples (Fig. 6(b) – (d)). The carbon may come from rGO material loading, since the latter was a carbon derivative [3,9,10]. As can be seen from the EDS mapping, the percentages (%) ratios of the Te elemental was decreased along with the increasing of rGO loading, whereas Bi element was increased. This may be due to the fact that the percentage (%) ratio of carbon atom might be error due to the impurity molecules like CO₂ or CO in air adsorbed on the Bi₂Te₃ + rGO to affect the percentage (%) ratio of Bi atom. Noted that although the amounts of rGO (1, 3 and 5 wt%) loading of Bi₂Te₃ + rGO composites were increased but the percentage (%) ratios of carbon atom due to rGO were not increased, resulting the percentage (%) ratios of each element, Bi, Te, and C atoms not much accuracy with the trend of rGO loading. Additionally, the EDS mapping indicated that all elements were well-dispersed and incorporated on the particle surfaces of all the samples (see inset of Fig. 6(b) – (d)). These results indicated that all the elements of composite samples were present and well-combined in the grain boundary interfaces of rGO with Bi₂Te₃ after use of a simple ultrasonication method.

3.5. TGA of pristine Bi₂Te₃ and Bi₂Te₃ + rGO composite powders

Fig. 7(a) – (d) reveals the thermogravimetric analyses (TGA), weight loss and derivative weight) of the pristine Bi₂Te₃ and 1%, 3%, 5% Bi₂Te₃

+ rGO composite powders. This was done to study the thermal stability of the samples. The observed TGA results in the temperature range from ~375 to 600 °C of the pristine Bi₂Te₃ and 1%, 3%, and 5% Bi₂Te₃ + rGO composite samples reveal a continuous increase in the derivative weight signal without significant changes in the percentage weight loss. This may be associated with grain growth due to a slight inhomogeneity of the filler (rGO) distribution in the Bi₂Te₃ matrix. Moreover, at temperatures of 375 and 376 °C, based on derivative weight peak displayed, the initiation of oxidation occurs by an exothermic process with a peak ending at about 600 °C. According to our results, the remaining weight loss of pristine Bi₂Te₃ and 1%, 3%, and 5% Bi₂Te₃ + rGO composite samples from ~375 to 600 °C was 9.89, 12.59, 9.27, and 8.58%, respectively. According to Fig. 7(a) – (d), at temperatures greater than 600 °C, the weight loss under all conditions slightly increased with the residual mass by 2.96, 4.50, 3.76, and 3.36% for pristine Bi₂Te₃ and the 1%, 3% and 5% Bi₂Te₃ + rGO samples, respectively. This is due to ambient oxygen resulting from evaporation of absorbed water and the residual oxygen containing groups in the composite Bi₂Te₃ + rGO samples, which is in agreement with Music et al. [21].

3.6. UV-vis of pristine Bi₂Te₃ and Bi₂Te₃ + rGO composite powders

The UV-vis spectra of pristine Bi₂Te₃ and the 1%, 3% and 5% Bi₂Te₃ + rGO composite powders are shown in Fig. 8. The results showed an obviously broad-absorption peak for the pristine Bi₂Te₃ sample that appeared at approximately 210 nm, and a red shift towards higher wavelengths of 216, 227 and 235 nm for the 1%, 3% and 5% Bi₂Te₃ +

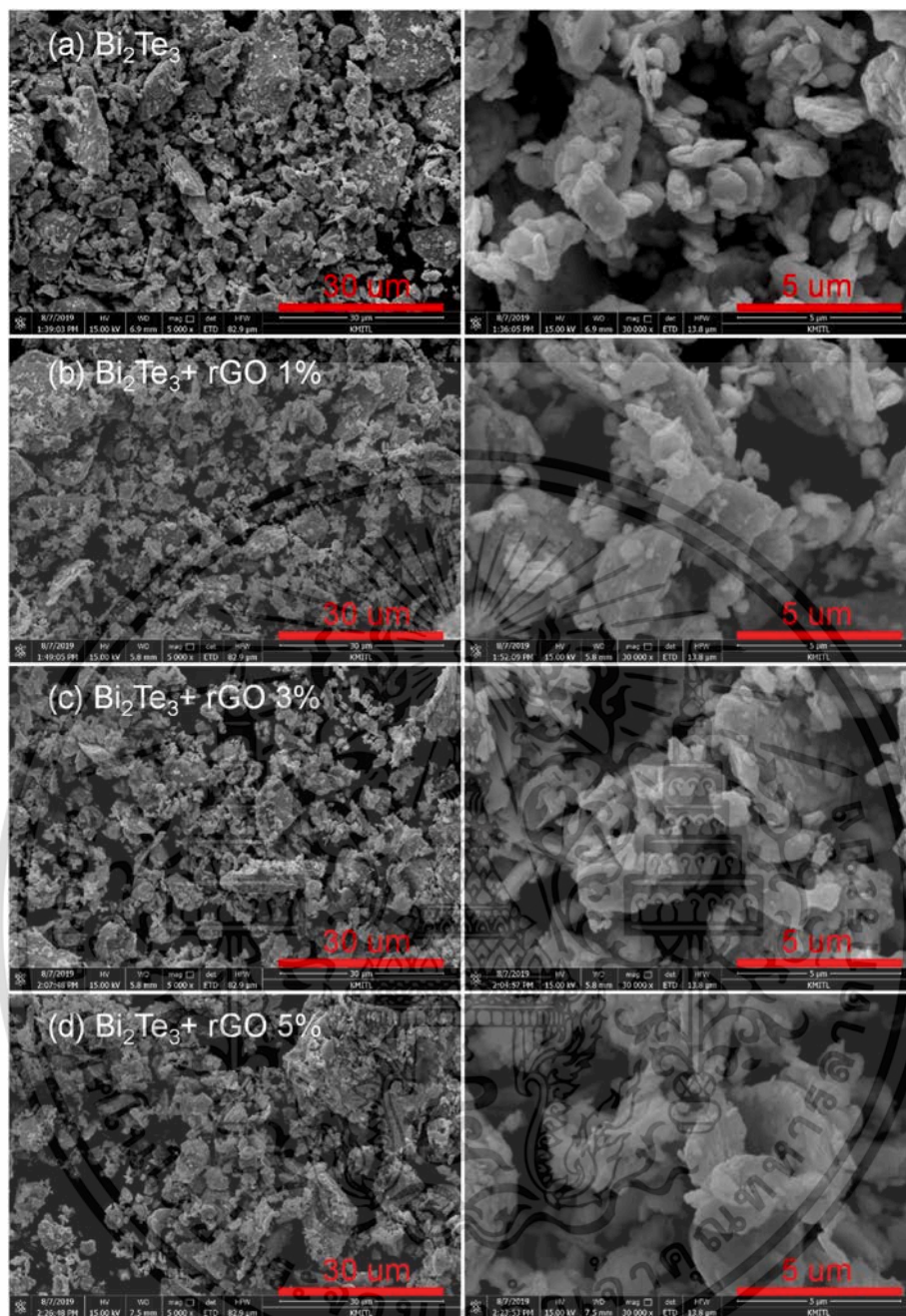


Fig. 5. SEM images and a high magnification view of (a) pristine Bi_2Te_3 and (b) – (d) 1%, 3% and 5% Bi_2Te_3 + rGO composite powders, respectively.

rGO samples, respectively. This effect resulted from electron transfer due to coupling between the eBi_2Te_3 structure and the oxygen containing functional groups of the rGO nanosheets [15]. The optical band gaps (E_g) were obtained by fitting the absorbance data to the direct transition equation [22], $(\alpha h\nu)^2 = k(h\nu - E_g)$, where E_g is the direct band gap, h is Planck’s constant, ν is the frequency of the incident photon, k is a constant and α is the absorption coefficient. From the plot of $(\alpha h\nu)^2$ vs. $h\nu$, shown in the inset of Fig. 8, the E_g value of each sample was determined by extrapolating the slope to the zero value of $(\alpha h\nu)^2$. The E_g value of the Bi_2Te_3 sample was 4.775 eV and the 1%, 3% and 5% Bi_2Te_3 + rGO samples were found to be 4.293, 4.004 and 3.629 eV, respectively. The E_g value monotonically decreased with increasing rGO concentration, which was caused by the red shift phenomenon in the UV absorption spectra. This is in agreement with Yin et al. [22].

3.7. Electrochemical properties of pristine Bi_2Te_3 and Bi_2Te_3 + rGO composite powders

Fig. 9(a) shows the CV curves of all electrodes at a scan rate of 50 mV s^{-1} in a potential window of $-0.7 \text{ V} - 0.0 \text{ V}$. It can be clearly seen that the pristine Bi_2Te_3 electrode displays poor capacitive behavior, while the Bi_2Te_3 composited 1%, 3% and 5% rGO nanosheets indicated clearly reversible reactions exhibiting capacitive behavior. The area of these CV curves gradually increased with rGO content. This indicates the storage charge mechanism of electrical double layer capacitors (EDLCs). Similarly, Fig. 9(b) presents the GCD curves of all electrodes within a potential window of $-0.7 \text{ V} - 0.0 \text{ V}$ at a scan rate of 0.25 A/g . The curves exhibit a symmetric shape, which clearly represents characteristic EDLC behavior [23,24]. The calculated specific capacitances (C_s) of all electrodes were determined from the discharge curves using the following

เอกสารนี้เป็นเอกสารที่สงวนไว้สำหรับการใช้งานเพื่อการศึกษาเท่านั้น ไม่อนุญาตให้นำไปใช้ประโยชน์ด้านการค้า
ไม่ว่ากรณีใดๆ ทั้งสิ้น อีกทั้งห้ามมิให้ตัดแปลงเนื้อหา และต้องอ้างอิงถึงเจ้าของเอกสารทุกครั้งที่มีการนำไปใช้

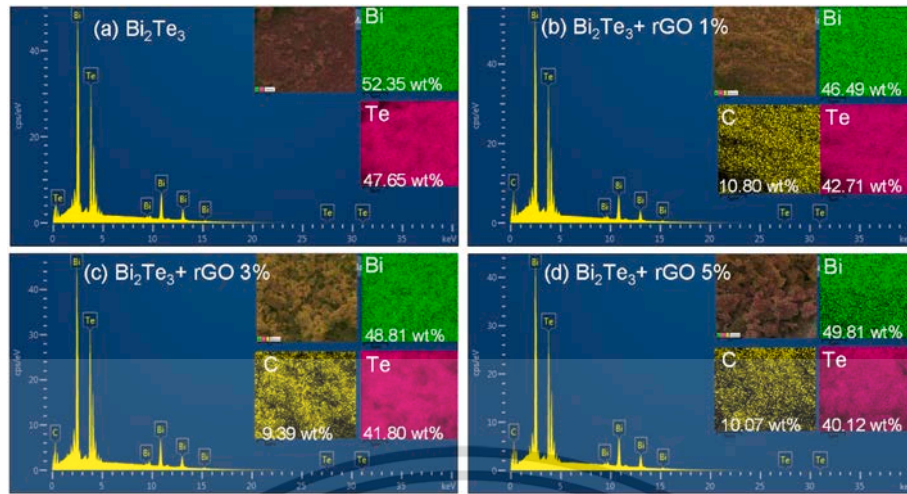


Fig. 6. EDS spectra and an inset showing the mapped images for Bi and Te of (a) pristine Bi_2Te_3 and Bi, Te and C for composite samples of (b) 1% $\text{Bi}_2\text{Te}_3 + \text{rGO}$, (c) 3% $\text{Bi}_2\text{Te}_3 + \text{rGO}$ and (d) 5% $\text{Bi}_2\text{Te}_3 + \text{rGO}$.

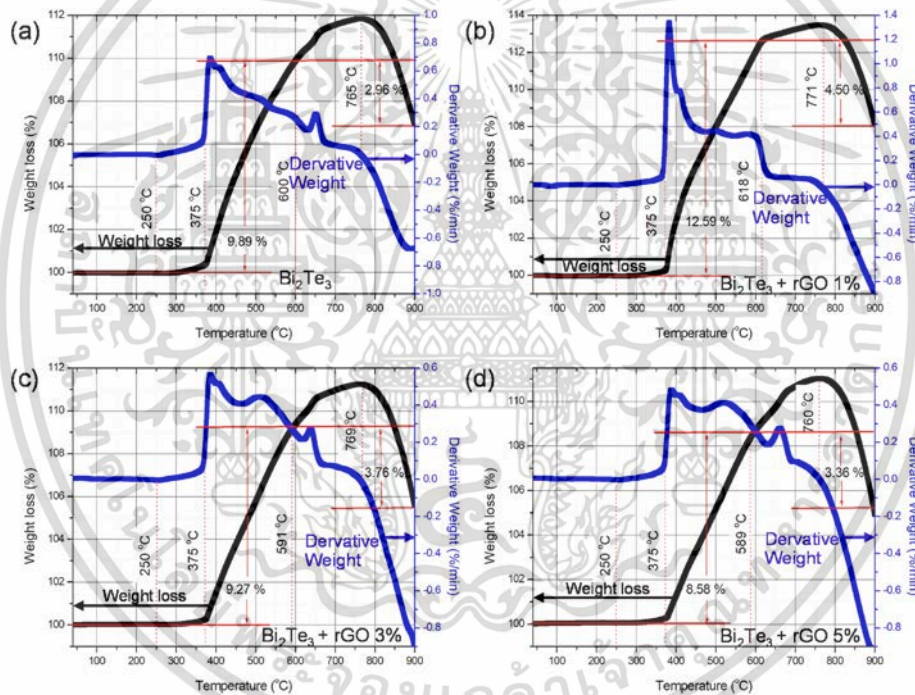


Fig. 7. TGA curves (weight loss and derivative weight) of (a) pristine Bi_2Te_3 and (b) – (d) 1%, 3% and 5% $\text{Bi}_2\text{Te}_3 + \text{rGO}$ composite powders, respectively.

equation:

$$C_s = I \Delta t / \Delta V, \quad (2)$$

where I is a constant current (A/g), Δt is the discharge time (s), ΔV is the potential window (V). Fig. 9(c) shows that the C_s values increased from 2.35 F/g for Bi_2Te_3 electrode to 16.50 F/g for the 5% $\text{Bi}_2\text{Te}_3 + \text{rGO}$ composite electrode. In fact, the increased C_s value was caused by the more efficient migration of OH^- ions through the porous structure and oxygen containing functional groups at surface of the rGO [24,25]. Additionally, the retention capacity after 1000 charge-discharge cycles at a current density of 1 A/g is shown in Fig. 9(d). Excellent cycling stability was exhibited. This showed that rGO nanosheet incorporation with Bi_2Te_3 materials improved the electrochemical properties of these materials.

3.8. Thermoelectric properties of pristine Bi_2Te_3 and $\text{Bi}_2\text{Te}_3 + \text{rGO}$ composite samples

Bulk samples of pristine Bi_2Te_3 and $\text{Bi}_2\text{Te}_3 + \text{rGO}$ composites were investigated in pelleted samples. The results are reported as follows.

3.8.1. XRD of pristine Bi_2Te_3 and $\text{Bi}_2\text{Te}_3 + \text{rGO}$ composite pellets

The XRD patterns and an enlargement of the (015) plane in the 2θ range of 27–30° of bulk pristine Bi_2Te_3 and 1%, 3% and 5% $\text{Bi}_2\text{Te}_3 + \text{rGO}$ composites are shown in Fig. 10(a). The results indicated that most diffraction peaks of the XRD patterns of powder samples present a rhombohedral Bi_2Te_3 structure as shown in Fig. 4(a). The lattice parameters (a , b , c) and cell volume (V) of bulk Bi_2Te_3 and 1%, 3% and 5% $\text{Bi}_2\text{Te}_3 + \text{rGO}$ samples are shown in Fig. 10(b). As can be seen in this figure, the lattice parameters (a , b , c) decreased with other parameters of the powder samples. The average crystalline sizes (D) decreased in the

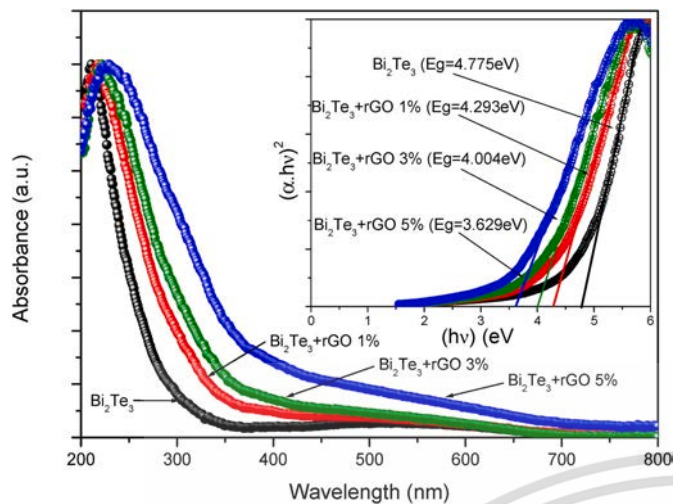


Fig. 8. UV-vis spectra with an inset showing direct band gap plots of $(\alpha h\nu)^2$ versus $h\nu$ of pristine 1%, 3% and 5% Bi_2Te_3 and $\text{Bi}_2\text{Te}_3 + \text{rGO}$ composite powders.

powder samples. They were found to be 26.316 ± 4.552 for the bulk Bi_2Te_3 sample and 35.776 ± 2.221 , 36.825 ± 3.049 and 30.892 ± 2.313 nm for the 1%, 3% and 5% bulk $\text{Bi}_2\text{Te}_3 + \text{rGO}$ composite samples, respectively.

3.9. SEM and EDS mapping of bulk pristine Bi_2Te_3 and $\text{Bi}_2\text{Te}_3 + \text{rGO}$ composite samples

The SEM images of bulk pristine Bi_2Te_3 and 1%, 3% and 5% $\text{Bi}_2\text{Te}_3 + \text{rGO}$ composite samples revealed their surface morphology after polishing, as shown in Fig. 11(a)–(d). It can be clearly seen in these figures that the high homogeneity of all bulk samples resulted in a highly dense microstructure. In the SEM images, it was found that the density value of bulk pristine Bi_2Te_3 was approximately 98%. However, the obtained

bulk $\text{Bi}_2\text{Te}_3 + \text{rGO}$ samples showed slightly decreased relative density values of 98%–96%, as the content of rGO increased. Furthermore, the EDS spectra and mapped images of bulk pristine Bi_2Te_3 and 1%, 3% and 5% $\text{Bi}_2\text{Te}_3 + \text{rGO}$ composites in Fig. 12(a)–(d) confirmed the presence of Bi and Te atoms in the bulk pristine Bi_2Te_3 sample, while Bi, Te and C were observed on the surfaces of bulk $\text{Bi}_2\text{Te}_3 + \text{rGO}$ composite samples. Moreover, C also was present on surfaces of the bulk $\text{Bi}_2\text{Te}_3 + \text{rGO}$ composite samples. These results confirmed the homogeneous distribution of all elements without no decomposition or transformation to the other phases during hot-press sintering at 450 °C for 1 h in the pelletization process.

3.9.1. Temperature dependence of the Seebeck coefficient (S) of bulk pristine Bi_2Te_3 and $\text{Bi}_2\text{Te}_3 + \text{rGO}$ composite samples

Fig. 13(a) shows the temperature dependence of the Seebeck coefficient of bulk pristine Bi_2Te_3 and 1%, 3% and 5% $\text{Bi}_2\text{Te}_3 + \text{rGO}$ composite samples over the temperature range 300 K–370 K. The bulk Bi_2Te_3 sample showed a positive of Seebeck coefficient value indicating a p-type thermoelectric material due to its role as a major hole carrier. The Seebeck coefficient values of the bulk Bi_2Te_3 sample decreased from 52 to 25 $\mu\text{V}/\text{K}$ as temperature was increased from 300 K to 370 K. The Seebeck coefficient values of the bulk Bi_2Te_3 samples were less than the values of a single crystal of Bi_2Te_3 previously reported by Jeon et al. [26]. Similarly, for decreased temperatures, the Seebeck coefficient for the sintered Bi_2Te_3 sample increased.

The 1%, 3% and 5% bulk $\text{Bi}_2\text{Te}_3 + \text{rGO}$ composite samples showed negative of Seebeck coefficient values, indicating that they were n-type thermoelectric materials and that electrical charges were transported mainly by electrons. The Seebeck coefficient values of the bulk $\text{Bi}_2\text{Te}_3 + \text{rGO}$ composite samples were constant over the tested temperature range. The Seebeck coefficient of Bi_2Te_3 pristine was p-type, while bulk $\text{Bi}_2\text{Te}_3 + \text{rGO}$ composite samples were n-type thermoelectric materials. This result was caused by the effect of the rGO composite in the structure of the materials, as it supplied electrical charge carriers. The Seebeck coefficient values of the bulk 1%, 3% and 5% $\text{Bi}_2\text{Te}_3 + \text{rGO}$ composite samples were found to be 78, 58 and 50 $\mu\text{V}/\text{K}$, respectively. The absolute

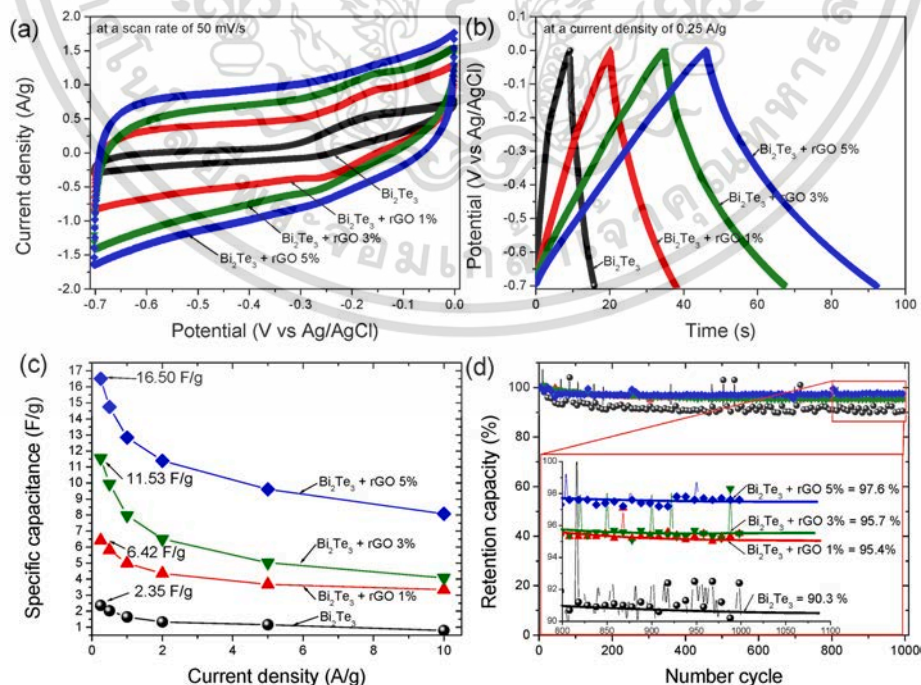


Fig. 9. (a) CV curves at a scan rate 50 mV s^{-1} , (b) GCD curves at a current density of 0.25 A/g , (c) specific capacitance plots at various current densities calculated by GCD test and (d) retention capacity using 1000 charge-discharge cycles at a current density of 1 A/g for pristine Bi_2Te_3 and 1%, 3% and 5% $\text{Bi}_2\text{Te}_3 + \text{rGO}$ composite powders in a 6 M KOH electrolyte.

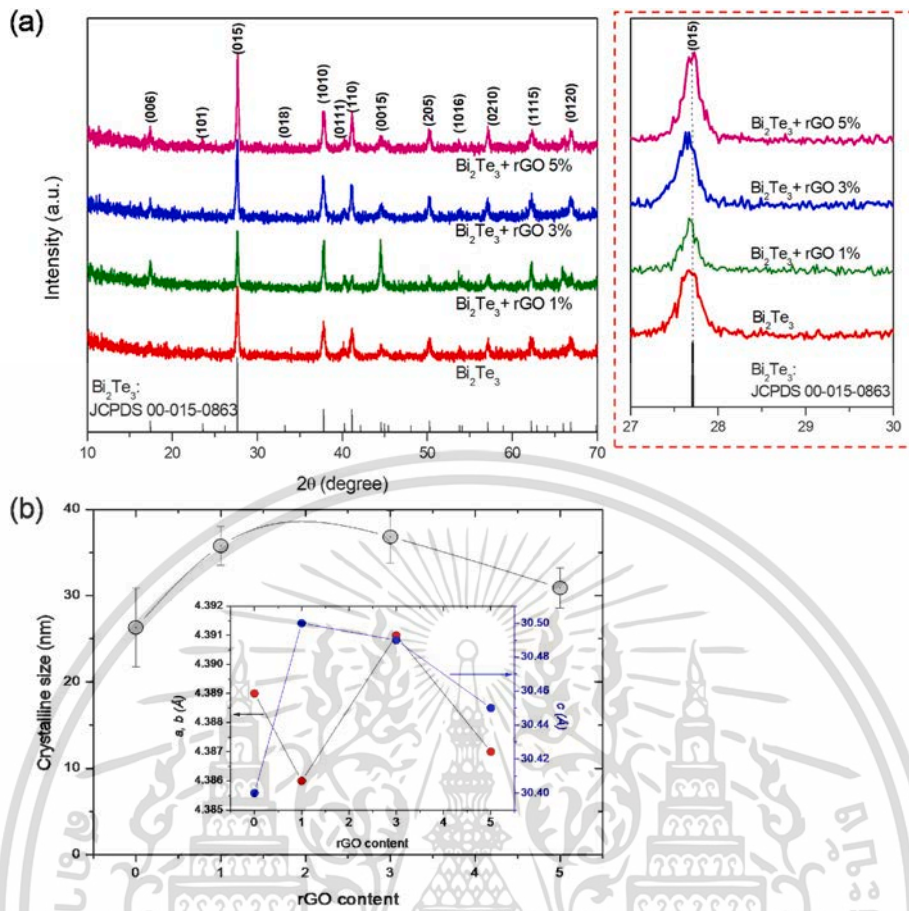


Fig. 10. (a) XRD patterns of bulk pristine Bi₂Te₃ and 1%, 3% and 5% Bi₂Te₃ + rGO composite samples and an inset showing enlargement of the (015) plane in the 2θ range of 27–30°, and (b) crystalline sizes and inset showing lattice parameters (a, b, c).

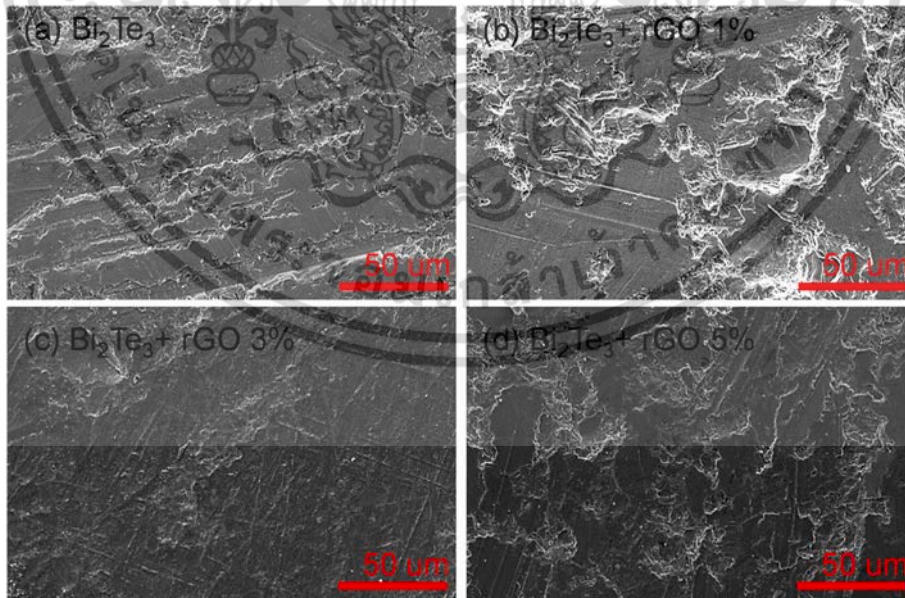


Fig. 11. SEM images of (a) pristine Bi₂Te₃ pellet, (b) 1% Bi₂Te₃ + rGO pellet, (c) 3% Bi₂Te₃ + rGO pellet and (d) 5% Bi₂Te₃ + rGO composite pellet.

Seebeck coefficient values of the bulk Bi₂Te₃ + rGO composite samples were greater than that of pristine Bi₂Te₃, and this value was decreased with increasing rGO content. The absolute values of Seebeck coefficient of a semiconductor [3,12] can be described by equation (3):

$$S = \frac{8\pi^2 k^2 T}{3qh^2} m_d^* \left(\frac{\pi}{3n}\right)^{2/3} \quad (3)$$

where q , k , T , h , m^* and n are the charge of the carrier, the Boltzmann

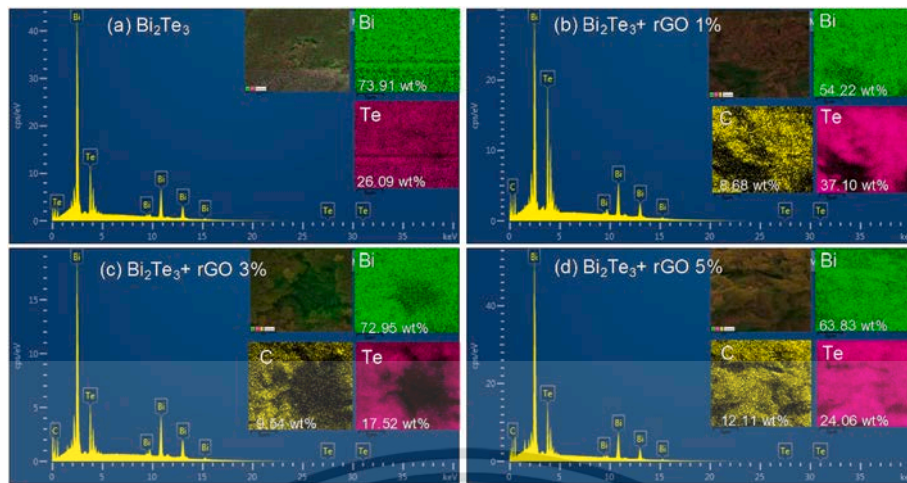


Fig. 12. EDS spectra and inset the mapped images for Bi, Te and C in bulk pristine Bi₂Te₃ and 1%, 3% and 5% Bi₂Te₃ + rGO composite pellets.

constant, absolute temperature, Planck's constant, the density of state (DOS) effective mass and the carrier concentration, respectively. Moreover, the Seebeck coefficient of bulk pristine Bi₂Te₃ decreased even at high temperatures. Increasing temperature resulted in an increased carrier concentration by intrinsic conduction. The positive Seebeck coefficient of bulk pristine Bi₂Te₃ confirmed that the electrical charge transport was controlled by hole carriers. Additionally, the Seebeck coefficient values of all bulk Bi₂Te₃ + rGO composite samples were constant over the tested temperature range. This occurred since the number of electron charge carriers did not change with temperature. However, the negative Seebeck coefficient of bulk Bi₂Te₃ + rGO composite samples confirmed the presence of electron carriers for electrical transport. These results revealed that the rGO content played an important role for supplying electron carriers. The absolute Seebeck coefficients of bulk 1% and 3% Bi₂Te₃ + rGO samples were larger than that of the Bi₂Te₃ sample. This confirmed that the rGO content enhanced the Seebeck coefficient of the Bi₂Te₃ by approximate doubled. The bulk 1%, 3% and 5% Bi₂Te₃ + rGO composite samples exhibited decreasing Seebeck coefficient values with increasing rGO content. This result was caused by an increased carrier concentration resulting from greater rGO content.

For a semiconductor material, activation energy to produce free carriers for electrical transport is expressed by equation (4) [27]:

$$S = \pm \frac{k_B}{e} \left(-\frac{E_s}{k_B T} + B_s \right), \quad (4)$$

where +/- is the p-type and n-type conductor, E_s is the activation energy for free carrier production and B_s is a constant, e is the electric charge carried, and k/e has a constant value of 86.17 $\mu\text{V}/\text{K}$. The E_s value was obtained by plotting S vs. $(1000/T)$. The slope of the resulting line was the E_s value. Fig. 13(b) shows temperature dependence of the Seebeck coefficient of sintered pristine Bi₂Te₃ and 1%, 3% and 5% Bi₂Te₃ + rGO composite samples with $1/T$. The results show the E_s value as the slope of the plot. Pristine Bi₂Te₃ had a larger than the 1%, 3% and 5% Bi₂Te₃ + rGO composite samples. This shows that bulk Bi₂Te₃ + rGO composite samples had lower activation energies for free carrier production. The free charge carriers were easily produced due to small thermal activation energy for free carrier production [26]. Fig. 13(c) shows the temperature dependence of the Seebeck coefficient for sintered pristine Bi₂Te₃ and 1%, 3% and 5% Bi₂Te₃ + rGO composite samples with inverse temperature.

Moreover, the changed sign of Seebeck coefficient from positive for the Bi₂Te₃ based-sample to negative for Bi₂Te₃ + rGO composite samples resulted from electron concentrations in the structures. Fig. 14 presents a schematic diagram of band alignment of the Bi₂Te₃ and rGO,

supporting the above observations. Exiting of the electron charge carriers can be described by the model of band alignment between Bi₂Te₃ and rGO according to Nam et al. [3] and Rahman et al. [9]. This approach can be explained via the relationship between the electron affinity (EA) of Bi₂Te₃, denoted as χ Bi₂Te₃, and the work function (WF) of rGO, denoted as W_{rGO} . The EA of Bi₂Te₃ was ~ 4.2 eV [28], remaining above the conduction band level of Bi₂Te₃. The WF of rGO was ~ 4.46 eV, remaining above the Fermi level of rGO. Also, the EA of Bi₂Te₃ was higher than the WF of rGO, as shown in Fig. 14. This result describes how the electrons in the conduction band of Bi₂Te₃ are transferred to the rGO at the interface, contributing of the electron charge carriers in the Bi₂Te₃ + rGO composite producing the effect of the grain boundary interfaces due to rGO incorporation with Bi₂Te₃ [3,9].

3.9.2. Temperature dependence of the electrical conductivity coefficient of pristine Bi₂Te₃ and Bi₂Te₃ + rGO composites

Fig. 15(a) shows electrical conductivity (σ) as a function of the temperature of bulk pristine Bi₂Te₃ and 1%, 3% and 5% Bi₂Te₃ + rGO composite samples. The σ value of pristine Bi₂Te₃ was approximately 2×10^4 S/m. This result closely matches the values for Bi₂Te_{2.7}Se_{0.3}, previously reported by Liao et al. [20]. Furthermore, the σ values of the 1%, 3% and 5% Bi₂Te₃ + rGO samples were approximately $4\text{--}9 \times 10^4$, 4 to 7×10^4 and 4 to 5×10^4 S/m, respectively. The σ values of sintered 1%, 3% and 5% Bi₂Te₃ + rGO composite samples were higher than that the sintered Bi₂Te₃ sample. The 1% Bi₂Te₃ + rGO composite sample exhibited the highest σ value in these experiments, close to those reported by Liang et al. [10] at high temperature (360 K). The σ values revealed that the rGO content with the Bi₂Te₃ increased electrical conduction in the Bi₂Te₃ + rGO composite samples. The electron conduction of bulk 1%, 3% and 5% Bi₂Te₃ + rGO samples was dominated by electron charge carriers, corresponding to their negative Seebeck coefficient values, as shown in Fig. 13. Moreover, the rGO contents contributed to the electron charge carriers for Bi₂Te₃ according to the schematic diagram of band alignment shown in Fig. 14.

Fig. 15(b) shows the logarithm of electrical conductivity ($\ln\sigma$) of the bulk pristine Bi₂Te₃ and Bi₂Te₃ + rGO composite samples as a function of $T^{-1/4}$. The linear slope of $\ln\sigma$ vs. $T^{-1/4}$ indicates the charge transfer between the bulk pristine Bi₂Te₃ and Bi₂Te₃ + rGO composite samples in a 3-dimensional variable-range hopping model according to Mott's equation. The electric conductor is expressed in Mott's equation by $\sigma = B \exp(T_0/T)^{-1/4}$, where B and T_0 are constants presenting the characteristic Mott's temperature [3,9,32]. The linear relationship between $\ln\sigma$ and $T^{-1/4}$ indicates a metallic-like behavior, and a zero value of the slope indicates metallic behavior. These results show that the bulk pristine Bi₂Te₃ and 1%, 3% and 5% Bi₂Te₃ + rGO composites have

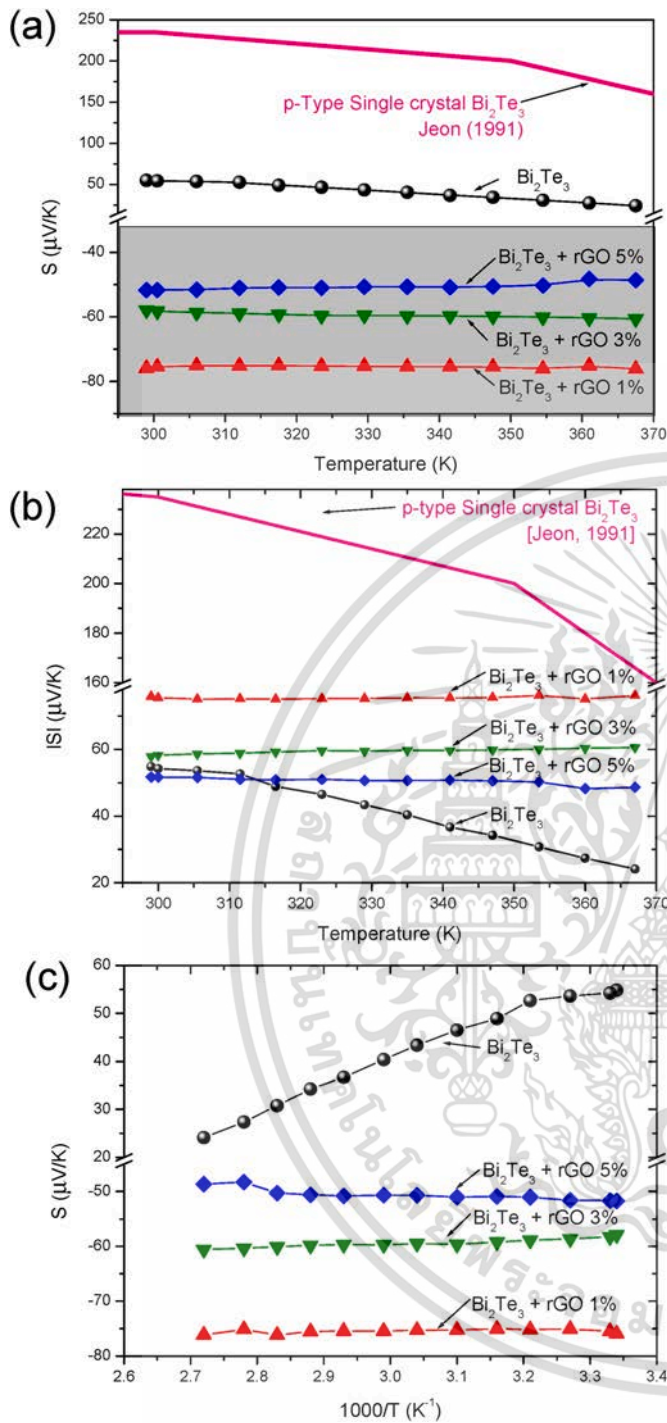


Fig. 13. (a) Temperature dependence of the Seebeck coefficient of bulk pristine Bi₂Te₃ (p-type), 1%, 3% and 5% Bi₂Te₃ + rGO composite (n-type) samples and single crystal Bi₂Te₃ (p-type) as reported by Jeon et al. [26] and (b) the absolute Seebeck coefficient |S| of bulk pristine Bi₂Te₃, 1%, 3% and 5% Bi₂Te₃ + rGO composite and (c) temperature dependence of the Seebeck coefficient of the sintered pristine Bi₂Te₃ and 1%, 3% and 5% Bi₂Te₃ + rGO composite samples with inverse temperature.

metallic-like behavior. Moreover, the slope of bulk pristine Bi₂Te₃ and Bi₂Te₃ + rGO 5% composite is closer to a zero value than the 1% and 3% Bi₂Te₃ + rGO composites. The above results show that a slight loading of rGO into pristine Bi₂Te₃ caused production of charge carrier transport in 1%, 3% and 5% Bi₂Te₃ + rGO composites in a metallic-like mechanism.

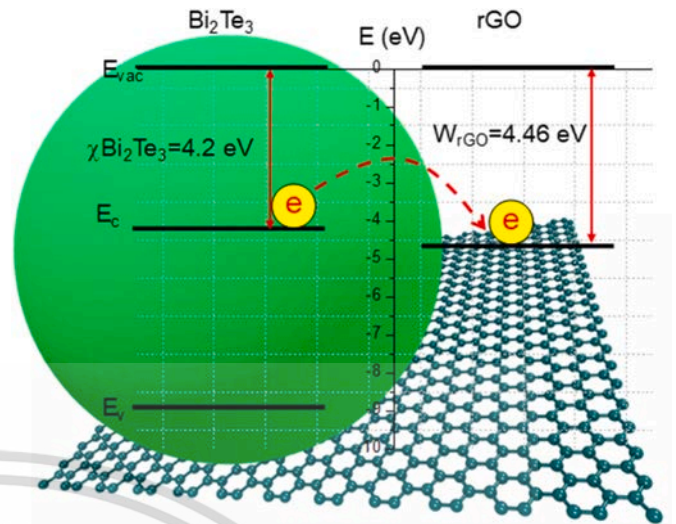


Fig. 14. A schematic diagram of band alignment of the Bi₂Te₃ and 2D rGO for electron charge transport in the Bi₂Te₃ + rGO composite as effected by grain boundary interfaces for rGO incorporated with Bi₂Te₃.

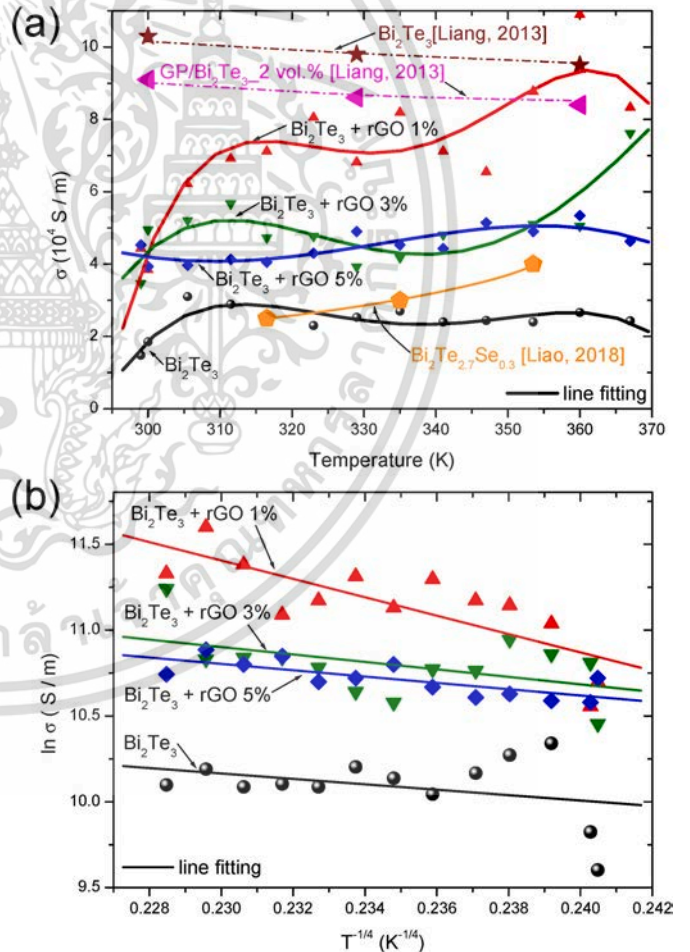


Fig. 15. (a) The conductivity coefficient (σ) and (b) showing the electric conduction of bulk pristine Bi₂Te₃ and 1%, 3% and 5% Bi₂Te₃ + rGO composites.

3.9.3. Power factor (PF) of pristine Bi₂Te₃ and Bi₂Te₃ + rGO composites

Fig. 16 shows a comparison of the power factor (PF) of bulk pristine Bi₂Te₃ and 1%, 3% and 5% Bi₂Te₃ + rGO composite samples calculated

เอกสารนี้เป็นเอกสารที่สงวนไว้สำหรับการใช้งานเพื่อการศึกษาเท่านั้น ไม่อนุญาตให้นำไปใช้ประโยชน์ด้านการค้า
ไม่ว่ากรณีใดๆ ทั้งสิ้น อีกทั้งห้ามมิให้ตัดแปลงเนื้อหา และต้องอ้างอิงถึงเจ้าของเอกสารทุกครั้งที่มีการนำไปใช้

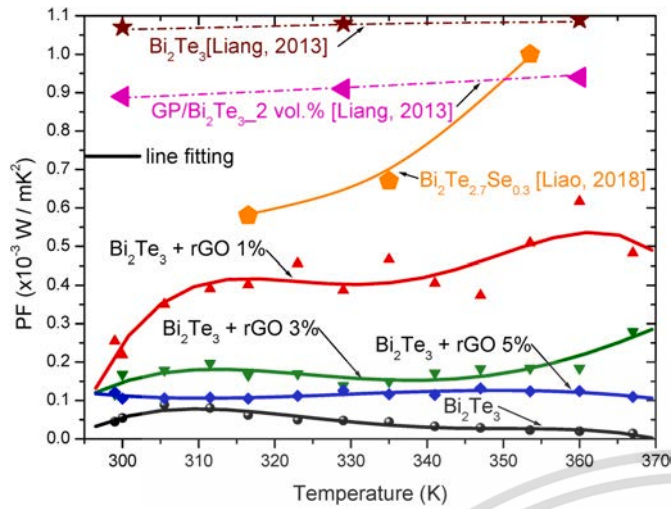


Fig. 16. Power factor (PF) of bulk pristine Bi_2Te_3 and 1%, 3% and 5% Bi_2Te_3 + rGO composite samples.

using equation (5):

$$PF = S^2 \times \sigma \quad (5)$$

The PF value of the bulk pristine Bi_2Te_3 based material was estimated to be $0.05 \times 10^{-3} \text{ W/mK}^2$ and it decreased with increasing temperature from 310 K to 370 K due to both a decreased Seebeck coefficient and electrical conductivity. However, the PF value of bulk 1% Bi_2Te_3 + rGO composite sample shows the highest PF value, of $0.4 \times 10^{-3} \text{ W/mK}^2$, owing to both high electrical conductivity and Seebeck coefficient. Thus, the PF values of the bulk Bi_2Te_3 + rGO composite samples remained less than those reported by Liang et al. [10] and Liao et al. [20].

As according to Liu et al. [29], thermoelectric performance can be enhanced using the energy band gap. Fig. 16 (b) shows the behavior, ZT ($=S^2 T \sigma / \kappa$), as a function of E_g for the Bi_2Te_3 + rGO composite samples. The results indicated that the ZT values of the Bi_2Te_3 + rGO samples were greatly decreased as E_g increased. By equation (3), the Seebeck value is related to the inverse of the carrier concentration (n). The intrinsic carrier concentration in a semiconductor at thermal equilibrium can be expressed as $n = N_s \exp\left(-\frac{E_g}{2k_B T}\right)$, where N_s is the number per unit volume of effective states available, E_g is the energy gap, and T is the absolute temperature. In the same way, the PF ($=S^2 \sigma$) and κ_e values are a function of n . Also, the values of ZT of the Bi_2Te_3 + rGO composite slightly decreased with increasing charge carrier concentration, depending on the degree of increased rGO content. This implies that the ZT value of the Bi_2Te_3 + rGO composites was related to the charge carrier concentration. For pristine Bi_2Te_3 , the Seebeck coefficient decreased with increasing temperature at high temperatures, as shown in Fig. 13(a). This results from an increased charge carrier concentration by intrinsic conduction with a temperature increase. This result is related to the previous work of Jeon et al. [26].

3.9.4. Temperature dependence on thermal conductivity of pristine Bi_2Te_3 and Bi_2Te_3 + rGO composites

Thermal conductivity (κ) was measured using a Nano-Flash thermal diffusivity analyser. The bulk density of the sample (D) [27,30] was 98% for sintered Bi_2Te_3 sample. It was from 96% to 98% for the sintered 1%, 3% and 5% Bi_2Te_3 + rGO composite samples. In Fig. 17(a), the thermal conductivity of the sintered pristine Bi_2Te_3 sample was 1–1.5 over temperature range of 300 K–530 K. It increased with temperature. The thermal conductivity of the bulk 1% Bi_2Te_3 + rGO composite sample was close to that of the pristine Bi_2Te_3 sample. Next, the κ of the bulk 3% Bi_2Te_3 + rGO composite was less than that of pristine Bi_2Te_3 , while the κ

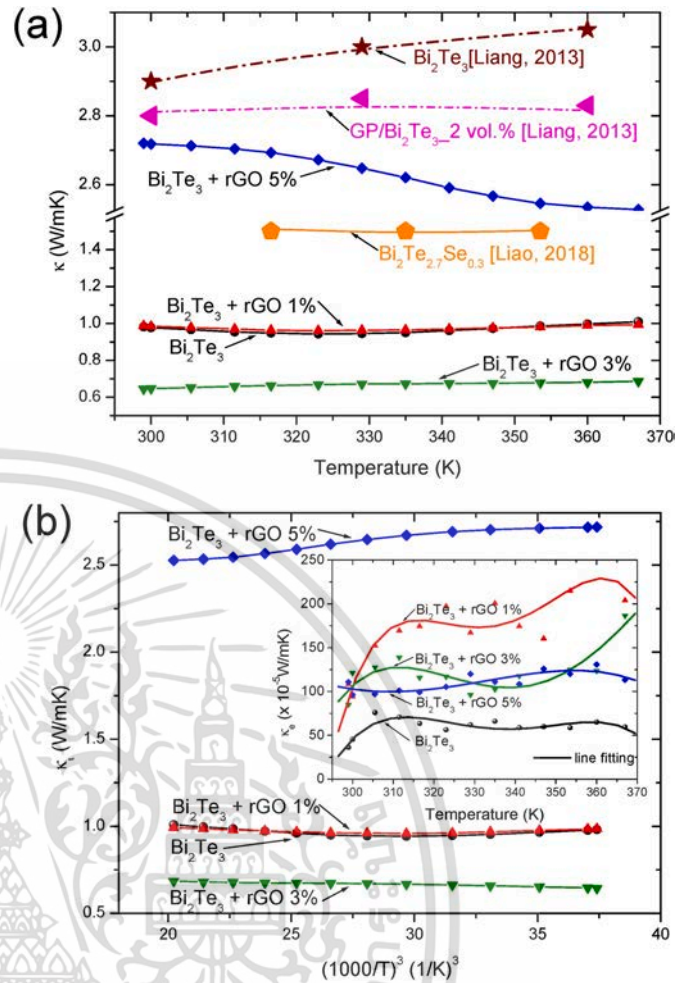


Fig. 17. (a) The temperature dependence of thermal conductivity (κ) and (b) the inverse absolute temperature dependence of lattice thermal conductivity (κ_l) with the insert, the temperature dependence of electronic thermal conductivity (κ_e) of bulk pristine Bi_2Te_3 and 1%, 3% and 5% Bi_2Te_3 + rGO composite samples.

value of the 5% Bi_2Te_3 + rGO composite was greater than the Bi_2Te_3 pristine sample. This highlights that the 3% rGO content with Bi_2Te_3 caused a reduction in thermal conductivity. However, the bulk 1% and 3% Bi_2Te_3 + rGO composites showed κ values that were less than those previously reported by Liang et al. [10] and Liao et al. [20], while the 5% Bi_2Te_3 + rGO composite sample value was close to those previously reported in the literature.

The thermal conductivity value can be expressed as a function of the electronic and lattice thermal conductivity as ($\kappa = \kappa_e + \kappa_l$). The κ_e value was obtained from the Wiedemann-Franz law: $\kappa_e = L_0 T \sigma$, where L_0 is the Lorenz number, $2.45 \times 10^{-8} \text{ V}^2 \text{ K}^{-2}$, and T is the absolute temperature [27,30].

The inset of Fig. 17(b) shows the κ_e values of the bulk pristine Bi_2Te_3 and 1%, 3% and 5% Bi_2Te_3 + rGO composite samples. It can be seen that all samples show very small values, $< 10^{-4} \text{ W/mK}$, compared with the total thermal conductivity value. Thus, κ_e arose from charge carriers in the structure. Moreover, the total thermal conductivity of all samples was dominated by the lattice thermal conductivity from the phonon mechanism, which played an important role in all samples.

κ_l is a function of the phonon relaxation time (τ_{ph}) via the relationship, $\frac{1}{\tau_{ph}} = \frac{1}{\tau_B} + \frac{1}{\tau_P} + \frac{1}{\tau_U}$ [9,30], where τ_B , τ_P and τ_U are the grain boundary, the point defect and the phonon-phonon processes, respectively. The low thermal conductivity was caused a low the τ_{ph} value. The τ_U term, the

เอกสารนี้เป็นเอกสารที่สงวนไว้สำหรับการใช้งานเพื่อการศึกษาเท่านั้น ไม่อนุญาตให้นำไปใช้ประโยชน์ด้านการค้า

ไม่ว่ากรณีใดๆ ทั้งสิ้น อีกทั้งห้ามมิให้ตัดแปลงเนื้อหา และต้องอ้างอิงถึงเจ้าของเอกสารทุกครั้งที่มีการนำไปใช้

phonon-phonon mechanism, can be expressed by $\frac{1}{\tau_U} = (B)\omega^2 T^3$, where B represents parameters independent of temperature. The τ_U term represents the relaxation time due to the phonon-phonon mechanism, which is inversely proportional to $1/T^3$. Fig. 17(a) shows a plot of the κ_l value of the sintered pristine Bi_2Te_3 and 1%, 3% and 5% $\text{Bi}_2\text{Te}_3 + \text{rGO}$ composite samples vs. the inverse absolute temperature cubed ($1/T^3$). It can be clearly seen that only the 5% $\text{Bi}_2\text{Te}_3 + \text{rGO}$ composite exhibited a κ value that was directly proportional to $1/T^3$. This implied that the behavior of Bi_2Te_3 was dominated (controlled) by the phonon-phonon mechanism. This result highlights that greater rGO contents increased thermal conductivity.

The τ_P term depicts a point defect mechanism that can be defined by $\frac{1}{\tau_P} = A\omega^4$, where A is a constant parameter independent of the temperature. The A parameter is a function mass and bond length disorder, expressed as $A = \frac{\delta^3}{4\pi v^3} (\Gamma_m + \Gamma_s)$, where δ^3 is the average atom volume, Γ_m is the mass fluctuation parameter, and Γ_s is the strain fluctuation parameter [31]. The τ_P term was affected by differences in the atomic mass and average atomic mass in the matrix sites within the structure of the materials. Therefore, this term was not changed in the bulk $\text{Bi}_2\text{Te}_3 + \text{rGO}$ 1% and 3% composite samples. The mechanism of the τ_B term can be expressed as $\frac{1}{\tau_B} = v/L$, where v is the phonon group velocity and L is the characteristic grain size that is affected by the grain boundary interfaces with rGO incorporation in Bi_2Te_3 [9]. The SEM results show the morphology of 1% and 3% $\text{Bi}_2\text{Te}_3 + \text{rGO}$ composite samples with rGO networks along the grain boundaries in the sample matrices. These provide grain boundary interfaces through rGO incorporation within Bi_2Te_3 . It is clear that the decreased thermal conductivity of the 1% and 3% $\text{Bi}_2\text{Te}_3 + \text{rGO}$ composite samples was caused by the rGO composite in the Bi_2Te_3 structure. The bulk 3% $\text{Bi}_2\text{Te}_3 + \text{rGO}$ composite had the lowest thermal conductivity value. Thus, an optimal 3% rGO content offered the minimum thermal conductivity value of the bulk $\text{Bi}_2\text{Te}_3 + \text{rGO}$ composite samples.

3.9.5. The figure of merit (ZT) of pristine Bi_2Te_3 and $\text{Bi}_2\text{Te}_3 + \text{rGO}$ composites

Fig. 18(a) shows a comparison of the figure of merit (ZT) of bulk pristine Bi_2Te_3 and 1%, 3% and 5% $\text{Bi}_2\text{Te}_3 + \text{rGO}$ composite samples, calculated using the equation, $ZT = (PF)/\kappa T$ [30]. The ZT value of the bulk pristine Bi_2Te_3 sample was approximately 0.02, whereas the 1%, 3% and 5% $\text{Bi}_2\text{Te}_3 + \text{rGO}$ composite samples showed decreased values with increased rGO contents of around 0.17, 0.1, and 0.02, respectively. It can be clearly seen that the 1% bulk $\text{Bi}_2\text{Te}_3 + \text{rGO}$ composite had the highest ZT value, however, its ZT value was about 10 times greater than the bulk pristine Bi_2Te_3 sample. It was close to the ZT value of a $\text{Bi}_2\text{Te}_{2.7}\text{Se}_{0.3}$ sample previously reported by Liao et al. [20], and higher than ZT value of Bi_2Te_3 and GP/ Bi_2Te_3 previously reported by Liang et al. [10]. Furthermore, an optimum 1% rGO content showed greatly improved thermoelectric properties of the n-type Bi_2Te_3 which is correspond to the fitting between E_g and ZT of bulk pristine Bi_2Te_3 and 1%, 3% and 5% $\text{Bi}_2\text{Te}_3 + \text{rGO}$ composite samples as shown in Fig. 18(b). Thus, this was effect of the rGO network along the grain boundaries in the Bi_2Te_3 matrix.

4. Conclusions

The electrochemical and thermoelectric properties of pristine Bi_2Te_3 were improved by compositing it with rGO nanosheets in the proportions of 1, 3, and 5% based on stoichiometric weight. $\text{Bi}_2\text{Te}_3 + \text{rGO}$ composite powders were prepared using a simple ultrasonic method, and bulk samples were hot-pressing sintered. The results show that the XRD phase of the $\text{Bi}_2\text{Te}_3 + \text{rGO}$ composite samples corresponded to a Bi_2Te_3 standard phase. Pristine Bi_2Te_3 and 1%, 3% and 5% $\text{Bi}_2\text{Te}_3 + \text{rGO}$ composite electrodes exhibited reversible reactions displaying capacitive behavior that gradually increased with their rGO content, demonstrating a charge storage mechanism with an EDLC behavior. The

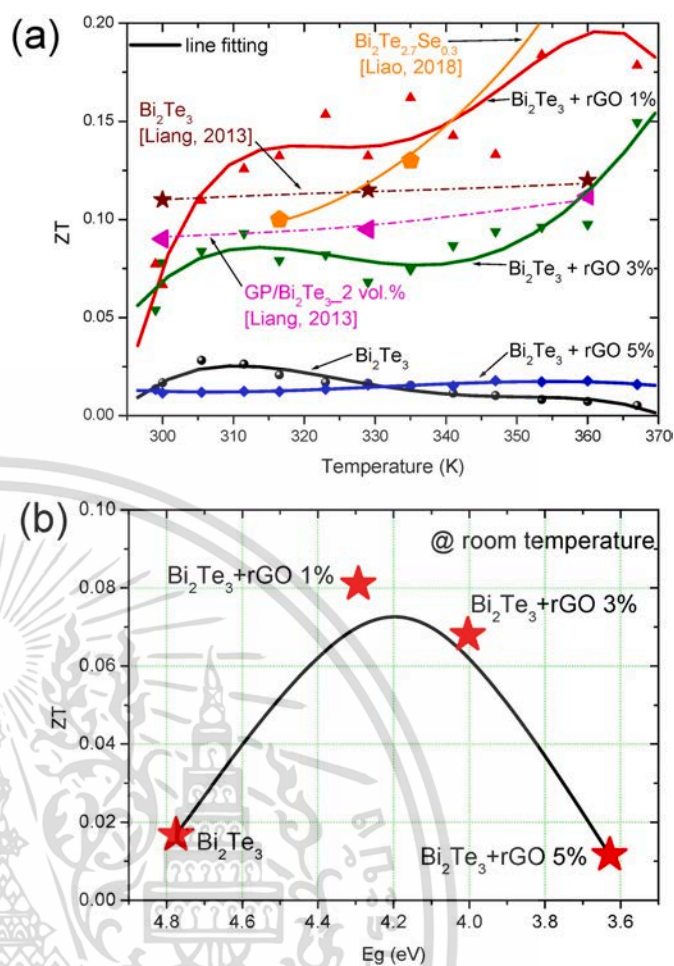


Fig. 18. The figure of merit (ZT) (a) and the fitting between E_g and ZT, (b) of bulk pristine Bi_2Te_3 and 1%, 3% and 5% $\text{Bi}_2\text{Te}_3 + \text{rGO}$ composite samples.

thermoelectric properties of the bulk pristine Bi_2Te_3 exhibited a positive Seebeck coefficient indicating that it was thermoelectric material. However, the bulk 1%, 3% and 5% $\text{Bi}_2\text{Te}_3 + \text{rGO}$ composites exhibited negative Seebeck coefficients. The Seebeck coefficients of bulk 1% and 3% $\text{Bi}_2\text{Te}_3 + \text{rGO}$ composites were larger than that of pristine Bi_2Te_3 . The electrical conductivity of the bulk 1% $\text{Bi}_2\text{Te}_3 + \text{rGO}$ composite showed the highest σ value, five times that of pristine Bi_2Te_3 . The lowest thermal conductivity was exhibited by the bulk 3% $\text{Bi}_2\text{Te}_3 + \text{rGO}$ sample. The highest ZT value, 0.07, was presented by the bulk 1% $\text{Bi}_2\text{Te}_3 + \text{rGO}$ sample. Clearly, the enhanced electrochemical and thermoelectric properties of Bi_2Te_3 material were affected by the rGO nanosheets composited with Bi_2Te_3 . This was due to the grain boundary interfaces of rGO within Bi_2Te_3 when prepared using a simple ultrasonic method. This method promoted a continuous network structure of rGO nanosheets in the $\text{Bi}_2\text{Te}_3 + \text{rGO}$ composite structures, contributing to exiting of electron charge carriers according to the model of band alignment between Bi_2Te_3 and rGO nanosheets. The effect of the grain boundary interfaces in $\text{Bi}_2\text{Te}_3/\text{rGO}$ nanosheet composites was the enhanced electrochemical and thermoelectric properties of these materials.

Declaration of competing interest

The authors declare no competing financial interests.

CRediT authorship contribution statement

Wannisa Thongsamrit: Conceptualization, Data curation, Formal analysis, Methodology. Chaiwat Phrompet: Data curation, Formal

analysis. **Keerati Maneesai**: Formal analysis. **Attaphol Karaphun**: Formal analysis, Writing - original draft. **Wattana Tuichai**: Formal analysis, Writing - original draft. **Chaval Sriwong**: Formal analysis, Visualization, Investigation, Visualization, Writing - original draft. **Chesta Ruttanapun**: Conceptualization, Formal analysis, Funding acquisition, Visualization, Project administration, Resources, Supervision, Validation, Visualization, Writing - original draft, Writing - review & editing.

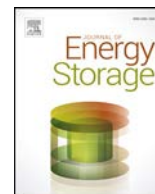
Acknowledgements

The authors would like to thank, King Mongkut's Institute of Technology Ladkrabang (KMITL), Ladkrabang, Bangkok, Thailand for funding our research [Grant Number: KREF046304].

References

- [1] A. Morata, M. Pacios, G. Gadea, C. Flox, D. Cadavid, A. Cabot, A. Tarancón, Large-area and adaptable electrospun silicon-based thermoelectric nanomaterials with high energy conversion efficiencies, *Nat. Commun.* 9 (2018) 4759.
- [2] J.P. Rojas, D. Singh, S.B. Inayat, G.A. Torres Sevilla, H.M. Fahad, M.M. Hussain, Micro and nano-engineering enabled new generation of thermoelectric generator devices and applications, *ECS J. Solid State Sci. Technol.* 6 (2017) N3036–N3044.
- [3] W.H. Nam, Y.S. Lim, W. Kim, H.K. Seo, K.S. Dae, S. Lee, W.-S. Seo, J.-Y. Lee, A gigantically increased ratio of electrical to thermal conductivity and synergistically enhanced thermoelectric properties in interface-controlled TiO_2 -RGO nanocomposites, *Nanoscale* 9 (2017) 7830.
- [4] Q. Jin, S. Jiang, Y. Zhao, D. Wang, J. Qiu, D.-M. Tang, J. Tan, D.-M. Sun, P.-X. Hou, X.-Q. Chen, K. Tai, N. Gao, C. Liu, H.-M. Cheng, X. Jiang, Flexible layer-structured Bi_2Te_3 thermoelectric on a carbon nanotube scaffold, *Nat. Mater.* 18 (2019) 62–68.
- [5] R. Liu, X. Tan, G. Ren, Y. Liu, Z. Zhou, C. Liu, Y. Lin, C.-Nan, Enhanced thermoelectric performance of Te-doped $\text{Bi}_2\text{Te}_{3-x}\text{Te}_x$ bulks by self-propagating high-temperature synthesis, *Crystals* 7 (2017) 257.
- [6] J.H. Lee, K.H. Lee, S.W. Kim, S. Kim, S.M. Choi, J.Y. Kim, S.Y. Kim, J.W. Roh, H. J. Park, Doping and band engineering by vanadium to enhance the thermoelectric performance in n-type $\text{Cu}_{0.008}\text{Bi}_2\text{Te}_{2.7}\text{Se}_{0.3}$, *Physica B* 517 (2017) 1–5.
- [7] H. Cho, J.H. Kim, S.Y. Back, K. Ahn, J.-S. Rhyee, S.-D. Park, Enhancement of thermoelectric properties in Cu-doped $\text{Bi}_2\text{Te}_{2.7}\text{Se}_{0.3}$ by hot-deformation, *J. Alloys Compd.* 731 (2018) 531–536.
- [8] K. Ahmad, C. Wan, M.A. Al-Eshaikh, A.N. Kadachi, Enhanced thermoelectric performance of Bi_2Te_3 based graphene nanocomposites, *Appl. Surf. Sci.* 474 (2019) 2–8.
- [9] J.U. Rahman, N.V. Du, W.H. Nam, W.H. Shin, K.H. Lee, W.-S. Seo, M.H. Kim, S. Lee, Grain boundary interfaces controlled by reduced graphene oxide in nonstoichiometric SrTiO_{3-x} thermoelectrics, *Sci. Rep.* 9 (2019) 8624.
- [10] B. Liang, Z. Song, M. Wang, L. Wang, Wan Jiang, Fabrication and thermoelectric properties of graphene/ Bi_2Te_3 composite materials, *J. Nanomater.* 5 (2013), 7–5.
- [11] H.J. Kim, S.-M. Lee, Y.-S. Oh, Y.-H. Yang, Y.S. Lim, D.H. Yoon, C. Lee, J.-Y. Kim, R. S. Ruoff, Unoxidized graphene/alumina nanocomposite: fracture- and wear-resistance effects of graphene on alumina matrix, *Sci. Rep.* 4 (2014) 5176.
- [12] Y. Du, J. Li, J. Xu, P. Eklund, Thermoelectric properties of reduced graphene oxide/ Bi_2Te_3 nanocomposites, *Energies* 12 (2019) 2430.
- [13] M. Mitra, C. Kulsi, K. Chatterjee, K. Kargupta, S. Ganguly, D. Banerjee, S. Goswami, Reduced graphene oxide-polyaniline composites synthesis, characterization and optimization for thermoelectric applications, *RSC Adv.* 5 (2015) 31039.
- [14] K. Xu, G. Chen, D. Qiu, Convenient construction of poly(3,4-ethylenedioxythiophene)-graphene pie-like structure with enhanced thermoelectric performance, *J. Mater. Chem. A.* 1 (2013) 12395.
- [15] C. Phrompet, C. Sriwong, C. Ruttanapun, Mechanical, dielectric, thermal and antibacterial properties of reduced graphene oxide (rGO)-nanosized C3AH6 cement nanocomposites for smart cement-based materials, *Compos. B Eng.* 175 (2019) 107128.
- [16] P. Wongjom, W. Thongsamrit, H. Ramamoorthy, S. Chinwong, R. Somphonsane, C. Ruttanapun, Cost-effective experimental setup for studies of spin Seebeck effect and electrical transport in thermoelectric materials, *IEEE Trans. Instrum. Meas.* (2019), <https://doi.org/10.1109/TIM.2019.2935597>.
- [17] K.T. Kim, S.Y. Choi, E.H. Shin, K.S. Moon, H.Y. Koo, G.-G. Lee, G.H. Ha, The influence of CNTs on the thermoelectric properties of a CNT/ Bi_2Te_3 composite, *Carbon* 52 (2013) 541–549.
- [18] M.-K. Han, Y. Jin, D.-H. Lee, Sung-Jin Kim, Thermoelectric properties of Bi_2Te_3 :CuI and the effect of its doping with Pb atoms, *Materials* 10 (2017) 1235.
- [19] S. Kumar, S. Singh, P.K. Dhawan, R.R. Yadav, N. Khare, Effect of graphene nanofillers on the enhanced thermoelectric properties of Bi_2Te_3 nanosheets: elucidating the role of interface in de-coupling the electrical and thermal characteristics, *Nanotechnology* 29 (2018) 135703.
- [20] M.-H. Liao, K.-C. Huang, F.-A. Tsai, C.-Y. Liu, C. Lien, M.-H. Lee, Thickness dependence of electrical conductivity and thermo-electric power of $\text{Bi}_{2.0}\text{Te}_{2.7}\text{Se}_{0.3}/\text{Bi}_{0.4}\text{Te}_{3.0}\text{Sb}_{1.6}$ thermoelectric devices, *AIP Adv.* 8 (2018), 015020.
- [21] D. Music, K. Chang, P. Schmidt, F.N. Braun, M. Heller, S. Hermsen, P.J. Pöllmann, T. Schulzendorff, C. Wagner, On atomic mechanisms governing the oxidation of Bi_2Te_3 , *J. Phys. Condens. Matter* 29 (2017) 485705.
- [22] K. Yin, Z.D. Cui, X.R. Zheng, X.J. Yang, S.L. Zhu, Z.Y. Li, Y.Q. Liang, Bi_2Te_3 @CoNiMo composite as a high performance bi functional catalyst for the hydrogen and oxygen evolution reactions, *J. Mater. Chem. A.* 3 (45) (2015).
- [23] J.P.L. Lazarte, R.C. Dipasupil, G.Y.S. Pasco, R.C.P. Eusebio, A.H. Orbecido, R. Doong, L.B. Patacsil, Synthesis of reduced graphene oxide/titanium dioxide nanotubes (rGO/TiO₂) composites as an electrical double layer capacitor, *J. Nanomater.* 8 (2018) 934.
- [24] P.K. Jha, S.K. Singh, V. Kumar, S. Rana, S. Kurungot, N. Ballav, High-level supercapacitive performance of chemically reduced graphene oxide, *Inside Chem.* 3 (2017) 846–860.
- [25] M. Wang, L.D. Duong, N.T. Mai, S. Kim, Y. Kim, H. Seo, Y.C. Kim, W. Jang, Y. Lee, J. Suhr, J.-D. Nam, All-solid-state reduced graphene oxide supercapacitor with large volumetric capacitance and ultralong stability prepared by electrophoretic deposition method, *ACS Appl. Mater. Interfaces* 72 (2015) 1348–1354.
- [26] H.-W. Jeon, H.-P. Ha, D.-B. Hyun, J.-D. Shim, Electrical and thermoelectrical properties of undoped Bi_2Te_3 -Sb Te_3 and Bi_2Te_3 -Sb Te_3 -Sb Se_3 single crystals, *J. Phys. Chem. Solid.* 52 (4) (1991) 579–585.
- [27] C. Ruttanapun, S. Maensiri, Effects of spin entropy and lattice strain from mixed-valent $\text{Fe}^{3+}/\text{Cr}^{3+}$ on the electronic, thermoelectric and optical properties of delafossite $\text{CuFe}_{1-x}\text{Cr}_x\text{O}_2$ ($x = 0.25, 0.5, 0.75$), *J. Phys. D.* 48 (49) (2015) 495103.
- [28] H. He, D. Huang, X. Zhang, G. Li, Characterization of hexagonal Bi_2Te_3 nanosheets prepared by solvothermal method, *Solid State Commun.* 152 (2012) 810–815.
- [29] Y. Liu, J. Lan, W. Xu, Y. Liu, Y.-L. Pei, B. Cheng, D.-B. Liu, Y.-H. Lin, L.-D. Zhao, Enhanced thermoelectric performance of a BiCuSeO system via band gap tuning, *Chem. Commun.* 49 (2013) 8075–8077.
- [30] S. Jantrasee, P. Moontragoon, S. Pinitsoontorn, C. Ruttanapun, Enhancing thermoelectric properties of nanostructure Ga-doped ZnO prepared by microwave-hydrothermal synthesizing with comparing to calculation results, *Mater. Res. Express* (2019), <https://doi.org/10.1088/2053-1591/aafc39>.
- [31] D. An, S. Chen, Z. Lu, R. Li, W. Chen, W. Fan, W. Wang, Y. Wu, Low thermal conductivity and optimized thermoelectric properties of p-type $\text{Te-Sb}_2\text{Se}_3$: synergistic effect of doping and defect engineering, *ACS Appl. Mater. Interfaces* 11 (2019) 27788–27797.
- [32] C. Rudradawong, C. Ruttanapun, Effect of excess oxygen for $\text{CuFeO}_{2.06}$ delafossite on thermoelectric and optical properties, *Phys. B Condens. Matter* 526 (2017) 21–27.

เอกสารนี้เป็นเอกสารที่สงวนไว้สำหรับการใช้งานเพื่อการศึกษาเท่านั้น ไม่อนุญาตให้นำไปใช้ประโยชน์ด้านการค้า
ไม่ว่ากรณีใดๆ ทั้งสิ้น อีกทั้งห้ามมิให้ตัดแปลงเนื้อหา และต้องอ้างอิงถึงเจ้าของเอกสารทุกครั้งที่มีการนำไปใช้



Electrochemical properties of tricalcium aluminate hexahydrate – reduced graphene oxide nanocomposites for supercapacitor device

Chaiwat Phrompet^{a,b,c,e}, Keerati Maneesai^{a,b,c,e}, Wattana Tuichai^{a,b,c,e}, Attaphol Karaphun^{a,b,c,e}, Chaval Sriwong^{a,b,d,e}, Chesta Ruttanapun^{a,b,c,e,*}

^a Center of Excellence in Smart Materials Research and Innovation, King Mongkut's Institute of Technology Ladkrabang, Chalongkrung Road, Ladkrabang, Bangkok, 10520, Thailand

^b Smart Materials Research and Innovation Unit, Faculty of Science, King Mongkut's Institute of Technology Ladkrabang, Chalongkrung Road, Ladkrabang, Bangkok, 10520, Thailand

^c Department of Physics, Faculty of Science, King Mongkut's Institute of Technology Ladkrabang, Chalongkrung Road, Ladkrabang, Bangkok, 10520, Thailand

^d Department of Chemistry, Faculty of Science, King Mongkut's Institute of Technology Ladkrabang, Chalongkrung Road, Ladkrabang, Bangkok, 10520, Thailand

^e Thailand Center of Excellence in Physics, Ministry of Higher Education, Science, Research and Innovation, 328 Si Ayutthaya Road, Bangkok 10400, Thailand

ARTICLE INFO

Keywords:

Reduced graphene oxide (rGO)
Tricalcium aluminate hexahydrate (C3AH6)
Electrochemical properties
Supercapacitor device

ABSTRACT

In this study, the influence of reduced graphene oxide (rGO)–Tricalcium Aluminate Hexahydrate (C3AH6) cement nanocomposites on electrochemical properties was investigated. The rGO-C3AH6 nanocomposite samples with various of rGO loading, such as, C3AH6_rGO-1, 3, 5, 7, 10 and 20 wt.% were easily synthesized by a rapid cement hydration method. The maximum specific surface area and average pore size diameters were 74.20 m²/g and 11.72 nm for C3AH6_rGO-20%. The charge transferring in C3AH6_rGO nanocomposites was described using band alignments model occurring between C3AH6 and rGO. Interestingly, the increasing of both dielectric property and stability in frequency of C3AH6_rGO composite samples can be explained by the high density of free electron charges on the rGO surface. Moreover, the electrochemical properties of C3AH6_rGO electrodes had excellent capacitive properties displaying the storage charge mechanism of a hybridsupercapacitor behavior. The large rGO content of the C3AH6_rGO nanocomposite capacitor with electrolyte interfaces showed excellent electrochemical performance. The highest value of 80.479 F g⁻¹ was obtained from C3AH6_rGO-20% at a current density of 0.2 A g⁻¹ with cycling stability of 96.51% after 1000 cycles.

1. Introduction

Nowadays, supercapacitors have been attracted interest for storage applications in a cell phone, hybrid electrical vehicles, and back-up power systems [1–10]. Normally, a supercapacitor, an ultracapacitor, is a charge and storage energy device like conventional batteries [2,5,7]. Additionally, a supercapacitor is an energy storage device with high-capacity capacitors and high capacitance value capacitors [3,6–11]. Certainly, it has high power energy storage, rapid charging capabilities, and robust lifetimes [10–11]. Thus, the supercapacitive materials for various energy storage applications require excellent power and reasonably high energy density [4,13,14]. Conventionally, a supercapacitor cell consists of two electrodes, a separator, and an electrolyte. The structure cell is assembled into a sandwich-like stacked configuration of a electrode/separator/electrode materials [13]. Consistent with the energy storage mechanisms and the nature of the electrode

materials, supercapacitors can be classified into two types: An electrochemical double-layer capacitors (EDLCs), which the electrostatic charge accumulates at the interface between the electrode surface and the electrolyte, and pseudocapacitors with fast and reversible redox reactions (Faradaic processes) occurring on the surface of electrodes [15,16]. Therefore, the energy storage mechanism of EDLCs operates through ion adsorption without Faradic charge transfer. This leads to fast charge–discharge processes, high power densities, and great cycling stabilities which is agree to the electrode surface area play a crucial role in the performance of a capacitor. However, the limited surface area and pore size distribution of conventional electrode materials often cause relatively low energy densities (normally, <10 Wh/kg¹) [3,5,6,11,16–19]. There are three main types of the electrode materials: Carbon materials with high specific surface area, conducting polymers [20–24], and metal oxides [6–10,16–25]. The electrode from carbon-based materials has many advantages, including higher specific surface

* Corresponding author.

E-mail address: chesta.ru@kmitl.ac.th (C. Ruttanapun).

<https://doi.org/10.1016/j.est.2020.101474>

Received 9 January 2020; Received in revised form 20 April 2020; Accepted 20 April 2020

2352-152X/© 2020 Elsevier Ltd. All rights reserved.

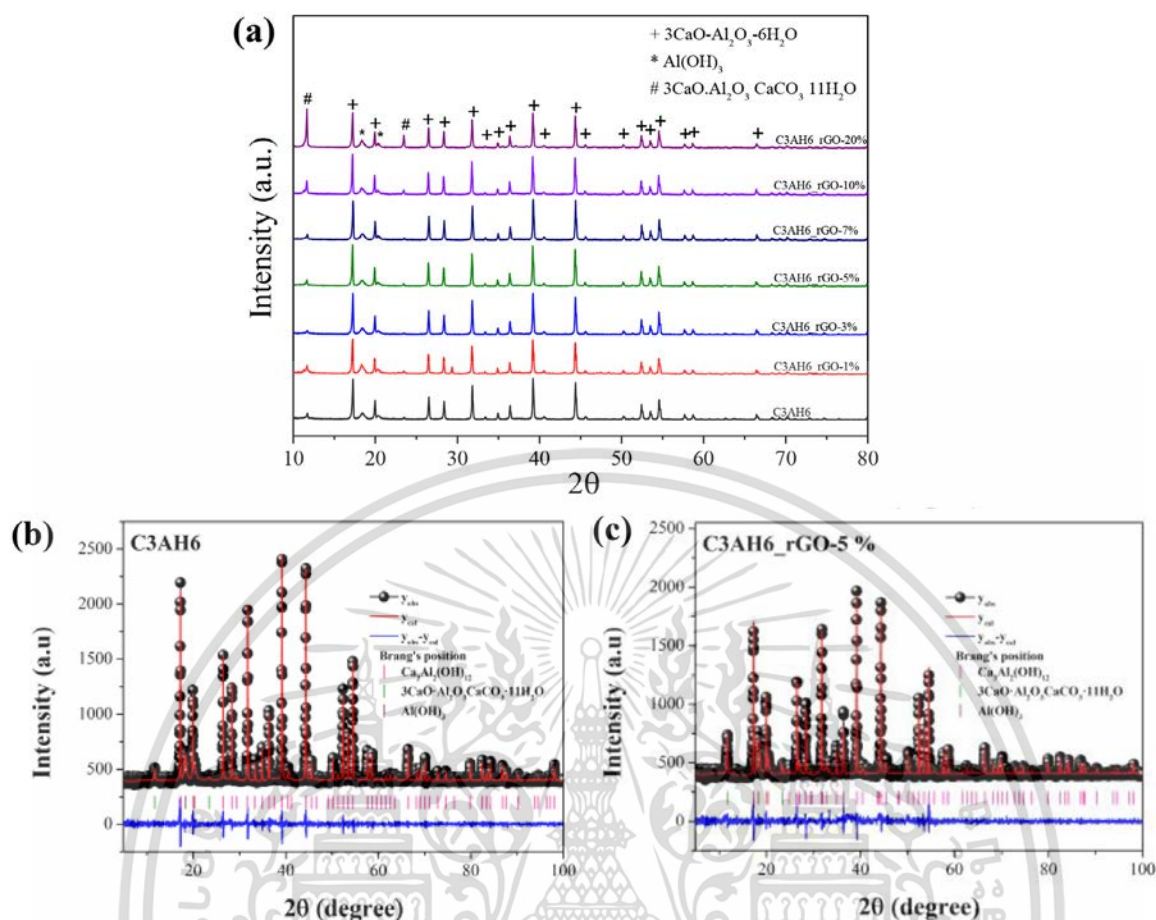


Fig. 1. (a) XRD patterns of pristine C3AH6 and C3AH6_rGO (1, 3, 5, 7, 10 and 20%) composites and (b) – (c) Rietveld refinement of pristine C3AH6 and C3AH6_rGO-5% composites, respectively.

Table 1

Lattice parameter (a), cell volume (V), structural data obtained from the Rietveld refinement and average crystallite size (D_{XRD}) of pristine C3AH6 and C3AH6_rGO (1, 3, 5, 7, 10 and 20%) composites.

Sample	Lattice parameter a (Å)	V (Å) ³	Density (g/cm ³)	R_{ex} (%)	R_p (%)	R_w (%)	GOF	D_{XRD} (nm)
C3AH6	12.582(2)	1991.79	2.5227	2.5352	7.3135	9.9601	2.5345	70.64 ± 4.54
C3AH6_rGO-1%	12.580(2)	1990.79	2.5252	2.6448	7.1462	9.7592	2.4396	69.38 ± 4.91
C3AH6_rGO-3%	12.579(7)	1990.38	2.5440	2.5996	7.1501	9.7086	2.4397	68.60 ± 4.65
C3AH6_rGO-5%	12.578(2)	1989.83	2.5251	2.6750	8.7805	11.9388	3.5822	65.89 ± 13.08
C3AH6_rGO-7%	12.579(2)	1990.31	2.5245	2.6887	9.0209	12.7044	4.0046	63.04 ± 10.85
C3AH6_rGO-10%	12.569(1)	1971.46	2.5487	2.7829	10.3829	14.5827	5.1147	61.99 ± 11.17
C3AH6_rGO-20%	12.565(4)	1968.53	2.5268	3.3081	12.7206	18.3919	8.4179	55.08 ± 20.84

area, good electronic conductivity, high chemical stability, lower cost with abundance and easy processing [26–27], and attention non toxic [28–30]. One type of carbon-based materials is reduced graphene oxide (rGO) which has been demonstrated as one class of the most promising and attractive electrode materials for supercapacitors because of their good conductivity, high surface area, exceptional intrinsic double-layer capacitance, and high theoretical capacitance [13,24,31–34]. Moreover, the challenge for high capacitance is its major focus on new electrode materials, which consist of high specific surface area, pore-size distribution, low internal electrical resistance, and better electrochemical and mechanical stability [1,3,4,6–12,16–18,25,26,35–36].

Bo et al. [11] and Divyashree et al. [31] have described the electrode of the structure part for storage electric charge at the interface between the surface of a conductive and an electrolyte through a mechanism of charge separated at a Helmholtz double layer to reach high electrostatic double-layer capacitance. Purkait et al. [32] have reported the advantage of storage electric charge occurring from the nanostructure

materials as affecting from high specific and surface area for shorting for ions and electrons diffusion and transport path. Jha et al. [4] used graphene oxide (GO) in FeCl₂/HCl aqueous medium for Supercapacitor device. Zhou et al. [37] proposed Mn₃O₄/rGO electrode material as displaying efficient Supercapacitor. All previous reports suggested the rGO nanocomposite materials were effective in the electrochemical electrodes. Kumar Jha et al. [4] and Farma et al. [41] reported that the H⁺ ions bonding to O²⁻ ions of the materials presented the special physical properties of ionic transport applied to supercapacitor devices. According to Phrompet et al. [38], rGO-nanosized Tricalcium Aluminate Hexahydrate (C3AH6) cement composites (with 4% weight of rGO) had high surface area materials due to an enrichment effect caused by diffusion within the modified electrode and a high useful surface area of rGO nanosheet. The nanocomposited rGO-C3AH6 structure consists of the Ca atom occupied by Ca²⁺, the Al atom occupied by Al³⁺ in framework of an octahedral and a tetrahedral, and the H⁺ ions linked to each of the four O atoms in the rGO surface. The

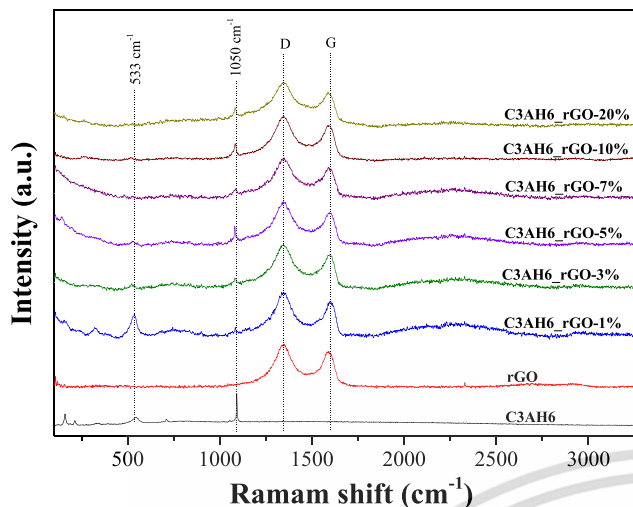


Fig. 2. Raman spectra of pristine C3AH6, rGO and C3AH6_rGO (1, 3, 5, 7, 10 and 20%) nanocomposites.

structure was responsible for free electron charge easy transferring between the electrode material and electrolyte [39–44]. The rGO-nanosized C3AH6 cement composites could be attracted attention for the supercapacitor devices because the nanostructure has high surface area and contains the free electron charge for ionic transport in the structure. All in all, Phrompet et al. [38] only reported the effects of rGO-nanosized C3AH6 cement composites on mechanical, dielectric, thermal and antibacterial properties. However, to the best of our knowledge, there are no reports on the electrochemical properties of rGO-nanosized C3AH6 cement composites for supercapacitor devices.

Hence, to further improve the supercapacitive property of the rGO-nanosized C3AH6 cement, this work is aimed to investigate influences of rGO loading contents mixed with Tricalcium Aluminate Hexahydrate (C3AH6_rGO) nanocomposites on dielectric and electrochemical properties. The C3AH6_rGO nanocomposite samples were easily prepared by a rapid cement hydration method with different amounts of rGO suspension loading (1, 3, 5, 7, 10 and 20 wt.%). The C3AH6_rGO-1, 3, 5, 7, 10 and 20% nanocomposite materials were characterized using XRD, SEM, Raman, TEM, FTIR, and BET. The dielectric constant (ϵ') and loss tangent ($\tan\delta$) of pristine C3AH6 and all C3AH6_rGO samples were observed at room temperature. The electrochemical performance (Cyclic Voltammetry (CV), Galvanostatic Charge/Discharge (GCD), and Electrochemical Impedance Spectroscopy (EIS)) and dielectric impedance of the C3AH6_rGO electrodes were tested.

2. Experimental details

2.1. Materials

A graphite powder (99% purity), an alumina powder (Al_2O_3 , 99.9% purity), a calcium carbonate powder (CaCO_3 , 99% purity), and hydrogen peroxide (H_2O_2 , 30%) were obtained from Sigma-Aldrich (USA). An ammonia solution (NH_3 , 28–30%) was supplied by Baker (USA). Sulfuric acid (H_2SO_4 , 98%), potassium permanganate (KMnO_4), and hydrochloric acid (HCl, 37%) were purchased from Merck (Germany). All chemicals were used as received without further purification.

2.2. Synthesis of C3AH6_rGO nanocomposite

2.2.1. Preparation of C12A7 cement

CaCO_3 and Al_2O_3 cement powders were used as starting materials. 12CaCO_3 and $7\text{Al}_2\text{O}_3$ powders were stoichiometrically mixed for the reaction [45]. The mixture was placed in an alumina crucible and

sintered in an electric furnace at 1200°C in an air atmosphere for 24 h. Finally, C12A7 powder was obtained.

2.2.2. Preparation of graphene oxide (GO)

Graphite oxide was synthesized through a modified Hummers method which is oxidizing graphite with a strong acid and oxidizing agent [38]. In brief, 2 g of graphite powder was firstly mixed with 6 g of KMnO_4 in a beaker. The mixed powder was poured into a 500 ml round bottom flask and cooled below 3°C . Second, 46 mL of H_2SO_4 was gradually added under stirring and cooling; then, maintained its temperature below 15°C , the mixture was stirred at 40°C for 30 min. Third, 90 mL of distilled water (DI water) was slowly added and heated under stirring of 95°C for 60 min. Subsequently, the reaction was stopped, and the metal residuals were removed by adding 250 mL DI water and 10 mL of H_2O_2 solution, respectively. The H_2O_2 was used as oxidizing agent to remove metal or metal oxide residuals (Mn or MnO_x). The obtained product was separated by centrifugation and washed with a 5% HCl solution to reduce sulfate. After that, it was filtered and washed several times with distilled water until the pH of filtered solution was about 7. The resulting solid paste product was dried in an oven at 65°C overnight. The synthesized graphite oxide powder (800 mg) was re-dispersed in distilled water (120 mL) under ultrasonication for 90 min, followed by centrifugation. Finally, the supernatant of an aqueous GO suspension was obtained.

2.2.3. Preparation of reduced graphene oxide (rGO)

Reduced graphene oxide (rGO) was prepared through a modified Dan Li method, which has been reported previously [34]. In a typical procedure, 100 mL of GO (2 mg/mL) suspension was mixed with 100 mL of DI water, 1 mL of ammonia (30%) solution and 0.1 mL of hydrazine hydrate (65%) solutions. In this method, ammonia was used as a stabilizer, whereas hydrazine hydrate was used as a reductant. After that, the obtained mixture was heated at 95°C and stirred for 45 min. Finally, a stable aqueous suspension of rGO was obtained. A stable of rGO aqueous suspension was obtained because of the effect of ammonia loading [34].

2.2.4. Preparation of C3AH6_rGO composite

The pristine C3AH6 and all C3AH6_rGO composite samples were prepared through rapid cement hydration method [38,40]. In this method, a $\text{Ca}_{12}\text{Al}_{14}\text{O}_{33}$ powder is used as the starting material. In order to prepare pristine C3AH6 cement, the C12A7 powder was used to suspend DI water through the chemical reaction, but there was no rGO loading for the experimental control. To prepare C3AH6_rGO composite samples, the C12A7 powder was dissolved with rGO aqueous suspension with varying load of 1, 3, 5, 7, 10 and 20 wt.%. The C3AH6_rGO composites were denoted by C3AH6_rGO-x%, where x is the weight percentage (wt.%) of rGO to the C12A7.

2.2.5. Preparation of tricalcium aluminate hexahydrate and all C3AH6_rGO electrodes

2.2.5.1. Slurries preparation. The active electrode slurry was made by ball milling method at room temperature for 24 h using Tricalcium Aluminate Hexahydrate (C3AH6) and all C3AH6_rGO samples (80 wt %), polyvinylidene fluoride (PVDF) (10 wt%) and ethylene black (10 wt %) with a N-methyl-2-pyrrolidone (NMP) 0.5 ml as a solvent at room temperature for 24 h.

2.2.5.2. Cells assembly of the active electrodes to measure a three-electrode cell system. The obtained slurries were prepared by coating $\sim 0.1 - 0.2$ ml active mass of slurry onto the ultrasonically cleaned nickel foam sheet within a coating area of $1 \times 1 \text{ cm}^2$ and oven dried at 80°C for 3 h. The mass of active material in pristine C3AH6 and C3AH6_rGO-1, 3, 5, 7, 10 and 20% electrodes were 2.94, 2.98, 3.11, 3.05, 3.21, 3.13 and 3.08 mg, respectively. Finally, all of these working active electrodes were pressed at 1.5 tons for 1 min using the uniaxial compression and

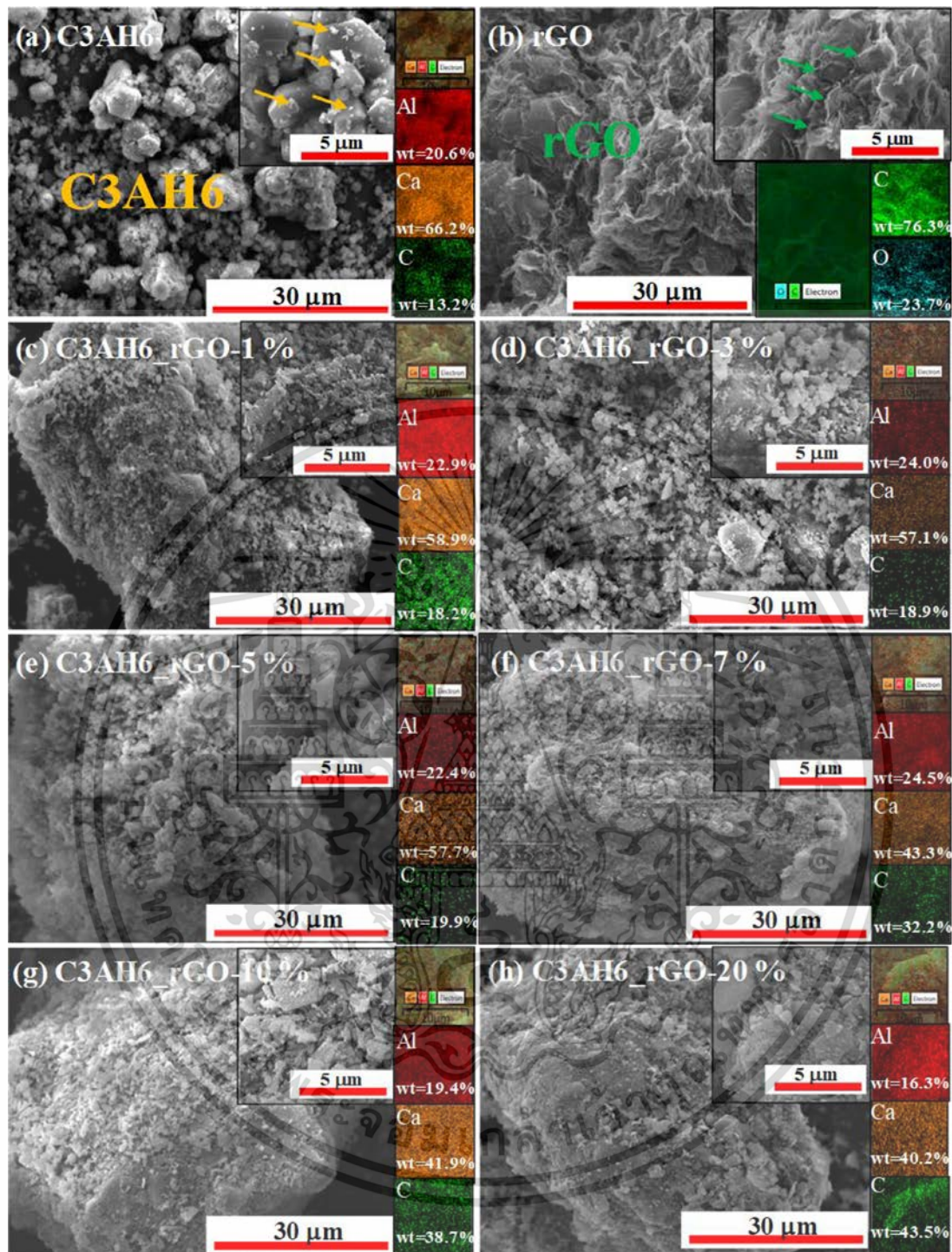


Fig. 3. (a) – (h) SEM images with inset a high magnification view of selected area, and displayed the EDS-mapping images for C and O elements of rGO and Al, Ca and C elements of pristine C3AH6, rGO and C3AH6_rGO (1, 3, 5, 7, 10 and 20% loading) composites, respectively.

soaked into 1.0 M KOH aqueous solution for 3 h before performing an electrochemical test.

2.2.5.3. Cells assembly of the as-fabricated symmetric C3AH6_rGO-20% supercapacitor cells. Two activated C3AH6_rGO-20% electrodes were fabricated by mixing 80 wt% of C3AH6_rGO-20% material, 10 wt% of ethylene black, 10 wt% of PVDF dispersed in NMP to produce a homogeneous slurry, and coated onto a copper plate ($1 \times 1 \text{ cm}^2$). Next, the fabricated electrodes were dried overnight at 50°C . The average mass of loaded activated materials in each electrode is

$\sim 3.5 \text{ mg}$. For PVA-6 KOH solid-electrolyte separator, 0.5 g of PVA was dissolved in 5 ml of DI water at 80°C under constant stirring for 2 h. After attaining clear PVA gel solution, 5 ml of 6 M KOH was added to this PVA gel solution and stirred at the same temperature for 3 h. For the C3AH6_rGO-20% supercapacitor cells fabrication, two activated C3AH6_rGO-20% electrodes were assembled into a sandwich-like stacked configuration of an activated C3AH6_rGO-20% electrode / PVA-6 KOH solid-electrolyte separator / activated C3AH6_rGO-20% electrodes and dried on the hot plate at 40°C for 1 h. Finally, the C3AH6_rGO-20% supercapacitor cells were sealed by a tape to form a

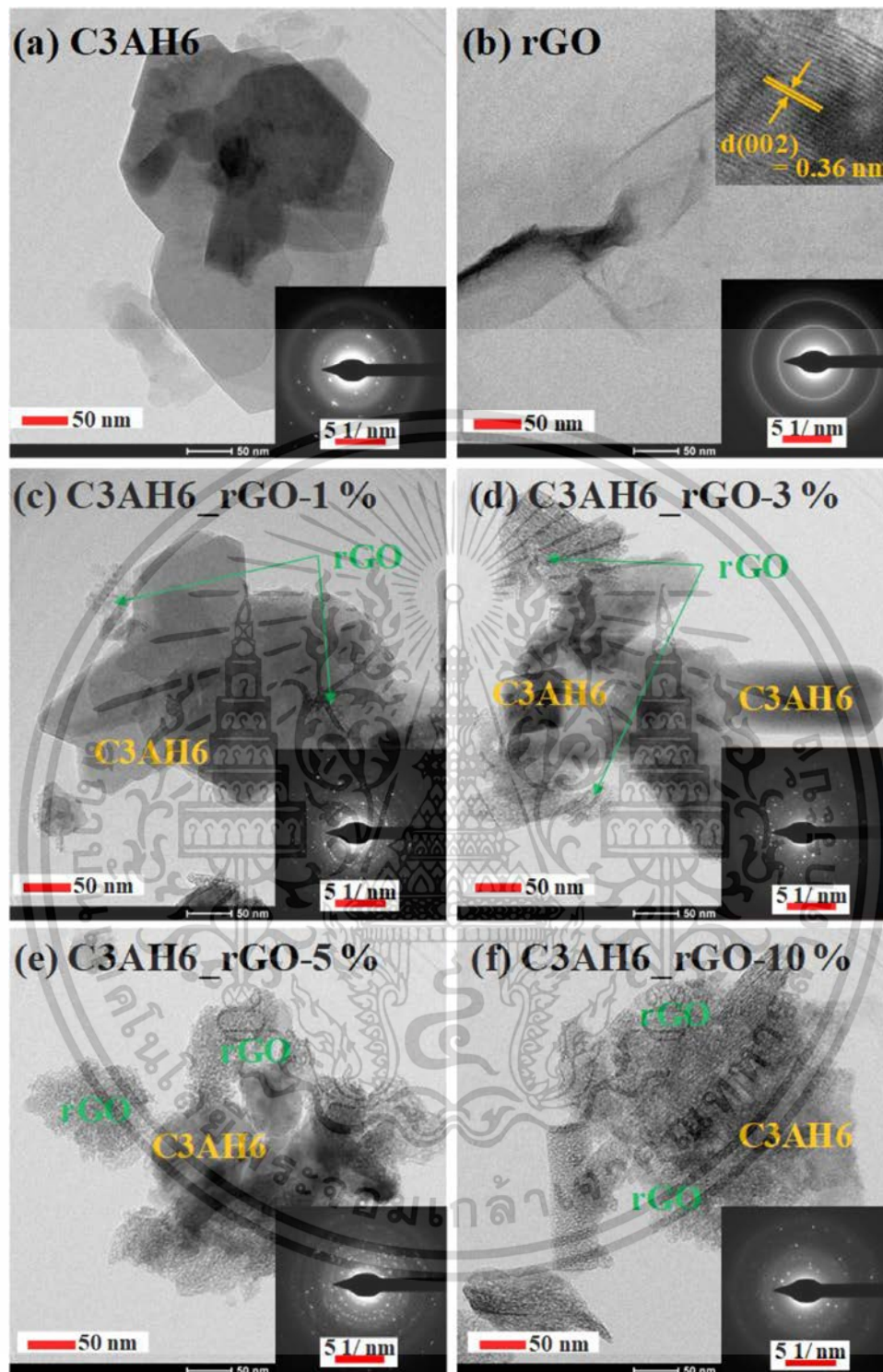


Fig. 4. (a) – (f) TEM images with inset a high magnification view of the selected area electron diffraction (SAED) patterns of pristine C3AH6, rGO and C3AH6_rGO_1, 3, 5 and 10% composites, respectively.

full cell.

2.3. Materials characterization

The X-Ray Diffraction (XRD) phase of the samples was analyzed using a powder XRD in a PHILIPS X'Pert's model (X-ray source λ $\text{CuK}\alpha = 1.5406 \text{ \AA}$). Raman spectroscopy was performed by a DXR Smart (Thermo Scientific) equipped with a 532 nm excitation. The morphology of the samples was observed by the SEM and TEM

techniques. The vibration mode of the atomic bonding was evaluated using FTIR, (Bruker, Senterra). The dielectric properties were determined through an impedance analyzer (KEYSIGHT E4990A). The electrochemical measurements (CV, GCD and EIS) were investigated using an electrochemical workstation (CS350 Potentiostat/Galvanostat, Wuhan Corrtest Instruments Corp Ltd.), which is measures a three-electrode cell system of the electrolyte 1.0 M KOH aqueous solution. The Ag/AgCl in 3.0 M HCl and platinum wire (diameter of 0.5 mm)

ไม่ว่ากรณีใดๆ ทั้งสิ้น อีกทั้งห้ามมิให้ตัดแปลงเนื้อหา และต้องอ้างอิงถึงเจ้าของเอกสารทุกครั้งที่มีการนำไปใช้

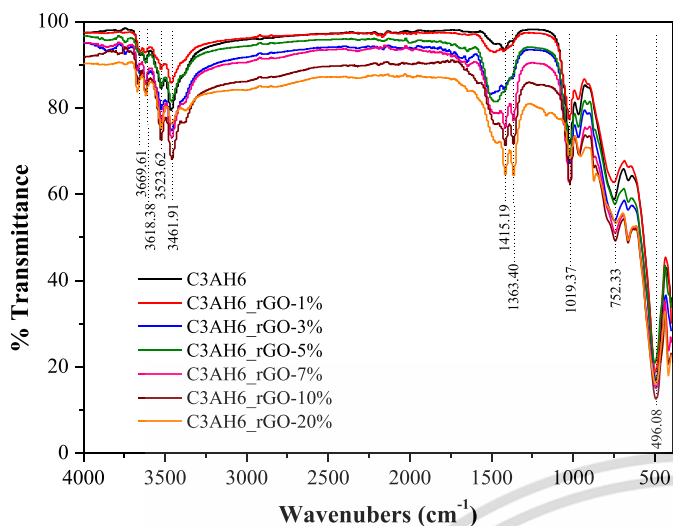


Fig. 5. FTIR spectra of pristine C3AH6 and C3AH6_rGO (1, 3, 5, 7, 10 and 20%) composites.

were used as reference and counter electrodes, respectively.

3. Results and discussions

3.1. XRD analysis

The XRD patterns of pristine C3AH6 and all C3AH6_rGO samples are shown in Fig. 1(a). The main diffraction peaks of pristine C3AH6 and all C3AH6_rGO samples are corresponded to the standard of JCPDS 03–0123 which have the cubic crystalline structures with a space group *Ia-3d* [38–40,46]. The characteristic XRD pattern of rGO ($2\theta = 25.2$) was not founded in all C3AH6_rGO samples due to an amorphous phase of rGO. In Fig. 1(a), it is observed that the secondary phase of Aluminum Hydroxide (Al(OH) 3) is appeared at the diffraction peak of 2θ approximately 18 and 23.5° of pristine C3AH6 and all C3AH6_rGO samples which is due to create during the hydration process of the C12A7 cement [45,47]. However, the $3\text{CaO}\cdot\text{Al}_2\text{O}_3\cdot\text{CaCO}_3\cdot 11\text{H}_2\text{O}$ phase, which is the supporter of the growth pristine C3AH6 nanosize in the rGO network of C3AH6_rGO samples, is observed in XRD results. The most dominant diffraction peaks in 2θ ranging from 10 to 55° consist of (211), (220), (321), (400), (332), (431), (521), (611), (552), (642) and (651) planes, corresponding to the diffraction angle 2θ of 17.2 , 19.9 , 26.5 , 28.3 , 33.4 , 36.4 , 39.2 , 44.3 , 52.4 , 53.5 and 54.5° , respectively. Clearly, these results can confirm the highly nano size pristine C3AH6 cement with increasing rGO concentrations [38]. Moreover, the Rietveld refinement method was used to determine the lattice constants (a), cell volume (V), reliability factors of weighted profile residual (R_{wp}), profile residual (R_p), expected residual (R_{ex}), and goodness of fit (GOF) of pristine C3AH6 and all C3AH6_rGO-5% samples. A space group *Ia-3d* of the standard Tricalcium Aluminate Hexahydrate was used for fitting, as shown in Fig. 1(b)–(c) and summarized in Table 1. As seen in Fig. 1(b)–(c) and Table 1, the excellent fitting of pristine C3AH6 and all C3AH6_rGO-5% samples were in agreement with the Tricalcium Aluminate Hexahydrate standard. Besides, the lattice constants (a) and cell volume (V) were decreased with increasing rGO concentrations, which suggests the decrease in C3AH6_rGO grain size. The average crystallite size (D_{XRD}) of pristine C3AH6 and all C3AH6_rGO-5% samples were calculated by the dominant peaks of the X-ray line broadening (211), (220), (321), (400), (332), (431), (521), (611), (552), (642) and (651) planes using the Scherrer formula equation as following [48]:

$$D_{XRD} = 0.9\lambda/\beta\cos\theta \quad (1)$$

where D_{XRD} is the crystallite size; λ is the wavelength of Cu-K α radiation; θ is the half of the diffraction peak angle; and β is the full width at half-maximum (FWHM) of the XRD peaks. The D_{XRD} values of pristine C3AH6 and all C3AH6_rGO samples with $x = 1, 3, 5, 7, 10$ and 20% were found to be 70.64 ± 4.54 , 69.38 ± 4.91 , 68.60 ± 4.65 , 65.89 ± 13.08 , 63.04 ± 10.85 , 61.99 ± 11.17 and 55.08 ± 20.84 nm, respectively (See Table 1). Interestingly, the nanometer crystallite sizes of all C3AH6_rGO samples ($x = 1, 3, 5, 7, 10$ and 20%) are decreased with increasing rGO concentrations, as corresponding to the lattice constants and cell volume.

3.2. Raman analysis

The Raman spectra measured in the spectral range from 100 cm^{-1} to 3000 cm^{-1} of pristine C3AH6, pristine rGO and all C3AH6_rGO samples are shown in Fig. 2(a). In Fig. 2(a), Raman spectra peak of C3AH6 sample showed two main peaks at around 533 and 1050 cm^{-1} as corresponding to the $[\text{AlO}_4^{5-}]$ stretching, which is the characteristic of pristine C3AH6 cement. For rGO spectra, the Raman spectra peak displayed two main peaks at around 1353 cm^{-1} and 1592 cm^{-1} , which correspond to the edges of the defected carbon layers due to the breakdown of translational symmetry (D band) and the second-order scattering (sp^2) of the graphitic carbon (G band) [13,38–41,45–49]. The characteristics of D band (~ 1300 cm^{-1}) and G band (~ 1600 cm^{-1}) were carefully observed. The I_D/I_G intensity ratio which confirmed that extensive oxidation and reduction have resulted in the GO led to large disorders in the rGO. Also, the ratio I_D/I_G is more than 1 conforming a large amount of GO transformation into rGO over chemical reduction using hydrazine reductant [13]. This is due to the decrease in both average size of the sp^2 domains and the removal of oxygen functional groups in chemical structure of GO [50–52]. Moreover, it was also observed that the two main peaks of D band and G band of rGO structure were found in all C3AH6_rGO samples, suggesting that the synthesis of C3AH6_rGO composites were successful, owing to the combination of pristine C3AH6 and rGO phases [38]. In addition, the ratio I_D/I_G of all C3AH6_rGO samples were strongly increased with greater amounts of rGO content. This result well confirmed that the content of rGO was increased into the C3AH6_rGO composite samples.

3.3. SEM analysis

The morphology of pristine C3AH6, rGO, and all C3AH6_rGO samples were analyzed by SEM images as shown in Fig. 3(a)–(h). As seen in Fig. 3(a), the morphology of pristine C3AH6 sample included the agglomerated irregular of edge shape particle with a micrometer size. For rGO morphology as shown in Fig. 3(b), the SEM image displayed the creases and wrinkles of thin sheet with high overlapping. As seen in Fig. 3(c)–(h), all C3AH6_rGO samples displayed similar edge shape particles, corresponding to the pristine C3AH6 sample, and illustrated the uniform shape of the continuous network rGO structure which presents the rGO incorporation with pristine C3AH6 cement. It shows a high magnification view in the inset Fig. 3(c)–(h). Interestingly, the surface of all C3AH6_rGO samples showed that the network structure of rGO sheet confirms the occurrence of grain boundary interfaces for rGO incorporation with pristine C3AH6 cement. The EDS-mapping images of pristine C3AH6, rGO and all C3AH6_rGO samples (See Fig. 3(a)–(h)) displayed the presence of C and O elements of rGO and Al, Ca and C elements of pristine C3AH6 sample and all C3AH6_rGO samples. These results confirmed the homogeneous distribution of a carbon compound in rGO composite on surface pristine C3AH6 cement.

3.4. TEM analysis

Fig. 4(a)–(f) shows TEM images of pristine C3AH6, pristine rGO and C3AH6_rGO-1, 3, 5 and 10% samples with an inset of the selected area electron diffraction (SAED) patterns. Fig. 4(a) shows that the

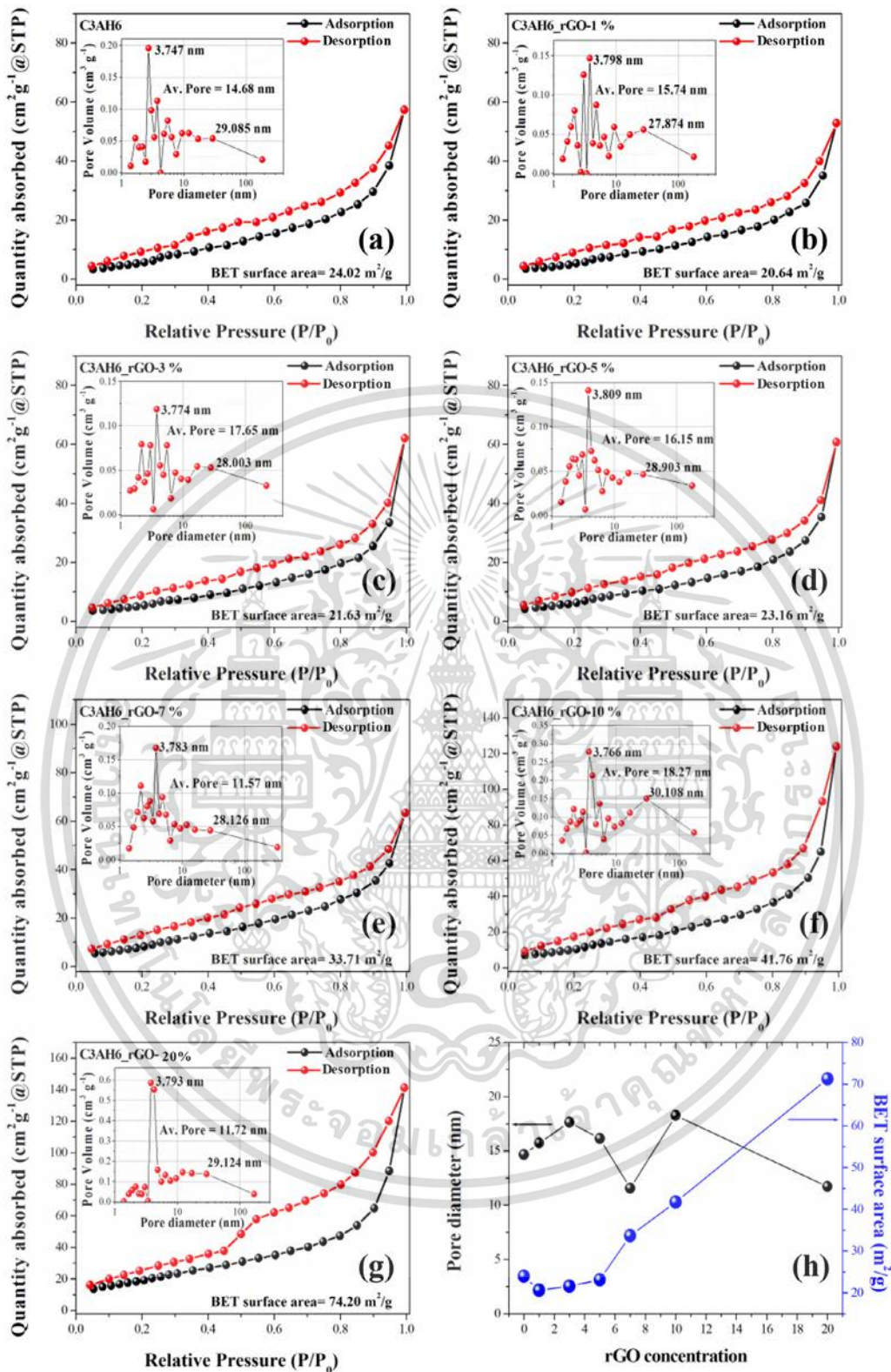


Fig. 6. (a) – (g) Nitrogen sorption isotherms with inset a pore-size distribution curves of C3AH6 and C3AH6_rGO (1, 3, 5, 7, 10 and 20%) composites, and (h) the plots of pore sizes and BET surface area as a function of rGO concentration.

particle of pristine C3AH6 sample had small grains and pores with nanosized approximately 100–200 nm. In addition, morphology of rGO nanosheet, shown in Fig. 4(b), indicated the translucent thin sheet. Regarding the C3AH6_rGO-1 and 3% samples, shown in Fig. 4(c) – (d), the morphology displayed similar flake-like shape, which is the rGO

incorporation with pristine C3AH6 cement. Fig. 4(e) – (f) clearly displayed the decrease of grain sizes with increasing rGO percent weight for the C3AH6_rGO-5 and 10% samples. Thus, the percent weight of rGO nanosheet can be affected by decreasing the grain sizes of the composites C3AH6_rGO samples. This is due to the rGO surface which

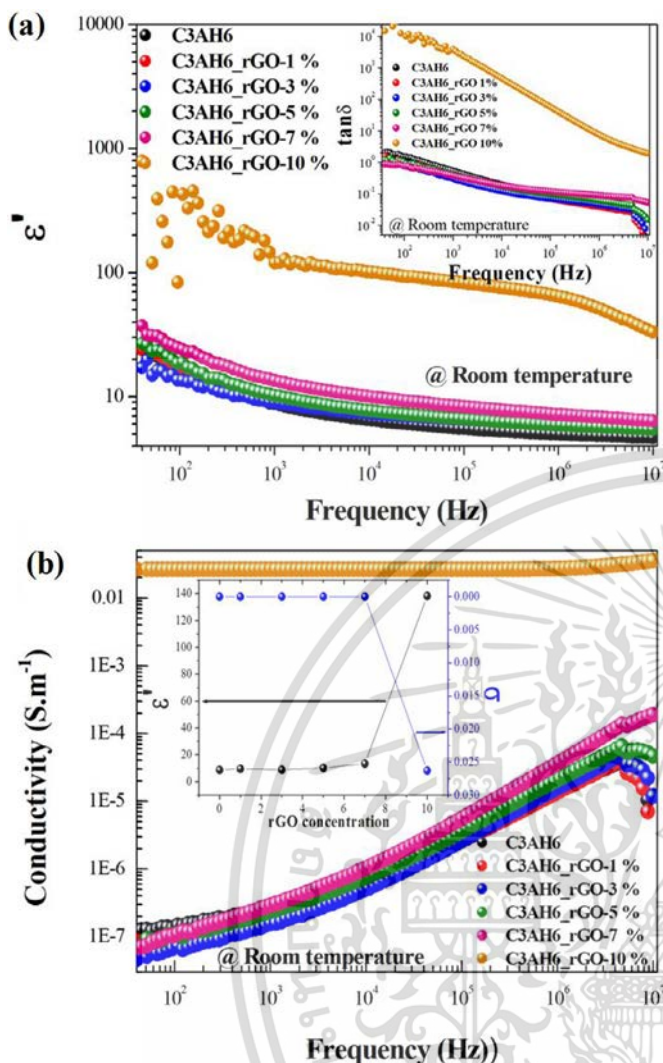


Fig. 7. (a) Frequency dependence of dielectric properties with inset showing $\tan\delta$ of C3AH6 and C3AH6_rGO (1, 3, 5, 7 and 10%) composites, and (b) AC conductivity at room temperature and inset of ϵ' and AC conductivity values at 1 kHz of C3AH6_rGO composites with various concentrations of rGO.

supports the constant growth of the nucleation pristine C3AH6 sites [38]. Moreover, SAED patterns of rGO sample revealed the diffraction ring, indicating a high poly crystalline. However, SAED patterns of C3AH6 and C3AH6_rGO-1, 3, 5 and 10% samples demonstrated a characteristic of the mixed diffraction ring and diffraction point as a result of combination of polycrystalline rGO and nanograin sized pristine C3AH6 cement.

3.5. FTIR analysis

The FTIR spectra of pristine C3AH6 and all C3AH6_rGO samples were measured in the region of $4000 - 400 \text{ cm}^{-1}$ the result of which is shown in Fig. 5(b). The appearance of vibrational peak at about 3669.61 cm^{-1} was attributed to the (ν_{as} O–H) stretching mode of water due to the formation of water adsorption on surface. And the 3669.61 , 3618.38 , 3523.62 and 3461.91 cm^{-1} were attributed to ν_{as} O–H stretching mode of AH_3 in pristine C3AH6 [38,53–55]. Moreover, the δ O–H stretching mode in AH_3 also showed vibrational peak at about 1019 cm^{-1} . The observed vibrational peak at about 1363.40 and 1415.19 cm^{-1} were attributed to the C–H stretching mode [46]. The strong vibrational peaks at band about $\sim 496.08 \text{ cm}^{-1}$ were attributed to the ν Al–O stretching mode in hydr ogarnet [46]. These obtained

results can confirm the structure of pristine C3AH6.

3.6. BET analysis

Fig. 6(a) – (h) shows the Nitrogen sorption isotherms of pristine C3AH6 and C3AH6_rGO samples. The pore-size distributions of these samples and plots of BET surface area and pore sizes were a function of the rGO concentrations. As seen in Fig. 6(a) – (h), a typical type-IV isotherm indicates the characteristic of mesoporous structure in particles [24,53,56]. The specific BET surface area of pristine C3AH6 and all C3AH6_rGO samples were found to be increased with increasing rGO content as summarized in Fig. 6(g). The maximum specific BET surface area was $74.20 \text{ m}^2/\text{g}$ for C3AH6_rGO-20% sample. Moreover, the calculated pore-size distributions of C3AH6 and all C3AH6_rGO samples using BJG technique are shown in Fig. 6(a) – (h) and average pore size diameters of these samples are summarized in Fig. 6(g). The average pore size diameters of pristine C3AH6 and C3AH6_rGO-1, 3, 5, 7, 10 and 20% were found to be 14.68, 15.74, 17.65, 16.15, 11.57, 18.27 and 11.72 nm, respectively.

3.7. Dielectric properties

The frequency dependence of the dielectric behavior of pristine C3AH6 and C3AH6_rGO-1, 3, 5, 7 and 10% samples revealed the dielectric constant (ϵ') and $\tan\delta$ shown in Fig. 7(a). The ϵ' and $\tan\delta$ of pristine C3AH6 and all C3AH6_rGO samples were observed at room temperature. As seen in Fig. 7(a), the pristine C3AH6 and C3AH6_rGO samples with loading low rGO content (1, 3 and 5%) demonstrate that the ϵ' value was not changed. On the other hand, the C3AH6_rGO samples (7 and 10%) showed that the ϵ' values gradually increase with increasing the rGO content. The ϵ' values are observed at 1 kHz of the pristine C3AH6 and the C3AH6_rGO samples with 1, 3, 5, 7 and 10% of 8.78, 9.66, 8.94, 10.23, 13.48 and 138.23, respectively. The ϵ' value of the C3AH6_rGO-10% is higher than that of pristine C3AH6 with approximately ~ 15 times, which is in agreement with the previous result of the reduced graphene oxide/ Mn_3O_4 nanocomposites [57–58]. Likewise, the ϵ' value of C3AH6_rGO-10% sample was nearly independent on frequency with a behavior similar to the one observed in poly (vinylidene fluoride)/nano-sized $\text{La}_2\text{NiO}_{4.8}$ (PVDF/LNO) nanocomposite films [58]. Meeporn et al. [59] reported that the ϵ' stability of frequency can be explained by the effect of density of free electron charges in the conductive particles. It is noteworthy that the obtained free electron charges of pristine C3AH6 were accumulated on the rGO surface interface [57–58]. Therefore, the enhanced ϵ' value was observed with increasing rGO content due to many free electron charges on the rGO surface [59]. The accumulated free electron charges on rGO surface are given rise to high polarization. These results clearly indicate that the interfacial polarization on the surface of C3AH6_rGO samples were used to explain the high ϵ' and high $\tan\delta$, especially at low frequency shown in Fig. 7(a), respectively [32,60–63]. This finding depends on the high AC conductivity (σ) in material [64–65]. The AC conductivity at room temperature and inset of ϵ' and σ values at 1 kHz of pristine C3AH6 and C3AH6_rGO-1, 3, 5, 7 and 10% samples with various of rGO concentrations are shown in Fig. 9(b). According to Fig. 7(b), the pristine C3AH6 and C3AH6_rGO samples with loading low rGO content (1, 3, 5 and 7%) show that the σ value was not changed at low frequencies whereas the C3AH6_rGO-10% sample exhibited the high σ value. Interestingly, the σ values of C3AH6_rGO-10% sample were independent of frequency. This result can prove that the conduction of rGO network was arisen by the obtained free electron charges from pristine C3AH6 which provide the high $\tan\delta$. According to Fig. 7(a) – (b), the conductivity of materials has strongly influenced the dielectric properties. Consequently, high ϵ' value and stability on frequency of the C3AH6_rGO-10% sample can be explained by the high density of free electron charges for the interfacial polarization on the rGO surface.

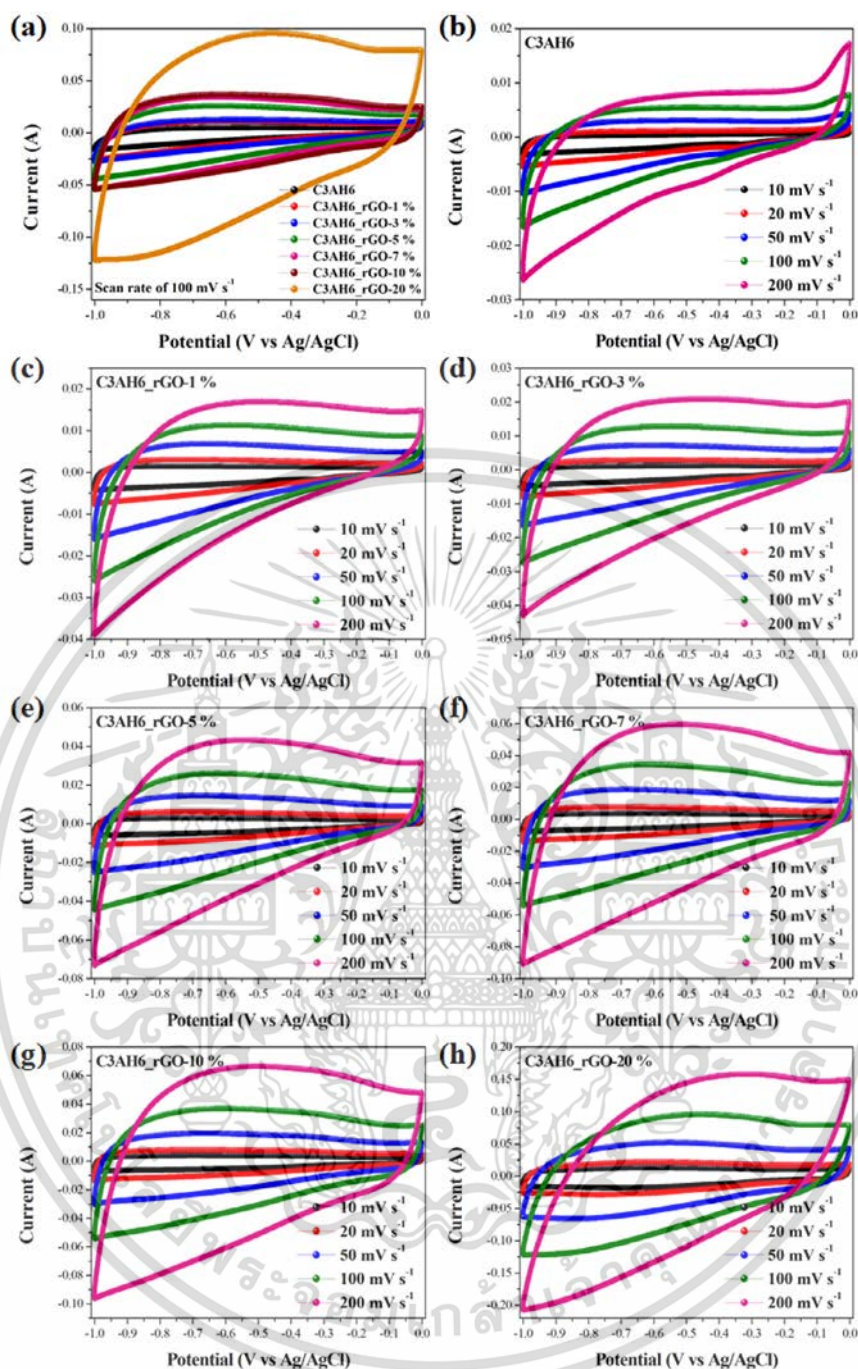


Fig. 8. (a) CV curves at a scan rate of 100 mV s^{-1} of C3AH6 and C3AH6_rGO (1, 3, 5, 7, 10 and 20%) electrodes, (b) – (h) CV curves at different scan rates of C3AH6 and C3AH6_rGO (1, 3, 5, 7, 10 and 20%) electrodes, respectively.

3.8. Electrochemical studies

Fig. 8(a) shows CV curves of pristine C3AH6 and all C3AH6_rGO electrodes at a scan rate of 100 mV s^{-1} in a potential window of $-0.1 - 0.0 \text{ V}$. It can be seen in Fig. 8(a) that the CV curves of pristine C3AH6 electrode display a small reversible reaction as a poor capacitive behavior, whereas the electrodes of rGO including the C3AH6 cement show gradual increase in the area of the reversible reaction with increasing the rGO content. In fact, these CV curves of all C3AH6_rGO electrodes are close to quasi-rectangular shape. This indicates a good capacitive behavior owing to clearly reversible reaction of a capacitive behavior which takes place at the interface of electrode and electrolyte. Which suggested the storage charge mechanism of electrochemical

double layer capacitors (EDLCs) behavior [13,25–26,51]. It can be seen in Fig. 8(b) – (h) that the CV curves of pristine C3AH6 and all C3AH6_rGO electrodes at scan rates from 10 to 200 mV s^{-1} , which shows the intensity and area of those CV curves, gradually increase with increasing the scan rate. This is because of the efficient migration of OH^- ions through the porous structure, the effect of the decreased C3AH6 size due to C3AH6 cement composited with rGO sheets, and oxygen containing functional groups at electrode surface of rGO connections [24,31–32,38,51]. As seen in Fig. 8(h), the area of closed CV curve of C3AH6_rGO-20% electrode was larger than that of other C3AH6_rGO electrodes, which can be an indicator of the superior electrochemically performance supercapacitor of C3AH6_rGO-20% electrode. The specific capacitance (C_{cs}) values of all working electrodes

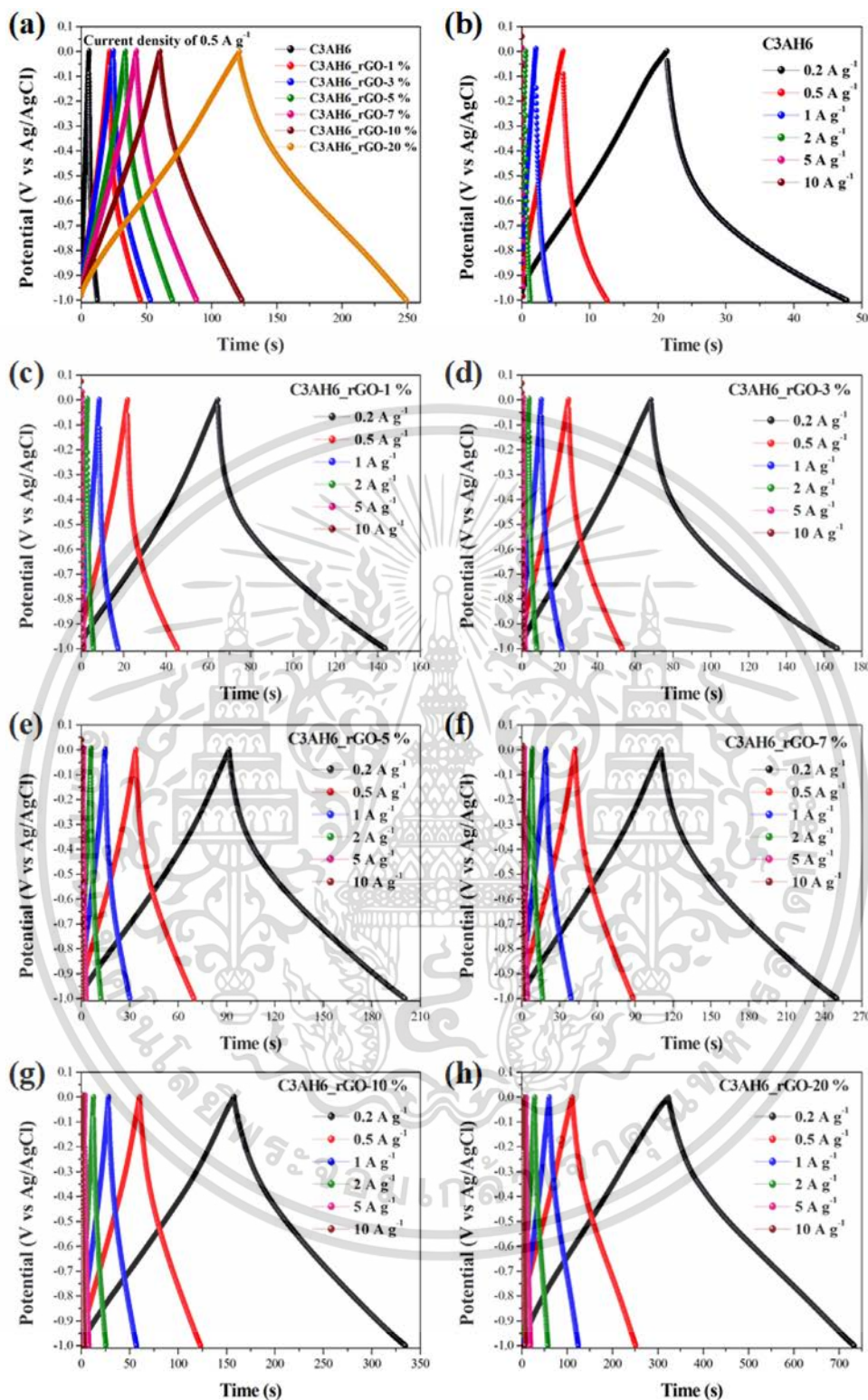


Fig. 9. (a) GCD curves at a scan rate of 0.5 A g^{-1} of C3AH6 and C3AH6_rGO (1, 3, 5, 7, 10 and 20%) electrodes, (b) – (h)GCD curves at different current densities of C3AH6 and C3AH6_rGO (1, 3, 5, 7, 10 and 20%) electrodes, respectively.

were calculated from the integral area of closed CV curves [25] using the following equation:

$$C_{sc} = \frac{\int i dV}{2mv\Delta V} \quad (3)$$

Where C_{sc} is the specific capacitance (F g^{-1}); i is the measured current (A); v is scan rate; m is the mass of active materials in each electrodes

(g); and ΔV is the total potential deviation (V). The C_{sc} was found to be 5.348, 12.740, 13.775, 16.685, 19.927, 26.650 and 64.067 F g^{-1} at 10 mV s^{-1} for pristine C3AH6 and all C3AH6_rGO electrodes, respectively. The C3AH6_rGO-20% shows higher C_{sc} than other compositions. As a matter of fact, the performance of the C3AH6_rGO-20% electrode was at maximum C_{sc} values due to its smaller particle size than other compositions. This helps enhance the surface area and have

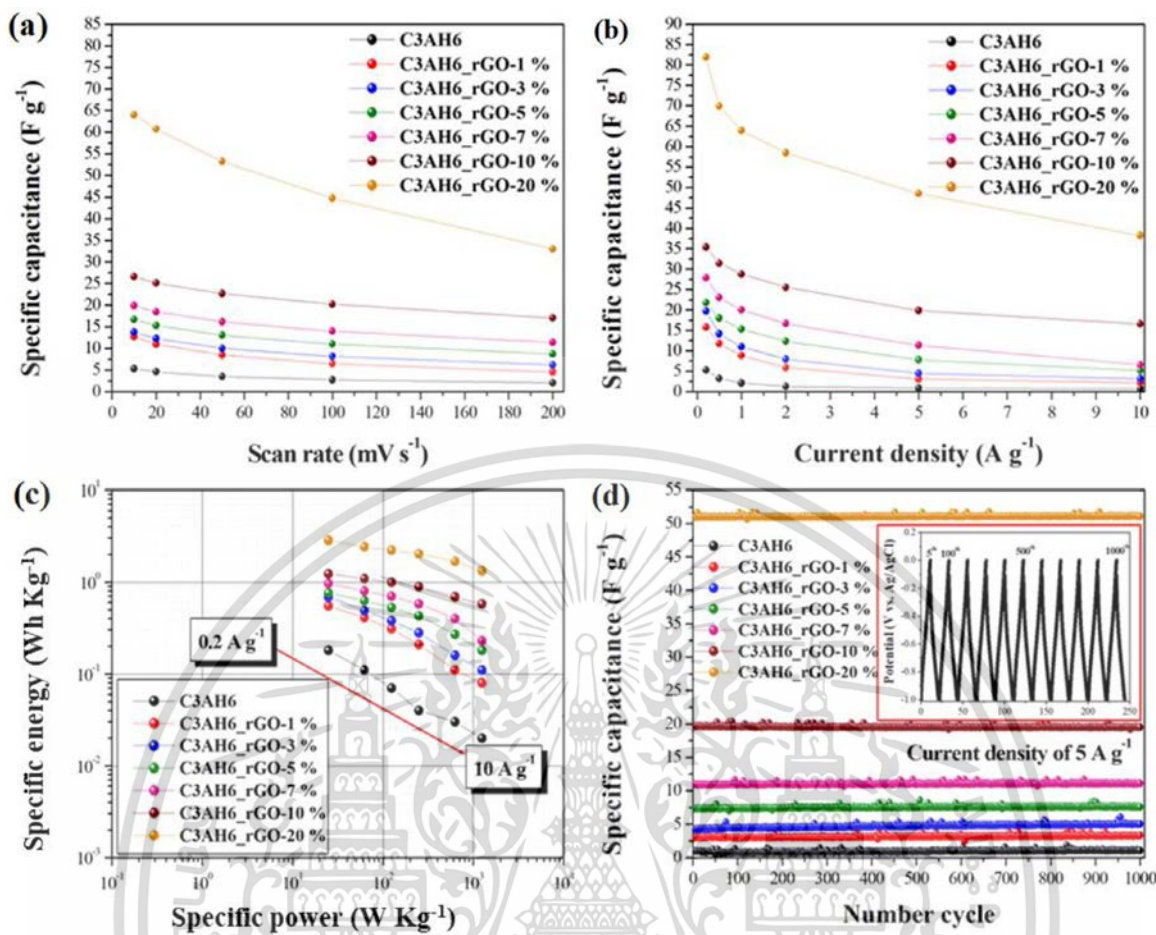


Fig. 10. (a) – (b) Specific capacitance plot of C3AH6 and C3AH6_rGO (1, 3, 5, 7, 10 and 20%) electrodes at different scan rates and current densities were calculated by CV and GCD test, respectively, (c) – (d) Ragone plots and cycling stability of C3AH6 and C3AH6_rGO (1, 3, 5, 7, 10 and 20%) electrodes using GCD test at a current density of 5 A g⁻¹, respectively.

Table 2

C_{sc} value at different scan rates and current densities were calculated by CV and GCD test, respectively, and EIS analysis of pristine C3AH6 and C3AH6_rGO (1, 3, 5, 7, 10 and 20%) electrodes.

Parameters	Electrodes C3AH6	C3AH6_rGO-1%	C3AH6_rGO-3%	C3AH6_rGO-5%	C3AH6_rGO-7%	C3AH6_rGO-10%	C3AH6_rGO-20%
C _{sc} (F g ⁻¹) by CV							
10 mV s ⁻¹	5.35	12.74	13.77	16.69	19.93	26.65	64.07
20 mV s ⁻¹	4.61	11.01	12.30	15.32	18.51	25.14	60.77
50 mV s ⁻¹	3.55	8.50	10.06	13.07	16.20	22.70	53.28
100 mV s ⁻¹	2.75	6.50	8.14	11.03	14.00	20.28	44.79
200 mV s ⁻¹	2.04	4.61	6.22	8.72	11.41	17.08	33.06
C _{sc} (F g ⁻¹) by GCD							
0.2 A g ⁻¹	5.30	15.83	19.76	21.79	27.91	35.42	81.95
0.5 A g ⁻¹	3.24	11.81	14.21	18.04	23.10	31.46	69.96
1 A g ⁻¹	2.12	8.86	11.04	15.32	20.08	28.82	63.96
2 A g ⁻¹	1.28	5.92	8.00	12.36	16.72	25.60	58.52
5 A g ⁻¹	0.90	3.10	4.50	7.80	11.40	19.90	48.55
10 A g ⁻¹	0.80	2.20	3.20	5.20	6.60	16.60	38.30
EIS analysis							
R _s (Ω)	1.003	0.932	0.945	1.051	0.929	1.060	0.855
(%error)	(1.301)	(1.366)	(1.467)	(1.310)	(1.436)	(1.384)	(2.075)
R _{ct} (Ω)	1.642	1.021	0.761	0.618	0.539	0.448	0.297
(%error)	(16.635)	(21.665)	(15.775)	(11.043)	(13.42)	(10.888)	(7.786)
C _p (F)	0.003	0.008	0.019	0.024	0.042	0.080	0.745
(%error)	(7.782)	(11.401)	(8.657)	(5.780)	(7.139)	(6.044)	(3.394)
DE-R (Ω)	3.064	1.380	4.693	1.279	0.780	0.942	0.834
(%error)	(27.011)	(44.401)	(31.807)	(31.610)	(48.185)	(60.441)	(32.548)

เอกสารนี้เป็นเอกสารที่สงวนไว้สำหรับการใช้งานเพื่อการศึกษาเท่านั้น ไม่อนุญาตให้นำไปใช้ประโยชน์ด้านการค้า
ไม่ว่ากรณีใดๆ ทั้งสิ้น อีกทั้งห้ามมิให้ตัดแปลงเนื้อหา และต้องอ้างอิงถึงเจ้าของเอกสารทุกครั้งที่มีการนำไปใช้

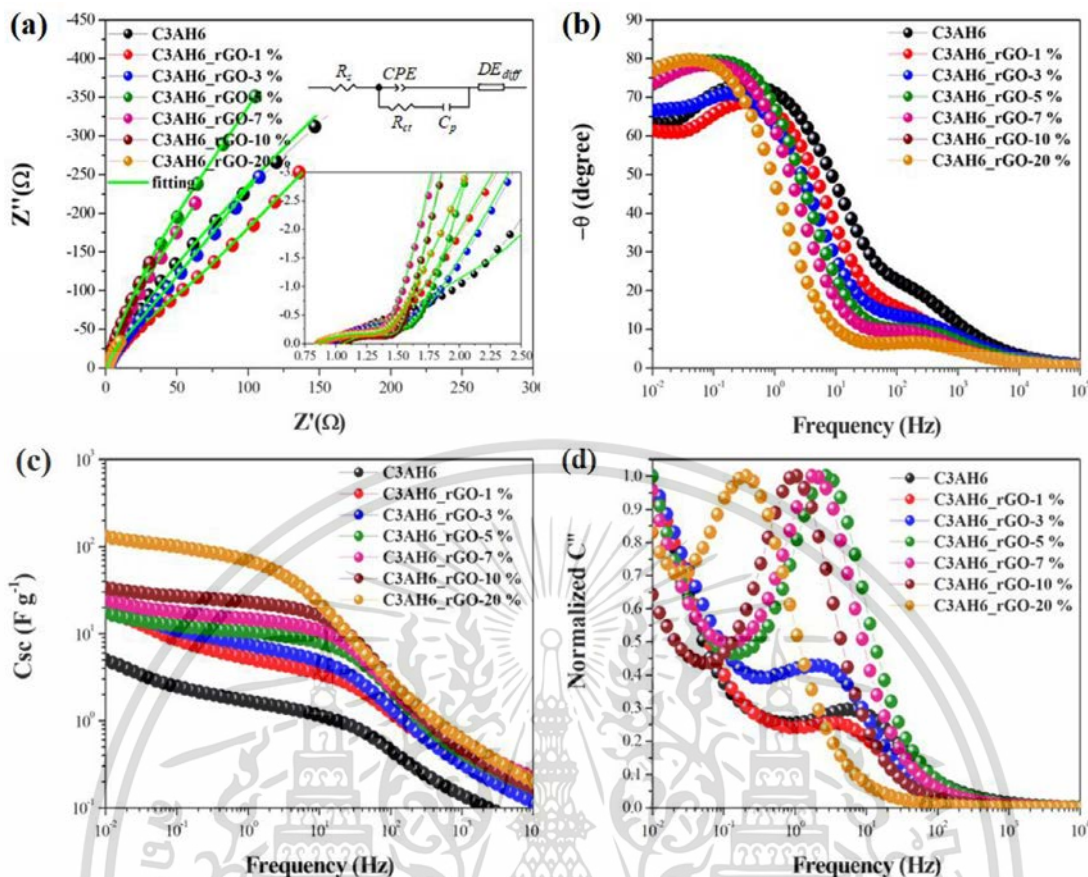


Fig. 11. (a) The fitting Nyquist impedance plots with inset the enlargement of the plots near origin of C3AH6 and C3AH6_rGO (1, 3, 5, 7, 10 and 20%) electrodes and showing an equivalent circuit, (b) – (d) Bode plots (phase angles and magnitudes plotted against the frequency) and showing of specific capacitance (c) and normalized imaginary part of the capacitance (d) versus frequency curves of C3AH6 and C3AH6_rGO (1, 3, 5, 7, 10 and 20%) electrodes, respectively.

larger energy storage [38,51].

Fig. 9(a) – (h) present the supercapacitor characteristics of pristine C3AH6 and all C3AH6_rGO electrodes. The characteristics can also be observed in GCD curves of pristine C3AH6 and all C3AH6_rGO electrodes performed within a potential window of $-0.1 - 0.0$ V at a scan rate of 0.5 A g^{-1} and different current densities from 0.2 to 10 A g^{-1} . It was clear that all GCD curves were almost linear in the range of voltage with constant slopes as an indicator of the double layer capacitor behavior [13,25,51]. In addition, it could be observed that the capacitive behavior decreased as the current density increased because the high current density accelerated and the charge/discharge rate of the ions in electrolyte could not be totally diffused onto electrode surface, which showed the internal resistance (R_i drop). The C_{sc} values were estimated based on the obtained GCD curves [31,53] using the following equation:

$$C_{sc} = \frac{i}{m(\frac{\Delta V}{\Delta t})} \quad (4)$$

Where i is the discharge current density (A g^{-1}); $\Delta V/\Delta t$ is the slope of discharge curves after the R_i drop. The C_{sc} of pristine C3AH6 and all C3AH6_rGO electrodes were calculated based on the integral area of closed CV curve and discharge curves as shown in Fig. 10(a) – (b). In Fig. 10(a) – (b), the C_{sc} values decreased with increasing the current density owing to the imperfection of electrodes preventing the electrolyte ions from being diffused and penetrated into the active sites of electrode materials. However, the enhanced C_{sc} of C3AH6_rGO-20% electrode could be attributed to the increase in the electrochemically active surface area for the formation of the EDLCs behavior and the effects of high surface area rGO connections [13,18,24–25,51,60–67].

In addition, the small particle size of pristine C3AH6 could result in high surface area and large mesopore of active redox sites for more OH^- ions to be accessible in electrolyte confirming the surface area and porous structure by BET results [24,52]. In line with the CV results, the C3AH6_rGO-20% composition showed higher C_{cs} (calculated from discharge curves) comparing to other compositions. Therefore, the enhanced activity of the composites has been due to an enrichment effect via diffusion within the modified electrode and the high useful surface area of rGO sheet. The free electron charge transfers through the electrode surfaces. The KOH electrolyte can be increased by the presence of rGO sheets composite with the pristine C3AH6 cement [38].

The specific energy (E_{sp} , Wh kg^{-1}) and specific power (P_{sp} , kW kg^{-1}) values of all working electrodes were calculated from the specific cell capacitance ($C_{sc, cell}$) which corresponds to $1/4$ of the C_{sc} in the GCD curves for the three electrode systems [25] using the following equation:

$$\frac{1}{C_{cell}} = \frac{1}{C_+} + \frac{1}{C_-} = \frac{1}{(m_+ \times C_{sc})} + \frac{1}{(m_- \times C_{sc})} = \frac{2}{(m \times C_{sc})}$$

Where m_+ and m_- are the effective masses of the active electrodes on the positive and negative electrodes ($m_+ = m_- = m$ for a symmetric supercapacitor). The C_{cell} is presented by $C_{cell} = \frac{(m \times C_{sc})}{2}$ and $C_{sc, cell}$ is

presented by $C_{sc, cell} = \frac{C_{cell}}{2 \times m} = \frac{(\frac{m \times C_{sc}}{2})}{2 \times m} = \frac{C_{sc}}{4}$. In this case, the C_{sc} and ΔV are used for the calculation of E_{sp} values as the following equation:

$$E_{sp} = \frac{1}{2} \frac{(C_{sc, cell} \times (\Delta V)^2)}{3.6} = \frac{1}{2} \frac{(\frac{C_{sc}}{4} \times (\Delta V)^2)}{3.6} = \frac{1}{8} \frac{(C_{sc} \times (\Delta V)^2)}{3.6} \quad (5)$$

The P_{sp} can be derived from E_{sp} divided by the discharge time t as

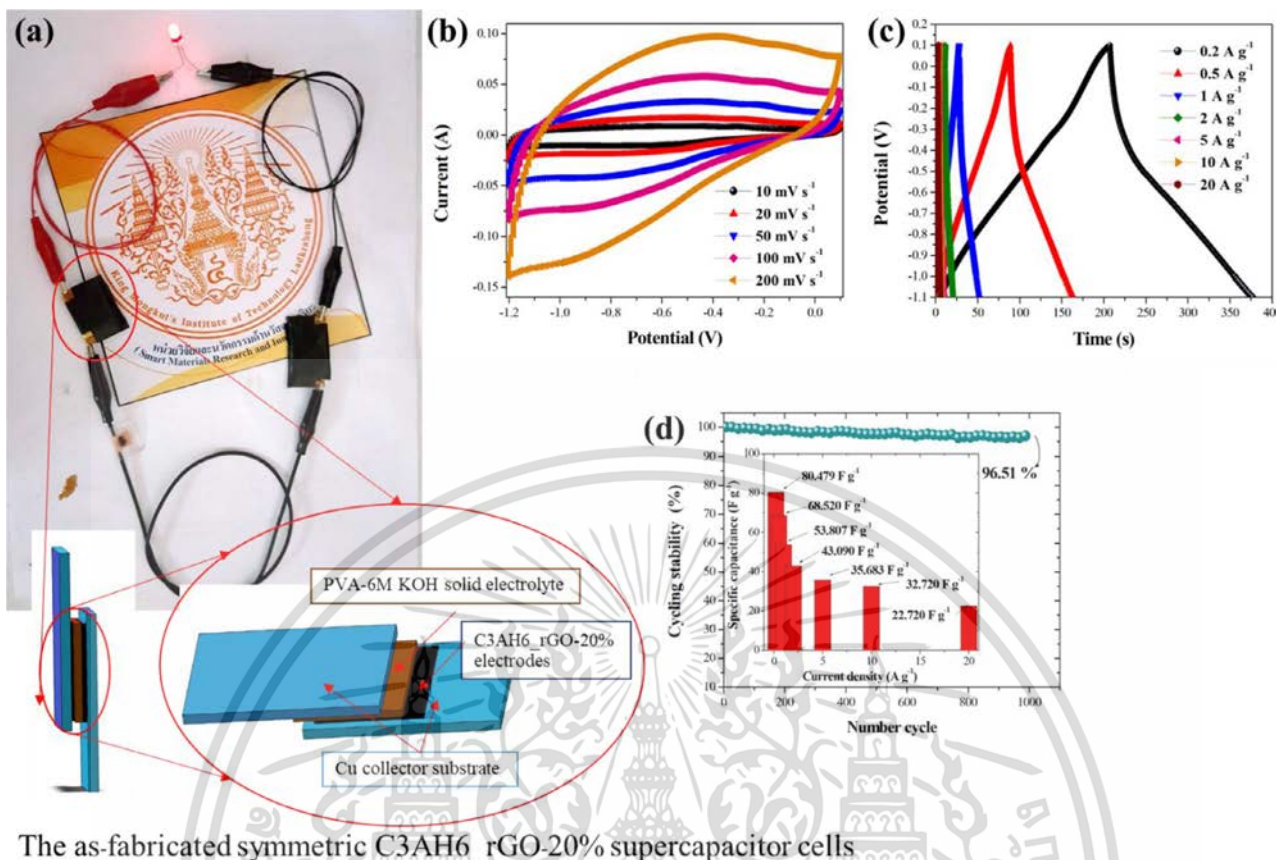


Fig. 12. (a) The photographic image of the as-fabricated symmetric C3AH6_rGO-20% supercapacitor cells which made from two activated C3AH6_rGO-20% electrodes and PVA-6 KOH solid-electrolyte, (b) the CV curves at different scan rates, (c) the GCD curves at different current densities and (d) the efficiency of the cycling stability.

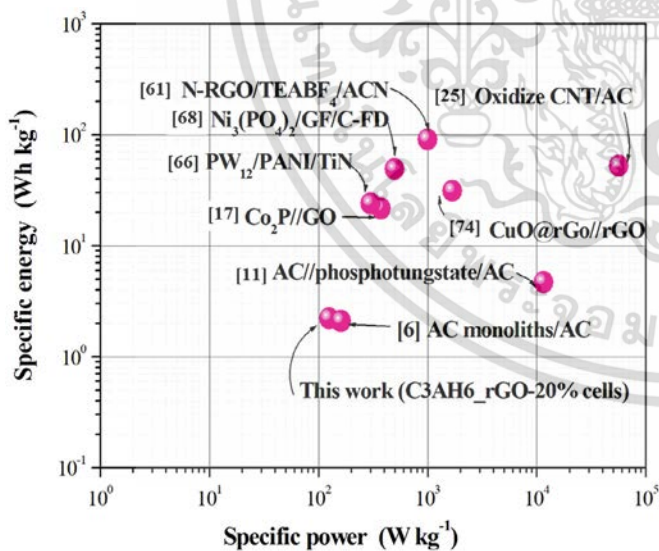


Fig. 13. Ragone plots of as-fabricated symmetric C3AH6_rGO-20% supercapacitor cells are comparable with values reported in previous studies.

the following equation:

$$P_{sp} = \frac{E_{sp} \times 3600}{t} \tag{6}$$

Fig. 10(c) displays the Ragone plot of pristine C3AH6 and all C3AH6_rGO electrodes. E_{sp} and P_{sp} values were found to be ranging from 0.02 to 2.85 Wh kg⁻¹ and 25 to 1250 W kg⁻¹, respectively, with

current densities of 0.2 to 10 A g⁻¹ in the KOH electrolyte which operates within a potential window of -0.1 - 0.0 V. The C3AH6_rGO-20% electrode clearly gave the highest specific power of 2.22 kW kg⁻¹ at a specific energy of 125 Wh kg⁻¹. Moreover, the E_{sp} and P_{sp} of C3AH6_rGO-20% electrode was comparable with values reported in previous studies as shown in Fig. 13. However, the cycling stability of pristine C3AH6 and all C3AH6_rGO electrodes were continuously investigated 1000 cycles by GCD test at a current density of 5 A g⁻¹, it was found that all C3AH6_rGO electrodes provided excellent cycling stability, as shown in Fig. 10(d).

Fig. 10(a) shows the Nyquist plots of pristine C3AH6 and all C3AH6_rGO electrodes which were analyzed by fitting the experimental data to the equivalent circuit model (inset in Fig. 10(a)) using ZView software. The main elements of the equivalent circuit were the solution resistance (R_s), charge transfer resistance (R_{ct}), a pseudocapacitive element (C_p) from redox process of active materials, constant phase element (CPE) to account for the double-layer capacitance, and diffusion resistance (DE_{diff}) [18,32,66,68-70]. The obtained values are summarized in Table 2. Generally, the intercept on Z' axis in a high frequency region was related to the R_s of the interface between an electrolyte solution and intrinsic resistance of active materials at surface electrodes. A semicircular curve was principally assigned to the R_{ct} according to the charge transfer process arisen at the interface of surface electrode and KOH electrolyte. As seen in Fig. 11(a), pristine C3AH6 and all C3AH6_rGO electrodes displayed a small semicircle in a high frequency region and straight line in a low frequency region. The C3AH6 electrode exhibited a higher R_{ct} value, whereas pristine C3AH6 with composite rGO electrodes was decreased from 1.642 to 0.292 Ω with increasing rGO content. It suggests that rGO provides great electrical conductivity to promote a faster charge transfer process. In

addition, in a low frequency region of Nyquist plots, the slopes of all C3AH6_rGO electrodes were higher than that of pristine C3AH6 electrode. It indicates a good electrical conductivity due to the high surface area of rGO connection and the low diffusion resistance (DE_{diff}) [66,68,71]. The low DE_{diff} values of C3AH6_rGO-7, 10 and 20% were obtained from the easy diffusion, proving that electrolyte ions can move more easily to the surface of the electrodes. This result showed that the pristine C3AH6 with composite rGO was a promising electrode material of supercapacitors.

The Bode plot in Fig. 11(b) shows the phase angle as a function of frequency, and this presents the phase angle value of about -60 to 80° in the low-frequency region. It suggests that the pristine C3AH6 with composite rGO electrodes approximates the ideal double layer charge storage capacitive behavior [18,68]. The specific capacitance (C_{sc}) and normalized capacitance (C'') as a function of the frequency of the pristine C3AH6 and all C3AH6_rGO electrodes were calculated by the following equations [25], respectively:

$$C_{sc} = \frac{-2}{\omega Z''^m} \quad (7)$$

and

$$C'' = \frac{Z'}{\omega |Z|^2} \quad (8)$$

Where ω is the angular frequency, Z' , Z'' and $|Z|$ are the real part, imaginary part and magnitude of impedance, respectively, and m is the mass of the active material on each electrode. As can be observed in Fig. 11(c), the C_{sc} completely depends on the frequency below approximately 1 Hz. Particularly for the C3AH6_rGO-20% electrode, a maximum C_{sc} is shown throughout the entire frequency region due to the high interfacial polarizations of ions on the surface electrodes [24–25,64–65]. The normalized capacitance (C''), which as a function of the frequency of the pristine C3AH6 and all C3AH6_rGO electrodes, as shown in Fig. 11(d). The characteristic of frequency at a maximum peak frequency was known as knee frequency (f_0) in which the capacitive and the resistive impedances are equal [66–67]. At higher frequencies from this point, the supercapacitors show more resistive behavior. On the other hand, the reciprocal of this f_0 represented the lowest time, which is associated with a short relaxation time constant ($t_0 = f_0^{-1}$). It can be used to define the boundary of the electrochemical capacitor from capacitive to resistive behavior [17,18,25,41,68]. Consequently, t_0 indicates a fast frequency response of the supercapacitor. The t_0 of pristine C3AH6 was 0.13 s, which was lower than that of all C3AH6_rGO electrodes found in the range from 0.23 to 4.45 s owing to the increase in rGO concentration. t_0 values of pure rGO film electrodes were usually found to be ~ 6.3 s [71]. In addition, the t_0 corresponds to the conductivity of materials at surface electrodes which have a great influence on the diffusion of free electron charges for the polarization on the rGO surface [25,32,71–73]. Therefore, t_0 of pristine C3AH6 was lower than that of all C3AH6_rGO electrodes due to the low conductivity and high intrinsic resistance of electrode materials, comparing with the electrodes of rGO having C3AH6 cement.

Fig. 12(a) shows that the photographic image of the as-fabricated symmetric C3AH6_rGO-20% supercapacitor cells were made from two activated C3AH6_rGO-20% electrodes and PVA-6 KOH solid-electrolyte. In Fig. 12(b), the CV curves of symmetric C3AH6_rGO-20% cells were determined by a potential window of $-1.2 - 0.1$ V for various scan rates from 10 to 200 mV s^{-1} . In the CV curves, the small swelling at about -0.22 and 0.61 clearly shows the small reversible redox reaction of rGO surface which an increase in current depends the increase in scan rate [4]. The appearance of the almost rectangular shape confirms that the capacitor behavior is largely contributed by double layer formation combined with the slightly pseudocapacitive process. Similarly, the GCD curves as shown in Fig. 12(c) displayed nearly typical symmetrical triangular shapes, suggesting that the capacitance originates from the hybrid supercapacitor behavior at the C3AH6_rGO-20% electrodes and

electrolyte interfaces. As seen in Fig. 12(d), the efficiency of the cycling stability is about 96.51% after 1000 cycles, whereas the maximum specific capacitance of symmetric C3AH6_rGO-20% cells was calculated and found to be 80.479 F g^{-1} at 0.2 A g^{-1} .

Fig. 13 shows the Ragone plots of symmetric C3AH6_rGO-20% supercapacitor cells. The result was comparable with values reported in previous studies. Obviously, the as-fabricated symmetric C3AH6_rGO-20% electrode shows an equal specific energy and specific power with activated carbon monoliths (ACMs) [18], which represent the characteristic of EDLCs behavior. Similarly, the range of specific power value of symmetric C3AH6_rGO-20% cells was observed from 100 to 10 kW kg^{-1} corresponding to AC//phosphotungstate/AC [11]. However, these values are lower than those of the reported symmetric supercapacitors, such as $\text{PW}_{12}/\text{PANI}/\text{TiN}$ (21.6 Wh kg^{-1} , 375 W kg^{-1}) [66], $\text{CoP}_2/\text{graphene}$ (24 Wh kg^{-1} , 300 W kg^{-1}) [17], and $\text{Ni}_3(\text{PO}_4)_2/\text{GO}/\text{C-FD}$ (49 Wh kg^{-1} , 499 W kg^{-1}) [68]. It is also comparable to the high specific energy and specific power of N-RGO/TEABF₄/ACN electrode (91.0 Wh kg^{-1} , 1 kW kg^{-1}) [61], CuO@rGO (31.2 Wh kg^{-1} , 1.69 kW kg^{-1}) [74], and Oxidize CNT (52.6 Wh kg^{-1} , 56.3 kW kg^{-1}) [25] which is a potential electrode for pseudocapacitors. In fact, this study indicated that the C3AH6_rGO composites are environmentally friendly, safe, and healthy built with energy-efficient and low-cost materials for supercapacitor applications [38].

4. Conclusions

The C3AH6_rGO-1, 3, 5, 10, and 20 wt.% nanocomposites were successfully synthesized by a rapid cement hydration method. XRD result and Rietveld refinement method showed excellent fitting and agreement with the pristine C3AH6 standard. SEM and TEM images displayed similar flake-like shape well confirming the rGO incorporation with pristine C3AH6 cements. EDS mapping image revealed the homogeneous distribution of a carbon compound in rGO composites on surface pristine C3AH6 cement. Raman spectra well confirmed the pristine rGO, pristine C3AH6 cement, and C3AH6_rGO nanocomposite with the appearance of the combination pristine C3AH6 and rGO. Nitrogen sorption isotherms of all samples displayed a typical type-IV isotherm with maximum specific BET surface area of $74.20 \text{ m}^2/\text{g}$ for C3AH6_rGO-20% sample. Interestingly, high dielectric property and stability on frequency of C3AH6_rGO-10% sample can be explained by the high density of free electron charges for the interfacial polarization on the rGO surface. Moreover, the electrochemical properties of pristine and all C3AH6_rGO electrodes had excellent capacitive properties, presenting the storage charge mechanism of a hybrid supercapacitor behavior. Interesting, the highest C_{sc} value of 80.479 F g^{-1} at a current density of 0.2 A g^{-1} with excellent cycling stability of 96.51% after 1000 cycles was obtained in symmetric C3AH6_rGO-20% supercapacitors. These results indicated that the enhanced activity of the composites may have been due to an enrichment effect via diffusion within the modified electrode and the highly usefull rGO surface area. This area allows free electron charges to transfer onto the electrode surface and the electrolyte can be increased by the presence of rGO sheets composited with the C3AH6 cement. Therefore, the nanocomposites material of reduced graphene oxide mixed with hydrogenated cement is an excellent ideal for supercapacitor electrode materials.

CRedit authorship contribution statement

Chaiwat Phrompet: Conceptualization, Data curation, Formal analysis. **Keerati Maneesai:** Data curation, Formal analysis. **Wattana Tuichai:** Data curation, Formal analysis, Writing - original draft. **Attaphol Karaphun:** Data curation, Formal analysis, Writing - original draft. **Chaval Sriwong:** Data curation, Formal analysis, Visualization, Investigation, Writing - original draft. **Chesta Ruttanapun:** Conceptualization, Formal analysis, Funding acquisition, Visualization, Resources, Supervision, Validation, Writing - original draft, Writing -

review & editing.

Declaration of Competing Interest

The authors declare no competing financial interests.

Acknowledgments

We express our sincere appreciation to the Faculty of Science, King Mongkut's Institute of Technology Ladkrabang (KMUTL) for funding our research grant [grant number: 2562-01-05-50].

Supplementary materials

Supplementary material associated with this article can be found, in the online version, at doi:10.1016/j.est.2020.101474.

References

- [1] Y. Wang, Y. Song, Y. Xia, *Chem. Soc. Rev.* 45 (2016) 5925.
- [2] B.E. Conway, *J. Electrochem. Soc.* 138 (1991) 1539.
- [3] P. Simon, Y. Gogotsi, *Nat. Mater.* 7 (2018) 845–854.
- [4] P.K. Jha, S.K. Singh, V. Kumar, S. Rana, S. Kurungot, N. Ballav, *Chem.* 3 (2017) 846–860.
- [5] M. Armand, J.M. Tarascon, *Nature* 451 (2008) 652–657.
- [6] G. Wang, L. Zhang, J. Zhang, *Chem. Soc. Rev.* 41 (2012) 797–828.
- [7] M. Vangari, T. Pryor, L. Jiang, *J. Energy Eng.* 139 (2) (2013) 72–79.
- [8] M.D. Stoller, S. Park, Y. Zhu, J. An, R.S. Ruoff, *Nano Lett.* 8 (10) (2008) 3498–3502.
- [9] S. Arepalli, *JOM* 57 (12) (2005) 26–31.
- [10] Z.S. Iro, C. Subramani, S.S. Dash, *Int. J. Electrochem. Sci.* 11 (2016) 10628–10643.
- [11] Z. Bo, Z. Wen, H. Kim, G. Lu, K. Yu, J. Chen, *Carbon N Y* 50 (2012) 4379–4387.
- [12] C. Liu, Z. Yu, D. Neff, A. Zhamu, B.Z. Jang, *Nano Lett.* 10 (12) (2010) 4863–4868.
- [13] H.T. Das, K. Mahendraprabhu, T. Maityalagan, P. Elumalai, *Sci. Rep.* 7 (2017) 15342.
- [14] S. Borhani, M. Moradi, M.A. Kiani, S. Hajati, J. Toth, *Ceram. Int.* 43 (16) (2017) 14413–14425.
- [15] S.H. Kazemi, B. Hosseinzadeh, H. Kazemi, M.A. Kiani, S. Hajati, *ACS Appl. Mater. Interfaces* 10 (2018) 23063–23073.
- [16] S. Ghosh, G. Sahoo, S.R. Polaki, N.G. Krishna, M. Kamruddin, T. Mathew, *J. Appl. Phys.* 122 (2017) 214902.
- [17] J. Suarez-Guevara, V. Ruiz, P. Gomez-Romero, *J. Mater. Chem. A* 2 (2014) 1014–1021.
- [18] N.A. Kumar, H.-J. Choi, Y.R. Shin, D.W. Chang, L. Dai, J.-B. Baek, *ACS Nano* 6 (2) (2012) 1715–1723.
- [19] V.K. Gupta, M.R. Ganjali, P. Norouzi, H. Khani, A. Nayak, S. Agarwal, *Crit. Rev. Anal. Chem.* 41 (4) (2011) 282–313.
- [20] R.N. Goyal, V.K. Gupta, M. Oyama, N. Bachheti, *Talanta* 71 (2007) 1110–1117.
- [21] R.N. Goyal, V.K. Gupta, A. Sangal, N. Bachheti, *Electroanal* 17 (2005) (2005) 2217–2223.
- [22] R.N. Goyal, V.K. Gupta, S. Chatterjee, *Biosensors* 24 (2009) 1649–1654.
- [23] A. Asfaram, M. Ghaedi, S. Agarwal, I. Tyagi, V.K. Gupta, *RSC Adv.* 5 (2015) 18438–18450.
- [24] H.-C. Youn, S.-M. Bak, M.-S. Kim, C. Jaye, D.A. Fischer, C.-W. Lee, X.-Q. Yang, K.C. Roh, K.-B. Kim, *Chem. Sus. Chem.* 8 (2015) 1875–1884.
- [25] B. Kim, H. Chung, W. Kim, *Nanotechnology* 23 (2012) 155401.
- [26] D.P. Dubal, N.R. Chodankar, G.S. Gund, R. Holze, C.D. Lokhande, P.G. Romero, *Energy Technol.* 3 (2015) 168–176.
- [27] S. Tursynbolat, Y. Bakytkarim, J. Huang, L. Wang, *J. Pharm. Anal.* 9 (2019) 358–366.
- [28] V.K. Gupta, L.P. Singh, Rakesh Singh, N. Upadhyay, S.P. Kaur, Bhavana Sethi, *J. Mol. Liq.* 174 (2012) 11–16.
- [29] V.K. Gupta, S. Kumar, R. Singh, L.P. Singh, S.K. Shoor, B. Sethi, *J. Mol. Liq.* 195 (2014) 65–68.
- [30] V.K. Gupta, B. Sethi, R.A. Sharma, Shilpi Agarwal, Arvind Bharti, *J. Mol. Liq.* 177 (2013) 114–118.
- [31] A. Divyashree, G. Hegde, *RSC Adv.* 5 (2015) 88339.
- [32] T. Purkait, G. Singh, D. Kumar, M. Singh, R. Sundar, *Sci. Rep.* 8 (2018) 640.
- [33] M.L. Yola, V.K. Gupta, T. Eren, A.E. Sen, N. Atar, *Electrochim. Acta.* 120 (2014) 204–211.
- [34] D. Li, M.B. Muller, S. Gilje, R.B. Kaner, G.G. Wallace, *Net. Nanotechnol.* 3 (2008) 101–105.
- [35] V.K. Gupta, R.N. Goyal, R.A. Sharma, *Anal. Chim. Acta.* 647 (2009) 66–71.
- [36] R.N. Goyal, V.K. Gupta, S. Chatterjee, *Biosens Bioelectron.* 24 (2009) 3562–3568.
- [37] Y. Zhou, L. Guo, W. Shi, X. Zou, B. Xiang, S.X. ing, *Materials (Basel)* 6 (2018) 881.
- [38] C. Phrompet, C. Sriwong, C. Ruttanapun, *Comp. Part. B.* 175 (2019) 107128.
- [39] G. Guoqing, L. Jiaqi, Y.-S. Yu, S. David A, K. David AL, M. Paulo JM, *Cryst. Growth. Des.* 17 (2017) 4246–4253.
- [40] C. Phrompet, C. Sriwong, M. Santi, P. Chindaprasirt, C. Ruttanapun, *Constr. Build. Mater.* 179 (2018) 57–65.
- [41] R. Farma, M. Deraman, I.A.Talib Awitdrus, R. Omar, J.G. Manjunatha, M.M. Ishak, N.H. Basri, B.N.M. Dolah, *Int. J. Electrochem. Sci.* 8 (2013) 257–273.
- [42] V.K. Gupta, A.K. Singh, L.K. Kumawat, *Sens. Actuator B-Chem.* (2014) 19598–108.
- [43] V.K. Gupta, N. Mergu, L.K. Kumawat, A.K. Singh, *Talanta* 144 (2015) 80–89.
- [44] V.K. Gupta, N. Mergu, L.K. Kumawat, A.K. Singh, *Sens. Actuator B-Chem.* 207 (2015) 216–223.
- [45] C. Phrompet, C. Sriwong, P. Srepusharwoot, S. Maensiri, P. Chindaprasirt, C. Ruttanapun, *Heliyon* 5 (5) (2019) e01808.
- [46] A. Hidalgo, J.L. Garcia, M.C. Alonso, L. Fernandez, C. Andrade, J. Therm. Anal. Calorim. 96 (2) (2009) 335–345.
- [47] S. Ahmadsreza, M.K. Ram, A. Zayed, K. Rajeev, S. Natallia, *J. Compos. Mater.* 4 (2014) 12–21.
- [48] B.D. Cullity, Stock S.R., *Elements of X-ray Diffraction*, 3rd edn., Prentice Hall, New Jersey, 2001.
- [49] W. Zhang, Y. Li, S. Peng, X. Cai, *Beilstein. J. Nanotechnol.* 5 (2014) 801–811.
- [50] B. Paulchamy, *J. Nanomed, Nanotechnology* 6 (2015) 1–4.
- [51] C. Gu, H. Zhang, X. Wang, J. Tu, *RSC Adv.* 3 (2013) 11807.
- [52] S. Stankovich, D.A. Dikin, R.D. Piner, K.A. Kohlhaas, A. Kleinhammes, Y. Jia, Y. Wu, S.T. Nguyen, R.S. Ruoff, *Carbon N. Y.* 45 (2007) 1558–1565.
- [53] L. Fernandez-Carrasco, F. Puertas, M.T. Blanco-Varela, T. Vazquez, *Mater. Constr.* 51 (2001) 127–136.
- [54] D. Rong, F. Qiu, C. Zhang, L. Fu, Y. Wang, D. Yang, *Ceram. Int.* 41 (2015) 2502.
- [55] M.H. Dehghani, D. Sanaei, I. Ali, A. Bhatnagar, *J. Mol. Liq.* 215 (2016) 671–679.
- [56] A. Karaphun, S. Maensiri, E. Swatsitang, *J. Mater. Sci. Mater. Electron.* 30 (2019) 3019.
- [57] C. Ruttanapun, P. Srepusharwoot, S. Maensiri, *Chin. J. Phys.* 56 (1) (2018) 252–260.
- [58] Y. Wang, H. Guan, C. Dong, X. Xiao, S. Du, Y. Wang, *Ceram. Int.* 42 (2016) 936–942.
- [59] K. Meeporn, S. Maensiri, P. Thongbai, *Appl. Surf. Sci.* 380 (2016) 67–72.
- [60] W. Tuichai, S. Danwittayakul, P. Thongbai, *Ceram. Int.* 44 (2018) S133–S136.
- [61] K. Yang, X. Huang, J. He, P. Jiang, *Adv. Mater. Interfaces* 2 (2015) 1500361.
- [62] J. Ma, J. Shu, W. Cao, M. Zhang, X. Wang, J. Yuan, M. Cao, *Comp. Part. B.* 166 (2019) 187–195.
- [63] W. Hu, Y. Liu, R.L. Withers, T.J. Frankcombe, L. Norén, A. Snashal, M. Kitchin, P. Smith, B. Gong, H. Chen, J. Schiemer, F. Brink, J. Wong-Leung, *Nat. Mater.* 12 (2012) 821–826.
- [64] S. Vangchangyia, E. Swatsitang, P. Thongbai, S. Pinitsoontorn, T. Yamwong, S. Maensiri, V. Amornkitbamrung, P. Chindaprasirt, *J. Am. Ceram. Soc.* 52 (2012) 1–4.
- [65] L. Lu, Y. Xie, *New. J.Chem.* 41 (2017) 335.
- [66] D. Kumar, A. Banerjee, S. Patil, A.K. Shukla, *Bull. Mater. Sci.* 38 (6) (2015) 1507–1517.
- [67] A.A. Mirghni, M.J. Madito, K.O. Oyedotun, T.M. Masikhwa, N.M. Ndiaye, S.J. Ray, N. Manyala, *RSC Adv.* 8 (2018) 11608.
- [68] H. Karimi-Maleh, F. Tahernejad-Javazmi, N. Atar, M.L. Yola, V.K. Gupta, A.A. Ensaifi, *Ind. Eng. Chem. Res.* 54 (2015) 3634–3639.
- [69] V.K. Gupta, H. Karimi-Maleh, R. Sadegh, *Int. J. Electrochem. Sci.* 10 (2015) 303–316.
- [70] Z. Ma, X. Zhou, W. Deng, D. Lei, Z. Liu, *ACS Appl. Mater. Interfaces* 10 (2018) 3634–3643.
- [71] W. Liu, *J. Mater. Chem. A* 4 (2016) 3754–3764.
- [72] M. Beidaghi, C. Wang, *Adv. Funct. Mater.* 22 (2012) 4501–4510.
- [73] X.-J. Ma, W.-B. Zhang, L.-B. Kong, Y.-C. Luo, L. Kang, *RSC Adv.* 6 (2016) 40077–40085.
- [74] D.P. Dubal, N.R. Chodankar, G.S. Gund, R. Holze, C.D. Lokhande, P. Gomez-Romero, *Energy Technol.* 3 (2015) 168–176.

เอกสารนี้เป็นเอกสารที่สงวนไว้สำหรับการใช้งานเพื่อการศึกษาเท่านั้น ไม่อนุญาตให้นำไปใช้ประโยชน์ด้านการค้า
ไม่ว่ากรณีใดๆ ทั้งสิ้น อีกทั้งห้ามมิให้ตัดแปลงเนื้อหา และต้องอ้างอิงถึงเจ้าของเอกสารทุกครั้งที่มีการนำไปใช้

Author biography

Name	Acting Sub Lt. Chaiwat Phrompet
Date of Birth	08 January 1985
Address	441/1 Moo.9, Falami Thuan, Pak-Phayun district, Phatthalung, 93120
Education	(2008) Bachelor of Science in Applied Physics-Energy GPA 2.66 (Thaksin University) (2013) Master of Engineering in Mechanical Engineering GPA 3.08 (Prince of Songkla University)
Scholarship	Thailand Research Fund (TRF) (Contract Number: PHD60I0046)
Research Experienced and Interesting	1) Thermoelectric Materials and Renewable energy 2) Smart cement-based materials, Cement nanocomposite materials. 3) Graphene Oxide (GO), Reduced Graphene oxide (rGO), Nano-Sheets and Its Applications
Job history	1) 2015-2016: Special Lecturer, Positions Place Program in Physics and General Science, Faculty of Science and Technology, Nakhon Ratchasima Rajabhat University. 2) 2008-2009: Research Assistant, Position at Alternative Energy Research Center, Department of Physics, Faculty of Science, Thaksin University.

เอกสารนี้เป็นเอกสารที่สงวนไว้สำหรับการใช้งานเพื่อการศึกษาเท่านั้น ไม่อนุญาตให้นำไปใช้ประโยชน์ด้านการค้า ไม่ว่าจะกรณีใดๆ ทั้งสิ้น อีกทั้งห้ามมิให้ดัดแปลงเนื้อหา และต้องอ้างอิงถึงเจ้าของเอกสารทุกครั้งที่มีการนำไปใช้

Academic Publications

- 1) Chaiwat Phrompet, Chaval Sriwong, Santi Maensiri, Prinya Chindaprasirt, Chesta Ruttanapun, “Optical and dielectric properties of nano-sized tricalcium aluminate hexahydrate (C₃AH₆) cement”, *Construction and Building Materials*, 179 (2018) 57–65. (ISI, IF: 4.046) (Scimago Q1) (Web of Science Q1)
- 2) Chaiwat Phrompet, Chaval Sriwong, Chesta Ruttanapun, “Mechanical, dielectric, thermal and antibacterial properties of reduced graphene oxide (rGO)-nanosized C₃AH₆ cement nanocomposites for smart cement-based materials”, *Composites Part B: Engineering*, 175 (2019) 107128 (ISI, IF: 6.864) (Scimago Q1) (Web of Science Q1)
- 3) Chaiwat Phrompet, Chaval Sriwong, Pornjuk Srepusharawoot, Santi Maensiri, Prinya Chindaprasirt, Chesta Ruttanapun, “Effect of free oxygen radical anions and free electrons in a Ca₁₂Al₁₄O₃₃ cement structure on its optical, electronic and antibacterial properties”, *Heliyon*, 5 (2019) e01808. (ISI) (Scimago Q1)
- 4) Wannisa Thongsamrit, Chaiwat Phrompet, Keerati Maneesai, Attaphol Karaphun, Wattan Tuichai, Chaval Sriwong and Chesta Ruttanapun, “Effect of grain boundary interfaces on electrochemical and thermoelectric properties of a Bi₂Te₃/reduced graphene oxide composites”, *Materials Chemistry and Physics* Volume 250, 1 August 2020, 123196. (ISI, IF: 2.781) (Scimago Q2)
- 5) Chaiwat Phrompet, Keerati Maneesai, Wattan Tuichai, Attaphol Karaphun, Chaval Sriwong and Chesta Ruttanapun, “Electrochemical properties of tricalcium aluminate hexahydrate–reduced graphene oxide nanocomposites for supercapacitor device”, *Journal of Energy Storage* Volume 30, August 2020, 101474. (ISI, IF: 3.517) (Scimago Q1)

เอกสารนี้เป็นเอกสารที่สงวนไว้สำหรับการใช้งานเพื่อการศึกษาเท่านั้น ไม่อนุญาตให้นำไปใช้ประโยชน์ด้านการค้า ไม่ว่าจะกรณีใดๆ ทั้งสิ้น อีกทั้งห้ามมิให้ตัดแปลงเนื้อหา และต้องอ้างอิงถึงเจ้าของเอกสารทุกครั้งที่มีการนำไปใช้